frontiers | Research Topics

Advances and applications of passive seismic source characterization

Edited by
Lei Li, Francesco Grigoli, Kit Chambers, Frantisek Stanek and Nori Nakata

Published in
Frontiers in Earth Science

ISSN 1664-8714
ISBN 978-2-8325-3557-8
DOI 10.3389/978-2-8325-3557-8

About Frontiers

Frontiers is more than just an open access publisher of scholarly articles: it is a pioneering approach to the world of academia, radically improving the way scholarly research is managed. The grand vision of Frontiers is a world where all people have an equal opportunity to seek, share and generate knowledge. Frontiers provides immediate and permanent online open access to all its publications, but this alone is not enough to realize our grand goals.

Frontiers journal series

The Frontiers journal series is a multi-tier and interdisciplinary set of open-access, online journals, promising a paradigm shift from the current review, selection and dissemination processes in academic publishing. All Frontiers journals are driven by researchers for researchers; therefore, they constitute a service to the scholarly community. At the same time, the *Frontiers journal series* operates on a revolutionary invention, the tiered publishing system, initially addressing specific communities of scholars, and gradually climbing up to broader public understanding, thus serving the interests of the lay society, too.

Dedication to quality

Each Frontiers article is a landmark of the highest quality, thanks to genuinely collaborative interactions between authors and review editors, who include some of the world's best academicians. Research must be certified by peers before entering a stream of knowledge that may eventually reach the public - and shape society; therefore, Frontiers only applies the most rigorous and unbiased reviews. Frontiers revolutionizes research publishing by freely delivering the most outstanding research, evaluated with no bias from both the academic and social point of view. By applying the most advanced information technologies, Frontiers is catapulting scholarly publishing into a new generation.

What are Frontiers Research Topics?

Frontiers Research Topics are very popular trademarks of the *Frontiers journals series*: they are collections of at least ten articles, all centered on a particular subject. With their unique mix of varied contributions from Original Research to Review Articles, Frontiers Research Topics unify the most influential researchers, the latest key findings and historical advances in a hot research area.

Find out more on how to host your own Frontiers Research Topic or contribute to one as an author by contacting the Frontiers editorial office: frontiersin.org/about/contact

Advances and applications of passive seismic source characterization

Topic editors

Lei Li — Central South University, China
Francesco Grigoli — University of Pisa, Italy
Kit Chambers — Motion Signal Technologies Limited, United Kingdom
Frantisek Stanek — Czech Academy of Sciences, Czechia
Nori Nakata — Massachusetts Institute of Technology, United States

Citation

Li, L., Grigoli, F., Chambers, K., Stanek, F., Nakata, N., eds. (2023). *Advances and applications of passive seismic source characterization*.
Lausanne: Frontiers Media SA. doi: 10.3389/978-2-8325-3557-8

Table of contents

frontiers | Frontiers in Earth Science

TYPE Editorial
PUBLISHED 11 September 2023
DOI 10.3389/feart.2023.1284106

OPEN ACCESS

EDITED AND REVIEWED BY
Jeroen Van Hunen,
Durham University, United Kingdom

*CORRESPONDENCE
Lei Li,
leileely@126.com

†PRESENT ADDRESS
František Staněk,
Silixa Ltd., Elstree, United Kingdom

RECEIVED 27 August 2023
ACCEPTED 04 September 2023
PUBLISHED 11 September 2023

CITATION
Li L and Staněk F (2023), Editorial: Advances and applications of passive seismic source characterization. *Front. Earth Sci.* 11:1284106. doi: 10.3389/feart.2023.1284106

Editorial: Advances and applications of passive seismic source characterization

Lei Li[1,2,3]* and František Staněk[4†]

[1]Key Laboratory of Metallogenic Prediction of Nonferrous Metals and Geological Environment Monitoring (Central South University), Ministry of Education, Changsha, China, [2]Hunan Key Laboratory of Nonferrous Resources and Geological Hazard Exploration, Changsha, China, [3]School of Geosciences and Info-Physics, Central South University, Changsha, China, [4]Colorado School of Mines, Golden, CO, United States

KEYWORDS

passive seismic, source characterization, microseismic monitoring, induced seismicity, seismic imaging

Editorial on the Research Topic
Advances and applications of passive seismic source characterization

Introduction

Source characterization is a fundamental task of passive seismic monitoring. Spatial-temporal evolution of both, point sources and finite-fault source, provides essential information for timely seismic hazard assessment and advanced analysis of the seismicity in the monitored areas. During the past few decades, the rise of dense seismic arrays and development of advanced array-based techniques lead to studies using recorded wavefields in great detail. Moreover, emerging technologies like distributed acoustic sensing (DAS) and machine learning also show great potential in advancing passive seismic imaging and source characterization. Besides, non-earthquake sources and ambient noise are also contributing to infrastructure monitoring and subsurface imaging, due to the utilization of sensitive sensors and modern techniques like seismic interferometry.

An improved characterization of passive seismic sources is beneficial to a better understanding of physical source properties, including both industry-related microseismicity and tectonic-related earthquakes. Microseismic monitoring is an important means to characterize small-scale fractures and reservoirs. Besides, microseismic events are crucial for mapping fault geometry, stress changes, fluid migration, and identifying seismogenic mechanisms. Passive seismic sources also play an important role in characterizing velocity structures by tomographic techniques. However, there are still many new challenges and opportunities in this field. For example, the full potential of dense arrays requires further exploration, the influence of different factors on source characterization at

different scales has not been thoroughly studied, and the applicability and performance of machine learning algorithms in seismic source inversion and imaging require more investigations.

Progress in the Research Topic

The introduced Research Topic was organized to collect theoretical and methodological progress related to passive seismic source characterization associated with different scenarios, and promote development and application of advanced seismic source imaging and inversion at different scales. There are 11 papers from 59 authors in the Research Topic. We summarize the contributions as three aspects and provide comments on the related prospects.

Microseismic data processing and inversion

To better understand the impacts of model parameters on microseismic location, Zheng et al. analyze the sensitivities for anisotropic parameters and event locations in a vertical transversely isotropic (VTI) media. Yu et al. introduce a novel probabilistic method of P-wave polarization analysis for receiver orientation and event back-azimuth estimation in downhole microseismic monitoring. The method can improve the accuracy of the receiver orientation angles and event back-azimuths. Anikiev et al. propose to use a feed-forward artificial neural network (ANN) for microseismic source location by training it on synthetic travertine data. The method is suitable for monitoring areas with no previously observed microseismicity. Real data examples demonstrate the method is efficient and exhibits a high location accuracy. Adinolfi et al. design a software platform, TREMOR, for efficient and reliable characterization of microseismicity. The platform integrates several open-source seismological algorithms and has great potential for natural or induced microseismicity monitoring.

Advanced and comprehensive techniques are urgently needed to tackle the challenges of a large data volume, low signal-to-noise ratio, and high frequency components associated with microseismic data. Machine learning algorithms can help achieve more efficient and reliable microseismic event detection and source characterization. More integrated workflows will be proposed to promote microseismic processing and interpretation.

Natural earthquake studies

Zhou et al. investigate velocity changes associated with the 2021 M_S 6.4 Yangbi earthquake by passive seismic interferometry, which is based on cross-correlation and autocorrelation of continuous ambient noise waveforms. They interpret the velocity changes as a combined effect of near-surface physical damage and static stress changes. Sun et al. perform a three-dimensional (3D) P-wave velocity structure analysis and seismic relocation using double-difference tomography based on over 13,000 earthquakes in the Yunnan area, China. The tomography results indicate that the Yangbi earthquake might have been related to the intrusion of the soft material flow. Song et al. evaluate the effects of 3D velocity heterogeneity on source mechanism inversion, and present an improved moment tensor catalog based on 3D full-waveform simulations in the southern Korean Peninsula (KP). They conclude that improved source mechanisms could benefit a reliable assessment of seismic hazards in regions with complex structures and sedimentary basins. Luo et al. adopt the natural orthogonal method to calculate the strain fields of 3 Ms > 6 earthquakes in Menyuan, Qinghai, China. They reveal that the method could help obtain the spatiotemporal anomalies of strain field preceding strong earthquakes, when combined with numerical simulations.

Natural earthquakes are important data sources for subsurface velocity imaging, and strong earthquakes are disasters that can directly endanger human safety. Along with dense monitoring networks and comprehensive geological knowledge, seismic imaging and inversion can help us reveal velocity anomalies in detail and better understand seismogenic mechanisms. More reliable seismic processing is needed to achieve more reasonable interpretation, timely hazard evaluation, and effective earthquake prediction.

Advanced techniques associated with passive seismic sources

Hu et al. propose the Waveform Energy Focusing Tomography (WEFT) method for passive seismic tomography. The method updates the velocity model by maximizing the stacking energy of the moment time functions and can provide an intermediate and more accurate velocity model for subsequent inversion. Anyiam et al. apply Vp/Vs consistency-constrained double-difference seismic tomography to determine high-resolution velocity models and constructed a structural framework for induced seismicity in the southern Sichuan Basin, China. The 3D crustal velocity analyses show that seismicity beneath the Changing salt mining area and the Xingwen shale gas block are caused by unique inducing mechanisms. Lecoulant et al. attempt to invert seismic moment tensors of induced microearthquakes recorded by distributed acoustic sensing (DAS) observations. They develop the strain-based forward modeling and prove the reliability of the method with both synthetic and field data.

Advanced techniques have been successfully utilized for source and structure characterization varying from induced microearthquakes to natural regional earthquakes. Novel algorithms and methodologies are still needed to handle new data acquisitions, such as DAS and highly dense networks in more complex environments.

Author contributions

LL: Conceptualization, Funding acquisition, Project administration, Writing–original draft. FS: Conceptualization, Investigation, Writing–review and editing.

Funding

This study was supported by the Natural Science Foundation for Excellent Young Scholars of Hunan Province, China (2022JJ20057) and Central South University Innovation-Driven Research Programme (2023CXQD063).

Acknowledgments

We thank the various authors for submitting their work to this Research Topic and the reviewers who helped to review individual contributions.

Conflict of interest

The authors declare that the research was conducted in the absence of any commercial or financial relationships that could be construed as a potential conflict of interest.

Publisher's note

frontiers | Frontiers in Earth Science

METHODS
published: 13 June 2022
doi: 10.3389/feart.2022.900435

Waveform Energy Focusing Tomography With Passive Seismic Sources

Yueqiao Hu[1], *Junlun Li*[1,2]* *and Haijiang Zhang*[1,2]

[1]*Laboratory of Seismology and Physics of Earth's Interior, School of Earth and Space Sciences, University of Science and Technology of China, Hefei, China,* [2]*Mengcheng National Geophysical Observatory, University of Science and Technology of China, Hefei, China*

By taking advantage of the information carried by the entire seismic wavefield, Full Waveform Inversion (FWI) is able to yield higher resolution subsurface velocity models than seismic traveltime tomography. However, FWI heavily relies on the knowledge of source information and good initial models, and could be easily trapped into local minima caused by cycle skipping issue because of its high nonlinearity. To mitigate these issues in FWI, we propose a novel method called Waveform Energy Focusing Tomography (WEFT) for passive seismic sources. Unlike conventional FWI, WEFT back-propagates the seismic records directly instead of the data residuals, and updates the velocity models by maximizing the stacking energy for all the moment tensor components from back-propagated wavefields around the sources. Therefore, except for source locations and origin times, WEFT does not require other source attributes in advance for the inversion. Since WEFT does not aim at fitting synthetic and observed waveforms, it has lower nonlinearity and is less prone to the cycle skipping issue compared to FWI. For the proof of concept, we have validated WEFT using several 2D synthetic tests to show it is less affected by inaccurate source locations and data noise. These advantages render WEFT more applicable for tomography using passive seismic sources when the source information is generally not accurately known. Although the inverted model from WEFT is inevitably influenced by the source distribution as well as its radiation patterns, and its resolution is likely lower than that of FWI, it can act as an intermediate step between traveltime tomography and FWI by providing a more reliable and accurate velocity model for the latter.

Keywords: waveform tomography, passive seismic sources, energy focusing, seismic moment tensor, time-reversal method

OPEN ACCESS

Edited by:
Tariq Alkhalifah, King Abdullah University of Science and Technology, Saudi Arabia

Reviewed by:
Hanchen Wang, Los Alamos National Laboratory (DOE), United States
Denis Anikiev, GFZ German Research Centre for Geosciences, Germany

***Correspondence:**
Junlun Li
lijunlun@ustc.edu.cn

Specialty section:
This article was submitted to Solid Earth Geophysics, a section of the journal Frontiers in Earth Science

Received: *20 March 2022*
Accepted: *09 May 2022*
Published: *13 June 2022*

Citation:
Hu Y, Li J and Zhang H (2022) Waveform Energy Focusing Tomography With Passive Seismic Sources. Front. Earth Sci. 10:900435. doi: 10.3389/feart.2022.900435

INTRODUCTION

Seismic tomography is an essential approach for imaging the subsurface structure. The well-established seismic traveltime tomographic methods based on ray theory have had many successful applications in imaging structures at different scales in the past few decades (e.g., Bording et al., 1987; Lanz et al., 1998; Rawlinson and Sambridge, 2003; Zhang and Thurber, 2003). More recently, Full Waveform Inversion (FWI) has also been developed and applied at many different scales (Ravaut et al., 2004; Bleibinhaus et al., 2007; Fichtner et al., 2013; Adamczyk et al., 2015; Bozdağ et al., 2016), as it can potentially obtain models with higher resolution by using more information carried in the waveforms (Virieux and Operto, 2009; Alkhalifah, 2014).

Traditional FWI inverts for subsurface velocities by minimizing the L2-norm misfit between the observed and simulated seismic waveforms (Tarantola, 1984; Pratt and Worthington, 1990). In spite of some successful applications on both active and passive seismic data (Brenders and Pratt, 2007; Fichtner et al., 2009, 2013; Tape et al., 2009, 2010; Warner et al., 2013; Operto et al., 2015), there are still practical issues and challenges yet to be solved in FWI. One of the critical issues is that FWI tends to fall into local minima when the time delay between the synthetic and observed waveforms is larger than half a cycle due to inaccurate starting velocity models, which is referred to as the cycle skipping (Virieux and Operto, 2009). Many efforts have been devoted to solving this problem from different aspects. For example, the multiscale strategy (Bunks et al., 1995; Sirgue and Pratt, 2004), which sequentially performs inversion from lower to higher frequencies, can efficiently avoid cycle skipping since waveforms at lower frequencies have broader cycles. Shin and Cha (2008), Shin and Cha (2009) extended the time-domain FWI to the Laplace-domain and Laplace-Fourier domain to build long-wavelength velocity models and increase the stability of the inversion. Choi and Alkhalifah (2015) developed the unwrapped phase inversion combined with exponential damping, which can avoid cycle-based jumps even when low-frequency information is missing.

Since the objective function based on the L2-norm often has stronger nonconvexity, a variety of misfit functionals have been proposed to measure the discrepancies between the observed and synthetic waveforms. The cross-correlation based objective functions (e.g., Luo and Schuster, 1991; van Leeuwen and Mulder, 2010) were proposed to measure the similarity between the observed and synthetic data, which are more dependent on the waveform kinematics and thus mitigate issues related to amplitudes. Although these objective functions are less susceptible to cycle skipping, a band-limited or non-impulsive source function may still affect the measurement of waveform discrepancies. The deconvolution-based objective function (Luo and Sava 2011) is thus proposed to alleviate the issue. The misfit measured by the discrepancy in waveform envelopes can be used to retrieve the long-wavelength component of a velocity model, and thus reduce the dependence of FWI on the initial model (Bozdağ et al., 2011; Wu et al., 2014; Luo and Wu, 2015; Oh and Alkhalifah, 2018). In addition, the misfit functions based on the optimal transport provide an alternative in an attempt to overcome the cycle skipping issue (Engquist and Froese, 2013; Métivier et al., 2016; Yang and Engquist, 2018). Recently, the new methods related to non-physical model extensions, such as reconstructed wavefields (van Leeuwen and Herrmann, 2013; Wang et al., 2016; Alkhalifah and Song, 2019), time lag extension (Yang and Sava, 2013; Biondi and Almomin, 2014), and matching filter (Luo and Sava, 2011; Warner and Guasch, 2016; Huang et al., 2017; Sun and Alkhalifah, 2019; Li and Alkhalifah, 2021) are also attractive for their stronger resistance to cycle skipping.

The source information is essential for FWI when calculating the synthetic waveforms, which is oftentimes inaccurate or even unknown. For an active seismic survey, though the source wavelet (or source time function) can be extracted directly from the near-offset traces (Schuster, 2017), the extraction is often successful only for data with high signal-to-noise ratios (SNRs). Owing to the linear relationship between the source attributes and the seismic data, the source wavelet can be obtained by solving a linear equation by assuming a relatively accurate velocity model is available (Pratt, 1999). Additionally, several strategies were also proposed to remove the influence of source wavelet based on convolution (Choi et al., 2005; Cheong et al., 2006; Choi and Alkhalifah, 2011; Wang and Alkhalifah, 2018; Wang et al., 2020) or deconvolution (Lee and Kim, 2003; Xu et al., 2006) of reference traces in both time and frequency domains. However, it may not be a trivial task to choose a reference trace for real-data applications.

In addition to the source time function, for passive seismic sources, the source moment tensor is also needed for FWI. Using the information from first motion polarities (e.g., Rau et al., 1996; Hardebeck and Shearer 2002), and/or the S/P amplitude ratios (Julian et al., 1998; Hardebeck and Shearer, 2003), to full waveforms (Li et al., 2011; Zhu and Ben-Zion, 2013; Willacy et al., 2019), source moment tensors can be characterized with increasing reliability. However, the inversion process inevitably becomes more computationally expensive and more complicated, and it generally requires a more accurate velocity model (Kim et al., 2011; Eyre and van der Baan, 2015). When the surface seismic acquisition array is dense, Time Reversal (TR) methods (Larmat et al., 2006; Kawakatsu and Montagner, 2008; Artman et al., 2010; Gharti et al., 2011; Chambers et al., 2014; Nakata and Beroza, 2016; Sun et al., 2016) based on seismic migration can be used to image the source attributes directly by back-propagating the observed data. For instance, for the microseismic datasets which have relatively lower SNR, not only phase picking is avoided, but also the influence of noise can be mitigated by stacking the back-propagated wavefields from many individual receivers with the TR methods (Gharti et al., 2011). However, the source attributes may not be well reconstructed if the observation array cannot record a sufficient amount of wavefield information from the source (Bazargani and Snieder, 2016). Furthermore, methods based on the machine learning, which demand less processing effort and computational costs, have become more appealing for obtaining the information of passive seismic sources (Kriegerowski et al., 2019; van den Ende and Ampuero, 2020; Wang and Alkhalifah, 2021; Smith et al., 2022). The seismic moment tensor can be determined according to the first-motion polarities picked by deep learning (Ross et al., 2018; Hara et al., 2019; Uchide, 2020). Kuang et al. (2021) proposed the Focal Mechanism Network (FMNet) to determine the seismic moment tensor directly from seismic waveforms. Based on the Bayesian Neural Networks (BNNs), Steinberg et al. (2021) estimated the moment tensor of earthquakes as well as parameter uncertainties. Although the machine-learning based methods can efficiently estimate source mechanisms, those methods are still limited by predefined Earth models and station distributions used for training the neural networks.

In order to overcome the aforementioned problems, many methods have been developed to invert for the velocity models with passive seismic sources. Using the variable projection

method, Sun et al. (2016) developed a framework of joint full-waveform inversion to obtain velocity models and passive seismic source locations simultaneously. Song et al. (2019a) proposed an objective function to invert for velocities and estimate source locations together by penalizing source energy away from the source location. Based on the geometric-mean imaging condition (Nakata and Beroza, 2016), Lyu and Nakata (2020) performed passive-source location and velocity inversion using FWI iteratively. However, these methods failed to consider the influence of the source radiation pattern, and corresponding FWI schemes still have high nonlinearity. By focusing different modes (PP, SS and PS) of the source images, a variety of methods for determining source locations as well as velocity models (Vp, Vs.) (Witten and Shragge, 2017; Rocha et al., 2019; Oren and Shragge, 2021; Oren and Shragge, 2022) have been developed using different imaging conditions. Since modeling elastic wavefields (both P- and S wave) is necessary for these methods, the computational cost is rather demanding, especially for 3D cases. Inspired by the TR principle, Lellouch and Landa (2018) used a minimum variation criterion to evaluate the coherency among focused sources and estimated the velocity model. Nevertheless, the influence of the source radiation pattern from different source mechanisms was still ignored, and trace normalization was used instead to mitigate the source effect.

For seismic exploration data using active seismic sources, to mitigate the aforementioned challenges in FWI, Zhang and Wang (2009) proposed a new method implemented in the tau-p domain by maximizing the stacking energy of the back-propagated wavefield at the source locations. Jin and Plessix (2013) further modified this method and used a volume centered at the source position instead of a single grid point for energy stacking in the data domain. Though the dependence on waveform fitting and the initial model is largely relaxed with the energy stacking approach, their methods were designed for active sources and are not directly applicable for earthquake sources with distinct source radiation patterns, which emanate waves with varying amplitudes and polarities in different directions.

In this study, we further extend the method of Jin and Plessix (2013) to passive sources. Since the locations of passive seismic sources and accompanying 1D layered structures (Kissling et al., 1995) or full 3D velocity models (Thurber, 1992) can be determined simultaneously using arrival times picked manually or automatically, we assume that the rough source locations are known a priori in this study while the uncertainties are also taken into consideration. The new method inverts for the velocity model by maximizing the spatiotemporally stacking energy for all the moment time functions from the back-propagated wavefields around the source location over a short time window and a limited volume, and the source attributes except for the rough source locations are therefore not required in advance. A multiscale strategy is also applied to stabilize the inversion. We will first present the newly proposed method and then validate the method with several numerical examples in two dimensions for simplicity.

WAVEFORM ENERGY FOCUSING TOMOGRAPHY FOR PASSIVE SEISMIC SOURCES

Based on the reversibility of wave propagation through simulation means, the time-reversal technique can refocus the back-propagated wavefields and maximize the stacking energy at the source location and origin time if the velocity model is correct (McMechan, 1982; Fink, 1997). Therefore, the amount of energy focused around the source can be used as the criterion for optimizing a velocity model when the source location is roughly known (Zhang and Wang, 2009; Jin and Plessix, 2013). For passive seismic sources, we measure the stacking energy for all the moment time functions from back-propagated wavefields. For simplicity, we first propose the method based on the 2D observation geometry in this study. The corresponding objective function in 2D is

$$\boldsymbol{E}(v) = -\frac{1}{2}\int_{\tilde{t}_0}^{t_{\max}} \left(\hat{M}_{xx}^{TR^2}(\boldsymbol{\xi},t) + \hat{M}_{xz}^{TR^2}(\boldsymbol{\xi},t) + \hat{M}_{zx}^{TR^2}(\boldsymbol{\xi},t) + \hat{M}_{zz}^{TR^2}(\boldsymbol{\xi},t) \right) dt \quad (1)$$

where $\hat{M}_{ij}^{TR}(\boldsymbol{\xi},t)$ denotes the moment tensor components estimated from the back-propagated wavefields at the source location $\boldsymbol{\xi}$, and $\hat{M}_{ij^2}^{TR}(\boldsymbol{\xi},t)$ denotes the stacking energy. The $\tilde{t}_0$ and t_{max} define the time duration for stacking. With a negative sign, the criterion is to minimize the negative of the stacking energy.

With the time-reversal imaging (TRI), $\hat{M}_{ij}^{TR}(\boldsymbol{\xi},t)$ can be estimated by (Kawakatsu and Montagner, 2008)

$$\hat{M}_{ij}^{TR}(\boldsymbol{\xi},t) = E_{ijn}(\boldsymbol{\xi},t;\mathbf{x}_r,0) * u_n(\mathbf{x}_r,-t) \quad (2)$$

where $u_n(\mathbf{x}_r,-t)$ is the nth component of time-reversed version of the observed displacement at the receiver location $\mathbf{x}_r$, the symbol $*$ denotes convolution, and E_{ijn} is the strain Green's tensor defined as

$$E_{ijn}(\boldsymbol{\xi},t;\mathbf{x}_r,0) = c_{ij}\left(\frac{\partial G_{in}(\boldsymbol{\xi},t;\mathbf{x}_r,0)}{\partial \xi_j} + \frac{\partial G_{jn}(\boldsymbol{\xi},t;\mathbf{x}_r,0)}{\partial \xi_i} \right) \quad (3)$$

in which $c_{ij} = 1/2$ for $i = j$ and $c_{ij} = 1$ otherwise. Thus, **Equation 2** can be rewritten as

$$\hat{M}_{ij}^{TR}(\boldsymbol{\xi},t) = \begin{cases} \dfrac{\partial G_{in}(\boldsymbol{\xi},t;\mathbf{x}_r,0)}{\partial \xi_i} * u_n(\mathbf{x}_r,-t), & i = j \\ \left(\dfrac{\partial G_{in}(\boldsymbol{\xi},t;\mathbf{x}_r,0)}{\partial \xi_j} + \dfrac{\partial G_{jn}(\boldsymbol{\xi},t;\mathbf{x}_r,0)}{\partial \xi_i} \right) * u_n(\mathbf{x}_r,-t), & i \neq j \end{cases} \quad (4)$$

Using the relationship with differentiation, the estimated moment tensor components can be derived by taking a partial derivative of back-propagated wavefield $u_i^b(x,t)$ with respect to the source coordinates ξ_j

$$\hat{M}_{ij}^{TR}(\boldsymbol{\xi},t) = \begin{cases} \dfrac{\partial u_i^b(\mathbf{x},t)}{\partial \xi_i}, & i = j \\ \dfrac{\partial u_i^b(\mathbf{x},t)}{\partial \xi_j} + \dfrac{\partial u_j^b(\mathbf{x},t)}{\partial \xi_i}, & i \neq j \end{cases} \quad (5)$$

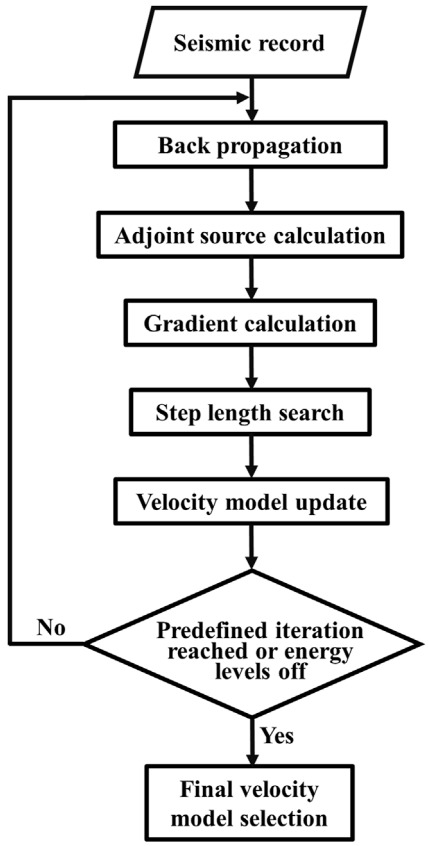

FIGURE 1 | The workflow of WEFT for passive source tomography.

Considering that many well-established seismic location methods, including the ray-based (Waldhauser and Ellsworth, 2000; Zhang and Thurber, 2003; Eisner et al., 2009), migration-based (McMechan, 1982; Artman et al., 2010; Sava, 2011; Nakata and Beroza, 2016; Song and Alkhalifah, 2019; Song et al., 2019b) and full-waveform-based (Kaderli et al., 2015; Wang and Alkhalifah, 2018; Willacy et al., 2019) methods, have been widely employed, we assume that the source locations are provided *a priori* and the influence of location error will be discussed later. To mitigate the effect of the source location error, a spatialtemporal weighting function $w(\mathbf{x},t)$ is defined for calculating the stacking energy around the source location. Thus, the objective function in **Equation 1** can be rewritten as

$$\boldsymbol{E}(v) = -\frac{1}{2}\int_{\tilde{t}_0}^{t_{\max}} \int_{x} w(\mathbf{x},t)\left(\left(\frac{\partial u_x^b}{\partial x}\right)^2 + 2\left(\frac{\partial u_x^b}{\partial z}+\frac{\partial u_z^b}{\partial x}\right)^2 + \left(\frac{\partial u_z^b}{\partial z}\right)^2\right)dtd\mathbf{x} \quad (6)$$

where $\mathbf{x}$ represents spatial coordinates $[x,z]$ in the 2D domain. The spatiotemporal weighting function $w(\mathbf{x},t)$, which defines a small spatiotemporal cube centered at the source, is given as

$$w(\mathbf{x},t) = \prod_{\gamma\,=\,x,z,t} f\left(\frac{\gamma-\gamma_s}{l_\gamma}\right)T\left(\frac{\gamma-\gamma_s}{l_\gamma}\right) \quad (7)$$

where $\gamma_s \in \{\xi_x, \xi_z, \tilde{t}_0\}$ is the spatiotemporal coordinate of the source, $f\left(\frac{\gamma-\gamma_s}{l_\gamma}\right)$ is a boxcar function whose value is one for $\left|\frac{\gamma-\gamma_s}{l_\gamma}\right| \le 1$ and zero otherwise, and l_γ defines a small aperture centered at each source coordinate γ_s. $T\left(\frac{\gamma-\gamma_s}{l_\gamma}\right)$ can be a Gaussian taper, a cosine taper, or other types of tapers that make the weighting function smoother. While the temporal aperture (i.e., duration) is determined by the frequency range of the used data, the spatial aperture could be a small value if the initial velocity model and the pre-determined source location are relatively accurate. Otherwise, a larger spatial aperture should be used when the initial velocity model or the pre-determined source location is not accurate.

To update the velocity model, we need to calculate the derivative of $\boldsymbol{E}(v)$ with respect to the velocity $v(\mathbf{X})$ and the adjoint-state method is used (Plessix, 2006). Using the 2D acoustic wave equation, the back-propagation of the wavefield can be expressed as

$$\begin{cases} \dfrac{\partial v_x^b}{\partial t} + \dfrac{1}{\rho}\dfrac{\partial p^b}{\partial x} = f_x \\ \dfrac{\partial v_z^b}{\partial t} + \dfrac{1}{\rho}\dfrac{\partial p^b}{\partial z} = f_z \\ \dfrac{\partial p^b}{\partial t} + \rho v^2\left(\dfrac{\partial v_x^b}{\partial x} + \dfrac{\partial v_z^b}{\partial z}\right) = 0 \end{cases} \quad (8)$$

where v_x^b and v_z^b are particle velocities and p^b is the pressure. The source f_i is the time-reversed version of observed seismic data d_i $(i \in [x,z])$:

$$f_i(\mathbf{x},t) = \sum_{r=1}^{nr} \delta(\mathbf{x}-\mathbf{x}_r)d_i(\mathbf{x}_r, t_{max}-t) \quad (9)$$

According to the Lagrange multiplier method (Hestenes, 1969), we define a new function

$$\boldsymbol{S}(v) = \boldsymbol{E}(v) + \int_{\tilde{t}_0}^{t_{max}} \int_{\chi} \boldsymbol{\lambda}(\mathbf{x},t)\boldsymbol{F}(v)d\mathbf{x}dt \quad (10)$$

where $\lambda(\mathbf{x},t) = (\lambda_x,\ \lambda_z,\ \lambda_p)^T$ denotes the adjoint-wavefield and **Equation 8** can be obtained by setting $F(v)=0$. Substituting **Equations 6**, **8** into **Equation 10**, we obtain

$$\begin{aligned} \boldsymbol{S}(v) = &-\frac{1}{2}\int_{\tilde{t}_0}^{t_{max}} \int_{\chi} w(\mathbf{x},t)\left(\left(\frac{\partial u_x^b}{\partial x}\right)^2 + 2\left(\frac{\partial u_x^b}{\partial z}+\frac{\partial u_z^b}{\partial x}\right)^2 + \left(\frac{\partial u_z^b}{\partial z}\right)^2\right)dtd\mathbf{x} + \\ &\int_{\tilde{t}_0}^{t_{max}} \int_{\chi} \lambda_x\left(\frac{\partial v_x^b}{\partial t} + \frac{1}{\rho}\frac{\partial p^b}{\partial x} - f_x\right)dtd\mathbf{x} + \int_{\tilde{t}_0}^{t_{max}} \int_{\chi} \lambda_z\left(\frac{\partial v_z^b}{\partial t} + \frac{1}{\rho}\frac{\partial p^b}{\partial z} - f_z\right)dtd\mathbf{x} + \\ &\int_{\tilde{t}_0}^{t_{max}} \int_{\chi} \lambda_p\left[\frac{\partial p^b}{\partial t} + \rho v^2\left(\frac{\partial v_x^b}{\partial x} + \frac{\partial v_z^b}{\partial z}\right)\right]dtd\mathbf{x} \end{aligned} \quad (11)$$

where the displacement u_i in the i direction can be expressed as

$$u_i = \int_0^t v_i dt \quad (12)$$

After substituting **Equation 12** into (**Equation 11**) and letting the partial derivatives of **Equation 11** with respect to v_x^b, v_z^b and p^b equal to zero, we obtain the adjoint-state equation system

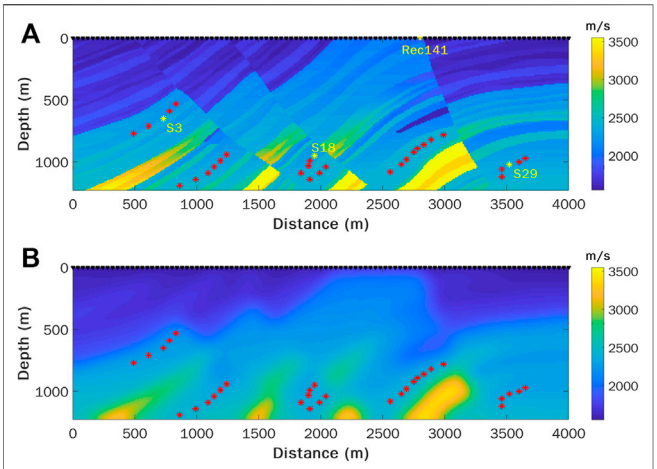

FIGURE 2 | 2D velocity models used for synthetic tests with WEFT. **(A)** The true model adapted from the Marmousi model. **(B)** The initial model used for WEFT. The inverted triangles at the top of the model denote the 201 receivers with an interval of 20 m, and the asterisks within the model denote the 31 earthquake sources. The yellow asterisks and the yellow inverted triangle indicate the sources and receiver used for the data comparison in **Figure 8**.

$$\begin{cases} \dfrac{\partial \lambda_x}{\partial t} + \rho v^2 \dfrac{\partial \lambda_p}{\partial x} = -\displaystyle\int_{\tilde{t}_0}^{t} w(\mathbf{x},t)\left(\frac{\partial^2 u_x^b}{\partial x^2} + 2\frac{\partial^2 u_z^b}{\partial x \partial z} + 2\frac{\partial^2 u_x^b}{\partial z^2}\right)dt \\ \dfrac{\partial \lambda_z}{\partial t} + \rho v^2 \dfrac{\partial \lambda_p}{\partial z} = -\displaystyle\int_{\tilde{t}_0}^{t} w(\mathbf{x},t)\left(\frac{\partial^2 u_z^b}{\partial z^2} + 2\frac{\partial^2 u_x^b}{\partial x \partial z} + 2\frac{\partial^2 u_z^b}{\partial x^2}\right)dt \\ \dfrac{\partial \lambda_p}{\partial t} + \dfrac{1}{\rho}\left(\dfrac{\partial \lambda_x}{\partial x} + \dfrac{\partial \lambda_z}{\partial z}\right) = 0 \end{cases} \tag{13}$$

For time-reversal imaging, **Equation 13** can be expressed as

$$\begin{cases} \dfrac{\partial \lambda_x}{\partial t} + \rho v^2 \dfrac{\partial \lambda_p}{\partial x} = -\displaystyle\int_{\tilde{t}_0}^{t} w(\mathbf{x},t)\left(\frac{\partial \hat{M}_{xx}^{TR}(\mathbf{x},t)}{\partial x} + 2\frac{\partial \hat{M}_{xz}^{TR}(\mathbf{x},t)}{\partial z}\right)dt \\ \dfrac{\partial \lambda_z}{\partial t} + \rho v^2 \dfrac{\partial \lambda_p}{\partial z} = -\displaystyle\int_{\tilde{t}_0}^{t} w(\mathbf{x},t)\left(\frac{\partial \hat{M}_{zz}^{TR}(\mathbf{x},t)}{\partial z} + 2\frac{\partial \hat{M}_{zx}^{TR}(\mathbf{x},t)}{\partial x}\right)dt \\ \dfrac{1}{\rho}\left(\dfrac{\partial \lambda_x}{\partial x} + \dfrac{\partial \lambda_z}{\partial z}\right) + \dfrac{\partial \lambda_p}{\partial t} = 0 \end{cases} \tag{14}$$

and the adjoint source of WEFT can be defined as

$$S_i = -\int_{\tilde{t}_0}^{t} \sum_{j=1}^{2} c_{ij} w(\mathbf{x}) \frac{\partial \hat{M}_{ij}^{TR}(\mathbf{x},t)}{\partial j} dt \tag{15}$$

in which $c_{ij} = 1$ for $i = j$ and $c_{ij} = 2$ otherwise, the adjoint-state equation system can be written as

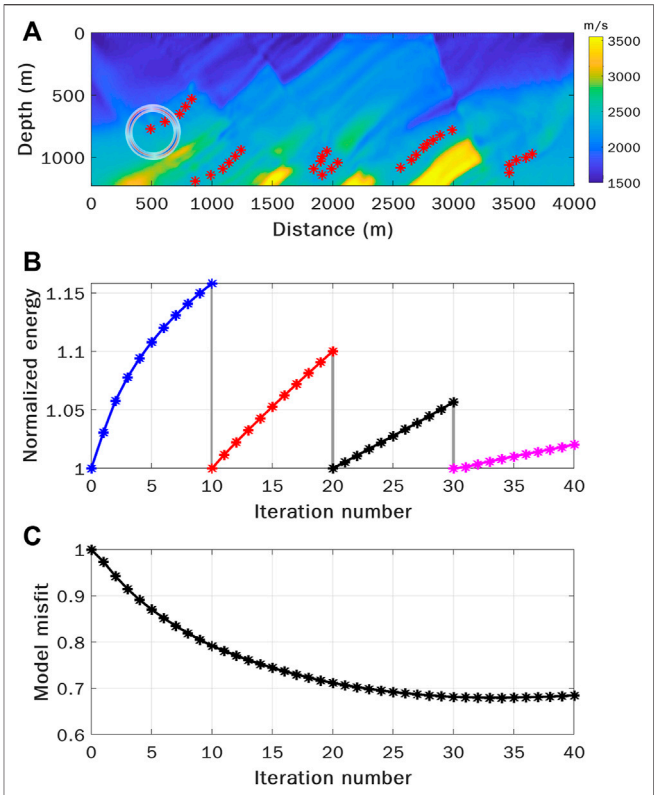

FIGURE 3 | Velocity inversion with WEFT using passive sources with a uniform radiation pattern. **(A)** The inverted velocity model by WEFT using the multiscale strategy. The source radiation pattern is indicated by the small adjacent ring. **(B)** The focused energy with iterations at the source locations. For the focused energy, their values are renormalized by the respective values at the first iteration in every frequency band (indicated by different colors). Waveforms in four frequency bands, 1–5 Hz, 1–9 Hz, 1–16 Hz, and 1–28 Hz are sequentially used for updating the velocity model, with 10 iterations in each band. **(C)** The normalized model misfit measured by L2-norm as a function of iterations.

$$\begin{cases} \dfrac{\partial \lambda_x}{\partial t} + \rho v^2 \dfrac{\partial \lambda_p}{\partial x} = S_x \\ \dfrac{\partial \lambda_z}{\partial t} + \rho v^2 \dfrac{\partial \lambda_p}{\partial z} = S_z \\ \dfrac{\partial \lambda_p}{\partial t} + \dfrac{1}{\rho}\left(\dfrac{\partial \lambda_x}{\partial x} + \dfrac{\partial \lambda_z}{\partial z}\right) = 0 \end{cases} \tag{16}$$

which is similar to **Equation 8**.

Solving **Equation 11**, the gradient of the objective function can be expressed as

$$\frac{\partial \boldsymbol{E}}{\partial v(\mathbf{x})} = \frac{\partial \boldsymbol{S}(v)}{\partial v(\mathbf{x})} = 2\rho v \int_{\tilde{t}_0}^{t_{max}} \lambda_p \left(\frac{\partial v_x^b}{\partial x} + \frac{\partial v_z^b}{\partial z}\right) dt \tag{17}$$

According to the relationship between the pressure and particle velocity in **Equation 8**, the gradient can be written as

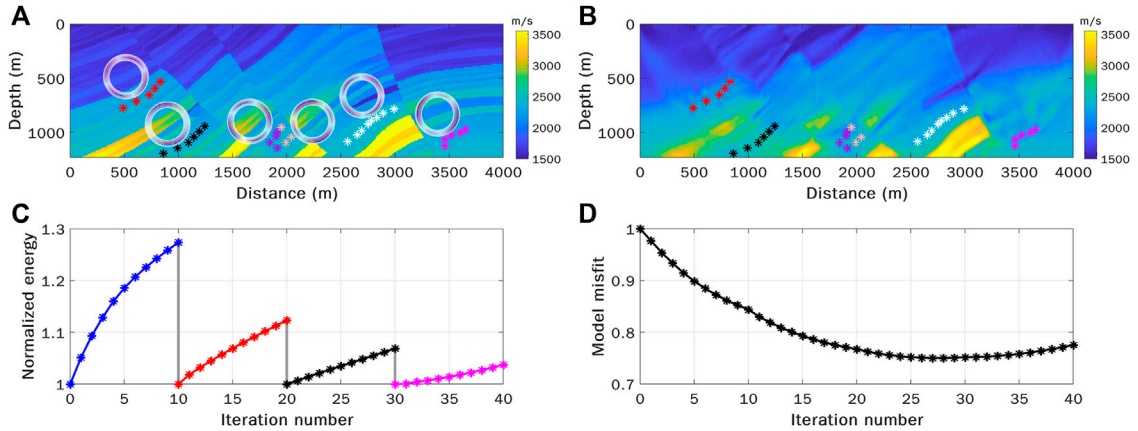

FIGURE 4 | Velocity inversion with WEFT using passive sources with varying radiation patterns. **(A)** Distribution of six seismic clusters (colored asterisks), each of which has a distinct radiation pattern indicated by small adjacent rings. The true velocity model is shown in the background. **(B)** The model inverted by multiscale WEFT with seismic sources in **(A)**. **(C)**The focused energy with iterations at the source locations. **(D)** The normalized model misfit measured by L2-norm as a function of iterations.

$$\frac{\partial E}{\partial v(\mathbf{x})} = -\frac{2}{v}\int_{t_0}^{t_{max}} \lambda_p(\mathbf{x},t;\boldsymbol{\xi})\frac{\partial p^b(\mathbf{x},t;\mathbf{x}_r)}{\partial t}dt \tag{18}$$

where $\lambda_p(\mathbf{x},t;\boldsymbol{\xi})$ denotes the forward-propagated pressure wavefield excited by the adjoint source of WEFT S_i, and $p^b(\mathbf{x},t;\mathbf{x}_r)$ denotes the back-propagated pressure wavefield. **Equation 18** means the gradient in WEFT can be calculated by correlating the time derivative of the back-propagated wavefield with forward-propagated wavefield defined by the equation system (**Eq. 16**), which is very similar to FWI (Zhong and Liu, 2019).

The workflow of WEFT is summarized in **Figure 1**. In each iteration, there are two essential steps: 1) the observed data are first back-propagated and the adjoint source is constructed; 2) the gradient is calculated by correlating the time derivative of back-propagated wavefield with the forward wavefield emanating from the adjoint source according to **Equation 18**. Then the conjugate gradient method (Mora, 1987) is used to update the velocity model iteratively and the backtracking line search method is applied to determine the proper step length. When the pre-defined number of iterations is reached or the increase in energy levels off, the inversion is terminated. Though there are many similarities in the implementation between WEFT and FWI, some noticeable differences still exist. The major difference is that WEFT back-propagates the recorded seismic data, whereas FWI back-propagates the residual waveforms between the recorded and synthetic data. Moreover, the moment time functions for a source must be provided *a priori* in FWI, whereas the source attributes except for rough source locations are not required for WEFT in advance.

NUMERICAL TESTS

To validate WEFT, we perform a series of synthetic tests using heterogeneous models in 2D. The true velocity model (**Figure 2A**) used for the following numerical experiments is adapted from the widely used Marmousi model (Martin et al., 2002). Both the true and smooth initial velocity models (**Figures 2A,B**) are from Schuster (2017). A Ricker wavelet with central frequency of 15 Hz is chosen as the source time function. The source-receiver configuration consists of 201 receivers on the surface with an interval of 20 m, and 31 passive sources located in the subsurface (**Figure 2**). These sources are distributed into 6 clusters. We should emphasize that the synthetic model used here is for the proof of concept for the proposed WEFT method and may not follow the actual scenarios for earthquake monitoring. However, with more and more dense seismic arrays used for monitoring induced seismicity, the distribution of dense receivers and shallow passive seismic sources are actually expected, such as the dense geophones used for monitoring shale gas hydraulic fracturing (Eisner et al., 2010; Staněk and Eisner, 2013; Anikiev et al., 2014).

Following the approach now commonly used in FWI, which sequentially utilizes observed data with increasing frequencies (Bunks et al., 1995), a multiscale strategy is also adopted in WEFT. After a predefined number of iterations is reached for a certain frequency band, the final velocity model is used as the initial model for the next frequency band. Since the source location used in this case is accurate, we choose a small spatial aperture $l_x = l_z = 40\ m$, and the temporal aperture is larger than the half-width of the source wavelet. To improve the resolution of the inverted model, the spatial aperture $l_{x,z}$ in **Eq. 7** for evaluating the focused energy is gradually decreased with increasing frequencies. We first test the WEFT using passive seismic sources with a uniform radiation pattern (indicated by the small adjacent ring in **Figure 3A**). Four frequency bands of 1–5 Hz, 1–9 Hz, 1–16 Hz, and 1–28 Hz are adopted. It can be seen that the inverted model (**Figure 3A**) is hardly affected by the source radiation pattern although the source moment time function is not provided for the inversion. The focused energy (**Figure 3B**) increases with iterations in each frequency band and

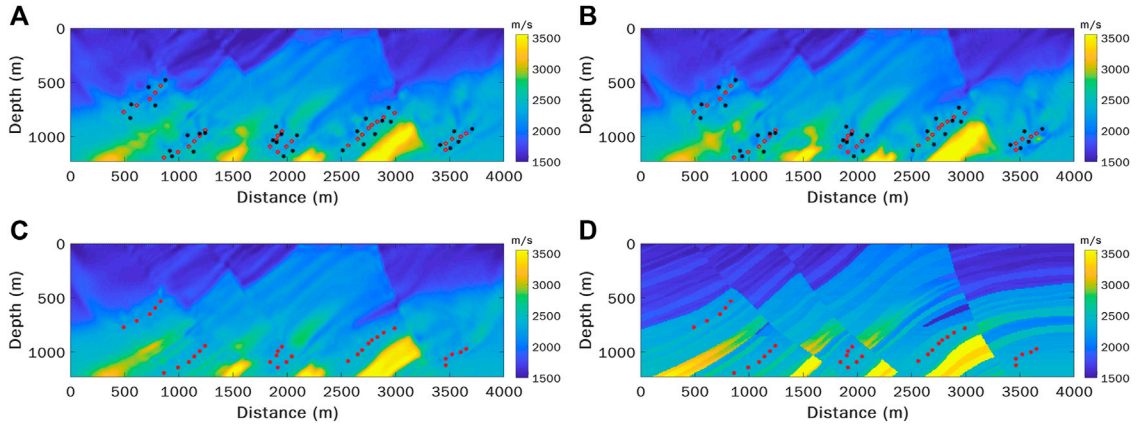

FIGURE 5 | Comparison of the velocity inversion results with different focusing apertures and with or without source location errors. **(A)** The model inverted with the smaller apertures ($l_x = l_z = 40$ m) while the source locations (black asterisks) deviate from their correct positions (red circles). **(B)** The model inverted with larger apertures ($l_x = l_z = 100\,m$) under the same conditions as **(A)**. **(C)** The model inverted with smaller apertures as **(A)** when source locations are accurate (red asterisks). **(D)** The true model for comparison.

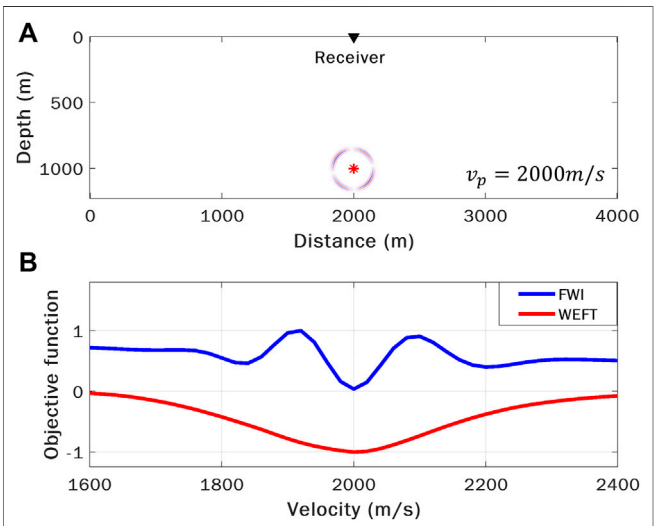

FIGURE 6 | Comparison of the objective functions between FWI and WEFT. **(A)** The source-receiver configuration used for calculating the objective functions. The source radiation pattern is indicated by the small adjacent ring. The velocity model is homogenous with Vp equal to 2000 m/s. **(B)** Comparison of the normalized objective functions for FWI (blue) and WEFT (red) with respect to different velocities.

its growth levels off gradually. Meanwhile, the model misfit measured by the L2-norm also decreases with iterations, as shown in **Figure 3C**.

We further test a more complicated scenario where six seismic clusters having different types of source moment tensors (**Figure 4A**). The spatialtemporal aperture used here is the same as in the previous case. The model inverted by the multiscale WEFT is shown in **Figure 4B**. Though the varying

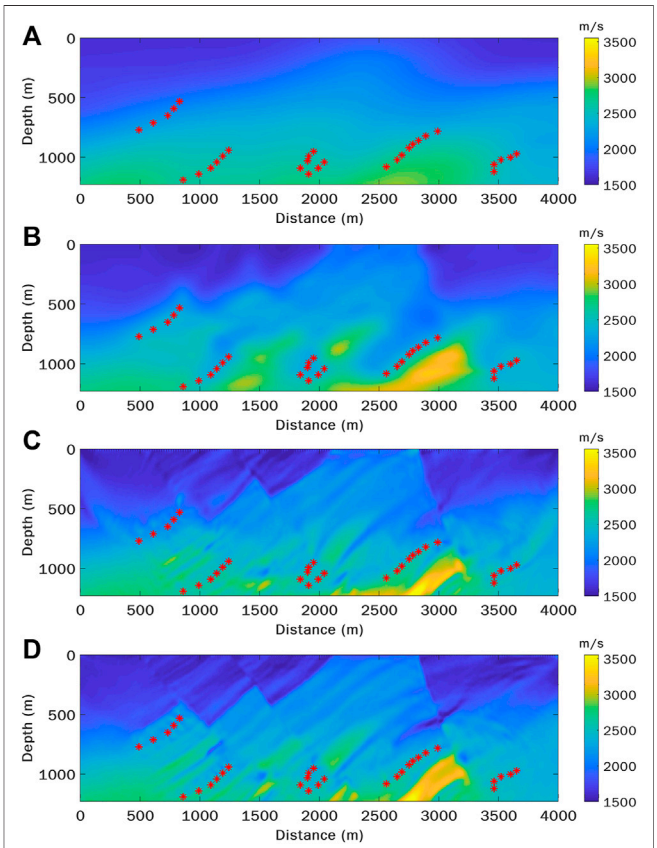

FIGURE 7 | The inverted models using traveltime tomography and WEFT from a rather smooth initial model. **(A)** The rather smooth initial model. **(B)** The model inverted by traveltime tomography. **(C)** The model inverted by multiscale WEFT. **(D)** The model further inverted by multiscale FWI starting from the WEFT model in **(C)**.

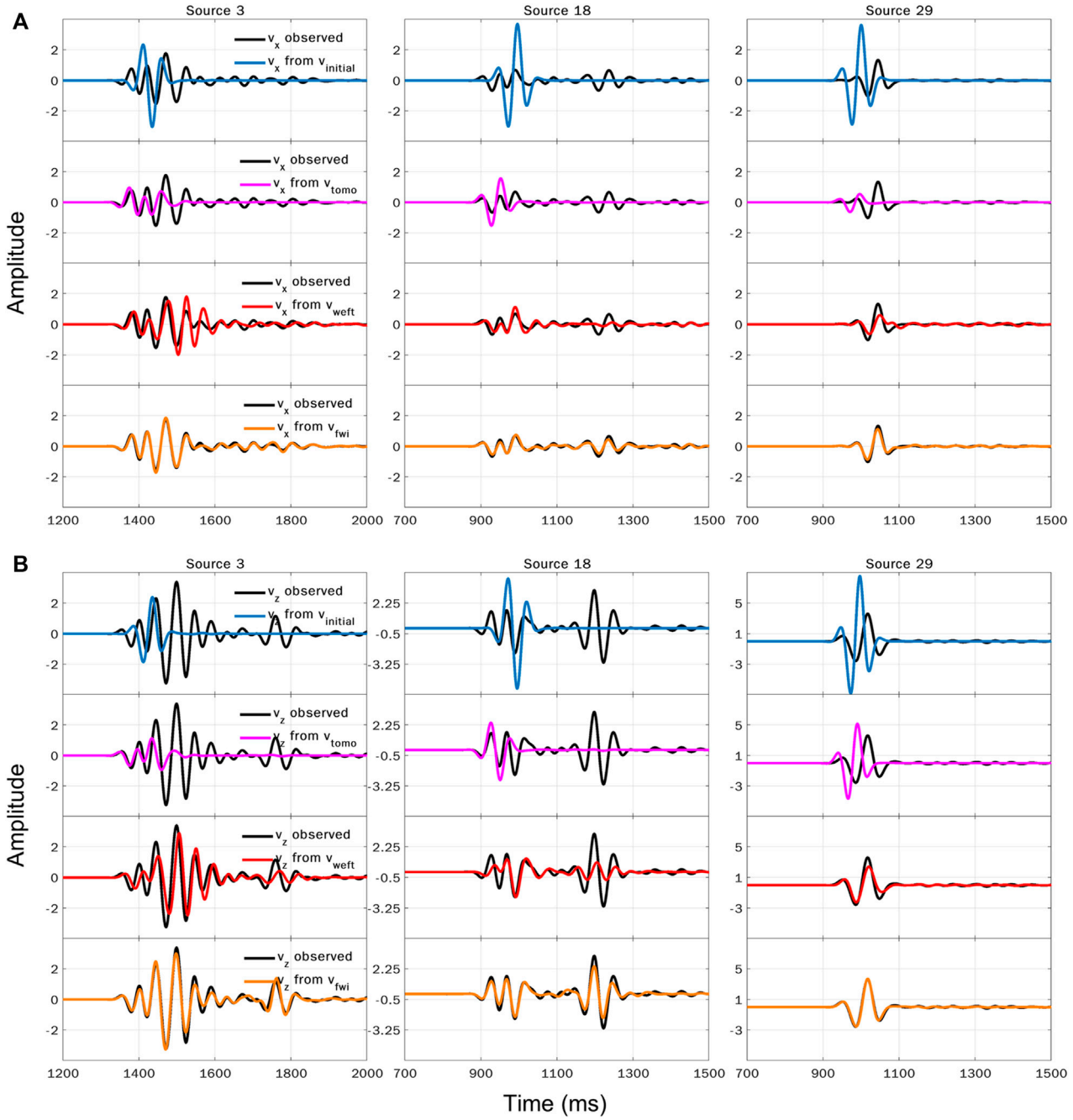

FIGURE 8 | Comparison of waveforms for the **(A)** v_x and **(B)** v_z components at a particular receiver from different sources using various velocity models. The black lines denote the observed data. The blue, magenta, red and orange lines denote the synthetic data with the initial model (**Figure 7A**), the final velocity models from traveltime tomography (**Figure 7B**), WEFT (**Figure 7C**) and FWI (**Figure 7D**), respectively. The subplots in each column show data from a different source. The locations of the receiver (yellow triangle) and the sources (yellow asterisks) are shown in **Figure 2A**. The waveforms are filtered between 1 and 28 Hz, and the true source moment time functions are used.

radiation patterns from different clusters pose a considerable challenge for waveform inversion, WEFT still inverts for the heterogeneous Marmousi model accurately. Compared to the true model, there are some minor artifacts in the inverted model, which are probably caused by the varying radiation patterns that can result in complicated directional illuminations in resolving the model. Although the stacking energy (**Figure 4C**) increases with iteration in each frequency band as expected, the model misfit (**Figure 4D**) undesirably also increases slightly in the last frequency band, which suggests the inversion was trapped in a local minimum for high-frequency data. Nevertheless, this example demonstrates that WEFT can be applied directly to

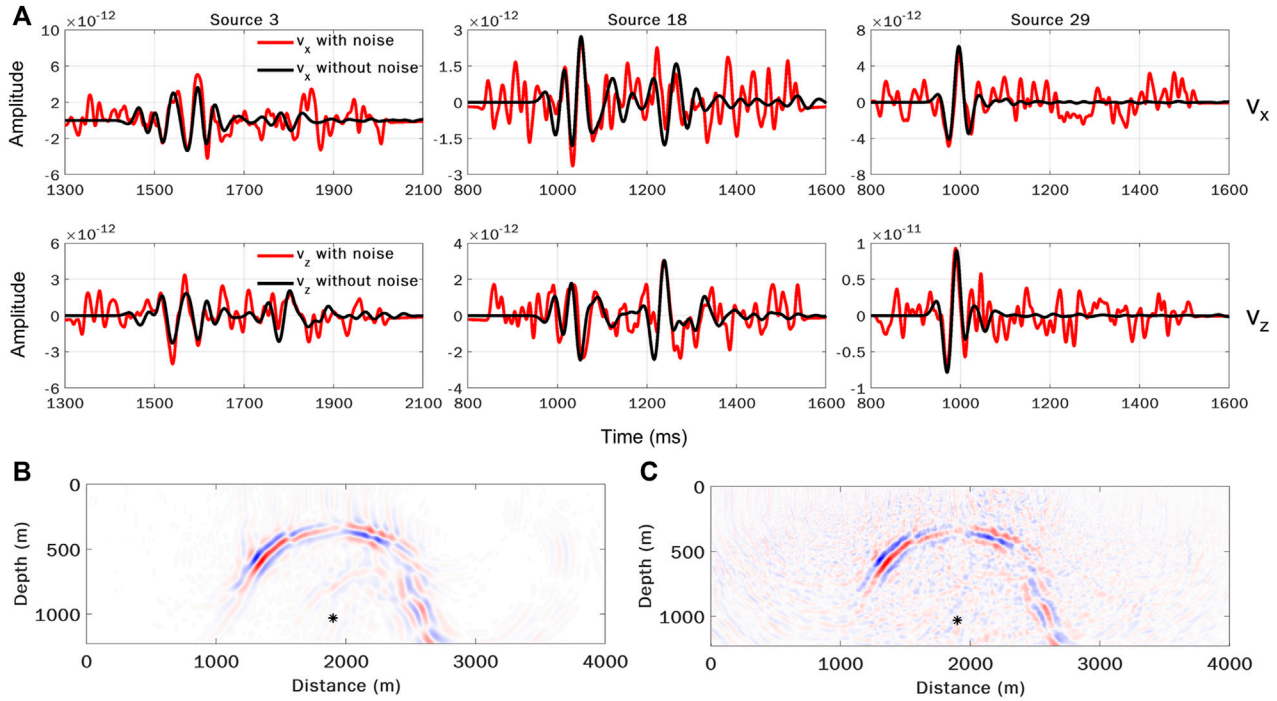

FIGURE 9 | The comparison between the noisy and noise-free synthetic data used for WEFT. **(A)** Noisy and noise-free traces at selected receivers. The source radiation pattern is the same as that shown in **Figure 3**. The black lines indicate the noise-free data, and the red lines indicate the noisy data by superposing the noise-free data with random Gaussian noise with limited bandwidth. The distributions of the sources and receivers are the same as those shown in **Figure 2**. **(B)** and **(C)** show the snapshots of the back-propagated wavefield with noise-free and noisy data, respectively.

surface seismic monitoring datasets in which seismic sources occur on different faults are with varying orientations and slipping angles.

DISCUSSIONS

Influence of Uncertainty in Source Location

In WEFT, the source location is used to determine the spatial volume for evaluating the focused energy (**Equation 7**), and for the adjoint source injection when calculating the adjoint wavefield (λ_p in **Equation 15**). As discussed earlier, in WEFT it is assumed that the source location and origin time are predetermined from other methods, e.g., the NonLinLoc method (Lomax et al., 2000), the double-difference location method based on traveltimes (Waldhauser and Ellsworth, 2000; Zhang and Thurber, 2003), or the recently developed location methods based on machine learning (Kriegerowski et al., 2019; Zhang et al., 2020; Wang and Alkhalifah, 2021). Thus, the source location may deviate from its true position owing to an inaccurate velocity model (Thurber, 1992) and arrival times. In WEFT, a way to mitigate the influence of inaccurate source locations is to expand the spatial aperture for evaluating the focused energy (determined by l_x and l_z in **Equation 7**). That is, the spatial aperture should be designed based on the source location uncertainty so that the true location is contained in the volume for evaluating the focused energy. To some extent, however, this strategy may also compromise the accuracy and resolution of the inverted velocity model, since the back-propagated wavefields using a slightly incorrect model may still focus well within an enlarged volume. When the source locations are known accurately, the inverted model using a smaller spatial aperture with $l_x = l_z = 40$ m is shown in **Figure 5C**, and the model misfit is reduced by about 30%. However, when the source locations are not accurate, the result using the same spatial apertures shows a slightly distorted inclined high-velocity layer at the bottom of the model ($x \approx 3000\,m$, $z \approx 1000\,m$) and a blurred inclined thin layer with low velocity ($x \approx 3000\,m$, $z \approx 600\,m$) (**Figure 5A**). The model misfit in this case is only reduced by 10%. If we enlarge the apertures to $l_x = l_z = 100$ m, not only the model misfit is reduced by about 18% of the original, but also the distortion is suppressed and the low-velocity thin layer is better recovered (**Figure 5B**). By comparing models in **Figure 5A,B,C**, we notice that some artifacts around the sources are introduced with inaccurate source locations.

Comparison With Full Waveform Inversion and Seismic Travel Time Tomography

Since WEFT evaluates the magnitudes of the back-propagated energy focused around the hypocenters instead of matching the wiggles between the observed and synthetic waveforms at the receivers, the proposed method has less nonlinearity and is more

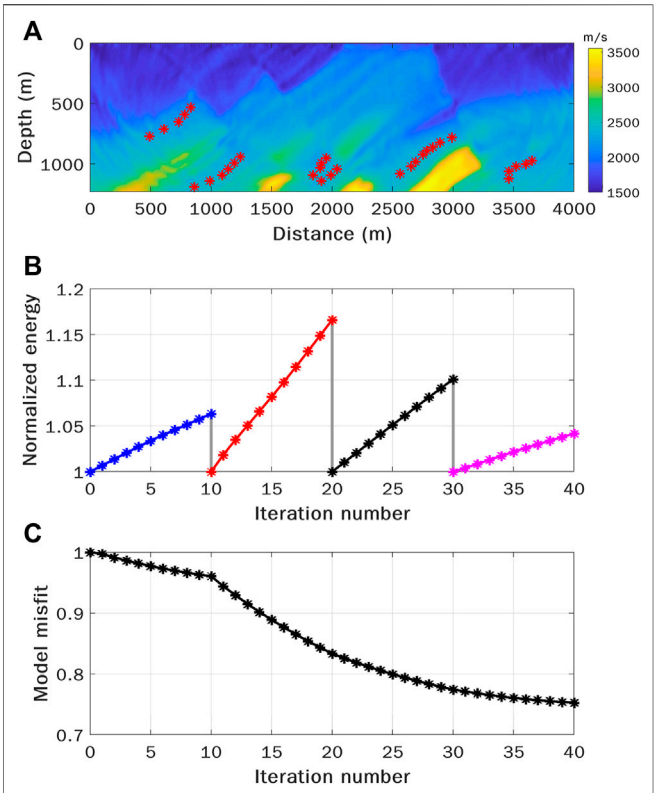

FIGURE 10 | Results of multiscale WEFT using data with random Gaussian noise with limited bandwidth. **(A)** The inverted velocity model with multiscale WEFT. **(B)** The focused energy with iterations at the source locations. The parameters used in the inversion are similar to those used in **Figure 3**. **(C)** The normalized model misfit measured by L2-norm as a function of iterations.

robust since there is less cycle-skipping issues as commonly seen in conventional FWI. **Figure 6B** shows a comparison of objective functions of FWI and WEFT for a simple source-receiver configuration (**Figure 6A**), where the passive source is located at 1,000 m in depth and a single receiver is on the surface. It is obvious that the objective function of FWI has multiple local minima compared to that of WEFT, which has a more convex behavior globally and has only a single global minimum for this scenario.

The lower nonlinearity of WEFT can also facilitate velocity inversion from a poor initial velocity model. In **Figure 7**, we further compare the inversion results between WEFT and conventional traveltime tomography using an even smoother initial velocity model (**Figure 7A**). Compared to the true model, many small heterogeneities and contrasts are recovered in the inverted model by WEFT (**Figure 7C**), while only the tilted high-velocity bodies at the bottom of the model are distorted. In comparison, the inverted model by traveltime tomography (**Figure 7B**) appears much smoother and lack fine details. Starting from the final inverted model from WEFT, we perform FWI to further update the velocity (**Figure 7D**), and even more details are added to the model. It should be stressed again that WEFT does not require source moment time functions in the inversion, while FWI does. Using the final velocity models inverted by WEFT and traveltime tomography shown in **Figure 7**, we generate synthetic waveforms and compare the v_x and v_z components (**Figure 8**). Significant time delays can be found between the "observed" data from the true model (black lines) and the 'synthetic' data generated based on the initial model (blue lines). Although the model inverted by traveltime tomography considerably mitigates the time delays between the observed and synthetic data, wiggles in the two datasets still differ markedly. In comparison, the waveform matching between the synthetic and observed data improves considerably using the velocity model derived by WEFT, with many later-arrived wiggles successfully modeled. When using the model inverted by FWI starting from the final model of WEFT, the synthetic and observed waveforms are almost the same. This nice agreement in waveforms indicates that though the objective function of WEFT only considers the energy focusing at the sources directly, the waveform matching at the receivers is nevertheless satisfactory owning to a correctly updated model.

Influence of Noise

We further test the stability and accuracy of WEFT with noisy observed data (**Figure 9A**). In this experiment, the synthetic data are contaminated by random Gaussian noise, which is not coherent among receivers, and the SNR is about 0.3. For the noisy data, it is difficult to obtain a relatively accurate velocity model by conventional FWI without sophisticated data preprocessing. However, it is still possible to apply WEFT with the noisy data. This is because although the seismic signals are initially buried in the noise, the coherent signals can be gradually enhanced against the inherent noise with back-propagation. In other words, wavefield back-propagation specifically focuses the energy of the microseismic event and thus suppresses incoherent noise, which can be seen in the snapshots of the back-propagated wavefields at a certain time with noise-free and noisy data (**Figures 9B,C**, respectively). Compared with the inverted model from the noise-free data (**Figure 3**), the inverted model with the noisy data is similar (**Figure 10A**), and the model misfit (**Figure 10C**) still shows a considerable reduction. This test demonstrates that WEFT is rather resilient to incoherent noise, which can be a considerable advantage over FWI.

Influence of Source Distribution

Considering that the distribution of sources and the source mechanisms may have a noticeable influence on the inverted model, we further perform a challenging test where 10 earthquakes with a uniform radiation pattern are distributed within a narrow depth range of 60 m, as shown in **Figure 11A**. Starting from the initial model shown in **Figure 11B**, two distinct source mechanisms are used for comparison. The inverted models using sources with different radiation patterns (indicated by the small adjacent ring) are shown in **Figures 11C,E**, respectively. The comparison of the velocity profiles at the position x = 2,310 m is shown in **Figures 11D,F**, respectively. We found that, as expected, most of the effective update is within the central part of the model above the earthquake sources due to the limited source illumination.

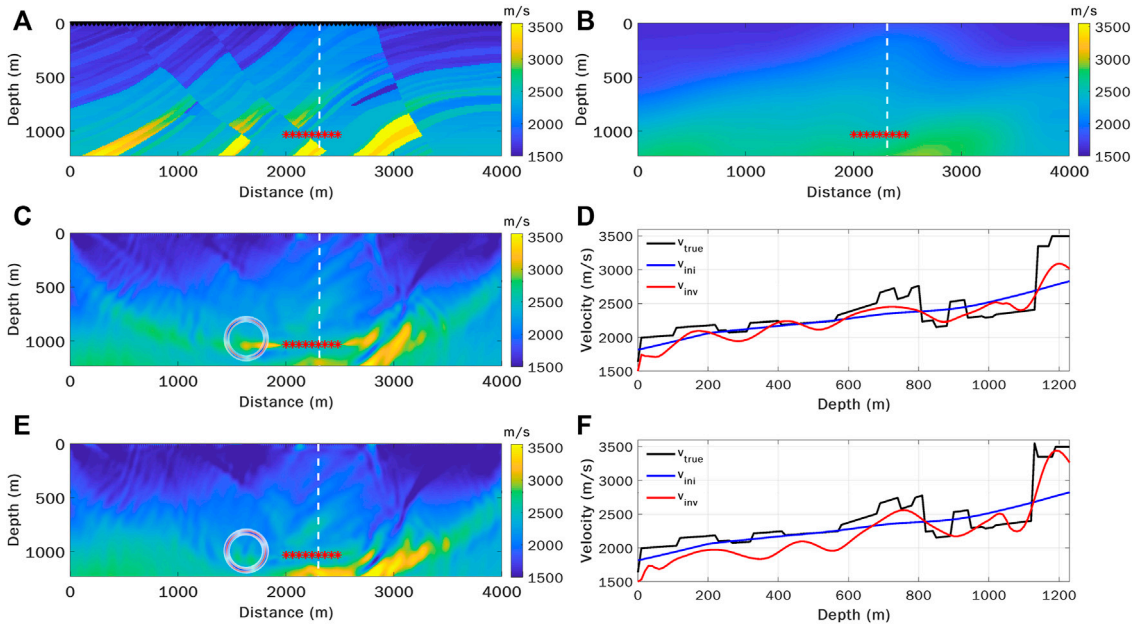

FIGURE 11 | Comparison of the velocity inversion results using clustered earthquakes in a narrow depth range with uniform focal mechanisms. **(A)** The distributions of 10 sources (red asterisks) and 199 receivers (black inverted triangles) with the true model in the background. **(B)** The initial model used for WEFT. **(C)** and **(E)** are the inverted models using sources with two distinct focal mechanisms (indicated by small adjacent rings). **(D)** and **(F)** are the corresponding comparisons of the true (black), initial (blue) and inverted (red) velocity profiles at x = 2,310 m (indicated by a white dash line).

Besides, different source mechanisms, which result in varying illumination patterns, inevitably have an impact on the inverted models. Due to the poor source distribution, the recovered models are not as good as those shown before. However, both inverted models are updated successfully compared to the initial one, especially the model shown in **Figures 11C,D**.

CONCLUSION

We propose a new seismic tomography method called Waveform Energy Focusing Tomography for passive seismic sources. Compared to FWI, WEFT inverts for the velocity model by maximizing the energy of the moment time functions from back-propagated wavefields around the sources, instead of matching synthetic and observed waveforms at the receivers. As a result, WEFT has lower nonlinearity in the inversion and can avoid the cycle skipping issue in FWI. More importantly, except for the source locations and origin times, WEFT does not require other source attributes including source time functions and focal mechanisms. This means that more earthquakes with smaller magnitudes and unknown source mechanisms can also be used by WEFT.

We have shown the effectiveness and advantages of WEFT through several 2D synthetic tests based on the Marmousi model. WEFT can still perform well on different challenging cases when passive seismic sources have different radiation patterns, when the initial velocity model is rather smooth, and when waveforms are very noisy. Nevertheless, the quality of inverted models can still be affected by uneven illumination due to distributions and mechanisms of sources. Although waveform matching at the receivers is not directly considered in the objective function of WEFT, the synthetic tests show that the waveform matching using the inverted model by WEFT is still satisfactory, much better than the velocity model inverted by traveltime tomography using arrival times. It should be noted that WEFT yields velocity models with slightly lower resolution compared to FWI. Therefore, WEFT can act as an intermediate step between seismic traveltime tomography and FWI by providing a more accurate and reliable starting velocity model for the latter.

In this study, for simplicity we validate WEFT with passive seismic sources under the 2D acoustic assumption. This method can also be extended to 3D for real applications such as dense-array monitoring of local seismicity from fault zones or hydraulic fracturing when the receivers are not distributed along a straight line or the passive sources have an areal distribution, which will be shown in a future study.

DATA AVAILABILITY STATEMENT

The raw data supporting the conclusions of this article will be made available by the authors, without undue reservation.

AUTHOR CONTRIBUTIONS

YH, JL, and HZ all contributed to the study. YH performed the numerical tests and wrote the first draft of the manuscript. All authors contributed to the revision and approved the submitted version.

FUNDING

This research is supported by the National Natural Science Foundation of China under grants 41961134001 and 41874048, and supported by the National Key Research and Development Projects 2021YFC3000602 and 2018YFC1504102.

ACKNOWLEDGMENTS

The authors would like to thank Haipeng Li for his many helpful discussions. We also thank two reviewers and editor Tariq Alkhalifah for their very helpful comments in improving our manuscript.

REFERENCES

Adamczyk, A., Malinowski, M., and Górszczyk, A. (2015). Full-waveform Inversion of Conventional Vibroseis Data Recorded along a Regional Profile from Southeast Poland. *Geophys. J. Int.* 203, 351–365. doi:10.1093/gji/ggv305

Alkhalifah, T. (2014). *Full Waveform Inversion in an Anisotropic World: Where Are the Parameters Hiding*. European Association of Geoscientists and Engineers (EAGE).

Alkhalifah, T., and Song, C. (2019). An Efficient Wavefield Inversion: Using a Modified Source Function in the Wave Equation. *Geophysics* 84, R909–R922. doi:10.1190/geo2018-0759.1

Anikiev, D., Valenta, J., Staněk, F., and Eisner, L. (2014). Joint Location and Source Mechanism Inversion of Microseismic Events: Benchmarking on Seismicity Induced by Hydraulic Fracturing. *Geophys. J. Int.* 198 (1), 249–258. doi:10.1093/gji/ggu126

Artman, B., Podladtchikov, I., and Witten, B. (2010). Source Location Using Time-Reverse Imaging. *Geophys. Prospect.* 58, 861–873. doi:10.1111/j.1365-2478.2010.00911.x

Bazargani, F., and Snieder, R. (2016). Optimal Source Imaging in Elastic Media. *Geophys. J. Int.* 204, 1134–1147. doi:10.1093/gji/ggv494

Biondi, B., and Almomin, A. (2014). Simultaneous Inversion of Full Data Bandwidth by Tomographic Full-Waveform Inversion. *Geophysics* 79, WA129–WA140. doi:10.1190/geo2013-0340.1

Bleibinhaus, F., Hole, J. A., Ryberg, T., and Fuis, G. S. (2007). Structure of the California Coast Ranges and San Andreas Fault at SAFOD from Seismic Waveform Inversion and Reflection Imaging. *J. Geophys. Res. Solid Earth* 112, 4611. doi:10.1029/2006jb004611

Bording, R. P., Gersztenkorn, A., Lines, L. R., Scales, J. A., and Treitel, S. (1987). Applications of Seismic Travel-Time Tomography. *Geophys. J. Int.* 90, 285–303. doi:10.1111/j.1365-246x.1987.tb00728.x

Bozdağ, E., Peter, D., Lefebvre, M., Komatitsch, D., Tromp, J., Hill, J., et al. (2016). Global Adjoint Tomography: First-Generation Model. *Geophys. J. Int.* 207, 1739–1766. doi:10.1093/gji/ggw356

Bozdağ, E., Trampert, J., and Tromp, J. (2011). Misfit Functions for Full Waveform Inversion Based on Instantaneous Phase and Envelope Measurements. *Geophys. J. Int.* 185, 845–870. doi:10.1111/j.1365-246X.2011.04970.x

Brenders, A. J., and Pratt, R. G. (2007). Full Waveform Tomography for Lithospheric Imaging: Results from a Blind Test in a Realistic Crustal Model. *Geophys. J. Int.* 168, 133–151. doi:10.1111/j.1365-246x.2006.03156.x

Bunks, C., Saleck, F. M., Zaleski, S., and Chavent, G. (1995). Multiscale Seismic Waveform Inversion. *Geophysics* 60, 1457–1473. doi:10.1190/1.1443880

Chambers, K., Dando, B. D. E., Jones, G. A., Velasco, R., and Wilson, S. A. (2014). Moment Tensor Migration Imaging. *Geophys. Prospect.* 62, 879–896. doi:10.1111/1365-2478.12108

Cheong, S., Pyun, S., and Shin, C. (2006). Two Efficient Steepest-Descent Algorithms for Source Signature-free Waveform Inversion: Synthetic Examples. *J. Seismic Explor.* 14, 335.

Choi, Y., and Alkhalifah, T. (2011). Source-independent Time-Domain Waveform Inversion Using Convolved Wavefields: Application to the Encoded Multisource Waveform Inversion. *Geophysics* 76, R125–R134. doi:10.1190/geo2010-0210.1

Choi, Y., and Alkhalifah, T. (2015). Unwrapped Phase Inversion with an Exponential Damping. *Geophysics* 80, R251–R264. doi:10.1190/geo2014-0498.1

Choi, Y., Shin, C., Min, D.-J., and Ha, T. (2005). Efficient Calculation of the Steepest Descent Direction for Source-independent Seismic Waveform Inversion: An Amplitude Approach. *J. Comput. Phys.* 208, 455–468. doi:10.1016/j.jcp.2004.09.019

Eisner, L., Duncan, P. M., Heigl, W. M., and Keller, W. R. (2009). Uncertainties in Passive Seismic Monitoring. *Lead. Edge* 28, 648–655. doi:10.1190/1.3148403

Eisner, L., Williams-Stroud, S., Hill, A., Duncan, P., and Thornton, M. (2010). Beyond the Dots in the Box: Microseismicity-Constrained Fracture Models for Reservoir Simulation. *Lead. Edge* 29 (3), 326–333. doi:10.1190/1.3353730

Engquist, B., and Froese, B. D. (2013). Application of the Wasserstein Metric to Seismic Signals. arXiv preprint arXiv:1311.4581.

Eyre, T. S., and van der Baan, M. (2015). Overview of Moment-Tensor Inversion of Microseismic Events. *Lead. Edge* 34, 882–888. doi:10.1190/tle34080882.1

Fichtner, A., Kennett, B. L. N., Igel, H., and Bunge, H.-P. (2009). Full Seismic Waveform Tomography for Upper-Mantle Structure in the Australasian Region Using Adjoint Methods. *Geophys. J. Int.* 179, 1703–1725. doi:10.1111/j.1365-246x.2009.04368.x

Fichtner, A., Trampert, J., Cupillard, P., Saygin, E., Taymaz, T., Capdeville, Y., et al. (2013). Multiscale Full Waveform Inversion. *Geophys. J. Int.* 194, 534–556. doi:10.1093/gji/ggt118

Fink, M. (1997). Time Reversed Acoustics. *Phys. today* 50, 34–40. doi:10.1063/1.881692

Gharti, H. N., Oye, V., Kühn, D., and Zhao, P. (2011). "Simultaneous Microearthquake Location and Moment-Tensor Estimation Using Time-Reversal Imaging," in 81st Annual International Meeting, SEG Technical Program Expanded Abstracts 2011, San Antonio, 1632–1637.

Hara, S., Fukahata, Y., and Iio, Y. (2019). P Wave First-Motion Polarity Determination of Waveform Data in Western Japan Using Deep Learning. *Earth Planets Space* 71, 1–11. doi:10.1186/s40623-019-1111-x

Hardebeck, J. L., and Shearer, P. M. (2002). A New Method for Determining First-Motion Focal Mechanisms. *Bull. Seismol. Soc. Am.* 92, 2264–2276. doi:10.1785/0120010200

Hardebeck, J. L., and Shearer, P. M. (2003). Using S/P Amplitude Ratios to Constrain the Focal Mechanisms of Small Earthquakes. *Bull. Seismol. Soc. Am.* 93, 2434–2444. doi:10.1785/0120020236

Hestenes, M. R. (1969). Multiplier and Gradient Methods. *J. Optim. Theory Appl.* 4, 303–320. doi:10.1007/bf00927673

Huang, G., Nammour, R., and Symes, W. (2017). Full-waveform Inversion via Source-Receiver Extension. *Geophysics* 82, R153–R171. doi:10.1190/geo2016-0301.1

Jin, S., and Plessix, R.-É. (2013). "Stack-based Full Wavefield Velocity Tomography," in 83rd Annual International Meeting, SEG Technical Program Expanded Abstracts 2013, Houston, 1095–1099. doi:10.1190/segam2013-1027.1

Julian, B. R., Miller, A. D., and Foulger, G. R. (1998). Non-double-couple Earthquakes 1. Theory. *Rev. Geophys.* 36, 525–549. doi:10.1029/98rg00716

Kaderli, J., McChesney, M. D., and Minkoff, S. E. (2015). "Microseismic Event Estimation in Noisy Data via Full Waveform Inversion," in 85th Annual International Meeting, SEG Technical Program Expanded Abstracts 2015, New Orleans, 1159–1164. doi:10.1190/segam2015-5867154.1

Kawakatsu, H., and Montagner, J.-P. (2008). Time-reversal Seismic-Source Imaging and Moment-Tensor Inversion. *Geophys. J. Int.* 175, 686–688. doi:10.1111/j.1365-246x.2008.03926.x

Kim, Y., Liu, Q., and Tromp, J. (2011). Adjoint Centroid-Moment Tensor Inversions. *Geophys. J. Int.* 186, 264–278. doi:10.1111/j.1365-246x.2011.05027.x

Kissling, E., Kradolfer, U., and Maurer, H. (1995). *Program VELEST User's Guide-Short Introduction*. ETH Zurich: Institute of Geophysics.

Kriegerowski, M., Petersen, G. M., Vasyura-Bathke, H., and Ohrnberger, M. (2019). A Deep Convolutional Neural Network for Localization of Clustered Earthquakes Based on Multistation Full Waveforms. *Seismol. Res. Lett.* 90, 510–516. doi:10.1785/0220180320

Kuang, W., Yuan, C., and Zhang, J. (2021). Real-time Determination of Earthquake Focal Mechanism via Deep Learning. *Nat. Commun.* 12, 1–8. doi:10.1038/s41467-021-21670-x

Lanz, E., Maurer, H., and Green, A. G. (1998). Refraction Tomography over a Buried Waste Disposal Site. *Geophysics* 63, 1414–1433. doi:10.1190/1.1444443

Larmat, C., Montagner, J. P., Fink, M., Capdeville, Y., Tourin, A., and Clévédé, E. (2006). Time-reversal Imaging of Seismic Sources and Application to the Great Sumatra Earthquake. *Geophys. Res. Lett.* 33, 26336. doi:10.1029/2006GL026336

Lee, K. H., and Kim, H. J. (2003). Source-independent Full-waveform Inversion of Seismic Data. *Geophysics* 68, 2010–2015. doi:10.1190/1.1635054

Lellouch, A., and Landa, E. (2018). Seismic Velocity Estimation Using Time-Reversal Focusing. *Geophysics* 83 (4), U43–U50. doi:10.1190/geo2017-0569.1

Li, J., Zhang, H., Sadi Kuleli, H., and Nafi Toksoz, M. (2011). Focal Mechanism Determination Using High-Frequency Waveform Matching and its Application to Small Magnitude Induced Earthquakes. *Geophys. J. Int.* 184, 1261–1274. doi:10.1111/j.1365-246x.2010.04903.x

Li, Y., and Alkhalifah, T. (2021). Extended Full Waveform Inversion with Matching Filter. *Geophys. Prospect.* 69 (7), 1441–1454. doi:10.1111/1365-2478.13121

Lomax, A., Virieux, J., Volant, P., and Berge-Thierry, C. (2000). "Probabilistic Earthquake Location in 3D and Layered Models," in *Advances in Seismic Event Location*. Editors C. H. Thurber and N. Rabinowitz (Amsterdam: Kluwer), 101–134. doi:10.1007/978-94-015-9536-0_5

Luo, J., and Wu, R.-S. (2015). Seismic Envelope Inversion: Reduction of Local Minima and Noise Resistance. *Geophys. Prospect.* 63, 597–614. doi:10.1111/1365-2478.12208

Luo, S., and Sava, P. (2011). "A Deconvolution-Based Objective Function for Wave-Equation Inversion," in 81st Annual International Meeting, SEG Technical Program Expanded Abstracts 2011, San Antonio, 2788–2792. doi:10.1190/1.3627773

Luo, Y., and Schuster, G. T. (1991). Wave-equation Traveltime Inversion. *Geophysics* 56, 645–653. doi:10.1190/1.1443081

Lyu, B., and Nakata, N. (2020). Iterative Passive-Source Location Estimation and Velocity Inversion Using Geometric-Mean Reverse-Time Migration and Full-Waveform Inversion. *Geophys. J. Int.* 223, 1935–1947. doi:10.1093/gji/ggaa428

Martin, G. S., Marfurt, K. J., and Larsen, S. (2002). "Marmousi-2: An Updated Model for the Investigation of AVO in Structurally Complex Areas," in SEG International Exposition and 72nd Annual International Meeting, SEG Technical Program Expanded Abstracts 2002, Salt lake City, UT.

McMechan, G. A. (1982). Determination of Source Parameters by Wavefield Extrapolation. *Geophys. J. Int.* 71, 613–628. doi:10.1111/j.1365-246x.1982.tb02788.x

Métivier, L., Brossier, R., Merigot, Q., Oudet, É., and Virieux, J. (2016). An Optimal Transport Approach for Seismic Tomography: Application to 3D Full Waveform Inversion. *Inverse Probl.* 32, 115008. doi:10.1088/0266-5611/32/11/115008

Mora, P. (1987). Nonlinear Two-dimensional Elastic Inversion of Multioffset Seismic Data. *Geophysics* 52, 1211–1228. doi:10.1190/1.1442384

Nakata, N., and Beroza, G. C. (2016). Reverse Time Migration for Microseismic Sources Using the Geometric Mean as an Imaging Condition. *Geophysics* 81, KS51–KS60. doi:10.1190/geo2015-0278.1

Oh, J.-W., and Alkhalifah, T. (2018). Full Waveform Inversion Using Envelope-Based Global Correlation Norm. *Geophys. J. Int.* 213, 815–823. doi:10.1093/gji/ggy031

Operto, S., Miniussi, A., Brossier, R., Combe, L., Métivier, L., Monteiller, V., et al. (2015). Efficient 3-D Frequency-Domain Mono-Parameter Full-Waveform Inversion of Ocean-Bottom Cable Data: Application to Valhall in the Visco-Acoustic Vertical Transverse Isotropic Approximation. *Geophys. J. Int.* 202, 1362–1391. doi:10.1093/gji/ggv226

Oren, C., and Shragge, J. (2022). Passive-seismic Image-Domain Elastic Wavefield Tomography. *Geophys. J. Int.* 228 (3), 1512–1529. doi:10.1093/gji/ggab415

Oren, C., and Shragge, J. (2021). PS Energy Imaging Condition for Microseismic Data - Part 1: Theory and Applications in 3D Isotropic Media. *Geophysics* 86 (2), KS37–KS48. doi:10.1190/geo2020-0476.1

Plessix, R.-E. (2006). A Review of the Adjoint-State Method for Computing the Gradient of a Functional with Geophysical Applications. *Geophys. J. Int.* 167, 495–503. doi:10.1111/j.1365-246x.2006.02978.x

Pratt, R. G. (1999). Seismic Waveform Inversion in the Frequency Domain, Part 1: Theory and Verification in a Physical Scale Model. *Geophysics* 64, 888–901. doi:10.1190/1.1444597

Pratt, R. G., and Worthington, M. H. (1990). Inverse Theory Applied to Multi-Source Cross-Hole Tomography. Part 1: Acoustic Wave-Equation Method1. *Geophys. Prospect* 38, 287–310. doi:10.1111/j.1365-2478.1990.tb01846.x

Rau, R.-J., Wu, F. T., and Shin, T.-C. (1996). Regional Network Focal Mechanism Determination Using 3D Velocity Model and SH/P Amplitude Ratio. *Bull. Seismol. Soc. Am.* 86, 1270–1283.

Ravaut, C., Operto, S., Improta, L., Virieux, J., Herrero, A., and Dell'Aversana, P. (2004). Multiscale Imaging of Complex Structures from Multifold Wide-Aperture Seismic Data by Frequency-Domain Full-Waveform Tomography: Application to a Thrust Belt. *Geophys. J. Int.* 159, 1032–1056. doi:10.1111/j.1365-246x.2004.02442.x

Rawlinson, N., and Sambridge, M. (2003). Seismic Traveltime Tomography of the Crust and Lithosphere. *Adv. Geophys.* 46, 81–198. doi:10.1016/s0065-2687(03)46002-0

Rocha, D., Sava, P., Shragge, J., and Witten, B. (2019). 3D Passive Wavefield Imaging Using the Energy Norm. *Geophysics* 84 (2), KS13–KS27. doi:10.1190/geo2018-0251.1

Ross, Z. E., Meier, M. A., and Hauksson, E. (2018). P Wave Arrival Picking and First-Motion Polarity Determination with Deep Learning. *J. Geophys. Res. Solid Earth* 123, 5120–5129. doi:10.1029/2017jb015251

Sava, P. (2011). Micro-earthquake Monitoring with Sparsely Sampled Data. *J. Pet. Explor Prod. Technol.* 1, 43–49. doi:10.1007/s13202-011-0005-7

Schuster, G. T. (2017). *Seismic Inversion*. Society of Exploration Geophysicists (SEFG). Available at: https://csim.kaust.edu.sa/files/ErSE328.2013/LAB/Chapter.FWIa/index.html.

Shin, C., and Cha, Y. H. (2009). Waveform Inversion in the Laplace-Fourier Domain. *Geophys. J. Int.* 177, 1067–1079. doi:10.1111/j.1365-246x.2009.04102.x

Shin, C., and Cha, Y. H. (2008). Waveform Inversion in the Laplace Domain. *Geophys. J. Int.* 173, 922–931. doi:10.1111/j.1365-246x.2008.03768.x

Sirgue, L., and Pratt, R. G. (2004). Efficient Waveform Inversion and Imaging: A Strategy for Selecting Temporal Frequencies. *Geophysics* 69, 231–248. doi:10.1190/1.1649391

Smith, J. D., Ross, Z. E., Azizzadenesheli, K., and Muir, J. B. (2022). HypoSVI: Hypocenter Inversion with Stein Variational Inference and Physics Informed Neural Networks. *Geophys. J. Int.* 228, 698–710. doi:10.1093/gji/ggab309

Song, C., and Alkhalifah, T. (2019). Microseismic Event Estimation Based on an Efficient Wavefield Inversion. *IEEE J. Sel. Top. Appl. Earth Obs. Remote Sens.* 12, 4664–4671. doi:10.1109/jstars.2019.2946903

Song, C., Alkhalifah, T., and Wu, Z. (2019b). Microseismic Event Estimation and Velocity Analysis Based on a Source-Focusing Function. *Geophysics* 84 (3), KS85–KS94. doi:10.1190/geo2018-0205.1

Song, C., Wu, Z., and Alkhalifah, T. (2019a). Passive Seismic Event Estimation Using Multi-Scattering Waveform Inversion. *Geophysics* 84, KS59–KS69. doi:10.1190/geo2018-0358.1

Stanek, F., and Eisner, L. (2013). "New Model Explaining Inverted Source Mechanisms of Microseismic Events Induced by Hydraulic Fracturing," in 83rd Annual International Meeting, SEG Technical Program Expanded Abstracts 2013, Houston, 2201–2205. doi:10.1190/segam2013-0554.1

Steinberg, A., Vasyura-Bathke, H., Gaebler, P., Ohrnberger, M., and Ceranna, L. (2021). Estimation of Seismic Moment Tensors Using Variational Inference Machine Learning. *J. Geophys. Res. Solid Earth* 126, e2021JB022685. doi:10.1029/2021jb022685

Sun, B., and Alkhalifah, T. (2019). A Robust Waveform Inversion Using a Global Comparison of Modeled and Observed Data. *Lead. Edge* 38 (3), 185–192. doi:10.1190/tle38030185.1

Sun, J., Xue, Z., Formel, S., Zhu, T. Y., and Nakata, N. (2016). "Full Waveform Inversion of Passive Seismic Data for Sources and Velocities: 86th Annual International Meeting," in SEG International Exposition and 86th Annual International Meeting, SEG Technical Program Expanded Abstracts 2016, 1405–1410.

Tape, C., Liu, Q., Maggi, A., and Tromp, J. (2009). Adjoint Tomography of the Southern California Crust. *Science* 325, 988–992. doi:10.1126/science.1175298

Tape, C., Liu, Q., Maggi, A., and Tromp, J. (2010). Seismic Tomography of the Southern California Crust Based on Spectral-Element and Adjoint Methods. *Geophys. J. Int.* 180, 433–462. doi:10.1111/j.1365-246x.2009.04429.x

Tarantola, A. (1984). Inversion of Seismic Reflection Data in the Acoustic Approximation. *Geophysics* 49, 1259–1266. doi:10.1190/1.1441754

Thurber, C. H. (1992). Hypocenter-velocity Structure Coupling in Local Earthquake Tomography. *Phys. Earth Planet. Interiors* 75, 55–62. doi:10.1016/0031-9201(92)90117-e

Uchide, T. (2020). Focal Mechanisms of Small Earthquakes beneath the Japanese Islands Based on First-Motion Polarities Picked Using Deep Learning. *Geophys. J. Int.* 223, 1658–1671. doi:10.1093/gji/ggaa401

van den Ende, M. P., and Ampuero, J. P. (2020). Automated Seismic Source Characterization Using Deep Graph Neural Networks. *Geophys. Res. Lett.* 47, e2020GL088690. doi:10.1029/2020gl088690

Van Leeuwen, T., and Herrmann, F. J. (2013). Mitigating Local Minima in Full-Waveform Inversion by Expanding the Search Space. *Geophys. J. Int.* 195, 661–667. doi:10.1093/gji/ggt258

Van Leeuwen, T., and Mulder, W. A. (2010). A Correlation-Based Misfit Criterion for Wave-Equation Traveltime Tomography. *Geophys. J. Int.* 182, 1383–1394. doi:10.1111/j.1365-246x.2010.04681.x

Virieux, J., and Operto, S. (2009). An Overview of Full-Waveform Inversion in Exploration Geophysics. *Geophysics* 74, WCC1–WCC26. doi:10.1190/1.3238367

Waldhauser, F., and Ellsworth, W. L. (2000). A Double-Difference Earthquake Location Algorithm: Method and Application to the Northern Hayward Fault, California. *Bull. Seismol. Soc. Am.* 90, 1353–1368. doi:10.1785/0120000006

Wang, C., Yingst, D., Farmer, P., and Leveille, J. (2016). "Full-waveform Inversion with the Reconstructed Wavefield Method," in SEG International Exposition and 86th Annual International Meeting, SEG Technical Program Expanded Abstracts 2016, 1237–1241. doi:10.1190/segam2016-13870317.1

Wang, H., and Alkhalifah, T. (2021). Direct Microseismic Event Location and Characterization from Passive Seismic Data Using Convolutional Neural Networks. *Geophysics* 86, KS109–KS121. doi:10.1190/geo2020-0636.1

Wang, H., and Alkhalifah, T. (2018). Microseismic Imaging Using a Source Function Independent Full Waveform Inversion Method. *Geophys. J. Int.* 214, 46–57. doi:10.1093/gji/ggy121

Wang, H., Guo, Q., Alkhalifah, T., and Wu, Z. (2020). Regularized Elastic Passive Equivalent Source Inversion with Full-Waveform Inversion: Application to a Field Monitoring Microseismic Data Set. *Geophysics* 85 (6), KS207–KS219. doi:10.1190/geo2019-0738.1

Warner, M., and Guasch, L. (2016). Adaptive Waveform Inversion: Theory. *Geophysics* 81, R429–R445. doi:10.1190/geo2015-0387.1

Warner, M., Ratcliffe, A., Nangoo, T., Morgan, J., Umpleby, A., Shah, N., et al. (2013). Anisotropic 3D Full-Waveform Inversion. *Geophysics* 78, R59–R80. doi:10.1190/geo2012-0338.1

Willacy, C., van Dedem, E., Minisini, S., Li, J., Blokland, J.-W., Das, I., et al. (2019). Full-waveform Event Location and Moment Tensor Inversion for Induced Seismicity. *Geophysics* 84, KS39–KS57. doi:10.1190/geo2018-0212.1

Witten, B., and Shragge, J. (2017). Image-domain Velocity Inversion and Event Location for Microseismic Monitoring. *Geophysics* 82 (5), KS71–KS83. doi:10.1190/geo2016-0561.1

Wu, R.-S., Luo, J., and Wu, B. (2014). Seismic Envelope Inversion and Modulation Signal Model. *Geophysics* 79, WA13–WA24. doi:10.1190/geo2013-0294.1

Xu, K., Greenhalgh, S. A., and Wang, M. (2006). Comparison of Source-independent Methods of Elastic Waveform Inversion. *Geophysics* 71, R91–R100. doi:10.1190/1.2356256

Yang, T., and Sava, P. (2013). "3D Image-Domain Wavefield Tomography Using Time-Lag Extended Images," in 83rd Annual International Meeting, SEG Technical Program Expanded Abstracts 2013, Houston, 4816–4821. doi:10.1190/segam2013-0279.1

Yang, Y., and Engquist, B. (2018). Analysis of Optimal Transport and Related Misfit Functions in Full-Waveform Inversion. *Geophysics* 83, A7–A12. doi:10.1190/geo2017-0264.1

Zhang, H., and Thurber, C. H. (2003). Double-difference Tomography: The Method and its Application to the Hayward Fault, California. *Bull. Seismol. Soc. Am.* 93, 1875–1889. doi:10.1785/0120020190

Zhang, X., Zhang, J., Yuan, C., Liu, S., Chen, Z., and Li, W. (2020). Locating Induced Earthquakes with a Network of Seismic Stations in Oklahoma via a Deep Learning Method. *Sci. Rep.* 10, 1–12. doi:10.1038/s41598-020-58908-5

Zhang, Y., and Wang, D. (2009). Traveltime Information-Based Wave-Equation Inversion. *Geophysics* 74, WCC27–WCC36. doi:10.1190/1.3243073

Zhong, Y., and Liu, Y. (2019). Time-domain Acoustic Full-Waveform Inversion Based on Dual-Sensor Seismic Acquisition System. *J. SEISMIC Explor.* 28, 103–120.

Zhu, L., and Ben-Zion, Y. (2013). Parametrization of General Seismic Potency and Moment Tensors for Source Inversion of Seismic Waveform Data. *Geophys. J. Int.* 194, 839–843. doi:10.1093/gji/ggt137

Conflict of Interest: The authors declare that the research was conducted in the absence of any commercial or financial relationships that could be construed as a potential conflict of interest.

Publisher's Note: All claims expressed in this article are solely those of the authors and do not necessarily represent those of their affiliated organizations, or those of the publisher, the editors and the reviewers. Any product that may be evaluated in this article, or claim that may be made by its manufacturer, is not guaranteed or endorsed by the publisher.

frontiers | Frontiers in Earth Science

ORIGINAL RESEARCH
published: 05 July 2022
doi: 10.3389/feart.2022.945022

Moment Tensor Solutions for Earthquakes in the Southern Korean Peninsula Using Three-Dimensional Seismic Waveform Simulations

Jung-Hun Song[1], *Seongryong Kim*[2]*, *Junkee Rhie*[1] *and Donghee Park*[1,3]

[1]School of Earth and Environmental Sciences, Seoul National University, Seoul, South Korea, [2]Department of Earth and Environmental Sciences, Korea University, Seoul, South Korea, [3]Central Research Institute, Korea Hydro & Nuclear Power Co., Ltd., Daejeon, South Korea

Precise estimates of earthquake source properties are crucial for understanding earthquake processes and assessing seismic hazards. Seismic waveforms can be affected not only by individual event properties, but from the Earth's interior heterogeneity. Therefore, for accurate constraints on earthquake source parameters, the effects of three-dimensional (3D) velocity heterogeneity on seismic wave propagation need evaluation. In this study, regional moment tensor solutions for earthquakes around the southern Korean Peninsula were constrained based on the spectral-element moment tensor inversion method using a recently developed high-resolution regional 3D velocity model with accurate high-frequency waveform simulations. Located at the eastern margin of the Eurasian plate, the Korean Peninsula consists of complex geological units surrounded by thick sedimentary basins in oceanic areas. It exhibits large lateral variations in crustal thickness (> 10 km) and seismic velocity (>10% dlnVs) at its margins in the 3D model. Seismic waveforms were analyzed from regional earthquakes with local magnitudes > 3.4 that occurred within and around the peninsula recorded by local broadband arrays. Moment tensor components were inverted together with event locations using the numerically calculated Fréchet derivatives of each parameter at periods ≥ 6 s. The newly determined solutions were compared with the results calculated from the one-dimensional (1D) regional velocity model, revealing a significant increase in a double-couple component of > 20% for earthquakes off of the coastal margins. Further, compared to initial solutions, ≤ 5 km change in depth was observed for earthquakes near the continental margin and sedimentary basins. The combination of a detailed 3D crustal model and accurate waveform simulations led to an improved fit between data and synthetic seismograms. Accordingly, the present results provide the first confirmation of the effectiveness of using 3D velocity structures for accurately constraining earthquake source parameters and the resulting seismic wave propagation in this region. We suggest that accurate 3D wave simulations, together with improved source mechanisms, can contribute a reliable assessment of seismic hazards in regions with complex continental margin structures and sedimentary basins

OPEN ACCESS

Edited by:
Mourad Bezzeghoud, Escola de Ciência e Tecnologia, Universidade de Évora, Portugal

Reviewed by:
Rohtash Kumar, Banaras Hindu University, India
Bouhadad Youcef, National Earthquake Engineering Center (CGS), Algeria
José Borges, University of Evora, Portugal

***Correspondence:**
Seongryong Kim
seongryongkim@korea.ac.kr

Specialty section:
This article was submitted to Solid Earth Geophysics, a section of the journal Frontiers in Earth Science

Received: *16 May 2022*
Accepted: *14 June 2022*
Published: *05 July 2022*

Citation:
Song J-H, Kim S, Rhie J and Park D (2022) Moment Tensor Solutions for Earthquakes in the Southern Korean Peninsula Using Three-Dimensional Seismic Waveform Simulations. Front. Earth Sci. 10:945022. doi: 10.3389/feart.2022.945022

from offshore earthquakes whose seismic waveforms can be largely affected by 3D velocity structures.

Keywords: earthquake source parameters, seismic waveform simulation, 3D velocity model, spectral-element method, Southern Korean Peninsula

INTRODUCTION

Accurate determination of earthquake source parameters (e.g., hypocenter, focal mechanisms, and moment tensors) is important for understanding earthquake processes, elastic responses of a medium to tectonic stresses, and strong ground motions affected by the sources (Talwani, 2014; Gallovič et al., 2019). Notably, seismic waveforms have been routinely used to improve source property estimates (Ekström et al., 2012), as they contain more information due to the superposition of different seismic signals across amplitudes and phases (Dreger and Helmberger, 1993; Kim et al., 2011). Seismic waveforms are responses to wave propagation through the Earth's structure, as well as earthquake processes. Though averaged one-dimensional (1D) structural models are useful in most practices (Dreger and Helmberger, 1993; Ford et al., 2009), constrained source properties can often be biased from unaccounted for three-dimensional (3D) structural heterogeneity (Hejrani et al., 2017; Li et al., 2018), such as thick sedimentary basins, or sharp lateral variations in crustal thickness at the continental margin (Tape et al., 2010). Additionally, signals from small-to-moderate regional earthquakes (moment magnitude (M_w) ~3.0–5.5) are generally detected by regional arrays (epicentral distance < 500 km) over relatively shorter period bands (< 40 s), in which seismic wave propagation becomes increasingly sensitive to smaller volumetric or sharp interfacial structures in the crust and upper mantle (e.g., Fichtner and Tkalčić, 2010). Therefore, for more precise constraints on earthquake source parameters across various magnitudes, the effects of 3D velocity heterogeneity on seismic wave propagation require evaluation.

With recent advancements in computational capacity, the calculation of 3D seismic wave simulations has become more readily attainable and has been successfully applied for synthesizing full seismic waveforms and ground shaking with the inclusion of more accurate 3D Earth structures (Liu et al., 2004; Lee et al., 2022). Indeed, 3D velocity model analyses have shown to improve moment tensor solutions for a more accurate alignment with actual regional tectonic features (Hejrani et al., 2017; Takemura et al., 2020). Further, accurate wave simulations enabled with a 3D velocity model show that slip processes can be resolved more precisely at higher frequencies (> 0.1 Hz) for earthquakes at shallow depths (< 2 km; Hejrani and Tkalčić, 2020) or complex tectonic systems (Julian et al., 1997; Vavryčuk, 2011). Despite the effectiveness of considering 3D velocity structures, the number of local and regional studies constraining earthquake source parameters based on the calculations of 3D wave propagations is limited to Iceland (Fichtner and Tkalčić, 2010), Taiwan (Lee et al., 2010), the Australian region (Hingee et al., 2011; Hejrani and Tkalčić, 2020), Papua New Guinea and the Solomon Islands (Hejrani et al., 2017), the Kanto region (Takemura et al., 2020), Los Angeles region (Wang and Zhan, 2020), Groningen Field (Willacy et al., 2018), and the southern Sichuan Basin (Huo et al., 2021). In part, this limitation is due to the lack of regional 3D velocity models with reasonable resolutions and/or insufficient computational resources to accommodate accurate 3D wave simulations.

Here, we present a newly estimated moment tensor catalog based on 3D full-waveform simulations in the southern Korean Peninsula (KP). The combined presence of a regional high-resolution 3D velocity model and accelerated processing through advanced graphical processing units (GPUs) allow for the more efficient calculation of synthetic waveforms reflecting the 3D heterogeneity. The KP is a continental part at the eastern margin of the Eurasian plate. Tectonically, the KP is under a stable intraplate regime, with compressive tectonic forces controlled by the convergence of the Eurasian plate (EP), Philippine Sea plate (PSP), and the Pacific plate (PP; **Figure 1**). Although this region has been classified as a tectonically stable intraplate area, several small-to-moderate sized earthquakes (M_w ~3–5) occur annually, with two of the largest earthquakes (M_w > 5.4) in instrumentally recorded history (generating ground shaking-caused damages near the epicenters and felt throughout the southern KP) occurring within the last 5 years, (Kim Y. et al., 2016; Kim K. H. et al., 2018). Previous studies have applied various techniques for estimating detailed earthquake moment tensors and resultant ground shaking based on 1D regional velocity models (Rhie and Kim, 2010; Kim et al., 2011; Hong and Choi, 2012; Hong et al., 2020; Park et al., 2020). With increasing concern of possible damaging earthquakes, several seismic stations have been deployed over the past decade in the southern KP (**Figure 1A**). The accumulated continuous waveform records from these stations have enabled the development of high-resolution crust and upper mantle velocity models through ambient noise tomography for the southern KP and northeast Asia, resolving lateral structures down to ~20 km (Lee et al., 2015; Kim. et al., 2016b; Rhie et al., 2016). Elsewhere, a regional 3D velocity model has successfully enhanced the accuracy of hypocenter locations of the 2017 Pohang earthquake sequences (Jung et al., 2022). Further, seismic wave propagation simulations calculated with the 3D velocity model have shown that local amplification of ground motions caused by complex wave propagation effects can be reproduced accurately up to 1 Hz, with improved predictive accuracy (Lee et al., 2022). These results support that 3D models well represent fine details of velocity heterogeneity in this region. Furthermore, GPUs were employed here to accelerate the spectral element wavefield simulation (Komatitsch et al., 2010), as they can reduce the computational time of synthetic wave propagation

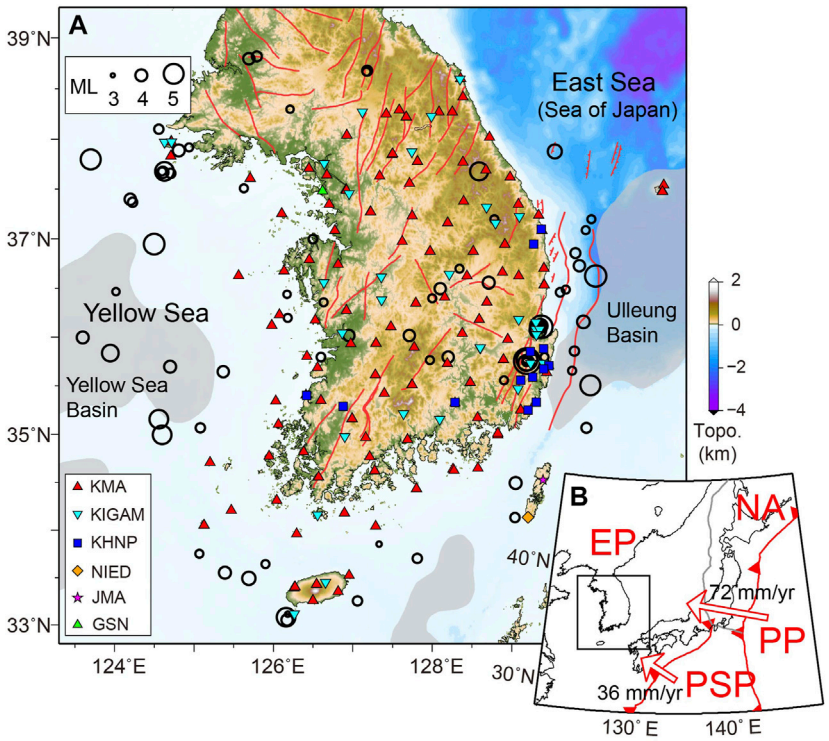

FIGURE 1 | Distribution of seismic stations and earthquakes within the study area. **(A)** Stations are indicated by solid symbols, with different colors and shapes for different networks—KMA, Korea Meteorological Administration; KIGAM, Korea Institute of Geoscience and Mineral Resources, KHNP, Korea Hydro & Nuclear Power; NIED, National Research Institute for Earth Science and Disaster Resilience; JMA, Japan Meteorological Agency; GSN, Global Seismic Network. Black circles indicate local events (M_L > 3.4) occurring between 2003 and 2021, with corresponding circle sizes indicating magnitude. Red lines delineate major faults (Chough et al., 2018), whereas gray shaded regions indicate sedimentary basins with a thickness > 1 km (Straume et al., 2019). **(B)** a regional tectonic setting, where subduction boundaries are indicated by red saw-toothed lines, while other convergent plate boundaries are indicated by gray lines (Bird, 2003). Red arrows indicate the movement direction of the Philippine Sea and Pacific plates with respect to the Eurasian Plate (velocities indicated). The study area is indicated by the black square. EP, Eurasian Plate; PP, Pacific Plate; PSP, Philippine Sea Plate; NA, North American Plate.

by ≤ 20-times compared to CPU clusters (Komatitsch et al., 2010). Synthetics and their Fréchet derivatives were computed for six moment tensor components and three location parameters (longitude, latitude, and depth) to be used for the inversion of earthquake source parameters for each earthquake. In particular, shorter period waveforms (6–30 s) were incorporated to better resolve source complexities and reduce moment tensor dependencies in source depth (Julian et al., 1997; Mustać et al., 2020). The inversion results and synthetic waveforms obtained with the regional 3D and 1D velocity models were compared, ultimately revealing that the more accurate waveform simulation technique with the 3D velocity model resulted in generally better fits between data and synthetic seismograms, with more reliable focal mechanism solutions in this region.

DATA AND METHOD

Event Data and Initial Solutions

Regional earthquakes with local magnitudes (M_L) > 3.4 occurring between 2003 and 2021 within and around the southern KP (33.0°–38.2° N, 123.8°–130.3° E) were identified from the event catalog of the Korean Meteorological Agency (KMA; N = 73 events). Further, we obtained three-component seismic waveforms for these events recorded by broadband seismometers from various networks (**Figure 1A**). The raw seismogram data were deconvolved from instrument responses and converted to displacement. Two horizontal components (E and N components) were rotated to radial (R) and tangential (T) components based on the KMA-provided event locations. Station orientations were corrected based on the measurement of seismometer misorientation by teleseismic P-wave polarization (Son et al., 2021). To obtain initial earthquake moment tensor solutions for the subsequent 3D analysis and reject earthquakes with poor data quality, we performed 1D time-domain moment tensor inversions (TDMT, Dreger and Helmberger, 1993) with a regional 1D velocity model (Kim et al., 2011). Green's functions were calculated using a frequency-wavenumber integration method (Saikia, 1994) based on the actual epicentral distances of each station. For larger earthquakes, we applied a 20–40 s band-pass filter, and for smaller events (M_w < 4), a relatively short-period band of 10–30 s was used to account for frequency contents of corresponding earthquakes and to increase signal-to-noise ratios of the observed waveforms (Rhie and Kim, 2010). We

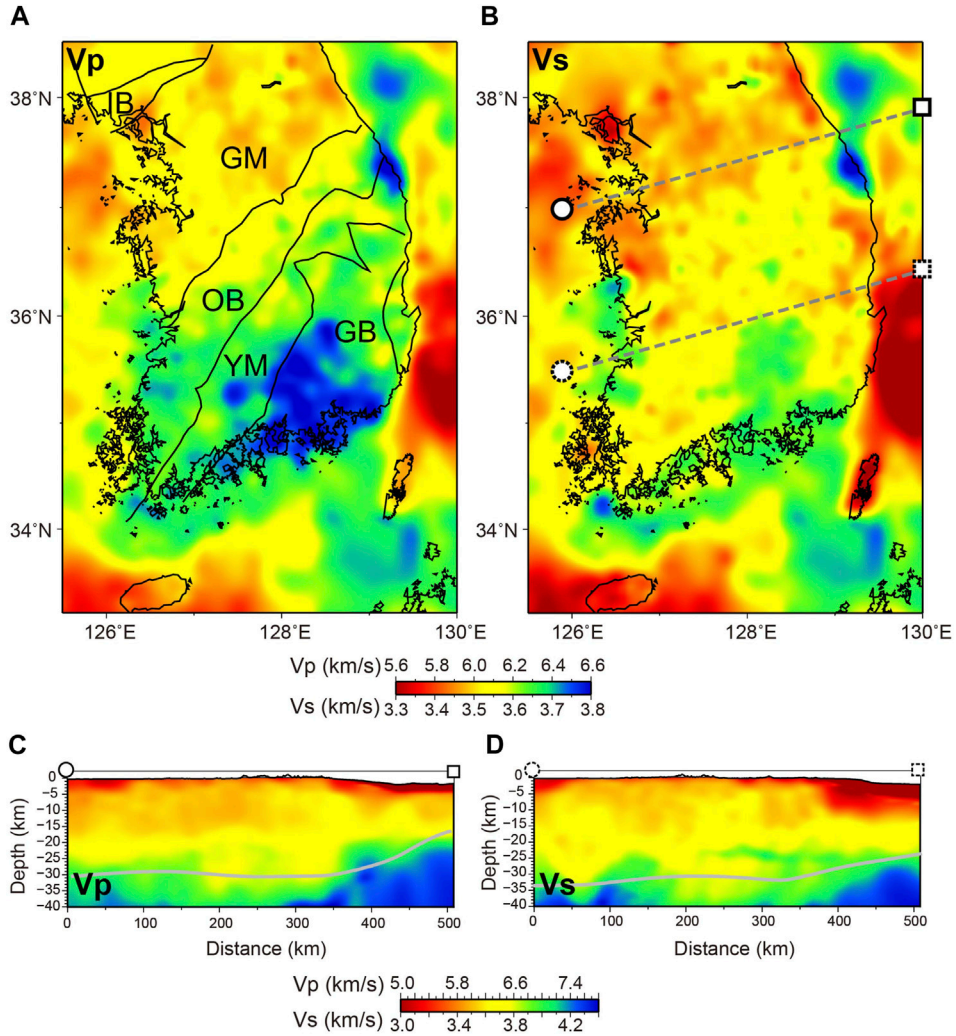

FIGURE 2 | Regional three-dimensional seismic velocity model of the southern Korean Peninsula: **(A)** Horizontal cross-section of P-wave velocity at 10 km depth. Black solid lines indicate the boundaries of different geologic provinces; **(B)** Horizontal cross-section of S-wave velocity at 10 km depth; **(C,D)** represent vertical cross-sections of P- and S-wave velocities, respectively. Gray solid curves are Moho depths from receiver function studies (e.g., Chang and Baag, 2007; Kim et al., 2015). Locations of vertical profiles are indicated in **B**: GB, Gyeongsang Basin; GM, Gyeonggi Massif; IB, Imjingang Belt; OB, Okcheon Belt; YM, Yeongnam Massif.

inverted for deviatoric moment tensor solutions of each event with varying centroid depths, while fixing lateral locations (i.e., longitude and latitude), as provided by the earthquake catalog. The event depth varied between 0 and 30 km at increments of 0.5 km, and the final depth was determined to have the lowest misfit between the synthetic and observed waveforms. During the inversion process, time shifts of each station were determined for the alignment of synthetic seismograms with the observed waveforms based on cross-correlations to account for unmodeled propagation effects. Ultimately, 45 events were obtained for which both moment tensors and centroid depths could be stably determined, with variance reductions > 60% and the number of stations showing clear three-component waveforms > 10. Events that occurred in the northern KP were excluded due to limited regional resolution of 1D and 3D velocity structures. The chosen events were analyzed further in the moment tensor inversion *via* the 3D waveform simulation.

Three-Dimensional Velocity Model

The 3D regional velocity model of the southern KP was constructed based on ambient noise tomography (**Figure 2**). The model data were obtained from multiple regional ambient noise datasets with different spatial scales. In the southern KP, the velocity model was constructed using 1–6 s group velocity data measured at 150 accelerometer stations and 5–30 s group and phase velocity data estimated at 37 regional broadband stations (Rhie et al., 2016). The velocity model outside the southern KP was constrained by 25–40 s phase velocity data collected at broadband stations in northeast Asia (Kim. et al., 2016b). The lateral variations of phase and group velocity for period ranges ≤ 1 Hz were calculated based on the trans-dimensional and

hierarchical Bayesian inversion technique (Kim. et al., 2016a; Rhie et al., 2016). The 1D depth profiles from surface-wave dispersions were inverted *via* a Bayesian approach and used to construct the 3D shear velocity model (Kim et al., 2017). Based on the lateral variation of the compressional to shear-wave velocity ratio (Vp/Vs) estimated from the receiver function method (Chang and Baag, 2007), 3D modeled P-wave velocities were converted from the shear velocity. A simple empirical relationship between seismic velocity and density (Christensen and Mooney, 1995) was employed to construct a density model covering the southern KP and its coastal regions, including the western part of the East Sea (Sea of Japan) and the eastern Yellow Sea, extending to depths of 120 km. For the crust and uppermost mantle, the horizontal resolution of the 3D model extended to 25–30 km within the continental area and 50–75 km in the offshore regions. These resolutions were determined based on synthetic recovery test results using checkerboard and structural patterns (Kim. et al., 2016b; Rhie et al., 2016). We confirmed that the modeled region successfully recovered the original input pattern. The velocity grids in the continental and oceanic regions were sampled at horizontal intervals of 5 and 25 km, respectively, with a common depth spacing of 0.5 km.

Waveform Simulations Using Spectral-Element Method

The spectral-element method implemented in the SPECFEM3D Cartesian software package (Komatitsch and Tromp, 1999) was used for the accurate calculation of 3D elastic wave propagation. This method has previously been used to simulate seismic wave propagation on both global and regional scales with 3D Earth structures (Komatitsch and Tromp, 2002; Tape et al., 2009). Further, this method exploits the geometric flexibility of the finite-element method with an accurate representation of the wave fields based on high-degree Lagrange polynomials *via* pseudospectral techniques (Komatitsch et al., 2004). Surface topography, bathymetry, and internal discontinuities (e.g., Moho) can be accommodated into the spectral element mesh. We constructed a mesh that covers 817.1 x 713.4 km (123.5°–132.5° E and 32.8°–39.3° N) and extends to 85 km depth. The mesh encompasses all stations and earthquakes in the southern KP, as well as its coastal regions (**Figure 1A**). Spectral elements were defined to maintain a regular spacing of ~3 km in the model domain, which contained 1.89 x 10^6 elements with 1.19 x 10^8 grid points. We applied a free surface condition at the topographic surface and the Stacey absorbing boundary condition at the bottom and sides (Komatitsch and Tromp, 2003). Based on the minimum shear wave velocity of the regional velocity model and spacing of spectral elements, synthetic seismograms could be resolved up to 0.5 Hz. We employed a GPU-enabled spectral-element solver of the seismic wave equation.

Moment Tensor Inversion

A seismic moment tensor and event location were determined using the regional 3D velocity model based on the spectral-element moment tensor inversion method (Liu et al., 2004). This method uses spectral-element simulations to calculate the sensitivity of seismic waveforms to source parameters (i.e., the Fréchet derivatives). For each earthquake, we inverted six moment tensor components (Mrr, Mtt, Mpp, Mrt, Mrp, and Mtp) and three location components (longitude, latitude, and depth). Accordingly, a total of 10 simulations were conducted, of which 9 consisted of calculating synthetics for the Fréchet derivatives, and the remaining simulation constructed synthetic seismograms with an initial moment tensor solution determined by the TDMT method. As the synthetics (s) can be represented by linear combinations of the moment tensor elements (m), the derivatives $\frac{ds}{dm_i}$ (where index i varies from 1 to 6) can be obtained by forward calculations for moment tensors that have a nonzero element for an individual ith component, while all other elements are zero. In the case of an inversion for the six elements of the moment tensor m = [Mrr, Mtt, Mpp, Mrt, Mrp, Mtp] , the synthetics $s(t, m)$ may be represented by linear combinations of the Fréchet derivatives with respect to moment tensor elements: **Eq. 1**

$$s(t,m) = \sum_{i=1}^{6} \frac{ds}{dm_i}(t) m_i \tag{1}$$

The Fréchet derivatives of location parameters can be constructed based on the differences between synthetic seismograms computed with a moment tensor, that is, spatially separated from the initial location and the initial synthetic seismograms. In contrast to the moment tensor components, the synthetic waveforms have a nonlinear relationship with location parameters. Assuming that the initial solution was close to the true solution, a linear gradient calculated with step lengths of 1 km for depth, and 250 m for latitude and longitude, was applied from the initial location. Step lengths were determined based on the numerical test results showing the quasi-linearity of gradients around the initial location (Liu et al., 2004). Using the initial point-source parameters as the starting solution (m^0) , the synthetics can be linearized with respect to the initial parameters as **Eq. 2**

$$s(t,m) = s(t,m^0) + \sum_{i=1}^{n} \frac{ds}{dm_i}(t,m^0)(m_i - m_i^0), \tag{2}$$

where n is the number of inversion parameters, which include six elements of moment tensor with three location parameters. Given a set of source parameters, the misfit between the data and the synthetics was defined as the least-square waveform misfit function **Eq. 3**

$$E(m) = \frac{1}{2A} \sum_{j=1}^{N} w_j \int \left[d_j(t) - s_j(t,m) \right]^2 dt, \tag{3}$$

where A is a normalization factor, N is the number of individual waveforms, and w_j is the weights of j^{th} station data, which is based upon the station's azimuth, epicentral distance, and data components (Liu et al., 2004). The nonlinear Newton's iterative solver (Conte and Boor, 1980) was applied to resolve this nonlinear equation that minimizes a waveform misfit function based on the calculated gradients (For details about derivation of the nonlinear equation and data weights, see the appendix of Liu et al., 2004).

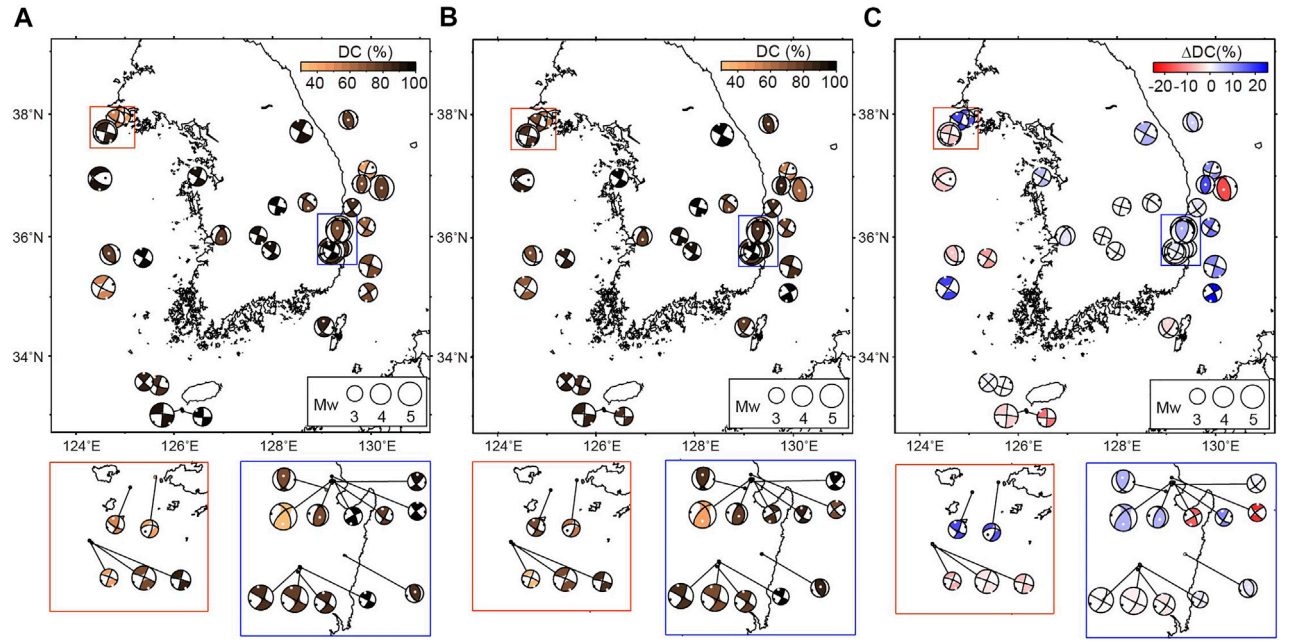

FIGURE 3 | Moment tensor solutions obtained with the: **(A)** regional 1D velocity model and **(B)** regional 3D velocity model. Beach balls in **A** and **B** indicate focal mechanisms, with the projection of the fault orientation and slip on the lower half of a sphere surrounding the hypocenter, and the colored (non-colored) quadrants indicating motion towards (away) those quadrants. Colors of each beachball indicate the proportion of a double couple component (DC %). **(C)** Differences in the DC component proportions between 3D and 1D focal mechanisms. Black and white circles on each beach ball indicate the directionality of the maximum and minimum principal compressive stresses P and T axes, respectively. Colored boxes at the bottom are enlarged maps of regions indicated by orange and blue squares.

We applied a band-pass filter with a period range from 6 to 30 s for the synthetic seismograms, their derivatives, and observed data. Time windows of waveforms were selected to be used for the inversion process *via* an automated time-window selection software (FLEXWIN, Maggi et al., 2009). This program automatically selects time windows around potential seismic phases based on quantities evaluating waveform shape (e.g., amplitudes, signal-to-noise ratio, short-term-average/long-term averages) for comparing synthetic and observed seismograms. Selected time windows were manually checked for all seismograms. Only those that included waveforms showing high similarities (cross-correlation coefficients > 0.7, log amplitude ratios < 1.5) between the observed and synthetics generated by the initial focal mechanism were incorporated. During the inversion process, time shifts of the synthetics with respect to the data were applied to obtain the optimal correlation between the two, as such calculations help extract the contributions of the 3D velocity structure to seismic waveforms and source parameters by removing time shifts originating from errors in event origin time, location, or derived from inaccuracies in the 3D velocity structure due to limited resolution (Komatitsch et al., 2004; Hejrani et al., 2017). Although the application of time shifts has been demonstrated to be useful for reducing travel time effects of lateral velocity heterogeneity (Zhao and Helmberger, 1994), they cannot fully account for the complex nature of 3D wave propagation effects in regions where seismic phases and amplitudes can be distorted (Liu et al., 2004).

Bootstrap analyses were conducted to assess uncertainties of the determined source parameters and the reliability of reduction of an amplitude misfit following inversion. We generated 100 solutions based on randomly selected seismograms of each event and calculated averages and standard deviations of locations, moment tensor components, a percentage of a double couple (DC) component, and the misfit between synthetic and observed waveforms.

RESULTS

We compared the inversion results obtained with waveform simulations using the 3D and the 1D velocity models, and **Figure 3** shows focal mechanism solutions and percentages of the DC component for each event. The results indicated general increases in the proportion of DC components (3–25%) for the earthquakes in the continental southern KP, as well as the continental margin off the east coast when the 3D velocity model was used (**Figure 3A**). The continental events exhibited high DC proportions overall (> 80%) in both models (**Figures 3A,B**), with small increases (3–7%) in the 3D model. These increases in the DC component were considered reliable given that the moment tensor components were determined with small uncertainties (< 3%) (**Figure 4B**). Relatively large increases in DC components (15–25%) were found for earthquakes in the offshore southeastern continental margin, and these increments were deemed reliable given that the uncertainty of a DC component

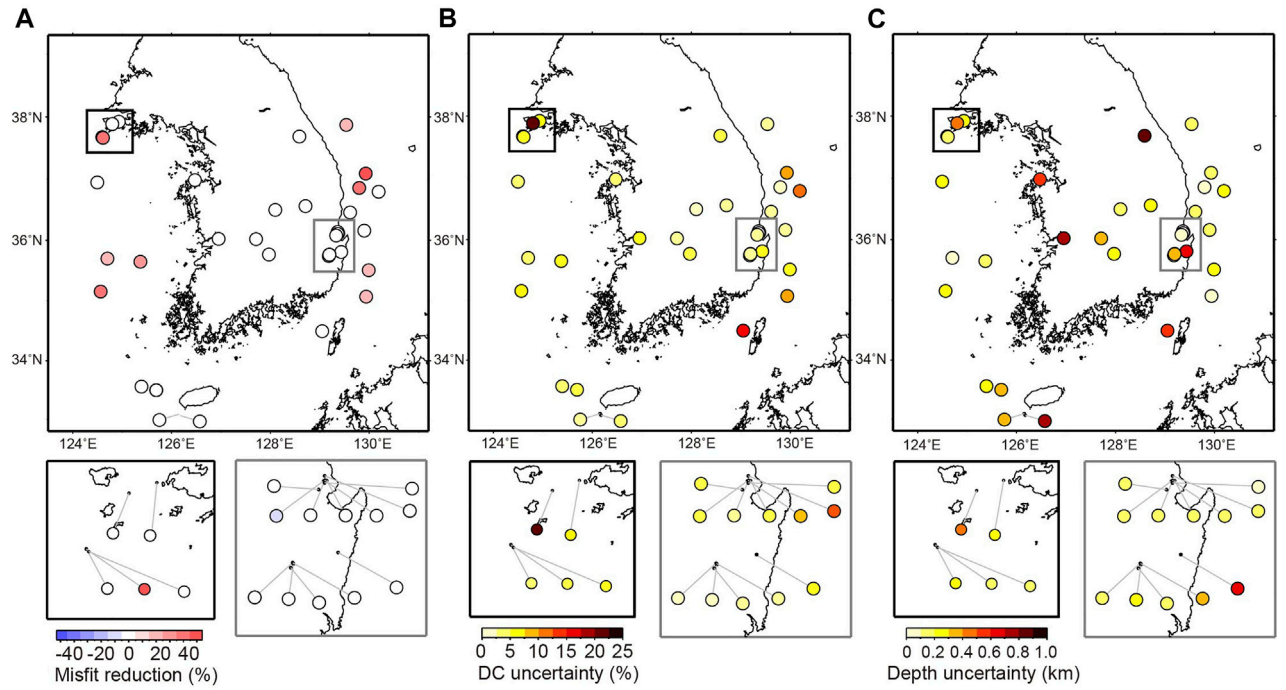

FIGURE 4 | (A) Reduction of amplitude misfits between the observed and synthetic seismograms for the wave simulations using source parameters constrained by the 3D vs. 1D velocity models. The misfit reduction was calculated as $100 \times (\frac{\textit{residual misfit in 1D}-\textit{residual misfit in 3D}}{\textit{residual misfit in 1D}})$, where residual misfits indicate the remaining amplitude misfits following the source parameter inversion process. Only misfit reduction values > 1 standard deviation (as determined by bootstrap analysis) are colored. **(B)** Uncertainties in the proportion of DC components for the focal mechanism solutions, as determined by the 3D velocity model. **(C)** Uncertainties in focal depth determined with the 3D velocity model. Boxes at the bottom are enlarged maps of regions indicated by black and gray squares.

was determined to be < 10% for these earthquakes (**Figure 4B**). Meaningful increases in the percentage of DC components also exist for earthquakes in the Yellow Sea and the northwestern continental margin of the southern KP. The mainshock (M_w = 5.4) of the earthquake sequences in the Pohang area (**Figure 3**, top of the blue box) and a moderate-sized (M_w ~5) earthquake offshore of Uljin in the eastern continental margin show comparably low DC percentage than other earthquakes in the 3D model.

All comparisons between the observed and synthetic waveforms calculated using the 1D and 3D models were made after applying a band pass filter to each dataset within a common period range. A meaningful decrease in waveform misfit (~5–50%) between synthetic and observed waveforms was found when the 3D velocity model was used (**Figure 4**). Notable improvements (> 30%) in waveform fitting were found for the events in the offshore eastern and western coastal margins. There were notable differences in amplitudes and arrival times of surface waves for the synthetic waveforms between the 1D and 3D velocity models when assessing offshore earthquakes (**Figure 5**), where 3D model synthetic waveforms showed a better fit with observations.

Figure 6 shows the changes in centroid depths for source parameters determined with the 3D velocity model as compared to the initial solutions, revealing an overall increase in depth (~1–5 km) for the offshore events along the eastern continental margin. Given that uncertainties in centroid depth were estimated as ~0.3 km (**Figure 4C**), the observed depth changes were significant. The determined centroid depths here for events at the offshore eastern coastal margins extended deeply to ~19 km (**Figure 6A**, cross-section a-a').

Figure 7 compares the moment magnitude (M_w) constrained with 3D and 1D velocity models. Generally, the magnitude values showed a 1:1 correlation between estimates. Relatively large discrepancies (~0.05–0.1) were found for those that occurred in the offshore continental margin.

DISCUSSIONS

The overall high DC values (>80%) of continental earthquakes indicated that the moment tensor of earthquakes was well represented by shear slip on a planar fault. Most of the regional earthquakes in the southern KP exhibited shear slip on a planar fault with a high DC percentage (>80%) (e.g., Rhie and Kim, 2010; Kim Y. et al., 2016), which can be reasonably considered as point sources with minimal fault geometry and slip history complexity, owing to their small magnitudes (Mw < 5). Therefore, additional increases in DC values with the 3D model potentially suggest that the moment tensor solutions can be more precisely constrained *via* the calculation of accurate wave propagations.

Except for some earthquakes (especially in volcanic and geothermal areas) or explosions, rupture processes of most small-to-moderate sized tectonic earthquakes can be represented by shear

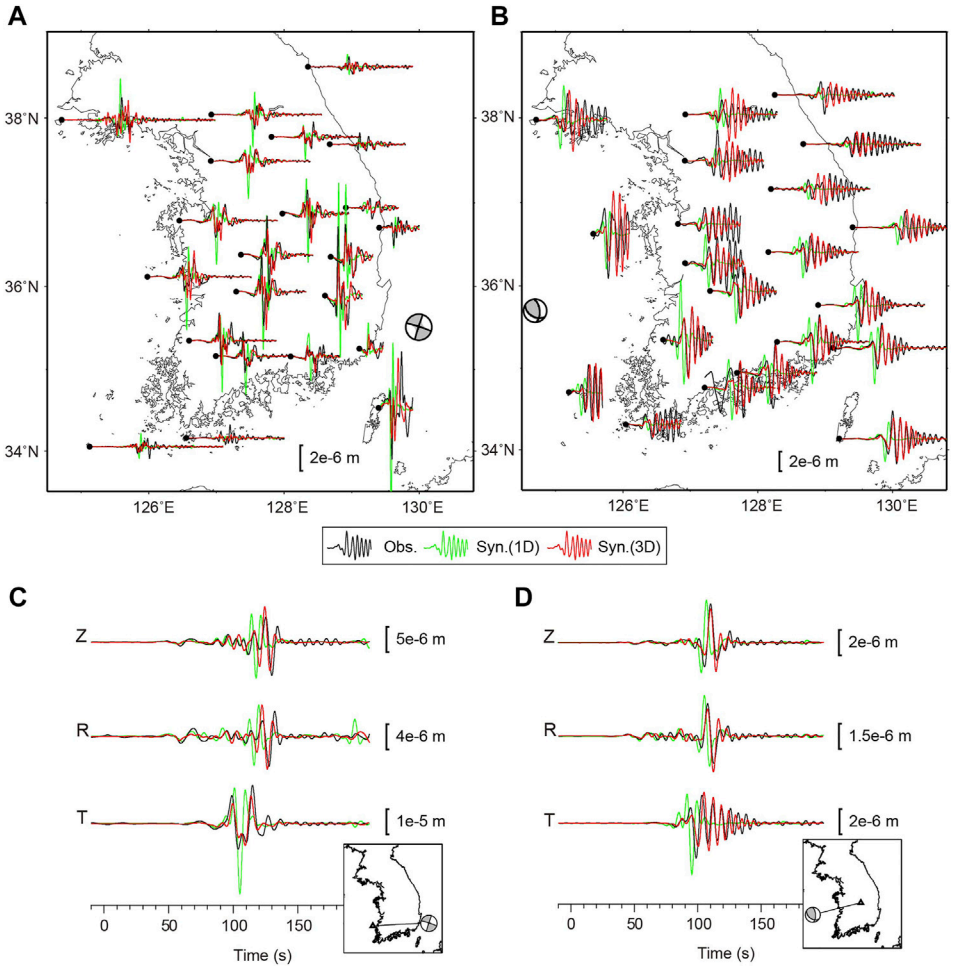

FIGURE 5 | Example comparisons of synthetic seismograms and observations: **(A,C)** Waveforms of the event (moment magnitude (M_w) 4.7) that occurred along the southeastern offshore of the Korean Peninsula at 11:33:03 (UTC) on 7-5-2016, and **(B,D)** Waveforms of the event (M_w 4.1) that occurred in the Yellow Sea at 00:40:40 (UTC) on 8-21-2021. **A** and **B** show tangential component waveforms, where wiggles in black are the observed seismograms, while those in green are the synthetic seismograms calculated with moment tensor solutions constrained by time-domain moment tensor inversions (TDMTs) *via* the regional 1D velocity model. Red seismograms are the synthetics of 3D waveform simulation calculated with moment tensor solutions obtained from the regional 3D velocity model. Beach balls in gray indicate focal mechanisms of each event. Frequency bands for the waveforms in **A** and **C** ranged from 0.033 to 0.33 Hz, whereas those in **B** and **D** ranged from 0.033 to 0.18 Hz.

faulting on a planar fault, in which the moment tensor components are composed solely of DC components (i.e., DC = 100%; Julian et al., 1998); however, the moment tensors constrained with real datasets often reveal DC percentages < 100%. Such decreases in DC percentage can be derived from various origins, including uncertainties in source parameters due to limited station azimuthal coverage, lower signal-to-noise ratios of the observed waveforms, inaccurate waveform predictions due to unaccounted for 3D heterogeneity, or complex source properties (e.g., slip on a non-planar fault) (Julian et al., 1998). Under the same condition in dataset and source-receiver pairs, the meaningful increases in DC components with the 3-D regional velocity model here indicate that portions of a non-DC component of source parameters can be reduced by accounting for lateral velocity variations. Relatively large increases in DC components (15–25%) were observed for earthquakes in the offshore southeastern continental margin, where large lateral velocity variations (> 10%) in the crust existed for the eastern continental margin of the KP. The structures reflect transitions from the continental to oceanic crust, or thick sedimentary basins formed by late Cretaceous to Cenozoic rifting processes (Cho et al., 2004; Hong, 2010; Kim et al., 2019). The present results show that these complex structures were well reflected in the regional 3D velocity model (**Figure 2B**), thereby improving the depiction of seismic full waveforms by accurately constraining moment tensors for offshore events.

Even with datasets of clear waveforms and good azimuthal coverage, the mainshock (M_w = 5.4) of the earthquake sequences in the Pohang area (**Figure 3**, top of the blue box), consistently showed low DC percentage in both models (1D ~ 35%, 3D ~ 45%). Notably, this event has been reported to be the first non-DC event in South Korea (Song et al., 2018; Lee et al., 2020). Further, there are general increments in DC percentage with overall high DC

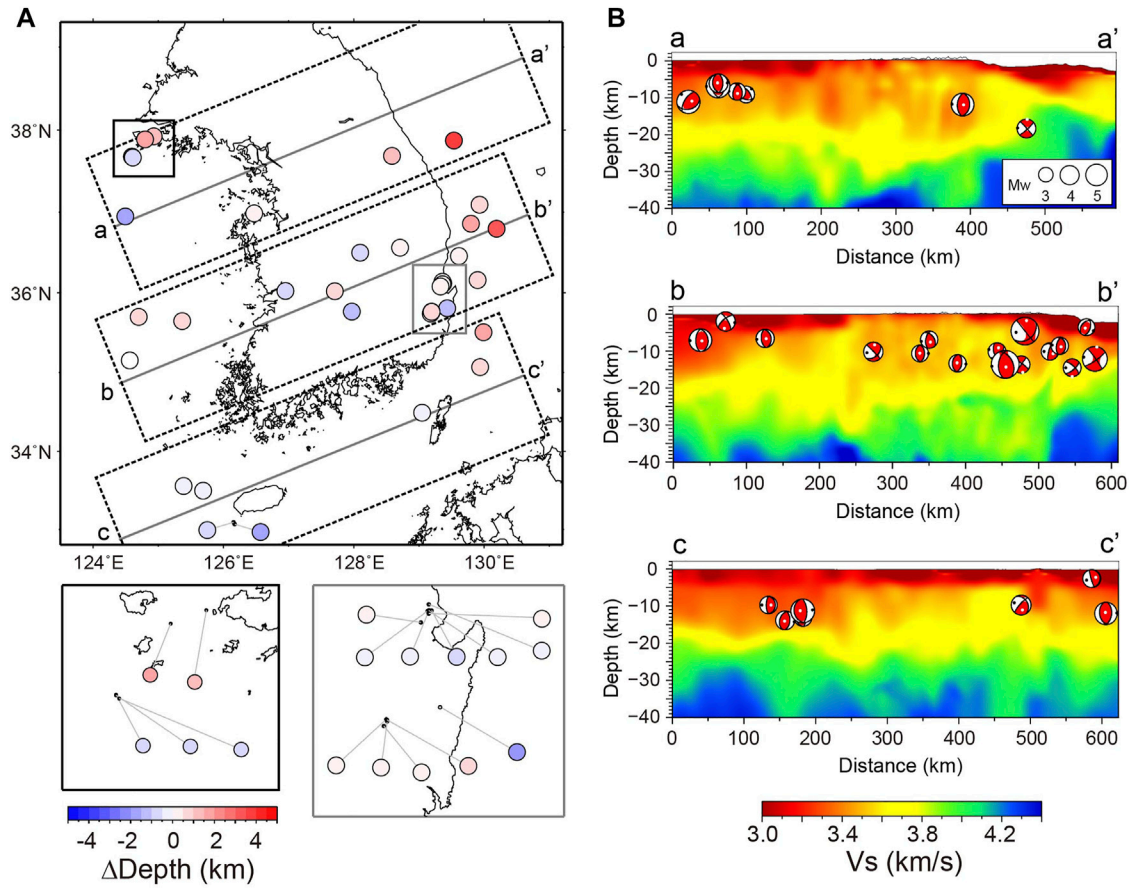

FIGURE 6 | (A) Variation in centroid depth of events constrained with the 3D velocity model compared to the initial solutions determined using the TDMT method (Dreger and Helmberger, 1993). **(B)** Event locations with moment tensor solutions constrained by the 3D velocity model at different cross-sections. Locations of velocity profiles are shown as gray lines in A, with the range of plotted focal mechanisms indicated by dashed rectangles.

values for nearby earthquakes when the 3D velocity model was used, indicating that the origin of a high non-DC component for the Pohang mainshock could be attributable to its source properties. Previously, the large non-DC component was explained by the slip motions on two intersecting faults (Grigoli et al., 2018; Son et al., 2020; Woo et al., 2020). Similar to the Pohang mainshock, there was a moderate-sized (M_w ~5) earthquake with a relatively lower DC percentage (~65%) offshore of Uljin in the eastern continental margin (**Figure 1A**). This event occurred on a deep-seated (> 10 km) pre-existing feature that was expressed on the surface as the basement escarpment along the western slope of the Ulleung Basin (Kim G. B. et al., 2018). Given that other adjacent earthquakes generally showed increases in DC percentages for the 3D velocity model (producing overall high DC values > 80%), the relatively high non-DC fraction of this earthquake could be due to complex source processes (e.g., non-planar fault slips). Structures of curved dipping faults (i.e., listric faults) have been found on the eastern continental shelf (e.g., Han et al., 2019; Moon et al., 2022). There were formed by tectonic processes associated with back-arc rifting and breakup in the East Sea during the late Oligocene to early Miocene (Chough et al., 2018) and perhaps being reactivated by an east-west compressional stress regime in the late Cenozoic (Kim et al., 2006; Choi et al., 2012). Pre-existing fault structures with curvature could accommodate slips that could not be represented by those on a single planar fault, potentially generating high non-DC components (Julian et al., 1998). Relatively small decreases (5–10%) in DC percentages were observed in the 3D velocity model, especially for those of small magnitudes (M_w < 4). This could be due to uncertainties in source parameters constrained by datasets with limited azimuthal (or distance) coverages maintaining low signal-to-noise ratios, or the inaccuracy of 3D velocity structures due to limited resolutions at model boundaries; however, complex rupture characteristics cannot be ruled out for moderate-sized (M_w ~ 4–5) earthquakes in the Yellow Sea or southern offshore region of the continental margin.

It was also noticed that the proportion of DC components increased by 15–20% for the offshore earthquakes (**Figure 3C**), where there were large lateral velocity gradients in the crust (dlnVs/Horizontal distance ~ 10%/50 km; **Figure 2A**). The reduced waveform misfits between the observed and synthetic values, together with decreases in DC fractions of focal mechanisms, strongly supported the efficacy of using the 3D velocity model for reproducing more accurate seismic wave

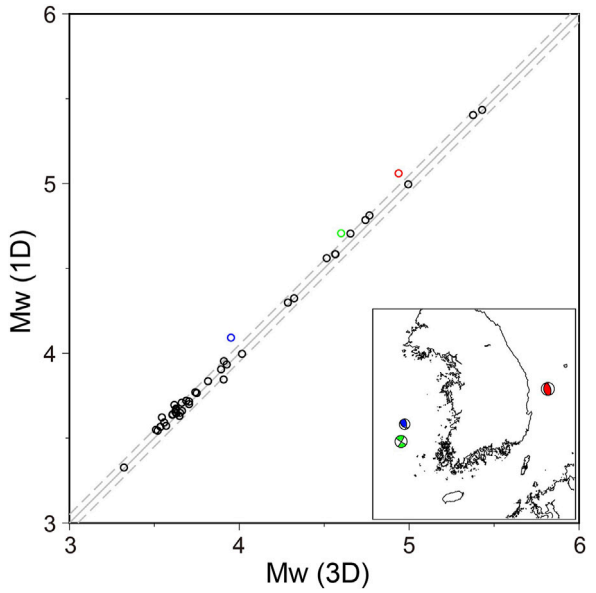

FIGURE 7 | Comparisons of event magnitude determined *via* the 3D and 1D velocity models. Circles indicate the magnitudes of the analyzed events. Gray solid and dashed lines indicate a 1:1 correlation between the magnitudes, and its two standard deviations (~0.05), as calculated based on the uncertainties of moment tensor components from bootstrap analyses averaged over all events. Blue, green, and red circles indicate events (M_w > 4) whose magnitude differences exceeded the uncertainty ranges, and the corresponding focal mechanisms are shown in the inset map in the lower right.

propagations with improved constraints of source parameters (Hejrani et al., 2017). The improvements in waveform fitting are likely attributable to a better depiction of marginal structures in the 3D velocity model (**Figure 2**), and the more accurate reproductions of seismograms leading to improvements in the focal mechanism solutions (**Figure 3B**). A similar example showing waveform complexity that can be reproduced by the 3D velocity model was found for a Yellow Sea event (**Figure 5B**) occurring at a very shallow depth (~2 km), adjacent to a sedimentary basin with a thickness of > 1 km (**Figure 1A**). Surface waves originating from this event were strongly dispersed while propagating through the sedimentary basin with low shear wave velocity (< 2 km s^{-1}; **Figure 5B**, cross-section b-b'; Feng and Ritzwoller, 2017), which were successfully reproduced in the 3D model.

The variations of centroid depths were meaningful, while lateral locations were not significantly changed compared to initial values. Previous studies have found increases in crustal velocity from the eastern margin of the KP towards the East Sea correlated with decreasing crustal thickness (Kim et al., 2003). Since the regional 1D velocity model was constructed for the continental KP (Kim et al., 2011), this model exhibited relatively slower velocities than the 3D model at the continental margin. Accordingly, using the 1D velocity model for the analysis of initial source mechanisms could create biases towards shallower depths by predicting delayed arrival times. The crust thins out towards the east and reached ~20–25 km (**Figure 2C**). Seismogenic depths ≤ 19 km potentially indicate that pre-existing features extend down to lower crusts (as suggested by previous studies—Kim et al., 2006; Moon et al., 2022), along with rheological condition changes (Prieto et al., 2017; Tape et al., 2018), or crustal thickening due to more mafic lower crustal compositions (Albaric et al., 2009). There were slight decreases (~0.1–0.6 km) in centroid depths from 2–7 km to 1.4–6.7 km for the Pohang area earthquake sequences. These results are consistent with hypocenters determined *via* travel time calculations using local 3D velocity structures (Jung et al., 2022). Earthquake depths in the KP inland generally ranged from 1.4 to 15 km, corresponding to the upper to middle crust (Kim et al., 2011). Events at comparably shallow depths (< 2 km) were mostly found adjacent to sedimentary basins in oceanic regions.

A clear 1:1 correlation between the moment magnitudes estimated from the 1D and 3D velocity models indicates that the event magnitudes can be determined consistently by both models, which agrees with previous findings indicating that the moment magnitude was less dependent on the velocity model (Hejrani et al., 2017). Relatively large discrepancies (~0.05–0.1) between the two magnitudes found for those occurred in the offshore continental margin, possibly due to the effects of 3D heterogeneity, which can cause non-radial seismic energy propagation from the source due to refraction (Koketsu and Kikuchi, 2000) or waveguide effects (Denolle et al., 2014). These effects could lead to the variable intensity and magnitude estimates depending on station locations. Other effects of 3D heterogeneity include seismic attenuation, where a portion of seismic energies can be dissipated *via* anelastic properties of the medium, resulting in apparently lower magnitudes if left unaccounted for (Hong, 2010). For more detailed analyses of event magnitudes, further investigations are needed accounting for attenuation effects with precise information of event locations, and constrained by 3D velocity models.

The results here show that the combination of improved source parameters and accurate wave propagation calculations in 3D mediums can reproduce synthetic waveforms that are more comparable to observations. Improvements in moment tensor solution quality *via* 3D waveform simulations have been reported for other geographic regions. For example, a new centroid moment tensor catalog based on a 3D Earth model for northern Australia (Hejrani et al., 2017; Hejrani and Tkalčić, 2020) produced a meaningful increase in the DC percentage (up to 70%) compared to the Global Centroid Moment Tensor solutions (Ekström et al., 2012), with a source mechanism that was in better accordance with local tectonic features. In addition, studies that analyzed source parameters of earthquakes in Southern California found that waveform simulations with a high-resolution 3D velocity model yielded substantial reductions in the uncertainties and non-DC components by reproducing the observed waveforms with reduced misfits (Liu et al., 2004; Wang and Zhan, 2020). Similar results obtained in this study support the use of a regional 3D velocity model for more accurate constraints on the source mechanism and seismic waveforms. Compared to the 1D velocity model, we found significant differences in waveform shapes and amplitudes when a 3D velocity effect was considered, particularly for earthquakes adjacent to coastal and offshore areas. From 2003

to 2021, > 50% of the events with M_w > 3.3 occurred in offshore regions. Placing accurate constraints on source parameters and the resultant ground shaking calculated *via* the high-resolution regional 3D velocity model, can thereby contribute to improved assessments of potential seismic hazards from these earthquakes to major cities with high populations or nuclear power plants adjacent to the coastal regions (**Figure 1A**).

CONCLUSION

We determined the regional moment tensor and locations of seismic events that occurred in and around the southern KP based on the spectral element moment tensor inversion method with a regional 3D crustal and upper mantle model. The recent development of a high-resolution 3D velocity model in this region, together with a high-performance computing system, allowed for the calculation of full waveforms and their derivatives with respect to source parameters in the 3D velocity model. The 3D model depicted lateral variation in seismic velocity that accords with surface geological and tectonic features. Synthetic waveforms and their derivatives were accurately calculated for source parameters using the spectral element method and 3D velocity model at periods ≥ 6 s. Ultimately, improvements in waveform fitting between synthetic and observation values were observed, particularly for events that occurred in the offshore areas when the moment tensor solutions and wave propagations were determined with the regional 3D velocity model. The results indicated the importance of employing a 3D velocity model for accurately constraining source parameters and the resultant ground shaking. Accordingly, we anticipate that the accurate wave simulations, together with improved source mechanisms determined *via* the 3D velocity model, can be applied for the reliable assessment of seismic hazards in regions with complex velocity structures (e.g., continental margin, sedimentary basins).

DATA AVAILABILITY STATEMENT

The original contributions presented in the study are included in the article/**Supplementary Material**, further inquiries can be directed to the corresponding author.

AUTHOR CONTRIBUTIONS

J-HS was responsible for data acquisition, processing, and writing of the original manuscript. SK and JR conceptualized the study and participated in writing the manuscript. DP helped analyze the results and review the original draft. All authors have read and approved the final version of the submitted manuscript.

FUNDING

This work was funded by the Korea Meteorological Institute under Grant KMI 2021-02010.

ACKNOWLEDGMENTS

We thank KMA, KIGAM, KHNP, NIED, and JMA for providing continuous waveform data. Most figures were generated using Generic Mapping Tools (Wessel et al., 2013). We acknowledge Jeong-Ung Woo for instructing numerical mesh generation, and Hwa Sung Cheon for installing SPECFEM3D with GPUs.

SUPPLEMENTARY MATERIAL

The Supplementary Material for this article can be found online at: https://www.frontiersin.org/articles/10.3389/feart.2022.945022/full#supplementary-material

REFERENCE

Albaric, J., Déverchère, J., Petit, C., Perrot, J., and Le Gall, B. (2009). Crustal Rheology and Depth Distribution of Earthquakes: Insights from the Central and Southern East African Rift System. *Tectonophysics* 468, 28–41. doi:10.1016/j.tecto.2008.05.021

Bird, P. (2003). An Updated Digital Model of Plate Boundaries. *Geochem. Geophys. Geosyst.* 4, 1027. doi:10.1029/2001GC000252

Chang, S.-J., and Baag, C.-E. (2007). Moho Depth and Crustal Vp/Vs Variation in Southern Korea from Teleseismic Receiver Functions: Implication for Tectonic Affinity between the Korean Peninsula and China. *Bull. Seismol. Soc. Am.* 97, 1621–1631. doi:10.1785/0120050264

Cho, H.-M., Kim, H.-J., Jou, H.-T., Hong, J.-K., and Baag, C.-E. (2004). Transition from Rifted Continental to Oceanic Crust at the Southeastern Korean Margin in the East Sea (Japan Sea). *Geophys. Res. Lett.* 31, L07606. doi:10.1029/2003GL019107

Choi, H., Hong, T.-K., He, X., and Baag, C.-E. (2012). Seismic Evidence for Reverse Activation of a Paleo-Rifting System in the East Sea (Sea of Japan). *Tectonophysics* 572-573, 123–133. doi:10.1016/j.tecto.2011.12.023

Chough, S. K., Shinn, Y. J., and Yoon, S. H. (2018). Regional Strike-Slip and Initial Subsidence of Korea Plateau, East Sea: Tectonic Implications for the Opening of Back-Arc Basins. *Geosci. J.* 22, 533–547. doi:10.1007/s12303-018-0017-0

Christensen, N. I., and Mooney, W. D. (1995). Seismic Velocity Structure and Composition of the Continental Crust: a Global View. *J. Geophys. Res.* 100, 9761–9788. doi:10.1029/95JB00259

Conte, S. D., and Boor, C. (1980). *Elementary Numerical Analysis: An Algorithm Approach*. New York: McGraw-Hill.

Denolle, M. A., Dunham, E. M., Prieto, G. A., and Beroza, G. C. (2014). Strong Ground Motion Prediction Using Virtual Earthquakes. *Science* 343, 399–403. doi:10.1126/science.1245678

Dreger, D. S., and Helmberger, D. V. (1993). Determination of Source Parameters at Regional Distances with Three-Component Sparse Network Data. *J. Geophys. Res.* 98, 8107–8125. doi:10.1029/93JB00023

Ekström, G., Nettles, M., and Dziewoński, A. M. (2012). The Global CMT Project 2004-2010: Centroid-Moment Tensors for 13,017 Earthquakes. *Phys. Earth Planet. Interiors* 200-201, 1–9. doi:10.1016/j.pepi.2012.04.002

Feng, L., and Ritzwoller, M. H. (2017). The Effect of Sedimentary Basins on Surface Waves that Pass through Them. *Geophys. J. Int.* 211, 572–592. doi:10.1093/gji/ggx313

Fichtner, A., and Tkalčić, H. (2010). Insights into the Kinematics of a Volcanic Caldera Drop: Probabilistic Finite-Source Inversion of the 1996 Bárdarbunga, Iceland, Earthquake. *Earth Planet. Sci. Lett.* 297, 607–615. doi:10.1016/j.epsl.2010.07.013

Ford, S. R., Dreger, D. S., and Walter, W. R. (2009). Identifying Isotropic Events Using a Regional Moment Tensor Inversion. *J. Geophys. Res.* 114, 11. doi:10.1029/2008JB005743

Gallovič, F., Valentová, Ľ., Ampuero, J. P., and Gabriel, A. A. (2019). Bayesian Dynamic Finite-Fault Inversion: 2. Application to the 2016 M W 6.2 Amatrice, Italy, Earthquake. *J. Geophys. Res. Solid Earth* 124 (7), 6970–6988. doi:10.1029/2019JB017512

Grigoli, F., Cesca, S., Rinaldi, A. P., Manconi, A., López-Comino, J. A., Clinton, J. F., et al. (2018). The November 2017 M W 5.5 Pohang Earthquake: a Possible Case of Induced Seismicity in South Korea. *Science* 360, 1003–1006. doi:10.1126/science.aat2010

Han, M., Kim, H.-J., Kang, S. Y., Kim, K.-H., Yoon, S.-H., and Kyung, J. B. (2019). Detection of Microearthquakes and Identification of Their Causative Structures in the Eastern Offshore Region of South Korea. *Tectonophysics* 750, 36–44. doi:10.1016/j.tecto.2018.11.003

Hejrani, B., Tkalčić, H., and Fichtner, A. (2017). Centroid Moment Tensor Catalogue Using a 3-D Continental Scale Earth Model: Application to Earthquakes in Papua New Guinea and the Solomon Islands. *J. Geophys. Res. Solid Earth* 122, 5517–5543. doi:10.1002/2017JB014230

Hejrani, B., and Tkalčić, H. (2020). Resolvability of the Centroid-Moment-Tensors for Shallow Seismic Sources and Improvements From Modeling High-Frequency Waveforms. *J. Geophys. Res. Solid Earth* 125, e2020JB019643. doi:10.1029/2020JB019643

Hingee, M., Tkalčić, H., Fichtner, A., and Sambridge, M. (2011). Seismic Moment Tensor Inversion Using a 3-D Structural Model: Applications for the Australian Region. *Geophys. J. Int.* 184, 949–964. doi:10.1111/j.1365-246X.2010.04897.x

Hong, T.-K., and Choi, H. (2012). Seismological Constraints on the Collision Belt between the North and South China Blocks in the Yellow Sea. *Tectonophysics* 570-571, 102–113. doi:10.1016/j.tecto.2012.08.034s

Hong, T.-K. (2010). Lg Attenuation in a Region with Both Continental and Oceanic Environments. *Bull. Seismol. Soc. Am.* 100, 851–858. doi:10.1785/0120090057

Hong, T.-K., Park, S., Lee, J., Chung, D., and Kim, W. (2020). One-off Deep Crustal Earthquake Swarm in a Stable Intracontinental Region of the Southwestern Korean Peninsula. *Phys. Earth Planet. Interiors* 308, 106582. doi:10.1016/j.pepi.2020.106582

Huo, Y., Zhang, W., and Zhang, J. (2021). Centroid Moment Tensor of the 2019 MW 5.7 Changning Earthquake Refined Using 3D Green's Functions Considering Surface Topography. *Front. Earth Sci.* 9, 642721. doi:10.3389/feart.2021.642721

Julian, B. R., Miller, A. D., and Foulger, G. R. (1997). Non-double-couple Earthquake Mechanisms at the Hengill-Grensdalur Volcanic Complex, Southwest Iceland. *Geophys. Res. Lett.* 24, 743–746. doi:10.1029/97GL00499

Julian, B. R., Miller, A. D., and Foulger, G. R. (1998). Non-double-couple Earthquakes 1. Theory. *Rev. Geophys.* 36, 525–549. doi:10.1029/98RG00716

Jung, Y., Woo, J.-U., and Rhie, J. (2022). Enhanced Hypocenter Determination of the 2017 Pohang Earthquake Sequence, South Korea, Using a 3-D Velocity Model. *Geosci. J.* 26 , 1–13. doi:10.1007/s12303-021-0043-1

Kim, G. B., Yoon, S.-H., Kim, S.-S., and So, B.-D. (2018). Transition from Buckling to Subduction on Strike-Slip Continental Margins: Evidence from the East Sea (Japan Sea). *Geology* 46, 603–606. doi:10.1130/G40305.1

Kim, H.-J., Jou, H.-T., Cho, H.-M., Bijwaard, H., Sato, T., Hong, J.-K., et al. (2003). Crustal Structure of the Continental Margin of Korea in the East Sea (Japan Sea) from Deep Seismic Sounding Data: Evidence for Rifting Affected by the Hotter Than Normal Mantle. *Tectonophysics* 364, 25–42. doi:10.1016/S0040-1951(03)00048-9

Kim, H.-J., Kim, C.-H., Hao, T., Liu, L., Kim, K.-H., Jun, H., et al. (2019). Crustal Structure of the Gunsan Basin in the SE Yellow Sea from Ocean Bottom Seismometer (OBS) Data and its Linkage to the South China Block. *J. Asian Earth Sci.* 180, 103881. doi:10.1016/j.jseaes.2019.103881

Kim, K. H., Ree, J.-H., Kim, Y., Kim, S., Kang, S. Y., and Seo, W. (2018). Assessing whether the 2017 M W 5.4 Pohang Earthquake in South Korea Was an Induced Event. *Science* 360, 1007–1009. doi:10.1126/science.aat6081

Kim, S., Dettmer, J., Rhie, J., and Tkalčić, H. (2016a). Highly Efficient Bayesian Joint Inversion for Receiver-Based Data and its Application to Lithospheric Structure beneath the Southern Korean Peninsula. *Geophys, J. Int.* 206, 328–344. doi:10.1093/gji/ggw149

Kim, S., Rhie, J., and Kim, G. (2011). Forward Waveform Modelling Procedure for 1-D Crustal Velocity Structure and its Application to the Southern Korean Peninsula. *Geophys. J. Int.* 185, 453–468. doi:10.1111/j.1365-246X.2011.04949.x

Kim, S., Tkalčić, H., Rhie, J., and Chen, Y. (2016b). Intraplate Volcanism Controlled by Back-Arc and Continental Structures in NE Asia Inferred from Transdimensional Bayesian Ambient Noise Tomography. *Geophys. Res. Lett.* 43, 8390–8398. doi:10.1002/2016GL069483

Kim, S., Tkalčić, H., and Rhie, J. (2017). Seismic Constraints on Magma Evolution beneath Mount Baekdu (Changbai) Volcano from Transdimensional Bayesian Inversion of Ambient Noise Data. *J. Geophys. Res. Solid Earth* 122, 5452–5473. doi:10.1002/2017JB014105

Kim, W. Y., Noh, M. H., and Choi, H. S. (2006). The 29 May 2004 Offshore Southeast Coast of Korea Earthquake Sequence: Shallow Earthquakes in the Ulleung Back-Arc Basin, East Sea (Sea of Japan). *J. Korean Geophys. Soc.* 9, 249–262.

Kim, Y., Lee, C., and Kim, S.-S. (2015). Tectonics and Volcanism in East Asia: Insights from Geophysical Observations. *J. Asian Earth Sci.* 113, 842–856. doi:10.1016/j.jseaes.2015.07.032

Kim, Y., Rhie, J., Kang, T.-S., Kim, K.-H., Kim, M., and Lee, S.-J. (2016). The 12 September 2016 Gyeongju Earthquakes: 1. Observation and Remaining Questions. *Geosci. J.* 20, 747–752. doi:10.1016/j.jseaes.2015.07.03210.1007/s12303-016-0033-x

Koketsu, K., and Kikuchi, M. (2000). Propagation of Seismic Ground Motion in the Kanto Basin, Japan. *Science* 288, 1237–1239. doi:10.1126/science.288.5469.1237

Komatitsch, D., Erlebacher, G., Göddeke, D., and Michéa, D. (2010). High-order Finite-Element Seismic Wave Propagation Modeling with MPI on a Large GPU Cluster. *J. Comput. Phys.* 229, 7692–7714. doi:10.1016/j.jcp.2010.06.024

Komatitsch, D., Liu, Q., Tromp, J., Suss, P., Stidham, C., and Shaw, J. H. (2004). Simulations of Ground Motion in the Los Angeles Basin Based upon the Spectral-Element Method. *Bull. Seismol. Soc. Am.* 94, 187–206. doi:10.1785/0120030077

Komatitsch, D., and Tromp, J. (2003). A Perfectly Matched Layer Absorbing Boundary Condition for the Second-Order Seismic Wave Equation. *Geophys. J. Int.* 154, 146–153. doi:10.1046/j.1365-246X.2003.01950.x

Komatitsch, D., and Tromp, J. (1999). Introduction to the Spectral Element Method for Three-Dimensional Seismic Wave Propagation. *Geophys. J. Int.* 139, 806–822. doi:10.1046/j.1365-246x.1999.00967.x

Komatitsch, D., and Tromp, J. (2002). Spectral-element Simulations of Global Seismic Wave Propagation-I. Validation. *Valid. Geophys. J. Int.* 149, 390–412. doi:10.1046/j.1365-246X.2002.01653.x

Lee, J., Kim, S., and Marija, M. (2020). Uncertainty Estimation of Moment Tensor Solutions for the 2017 Mw 5.5 Pohang Earthquake Using Hierarchical Bayesian Inversion Method. *Abstr. retrieved Abstr. Am. Geophys. Union Fall Meet.* 2020, S011–S0001.

Lee, J., Song, J.-H., Kim, S., Rhie, J., and Song, S. G. (2022). Three-Dimensional Seismic-Wave Propagation Simulations in the Southern Korean Peninsula Using Pseudodynamic Rupture Models. *Bull. Seismol. Soc. Am.* 112, 939–960. doi:10.1785/0120210172

Lee, S.-J., Rhie, J., Kim, S., Kang, T.-S., and Kim, G. B. (2015). Ambient Seismic Noise Tomography of the Southern East Sea (Japan Sea) and the Korea Strait. *Geosci. J.* 19, 709–720. doi:10.1007/s12303-015-0012-7

Lee, S. J., Huang, B. S., Liang, W. T., and Kou-Cheng, C. (2010). Grid-based Moment Tensor Inversion Technique by Using 3-D Green's Functions Database: a Demonstration of the 23 October 2004 Taipei Earthquake. *Terr. Atmos. Ocean. Sci.* 21, 5. doi:10.3319/TAO.2010.01.25.02(TH)

Li, J., Zheng, Y., Thomsen, L., Lapen, T. J., and Fang, X. (2018). Deep Earthquakes in Subducting Slabs Hosted in Highly Anisotropic Rock Fabric. *Nat. Geosci.* 11, 696–700. doi:10.1038/s41561-018-0188-3

Liu, Q., Polet, J., Komatitsch, D., and Tromp, J. (2004). Spectral-element Moment Tensor Inversions for Earthquakes in Southern California. *Bull. Seismol. Soc. Am.* 94, 1748–1761. doi:10.1785/012004038

Maggi, A., Tape, C., Chen, M., Chao, D., and Tromp, J. (2009). An Automated Time-Window Selection Algorithm for Seismic Tomography. *Geophys. J. Int.* 178, 257–281. doi:10.1111/j.1365-246X.2009.04099.x

Moon, S., Kim, H.-J., Kim, K.-H., Yoo, D.-G., Lee, S.-H., Son, W.-H., et al. (2022). Correlation of Seismicity with Geologic Structures at the Middle Eastern Korean Margin in the East Sea (Japan Sea) and Seismic Hazard Assessment. *Mar. Geophys Res.* 43, 1–11. doi:10.1007/s11001-022-09479-9

Mustać, M., Hejrani, B., Tkalčić, H., Kim, S., Lee, S.-J., and Cho, C.-S. (2020). Large Isotropic Component in the Source Mechanism of the 2013 Democratic People's Republic of Korea Nuclear Test Revealed via a Hierarchical Bayesian Inversion. *Bull. Seismol. Soc. Am.* 110, 166–177. doi:10.1785/0120190062

Park, D., Song, S. G., and Rhie, J. (2020). Sensitivity Analysis of Near-Source Ground Motions to Pseudo-dynamic Source Models Derived with 1-point and 2-point Statistics of Earthquake Source Parameters. *J. Seismol.* 24, 397–422. doi:10.1007/s10950-020-09905-8

Prieto, G. A., Froment, B., Yu, C., Poli, P., and Abercrombie, R. (2017). Earthquake Rupture below the Brittle-Ductile Transition in Continental Lithospheric Mantle. *Sci. Adv.* 3, e1602642. doi:10.1126/sciadv.1602642

Rhie, J., and Kim, S. (2010). Regional Moment Tensor Determination in the Southern Korean Peninsula. *Geosci. J.* 14, 329–333. doi:10.1007/s12303-010-0038-9

Rhie, J., Kim, S., Woo, J. U., and Song, J. H. (2016). Three-dimensional Velocity Model of Crustal Structure in the Southern Korean Peninsula and its Full-Waveform Validations. *Am. Geophys. Union Fall Meet. 2016*, S43B–S2861.

Saikia, C. K. (1994). Modified Frequency-Wavenumber Algorithm for Regional Seismograms Using Filon's Quadrature: Modelling ofLgwaves in Eastern North America. *Geophys. J. Int.* 118, 142–158. doi:10.1111/j.1365-246X.1994.tb04680.x

Son, M., Cho, C. S., Lee, H. K., Han, M., Shin, J. S., Kim, K., et al. (2020). Partitioned Fault Movement and Aftershock Triggering: Evidence for Fault Interactions during the 2017 M W 5.4 Pohang Earthquake, South Korea. *JGR Solid Earth* 125, e2020JB020005. doi:10.1029/2020JB020005

Son, Y. O., Seo, M.-S., and Kim, Y. (2021). Measurement of Seismometer Misorientation Based on P-Wave Polarization: Application to Permanent Seismic Network in South Korea. *Geosci. J.* 26, 235–247. doi:10.1007/s12303-021-0031-5

Song, J. H., Woo, J. U., Rhie, J., Kim, S., and Kang, T. S. (2018). "Source Analysis of November 15, 2017 Pohang Earthquake Sequences: the First Non-double Couple Event Reported in South Korea," in Geosciences Union General Assembly Conference, Vienna, Austria, 4-13 April, 2018, 12279. Abstract retrieved from Abstracts in European.

Straume, E. O., Gaina, C., Medvedev, S., Hochmuth, K., Gohl, K., Whittaker, J. M., et al. (2019). GlobSed: Updated Total Sediment Thickness in the World's Oceans. *Geochem. Geophys. Geosyst.* 20, 1756–1772. doi:10.1029/2018GC008115

Takemura, S., Okuwaki, R., Kubota, T., Shiomi, K., Kimura, T., and Noda, A. (2020). Centroid Moment Tensor Inversions of Offshore Earthquakes Using a Three-Dimensional Velocity Structure Model: Slip Distributions on the Plate Boundary along the Nankai Trough. *Geophys. J. Int.* 222, 1109–1125. doi:10.1093/gji/ggaa238

P. Talwani (Editor) (2014). *Intraplate Earthquakes*. 1st ed. (New York: Cambridge University Press). doi:10.1017/CBO9781139628921

Tape, C., Holtkamp, S., Silwal, V., Hawthorne, J., Kaneko, Y., Ampuero, J. P., et al. (2018). Earthquake Nucleation and Fault Slip Complexity in the Lower Crust of Central Alaska. *Nat. Geosci.* 11, 536–541. doi:10.1038/s41561-018-0144-2

Tape, C., Liu, Q., Maggi, A., and Tromp, J. (2009). Adjoint Tomography of the Southern California Crust. *Science* 325, 988–992. doi:10.1126/science.1175298

Tape, C., Liu, Q., Maggi, A., and Tromp, J. (2010). Seismic Tomography of the Southern California Crust Based on Spectral-Element and Adjoint Methods. *Geophys. J. Int.* 180, 433–462. doi:10.1111/j.1365-246X.2009.04429.x

Vavryčuk, V. (2011). Detection of High-Frequency Tensile Vibrations of a Fault during Shear Rupturing: Observations from the 2008 West Bohemia Swarm. *Geophys. J. Int.* 186, 1404–1414. doi:10.1111/j.1365-246X.2011.05122.x

Wang, X., and Zhan, Z. (2020). Moving from 1-D to 3-D Velocity Model: Automated Waveform-Based Earthquake Moment Tensor Inversion in the Los Angeles Region. *Geophys. J. Int.* 220, 218–234. doi:10.1093/gji/ggz435

Wessel, P., Smith, W. H. F., Scharroo, R., Luis, J., and Wobbe, F. (2013). Generic Mapping Tools: Improved Version Released. *Eos Trans. AGU* 94, 409–410. doi:10.1002/2013EO450001

Willacy, C., van Dedem, E., Minisini, S., Li, J., Blokland, J. W., Das, I., et al. (2018). Application of Full-Waveform Event Location and Moment-Tensor Inversion for Groningen Induced Seismicity. *Lead. Edge* 37 (2), 92–99. doi:10.1190/tle37020092.1

Woo, J.-U., Kim, M., Rhie, J., and Kang, T.-S. (2020). Aftershock Sequence and Statistics of the 2017 Mw 5.5 Pohang, South Korea, Earthquake: Implications of Fault Heterogeneity and Postseismic Relaxation. *Bull. Seismol. Soc. Am.* 110, 2031–2046. doi:10.1785/0120200059

Zhao, L. S., and Helmberger, D. V. (1994). Source Estimation from Broadband Regional Seismograms. *Bull. Seismol. Soc. Am.* 84, 91–104. doi:10.1785/BSSA0840010091

Conflict of Interest: Author DP was employed by Korea Hydro & Nuclear Power Co., Ltd.

The remaining authors declare that the research was conducted in the absence of any commercial or financial relationships that could be construed as a potential conflict of interest.

Publisher's Note: All claims expressed in this article are solely those of the authors and do not necessarily represent those of their affiliated organizations, or those of the publisher, the editors and the reviewers. Any product that may be evaluated in this article, or claim that may be made by its manufacturer, is not guaranteed or endorsed by the publisher.

frontiers | Frontiers in Earth Science

TYPE Methods
PUBLISHED 25 October 2022
DOI 10.3389/feart.2022.1046258

OPEN ACCESS

EDITED BY
Eleftheria Papadimitriou,
Aristotle University of Thessaloniki,
Greece

REVIEWED BY
Gilda Maria Currenti,
Istituto Nazionale di Geofisica e
Vulcanologia (INGV), Italy
Veronica Pazzi,
University of Trieste, Italy

*CORRESPONDENCE
Denis Anikiev,
denis.anikiev@gfz-potsdam.de

SPECIALTY SECTION
This article was submitted to Solid Earth Geophysics,
a section of the journal
Frontiers in Earth Science

RECEIVED 16 September 2022
ACCEPTED 12 October 2022
PUBLISHED 25 October 2022

CITATION
Anikiev D, Waheed Ub, Staněk F, Alexandrov D, Hao Q, Iqbal N and Eisner L (2022), Traveltime-based microseismic event location using artificial neural network.
Front. Earth Sci. 10:1046258.
doi: 10.3389/feart.2022.1046258

Traveltime-based microseismic event location using artificial neural network

Denis Anikiev[1]*, Umair bin Waheed[2], František Staněk[3], Dmitry Alexandrov[4], Qi Hao[2], Naveed Iqbal[2] and Leo Eisner[4]

[1]Section 4.5—Basin Modelling, Department 4—Geosystems, GFZ German Research Centre for Geosciences, Potsdam, Germany, [2]King Fahd University of Petroleum and Minerals, Dhahran, Saudi Arabia, [3]Department of Geophysics, Colorado School of Mines, Golden, CO, United States, [4]Seismik s.r.o, Prague, Czechia

Location of earthquakes is a primary task in seismology and microseismic monitoring, essential for almost any further analysis. Earthquake hypocenters can be determined by the inversion of arrival times of seismic waves observed at seismic stations, which is a non-linear inverse problem. Growing amounts of seismic data and real-time processing requirements imply the use of robust machine learning applications for characterization of seismicity. Convolutional neural networks have been proposed for hypocenter determination assuming training on previously processed seismic event catalogs. We propose an alternative machine learning approach, which does not require any pre-existing observations, except a velocity model. This is particularly important for microseismic monitoring when labeled seismic events are not available due to lack of seismicity before monitoring commenced (e.g., induced seismicity). The proposed algorithm is based on a feed-forward neural network trained on synthetic arrival times. Once trained, the neural network can be deployed for fast location of seismic events using observed P-wave (or S-wave) arrival times. We benchmark the neural network method against the conventional location technique and show that the new approach provides the same or better location accuracy. We study the sensitivity of the proposed method to the training dataset, noise in the arrival times of the detected events, and the size of the monitoring network. Finally, we apply the method to real microseismic monitoring data and show that it is able to deal with missing arrival times in efficient way with the help of fine tuning and early stopping. This is achieved by re-training the neural network for each individual set of picked arrivals. To reduce the training time we used previously determined weights and fine tune them. This allows us to obtain hypocenter locations in near real-time.

KEYWORDS

microseismic, source location, machine learning, neural network, induced seismicity, earthquakes

1 Introduction

Earthquakes observed in the crust and the upper mantle are caused by natural forces or induced by human activity (possibly both in the case of triggered seismicity). Location of the observed earthquakes is one of the crucial tasks of seismology and microseismic monitoring as hypocenters play key role in interpretation for natural seismic hazards (earthquake disasters, tsunamis) or in mitigation of unwanted induced seismicity and interpretation of microseismicity related to human activity (oil and gas reservoirs, geothermal extraction, CO_2 sequestration, etc.). For example, a rapid and automated earthquake location using initially identified arrivals of direct P-waves is needed for early warning systems (e.g., Cremen and Galasso, 2020) or tsunamis to be able to determine size of the natural earthquake and mitigate hazards associated with unpredictable seismicity.

Induced seismicity, whether in mines (e.g., Foulger et al., 2018) or induced by unconventional production (Ellsworth, 2013) requires locations for mitigation of felt seismicity in previously seismically quiet intraplate areas in different parts of the world. The induced seismicity hazards use the so-called 'traffic light system' (TLS) originally developed for mitigation of seismicity in geothermal exploration (Häring et al., 2008) and later applied to a wide range of underground operations (e.g., Verdon and Bommer (2020); Schultz et al. (2020)). This TLS usually requires real-time detection, location and size characterization of induced seismicity. Real-time locations of weak induced earthquakes (microseismic events) are used to image subsurface stimulations, delineate fault movements and optimize energy extraction (Maxwell et al. (2010) or Duncan and Eisner (2010)). All of these methods utilize automatic location algorithms.

The automatic location methods for induced seismicity have been studied for at least two decades (see, e.g., Foulger et al. (2018) for an overview). Traditional location techniques use arrival times of the direct P- or S-waves and are mainly used in downhole monitoring (Rutledge and Phillips, 2003), while more recent techniques use diffraction stacking to locate microseismic events by enhancing signal-to-noise ratio (e.g. Duncan and Eisner, 2010; Anikiev et al., 2014). Both techniques are used for automated location from local monitoring arrays (with thousands of channels in surface monitoring). The advantage of using arrival times or diffraction stacking is in lower requirements on accuracy of velocity model, as only direct arrival times are needed.

At the same time, the full-waveform-based location methods do not require picking (e.g., Li et al., 2020) and allow implementations independent of variability in the acquisition geometry from event to event. This is not the same for picking-based locations where picks may and may not be available on certain stations as discussed later. In this study we focus on a location method using direct P-wave arrivals, a classical seismological problem which requires only the P-wave velocity model. This location method requires pre-existing picking (automated or manual) of multiple P-wave arrival times but is less sensitive to velocity model errors.

The machine learning (ML) methodologies are increasingly applied to seismic data processing to provide real-time results, deal with consistently increasing amount of data and take advantage of growing computational resources which can handle them. ML attracts increasing attention in geoscience (Dramsch, 2020) and geophysics (Yu and Ma, 2021) in general, as well as in seismology (Kong et al., 2019), mainly for detection and location tasks (e.g., Zhu and Beroza, 2018; Mousavi and Beroza, 2020; Mousavi et al., 2020; Saad and Chen, 2021), but also for de-noising (e.g., Saad et al., 2021; Birnie and Alkhalifah, 2022), source mechanism determination (e.g., Nooshiri et al., 2021; Steinberg et al., 2021), reconstruction of ground-shaking fields (e.g., Fornasari et al., 2022) and other purposes. The use of ML algorithms also brings consistency in processing rarely achievable by manual processing.

In supervised ML one constructs a mathematical model, which is trained by using labeled data (also called training data), to make predictions (of, e.g., hypocenter locations) from new unseen data (data which were not labeled). For example, Perol et al. (2018) studied induced seismicity in Oklahoma, United States, using a convolutional neural network (CNN). They trained the network on data from 2709 events recorded on two stations to roughly locate earthquakes belonging to one of six regions. Kriegerowski et al. (2018) applied CNN methodology to swarms of natural earthquakes from 8 to 12 km depth in West Bohemia, recorded on nine local stations, they located clustered earthquakes with greater consistency than manual processing. Tous et al. (2020) reported the results of applying a deep CNN for P-wave earthquake detection and source region estimation in North-Central Venezuela. Zhang et al. (2021) developed a deep learning early earthquake warning system that utilizes fully convolutional networks (FCN) to simultaneously detect earthquakes and estimate their source parameters from continuous seismic waveform streams. To train the network, they collected 773 cataloged earthquakes with magnitude ranging from 2.0 to 3.7.

Previously mentioned methods reveal a certain limitation, as they require large manually pre-processed historical catalogs for training the CNNs or FCNs. Generally, those solutions are quite demanding in terms of the amount of training data needed, as well as in terms of training time costs. For example, a CNN-based method that does not rely on the historical database was proposed by Vinard et al. (2021), who applied CNNs trained on synthetic data to improve result obtained by an imaging method based on a grid search. Usage of a neural network with a simpler architecture that needs less or no training data (and therefore is faster to train) is needed for induced seismicity as often there is no pre-processed historical dataset which can be

used. Simply there are many cases when there is no seismicity recorded prior to any activity that may induce it.

In this study, we propose a new method of utilizing a feed-forward artificial neural network (ANN) to determine hypocenters, which is trained on synthetic traveltime data to overcome the problem when there are no real samples in the study area. We found this easier to train than CNN and it does not require any historical dataset. Original methodology and tests on synthetic datasets are summarized in Hao et al. (2020) where an initial implementation of the idea was demonstrated on a 2D synthetic model. This was followed by the first testing on real data presented in Anikiev et al. (2021). In this paper, we extend the method and analyze the results to develop a practical location method based on our initial results reported earlier. In particular, here we study the method on 3-D synthetics and extend the analysis to field data towards developing a practical approach to the problem.

All earthquake location techniques require a seismic velocity model and depend on its accuracy. Our methodology assumes subsurface velocities to be known, so that calculation of the traveltimes from the subsurface locations can be performed properly. Using arrival times as an input automatically leads to averaging over the velocity model and results in lower requirements on the high resolution of the velocity model. This advantage is common for all traveltime-based location algorithms and the cost of that is the requirement of picked arrival times. Alternative location algorithms require more detailed knowledge of the velocities to model full waveforms (multiply scattered and trapped waves) and hence may result in large errors where such a model is not available. Recent progress in automated picking using machine learning (e.g., Wiszniowski et al. (2013); Zhu and Beroza (2018); Bhandarkar et al. (2019)) as well as template matching (Ross et al., 2019) represent various efficient solutions for picking that can be combined with a neural network location technique based on time of picked arrivals. By choosing the wave arrival times as an input for ANN, we pre-select the physically meaningful feature to be trained on. Therefore, we deliberately exclude the feature selection essential in training of more sophisticated networks like CNN.

Machine-learning-based methods outperform classical location algorithms in terms of computational efficiency because location using a trained network does not depend on the location grid size and step. Also, neural network provides natural interpolation of locations between the training grid nodes as the weights of the NN smooth the output. Classical location methods, instead, need to utilize probability density functions (see, e.g., Eisner et al., 2010) to smooth the misfit assuming Gaussian distribution of the image function. We show that the developed ML location is potentially more reliable due to high sensitivity of the estimated hypocenters to errors in picked arrival times.

In contrast to the published works of Perol et al. (2018), Kriegerowski et al. (2018) and Tous et al. (2020), we train the network using a synthetic dataset. This is particularly important for monitoring of induced seismicity because in most cases there are no recorded historical earthquakes in the area (before the purpose-built seismic receiver network). Training on synthetics does not require labeled earthquake data. Once trained, the neural network can be used to locate real events using their observed P-wave arrival times as an input.

We use synthetic data to analyze the factors that may affect the performance of the neural network. It is important to emphasize that in our study we consider a typical microseismic monitoring setting with many stations (usually several hundred) deployed over a relatively small area (usually about 5 km by 5 km). However, the methodology in general is not limited to this type of acquisition geometry. Through numerical tests, we explore the accuracy of the proposed method as a function of several parameters, including velocity model complexity, station network distribution, and the size of the training data. Finally, we apply the developed machine-learning methodology to location of microseismicity occurred during real hydraulic fracturing operations in the Arkoma basin in the United States of America. The resulting hypocenters are compared with locations obtained by a conventional traveltime-based location method (Eisner et al., 2010) based on the maximum likelihood principle (Anikiev et al., 2014; Anikiev, 2015). We show that the locations are similar if not better and the ANN-based methodology is less sensitive to gridding issues and more sensitive to outliers (false positive event detections) in data.

2 Methodology

To locate the earthquake hypocenters, we utilize an ANN trained on pre-processed traveltimes calculated from a grid of synthetic earthquake locations. The input is provided as a vector of size defined by the number of P-wave arrival time picks.

2.1 Feed-forward neural networks

A feed-forward neural network is a composition of neurons organized in layers. Each neuron represents a mathematical operation, whereby it takes a weighted sum of its inputs plus a bias term and passes them through an activation function. The output of a neuron is then passed on to subsequent neurons as their inputs. Mathematically, the output, ζ, of a neuron is given as:

$$\zeta = f\left(\sum_i w_i \chi_i + b\right), \tag{1}$$

where ω_i is the weight associated with the input χ_i, b is the bias term, and f () represents the activation function (Anikiev et al.,

2021). A nonlinear activation function is typically used to learn nonlinear relationships between the input and the output. Training of a neural network refers to the mechanism of adjusting the networks' weights and biases to correctly map the input to the output provided in the training data.

2.2 Event location using feed-forward neural networks

For the seismic event location problem, the input layer of the neural network comprises one neuron per station for the total number of recording stations in the monitoring network. The output layer will contain one neuron for each coordinate axis. Hidden layers of neurons are used to learn nonlinear relationships between the input and the output.

To locate the hypocenter of a detected seismic event that was recorded at the stations of an earthquake monitoring network, we use its registered P-wave arrival times. In order to get rid of dependence on the origin time, we use the deviation of arrival times from their mean as the input to the ANN, that is

$$\Delta t_i = t_i - \frac{1}{N}\sum_{i=1}^{N} t_i, \tag{2}$$

where t_i denotes the P-wave arrival time registered at the i-th station. N denotes the total number of the stations. Δt_i is the deviation of arrival time relative to the average arrival time. It is worth noting that even though the event origin time is not available, Δt_i is not affected by it due to the subtraction in Eq. 2. The proposed methodology allows us to locate events from P-wave arrival times only (or S-wave arrival times only). The generalization to combinations of P- and S-waves or more complex arrivals is discussed later.

Based on our experience in training an ANN model, we found the training to be often slow while directly using the input consisting of Δt_i. Therefore, we scale the input Δt_i to the range [0, 1] to accelerate the training process by using the following normalization:

$$\tau_i = \frac{\Delta t_i - \Delta t_{min}}{\Delta t_{max} - \Delta t_{min}}, \tag{3}$$

where Δt_{min} and Δt_{max} denote the minimum and maximum of all Δt_i values in the whole training data, respectively. It must be noted that for consistency Δt_{min} and Δt_{max} are used not only for training but also while evaluating the trained ANN model for predictions.

The training data for our network are generated synthetically. For a given velocity model that is discretized into regular grids, we define a number of potential source positions inside an identified seismic zone of interest and calculate the corresponding traveltimes using the factored fast sweeping method (Fomel et al., 2009). We define the arrival time as the time of observed arrival of a seismic wave (P-wave in our case), while traveltime is the synthetic time of the seismic wave propagation between a source and a receiver. Using Eq. 2, we compute the deviations of traveltimes for a set of training sources, and then scale them using Eq. 3 to obtain the scaled traveltime deviations which are then fed as input to the ANN model. The outputs of the ANN are the predicted coordinates of a source.

To build and train the feed-forward ANN, we use Keras API (Chollet, 2015)—an open-source neural network library that runs on top of Tensorflow (Abadi et al., 2015). We use the rectified linear unit as activation function for the hidden layers while the output layer uses a linear activation function. The loss function for training the ANN model is chosen to be the averaged squared L_2-norm of residuals between the predicted location and the associated label from the training set:

$$J = \frac{1}{L}\sum_{l=1}^{L} \|\mathbf{x}_{ANN}^{(l)} - \mathbf{x}_{Syn}^{(l)}\|_2^2, \tag{4}$$

where L is used to denote the total number of synthetic sources, while $\mathbf{x}_{ANN}$ and $\mathbf{x}_{Syn}$ denote the coordinate vectors for the predicted source location and true source location, respectively.

Then training the neural network amounts to being an optimization problem of minimizing the loss function given in Eq. 4. To do so, we use the Adam optimizer (Kingma and Ba, 2014) with mini-batch training. The training of the network terminates when the network's weights and biases are adjusted, misfit between the input and the output (defined by the loss function 4) is below a certain threshold. While increasing the hidden layers and/or the number of neurons in each hidden layer may result in improved performance on the training set, beyond a certain point, it leads to the problem of over-fitting, causing poor performance on test data. Hence, we deliberately designed the neural network architecture through trial and error (Hao et al., 2020).

2.3 Event location in case of missing data

In field data, it is often the case that some stations do not record a seismic event, or the records are too noisy leading to the inability to pick a wave arrival. Due to a fixed architecture, the ANN model expects input for all stations that it has been trained on. This makes the application of the proposed approach tricky in the case of field data. To overcome this problem, one approach is to retrain the ANN model only for the stations that have the observed P-wave arrival picks. However, it is time consuming to train the ANN each time from beginning, and, therefore, we propose to use fine tuning instead. Fine tuning is a machine

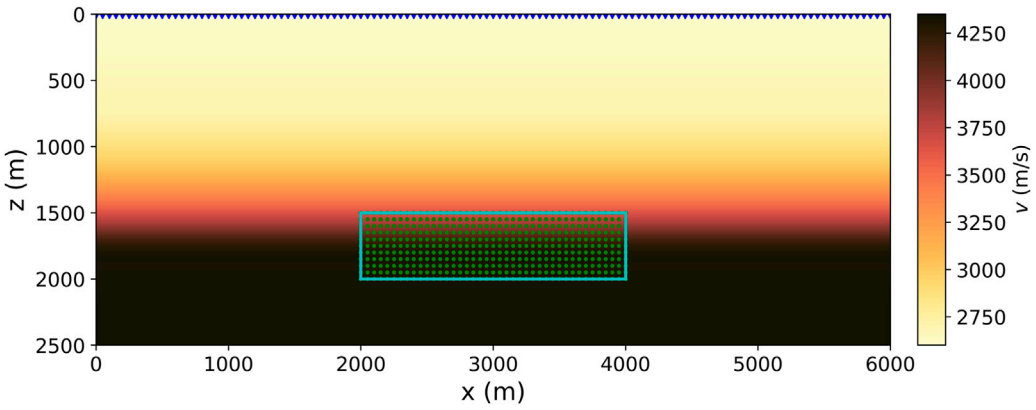

FIGURE 1
The 2-D P-wave velocity model considered for the tests. The cyan rectangular box shows the zone of interest with expected seismicity. Green dots represent 451 source positions used for training. Blue triangles on the top of the model denote 121 seismic stations. The model is taken from Hao et al. (2020).

learning technique where model parameters (weights, biases) trained for one task are reused as initial model parameters for another similar task (Anikiev et al. (2021) use a more broad term "transfer learning", but "fine tuning" is more appropriate in this case).

In this study, the network parameters obtained after training of the original neural network with all available receivers as input are used as starting weights for training of a new neural network with the reduced input. In other words, for each new seismic event, we re-train a reduced ANN that is limited to the distribution of stations on which this event has picked arrivals only. To make this re-training faster we use parameters initialized using those from the originally trained ANN with all available stations as input. We show that such re-training is fast and allows near-realtime location. The relevant weights and biases can be easily copied from the original trained neural network model with all available receivers given that the order of stations in the input layer is defined and is consistent between the models. Location using fine tuning significantly reduces the computational overhead without compromising on the accuracy of the predictions.

2.4 Origin time determination

Last but not least, apart from coordinates of a seismic source location algorithms usually provide also the origin time of event. In the proposed method, the origin time t_0 can be estimated by minimizing the least squares misfit $F(t_0)$ between the actual picked arrival times t_i and the traveltimes t_i^c computed for the corresponding receivers for the determined event location (x_0, y_0, z_0) shifted by t_0:

$$F(t_0) = \sum_{i=1}^{N} \left(t_i - \left(t_i^c(x_0, y_0, z_0) + t_0\right)\right)^2.$$

3 Synthetic data examples

To explore the sensitivity of the proposed methodology on different factors that affect the location accuracy, we design a set of simple 2-D synthetic numerical experiments. Figure 1 shows the P-wave velocity model considered for the tests. The model spans 6 km in horizontal direction and is 2.5 km in depth with a grid step of 10 m in both directions. The rectangular box (in cyan) shows the zone of interest (2000 m in x by 500 m in z at an average depth of 1750 m) where we model the synthetic earthquakes. The P-wave velocity distribution in the model is represented by a vertical gradient from 2.6 km/s to 4.35 km/s. In total 121 stations are evenly distributed on the surface (top of the model) with a 50 m interval (blue triangles in Figure 1). This ensures a minimum offset-to-depth ratio of 1:1.

The architecture of the feed-forward neural network is shown in Figure 2. The network consists of three hidden layers with 40 neurons ($M = 40$ in Figure 2) in each layer (Hao et al., 2020). The number of neurons in the input layer equals the number of stations ($N = 121$ in Figure 2), while two neurons in the output layer correspond to the two coordinate axes ($D = 2$ in Figure 2). The activation function for the hidden layer is the rectified linear unit (ReLU), a piecewise linear function, while the final layer has the linear activation function. ReLU is the default activation function for modern deep learning networks (e.g., Glorot et al. (2011)). The source code showing implementation of the described neural network model in Python is available in the Supplemental Material.

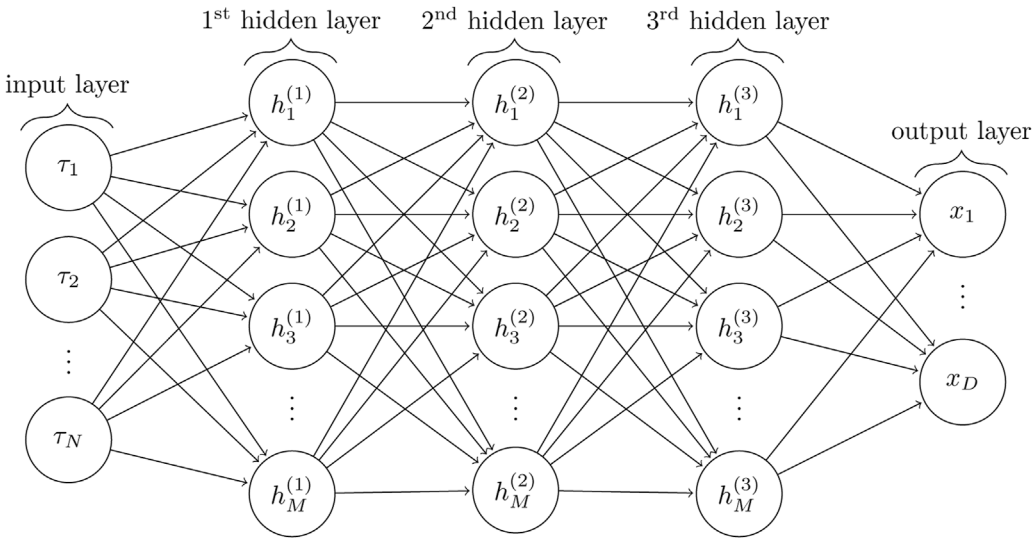

FIGURE 2
Network graph for a 3-layer perceptron with *N* input units and *D* output units, where *N* is a number of seismic stations with picked wave arrivals and *D* is a number of spatial dimensions. Each hidden layer contains *M* hidden units.

TABLE 1 Training time and standard deviation of location errors for different number of training sources and stations.

Number of training sources	Number of stations	Std. dev. Of x error (m)	Std. dev. Of z error (m)	Training time (s)
451	121	16.3	19.1	50.1
451	31	29.3	30.0	44.8
126	121	15.8	25.0	13.3
126	31	44.3	46.5	12.9
27	121	41.1	124.8	4.9
27	31	57.3	133.2	4.7

To train the network, we use synthetic data generated for a set of artificial sources placed on a regular grid in the zone of interest (the green dots and the rectangular box in Figure 1). Having trained the network on these sources, we test the method by feeding synthetic arrival times from 100 test sources randomly placed in the zone of interest. The traveltimes are calculated by the fast sweeping method (FSM, Zhao (2005)) at various station positions on the surface.

Following Hao et al. (2020), we present a systematic study of the different factors affecting the accuracy of the location with the ANN method. We used 1000 epochs to train the ANN in each numerical test, whereas the number of stations and the number of training grid points during these tests were varied (see Table 1). The result show that the accuracy of the located events slightly decreases with the number of training sources while training time is still very short.

3.1 Effect of noise in test data

To measure the sensitivity of the ANN to potential errors in picking P-wave arrival times, we test the network by feeding in traveltimes (of test events) contaminated by Gaussian noise. We train the network using traveltime data from 451 training sources located inside the rectangular box shown in Figure 1 and spaced at an interval of 50 m along both x and z axes. The times of wave arrivals are modelled at the 121 stations on the surface (see Figure 1). Assuming no systematic bias in picking, we consider that picking errors result from random errors (noise). We consider two noise levels by adding to the arrival times a random Gaussian noise with zero mean (μ) and standard deviations (σ) of 10 ms and 20 ms.

Figure 3 shows examples of arrival times of a single test event after subtracting the mean value (see Eq. 2),

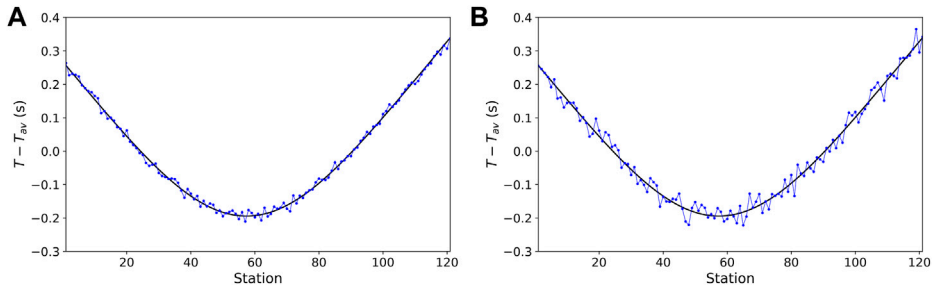

FIGURE 3
Illustration of synthetic arrival times for a test event after subtracting their mean (black curves). The arrival times contaminated with noise are shown with blue dots. **(A)** Arrival times contaminated with zero-mean Gaussian noise with noise level σ =10 ms. **(B)** Arrival times contaminated with zero-mean Gaussian noise with noise level σ =20 ms.

contaminated with Gaussian noise of two levels, corresponding to σ = 10 ms (Figure 3A) and σ = 20 ms (Figure 3B). Figures 4A,B show distribution of location error in x and z coordinates of the source locations for the two noise levels (true locations were subtracted from predicted). We observe that location errors increase as the noise in the arrival times increases. However, even for higher noise contamination in time picks, the maximum location error does not exceed 100 m. Generally the error distributions fit to the Gaussian as seen from the black curves in Figures 4A,B. Parameters of the resulting fitting distribution in each case are shown in the legends of Figures 4A,B.

3.2 Effect of the number of stations

Next, we study the effect of the number of stations (receivers) on location errors. The tested model is the same as in Figure 1, but the number of stations is reduced to 31 stations spaced at an interval of 200 m. Figure 4C shows location errors for test data from the same 100 sources with a Gaussian noise corresponding to σ = 10 ms. By comparing Figures 4A,C, we observe considerable reduction in location accuracy when the number of stations is reduced. We observe that the standard deviation of location errors considerably increases (almost twice).

Figure 4D shows location error histograms for the arrival time noise level of σ = 20 ms. We observe, similar to the previous case, that increased noise worsens the location accuracy (in agreement with Hao et al., 2020). However, when the number of stations in the monitoring array is reduced, the reduction in accuracy is greater, indicating increased sensitivity to noise. Since the monitoring array is horizontal and we are using P-wave traveltimes, the vertical location is less constrained, and therefore the vertical location errors increase more than the horizontal errors. However, even in the worst considered scenario, the maximum location error observed is around 150 m, which is about three steps of the training grid (50 m).

3.3 Effect of the number of training sources

Finally, we study the effect of the number of sources used to train the network. Table 1 shows the training times and standard deviations of x and z location errors for the neural network trained using 451, 126, and 27 sources, corresponding to regular intervals of 50 m, 100 m, and 250 m, and for different station distributions: with 31 and 121 stations. The test data in all cases were contaminated by Gaussian noise with σ = 10 ms. Computations were performed on a laptop with NVIDIA GeForce MX150 graphics card.

It is obvious that the training time reduces as the number of training sources decreases, but the reduction in accuracy is significant. The training time is also slightly less if fewer stations are used. This observation suggests using a higher number of sources will improve the location accuracy. It is worth noting that a smaller training grid but a denser station array gives higher horizontal accuracy than a larger training grid but a coarser station array. This is not always true for vertical accuracy, which seems to be more sensitive to the number of training nodes.

4 Real data examples

To test the ANN method on real data, we apply the methodology to the field microseismic monitoring dataset gathered on the Woodford shale reservoir (Figure 5) in Oklahoma, United States.

4.1 Real seismic monitoring setting

Figure 5 show the 3-D inhomogeneous isotropic P-wave velocity model (Figure 5A) and the microseismic data acquisition geometry (Figure 5B). The original grid spacing of the velocity model in x-, y- and z-directions is uniform and equal

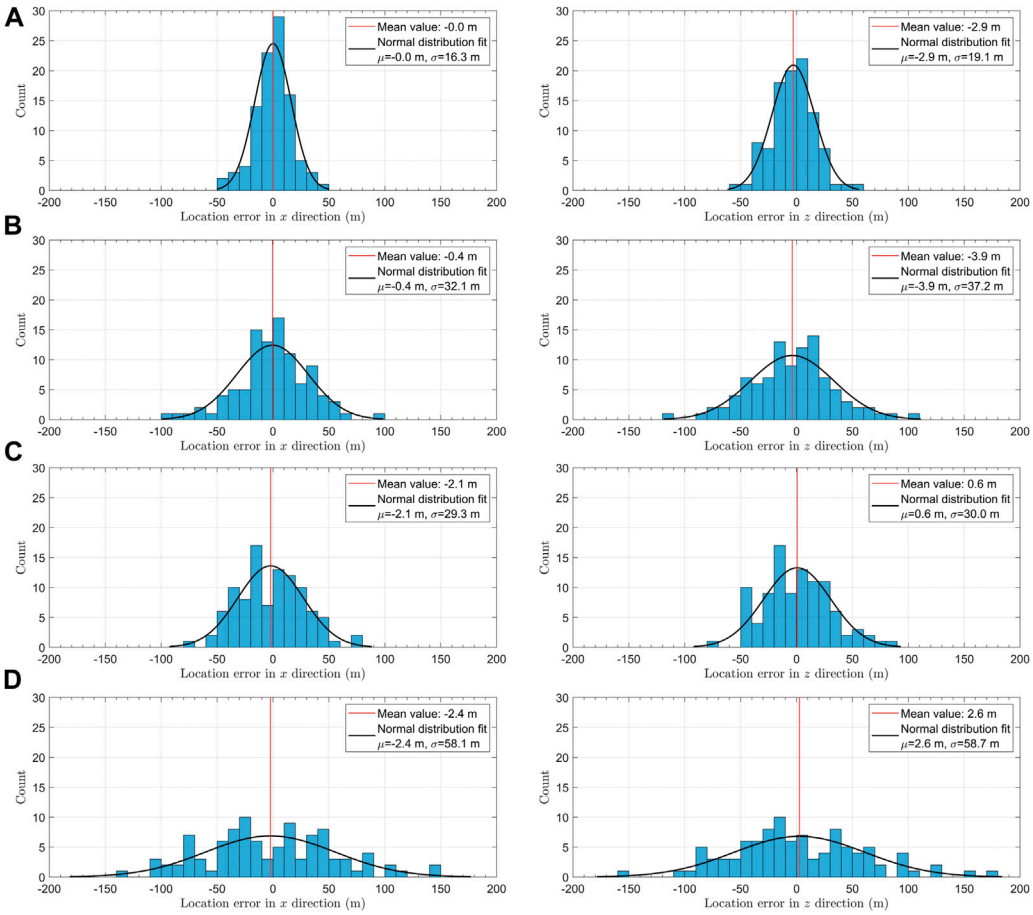

FIGURE 4
Location errors in *x* and *z* directions for 100 test sources with arrival times measured on 121 equispaced stations **(A and B)** and 31 equispaced stations **(C and D)**, and contaminated by noise with Gaussian distribution and σ =10 ms **(A and C)** and σ =20 ms **(B and D)**.

to 22.86 m (75 ft). Geophones recording vertical displacement component are distributed in the form of a star-like array with 10 arms (Figure 5B), comprising 911 seismic stations in total.

The same microseismic monitoring setting and dataset was used by Anikiev et al. (2014) to benchmark the diffraction stacking location technique (see also Anikiev (2015)). The velocity model was derived from the processing of active source data or sonic logs and calibrated with sources at known positions (Anikiev et al., 2014). In this paper we benchmark the ANN methodology by comparing it with the traveltime maximum likelihood (TML) method (Eisner et al., 2010), following Anikiev et al. (2014).

The TML algorithm minimizes the misfit between manually picked arrival times and synthetic traveltimes calculated for a reference velocity model (Anikiev et al., 2021). Hypocenter locations then are obtained from a resulting probability density function. Therefore, the TML: (i) uses the same input data as the ANN and (ii) is also based on residual minimization (Anikiev et al., 2021). This makes both ANN and TML methods suitable for comparison with the TML method used as a benchmark.

4.2 Preliminary synthetic ANN test for the real monitoring setting

Similar to a 2-D synthetic numerical study, for the 3-D case study we also design the feed-forward artificial neural network with three hidden layers (see Figure 2). Provided that synthetic data do not have gaps, the input layer consists of 911 neurons (N = 911 in Figure 2), each of which represents an arrival time deviation (Eq. 2) at the appropriate station. Each of the three hidden layers has 250 neurons (M = 250 in Figure 2). The array of seismic stations in this real example is larger than the one used in the 2-D study, leading to a larger amount of neurons in the hidden layers. The output layer now consists of 3 neurons (D = 3

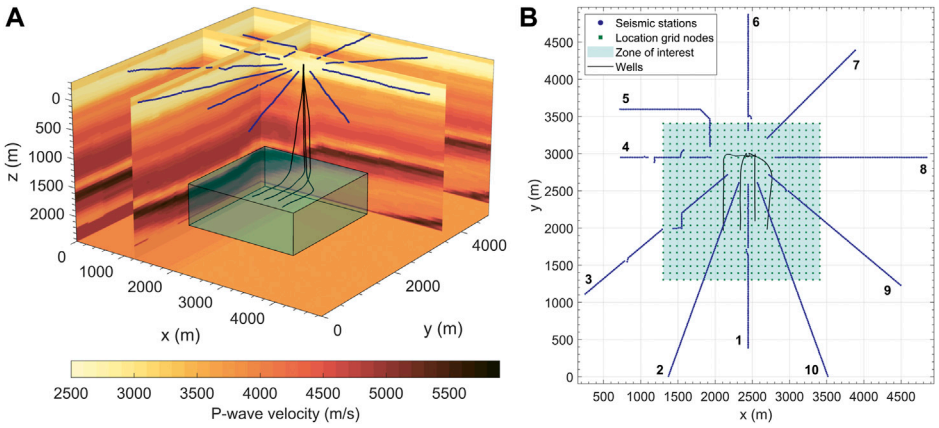

FIGURE 5
Microseismic monitoring setting at the Woodford shale reservoir in Oklahoma, United States: **(A)** P-wave velocity model and **(B)** data acquisition geometry. **(A)** 3-D view of the P-wave velocity model. The colorbar displays the color-coded P-wave velocities in m/s. The blue dots on the surface are seismic stations. The cyan rectangular box shows the zone of interest around lateral parts of the four wells (black lines). The zone ranges from 1303.02 m (4275 ft) to 3406.14 m (11175 ft) along the *x* (easting) and *y* (northing) axes, and from 1546.86 m (5075 ft) to 2278.38 m (7475 ft) along the *z* (depth) axis. **(B)** Map view of the data acquisition geometry: the star-like seismic station array with 10 arms (numbers) and 911 stations (blue dots), the 24 x 24 x 9 location grid with 5184 nodes (green squares show only 576 upper grid nodes), distributed over the zone of interest (cyan square), resulting in the grid spacing of 91.44 m (300 ft).

in Figure 2), which represent the predicted *x*-, *y*- and *z*-coordinates of the event hypocenter.

Location grid for TML is represented by an array of 5184 grid nodes consisting of 24 × 24 nodes in 9 vertical planes (Figure 5). The grid nodes are regularly distributed over the zone of interest (cyan rectangular block in Figure 5A) around lateral parts of the four wells (Figure 5B), so that the resulting grid spacing of the location grid is 91.44 m (300 ft) in all directions. For consistency, the same grid was used to produce the training data, i.e. 5184 training sources were placed to the positions of the location grid nodes, forming a training grid (see also Anikiev et al., 2021).

For each training source, we applied the 3-D factored FSM algorithm (Fomel et al., 2009) to obtain the synthetic traveltimes at all the stations. The factored FSM significantly reduces the location error, especially in depth, due to much higher accuracy of computed traveltimes at far offsets (Alexandrov et al., 2021). The computed traveltimes, after removing the mean (Eq. 2) and scaling (Eq. 3), are used as an input for the ANN, which is then trained until its output matches the coordinates of the training sources by minimizing the loss function 4.

In order to evaluate the performance of the ANN by using the synthetic data, we randomly generated 100 test sources inside the zone of interest (Figure 5) and computed the corresponding traveltimes from these sources to the seismic stations with the factored FSM using the known velocity model. Figure 6 shows the error distributions of the predicted source coordinates (true locations were subtracted from predicted). The maximum errors in the *x*- and *y*-coordinates do not exceed 10 m, and the maximum error in the *z*-coordinate is less than 20 m, which is close to the grid spacing interval of the velocity model (22.86 m) and much smaller than the training grid spacing (91.44 m). The mean values of the observed error distributions are close to zero. The forms of these distributions are similar to Gaussian, implying that the locations should be correct as long as the input arrival times are correct.

4.3 Benchmarking on real data

For benchmarking we selected 75 independent seismic events strong enough to be picked on majority of stations without stacking. Figure 7 shows deviation times (see Eq. 2) obtained from manual P-wave arrival time picking for all 75 events on 911 stations. White gaps correspond to the stations for which the picking was not possible or not reliable (Anikiev et al., 2021). The seismic events are sorted by the number of missing arrival time picks. This number varies from 41 for the best picked event (event 1, Figure 7) to 503 for the worst picked event (event 75, Figure 7). Figure 7 shows that even the most distinct event (event 1) has clear P-wave arrivals only on 870 stations out of 911.

Event 39 has different picking pattern due to an unusual distinctive moveout and apex point of the traveltime curve, indicating a unique epicenter position. Event 74 (second last) was incorrectly picked at several stations at the far offset of the 6-th arm (see Figure 5B). These picking errors result in the set of big negative deviations of arrival time (see Figure 7). We kept this incorrectly picked event to compare the sensitivity of the two methods to a real case scenario where either a human or a picking

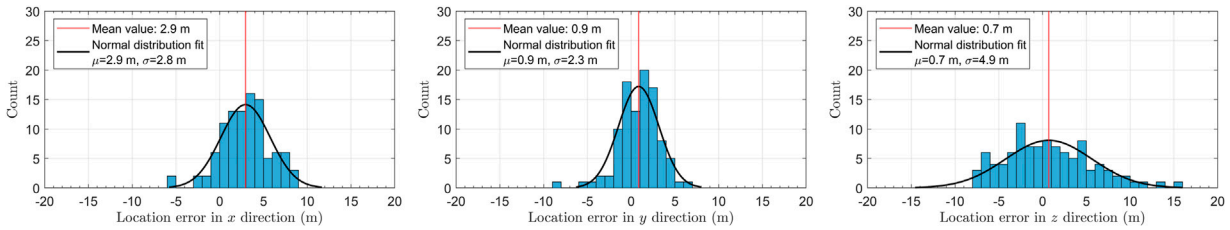

FIGURE 6
Location errors in three directions: *x* (left), *y* (middle) and *z* (right) for 100 test sources (without noise). Black curve in each panel show result of Gaussian distribution fit, corresponding parameters are listed in the panel legend.

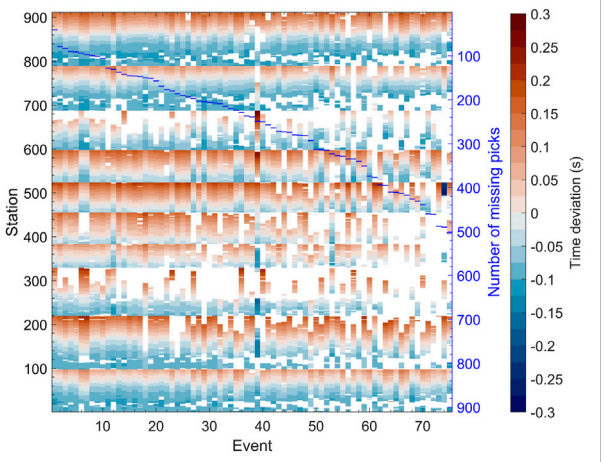

FIGURE 7
Deviation times obtained from manual P-wave arrival time picking for 75 real microseismic events recorded with 911 seismic stations. Blue horizontal dashes show number of missing (out of 911) time picks (right axis) for each event.

algorithm wrongly identifies the P-wave arrival. We observe that the ANN algorithm results in a similar location anomaly as the TML. Classical traveltime-based location methods like TML are flexible to missing data. In contrast to that, data gaps introduce a serious fundamental complexity for feed-forward ANNs, which require regular input.

As a proof of concept for real data, following Anikiev et al. (2021), we first tested a "brute-force" approach by training the ANN from scratch for each real event separately, taking into account only stations with available time picks. This means that we re-trained the neural network for each picked event using only the stations with available picks. In the data application of Anikiev et al. (2021) a fixed number of training epochs (4000) and an initial learning rate of 10^{-4} were used. This could result in an overfitting, especially when the validation set (100 random sources) has a similar distribution to the training data. Overfitting is a common problem in ML which occurs when the ANN fits the training data too well. In order to avoid overfitting we follow a different approach. We first split the training data and use 15% of initial dataset for validation and then implemented early stopping (e.g., Chollet, 2015), i.e. tracking the validation loss and stopping the training before overfitting occurs. This has also reduced the overall time cost of the training. We used a patience parameter of 100 as a stopping criteria in each case. The patience parameter is a number of epochs with no improvement after which training will be stopped (see Keras API documentation (Chollet, 2015). Moreover, we set a loss function value threshold of 391.9 m^2 as an additional criterion. If loss function goes lower than this threshold, the training stops. The threshold value was estimated from the velocity model grid step of 22.86 m: $3 \times (22.86/2)^2 = 391.9$. This means that if the misfit is corresponding to one-half of the velocity model grid step (used also for traveltime computation), the training already reaches the reasonable accuracy level, although some other multiples of the grid step might be also acceptable. Application of these two criteria provides the compromise between the accuracy and computation time of training with its numerical stability and helps to avoid overfitting, thus making the training flexible.

Figure 8 shows comparison of the TML locations (blue circles) with the ANN locations (orange circles) for all 75 events. To produce this result for each event, we performed re-training of the ANN from scratch. As seen from Table 2, the number of epochs until stopping varied from 674 to 1943 with an average of about 1214. Event 74, which was picked with several errors, is located by the ANN method at an extremely large depth of around 4500 m, outside of the training grid (green dots in Figure 8), whereas the TML locates it close to the lower bound of the grid. This indicates that the ANN is more sensitive to data with large uncertainty (outliers, e. g, false positive detections) than the TML. Such deviations can be used in quality control as indicators of input data errors. Location misfit for the event 74 in lateral direction is smaller, so the true epicenter is expected to be to the north from the wells. Event 39, which has the aforementioned dissimilar arrival time pattern

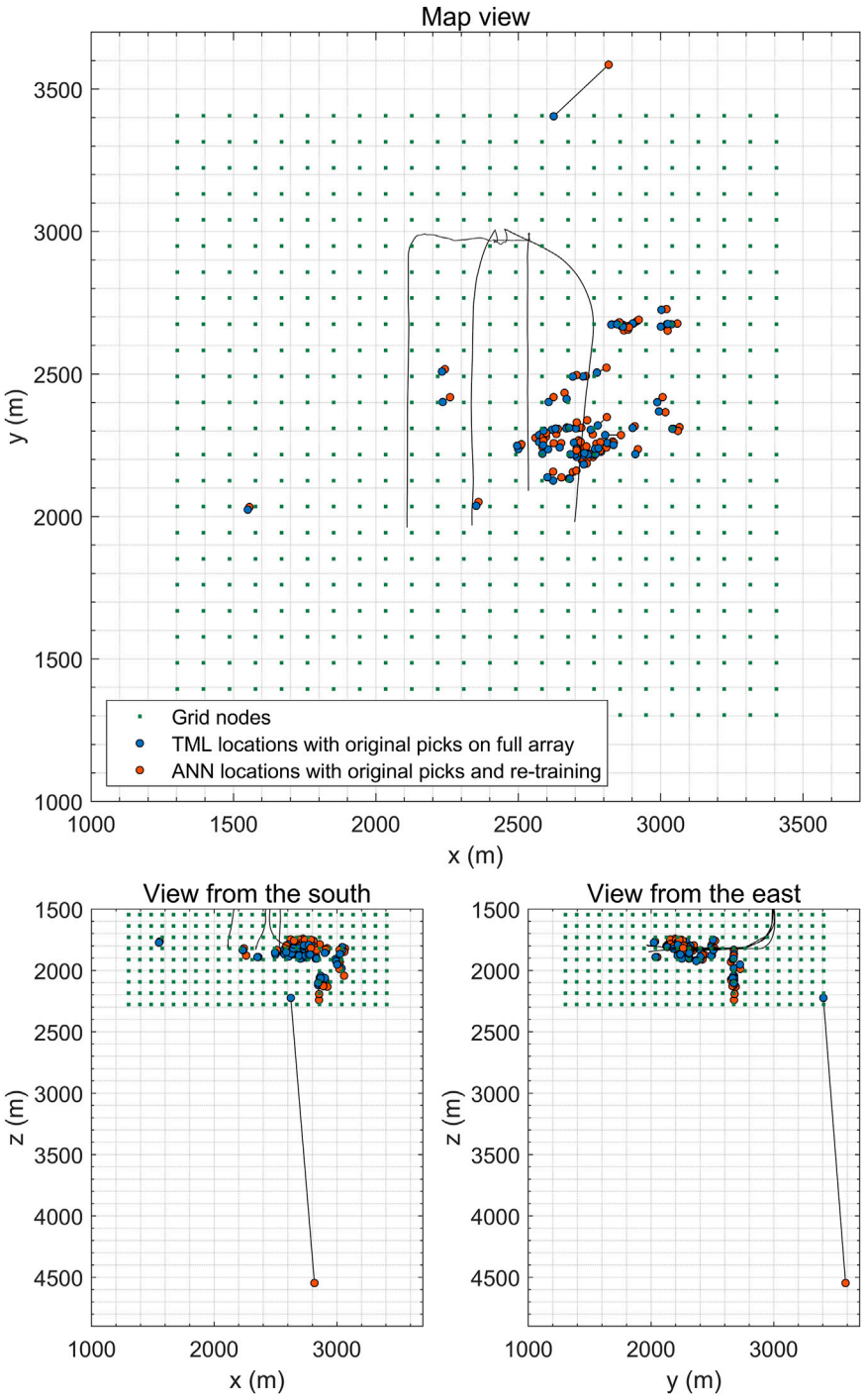

FIGURE 8
Comparison of TML locations (blue circles) with ANN locations (orange circles) obtained with re-training for all 75 events: map view (top panel), view from the south (left bottom panel), view from the east (right bottom panel). Two locations for the same event are connected with a black line. Green dots represent the grid nodes for the TML, also used as training sources for the ANN. Wells are shown with black lines.

(Figure 7), is predictably located by both methods to the south-southwest from the wells and the cluster of the remaining events.

If we take a closer look into the locations of the 74 reliably picked events (excluding the event 74), as displayed by Figure 9, we see that horizontal misfit between the locations by TML and

TABLE 2 Computation time costs for the ANN training and location of 75 events, and location misfits when compared with the TML.

Operation parameter	Training for all stations	Location with re-training	Location with fine tuning
Max. limit of training epochs	4000	4000 per event	100 per event
Min. number of epochs to stop	1027	674	17
Av. number of epochs to stop	1027	1214	39
Max. number of epochs to stop	1027	1943	71
Early stopping patience	100	100	5
Time cost (s)	472.6	40632.2	1610.4
Av. time cost per event (s)	-	541.8	21.5
Min. abs. misfit (m)	-	8.7	9.0
Av. abs. misfit (m)	-	35.5	32.1
Max. abs. misfit (m)	-	121.9	72.5

ANN does not exceed the spacing of the location (training) grid even for the distant event 39 (southwestern corner on the map view in Figure 9). Vertical misfit is generally larger but is comparable to the grid spacing as well (in agreement with Anikiev et al., 2021).

To avoid the time-consuming re-training from beginning, we propose to use fine tuning (transfer learning in Anikiev et al. (2021), i.e., make use of the weights of a pre-trained network to speed up adaptation to the new input pattern. Technically, fine tuning consists of unfreezing the initially trained model and further additional training on the new data with a lower learning rate. The neural network is first pre-trained on the complete array of stations with the same stopping criteria mentioned before. The trained weights and biases are then transferred into the corresponding layer of a new neural network that is designed for each event with its own input layer dimension according to the pattern of available P-wave arrival time picks. Finally, this newly set network is shortly trained (fine-tuned) with a patience of 5 and the last used learning rate taken from the pre-training.

Figure 10 shows the TML locations of the same 74 reliably picked events compared to the ANN location obtained with fine tuning. We observe that the locations obtained using fine tuning are similar to those obtained with the entirely re-trained neural network, but they are achieved much faster. The average misfit of locations obtained with fine tuning with TML locations is lower (see Table 2). At the same time fine tuning significantly reduces the amount of required training epochs and time cost. The average time cost with fine tuning is roughly 25 times lower. The pre-training stopped at 1027 epochs, which took less than 8 min (Table 2), while an average of 39 epochs in terms of fine tuning per each event provide sufficient accuracy in tens of seconds (Table 2, Figure 10). All computations were performed on the same machine as in the synthetic data case.

Figure 11, Figure 12 show histograms of misfit in x-, y- and z-directions together with absolute misfits for ANN with re-training and ANN with fine tuning, respectively. The lateral misfits in case of ANN with fine tuning do not exceed 40 m, which is twice as less than the training grid spacing of 91.44 m (Figure 12). The vertical misfits are predictably larger, especially in case of ANN with re-training, where it reaches 120 m (Figure 11). The standard deviations of the misfit distributions in lateral direction are similar for both results. In contrast, the standard deviation of the vertical misfit is smaller for locations in Figure 12 obtained with fine tuning. The distribution of the absolute misfits (square root of the sum of squared misfits in x-, y- and z-directions) in both cases fits well to the non-central χ distribution with 3 degrees of freedom. The latter is mathematically consistent with the distribution of the absolute value (square root of sum of squares) of the three independent normally distributed quantities with non-zero mean (e.g., Bhattacharya and Burman (2016). The distribution is described by the non-centrality parameter, reflecting the characteristic difference between the two results. Statistical distributions for both cases (ANN with re-training and with fine tuning) can be described with non-centrality parameter much smaller than the training grid step. The maximum absolute misfit for fine tuning (Figure 11) is less than 80 m, so it does not exceed the training grid step, whereas for ANN with re-training it exceeds it with values over 120 m.

Comparison of Figure 9 with Figure 10 and Figure 11 with Figure 12 shows that the proposed ANN methodology extended with fine tuning provides sufficient location accuracy without time consuming computations, as illustrated by Table 2.

5 Discussion

In the proposed ANN method the neural network is trained only with synthetic data, i.e., no existing seismic data are needed (although the method does not exclude the ability to use existing catalog locations), and so the training can be done before the

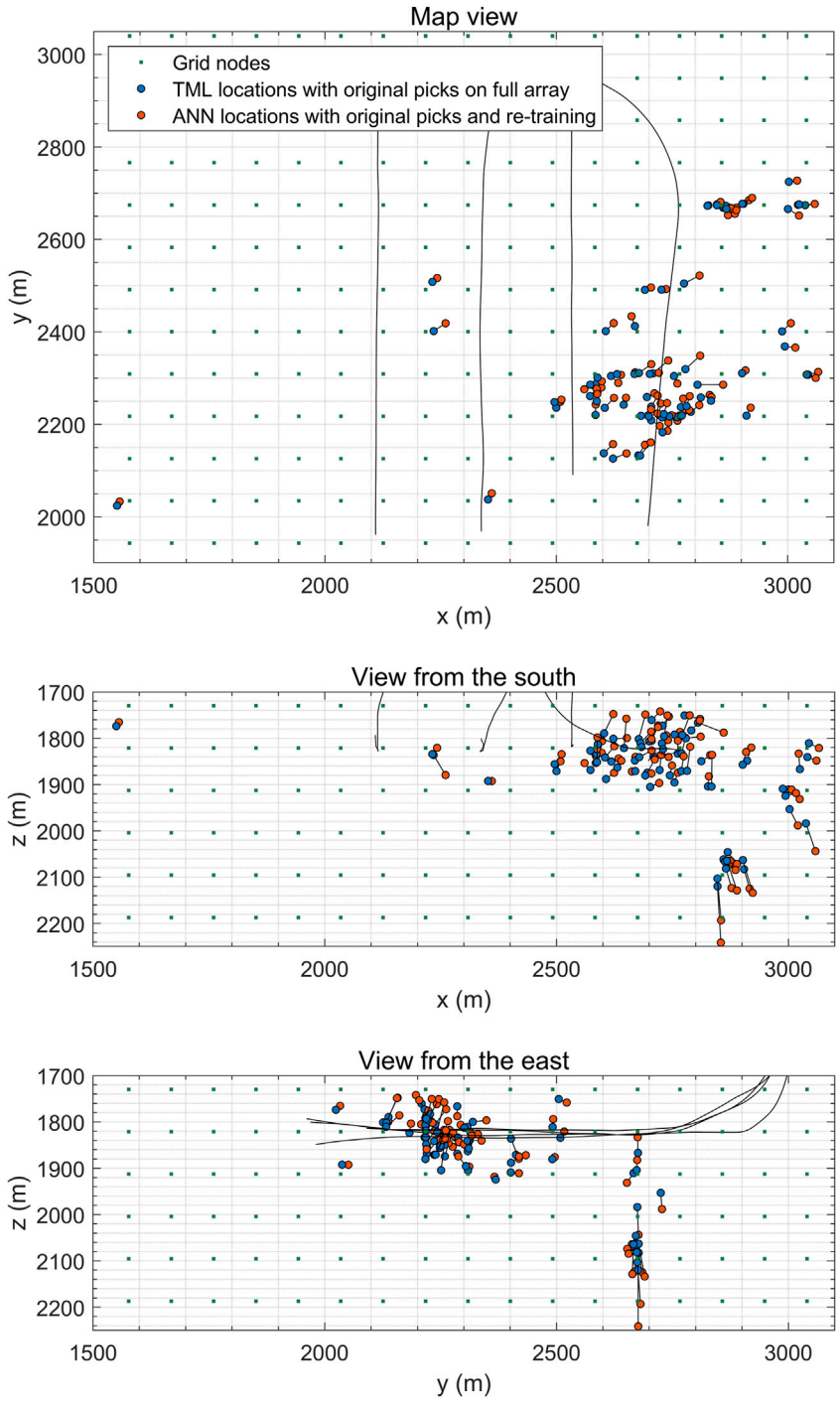

FIGURE 9
Comparison TML locations (blue circles) with ANN locations (orange circles) obtained with re-training for 74 reliably picked events: map view (top panel), view from the south (middle panel), view from the east (bottom panel). Two locations for the same event are connected with a black line. Green dots represent the grid nodes for the TML, also used as training sources for the ANN. Wells are shown with black lines.

monitoring starts. However, if enough seismic events in the area are observed previously, it can be trained using P-wave arrivals and locations of these real events. Obviously, the accuracy of the network trained with real events depends on number of events

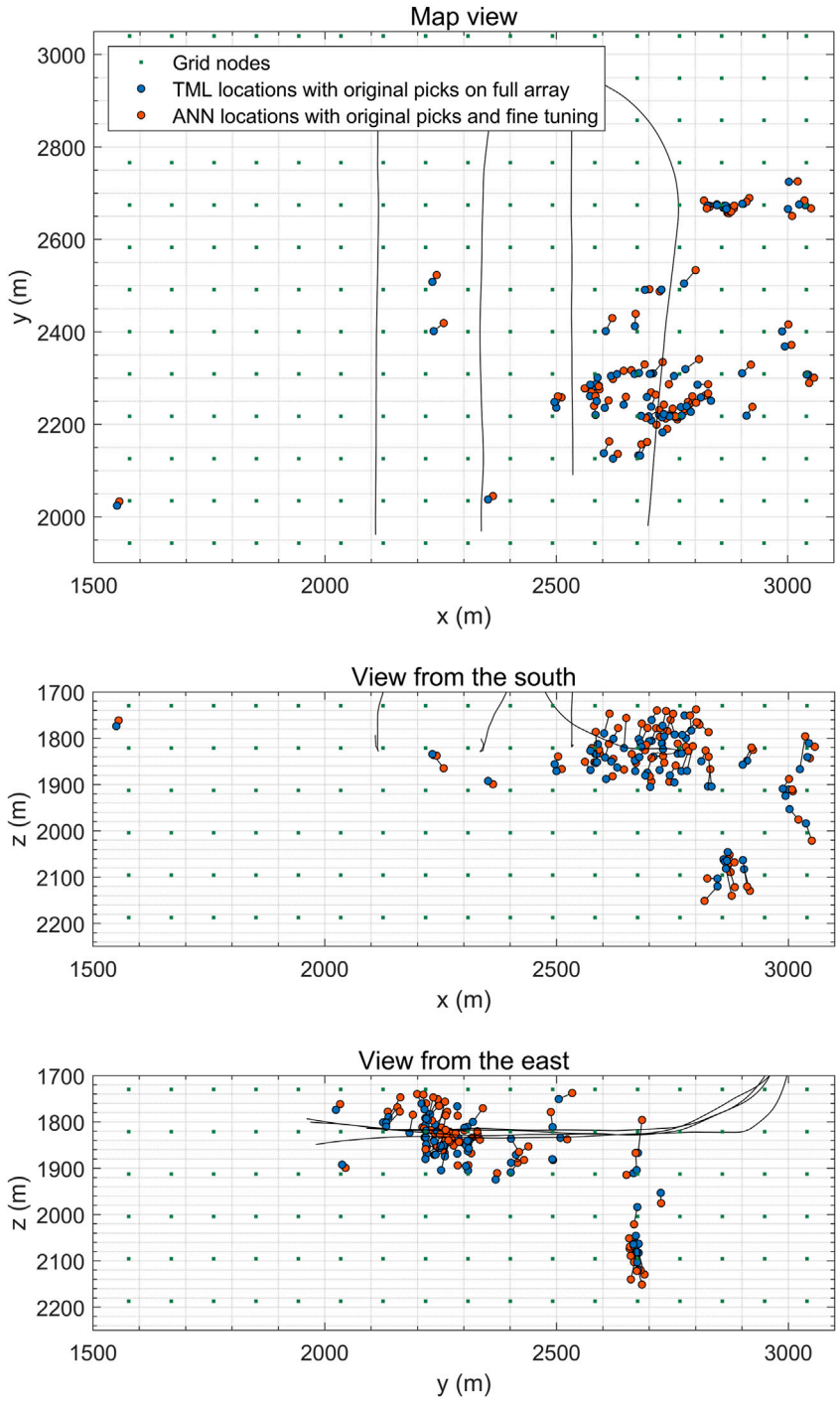

FIGURE 10
Comparison of TML locations (blue circles) with ANN locations (orange circles) obtained with fine tuning for 74 reliably picked events: map view (top panel), view from the south (middle panel), view from the east (bottom panel). Two locations for the same event are connected with a black line. Green dots represent the grid nodes for the TML, also used as training sources for the ANN. Wells are shown with black lines.

and spatial distribution of their locations. Training with synthetic data is more time consuming and computationally expensive but the accuracy of resulting ANN locations is higher. The time needed to locate a single event stays the same once the network is

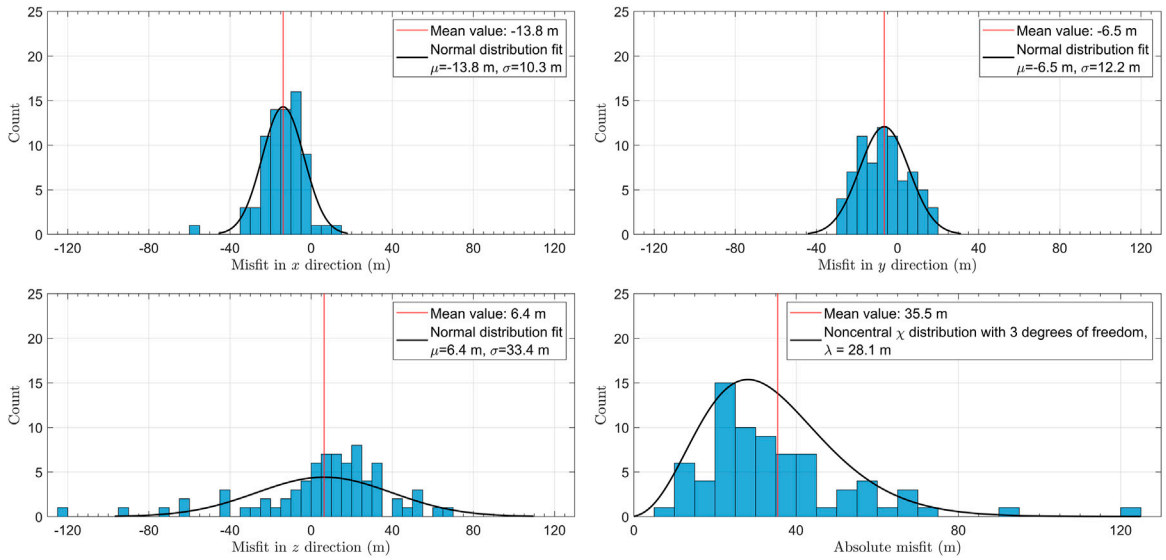

FIGURE 11
Histograms of misfits between TML locations and ANN locations obtained with re-training for 74 reliably picked events. Black curve in each panel shows the result of distribution fit with the corresponding parameters listed in the panel legend.

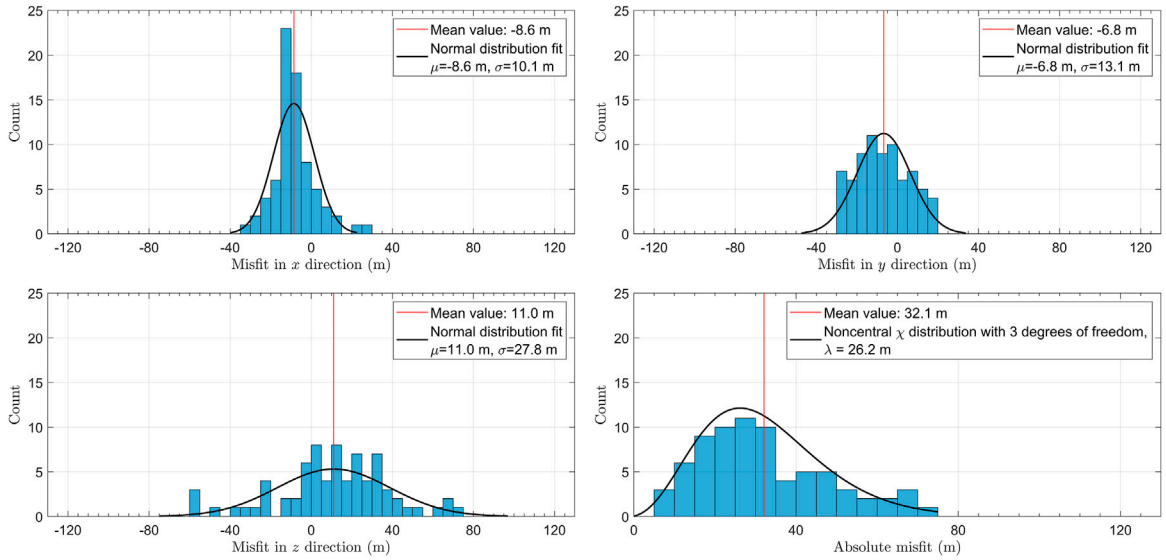

FIGURE 12
Histograms of misfits between TML locations and ANN locations obtained with fine tuning for 74 reliably picked events. Black curve in each panel shows the result of distribution fit with the corresponding parameters listed in the panel legend.

pre-trained, no matter whether the training is done with synthetic or real data.

A typical workflow for deployment of the proposed method for microseismic monitoring is represented in Figure 13. The most time consuming parts: computation of the traveltime lookup table and training of the ANN are performed before the monitoring starts. Real-time detection stage can also be implemented with the help of ML (out of the

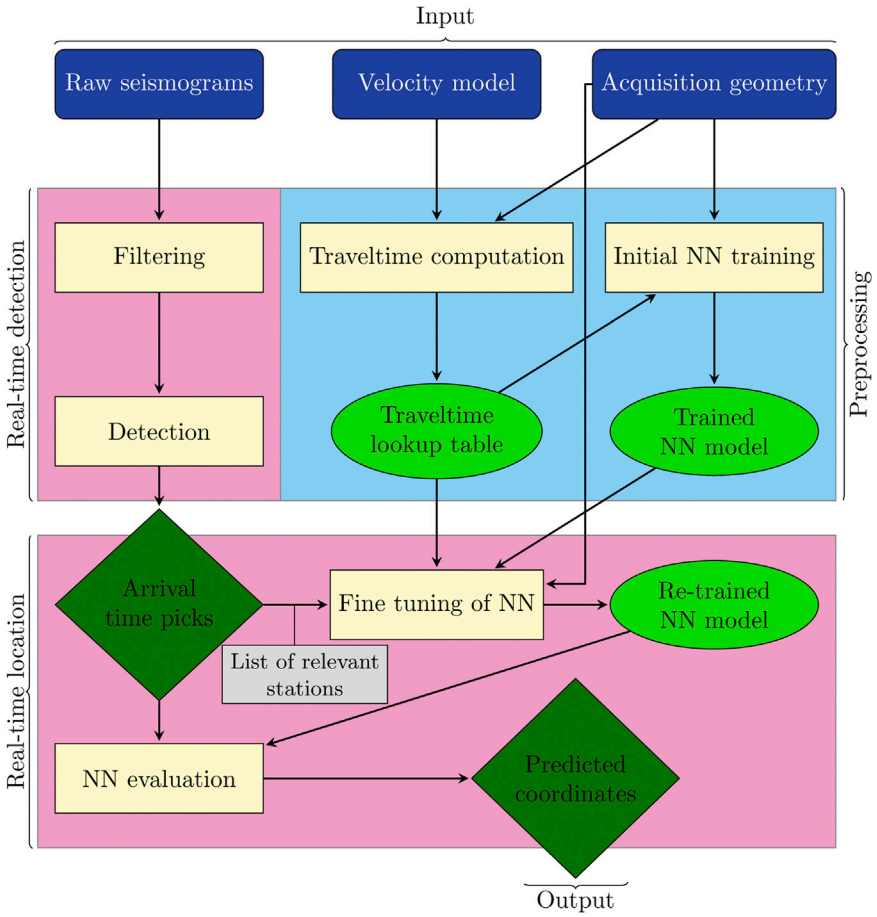

FIGURE 13
The flowchart showing a typical implementation of ANN-based location in real-time microseismic monitoring setting. Time consuming blocks in the blue zone belong to a pre-processing stage performed prior to the monitoring, while blocks in the reddish zones are in real time. Blue blocks represent input data, yellow blocks correspond to processes, green ellipses show intermediate products and deep-green diamonds show the output: arrival time picks and predicted hypocenter coordinates. Gray block denotes that fine tuning requires only the list of relevant stations, arrival time picks from raw seismograms are used for NN evaluation only.

scope of this paper). The essential part of detection stage is to provide the P-wave arrival times for a certain subset of stations (picking depends on the quality of the record and often cannot be done reliably on all stations). Real-time location then requires inexpensive fine tuning of the initially trained NN for the provided set of stations. The fine-tuned network model is stored and re-used for further events with the same subset of stations, thus reducing the processing time. We suggest to use the 3-layer perceptron architecture of the NN explained by Figure 2, where $M = 250$ is optimal for number of recording seismic stations N around 1000.

In real-time monitoring applications, time to deliver the source locations is important. We have shown that combining fine-tuning with early stopping and additional loss function threshold gives a compromise between the location accuracy and computation time required for additional training. The fine tuning step is done in seconds on a mobile mid-range GPU and won't be a bottleneck in real-time implementations on more performant GPU systems.

As we show on synthetic examples, the developed ANN method suffers from the same known limitations as all the other location methods when monitoring with surface array. The average location uncertainty in vertical direction is typically higher than in horizontal directions when only P-wave arrival times are input. If data quality allows, methods can be usually extended with S-wave arrivals and location accuracy improves. Location quality decreases with higher uncertainty of picks (related to SNR of arrivals in real data) and with coarser training grid. However, in our case, the latter can be easily eliminated as the ANN can be pre-trained with synthetic events in an arbitrarily dense training grid.

Location uncertainty estimates are highly dependent on the accuracy of the velocity model, which is always different. We have tested the accuracy of location based on synthetic tests and provided estimates of the standard deviation in each case. We consider this to be a fair representation of the potential location error. Integration of the dedicated uncertainty estimates into the ML prediction is a more sophisticated task which is out of the scope of the present manuscript. It is certainly one of the directions for further advanced studies.

In real data, signal-to-noise ratio varies for each event and consequently number of input stations with available picks changes, leading to gaps in the input data. In order to solve this problem we initially considered several options.

First, one can use interpolation of the data at the stations with missing time picks. Interpolation methods for uniform grids are not applicable in this case, as the stations are usually distributed irregularly. The kriging method (Stein, 1999) models the interpolated data through a Gaussian process governed by prior covariances, and it is applicable to irregular grids. The kriging algorithm performs well for small local gaps, e.g., when few stations with missing picks are surrounded by the stations with available time arrivals. However, it can introduce a significant bias in the case when the missing picks occur on the stations at the edge of the network or along a certain direction due to the radiation pattern defined by the source mechanism of an earthquake. Such a situation is typical when using star-like geometries (Anikiev et al., 2014; Staněk et al., 2015). Besides, any interpolation method is likely to introduce a non-physical distortion to the set of traveltimes in the case of a coarse network of stations.

The benchmark comparison with the TML method shows that the proposed location algorithm is as good as any other arrival time based location technique. It provides good location if the velocity model is good and arrival times are correctly picked. Velocity model errors are perhaps the most significant source of location biases in both surface and downhole monitoring (Eisner et al., 2010). Very much the same as for any other arrival time based method (e.g., for the mentioned TML method), the errors in velocity model in the proposed ANN approach influence only the traveltime computation. Therefore, we consider the accuracy of the velocity model to be a more general problem that has already been covered in literature. For instance, Eisner et al. (2009) presented an extensive study of the effect of errors in the velocity model on locations derived from arrival time picks by simulating uncertainties for frequently used borehole and surface acquisition receiver geometries and assuming a homogeneous medium.

Another option for benchmarking would be to use any other conventional location method to calculate the traveltimes based on the estimated location. This means that prior to the prediction of location by the ANN, the real traveltimes are "regularized" using the modeled ones. For such an approach, the TML methodology suits the best, as it is based on the maximum likelihood of traveltimes, which is consistent with the chosen cost function in our algorithm. However, there is an obvious disadvantage of this approach–for each event, it requires an additional step of location, therefore making the ANN-based location computationally less attractive.

Finally, in order to be independent of the missing data, one could pre-train many ANNs for different sets of available stations. Every possible combination of stations requires 2^N trainings with N being a number of seismic stations. It possible for very small N and is out of question for large N. Alternatively, we may consider training only for a certain set of "backbone" stations where all events are picked, and throwing away all other picks on the remaining stations.

After testing the aforementioned methods, we decided to use fine tuning to overcome the issue of missing picks. Fine tuning is an effective method taking advantage of weights of ANN obtained after training with full array of stations acquiring data. With a limited number of epochs, we are able to quickly train ANN specific for each individual event picked on a specific subset of stations. The other methods seem not to be as robust and accurate as the fine-tuning approach.

A ML location method that is flexible to the number of seismic stations was proposed by van den Ende and Ampuero (2020), who developed a graph neural network (GNN) approach which is also invariant to the order in which the stations are arranged. First, authors suggest to analyze the waveforms on each station using a CNN which extracts certain features, and then the location of stations is appended to form a feature vector that serves as an input for the second multilayer perceptron (MLP) component. After performing the operation on every station, the results are combined into a graph feature vector. So far we have considered to adapt this approach for traveltime-based location, where the selected feature at each station is the picked arrival time. GNN might result in potential improvement, but the challenge is in enforcing the feature to be the arrival time.

6 Conclusion

A machine learning methodology proposed earlier was extended in this paper into a practical technique capable of locating real microseismic events in a typical microseismic monitoring setting. This extension represents a non-trivial task which was not anticipated earlier.

The location method is based on P-wave arrival picks input and artificial neural network trained on a set of known locations. Its main advantage is a possibility to train the system only with

synthetic data, i.e., no existing seismic data are needed before its application. Therefore, the training can be successfully done even in areas where any prior seismicity has not been observed, and it can be done in advance, before the actual seismic monitoring starts.

The training dataset is computed with known velocity model, monitoring array, and a set grid of training locations in the subsurface. The ANN must be trained with the same (sub-)set of stations as the data of real event are from. However, in reality, a subset of stations with available picks for each event changes due to various reasons (variable SNR, missing stations, etc.). To overcome this problem, we use fine tuning: the weights of ANN obtained after training using full array of seismic stations are used as initial values and a new ANN can be quickly trained for each individual event picked on a specific subset of stations. In order to prevent overfitting we further investigated the use of early stopping by reserving part of the training data for validation and tracking the validation loss.

The extended methodology was tested on 2D and 3D synthetic examples that allowed us to determine optimal neural network parameters and estimate location errors. We showed that accuracy of resulting locations increases with density of training location grid, number of available seismic stations and quality of input data, which is in agreement with the behavior of classical location methods. The ANN method was benchmarked against a commonly used TML method on a real dataset acquired during hydraulic fracturing. We demonstrated that locations from both methods are comparable and the location misfit is similar to the training grid spacing when a reliable velocity model is used. However, the ANN-based location is less sensitive to gridding, more sensitive to data outliers, and implies simple and straightforward training. Use of the early stopping criterion presented in this study helped to significantly reduce the computation time both for initial training using the full set of seismic stations and for the fine-tuning training step.

Analysis of real data application results show that the proposed approach is efficient and can be applied during real-time monitoring when combined with reliable automatic event detection and arrival time picking algorithms. We proposed a workflow for implementation of the method in the real-time monitoring setting.

Data availability statement

The data analyzed in this study is subject to the following licenses/restrictions: The data underlying this article were provided by Newfield Exploration Mid Continent Inc. and MicroSeismic, Inc. by permission. Data will be shared on reasonable request to the corresponding author with permission of MicroSeismic, Inc. The source code showing implementation of the described neural network model in Python is available in the Supplemental Material. Other source codes will be shared on reasonable request to the corresponding author. Requests to access these datasets should be directed to denis.anikiev@gfz-potsdam.de.

Author contributions

This study was conceptualized by LE, UW and QH, with contributions from DAn and FS. The ANN model has been set up, trained and tested on synthetic data by QH with contributions from UW and DAn. FS prepared the real dataset and model with contributions by DAn. The methodology for real data processing was developed by DAn and UW with contributions from FS. The ANN model application to real data including the fine tuning approach was prepared by DAn. The artwork was prepared by DAn with contributions from QH. The results have been analysed by UW and LE with contributions by DAl, NI and QH. The final manuscript has been written by DAn and UW, with contributions by LE, FS, DAl, NI and QH.

Funding

The research is funded by the Helmholtz Centre Potsdam–GFZ German Research Centre for Geosciences (Germany), King Fahd University of Petroleum (Saudi Arabia) and Minerals and Seismik s. r.o (Czech Republic). Publication costs are supported within the funding programme “Open Access Publikationskosten” Deutsche Forschungsgemeinschaft (DFG, German Research Foundation) - Project Number 491075472.

Acknowledgments

The authors thank the College of Petroleum Engineering and Geosciences at KFUPM and Basin Modelling Section at GFZ for support. The Woodford field dataset and model is courtesy of Newfield Exploration Mid Continent Inc. and MicroSeismic, Inc. We are grateful to all the reviewers for their valuable and constructive comments which helped us to improve the manuscript.

Conflict of interest

Authors DAl and LE were employed by the company Seismik s.r.o.

The remaining authors declare that the research was conducted in the absence of any commercial or financial

relationships that could be construed as a potential conflict of interest.

Publisher's note

All claims expressed in this article are solely those of the authors and do not necessarily represent those of their affiliated organizations, or those of the publisher, the editors and the reviewers. Any product that may be evaluated in this article, or claim that may be made by its manufacturer, is not guaranteed or endorsed by the publisher.

Supplementary material

The Supplementary Material for this article can be found online at: https://www.frontiersin.org/articles/10.3389/feart.2022.1046258/full#supplementary-material

References

Abadi, M., Agarwal, A., Barham, P., Brevdo, E., Chen, Z., Citro, C., et al. (2015). TensorFlow: Large-scale machine learning on heterogeneous systems. Available at: http://download.tensorflow.org/paper/whitepaper2015.pdf.

Alexandrov, D., bin Waheed, U., and Eisner, L. (2021). Microseismic location error due to eikonal traveltime calculation. *Appl. Sci.* 11, 982. doi:10.3390/app11030982

Anikiev, D., bin Waheed, U., Staněk, F., Alexandrov, D., and Eisner, L. (2021). "Microseismic event location using artificial neural networks," in *First international meeting for applied geoscience & energy expanded abstracts* (Texas, United States: Society of Exploration Geophysicists), 1661–1665. doi:10.1190/segam2021-3582729.1

Anikiev, D. (2015). "Location and source mechanism determination of microseismic events," Ph.D. thesis (St. Petersburg, Russia: St. Petersburg State University).

Anikiev, D., Valenta, J., Staněk, F., and Eisner, L. (2014). Joint location and source mechanism inversion of microseismic events: Benchmarking on seismicity induced by hydraulic fracturing. *Geophys. J. Int.* 198, 249–258. doi:10.1093/gji/ggu126

Bhandarkar, T., K, V., Satish, N., Sridhar, S., Sivakumar, R., and Ghosh, S. (2019). Earthquake trend prediction using long short-term memory RNN. *Int. J. Electr. Comput. Eng. (IJECE)* 9, 1304. doi:10.11591/ijece.v9i2.pp1304-1312

Bhattacharya, P. K., and Burman, P. (2016). *Theory and methods of statistics*. Massachusetts, United States: Academic Press.

Birnie, C., and Alkhalifah, T. (2022). "Leveraging domain adaptation for efficient seismic denoising," in Energy in Data Conference, Austin, Texas, 20–23 February 2022, 11–15. Energy in Data. doi:10.7462/eid2022-04.1

Chollet, F. (2015). Keras. Available at: https://keras.io/.

Cremen, G., and Galasso, C. (2020). Earthquake early warning: Recent advances and perspectives. *Earth-Science Rev.* 205, 103184. doi:10.1016/j.earscirev.2020.103184

Dramsch, J. S. (2020). 70 years of machine learning in geoscience in review. *Adv. Geophys.* 61, 1–55. doi:10.1016/bs.agph.2020.08.002

Duncan, P. M., and Eisner, L. (2010). Reservoir characterization using surface microseismic monitoring. *Geophysics* 75, 75A139–75A146. doi:10.1190/1.3467760

Eisner, L., Duncan, P. M., Heigl, W. M., and Keller, W. R. (2009). Uncertainties in passive seismic monitoring. *Lead. Edge* 28, 648–655. doi:10.1190/1.3148403

Eisner, L., Hulsey, B. J., Duncan, P., Jurick, D., Werner, H., and Keller, W. (2010). Comparison of surface and borehole locations of induced seismicity. *Geophys. Prospect.* 58, 809–820. doi:10.1111/j.1365-2478.2010.00867.x

Ellsworth, W. L. (2013). Injection-induced earthquakes. *Science* 341, 1225942. doi:10.1126/science.1225942

Fomel, S., Luo, S., and Zhao, H. (2009). Fast sweeping method for the factored eikonal equation. *J. Comput. Phys.* 228, 6440–6455. doi:10.1016/j.jcp.2009.05.029

Fornasari, S. F., Pazzi, V., and Costa, G. (2022). A machine-learning approach for the reconstruction of ground-shaking fields in real time. *Bull. Seismol. Soc. Am.* 112, 2642–2652. doi:10.1785/0120220034

Foulger, G. R., Wilson, M. P., Gluyas, J. G., Julian, B. R., and Davies, R. J. (2018). Global review of human-induced earthquakes. *Earth-Science Rev.* 178, 438–514. doi:10.1016/j.earscirev.2017.07.008

Glorot, X., Bordes, A., and Bengio, Y. (2011). "Deep sparse rectifier neural networks," in Proceedings of the Fourteenth International Conference on Artificial Intelligence and Statistics. Editors G. Gordon, D. Dunson, and M. Dudík (Fort Lauderdale, FL, USA: JMLR Workshop and Conference Proceedings), 315–323. 15 of Proceedings of Machine Learning Research.

Hao, Q., Waheed, U., Babatunde, M., and Eisner, L. (2020). Microseismic hypocenter location using an artificial neural network. In 82nd EAGE Annual Conference & Exhibition European Association of Geoscientists & Engineers, December 8–11, 2022. 2020, 1–5. doi:10.3997/2214-4609.202010583

Häring, M. O., Schanz, U., Ladner, F., and Dyer, B. C. (2008). Characterisation of the basel 1 enhanced geothermal system. *Geothermics* 37, 469–495. doi:10.1016/j.geothermics.2008.06.002

Kingma, D. P., and Ba, J. (2014). Adam: A method for stochastic optimization. arXiv preprint arXiv:1412.6980. Availablble at: https://arxiv.org/abs/1412.6980 (Accessed Dec 22, 2014).

Kong, Q., Trugman, D. T., Ross, Z. E., Bianco, M. J., Meade, B. J., and Gerstoft, P. (2019). Machine learning in seismology: Turning data into insights. *Seismol. Res. Lett.* 90, 3–14. doi:10.1785/0220180259

Kriegerowski, M., Petersen, G. M., Vasyura-Bathke, H., and Ohrnberger, M. (2018). A deep convolutional neural network for localization of clustered earthquakes based on multistation full waveforms. *Seismol. Res. Lett.* 90, 510–516. doi:10.1785/0220180320

Li, L., Tan, J., Schwarz, B., Staněk, F., Poiata, N., Shi, P., et al. (2020). Recent advances and challenges of waveform-based seismic location methods at multiple scales. *Rev. Geophys.* 58, e2019RG000667. doi:10.1029/2019rg000667

Maxwell, S. C., Rutledge, J., Jones, R., and Fehler, M. (2010). Petroleum reservoir characterization using downhole microseismic monitoring. *Geophysics* 75, 75A129–75A137. doi:10.1190/1.3477966

Mousavi, S. M., and Beroza, G. C. (2020). A machine-learning approach for earthquake magnitude estimation. *Geophys. Res. Lett.* 47, e2019GL085976. doi:10.1029/2019gl085976

Mousavi, S. M., Ellsworth, W. L., Zhu, W., Chuang, L. Y., and Beroza, G. C. (2020). Earthquake transformer—An attentive deep-learning model for simultaneous earthquake detection and phase picking. *Nat. Commun.* 11, 3952. doi:10.1038/s41467-020-17591-w

Nooshiri, N., Bean, C. J., Dahm, T., Grigoli, F., Kristjánsdóttir, S., Obermann, A., et al. (2021). A multibranch, multitarget neural network for rapid point-source inversion in a microseismic environment: Examples from the hengill geothermal field, Iceland. *Geophys. J. Int.* 229, 999–1016. doi:10.1093/gji/ggab511

Perol, T., Gharbi, M., and Denolle, M. (2018). Convolutional neural network for earthquake detection and location. *Sci. Adv.* 4, e1700578. doi:10.1126/sciadv.1700578

Ross, Z. E., Trugman, D. T., Hauksson, E., and Shearer, P. M. (2019). Searching for hidden earthquakes in southern California. *Science* 364, 767–771. doi:10.1126/science.aaw6888

Rutledge, J. T., and Phillips, W. S. (2003). Hydraulic stimulation of natural fractures as revealed by induced microearthquakes, Carthage Cotton Valley gas field, east Texas. *Geophysics* 68, 441–452. doi:10.1190/1.1567214

Saad, O. M., Bai, M., and Chen, Y. (2021). Uncovering the microseismic signals from noisy data for high-fidelity 3D source-location imaging using deep learning. *Geophysics* 86, KS161–KS173. doi:10.1190/geo2021-0021.1

Saad, O. M., and Chen, Y. (2021). Earthquake detection and P-wave arrival time picking using capsule neural network. *IEEE Trans. Geosci. Remote Sens.* 59, 6234–6243. doi:10.1109/tgrs.2020.3019520

Schultz, R., Beroza, G., Ellsworth, W., and Baker, J. (2020). Risk-informed recommendations for managing hydraulic fracturing–induced seismicity via traffic light protocols. *Bull. Seismol. Soc. Am.* 110, 2411–2422. doi:10.1785/0120200016

Staněk, F., Anikiev, D., Valenta, J., and Eisner, L. (2015). Semblance for microseismic event detection. *Geophys. J. Int.* 201, 1362–1369. doi:10.1093/gji/ggv070

Stein, M. L. (1999). *Interpolation of spatial data: Some theory for kriging*. Berlin, Germany: Springer Science & Business Media.

Steinberg, A., Vasyura-Bathke, H., Gaebler, P., Ohrnberger, M., and Ceranna, L. (2021). Estimation of seismic moment tensors using variational inference machine learning. *J. Geophys. Res. Solid Earth* 126, e2021JB022685. doi:10.1002/essoar.10507484.1

Tous, R., Alvarado, L., Otero, B., Cruz, L., and Rojas, O. (2020). Deep neural networks for earthquake detection and source region estimation in north-central Venezuela. *Bull. Seismol. Soc. Am.* 110, 2519–2529. doi:10.1785/0120190172

van den Ende, M. P. A., and Ampuero, J.-P. (2020). Automated seismic source characterization using deep graph neural networks. *Geophys. Res. Lett.* 47, e2020GL088690. doi:10.1029/2020gl088690

Verdon, J. P., and Bommer, J. J. (2020). Green, yellow, red, or out of the blue? An assessment of traffic light schemes to mitigate the impact of hydraulic fracturing-induced seismicity. *J. Seismol.* 25, 301–326. doi:10.1007/s10950-020-09966-9

Vinard, N. A., Drijkoningen, G. G., and Verschuur, D. J. (2021). Localizing microseismic events on field data using a u-net-based convolutional neural network trained on synthetic data. *Geophysics* 87, KS33–KS43. doi:10.1190/geo2020-0868.1

Wiszniowski, J., Plesiewicz, B. M., and Trojanowski, J. (2013). Application of real time recurrent neural network for detection of small natural earthquakes in Poland. *Acta Geophys.* 62, 469–485. doi:10.2478/s11600-013-0140-2

Yu, S., and Ma, J. (2021). Deep learning for geophysics: Current and future trends. *Rev. Geophys.* 59, e2021RG000742. doi:10.1029/2021rg000742

Zhang, X., Zhang, M., and Tian, X. (2021). Real-time earthquake early warning with deep learning: Application to the 2016 m 6.0 central apennines, Italy earthquake. *Geophys. Res. Lett.* 48, 2020GL089394. doi:10.1029/2020gl089394

Zhao, H. (2005). A fast sweeping method for eikonal equations. *Math. Comput.* 74, 603–627. doi:10.1090/s0025-5718-04-01678-3

Zhu, W., and Beroza, G. C. (2018). PhaseNet: A deep-neural-network-based seismic arrival-time picking method. *Geophys. J. Int.* 216, 261–273. doi:10.1093/gji/ggy423

frontiers | Frontiers in Earth Science

TYPE Methods
PUBLISHED 11 November 2022
DOI 10.3389/feart.2022.1023141

OPEN ACCESS

EDITED BY
Lei Li,
Central South University, China

REVIEWED BY
Yuyang Tan,
Ocean University of China, China
Xinpeng Pan,
Central South University, China
Jie Tang,
Huadong, China

*CORRESPONDENCE
Yibo Wang,
wangyibo@mail.iggcas.ac.cn

SPECIALTY SECTION
This article was submitted to Solid Earth Geophysics,
a section of the journal
Frontiers in Earth Science

RECEIVED 19 August 2022
ACCEPTED 07 September 2022
PUBLISHED 11 November 2022

CITATION
Zheng Y and Wang Y (2022), Sensitivity analysis of anisotropic parameter inversion simultaneously with microseismic source location in layered VTI media.
Front. Earth Sci. 10:1023141.
doi: 10.3389/feart.2022.1023141

Sensitivity analysis of anisotropic parameter inversion simultaneously with microseismic source location in layered VTI media

Yikang Zheng[1,2] and Yibo Wang[1,2]*

[1]Key Laboratory of Petroleum Resource Research, Institute of Geology and Geophysics, Chinese Academy of Sciences, Beijing, China, [2]Innovation Academy for Earth Science, Chinese Academy of Sciences, Beijing, China

The hypocenters of microseismic events induced by hydraulic fracturing are conventionally located with an initial model established from well logs or perforation shots. In most geological settings, the arrival times are insufficiently explained without accounting for the velocity changes introduced by the reservoir stimulation process. The model parameters and source locations should be inverted simultaneously with arrival time information. Therefore, the joint inversion of event locations and velocity model requires the information of anisotropy parameters, which leads to the problem of the selection of degree of symmetry of anisotropic media in the inversion process. Since it is not possible to retrieve all elastic moduli from limited passive seismic data, the joint inversion is constrained to layered vertical transversely isotropic (VTI) media. Various methods have been proposed to invert the velocity model and source locations from the arrival times in anisotropic media, but the number of retrievable parameters in different parametrization types and acquisition scenarios have not been decisively discussed. We analyze the sensitivities for event locations and anisotropic parameters by the singular value decomposition (SVD) of the Fréchet derivatives in a layered anisotropic medium with vertical axis of symmetry. The singular values and eigenvectors obtained from SVD can be used to predict which unknown parameters are better constrained by the available traveltimes. The comparison of different parametrizations and monitoring array configurations allows to design a better inversion strategy to provide microseismic event locations and anisotropic parameters.

KEYWORDS

microseismic, source location, anisotropic parameter inversion, sensitivity analysis, layered VTI media

1 Introduction

Microseismic monitoring is an important diagnostic tool for hydraulic fracturing stimulation in unconventional reservoirs (Grechka, 2010; Maxwell et al., 2010; Li et al., 2019b; Pan et al., 2022). Locating induced microseismic events is the primary task in such monitoring, which requires the accurate velocity model (Eisner et al., 2009; Zimmer et al., 2009; Li et al., 2020). Traditionally, the velocity models are derived from sonic logs and perforation shots (Pei et al., 2009; Bardainne and Gaucher, 2010). As the perforation shots illuminate limited subsurface, the locations are prone to errors due to the unreliable velocity information (Grechka et al., 2011; Li et al., 2013; Li et al., 2019a). Additionally, the hydraulic stimulation and fractured shales in the reservoir may change the velocity model. The estimated velocity models may be updated based on the information supplied by the microseismic events, which is similar to the passive seismic tomography in global seismology (Thurber, 1986; Zhang and Thureber, 2003).

As the anisotropy commonly exists in shale (Eisner et al., 2011; Tsvankin, 2012) and shear wave splitting is commonly observed (Grechka and Yaskevich, 2014; Grechka, 2015), the isotropic velocity models are most likely insufficient to explain the recorded traveltimes in the estimation of velocity simultaneously with event locations. For example, Grechka et al. (2011) show that event locations lead to lower residuals when anisotropy is taken into account. Grechka and Duchkov (2011) propose that isotropic model is inadequate and develop methodology to estimate elements of elastic moduli from traveltimes observed in downhole geophones. The challenge of the inversion is that the phase and group velocities are represented in narrow angular apertures for typical downhole geometries. Grechka et al. (2011) estimated the anisotropy simultaneously with events locations in a single-well geometry. The analysis is based on stiffness tensor and only the downhole case is discussed. Li et al. (2013) proposed to use differential arrival times and differential azimuths for event location and anisotropic tomography, which is also discussed in a single well geometry. Grechka and Yaskevich (2014) used the traveltimes and polarizations to invert event locations and parameters for layer triclinic media using downhole microseismic data with wide aperture. Michel and Tsvankin (2016) developed an elastic waveform inversion algorithm to estimate the anisotropic parameter and source information in the layered vertical transversely isotropic (VTI) media. In this study, we do not use full waveforms as the amplitude is often contaminated by noise and compromised by receiver coupling in downhole monitoring. The arrival times of the direct P- and S- waves sometimes are more reliable than the waveforms in the source location.

In the above discussed studies, the downhole geophones in a single vertical monitoring well are usually assumed and the elastic stiffness tensor is used to delineate the anisotropic properties. Alternatively, surface or near-surface arrays are also used in monitoring hydraulic fracturing (Duncan and Eisner, 2010). In such geometry most of the rays travel through overburden which can be characterized as vertical transversely isotropic media (VTI), and it is enough to describe the observed direct arrival times in field data (Gei et al., 2011).

In this study, we derive the analytical sensitivities for the elastic moduli and Thomsen-type parameters (Thomsen, 1986) in the joint inversion of event locations, source origin times and anisotropic properties with layered anisotropy assumption. We investigate the sensitivities of the direct P- and S- arrival time inversion to source location and anisotropic parameters by using singular value decomposition (SVD). We compare the sensitivity matrices derived from microseismic data for downhole geometry and establish the methodology to judge the effectiveness and limits of using the traveltimes to invert the unknown parameters.

2 Methodology

2.1 Joint inversion of microseismic location and anisotropic parameters

The objective function in the joint inversion of the source location, origin times and anisotropic tomography is the traveltime differences between the observed arrival time and the corresponding modelled arrival time. The sensitivities of the arrival time with respect to the hypocenter $\boldsymbol{x}_i$, the origin times τ_i, the anisotropic parameters $\boldsymbol{m}$ and the layer thickness l_j are given by the Fréchet derivativest

$$\boldsymbol{\mathcal{F}} = \left[\frac{\partial t_Q}{\partial \boldsymbol{m}}, \frac{\partial t_Q}{\partial \boldsymbol{x}_i}, \frac{\partial t_Q}{\partial \tau_i}, \frac{\partial t_Q}{\partial l_j}\right], \tag{1}$$

where t_Q is the arrival time and Q is used to denote the wave types, which can be quasi-P (qP), quasi-SV (qSV) or SH waves in the anisotropic media (Grechka and Duchkov, 2011). $\frac{\partial t_Q}{\partial \boldsymbol{m}}$ are the derivatives of arrival times with respect to anisotropic parameters. Different parametrizations have been suggested to represent the anisotropic properties in homogeneous VTI medium. The first one is the combinaton of five elastic modulus, c_{11}, c_{33}, c_{55}, c_{66}, and c_{13}. Alternatively, Thomsen-type parameters can be used to define a VTI medium. Then $\boldsymbol{m}$ includes the vertical P- and S-wave velocities, V_{P0} and V_{S0}, and the anisotropic coefficients, ε, γ and δ. The derivatives can be calculated by the chain rule

$$\frac{\partial t_Q}{\partial \boldsymbol{m}} = \frac{\partial t_Q}{\partial g_Q}\frac{\partial g_Q}{\partial \boldsymbol{m}} = -\frac{t_Q}{g_Q}\frac{\partial g_Q}{\partial \boldsymbol{m}}, \tag{2}$$

where g_Q represents group velocities. The derivation of these derivatives for qP, qSV and SH is given in Supplementary Appendix S1.

The second part on the right side of Eq. 1 is the derivatives of traveltime t_Q with respect to source location coordinates $\boldsymbol{x} = \{x_1, x_2, x_3\}$. The location can be expressed by the event

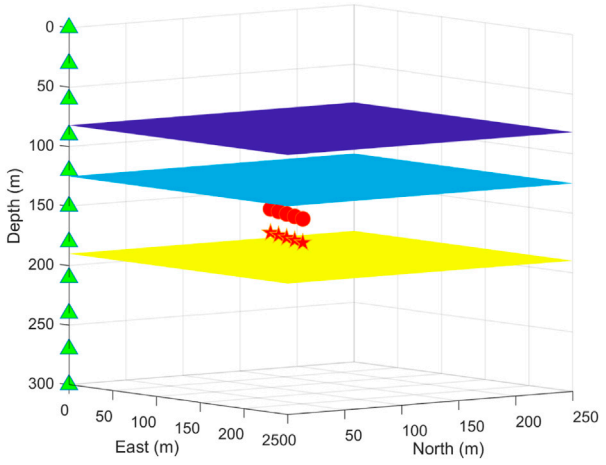

FIGURE 1
The layered anisotropic model used in synthetic tests. There are 11 receivers (green triangles) located in the monitoring well and two fracture systems in the third layer, which is associated with five microseismic events (red stars and red dots).

azimuth α, radial distance r and depth difference h in a cylindrical coordinate system with the origin at the receiver.

$$\boldsymbol{x} = \{x_1,\ x_2, x_3\} = \{rcos\alpha, rsin\alpha, h\}. \tag{3}$$

In our joint inversion approach, the event azimuth is assumed to be known as they are independently measured from particle polarization, from the work of Eisner et al., 2009. The sensitivity of arrival times with respect to hypocenter can be expressed as

$$\frac{\partial t_Q}{\partial \boldsymbol{x}} = \frac{\partial t_Q}{\partial \{r, h\}} = -\left\{p_r^Q, p_h^Q\right\}, \tag{4}$$

where p_r^Q and p_h^Q are the radial and vertical slowness, which are associated with anisotropic parameters and propagation angle.

The third part on the right side of Eq. 1 is the derivatives of arrival time t_Q with respect to the origin times τ_i. In the inversion, microseismic events are independently evaluated and the arrival time is only relevant with its own origin time. If the number of microseismic events is n, $\frac{\partial t_Q}{\partial \tau_i}$ is the $n \times n$ identity matrix. It's equal to I_{ij} for the *j-th* event.

The last part is the sensitivity with respect to the layer thickness. This problem has been discussed by Li et al. (2013). The sensitivity expression is

$$\frac{\partial t_Q}{\partial l_j} = p_r^Q\left(tan\,\varphi_2 - tan\,\varphi_1\right) + \frac{1}{cos\,\varphi_1 g_1^Q} - \frac{1}{cos\,\varphi_2 g_2^Q}, \tag{5}$$

To specify the case to calculate the derivatives in the equations, here we assume the ray travels downwards, the terms should be adjusted in upward cases. φ_1 and φ_2 are the group angles in the first and second layer, respectively. g_1^Q and g_2^Q represent the corresponding group velocities.

TABLE 1 The anisotropic parameters of the four layers.

Layer	1	2	3	4
c_{11} (km/s)^2	20.0111	22.8211	18.4782	23.7995
c_{33} (km/s)^2	16.4025	18.4041	13.1987	19.1932
c_{55} (km/s)^2	5.5885	6.4009	5.1984	7.1985
c_{66} (km/s)^2	7.1533	7.9371	7.2778	8.3502
c_{13} (km/s)^2	7.1810	7.9494	5.6091	8.4593
V_{P0} (km/s)	4.050	4.290	3.633	4.381
V_{S0} (km/s)	2.364	2.530	2.280	2.683
ε	0.11	0.12	0.20	0.12
γ	0.14	0.12	0.20	0.08
δ	0.13	0.14	0.25	0.22

As the derivatives $\{\frac{\partial t_Q}{\partial \boldsymbol{m}}, \frac{\partial t_Q}{\partial \boldsymbol{x}_i}, \frac{\partial t_Q}{\partial \tau_i}, \frac{\partial t_Q}{\partial l_j}\}$ have different unit dimensions, they should be scaled by factors to balance the contributions from different unknowns (Grechka et al., 2011). Here the factors we choose are the mean source-receiver distance $f(x) = mean(|\boldsymbol{x}|)$, the mean arrival times $f(\tau) = mean(|t_Q|)$ and the mean layer thickness $f(l) = mean(|l|)$. The matrix used in sensitivity analysis can be expressed as

$$\boldsymbol{\mathcal{F}} = \left[\left(\frac{f(x)}{f(\tau)}\right)^2\left\{\frac{\partial t_Q}{\partial c}\right\}, f(x)\frac{\partial t_Q}{\partial \boldsymbol{x}_i}, f(\tau)\frac{\partial t_Q}{\partial \tau_i}, f(l)\frac{\partial t_Q}{\partial l_j}\right], \text{or}$$
$$\boldsymbol{\mathcal{F}} = \left[\frac{f(x)}{f(\tau)}\left\{\frac{\partial t_Q}{\partial V_{P0}}, \frac{\partial t_Q}{\partial V_{S0}}\right\}, \left\{\frac{\partial t_Q}{\partial \varepsilon,}, \frac{\partial t_Q}{\partial \gamma}, \frac{\partial t_Q}{\delta}\right\}, f(x)\frac{\partial t_Q}{\partial \boldsymbol{x}_i}, f(\tau)\frac{\partial t_Q}{\partial \tau_i}, f(l)\frac{\partial t_Q}{\partial l_j}\right]. \tag{6}$$

2.2 Singular value decomposition

Singular Value Decomposition (SVD) of a matrix is a factorization into three parts. It indicates the algebraic properties and provides important geometrical insights of the original matrix. The quantitative assessment of the joint inversion can be obtained by applying singular value decomposition to the Fréchet derivatives (Grechka et al., 2011; Kazei and Alkhalifah, 2018)

$$\boldsymbol{\mathcal{F}} = \boldsymbol{u}\,\boldsymbol{s}\,\boldsymbol{w}^T, \tag{7}$$

where $\boldsymbol{u}$ is an orthogonal matrix and consists of eigenvectors of $\boldsymbol{\mathcal{F}}\boldsymbol{\mathcal{F}}^T$, $\boldsymbol{s}$ is a diagonal matrix with singular values on the diagonal, $\boldsymbol{w}$ is an orthogonal eigenvector matrix and consists of eigenvectors of $\boldsymbol{\mathcal{F}}^T\boldsymbol{\mathcal{F}}$, and $\boldsymbol{w}^T$ is the conjugate transpose of $\boldsymbol{w}$. The absolute magnitude of the diagonal elements of $\boldsymbol{s}$ show how perturbations in the corresponding eigenvectors shift the arrival times. And the values of the elements in each eigenvector show the relative weight of the parameters in

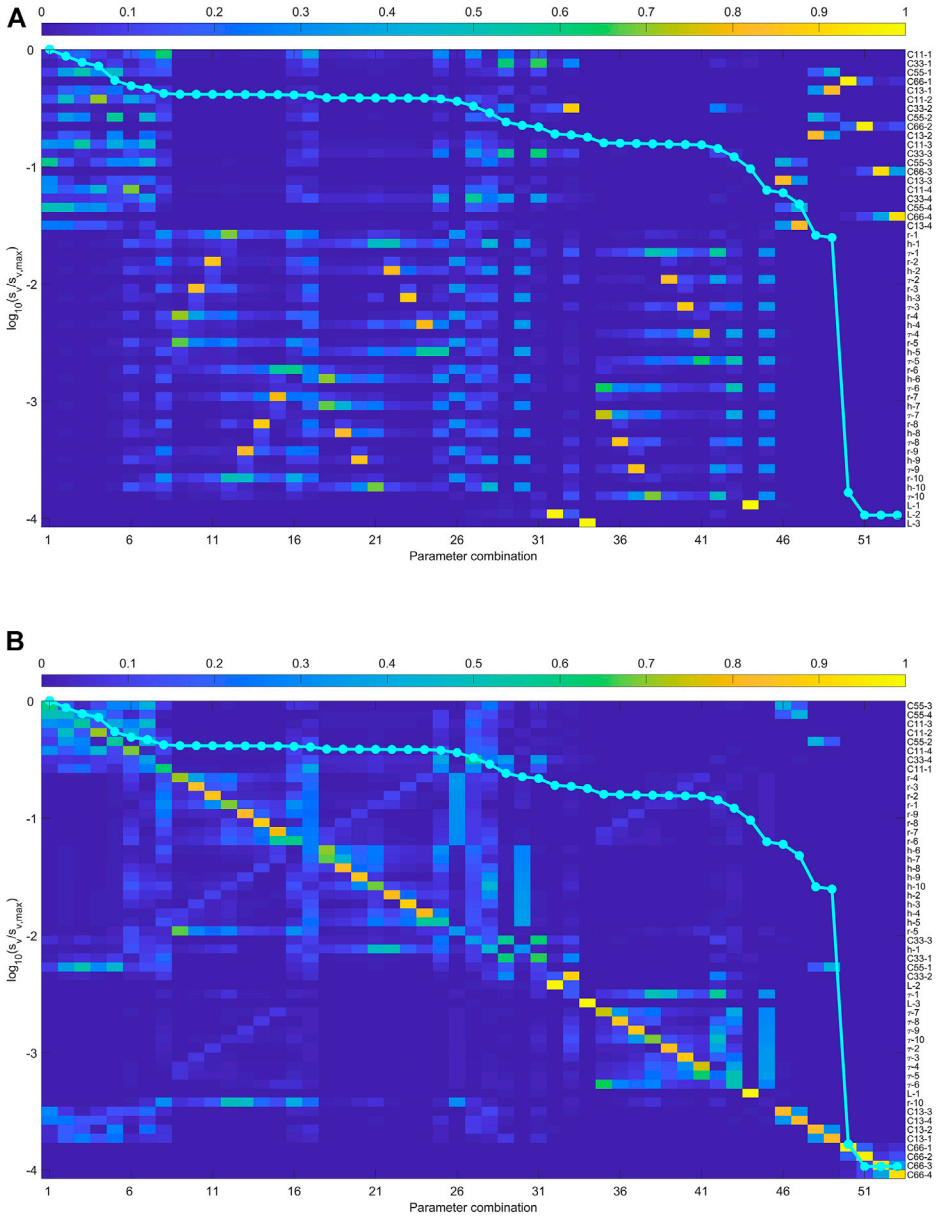

FIGURE 2
(A) The sensitivity analysis of the joint inversion using qP arrival times in the downhole array. The anisotropic is represented by c_{ij} parametrization. **(B)** the rows of eigenvector matrix are sorted to make it diagonally dominant as possible. The horizontal axis shows the index of eigenvectors, the vertical axis on the left shows the corresponding normalized singular values, and the vertical axis on the right shows the represented parameters. The blue solid dotted line in **(B)** indicates the suggestion inversion sequence of the unknowns. The singular values close to zero means the parameters on the right do not contribute to the observed data.

joint inversion. The number of non-zero values on the diagonal of matrix $\boldsymbol{s}$ indicates the invertible linear combinations of parameters. If it is less than the number of parameters, some trade-offs between the parameters exist in the inversion. As the eigenvectors are unit vectors and orthogonal to each other, the ideal parametrization is that each eigenvector has only one non-zero element. Then we could invert the parameter one by one, from the eigenvector with large singular value to small. Usually the eigenvectors have multiple non-zero elements and the crosstalk issues are introduced. Then, the rough inversion strategy is that we could sort the eigenvectors based on its corresponding singular values and invert the dominant diagonal elements sequentially.

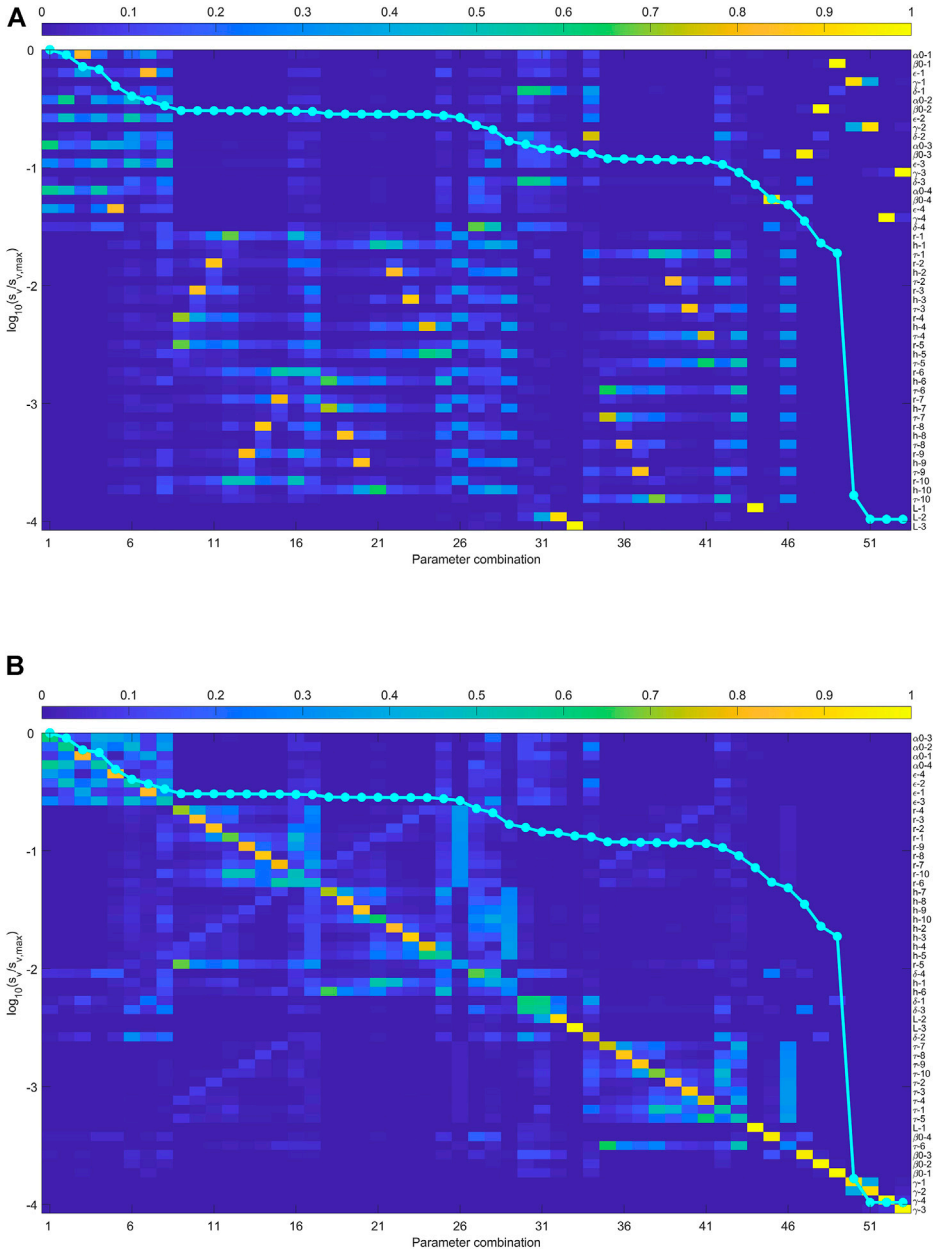

FIGURE 3
(A) The sensitivity analysis of the joint inversion using qP arrival times in the downhole array. The anisotropic is represented by Thomesen parametrization. **(B)** the rows of eigenvector matrix are sorted to make it diagonally dominant as possible. The singular values close to zero means the parameters on the right do not contribute to the observed data.

3 Synthetic examples

To illustrate the sensitivity analysis in the joint inversion, we use a model with four layers. It is shown in Figure 1. The anisotropic parameters (density-normalized stiffness matrix in Voigt notation) used in the synthetic tests are shown in Table 1 (Li et al., 2013; Huang et al., 2019). In the third layer, which is assumed to be the reservoir, there are ten events divided into two fracture systems. The arrival times of the microseismic events are calculated analytically.

As the data in microseismic is often not sufficient to pick all three waves (qP, qSV and SH), we discuss two cases that only the arrival times of P-wave are used or the arrival times of three wave types are all used in the joint inversion. For the application of field data, the initial guess of the anisotropic parameters is derived from the polarization analysis of the

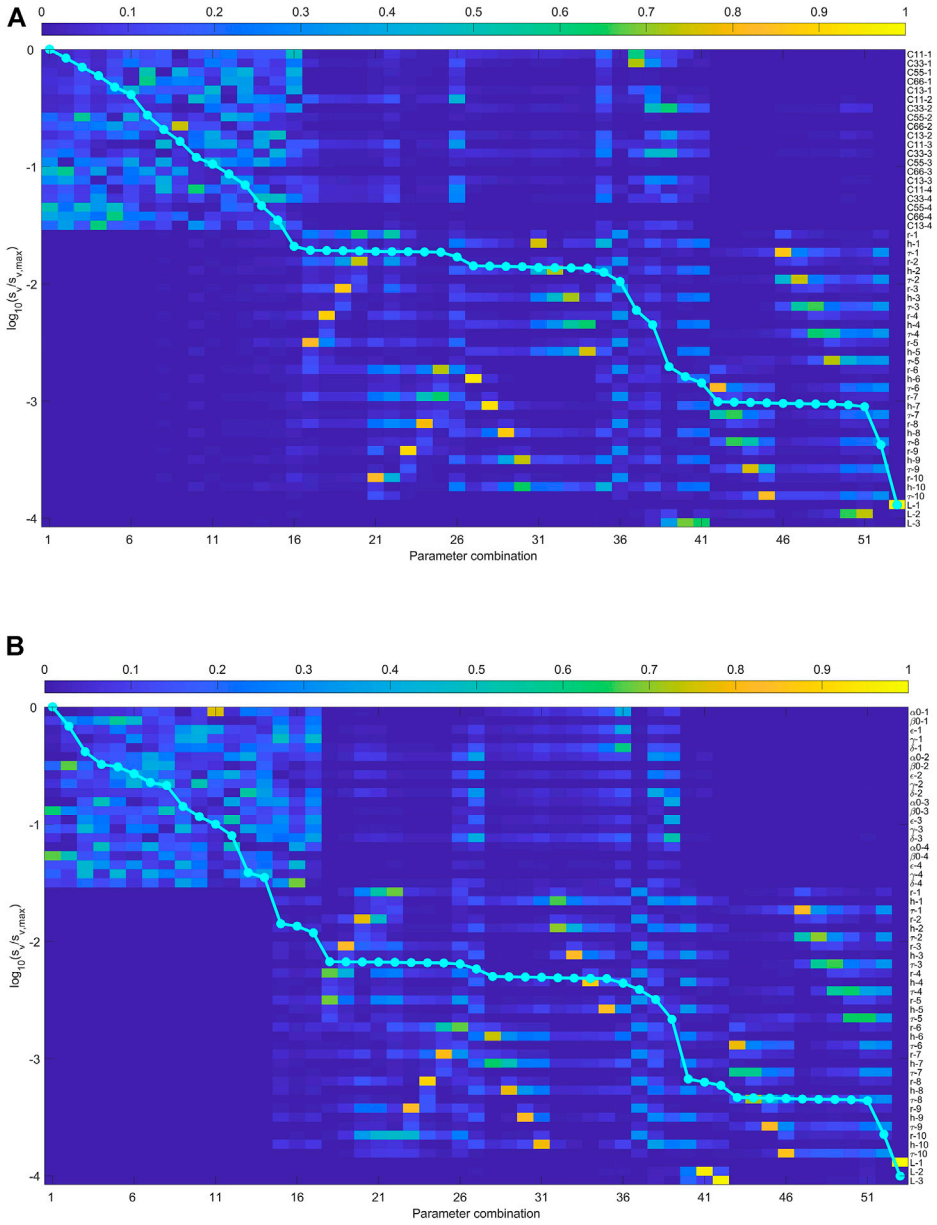

FIGURE 4
(A) The sensitivity analysis of the joint inversion using the arrival times of qP wave and two S- waves. The anisotropic is represented by c_{ij} parametrization. **(B)** the rows of eigenvector matrix are sorted to make it diagonally dominant as possible. The absence of singular values close to zero means all the parameters on the right contribute to the observed data.

seismic data (Grechka et al., 2011). A least-squares objective function is constructed to invert the anisotropic model with a local isotropic assumption (Grechka and Mateeva, 2007). As we are only focusing on the sensitivity analysis in this study, the parameters of mentioned above are directly used with 5% randomly perturbation. In the analysis of specific cases, firstly the Fréchet derivatives (Eq. 6) is calculated and used as the input for SVD. Then the eigenvectors are sorted by their corresponding singular values. Then the element in the column are automatically sequenced by the maximum value and formed the suggested inversion strategy. With less parameter with singular values close to zero, the inversion process is better constrained.

First, we use the qP arrival times of ten microseismic event recorded by all receivers in sensitivity analysis. When the elastic moduli are used to represent the anisotropic media, the results are shown in Figure 2. The singular values close to zero indicates there are four parameters that can not be

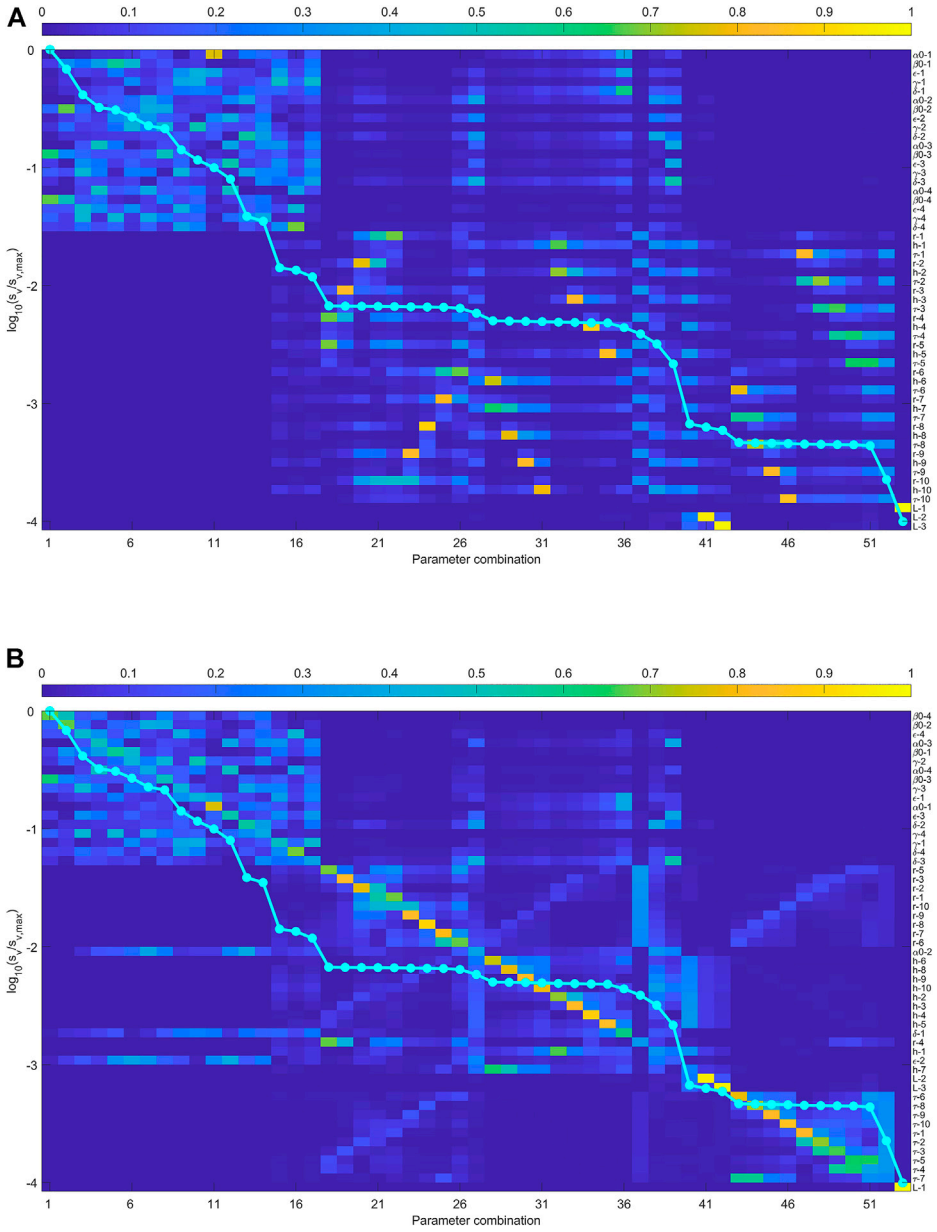

FIGURE 5
(A) The sensitivity analysis of the joint inversion using the arrival times of qP wave and two S- waves. The anisotropic is represented by Thomsen-type parametrization. **(B)** the rows of eigenvector matrix are sorted to make it diagonally dominant as possible. The absence of singular values close to zero means all the parameters on the right contribute to the observed data.

inverted. By resorting the rows to make it with best diagonal dominance, we can find that the smallest singular values correspond to c_{66}. They are poorly constrained as the arrival times of S- waves are not used.

When the initial model is close to the true solution, Figure 2B shows the methodology to invert the parameters in the downhole geometry shown in Figure 1. When only the arrival times of P- waves are used, the arrival times are strongly related with c_{66}, c_{11}, the radial distance r and the vertical distance h. The values of layer thickness l and the origin times τ have lower sensitivity to the arrival times. The value of c_{13} is least constrained in the joint inversion. When only the arrival times of P-wave are available, the columns that have non-zero singular values have off-diagonal elements with high values. It indicates the crosstalk between the parameters are introduced and some trade-off exist. The parameter array

on the right in Figure 2B shows the possible inversion sequence, from the best constrained parameter to the worst.

Figure 3 shows the result when the anisotropic media are represented by Thomsen-type parameters. In this case, the sensitivity analysis provided the relation sequence: V_{P0}, ε, r, h, δ, l and V_{S0}. It has four near-zero singular values corresponding to γ in the four layers, which means they can not be inverted in the joint inversion.

When the arrival times of three wave types are used, the anisotropic parameters are better constrained in the inversion. Figures 4, 5 show the result. Figure 4B indicates that c_{55}, c_{66}, c_{13} and c_{11} have the highest possibility to be inverted from the inversion. The second group is the radial and vertical distance r, h, and c_{33}. The similar colors of r and h in each column indicate that the two parameters trade-off with each other. The third group is the excitation time of ten events and the layer thickness. Figure 5B shows that the relation sequence becomes V_{S0}, V_{P0}, ε, γ, δ, r, h. The parameters that are not well constrained in the joint inversion are still the excitation times and layer thickness.

We used the downhole array to illustrate the proposed method, and it is also applicable to surface geometries or more mircoseismic events. The difference is the traveltimes calculation for the relative locations between receiver and microseismic sources. In the specific cases, the analysis process should be performed respectively and the terms in the derivatives need to be adjusted accordingly. The inferred inversion strategy highly depends on the locations of the events and receivers, but the main procedures are quite similar and not included here.

4 Conclusion

The sensitivity analysis of the joint inversion are obtained by the SVD of the Fréchet derivative matrix. As the monitoring arrays affect the measured quantities, this analysis should be done for each specific monitoring array. We use elastic moduli and Thomsen-type parametrization to describe the VTI media as the horizontal shale layers often have vertical axis of symmetry.

We derive the derivative of group velocity with respect to the elastic moduli and Thomsen-type parameters. We demonstrate how to establish the Fréchet derivative matrix in the joint inversion of anisotropic parameters and source locations. We show how to perform the sensitivity analysis to the monitoring array. It gives the tool to judge the constrain on the unknows in the joint inversion when limited data are obtained.

Data availability statement

The original contributions presented in the study are included in the article/Supplementary Material; further inquiries can be directed to the corresponding author.

Author contributions

YZ performed the data analysis. YW provided the research ideas and supervised the findings of this work. YZ and YW wrote and revised the manuscript.

Funding

This study was funded by the The Scientific Instrument Developing Project of the Chinese Academy of Sciences (Broadband fiber optic seismometer acquisition instrument and system), and Key Research Program of Frontier Sciences, Chinese Academy of Sciences (Grant No. QYZDY-SSW-DQC009).

Acknowledgments

We express our gratitude to Leo Eisner for the helpful discussions and comments.

Conflict of interest

The authors declare that the research was conducted in the absence of any commercial or financial relationships that could be construed as a potential conflict of interest.

Publisher's note

Supplementary material

The Supplementary Material for this article can be found online at: https://www.frontiersin.org/articles/10.3389/feart.2022.1023141/full#supplementary-material

References

Bardainne, T., and Gaucher, E. (2010). Constrained tomography of realistic velocity models in microseismic monitoring using calibration shots. *Geophys. Prospect.* 58 (5), 739–753. doi:10.1111/j.1365-2478.2010.00912.x

Duncan, P. M., and Eisner, L. (2010). Reservoir characterization using surface microseismic monitoring. *Geophysics* 75 (5), 75A139–75A146. doi:10.1190/1.3467760

Eisner, L., Duncan, P. M., Heigl, W. M., and Keller, W. R. (2009). Uncertainties in passive seismic monitoring. *Lead. Edge* 28 (6), 648–655. doi:10.1190/1.3148403

Eisner, L., Zhang, Y., Duncan, P., Mueller, M. C., Thornton, M. P., and Gei, D. (2011). Effective VTI anisotropy for consistent monitoring of microseismic events. *Lead. Edge* 30 (7), 772–776. doi:10.1190/1.3609092

Gei, D., Eisner, L., and Suhadolc, P. (2011). Feasibility of estimating vertical transverse isotropy from microseismic data recorded by surface monitoring arrays. *Geophysics* 76 (6), WC117–WC126. doi:10.1190/geo2011-0028.1

Grechka, V. (2010). Data-acquisition design for microseismic monitoring. *Lead. Edge* 29 (3), 278–282. doi:10.1190/1.3353723

Grechka, V., and Duchkov, A. A. (2011). Narrow-angle representations of the phase and group velocities and their applications in anisotropic velocity-model building for microseismic monitoring. *Geophysics* 76 (6), WC127–WC142. doi:10.1190/geo2010-0408.1

Grechka, V., and Mateeva, A. (2007). Inversion of P-wave VSP data for local anisotropy: Theory and case study. *Geophysics* 72 (4), D69–D79. doi:10.1190/1.2742970

Grechka, V., Singh, P., and Das, I. (2011). Estimation of effective anisotropy simultaneously with locations of microseismic events. *Geophysics* 76 (6), WC143–WC155. doi:10.1190/geo2010-0409.1

Grechka, V. (2015). Tilted TI models in surface microseismic monitoring. *Geophysics* 80 (6), WC11–WC23. doi:10.1190/geo2014-0523.1

Grechka, V., and Yaskevich, S. (2014). Azimuthal anisotropy in microseismic monitoring: A bakken case study. *Geophysics* 79 (1), KS1–KS12. doi:10.1190/geo2013-0211.1

Huang, G., Ba, J., Du, Q., and Carcione, J. M. (2019). Simultaneous inversion for velocity model and microseismic sources in layered anisotropic media. *J. Petroleum Sci. Eng.* 173, 1453–1463. doi:10.1016/j.petrol.2018.10.071

Kazei, V., and Alkhalifah, T. (2018). Waveform inversion for orthorhombic anisotropy with P waves: Feasibility and resolution. *Geophys. J. Int.* 213 (2), 963–982. doi:10.1093/gji/ggy034

Li, J., Zhang, H., Rodi, W. L., and Toksoz, M. N. (2013). Joint microseismic location and anisotropic tomography using differential arrival times and differential backazimuths. *Geophys. J. Int.* 195 (3), 1917–1931. doi:10.1093/gji/ggt358

Li, L., Tan, J., Schwarz, B., Staněk, F., Poiata, N., Shi, P., et al. (2020). Recent advances and challenges of waveform-based seismic location methods at multiple scales. *Rev. Geophys.* 58 (1), e2019RG000667. doi:10.1029/2019RG000667

Li, L., Tan, J., Wood, D. A., Zhao, Z., Becker, D., Lyu, Q., et al. (2019b). A review of the current status of induced seismicity monitoring for hydraulic fracturing in unconventional tight oil and gas reservoirs. *Fuel* 242, 195–210. doi:10.1016/j.fuel.2019.01.026

Li, L., Tan, J., Xie, Y., Tan, Y., Walda, J., Zhao, Z., et al. (2019a). Waveform-based microseismic location using stochastic optimization algorithms: A parameter tuning workflow. *Comput. Geosciences* 124, 115–127. doi:10.1016/j.cageo.2019.01.002

Maxwell, S. C., Rutledge, J., Jones, R., and Fehler, M. (2010). Petroleum reservoir characterization using downhole microseismic monitoring. *Geophysics* 75 (5), 75A129–75A137. doi:10.1190/1.3477966

Michel, O. J., and Tsvankin, I. (2016). "Anisotropic waveform inversion for microseismic velocity analysis and event location," in *SEG technical Program expanded abstracts 2016* (Texas United States: Society of Exploration Geophysicists), 296–300.

Pan, X., Du, X., Zhao, X., Ge, Z., Li, L., Zhang, D., et al. (2022). Seismic characterization of decoupled orthorhombic fractures based on observed surface azimuthal amplitude data. *IEEE Trans. Geosci. Remote Sens.* 60, 1–12. doi:10.1109/TGRS.2021.3105724

Pei, D., Quirein, J. A., Cornish, B. E., Quinn, D., and Warpinski, N. R. (2009). Velocity calibration for microseismic monitoring: A very fast simulated annealing (vfsa) approach for joint-objective optimization. *Geophysics* 74 (6), WCB47–WCB55. doi:10.1190/1.3238365

Thomsen, L. (1986). Weak elastic anisotropy. *Geophysics* 51 (10), 1954–1966. doi:10.1190/1.1442051

Thurber, C. H. (1986). Analysis methods for kinematic data from local earthquakes. *Rev. Geophys.* 24 (4), 793–805. doi:10.1029/rg024i004p00793

Tsvankin, I. (2012). *Seismic signatures and analysis of reflection data in anisotropic media*. Texas United States: Society of Exploration Geophysicists.

Zhang, H., and Thurber, C. H. (2003). Double-difference tomography: The method and its application to the Hayward fault, California. *Bull. Seismol. Soc. Am.* 93 (5), 1875–1889. doi:10.1785/0120020190

Zhang, J., and Toksoz, M. N. (1998). Nonlinear refraction travel time tomography. *Geophysics* 63, 1726–1737. doi:10.1190/1.1444468

Zhou, B., and Greenhalgh, S. A. (2005). Analytic expressions for the velocity sensitivity to the elastic moduli for the most general anisotropic media. *Geophys. Prospect.* 53 (4), 619–641. doi:10.1111/j.1365-2478.2005.00490.x

Zimmer, U., Bland, H., Jing, D., Warpinski, N., Sen, V., and Wolfe, J. (2009). "Accuracy of microseismic event locations recorded with single and distributed downhole sensor arrays," in *SEG technical Program expanded abstracts*. Houston, TX: Society of Exploration Geophysicists. 1519–1523.

frontiers | Frontiers in Earth Science

TYPE Original Research
PUBLISHED 04 January 2023
DOI 10.3389/feart.2022.1072017

OPEN ACCESS

EDITED BY
Lei Li,
Central South University, China

REVIEWED BY
Gaohua Zhu,
Institute of Oceanology (CAS), China
Huajian Yao,
University of Science and Technology of China, China

*CORRESPONDENCE
Cong Zhou,
zhoucong323@126.com

SPECIALTY SECTION
This article was submitted to Solid Earth Geophysics, a section of the journal Frontiers in Earth Science

RECEIVED 17 October 2022
ACCEPTED 09 December 2022
PUBLISHED 04 January 2023

CITATION
Zhou C, Fu L, Shi K, Zeng X and Zhang P (2023), Velocity changes after the 2021 M_S 6.4 Yangbi earthquake based on passive image interferometry. *Front. Earth Sci.* 10:1072017. doi: 10.3389/feart.2022.1072017

Velocity changes after the 2021 M_S 6.4 Yangbi earthquake based on passive image interferometry

Cong Zhou[1,2]*, Lei Fu[3], Kexu Shi[2], Xiangzhi Zeng[4] and Pei Zhang[2]

[1]Institute of Geophysics, China Earthquake Administration, Beijing, China, [2]The Second Monitoring and Application Center, China Earthquake Administration, Xi'an, China, [3]School of Geophysics and Geomatics, China University of Geosciences, Wuhan, China, [4]Jiangsu Donghai Continental Deep Hole Crustal Activity, National Observation and Research Station, Lianyungang, China

An M_S 6.4 earthquake occurred in Yangbi, Yunan Province, China, on 21 May 2021. The epicenter was on the blind branch fault in the west of the Weixi–Qiaohou–Weishan fault, but no surface rupture was obvious. In the present study, the continuous vertical component of waveforms that were recorded in six nearby permanent stations was collected and the noise cross-correlation and autocorrelation techniques were utilized to investigate velocity changes that were induced by the Yangbi Earthquake. Velocity changes based on the single-station autocorrelation method reveal mainly coseismic declines, and a maximum of .09% was recorded in the EYA station. Results from the cross-correlation technique show both positive and negative velocity changes, and these lasted for approximately 3 months. The volumetric strain that was generated by the Yangbi Earthquake at a depth of 5 km exhibits an obvious four-quadrant distribution. Station pairs in the dilatation region (e.g., EYA–HEQ) mainly display a decrease in velocity, whereas those in the contraction region (e.g., BAS–TUS, TUS–YUL, and LUS–TUS) show an increase in velocity. Based on the depth sensitivity of scattered waves, velocity changes that were obtained using the noise cross-correlation involve the highest weight coefficients near the related two stations. Regarding stations of one station pair in different stress loading regions, the static stress of the station that is nearest to the epicenter exerted a greater impact on the velocity change. The observed velocity changes are likely attributed to a combination of near-surface physical damage and static stress changes. The validation of clock errors with magnitudes of seconds that were obtained using the noise cross-correlation and effects of these errors on measured velocity changes are also discussed.

KEYWORDS

noise cross-correlation, autocorrelation, coda wave interferometry, the Yangbi earthquake, velocity change, clock error

1 Introduction

The state of stress and properties of the medium in a fault zone can change significantly during the nucleation and occurrence of an earthquake (Kanamori, 1994; Liu et al., 2014). Therefore, studies on changes in the medium are useful to understand the evolution and healing of faults, as well as the evolution of earthquake risk analysis. Seismologists have proposed the use of repeated earthquake data to characterize velocity perturbations in the crust because earthquakes, which originated from deep underground locations, reveal significant information of the source area (Poupinet et al., 1984; Peng and Ben-Zion, 2006). However, repeated earthquakes are spatiotemporally limited, and these are often associated with regions of high seismic activity. Artificial sources that produce similar waveforms are also useful for the monitoring of temporal changes in such media (Reasenberg and Aki, 1974; Vidale and Li, 2003; Wang et al., 2008). Su et al. (2022) reported coseismic velocity variations of .08%–.12% near the fault zone of the 2021 M_S 6.4 Yangbi Earthquake based on seismic wave signals that were generated using Binchuan Airgun. In the past decade, the passive monitoring of seismic velocity using interferometry increased significantly. This was utilized to monitor fault systems and landslides (Brenguier et al., 2008a; Liu et al., 2014; Liu et al., 2018; Boschelli et al., 2021; Huang et al., 2021; Le Breton et al., 2021), predict volcanic intrusions (Brenguier et al., 2008b; Liu et al., 2022), and explore changes in shallow groundwater (Clements and Denolle, 2018; Mao et al., 2022). These studies generally assumed that the coda part of noise cross-correlation functions travels a longer path that broadly samples the medium compared to direct waves, and is therefore more sensitive to small perturbations in the medium (Snieder et al., 2002; Sheng et al., 2021).

The methods that can be used to calculate the travel time shift δt between earthquake doublets can be divided into three categories: 1) Time-domain methods such as windowed cross correlation (Snieder et al., 2002), trace stretching (Sens-Schönfelder and Wegler, 2006; Obermann et al., 2016), and dynamic time warping (Meier et al., 2010); 2) Frequency-domain methods such as moving window cross spectrum (MWCS) (Poupinet et al., 1984; Liu et al., 2018); and 3) Wavelet-domain methods such as wavelet cross spectrum (Mao et al., 2020) and wavelet trace stretching (Yuan et al., 2021). Liu et al. (2010) compared and analyzed the advantages and disadvantages of four common methods and concluded that the MWCS performed better due to small measurement errors. Moreover, MWCS separates amplitude spectrum and phase spectrum before measurement, so it is less affected by the frequency of ambient noise (Zhan et al., 2013).

Mechanisms of velocity changes induced by earthquakes, such as static stress and pore pressure variations, as well as near-surface and fault zone physical damage remain controversial (Poupinet et al., 1984; Rubinstein and Beroza, 2004; Wegler et al., 2009; Sheng et al., 2021). On 21 May 2021, an M_S 6.4 earthquake (epicenter at 25.67°N and 99.87°E) occurred in Yangbi County in the west of Yunan province, China. The epicenter of the earthquake was on the blind branch fault in the west of the Weixi–Qiaohou–Weishan fault, and surveys revealed no obvious surface rupture (Li et al., 2021; Zhu et al., 2022). This was the strongest shallow earthquake in Yunnan in the past decade following the M_S 6.5 Ludian and M_S 6.6 Jinggu earthquakes (Zhang et al., 2021).

In the present study, continuous data that were recorded in six nearby permanent stations was collected and both the ambient noise cross-correlation and autocorrelation methods were utilized to characterize velocity changes induced by the Yangbi Earthquake. Unlike many previous cases, both positive and negative velocity changes were obtained by using cross-correlation method. Mechanisms involved in the velocity changes were then examined based on the distributions of sensitivity associated with scattered waves and the static stress field. We also found clock errors of up to 1 year and up to 1 s in the data recorded at the EYA and LUS stations, respectively. Effects of the clock errors on measured of velocity changes were then analyzed.

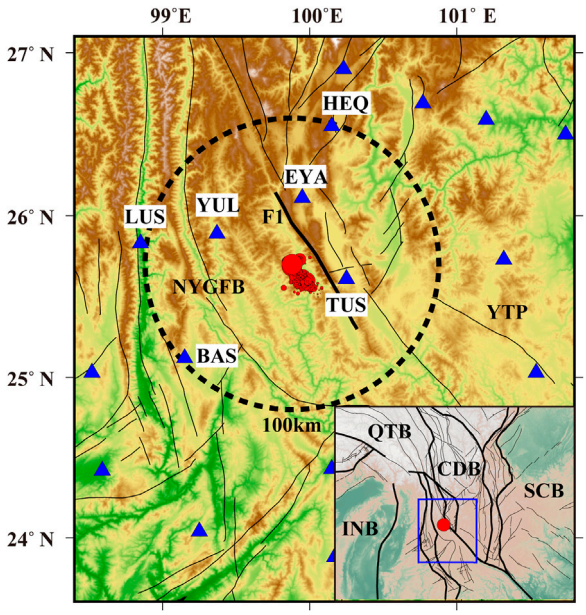

FIGURE 1
The tectonic background of the Yangbi earthquake sequence. Six broadband stations are located in the black circle area, which within approximately 100 km of the epicenter. F1 denotes the Weixi-Qiaohou-Weishan fault. The abbreviations denote the tectonic units. NYGFB, Northwest Yunnan geosynclinal fold belt; YTP, Yangtze Paraplatform; CDB, Chuandian Block; QTB, Qiangtang Block; SCB, South China Block; INB, Indian Block. The inset denotes the location of the research area. The red dot denotes the mainshock in both the main figure and the inset.

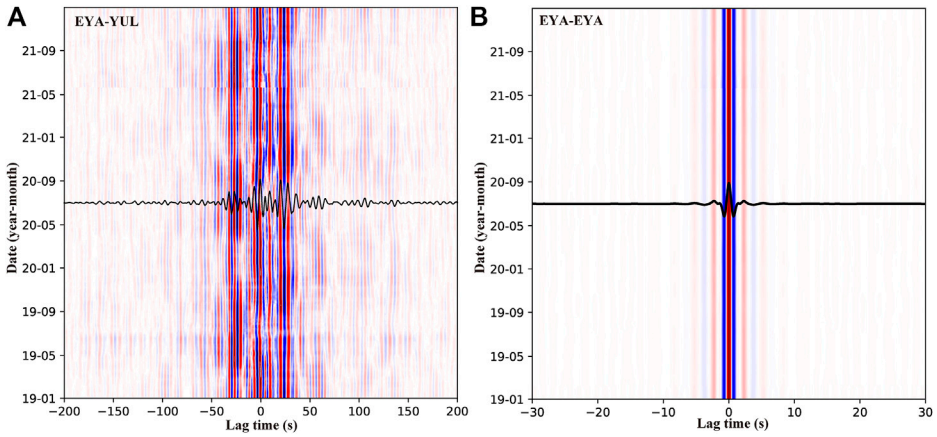

FIGURE 2
Daily CCFs for **(A)** EYA-YUL station pair in the period band of 1–10 s and **(B)** single station (EYA) in the period band of 1–3 s from January 2019 to December 2021. Waveforms in black represent reference CCFs, and red and blue correspondingly denote positive and negative.

2 Data and method

2.1 Data

The M_S 6.4 Yangbi earthquake is located in western Yunnan, which is located in the southeast margin of Tibet Plateau (Figure 1). It is the Yangtze paraplatform and northwest Yunnan geosynclinals fold belt junction area, which has strong characteristics of structural tension since the Quaternary period (Huang et al., 2014). In the present study, the vertical component of continuous waveforms (100 Hz) that were recorded in six broadband stations that are located within approximately 100 km of the epicenter of the Yangbi Earthquake between January 2019 and December 2021 was utilized (Figure 1). The area hosting the hypocenter was adequately covered by ten station pairs, and the minimum, maximum, and average distances between these stations pairs are 52, 143, and 97 km, respectively.

2.2 Green's function retrieval

The data preprocessing procedure that was utilized in the present study was described in Liu et al. (2014). Raw seismic data were partitioned into 1-day intervals and the vertical component data were then resampled at 10 Hz to improve computational efficiency. Temporal normalization and spectrum whitening in the 1–20 s range were applied to each segment to minimize earthquakes effects. Reference cross-correlation functions (CCFs) for station pairs were obtained *via* the stacking of CCFs covering the period from 1 January 2019, to 21 April 2021 (a month preceding the Yangbi Earthquake). To improve the signal-to-noise ratio of daily CCFs, these were derived through the stacking of CCFs for 61 d, which included 30 d before and after a target day. To prevent mixing of pre- and post-seismic signals, daily CCFs that were calculated for periods before and after the Yangbi Earthquake were stacked separately (Liu et al., 2014; Liu et al., 2022). For example, the daily CCF on 28 May 2021 is obtained from stacking only post-seismic daily CCFs from 22 May 2021 to 28 June 2021. Thus, the stacking days of daily CCFs is smaller than 61 d within a month before and after the main shock. Daily CCFs for the EYA–YUL station pair in the period band of 1–10 s from January 2019 to December 2021 are shown in Figure 2A, and clear surface and stable coda wave signals are obvious. Owing to the decrease of the coda wave coherence as the timelapse increases, the lapse window for the positive portion of CCFs was determined as 30–130 s after the arrival of Rayleigh waves in this period band (Supplementary Figure S1). The windows in the negative portion were symmetrical to that in the positive portion.

To supplement station pairs near the epicenter, the single-station autocorrelation approach was also considered. Autocorrelation functions mainly reflect changes in the shallow crust near a station, and the associated flow processing is similar to that for the cross-correlation of a station pair. Figure 2B shows the autocorrelation functions for the EYA station using 1–3 s band-pass filter from January 2019 to December 2021. The lapse windows for the autocorrelation were determined as the fixed windows with range of ±(5–55) s.

2.3 Velocity change measurement using coda wave interferometry

Large to medium velocity perturbations can be directly obtained by measuring the relative traveltimes of the direct

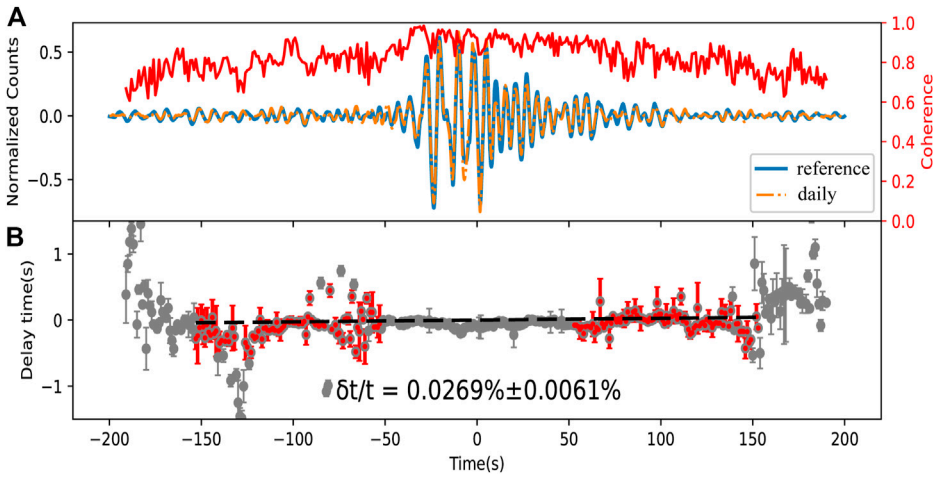

FIGURE 3
Example of a relative time shift (δt/t) that was estimated from CCFs in the period band of 1–10 s for the EYA–TUS station pair showing **(A)** waveforms of reference CCFs (blue) and daily CCFs for 1 April 2021 (yellow). The curve in red denotes the correlation coefficient. **(B)** The relative time shift (δt/t) for 1 April 2021. Circles containing error bars represent time shifts that were calculated in sliding windows, whereas the slope of the dash line in black was estimated using a weighted linear regression of all red time shifts.

waves. Studies on the detection of small–medium changes as a function of time have focused on seismic coda waves. Coda waves, which are also known as multiply scattered waves, usually arrive later than direct waves. The later the arrival of scattered wave phases at the receiver, the longer the associated propagation paths and the higher the sensitivity to minor perturbations in a medium (Snieder et al., 2002).

Assuming that the change of relative seismic wave velocity (δv/v) is spatially homogeneous, the travel time shift δt between CCFs is proportional to the lapse time t and can be calculated as δv/v = −δt/t (Poupinet et al., 1984; Snieder et al., 2002). Therefore, the measurement of the travel time shift δt is very important for coda wave interferometry. In the present study, the MWCS method was utilized to measure the relative time shift between a reference CCFs that corresponds to the initial state, and a current CCFs that has encountered a velocity change in the medium. With the MWCS method, a series of overlapping time windows are defined in the coda wave, and the time shifts in these windows are estimated by means of the cross-spectrum method. The cross-spectrum X(*f*) between the reference CCFs and current CCFs is calculated as follows (Clarke et al., 2011):

$$X(f) = F_{ref}(f) \cdot F^{*}_{cur}(f) \tag{1}$$

where F_{ref} and F_{cur} are the Fourier-transformed segments of the reference and current CCFs. The asterisk denotes the complex conjugation and f is the frequency. $X(f)$ can also be expressed by its amplitude $|X(f)|$ and phase $e^{i\phi(f)}$. If the time-shift is constant in each window segment, ϕ is linearly proportional to f:

$$\phi(f) = 2\pi\delta t f \tag{2}$$

The time shift for each window segment is the slope and the associated error e_m is caulcuated as

$$e_m = \sqrt{\sum_j \left(\frac{w_j v_j}{\sum_i w_i v_i^2}\right)^2 \frac{\sum_j (\phi_j - m v_j)^2}{N-1}} \tag{3}$$

where w are weights, m is the slope of ϕ, and v are $2\pi f$.

After all time shifts δt are measured in the window segments in an interest range of lapse time, the relative time shift $\delta t/t$ is estimated by a weighted linear regression passing through zero, and then $\delta v/v$ can be obtained by $-\delta t/t$ (Poupinet et al., 1984; Clarke et al., 2011). To evaluate the reliability and accuracy of the method, waveform modeling data that were reported in Yuan et al. (2021) were used, and the +.1% velocity perturbation that was determined in the model was correctly measured (Supplementary Figure S2).

Figure 3 shows an example of the relative time shift estimation using CCFs for the EYA–TUS station pair. Compared with the theoretical waveform in Supplementary Figure S2, CCFs of the EYA–TUS station pair produced a lower coherence and preserved the acausal signal. Regarding a 1–10 s period band and a station pair with distance of 62 km, the timelapse window is between 53 and 153 s and window segments are 18 s with a step of 1 s. Time shifts (δt) between reference and daily CCFs can be measured in each window segments by using the MWCS, and the slope (δt/t) can then be estimated *via* a weighted linear regression of the time shifts.

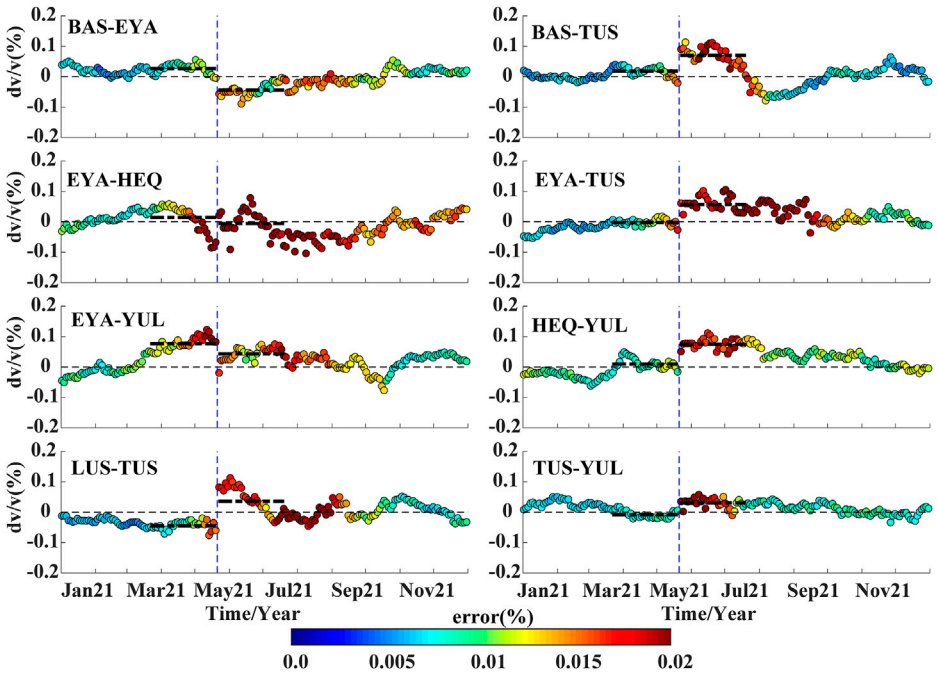

FIGURE 4
Continuous velocity changes obtained *via* the cross-correlation technique near the epicenter of the Yangbi Earthquake. The vertical dashed line in blue denotes the times of the earthquake, whereas the two thick dashed lines in black represent average values during the 2-month periods before and after the earthquake. The thin dashed line in black marks the zero levels, whereas dot colors highlight measurement errors, and the error scale is depicted.

3 Velocity changes caused by the Yangbi earthquake

Figure 4 shows continuous seismic velocity changes for the eight station pairs that cover the area of the epicenter of the Yangbi Earthquake. Coseismic velocity changes are observed in most station pairs, but unlike in many previous studies, velocity declines are evident in just three station pairs. Velocity changes of station pairs BAS-EYA, BAS-TUS, EYA-TUS, and LUS-TUS are relative stable and around the zero line before the main shock. The largest coseismic decrease is .06% for pair BAS-EYA, whereas the largest increasing is .14% for pair LUS–TUS that involves a path through the epicenter. These coseismic velocities are usually underestimated because of the long stacking days for the daily CCFs. Regardless of an increase or decrease in the coseismic velocity, the influence of the Yangbi Earthquake is evident for station pairs that display relatively stable results, such as the BAS–EYA, BAS–TUS, and LUS–TUS, and the influence last for approximately 3 months. Errors associated with the calculation of velocity changes are relatively high during the 1-month periods before and after the earthquake. These large errors are attributed to the reduction of stacking days because of the separation of stacking procedures of daily CCFs into those before and after the earthquake. Another reason is that because the Yangbi Earthquake is a typical foreshock–mainshock–aftershock type (Chen et al., 2022), the abundant foreshock and aftershock activities affect the stability of the empirical Green's functions.

Considering the average dv/v for the 2-month period preceding the earthquake as the reference value and that of the corresponding period after the earthquake minus the reference as the coseismic velocity change, a spatial distribution of coseismic velocity changes was obtained (Figure 5). Evidently, the Yangbi Earthquake mainly increased velocities in the study area. Station pairs of BAS-EYA, BAS-TUS, and EYA-TUS enclose the seismogenic fault and aftershock area. Coseismic velocity changes of pairs BAS-EYA and BAS-TUS, which across the fault zone, are −.07% and +.05%, whereas that of EYA-TUS on the east of the fault is +.06%. The relative velocity of the LUS–TUS station pair that involves a path through the epicenter increase by approximately .08%, but that of the TUS-YUL with a similar path increase slightly. Station pairs related to the TUS or YUL stations, which are in the near-field, are mainly characterized by an increase in velocity, whereas those involving the EYA station exhibit a decline.

Field surveys revealed that no obvious surface rupture was caused by the earthquake (Li et al., 2021; Zhu et al., 2022). According to simulations of strong ground motions, the peak ground acceleration exhibits a circular shape around the epicenter, and the ground motions beyond 60 km decay

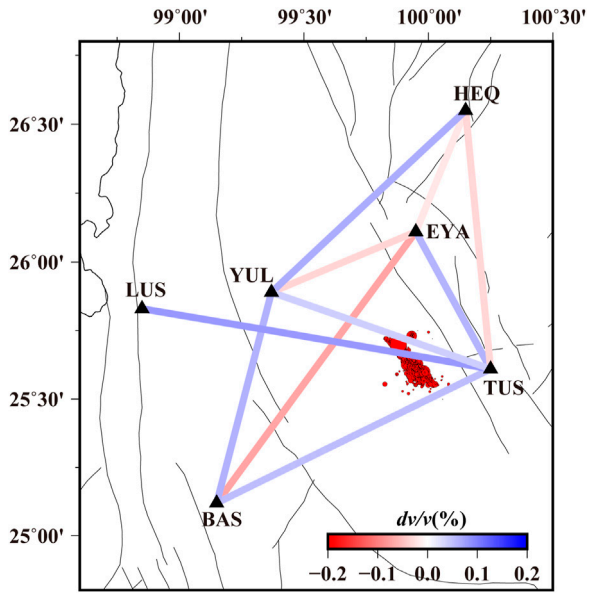

FIGURE 5
Spatial distribution of mean coseismic velocity changes. The mean coseismic velocity change is the difference between average velocity changes during the 2-month periods before and after the earthquake. Lines in blue indicate positive values, whereas those in red depict negative values.

rapidly (Zhou et al., 2021). To evaluate perturbations of the Yangbi Earthquake on the shallow crust in the near-field, the single-station autocorrelation method was used to obtain the continuous velocity changes for single stations in the period band of 1–3 s (Figure 6). The results show that, excluding the LUS station, which is farthest from the epicenter, the other five stations exhibit a decline in the coseismic velocity. The highest decline of .09% was obtained from the EYA station, and these effects of the earthquake lasted for approximately 2–3 months. Data for coseismic velocity changes that were obtained using the noise cross-correlation and autocorrelation techniques are presented in Table 1.

4 Discussion

There are four different mechanisms for velocity changes caused by earthquakes (Poupinet et al., 1984; Rubinstein and Beroza, 2004; Wegler et al., 2009; Boschelli et al., 2021; Sheng et al., 2021): 1) the change of the static stress results in positive and negative velocity changes; 2) the change of fluid content and pore pressure variations affects velocity; 3) the physical damage caused by fault motion; 4) near-surface physical damage caused by strong ground motion. Owing to the Yangbi Earthquake, excluding the LUS station (~104 km from the epicenter), which showed a slight increase in velocity, autocorrelation analysis results for the other five stations revealed declines in the coseismic velocity. These decreases in velocities are mainly attributed to near-surface physical damage caused by the strong ground motion. Conversely, results from the noise cross-correlation analysis are difficult to explain. But first and foremost, the clock error or instrumental time shift is needed to be considered in using passive image interferometry (Liu et al., 2010).

4.1 Clock errors and their effects on velocity changes

Variations in spatial distributions of noise sources and the instrumental clock errors can independently affect the measurement of the travel time shift (Stehly et al., 2007). Clock errors can produce an overall shift in the entire cross-correlation time, thereby increasing traveltimes in the positive portion and decreasing traveltimes in the negative portion, and *vice versa*. Comparatively to the measurement of velocity changes in a medium, a direct arrival surface wave was used instead of a coda wave to measure instrumental clock errors. Clock errors that was measured from the surface wave using the noise cross-correlation technique can be expressed as follows (Stehly et al., 2007):

$$\frac{\delta\tau(t)+\delta\tau(-t)}{2} = D(t) + \frac{\varepsilon(t)+\varepsilon(-t)}{2} \tag{4}$$

where $\delta\tau(t)$ denotes the variation in the traveltime of the surface wave that is measured in the positive or negative portion. $D(t)$ is the time shift caused by instrumental clock errors, and $\varepsilon(t)$ is the time shift associated with the spatial variation of noise sources. Therefore, clock errors can be estimated using Eq. 4 by assuming that $D(t)$ is greater than $\frac{\varepsilon(t)+\varepsilon(-t)}{2}$.

Following approaches that were advanced in Section 2.2 and Section 2.3, only the coda wave window was replaced with a surface wave window, that is, it starts 30 s before the surface wave time and ends 40 s after. Supplementary Figure S3 shows an example of clock errors that were estimated using data from the LUS–YUL station pair. The clock errors that were obtained on August 1 and October 20, for example, are .42 and −.04 s, respectively. The clock error on October 20 is less than one sampling rate, and thus, it can be considered as zero. Clock errors for these stations were evaluated for the period from 2019 to 2021, and results for station pairs with possible large clock errors are shown in Figure 7. The EYA station displays a clock drift of approximately −0.2 s throughout 2019, whereas LUS station exhibits a clock drift of −.6 s between July and August 2021. Considering that daily CCFs were obtained by stacking CCFs of 61 days, the estimated clock drifts are likely underestimated, in particular, the clock drifts from the LUS station may reach seconds.

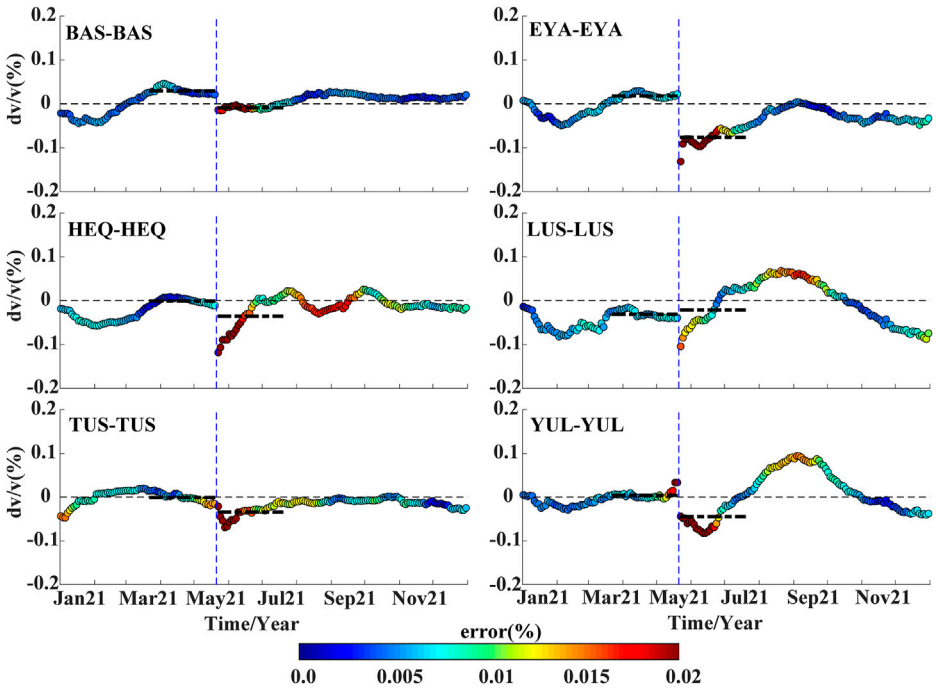

FIGURE 6
Continuous velocity changes near the epicenter of the Yangbi Earthquake that were derived using the autocorrelation technique. The vertical dashed line in blue denotes the time of the Yangbi Earthquake, whereas the two thick dashed lines in black are averages for the 2-month periods before and after the earthquake. The thin dashed line in black represents zero levels, whereas dot colors depict measurement errors, and the error scale is shown.

Two groups of teleseismic earthquakes that occurred in the Alaska Peninsula and the Philippines are selected to validate the clock drifts (Supplementary Tables S1, S2; Supplementary Figure S4). Differences in traveltimes of the phases between stations should essentially stable over time for nearby teleseismic earthquakes. But the reference arrivals of earthquakes on July 29 and 14 August 2021, were relatively early at the LUS station compared to that of other three earthquakes (Supplementary Figure S5). If the linear trend in Supplementary Figure S5B is eliminated, more intuitive reference arrivals relative to the distance from the epicenter can be obtained. Supplementary Figure S6A demonstrates that arrivals of earthquakes on July 29 and 14 August 2021, at the LUS station significantly differ from those of the other three earthquakes, and the drift is −1 s. Arrivals of all earthquakes at the other four stations do not show any obvious drift between 22 July 2020, and 11 October 2021. In addition, arrivals of earthquakes at the EYA station in 2019 slightly differ from those of the other three events, and the drift is −.3 s (Supplementary Figure S6B).

Considering the LUS–YUL station pair as an example, the velocity change that was calculated using the least squares fitting MWCS method is less than .02% for a clock error of 1 s (Figure 8). This minimal impact is probably because the slope of dt/t based on the MWCS method is unaffected by such an overall time drift of the cross-correlation time. However, a large clock error reduces the correlation between the reference and daily CCFs, and this affects subsequent calculations.

4.2 Static stress changes caused by the Yangbi earthquake

Positive and negative velocities linked to earthquakes may correspond to regions of increased and decreased stress, respectively (Rubinstein and Beroza, 2004). To explain observations from the noise cross-correlation, static stress changes caused by the earthquake were calculated using Coulomb 3.0 (Lin and Stein, 2004). The static slip distribution of the Yangbi Earthquake provided by Xu Zhang was utilized (https://www.cea.igp.ac.cn/kydt/278248.html, see Supplementary Figure S7), whereas the Poisson's ratio and shear modulus were set to .25 and 32 GPa, respectively. The calculated volumetric strains caused by fault slips at a depth of 5 km exhibit an obvious four-quadrant distribution (Figure 9). The EYA and HEQ stations are in the dilatation region, where a decrease in velocity is anticipated, in fact, the velocity changes for the EYA–HEQ station pair decreased by .02%. The other four stations fall within the contraction region, where a velocity increase is expected, in fact, velocity changes for the BAS–TUS, TUS–YUL, and LUS–TUS station

TABLE 1 Velocity changes caused by the Yangbi earthquake.

Station pairs	Cross-correlation (1–10 s)/autocorrelation (1–3 s)			Trend	Strain at 0 km
	dv/v (%) before earthquake	*dv/v* (%) after earthquake	Coseismic change (%)		
BAS-EYA	.0267	−.0443	−.0710	↓	——
BAS-TUS	.0180	.0700	.0519	↑	——
BAS-YUL	−.0449	.0166	.0615	↑	——
EYA-HEQ	.0144	−.0058	−.0202	↓	——
EYA-TUS	−.0023	.0572	.0595	↑	——
EYA-YUL	.0767	.0432	−.0335	↓	——
HEQ-TUS	.0110	−.0218	−.0328	↑	——
HEQ-YUL	.0098	.0746	.0648	↑	——
LUS-TUS	−.0446	.0359	.0805	↑	——
TUS-YUL	−.0086	.0306	.0393	↑	——
TUS-TUS	−.0011	−.0343	−.0331	↓	-1.3×10^{-7}
EYA- EYA	.0180	−.0763	−.0943	↓	6.5×10^{-8}
YUL-YUL	.0040	−.0448	−.0488	↓	-4.0×10^{-8}
LUS-LUS	−.0309	−.0209	.0100	↑	-1.1×10^{-8}
HEQ-HEQ	−.0009	−.0354	−.0345	↓	9.5×10^{-9}
BAS-BAS	.0298	−.0090	−.0387	↓	-2.7×10^{-9}

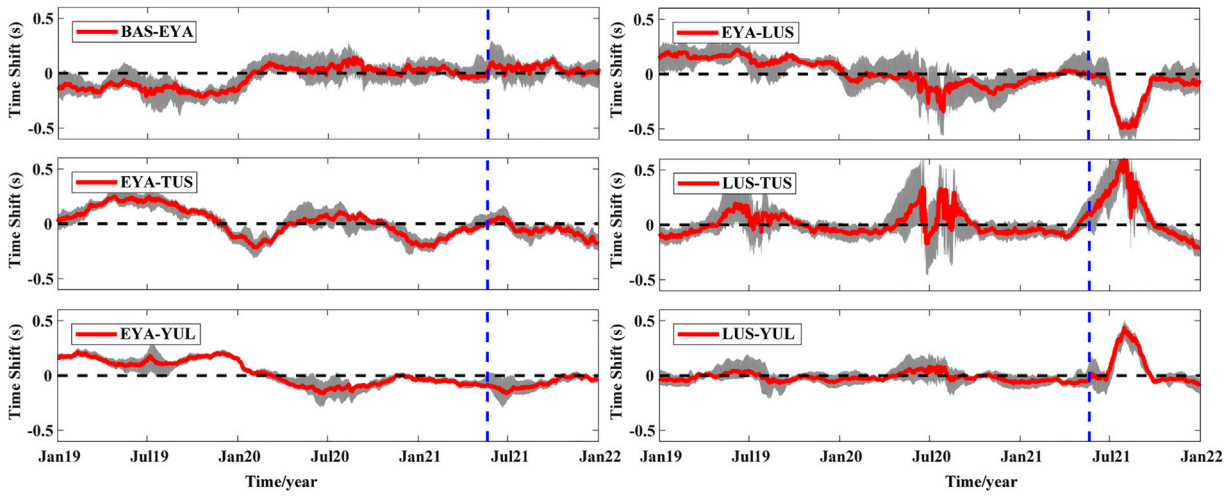

FIGURE 7
Clock errors for different station pairs between 2019 and 2021. The area shaded in gray represents the standard deviation, and this was used to highlight the calculation error. The vertical dashed line in blue denotes the time of the Yangbi Earthquake.

pairs corresponding increased by .05%, .04%, and .08%. However, how to decide if two stations are in different strain regions. For example, the velocity changes for the EYA–TUS station pair increased by .06%, whereas that for the EYA-YUL pair decreased by .03%. Therefore, an analysis of the spatial sensitivity distribution of coda waves is necessary.

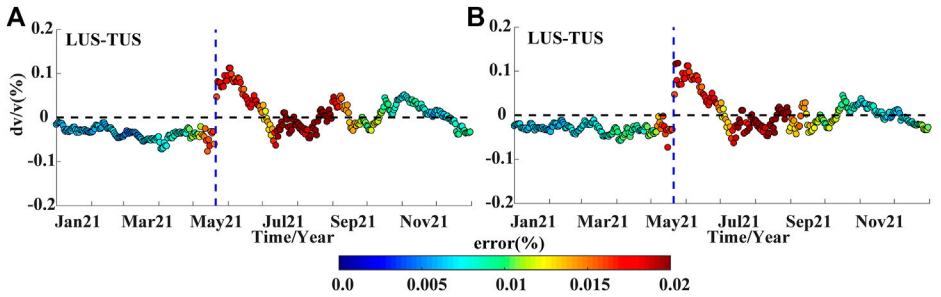

FIGURE 8
Velocity change measurements involving **(A)** no clock error correction and **(B)** with a clock error correction.

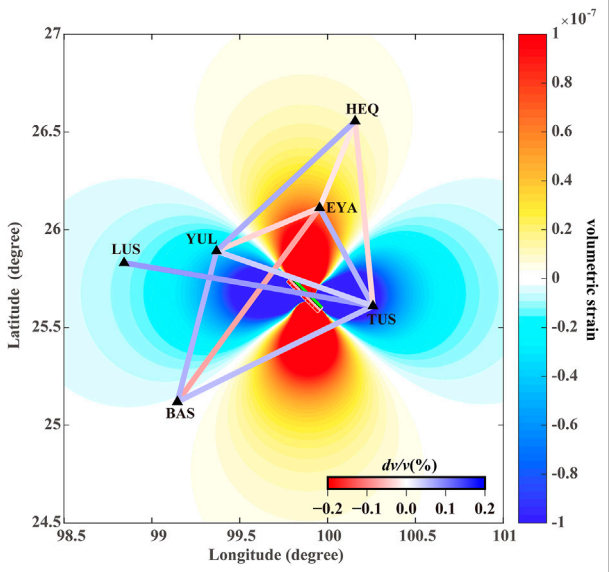

FIGURE 9
Volumetric strain changes caused by the Yangbi Earthquake at a depth of 5 km. The region of positive strain is dilatation and shown in red. Blue areas denote contraction. Lines connecting two stations correspond to the noise cross-correlation between the stations, and their values are presented in Table 1.

4.3 Depth sensitivity of coda waves

Based on numerical simulations of seismic waves in 2D and 3D heterogeneous elastic media, Obermann et al. (2013) suggested that the sensitivity of coda waves can be modeled as a linear combination of the sensitivities of body and surface waves. They indicated that early coda waves are dominated by fundamental surface waves, which mainly reflect shallow perturbations, whereas later coda waves are dominated by body waves. In the present study, the timelapse windows for CCFs were determined as 30–130 s after the arrivals of Rayleigh waves, and this contained sufficiently long signals. The sensitivity kernel that is expressed as follows can be used (Pacheco and Snieder, 2005):

$$K(\mathbf{S},\mathbf{R},\mathbf{r}_0,t)=\frac{1}{p(\mathbf{S},\mathbf{R},t)}\int_0^t p(\mathbf{S},\mathbf{r}_0,t')p(\mathbf{r}_0,\mathbf{R},t-t')dt' \quad (5)$$

where S and R are the positions of the source and receiver, respectively; r_0 is the position of the local velocity variation; t is the center timelapse for doublet analysis; and p (s, r, t) is the probability that the wave has traveled from s to r during t. This probability can be approximated using the full-space solution of the diffusion equation, which is expressed as follows (Mao et al., 2019):

$$p(\mathbf{s},\mathbf{r},t)=\frac{1}{(4\pi Dt)^{3/2}}e^{\frac{-\|s-r\|^2}{4Dt}} \quad (6)$$

where D is the diffusion constant. The multiply scattered waves that propagate in 3 dimensions can be described by D:

$$D=\frac{C_E * l^*}{3} \quad (7)$$

where C_E is the energy velocity and l^* is the scattering mean free path. Considering that S waves account for most of the energy in coda waves, a ratio of 9:1 was used to calculate C_E: $\frac{1}{C_E}=\frac{0.89}{Vs}+\frac{0.11}{Vp}$ (Obermann et al., 2016). Therefore, the key to determine the sensitivity kernel is to estimate the scattering mean free path l^*. In general, at a larger scale (e.g., crustal) the mean free path is fairly constant relative to the frequency, but this may not be applicable at local scales. Chaput et al. (2015) estimated that the scattering mean free path for the Erebus volcano in Antarctica at 1.5 Hz is ~2 km, and values slowly decreased as the frequency increased. Data for the scattering mean free path for the Yangbi area are scant, but theoretically values that involve 5%–10% heterogeneity are in the range of 2–10 km (Obermann et al., 2013). Here, l^* = 5 km was considered in the period band of 1–10 s for analysis. If the distance between two stations is 60 km and the center time of coda wave window is 100 s, the normalized depth sensitivity of the scattering waves can be obtained based on Eq. 5 (Figure 10).

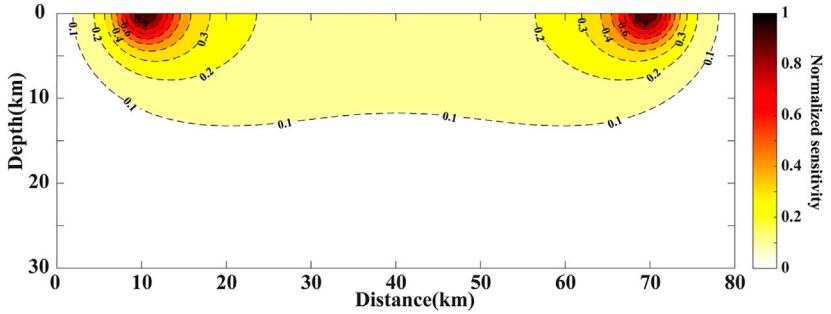

FIGURE 10
Normalized depth sensitivity of scattering waves.

The sensitivity of scattered waves is high near the source and receiving points and relatively low in the middle portion. It decays with increasing depth, and at ~12 km it reduces to 10% of the value at surface. The depth sensitivity for station pair LUS–TUS with path crossing through the fault zone shows that the epicenter of the Yangbi earthquake (marked by the red star in Supplementary Figure S8) is located in the weak sensitivity zone (smaller than 10%). The scatter waves for the existing station pairs may not be able to sample the major rupture area of the Yangbi earthquake. Velocity changes obtained using the noise cross-correlation technique can be considered weighting effects along propagation paths, and the largest weight coefficient is obtained near the related two stations.

Considering that the static stress rapidly decays as the distance from the epicenter increases, if two stations of a station pair are in different stress-loading regions, the static stress of the station closer to the epicenter exerts a greater impact on the velocity change. For example, the velocity changes for the EYA–TUS, EYA–YUL, BAS–EYA, and HEQ–YUL station pairs were attributed mainly to static stress of the stations closer to the epicenter. According to the meteorological observation data of the Dali Center of the China Earthquake Science Experiment Field, there is no obvious change in the rainfall before and after the main shock (Su et al., 2022). These results suggest that velocity changes are likely linked to a combination of near-surface physical damage and static stress changes. This also explains the inconspicuous drop in the coseismic velocity that was obtained using the autocorrelation for the TUS station, which is closest to the epicenter, compared to those of other nearby stations.

5 Conclusion

In the present study, temporal and spatial coseismic velocity changes were determined for the Yangbi Earthquake using the ambient noise cross-correlation and autocorrelation techniques. The mechanism involved in these velocity changes and effects of clock errors on the measurements were examined. The main conclusions are summarized as follows:

(1) Excluding the LUS station, which is farthest from the epicenter, velocity changes obtained using the single-station autocorrelation indicated declines in the period band of 1–3 s. In contrast, the noise cross-correlation produced both positive and negative velocity changes for 1–10-s period band, and the impact of the Yangbi Earthquake on these velocities lasted for approximately 3 months.
(2) Based on the depth sensitivity of scattering waves, velocity changes that were obtained using the noise cross-correlation produced the largest weight coefficients around the related stations. The static stress of the station closer to the epicenter exerted a greater impact on the velocity change. These observations demonstrated that velocity changes due to a combination of the near-surface physical damage and static stress changes.
(3) Clock errors were obtained in the EYA station, and the time shift for most of 2019 was ~−.3 s, whereas that for the LUS station between July and August 2021 was ~−1 s. These time shifts were validated using traveltimes of two groups of nearby teleseismic earthquakes. Clock errors of a few seconds minimally affected velocity measurements using the MWCS method, which estimated a change through linear regression.

Data availability statement

The original contributions presented in the study are included in the article/Supplementary Material, further inquiries can be directed to the corresponding author.

Author contributions

CZ and LF designed this study, analyzed the results, and drafted the manuscript. KS collected the earthquake catalogue and processed the data acquired. XZ and PZ contributed to the discussion and drafting.

Funding

This study is supported by the National Natural Science Foundation of China (Grant No. 41904063, 41974044) and Natural Science Basic Research Program of Shaanxi (Grant No. 2022JQ-256).

Acknowledgments

The authors would like to thank Professor Huajian Yao for using their software to calculate the cross-correlation and autocorrelation functions (http://yaolab.ustc.edu.cn/publication.php). The authors acknowledge that the Data Management Centre of China National Seismic Network at Institute of Geophysics provided the waveform data.

Conflict of interest

The authors declare that the research was conducted in the absence of any commercial or financial relationships that could be construed as a potential conflict of interest.

Publisher's note

Supplementary material

The Supplementary Material for this article can be found online at: https://www.frontiersin.org/articles/10.3389/feart.2022.1072017/full#supplementary-material

References

Boschelli, J., Moschetti, M. P., and Sens-Schönfelder, C. (2021). Temporal seismic velocity variations: Recovery following from the 2019 Mw 7.1 ridgecrest, California earthquake. *J. Geophys. Res. Solid Earth* 126, e2020JB021465. doi:10.1029/2020JB021465

Brenguier, F., Campillo, M., Hadziioannou, C., Shapiro, N. M., Nadeau, R. M., and Larose, E. (2008a). Postseismic relaxation along the San Andreas fault at Parkfield from continuous seismological observations. *Science* 321, 1478–1481. doi:10.1126/science.1160943

Brenguier, F., Shapiro, N. M., Campillo, M., Ferrazzini, V., Duputel, Z., Coutant, O., et al. (2008b). Towards forecasting volcanic eruptions using seismic noise. *Nat. Geosci.* 1, 126–130. doi:10.1038/ngeo104

Chaput, J., Campillo, M., Aster, R. C., Roux, P., Kyle, P. R., Knox, H., et al. (2015). Multiple scattering from icequakes at Erebus volcano, Antarctica: Implications for imaging at glaciated volcanoes. *J. Geophys. Res. Solid Earth* 120, 1129–1141. doi:10.1002/2014JB011278

Chen, J., Hao, J., Wang, Z., and Xu, T. (2022). The 21 may 2021 Mw 6.1 Yangbi earthquake—A unilateral rupture event with conjugately distributed aftershocks. *Seismol. Res. Lett.* 93, 1382–1399. doi:10.1785/0220210241

Clarke, D., Zaccarelli, L., Shapiro, N. M., and Brenguier, F. (2011). Assessment of resolution and accuracy of the Moving Window Cross Spectral technique for monitoring crustal temporal variations using ambient seismic noise. *Geophys. J. Int.* 186, 867–882. doi:10.1111/j.1365-246X.2011.05074.x

Clements, T., and Denolle, M. A. (2018). Tracking groundwater levels using the ambient seismic field. *Geophys. Res. Lett.* 45, 6459–6465. doi:10.1029/2018GL077706

Huang, H., Dai, S., and Xie, F. (2021). Monitoring *in-situ* seismic response on rock slopes using ambient noise interferometry: Application to the 2019 changning (mw 5.7) earthquake, China. *Front. Earth Sci.* 8. 610181, doi:10.3389/feart.2020.610181

Huang, X., Wu, Z., Li, J., Nima, C., Liu, Y., Huang, X., et al. (2014). Tectonic geomorphology and Quaternary tectonic activity in the northwest Yunnan rift zone. *Geol. Bull. China* 33, 578–593. (in Chinese with English abstract).

Kanamori, H. (1994). Mechanics of earthquakes. *Annu. Rev. Earth Planet. Sci.* 22, 207–237. doi:10.1146/annurev.ea.22.050194.001231

Le Breton, M., Bontemps, N., Guillemot, A., Baillet, L., and Larose, É. (2021). Landslide monitoring using seismic ambient noise correlation: Challenges and applications. *Earth-Science Rev.* 216, 103518. doi:10.1016/j.earscirev.2021.103518

Li, C., Zhang, J., Wang, W., Sun, K., and Shan, X. (2021). The seismogenic fault of the 2021 Yunnan Yangbi Ms6.4 earthquake. *Seismol. Geol.* 43, 706–721. (in Chinese with English abstract). doi:10.3969/j.issn.0253-4967.2021.03.015

Lin, J., and Stein, R. S. (2004). Stress triggering in thrust and subduction earthquakes and stress interaction between the southern San Andreas and nearby thrust and strike-slip faults. *J. Geophys. Res. Solid Earth* 109. 2003JB002607, doi:10.1029/2003JB002607

Liu, Z., Huang, J., He, P., and Qi, J. (2018). Ambient noise monitoring of seismic velocity around the Longmenshan fault zone from 10 years of continuous observation. *J. Geophys. Res. Solid Earth* 123, 8979–8994. doi:10.1029/2018JB015986

Liu, Z., Huang, J., and Li, J. (2010). Comparison of four techniques for estimating temporal change of seismic velocity with passive image interferometry. *Earthq. Sci.* 23, 511–518. doi:10.1007/s11589-010-0749-z

Liu, Z., Huang, J., Peng, Z., and Su, J. (2014). Seismic velocity changes in the epicentral region of the 2008 Wenchuan earthquake measured from three-component ambient noise correlation techniques. *Geophys. Res. Lett.* 41, 37–42. doi:10.1002/2013GL058682

Liu, Z., Liang, C., Huang, H., Wang, C., and Cao, F. (2022). Seismic velocity variations at different depths reveal the dynamic evolution associated with the 2018 Kilauea eruption. *Geophys. Res. Lett.* 49, e2021GL093691. doi:10.1029/2021GL093691

Mao, S., Campillo, M., van der Hilst, R. D., Brenguier, F., Stehly, L., and Hillers, G. (2019). High temporal resolution monitoring of small variations in crustal strain by dense seismic arrays. *Geophys. Res. Lett.* 46, 128–137. doi:10.1029/2018GL079944

Mao, S., Lecointre, A., van der Hilst, R. D., and Campillo, M. (2022). Space-time monitoring of groundwater fluctuations with passive seismic interferometry. *Nat. Commun.* 13, 4643. doi:10.1038/s41467-022-32194-3

Mao, S., Mordret, A., Campillo, M., Fang, H., and van der Hilst, R. D. (2020). On the measurement of seismic traveltime changes in the time–frequency domain with wavelet cross-spectrum analysis. *Geophys. J. Int.* 221, 550–568. doi:10.1093/gji/ggz495

Meier, U., Shapiro, N. M., and Brenguier, F. (2010). Detecting seasonal variations in seismic velocities within Los Angeles basin from correlations of ambient seismic noise. *Geophys. J. Int.* 181, 985–996. doi:10.1111/j.1365-246X.2010.04550.x

Obermann, A., Planès, T., Hadziioannou, C., and Campillo, M. (2016). Lapse-time-dependent coda-wave depth sensitivity to local velocity perturbations in 3-D heterogeneous elastic media. *Geophys. J. Int.* 207, 59–66. doi:10.1093/gji/ggw264

Obermann, A., Planès, T., Larose, E., Sens-Schönfelder, C., and Campillo, M. (2013). Depth sensitivity of seismic coda waves to velocity perturbations in an elastic heterogeneous medium. *Geophys. J. Int.* 194, 372–382. doi:10.1093/gji/ggt043

Pacheco, C., and Snieder, R. (2005). Time-lapse travel time change of multiply scattered acoustic waves. *J. Acoust. Soc. Am.* 118, 1300–1310. doi:10.1121/1.2000827

Peng, Z., and Ben-Zion, Y. (2006). Temporal changes of shallow seismic velocity around the Karadere-Düzce branch of the north Anatolian fault and strong ground motion. *Pure Appl. Geophys.* 163, 567–600. doi:10.1007/s00024-005-0034-6

Poupinet, G., Ellsworth, W. L., and Frechet, J. (1984). Monitoring velocity variations in the crust using earthquake doublets: An application to the calaveras fault, California. *J. Geophys. Res. Solid Earth* 89, 5719–5731. doi:10.1029/jb089ib07p05719

Reasenberg, P., and Aki, K. (1974). A precise, continuous measurement of seismic velocity for monitoring *in situ* stress. *J. Geophys. Res. Solid Earth* 79, 399–406. doi:10.1029/jb079i002p00399

Rubinstein, J. L., and Beroza, G. C. (2004). Evidence for widespread nonlinear strong ground motion in the MW 6.9 Loma Prieta earthquake. *Bull. Seismol. Soc. Am.* 94, 1595–1608. doi:10.1785/012004009

Sens-Schönfelder, C., and Wegler, U. (2006). Passive image interferometry and seasonal variations of seismic velocities at Merapi Volcano, Indonesia. *Geophys. Res. Lett.* 33, L21302. doi:10.1029/2006GL027797

Sheng, Y., Ellsworth, W. L., Lellouch, A., and Beroza, G. C. (2021). Depth constraints on coseismic velocity changes from frequency-dependent measurements of repeating earthquake waveforms. *J. Geophys. Res. Solid Earth* 126, e2020JB020421. doi:10.1029/2020JB020421

Snieder, R., Grêt, A., Douma, H., and Scales, J. (2002). Coda wave interferometry for estimating nonlinear behavior in seismic velocity. *Science* 295, 2253–2255. doi:10.1126/science.1070015

Stehly, L., Campillo, M., and Shapiro, N. M. (2007). Traveltime measurements from noise correlation: Stability and detection of instrumental time-shifts. *Geophys. J. Int.* 171, 223–230. doi:10.1111/j.1365-246X.2007.03492.x

Su, J., Yang, W., Li, X., Wang, W., Yang, J., and Chen, Y. (2022). Co-seismic velocity changes with Yunnan Yangbi Ms6.4 earthquake measured by airgun source. *Chin. J. Geophys.* 65, 649–662. (in Chinese with English abstract). doi:10.6038/cjg2022P0636

Vidale, J. E., and Li, Y.-G. (2003). Damage to the shallow Landers fault from the nearby Hector Mine earthquake. *Nature* 421, 524–526. doi:10.1038/nature01354

Wang, B., Zhu, P., Chen, Y., Niu, F., and Wang, B. (2008). Continuous subsurface velocity measurement with coda wave interferometry. *J. Geophys. Res. Solid Earth* 113, B12313. doi:10.1029/2007JB005023

Wegler, U., Nakahara, H., Sens-Schönfelder, C., Korn, M., and Shiomi, K. (2009). Sudden drop of seismic velocity after the 2004M_w6.6 mid-Niigata earthquake, Japan, observed with Passive Image Interferometry. *J. Geophys. Res. Solid Earth* 114, B06305. doi:10.1029/2008JB005869

Yuan, C., Bryan, J., and Denolle, M. (2021). Numerical comparison of time-frequency- and wavelet-domain methods for coda wave interferometry. *Geophys. J. Int.* 226, 828–846. doi:10.1093/gji/ggab140

Zhan, Z., Tsai, V. C., and Clayton, R. W. (2013). Spurious velocity changes caused by temporal variations in ambient noise frequency content. *Geophys. J. Int.* 194, 1574–1581. doi:10.1093/gji/ggt170

Zhang, B., Li, X., Rong, M., Yu, Y., Wang, Y., and Wang, J. (2021). Analysis of strong ground motion characteristics and earthquake damage for the Yangbi Ms6.4 earthquake, Yunnan. *Seismol. Geol.* 43, 1127–1139. (in Chinese with English abstract). doi:10.3969/j.issn.0253-4967.2021.05.006

Zhou, H., Li, Y., and Chang, Y. (2021). Simulation and analysis of spatial distribution characteristics of strong ground motions by the 2021 Yangbi, Yunnan Province Ms6.4 earthquake. *Chin. J. Geophys.* 64, 4526–4537. (in Chinese with English abstract). doi:10.6038/cjg2021P0421

Zhu, G., Yang, H., Tan, Y. J., Jin, M., Li, X., and Yang, W. (2022). The cascading foreshock sequence of the Ms 6.4 Yangbi earthquake in Yunnan, China. *Earth Planet. Sci. Lett.* 591, 117594. doi:10.1016/j.epsl.2022.117594

frontiers | Frontiers in Earth Science

TYPE Methods
PUBLISHED 05 January 2023
DOI 10.3389/feart.2022.1027216

OPEN ACCESS

EDITED BY
Lei Li,
Central South University, China

REVIEWED BY
Hongliang Zhang,
China National Offshore Oil Corporation, China
Xiao Tian,
East China University of Technology, China
Xiong Zhang,
East China University of Technology, China

*CORRESPONDENCE
Yuyang Tan,
tanyuyang@ouc.edu.cn

SPECIALTY SECTION
This article was submitted to Solid Earth Geophysics, a section of the journal Frontiers in Earth Science

RECEIVED 24 August 2022
ACCEPTED 15 September 2022
PUBLISHED 05 January 2023

CITATION
Yu Z, Huang D, Tan Y and He C (2023), Receiver orientation and event back-azimuth estimation for downhole microseismic monitoring using a probabilistic method based on P-wave polarization.
Front. Earth Sci. 10:1027216.
doi: 10.3389/feart.2022.1027216

Receiver orientation and event back-azimuth estimation for downhole microseismic monitoring using a probabilistic method based on P-wave polarization

Zhichao Yu[1], Dian Huang[1], Yuyang Tan[2]* and Chuan He[3]

[1]National Supercomputing Center in Shenzhen, Shenzhen, China, [2]Frontiers Science Center for Deep Ocean Multispheres and Earth System, Key Lab of Submarine Geosciences and Prospecting Techniques MOE, College of Marine Geosciences, Ocean University of China, Qingdao, China, [3]School of Earth and Space Sciences, Peking University, Beijing, China

Microseismic event back-azimuth is an indispensable parameter for source localization in downhole microseismic monitoring, and the accurate orientation of horizontal components of downhole seismic receivers is vital for reliably determining the event back-azimuth. Variation in the monitoring data quality may jeopardize the accuracy of receiver orientation which will further affect the event back-azimuth estimation. To mitigate this issue, we proposed a new probabilistic method based on P-wave polarization analysis for receiver orientation and event back-azimuth estimation. The algorithm constructs the von Mises distribution function using the polarization angle and corresponding rectilinearity of the P-wave, then determines the target angle using the maximum of the probability function. The receiver having the highest rectilinearity from the active-source event is used to quantify a reliable absolute orientation angle, and the relative orientation angles are calculated by the probability distributions based on the measurement angle differences and the associated averages of rectilinearity from all events. After receiver orientation, the P-wave polarization angles with different rectilinearity values are applied to construct the probability distribution functions to estimate the event back-azimuths. By using high-quality events and multi-receiver recordings, our methodology can greatly reduce the unintentional error in receiver orientation and increase event back-azimuth accuracy. We investigate the feasibility and reliability of the proposed method using both synthetic and field data. The synthetic data results demonstrate that, compared to the conventional methods, the proposed method can minimize the variance of the receiver orientation angle and back-azimuth estimation. The weighted standard deviation analysis demonstrates that the proposed method can reduce the orientation error and improve the event back-azimuth accuracy in the field dataset.

KEYWORDS

downhole microseismic monitoring, receiver orientation, event back-azimuth estimation, probability distribution, polarization analysis

Introduction

Microseismic monitoring technique is an efficient tool for evaluating the hydraulic fracture stimulation of unconventional reservoirs through recording and analyzing seismic signals caused by rock ruptures and/or fault reactivation (Maxwell, 2014; Grechka and Heigl, 2017; Li et al., 2019; Atkinson et al., 2020; Schultz et al., 2020). Downhole array is one of the common observatory systems for microseismic monitoring. It can provide higher quality data than surface/subsurface arrays due to its proximity to the fractured zone (Maxwell et al., 2010, 2012; Drew et al., 2012; Meng et al., 2018). For downhole microseismic monitoring, the determination of microseismic event back-azimuth is an important step in the data processing (Maxwell, 2014; Akram, 2020), and the accuracy of event back-azimuth has a significant impact on subsequent source location and fracture interpretation (Cipolla et al., 2011). Due to the influence of azimuth uncertainties, there is always error in the microseismic source location. Thus, it is critical to obtain accurate event back-azimuths to reduce the location errors to the utmost extent.

Three-component (3-C) geophones are normally placed in the vertical or deviated wells to record microseismic signals in mutually orthogonal directions. Because of rotation of the wireline during deployment, the orientation of the horizontal components of the receivers is unknown and usually random, which requires a receiver orientation correction approach to adjust them to the designated direction (for example, along the alignment between the calibration shot and monitoring well). By assuming that the polarization direction of the P-wave of the microseismic event coincides with its propagation direction, receiver orientation can be accomplished by performing polarization analysis using available calibration shots (e.g., perforation shots, string shots, ball-drop events, or vibroseis sources at the surface) to derive P-wave propagation direction, which can then be utilized to

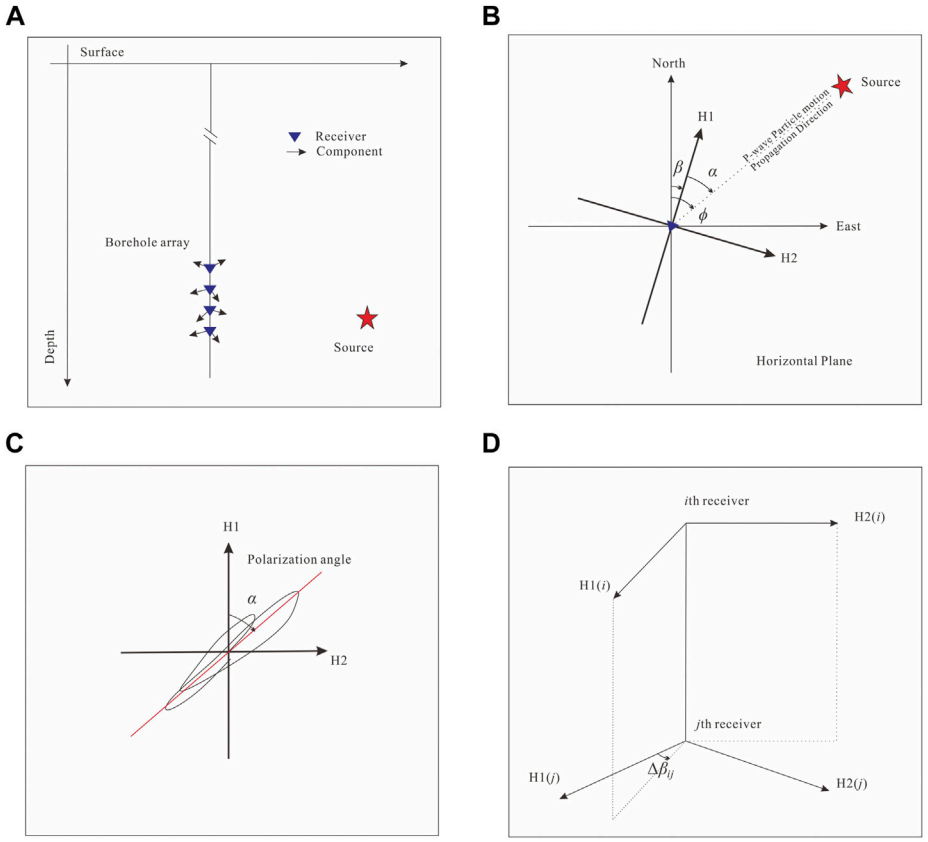

FIGURE 1
(A) Sketch of a vertical borehole with a linear array of receivers. **(B)** Illustration of the relationship among three angles: the event back-azimuth, the receiver orientation angle, and the polarization angle of the P-wave. **(C)** Schematic hodogram of particle motion. **(D)** Illustration of the relative angle between receivers.

TABLE 1 Symbols representing the angles.

Symbol	Definition	Detail description
ϕ	Event back-azimuth	1) ϕ_A and ϕ_E represent the back-azimuths of active-source event and microseismic event, respectively 2) $\phi_i(k)$represent the calculated potential back-azimuth on the ith receiver of the kth event 3) $\phi'(k)$ represent the calculated back-azimuth of the kth event
α	P-wave polarization angle	1) α_A represents the P-wave polarization angle of active-source event 2) $\alpha_i(k)$ represent the P-wave polarization angle on the ith receiver of the kth event
β	Receiver orientation angle	1) β_i represents the receiver orientation angle on the ith receiver. 2) β_i'represents the receiver orientation angle on the ith receiver by the proposed method
$\Delta\beta_{ij}$	Relative orientation angle between ith and jth receivers	1)$\Delta\beta_{ij}(k)$ represents the angle differences of the kth event 2) $\Delta\beta_{ij}'$represents the calculated relative orientation angle between ith and jth receivers

rotate the horizontal components to the correct direction (Nakamura et al., 1987; Menanno et al., 2013; Lagos and Velis, 2019; Huo et al., 2021). In addition to P-waves, Rayleigh waves have also been employed for receiver orientation (Niu and Li, 2011; Zha et al., 2013; Wang et al., 2016; Xu et al., 2018; Ensing and van Wijk, 2019; Takagi et al., 2019; Son et al., 2022; Yang et al., 2022). Receiver misorientations are defined as the deviations between the empirical and true back azimuths, and the relative-angle method by measuring the relative azimuth angle between receiver pairs is another strategy (Zeng and McMechan, 2006; Grigoli et al., 2012; Zhu et al., 2018; Ojo et al., 2019; Huo et al., 2021). The microseismic event back-azimuth can be obtained through statistical analysis of the P-wave polarization angles after receiver orientation (Chen et al., 2017; Meng et al., 2018; Tan et al., 2018). When the data quality of the P-wave is poor, the S-wave can also be applied for event azimuth estimation (Eisner et al., 2009; Yuan and Li, 2017).

Affected by the focal mechanism and background noise, the signal-to-noise ratio (S/N) of microseismic signals on different receivers is usually varied, which can also be reflected by the rectilinearity of the P-wave (Drew et al., 2008). Conventional methods of obtaining the receiver orientation angle from a single or several active-source events may contain unintended errors, which can be further transported to the event azimuth estimation. Additionally, after receiver orientation, the event back-azimuth estimation is also muddled because of the differences in the recording data quality among receivers. Apparently, more high-quality data may minimize the uncertainties in the azimuth results and the systematic deviation produced by a single dataset. For example, Huo et al. (2021) incorporate high-S/N microseismic events with unknown back-azimuths into the receiver orientation process to improve the accuracy of the relative orientation angles among all receivers.

In this study, by calculating the relative rotation angles between receivers, we develop a new receiver orientation and event back-azimuth estimation method for reducing the orientation error and enhancing the event back-azimuth accuracy. Firstly, we introduce the relationship between receiver orientation and event azimuth angles. Next, we calculate the probability density function (i.e., von Mises distribution function) using the polarization angle and corresponding rectilinearity of the P-wave to determine the relative orientation angles and then the event back-azimuths. Finally, we demonstrate the efficiency of the proposed method through synthetic and field data tests.

Methods

In this section, we first introduce the relationship among the event back-azimuth, the receiver orientation angle, and the polarization angle of the P-wave, as well as the definition of the relative orientation angle between receivers and potential back-azimuth angles on multi-level receivers. Then, we construct the probability density functions by using the polarization angle and rectilinearity of the P-wave to determine the relative orientation angle and event back-azimuth. Finally, we establish the processing workflow for receiver orientation and event back-azimuth estimation.

Receiver orientation and event back-azimuth

If the monitoring well is vertical (Figure 1A), we can assume that the horizontal components of the receivers are in a plane parallel to the surface. As shown in Figure 1B, we also assume that the 'North' component is misorientated by degrees defined clockwise from north. Table 1 summarizes the meaning of the adopted symbols in Figure 1 and following text.

For an incoming P-wave of an active-source event with a known location, the event back-azimuth ϕ_A can be determined directly using the horizontal coordinates of the source and receiver. Once the P-wave polarization angle α_A is obtained (Figure 1C), we can determine the receiver orientation angle β by

$$\beta = \phi_A - \alpha_A. \tag{1}$$

On the other hand, for a microseismic event whose location is unknown, we can calculate the event back-azimuth ϕ_E by using the estimated receiver orientation angle β and the P-wave polarization angle α_E,

$$\phi_E = \alpha_E + \beta. \tag{2}$$

In general, the receiver orientation angles at different receivers are determined individually based on P-wave polarization analysis of active-source events. However, the data S/N may vary on different receivers and events and this will introduce additional errors in the estimation of the receiver orientation angles. This kind of error is difficult to avoid when only a single or a small number of active-source events are available.

In fact, because the back-azimuth angles on different receivers in a vertical well are the same for every event (Figure 1D), the relative orientation angle between any two receivers is defined as

$$\Delta\beta_{ij}(k) = \alpha_j(k) - \alpha_i(k). \tag{3}$$

where $\Delta\beta_{ij}(k)$ is the relative orientation angle between the ith and jth receivers in kth event, $\alpha_i(k)$ and $\alpha_j(k)$are the P-wave polarization angle on ith and jth receivers of kth event, respectively. In real situations, the calculated relative angles are never the same due to the difference in data quality between events, but the relative angles from all events are focused on the true angles.

If a valid relative orientation angle can be acquired, a reliable absolute orientation angle and the relative angles can be used to drive the receiver angle, which is expressed as

$$\beta_i' = \beta_l + \Delta\beta_{il}', \tag{4}$$

where l denotes the reference receiver with the highest rectilinearity or S/N of P-wave, $\Delta\beta_{il}'$ is the obtained relative orientation angle between the ith and the reference receivers. The relative orientation angle can be obtained using the highest-quality event in the case of a small number of events, or can be obtained by statistical analysis of all events in the case of plenty events.

Once the receiver orientation angle β_i' is determined, the potential back-azimuths on different receivers for a microseismic event can be calculated as follow,

$$\phi_i(k) = \alpha_i(k) + \beta_i'. \tag{5}$$

where $\phi_i(k)$ is the potential back-azimuth (relative to the north) on the ith receiver of the kth microseismic event, $\alpha_i(k)$ and $\alpha_j(k)$ are the polarization angle on ith and jth receiver of kth event, respectively. For multiple receivers, the final event back-azimuth can be determined by the averaging $\phi_i(k)$ or choosing the one with the highest rectilinearity value.

Measurement of the P-wave polarization parameters

The polarization parameters of P-wave can be determined by calculating the eigenvalues and eigenvectors of a covariance matrix constructed using windowed waveforms around the P-wave arrival. The covariance matrix **C** for the two horizontal components is written as

$$\mathbf{C} = \frac{1}{N}\begin{bmatrix} n^T n & n^T e \\ e^T n & e^T e \end{bmatrix}. \tag{6}$$

We solve the eigenproblem and obtain the eigenvalues λ_1 and λ_2 ($\lambda_1 > \lambda_2$) and corresponding eigenvectors (u_1, u_2), in which $u_1 = [u_x, u_y]$ is the eigenvector associated with λ_1. According to Flinn (1965), the rectilinearity L and the polarization angle α for two component data can be calculated using the following equations,

$$L = 1 - \frac{\lambda_2}{\lambda_1}. \tag{7}$$

$$\alpha = \tan^{-1}\left(\frac{u_y}{u_x}\right). \tag{8}$$

The value of L lies in the range of 0–1, where L=0 indicates circular polarization trajectory and L =1 indicates linear trajectory. L characterize the linearity of the particle motion and can also affect the reliability of α.

Von Mises distribution

The von Mises distribution is a circular normal distribution and has been widely used to model circular data (Lark et al., 2014). It consists of two parameters which are the mean direction and concentration parameters. When the concentration parameter is zero, the distribution represents a uniform distribution over the unit circle (Lark et al., 2014). The expression of the von Mises distribution is

$$f(\theta; \mu, \kappa) = \frac{e^{\kappa\cos(\theta-\mu)}}{2\pi I_0(\kappa)}. \tag{9}$$

where $I_0(\kappa)$ is the modified Bessel function of the first kind and order zero, which is defined as

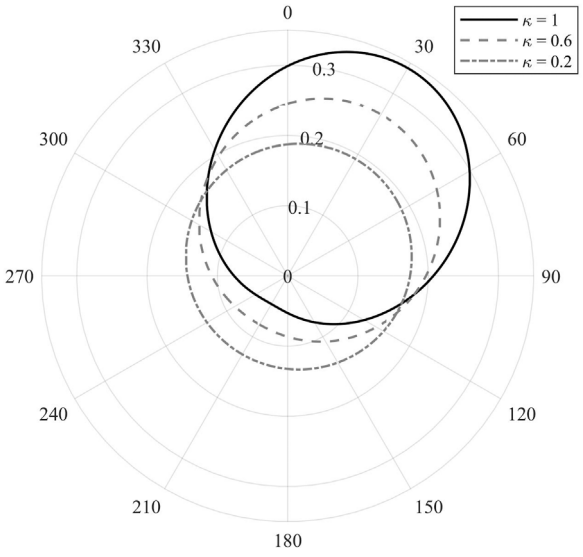

FIGURE 2
Probability density function $f(\theta)$ of a von Mises distribution with μ= 30° and three different values for κ.

$$I_0(\kappa) = \frac{1}{2\pi}\int_0^{2\pi} e^{\kappa\cos\theta}d\theta. \tag{10}$$

where μ is the mean direction and κ is the concentration parameter (Mardia and Jupp, 2000). The probability of deviations is the same on either side of the mean direction and decreases with increasing distance from the mean direction.

Figure 2 displays the examples of the von Mises distribution functions computed using μ=30° and different concentration parameters. We can see that as κ decreases, the shape of the distribution function becomes circular. In this study, we calculate the von Mises distribution function using L and α.

In practice, this von Mises distribution function is computed for each event and receiver, and then summed up to formulate one global function.

$$F(\theta) = \sum_{m=1}^{M} f_m(\theta). \tag{11}$$

where, M is the number of angles involved in the calculation. The maximum of this global function is taken as the optimal estimate of the target angle.

The proposed method

According to Eq. 3, we utilize all recorded microseismic events to compute relative orientation angles between receiver pairs. After rotating by these relative angles, all receivers will be orientated in the same direction with respect to an absolute azimuth. This absolute azimuth can be obtained by comparing the polarization angle of a reference receiver with the geometry angle of the active-source event. After removing the influence of receiver misorientation, we can determine all microseismic event back-azimuths using Eq. 5. We construct the von Mises distribution functions to determine the relative orientation angles by using all events and then the event back-azimuths by using multi-level recordings. The proposed method for receiver orientation and event back-azimuth estimation can be described as follow:

1) The polarization angle $\alpha_i(k)$ and the rectilinearity $L_i(k)$ are calculated using the P-wave waveforms on different receivers for all microseismic events.
2) Preliminary orientation angles β_i (i is the receiver number) are obtained from the active-source event, and the receiver having the highest rectilinearity in the active-source event is used to determine a reliable absolute orientation angle β_l.
3) The relative orientation angles $\Delta\beta_{il}$ are determined using the von Mises distribution functions constructed based on the polarization angle difference $\mu = \alpha_i(k) - \alpha_l(k)$ and the average rectilinearity $\kappa = [L_i(k) + L_l(k)]/2$ of all events recorded on ith and lth receivers. It should be noted that during the calculation of the relative orientation angles in all events, the relative orientation angles obtained from active-source event in step 2 can be used to resolve the 180° ambiguity.
4) After receiver orientation (Eq. 5), the potential angles $\mu = \phi_i(k)$with different P-wave rectilinearity $\kappa = L_i(k)$ are applied to construct the von Mises distribution functions to estimate the kth event back-azimuth $\phi'(k)$. It should be noted that the microseismic event is generally closer to fracturing stage can be used to resolve the 180°ambiguity in the event back-azimuth.

Numerical examples

In this section, we utilize synthetic data test to demonstrate the reliability of the proposed method. A 30 Hz Ricker wavelet is used as the synthetic source wavelet. Random waveform amplitudes and Gaussian noises are applied to generate the synthetic recordings with varying S/N. We ignore the arrival time differences (i.e., moveouts) at different receivers in the simulation because it has a very limited effect on determining the event back-azimuth. The results of the proposed method are compared with those of two other commonly used approaches, which determine the receiver orientation angle and event back-azimuth using the average value of the calculated angles and the angle corresponding to the maximum rectilinearity, respectively.

The first synthetic data example illustrates the accuracy in calculating the relative receiver orientation angle using the

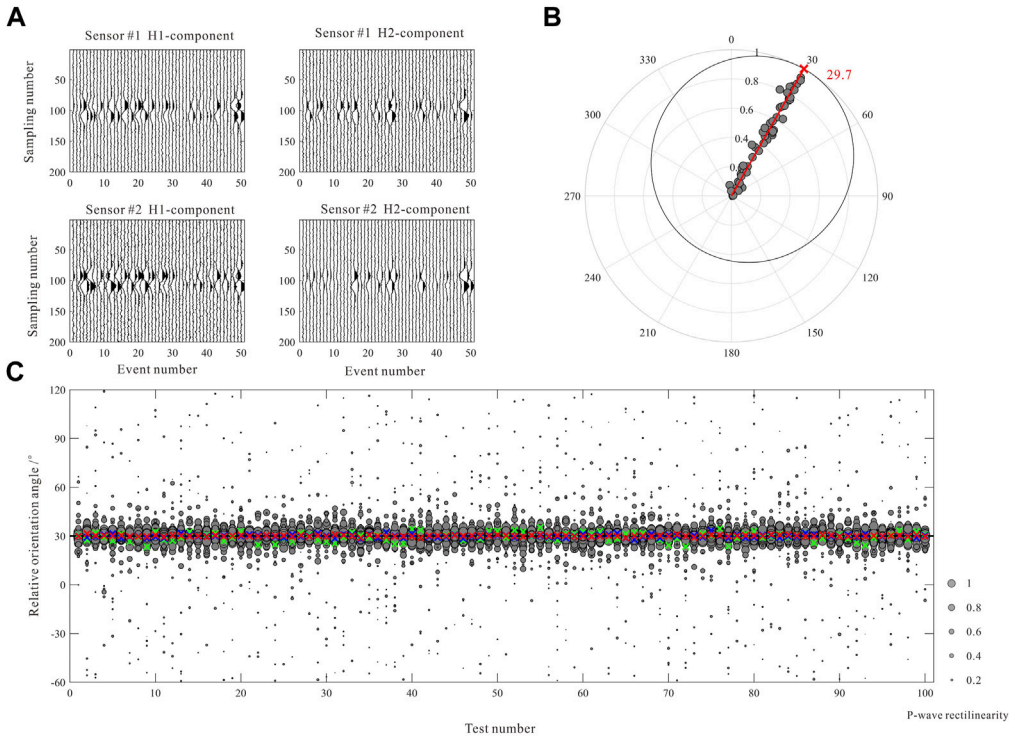

FIGURE 3
Comparisons of the relative orientation angle calculated by the proposed method and the conventional approaches. **(A)** Waveforms of the P-wave of 50 microseismic events recorded by 2 receivers. **(B)** The distribution of the polarization angle differences and the corresponding rectilinearity (the gray dots), and the normalized global probability distribution function (the black curve). The red cross indicates the angle corresponding to the maximum probability density. **(C)** The results of 100 groups of synthetic recordings with different random noises. The red, green, and blue crosses represent the results of the proposed method, the average values of the orientation angles at different receivers, and the angles corresponding to the receiver having the maximum rectilinearity, respectively. The size of the dots denotes the P-wave rectilinearity.

probability distribution function. 50 microseismic events at different locations are used to generate synthetic recordings at two receivers, and a predefined rotation angle (i.e., 30°) is adopted to rotate the synthetic waveforms on the second receiver to simulate the actual situation of different receiver orientation directions in a vertical well. Figure 3A shows the waveforms of two horizontal components of the P wave from the 50 synthetic microseismic events. We calculate the polarization angle and the rectilinearity of the P-wave of each event (i.e., each trace in Figure 3A) using Eqs 7, 8. The polarization angle differences between two receivers and the average rectilinearity values are applied to construct von Mises distribution functions, which are then summed up to formulate one global function (Eq. 11). Figure 3B shows the distribution of the angle differences and the rectilinearity values of these 50 events (the gray dots), and the polar radius coordinate denotes the average rectilinearity of the P-wave. We calculate the von Mises distribution functions of each event and obtained the normalized probability distribution function (the black curve). Note that the range of the probability density is 0–1. In this case, the angle corresponding to the maximum (equal to 1, denoted by the red cross) of the global function is 29.7°, which is only 0.3° away from the true value. Without loss of generality, the above test is repeated 100 times using synthetic data with different S/N (i.e., 0–40 dB) to verify the stability of the proposed method. We maintained the source locations and the predefined rotation angle consistent in the simulations. Figure 3C shows the results of the proposed method (the red crosses), the average relative orientation angles at different receivers (the green crosses), and the angles corresponding to the receivers having the maximum rectilinearity (the blue crosses). The standard deviations of the results of the three approaches are 0.42°, 2.65°, and 0.96°, respectively. This clearly indicates that our method can obtain more accurate relative orientation angles.

The second synthetic data example illustrates the accuracy in determining the event back-azimuth by the probability distribution function. Note that different from Figure 3A, Figure 4A shows the two horizontal components of the P-wave of one synthetic microseismic event recorded on ten receivers. The true back-azimuth of this event is set to 45°. Figure 4B shows the normalized probability distribution of the event back-azimuth. In this case, the angle corresponding to the

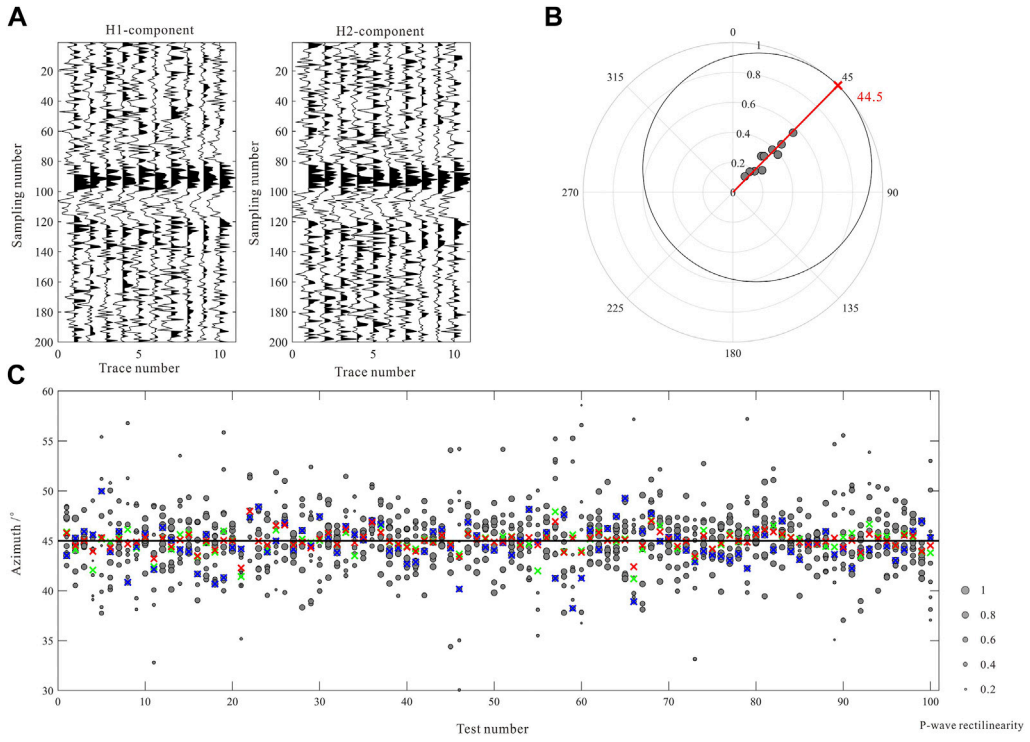

FIGURE 4
Comparisons of the event back-azimuth estimated by the proposed method and the conventional approaches. **(A)** Waveforms of the P-wave of one microseismic event recorded by 10 receivers. **(B)** The distribution of the polarization angles and corresponding rectilinearity (the gray dots), and the normalized global probability distribution function (the black curve). The red cross indicates the angle corresponding to the maximum probability density. **(C)** The result of 100 groups of synthetic event recordings with different random noises. The red, green, and blue crosses represent the results of the proposed method, the average values of the angles, and the angles corresponding to the maximum rectilinearity, respectively. The size of the dots reflects the P-wave rectilinearity.

maximum (equal to 1, denoted by the red cross) of the global function is 44.5°, which is 0.5° away from the true value. Similar to the first synthetic test, we also repeat this test 100 times and the results are shown in Figure 4C. It is shown that the results of the proposed method (the red crosses) are more accurate than the average values of the azimuths determined for all receivers (the green crosses) and the angles corresponding to the maximum rectilinearity (the blue crosses). The standard deviations of these three sets of results are 0.83°, 1.04°, and 1.59°, respectively, indicating that our method can also obtain more accurate event back-azimuth.

Field data application

In this section, we demonstrate the performance of the proposed method on real dataset. The real dataset was acquired from a fractured tight reservoir in the Shengli oil field of eastern China. A downhole array composed of 15 levels of 3-C geophones is deployed in a vertical monitoring well at depths from 2443 to 2673 m. The duration of the monitoring data is more than 27 h and the sampling interval is 0.5 ms. A perforation shot is fired in a third well located approximately 920 m northwest of the monitoring well before the hydraulic fracturing stimulation begins. Figure 5 shows the survey geometry of the real case. A total of 521 microseismic events are detected in the monitoring data, including 11 ball-drop events with known locations (Figure 5C). The P-wave arrival times of the microseismic events are determined using the joint STA/LTA-polarization-AIC method (Tan and He, 2016), and then refined by the global optimization method based on iterative cross-correlation (Leng et al., 2022).

Normally, all active-source events with known locations (e.g., the perforation shot or ball-drop event) should be utilized for receiver orientation. However, as shown in Figure 6, there are clearly discrepancies in the quality of real data. To show how data quality affects receiver orientation results, we perform receiver orientation using two independent events with known locations, which are the perforation shot and the first ball-drop event (Figure 5). Figure 7 shows P-wave waveforms after moveout correction of the perforation shot event and a microseismic

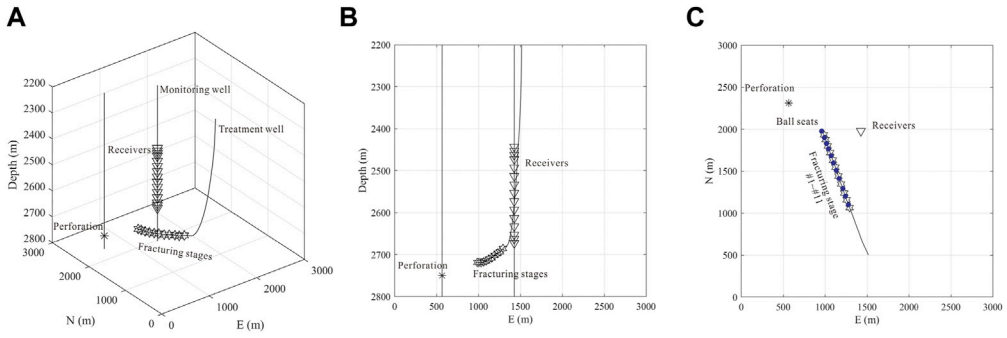

FIGURE 5
Survey geometry of the real data case. **(A)** 3D view; **(B)** depth view; **(C)** planar view. The triangles represent the receivers. The stars represent the fracturing stages. The asterisk represents the perforation shot. The blue circles represent the ball-drop locations.

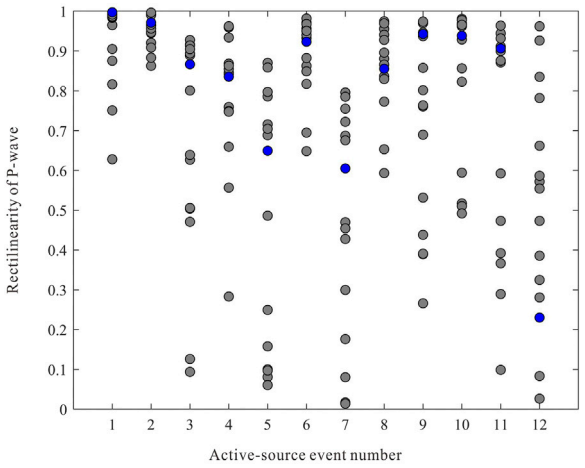

FIGURE 6
P-wave rectilinearity on different receivers from the 12 active-source events. The first event is the perforation shot and the others are ball-drop events. The blue circles represent the 6th receiver.

event, while Figure 8 shows the hodograms of two horizontal components of these events, as well as the calculated polarization angles and rectilinearity values at all receivers.

The receiver orientation results obtained from above two events are listed in Table 2. Because the P-wave of perforation shots on the 6th receiver in Figure 6 generally has the maximum rectilinearity, we choose the 6th receiver as the reference to calculate the relative orientation angles of other receivers. The relative angle differences and the average rectilinearity values from all recorded events are then utilized to construct the von Mises distribution functions and formulate the global functions. The relative orientation angles obtained from the perforation shot are used to correct the calculation of the relative orientation angles in all events for resolving the 180° ambiguity. Figure 9 depicts the polar diagrams of the relative angle differences and the average rectilinearity values from all events at those receivers. The relative receiver orientation angles can be obtained by calculating the maximum values of the probability density functions (denoted by the red crosses in Figure 9).

The results of the proposed method are compared with those of the conventional methods which only use one active-source event, as shown in Table 2. Conventional methods applied to two independent active source events provide various results, reflecting that the receiver orientation is greatly affected by the quality of event recordings. From Table 2, it can be seen that the maximum difference between the results obtained by the proposed method and the conventional method using the perforation shot is 12.2°, which can influence the accuracy of the estimated event back-azimuth. Thus, we adopt the event back-azimuths on different receivers after receiver orientation to analyze the accuracy of the receiver orientation results. Figure 10 depicts the angles on all receivers acquired by the three approaches using one ball-drop event and one microseismic event as examples. The figure demonstrates that, when compared with the conventional methods, the angles obtained by the proposed method are more concentrated, suggesting that the proposed method can more reliably determine the receiver orientations and hence the event back-azimuth.

The azimuths of the microseismic events can be calculated by using the von Mises distribution functions based on the angles after receiver orientation and corresponding rectilinearities, as shown in Figure 10. We calculate the back-azimuths of all 521 events using the proposed method, and the results are shown in Figure 11A. We adopt a principle that the event is closer to the perforation to resolve the 180°ambiguity in the event back-azimuth. The variation of the event azimuth reflects the sequencing of hydraulic fracturing stages in the horizontal well, which is overall consistent with the azimuth trend of the ball-drop events. Figure 11B shows the distribution of the highest rectilinearity value of the events. The azimuth distribution of

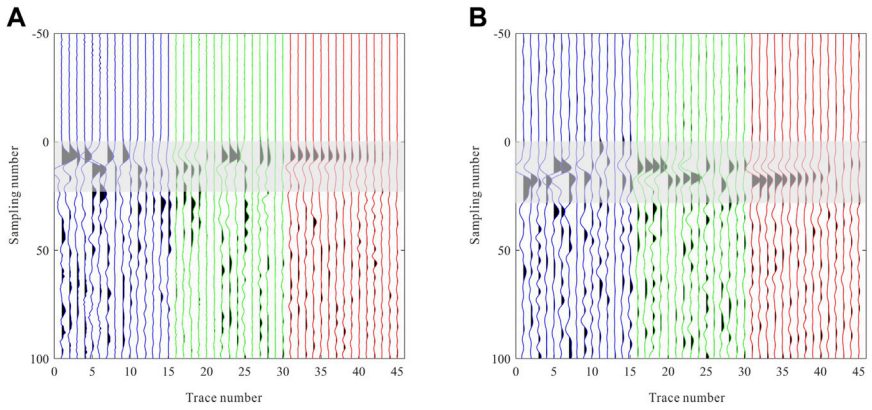

FIGURE 7
P wave after moveout correction. **(A)** P wave of the perforation shot event. **(B)** P wave of a microseismic event. Blue, green and red lines represent H1-, H2-, and vertical components respectively.

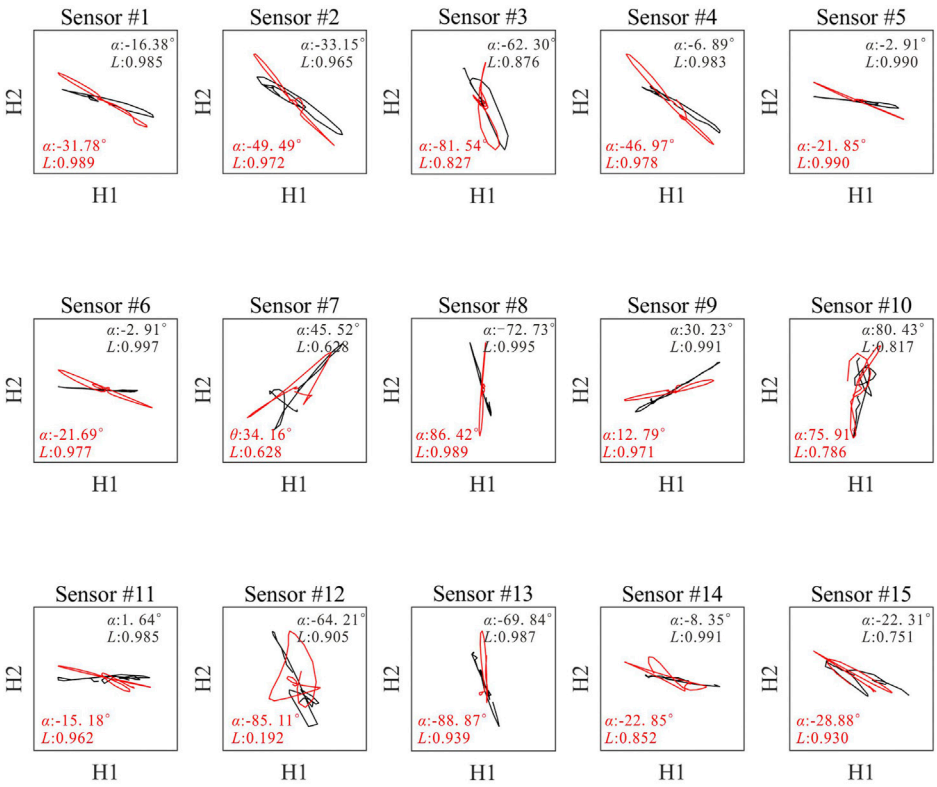

FIGURE 8
Hodograms of two horizontal components from two events shown in Figure 7. Black and red lines represent the perforation shot event and a microseismic event, respectively.

events from stages 3–7 (outlined by the blue box in Figure 11A) diverges, this may be due to the event data quality, the generation of the induced events around the former fracturing stages, or the extension of the fractures to larger distances. Microseismic events are located using the P- and S-wave arrival times and the velocity model between treatment and monitoring wells, and then the

TABLE 2 Comparison between orientation angles obtained with the conventional methods and our proposed method.

Receiver number	Conventional methods (°)		Method 3***(°)	Result differences (°)		
	Method 1*	Method 2**		Methods 1&2	Methods 3&1	Methods 3&2
1	143.61	348.59	342.88	−4.98	−0.73	−5.71
2	326.85	338.51	325.29	−4.98	−0.73	−5.71
3	297.63	301.39	305.07	−11.66	−1.56	−13.22
4	329.41	333.91	329.76	−3.76	7.43	3.68
5	173.14	180.08	174.65	−4.50	0.35	−4.15
6	177.07	184.32	177.07	−6.95	1.52	−5.43
7	45.10	43.58	42.58	−7.25	0.00	−7.25
8	106.27	119.47	104.35	1.52	−2.51	−0.99
9	30.23	25.48	30.09	−13.20	−1.92	−15.12
10	259.35	264.52	271.55	4.75	−0.14	4.61
11	181.76	180.46	181.42	−5.17	12.20	7.03
12	115.95	127.61	111.11	1.30	−0.34	0.96
13	109.97	114.08	110.37	−11.66	−4.84	−16.50
14	171.44	178.07	171.16	−4.11	0.40	−3.71
15	153.31	163.71	162.50	−6.63	−0.28	−6.92

*Method 1: receiver orientation by the perforation shot.
**Method 2: receiver orientation by the 1st ball-drop event.
***Method 3: the proposed method.

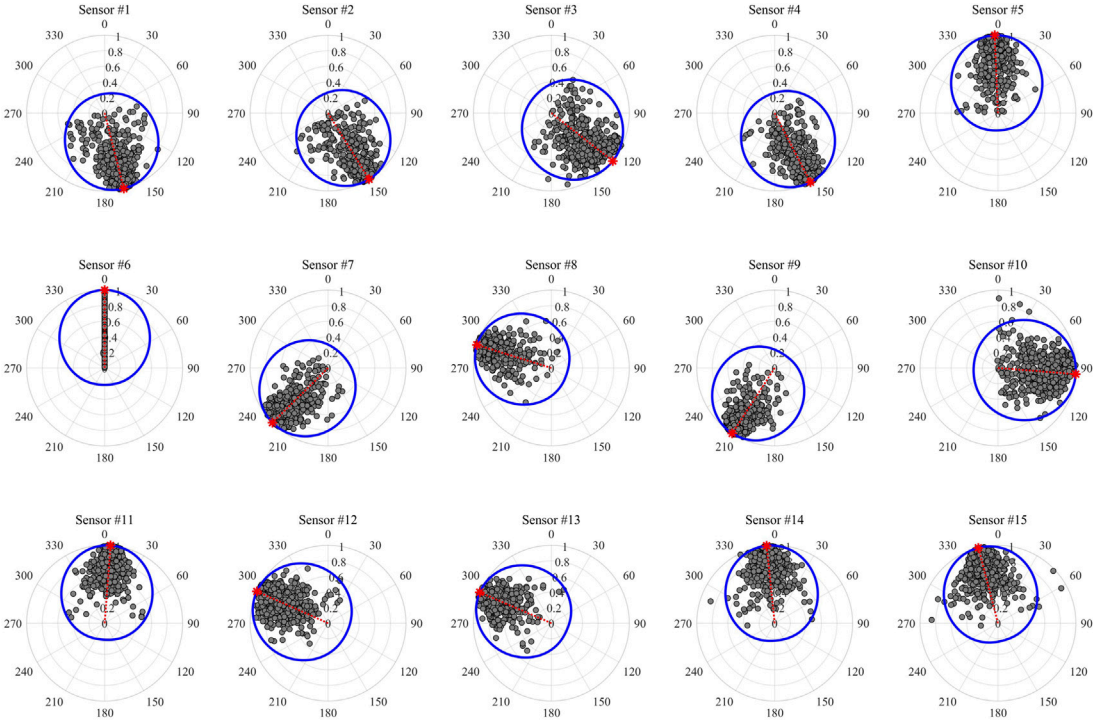

FIGURE 9
Diagram of relative orientation angle calculation. The grey dots represent the distribution of the polarization angle differences and the corresponding rectilinearity average, and the blue curve represents the normalized global probability distribution function. The red cross indicates the angle corresponding to the maximum probability density. The radius coordinate denotes both rectilinearity average of the P-waves and the normalized probability density.

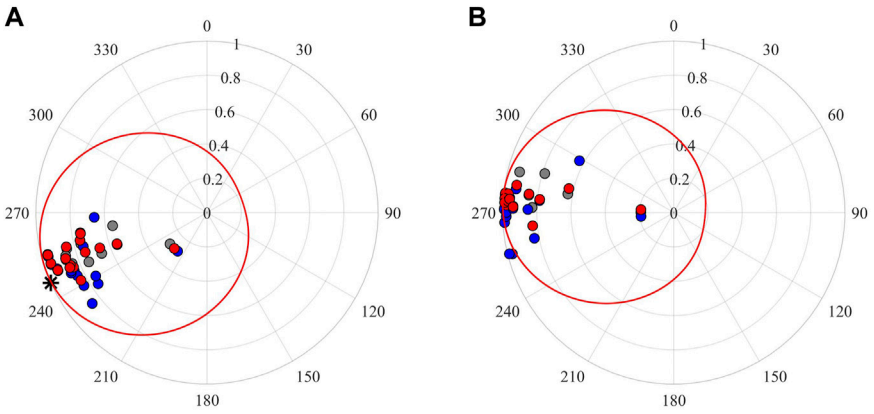

FIGURE 10
Distributions of the event potential back-azimuths on the 15 receivers by three approaches. **(A)** The back-azimuths of the 3rd ball-drop event. The black asterisk in Figure 10A represents the true ball-drop event azimuth. **(B)** The back-azimuths of the microseismic event (as shown in Figure 7A). The gray, blue, and red circles represent the results of those three methods in Table 2. The radius coordinate denotes the rectilinearity of the P-wave. The red curve represents the normalized global probability distribution function by using the back-azimuths from the proposed method.

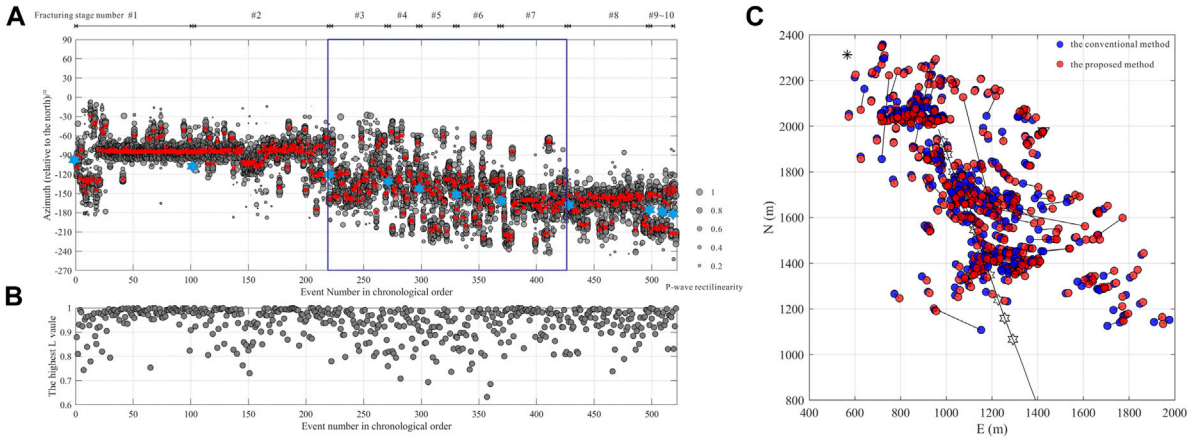

FIGURE 11
(A) Distributions of the 521 microseismic event back-azimuths. The gray dots represent the distribution of the potential back-azimuth angles after receiver orientation. The size of the dots reflects the P-wave rectilinearity. Red crosses represent the event back-azimuths calculated by the proposed method. The blue asterisks represent the ball-drop events. **(B)** Distributions of the P-wave rectilinearity average values of the 521 microseismic events. **(C)** Comparison of the source locations of the microseismic events by the conventional method and the proposed method.

hypocentral parameters in the Cartesian coordinate system are calculated using the event back-azimuths. We employ the comparison of source locations by the conventional method and the proposed method to introduce the effect of the back-azimuth error, as shown in Figure 11C. In the conventional method, the perforation shot event is used to correct the receiver orientation, and the average of the P-wave polarization angle after receiver orientation is obtained as the event back-azimuth.

We adopt a weighted standard deviation measurement of the azimuth results to illustrate the improvement of the proposed method for receiver orientation and event back-azimuth estimation. The weighted standard deviation is defined by

$$W(k) = \frac{1}{M}\sum_{i=1}^{M}\left[\left(\phi'(k) - \phi_i(k)\right)L_i(k)\right]. \quad (12)$$

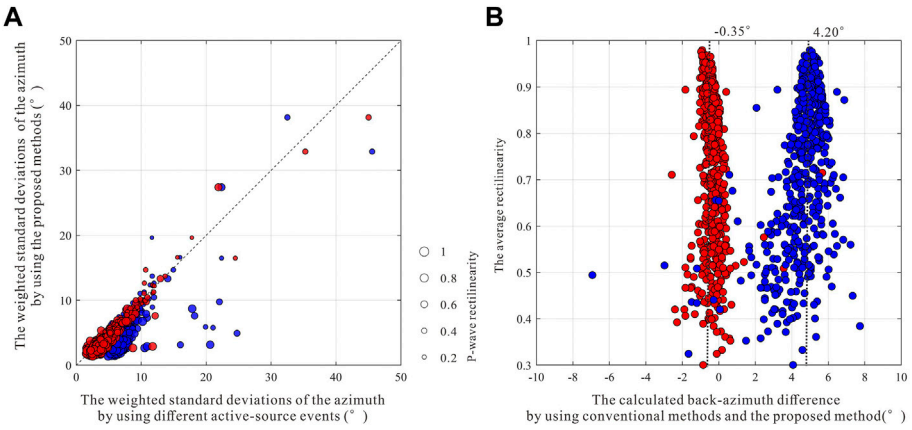

FIGURE 12
Comparisons of the azimuth results after receiver orientation using the conventional methods and the proposed method. **(A)** The weighted standard deviations. The size of the dots reflects the average value of P-wave rectilinearities in each microseismic event. **(B)** The back-azimuth difference. The red and blue circles represent receiver orientation angles calculated by the method 1 and 2 in Table 2, respectively.

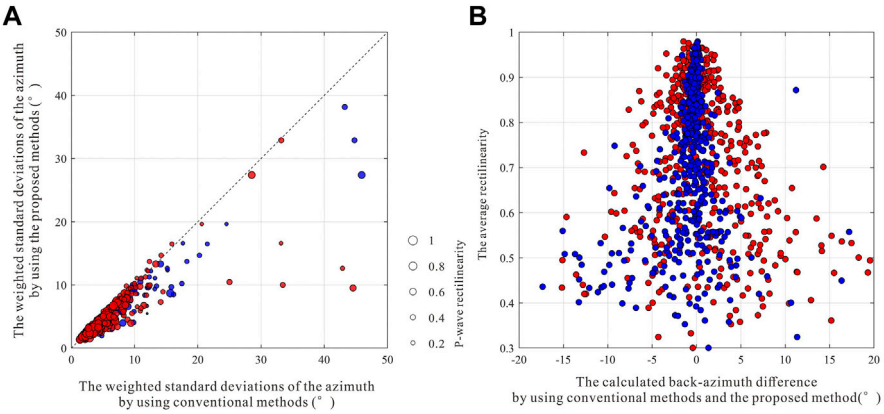

FIGURE 13
Comparisons of the azimuth results using the conventional methods and the proposed method. **(A)** The weighted standard deviations. The size of the dots reflects the average value of P-wave rectilinearities in each microseismic event. **(B)** The back-azimuth difference. The red and blue circles represent the results determined by the average angle and the angle corresponding to the maximum of P-wave rectilinearity, respectively.

where M is the receiver number, and $\phi'(k)$ is the calculated event back-azimuth. $\phi_i(k)$ and $L_i(k)$ are the potential azimuth angle after receiver orientation and the P-wave rectilinearity on the ith receiver, respectively. If W is reduced, the calculated azimuth becomes more dependable.

We firstly discuss the improvement of the proposed method in receiver orientation. The orientation angles acquired by the three methods (listed in Table 2) are used to obtain the potential event back-azimuths on different receivers, and the final event azimuths are also determined using the probability density distribution. The weighted standard deviations are then computed using the final event azimuths, and the comparisons are displayed in Figure 12A. It reveals that the quality of active-source events effects the receiver orientation results, with high-quality active-source event producing more accurate results. Furthermore, even when employing high-quality active source events, receiver orientation may still have unexpected and non-negligible errors on individual receivers, as shown in Figure 12B. When the signal-to-noise ratio of active-source

event is poor, the average azimuth deviation may approach 4.20°, therefore, this error should not be ignored. The weighted standard deviation distribution and the back-azimuth differences indicate that it can reduce the influence of a single active-source event in microseismic event back-azimuth estimation by using events with variable qualities.

We also illustrate the improvement of the proposed method in event back-azimuth estimation. We obtain the event back-azimuths using three strategies, including the average angle, the angle corresponding to the maximum rectilinearity, and the angle corresponding to the maximum value of the probability density in the proposed method. The weighted standard deviations are then computed correspondingly and compared in Figure 13A. The weighted standard deviation distribution indicates that it can reduce the influence of low-quality data in event back-azimuth estimation by integrating the angle information from multi-level receivers. By comparing the azimuth differences produced by the conventional method with the method presented in this study (as shown in Figure 13B), it is shown that using high signal-to-noise ratio recordings can increase back-azimuth accuracy.

Conclusion

In this study, we have developed a new probabilistic method for microseismic receiver orientation and event back-azimuth estimation. The von Mises distribution function, which serves as the probability density function in the new method, is constructed using the polarization angle and rectilinearity of the P-wave and applied in the estimation of the receiver orientation angles and event back-azimuths. The numerical examples have demonstrated that the proposed method has the advantage of minimizing the unintentional error in receiver orientation by employing high-quality events and increasing event back-azimuth accuracy by integrating the azimuths from multi-level receivers. We have also applied the proposed method to the field dataset. The results show that, compared with the conventional methods which generally utilize a single active-source event, our proposed method can increase the accuracy of the receiver orientation angles and microseismic event back-azimuths.

Data availability statement

The raw data supporting the conclusions of this article will be made available by the authors, without undue reservation.

Author contributions

ZY developed the method and wrote the original draft. YT revised the manuscript. All authors participated in designing this research work. All authors approved the final version of the manuscript.

Funding

This work is supported by the Key-Area Research and Development Program of Guangdong Province (Grant No. 2021B0101310002) and Science and Technology Program of Shenzhen Science and Technology Innovation Commission (Grant No. JSGG20201102160200001).

Acknowledgments

We would like to thank SINOPEC Geophysical Company, Shengli Branch for providing us the field data.

Conflict of interest

The authors declare that the research was conducted in the absence of any commercial or financial relationships that could be construed as a potential conflict of interest.

The handling editor LL declared a past co-authorship with the author YT.

Publisher's note

References

Akram, J. (2020). *Understanding downhole microseismic data analysis*. Berlin/Heidelberg, Germany: Springer International Publishing. doi:10.1007/978-3-030-34017-9

Atkinson, G. M., Eaton, D. W., and Igonin, N. (2020). Developments in understanding seismicity triggered by hydraulic fracturing. *Nat. Rev. Earth Environ.* Vol. 1, 264–277. doi:10.1038/s43017-020-0049-7

Chen, Y., Zhang, H., Miao, Y., Zhang, Y., and Liu, Q. (2017). Back azimuth constrained double-difference seismic location and tomography for downhole microseismic monitoring. *Phys. Earth Planet. Inter.* 264, 35–46. doi:10.1016/j.pepi.2016.10.003

Cipolla, C., Maxwell, S., Mack, M., and Downie, R. (2011). "A practical guide to interpreting microseismic measurements," in North American Unconventional Gas

Conference and Exhibition, The Woodlands, Texas, United States, June 2011 (OnePetro). doi:10.3997/2214-4609-pdb.285.spe144067

Drew, J., White, R., and Wolfe, J. (2008). "Microseismic event azimuth estimation: Establishing a relationship between hodogram linearity and uncertainty in event azimuth," in *SEG technical Program expanded abstracts 2008* (Society of Exploration Geophysicists), 1446–1450. doi:10.1190/1.3059186

Drew, J., Primiero, P., Brook, K., Raymer, D., Probert, T., Kim, A., et al. (2012). "Microseismic monitoring field test using surface, shallow grid, and downhole arrays," in *SEG technical Program expanded abstracts 2012* (Society of Exploration Geophysicists), 1–5. doi:10.1190/segam2012-0910.1

Eisner, L., Fischer, T., and Rutledge, J. T. (2009). Determination of S-wave slowness from a linear array of borehole receivers. *Geophys. J. Int.* 176 (1), 31–39. doi:10.1111/j.1365-246X.2008.03939.x

Ensing, J. X., and van Wijk, K. (2019). Estimating the orientation of borehole seismometers from ambient seismic noise. *Bull. Seismol. Soc. Am.* 109 (1), 424–432. doi:10.1785/0120180118

Flinn, E. A. (1965). Signal analysis using rectilinearity and direction of particle motion. *Proceed, IEEE* 53 (12), 1874–1876. doi:10.1109/PROC.1965.4462

Grechka, V. I., and Heigl, W. M. (2017). *Microseismic monitoring*. Tulsa, OK: Society of Exploration Geophysicists, 471. doi:10.1190/1.9781560803485

Grigoli, F., Cesca, S., Dahm, T., and Krieger, L. (2012). A complex linear least-squares method to derive relative and absolute orientations of seismic sensors. *Geophys. J. Int.* 188, 1243–1254. doi:10.1111/j.1365-246X.2011.05316.x

Huo, Y., Zhang, W., Zhang, J., and Yang, H. (2021). Using microseismic events to improve the accuracy of sensor orientation for downhole microseismic monitoring. *Geophys. Prospect.* 69 (6), 1167–1180. doi:10.1111/1365-2478.13099

Lagos, S., and Velis, D. (2019). A simple energy-based strategy for sensor orientation in borehole microseismic monitoring. *J. Geophys. Eng.* 16 (1), 85–91. doi:10.1093/jge/gxy007

Lark, R. M., Clifford, D., and Waters, C. N. (2014). Modelling complex geological circular data with the projected normal distribution and mixtures of von Mises distributions. *Solid Earth.* 5 (2), 631–639. doi:10.5194/se-5-631-2014

Leng, J., Yu, Z., Mao, Z., and He, C. (2022). Optimization and quality assessment of arrival time picking for downhole microseismic events. *Sensors (Basel).* 22 (11), 4065. doi:10.3390/s22114065

Li, L., Tan, J., Wood, D. A., Zhao, Z., Becker, D., Lyu, Q., et al. (2019). A review of the current status of induced seismicity monitoring for hydraulic fracturing in unconventional tight oil and gas reservoirs. *Fuel* 242, 195–210. doi:10.1016/j.fuel.2019.01.026

Mardia, K. V., and Jupp, P. E. (2000). *Directional statistics*. New York: Wiley. doi:10.1002/9780470316979

Maxwell, S. C., Rutledge, J., Jones, R., and Fehler, M. (2010). Petroleum reservoir characterization using downhole microseismic monitoring. *Geophysics* 75 (5), 75A129–75A137. doi:10.1190/1.3477966

Maxwell, S. C., Raymer, D., Williams, M., and Primiero, P. (2012). Tracking microseismic signals from the reservoir to surface. *Lead. Edge* 31 (11), 1300–1308. doi:10.1190/tle31111300.1

Maxwell, S. (2014). *Microseismic imaging of hydraulic fracturing: Improved engineering of unconventional shale reservoirs*. Tulsa, OK, United States: Society of Exploration Geophysicists. doi:10.1190/1.9781560803164

Menanno, G., Vesnaver, A., and Jervis, M. (2013). Borehole receiver orientation using a 3D velocity model. *Geophys. Prospect.* 61, 215–230. doi:10.1111/j.1365-2478.2012.01106.x

Meng, X., Chen, H., Niu, F., Tang, Y., Yin, C., and Wu, F. (2018). Microseismic monitoring of stimulating shale gas reservoir in SW China: 1. An improved matching and locating technique for downhole monitoring. *J. Geophys. Res. Solid Earth* 123 (2), 1643–1658. doi:10.1002/2017JB014488

Nakamura, Y., Donoho, P. L., Roper, P. H., and McPherson, P. M. (1987). Large-offset seismic surveying using ocean-bottom seismographs and air guns: Instrumentation and field technique. *Geophysics* 52 (12), 1601–1611. doi:10.1190/1.1442277

Niu, F., and Li, J. (2011). Component azimuths of the CEArray stations estimated from P-wave particle motion. *Earthq. Sci.* 24, 3–13. doi:10.1007/s11589-011-0764-8

Ojo, A. O., Zhao, L., and Wang, X. (2019). Estimations of sensor misorientation for broadband seismic stations in and around africa. *Seismol. Res. Lett.* 90 (6), 2188–2204. doi:10.1785/0220190103

Schultz, R., Skoumal, R. J., Brudzinski, M. R., Eaton, D., Baptie, B., and Ellsworth, W. (2020). Hydraulic fracturing-induced seismicity. *Rev. Geophys.* 58 (3), e2019RG000695. doi:10.1029/2019RG000695

Son, Y. O., Seo, M. S., and Kim, Y. (2022). Measurement of seismometer misorientation based on P-wave polarization: Application to permanent seismic network in South Korea. *Geosci. J.* 26 (2), 235–247. doi:10.1007/s12303-021-0031-5

Takagi, R., Uchida, N., Nakayama, T., Azuma, R., Ishigami, A., Okada, T., et al. (2019). Estimation of the orientations of the S-net cabled ocean-bottom sensors. *Seismol. Res. Lett.* 90 (6), 2175–2187. doi:10.1785/0220190093

Tan, Y., and He, C. (2016). Improved methods for detection and arrival picking of microseismic events with low signal-to-noise ratios. *Geophysics* 81 (2), KS93–KS111. doi:10.1190/geo2015-0213.1

Tan, Y., He, C., and Mao, Z. (2018). Microseismic velocity model inversion and source location: The use of neighborhood algorithm and master station method. *Geophysics* 83 (4), KS49–KS63. doi:10.1190/geo2017-0308.1

Wang, X., Chen, Q. F., Li, J., and Wei, S. (2016). Seismic sensor misorientation measurement using P-wave particle motion: An application to the NECsaids array. *Seismol. Res. Lett.* 87 (4), 901–911. doi:10.1785/0220160005

Xu, H., Luo, Y., Tang, C. C., Zhao, K., Xie, J., and Yang, X. (2018). Systemic comparison of seismometer horizontal orientations based on teleseismic earthquakes and ambient-noise data. *Bull. Seismol. Soc. Am.* 108 (6), 3576–3589. doi:10.1785/0120180087

Yang, Y., Qi, Q., Zhou, H., and Wang, Z. (2022). A novel method for determining geophone orientations from zero-offset VSP data constrained by scalar field. *Front. Earth Sci.* 10, 848954. doi:10.3389/feart.2022.848954

Yuan, D., and Li, A. (2017). Determination of microseismic event azimuth from S-wave splitting analysis. *J. Appl. Geophys.* 137, 145–153. doi:10.1016/j.jappgeo.2016.12.008

Zeng, X., and McMechan, G. A. (2006). Two methods for determining geophone orientations from VSP data. *Geophysics* 71 (4), V87–V97. doi:10.1190/1.2208935

Zha, Y., Webb, S. C., and Menke, W. (2013). Determining the orientations of ocean bottom seismometers using ambient noise correlation. *Geophys. Res. Lett.* 40 (14), 3585–3590. doi:10.1002/grl.50698

Zhu, Y., Lin, J., Zhao, F., Chen, Z., Sun, F., and Lv, H. (2018). A least squares method based on quaternions to derive absolute orientation of geophones with AHRS. *J. Geophys. Eng.* 15 (6), 2614–2624. doi:10.1088/1742-2140/aadd2f

frontiers | Frontiers in Earth Science

TYPE Original Research
PUBLISHED 19 January 2023
DOI 10.3389/feart.2022.1082122

OPEN ACCESS

EDITED BY
Lei Li,
Central South University, China

REVIEWED BY
Xinglin Lei,
National Institute of Advanced Industrial Science and Technology (AIST), Japan
German Rodriguez,
University of Bristol, United Kingdom

*CORRESPONDENCE
Haijiang Zhang,
zhang11@ustc.edu.cn
Yuyang Tan,
tanyuyang@ouc.edu.cn

SPECIALTY SECTION
This article was submitted to Solid Earth Geophysics, a section of the journal Frontiers in Earth Science

RECEIVED 27 October 2022
ACCEPTED 14 November 2022
PUBLISHED 19 January 2023

CITATION
Anyiam UO, Zhang H, Tan Y, Qian J, Gao L, Liu Y, Zuo K and Zhao C (2023), Enhanced 3D velocity structure, seismicity relocation and basement characterization of Changning shale gas and salt mining regions in southern Sichuan basin.
Front. Earth Sci. 10:1082122.
doi: 10.3389/feart.2022.1082122

Enhanced 3D velocity structure, seismicity relocation and basement characterization of Changning shale gas and salt mining regions in southern Sichuan basin

Uzonna Okenna Anyiam[1], Haijiang Zhang[1,2]*, Yuyang Tan[3]*, Jiawei Qian[4], Lei Gao[1], Ying Liu[1], Kezhen Zuo[5] and Cuiping Zhao[5]

[1]Laboratory of Seismology and Physics of Earth's Interior, School of Earth and Space Sciences, University of Science and Technology of China, Hefei, China, [2]Mengcheng National Geophysical Observatory, University of Science and Technology of China, Hefei, China, [3]Frontiers Science Center for Deep Ocean Multispheres and Earth System, Key Lab of Submarine Geosciences and Prospecting Techniques MOE, College of Marine Geosciences, Ocean University of China, Qingdao, China, [4]College of Oceanography, Hohai University, Nanjing, China, [5]Institute of Earthquake Forecasting, China Earthquake Administration, Beijing, China

Current extensive seismicity in southern Sichuan Basin is ascribed to the reactivation of pre-existing faults, as a result of prolonged fluid injection for salt mining and shale gas development, respectively. However, the structural framework of the region remains poorly understood. Here, we apply V_p/V_s consistency-constrained double-difference seismic tomography to high quality phase data from 36,314 earthquakes jointly recorded by our local array and a regional seismic network to determine high-resolution velocity models. Earthquake relocations reveal shallow hypocenters for the M_s>5.0 earthquakes and two distinct seismogenic zones corresponding to the salt mine and shale gas regions, with most induced seismic events forming widespread lineaments some of which extend to the basement and are remarkably similar to the fault and fracture trends interpreted on reflection seismic and outcrops, respectively. Our 3-D crustal velocity analyses show that seismicity beneath the Changing salt mining area is associated with a combination of relatively low V_p/V_s (1.6–1.74) and high V_p/V_s (1.75–1.86) expressions, while most of small earthquakes within the Xingwen shale gas block are associated with relatively high V_p/V_s values (1.77–1.87), indicating the earthquakes in these two areas are caused by unique inducing mechanisms. The two moderately strong 2018 Xingwen M_s5.7 and 2019 Gongxian M_s5.3 earthquakes in the Xingwen shale gas block are located around low V_p/V_s. zones, suggesting they could be structurally controlled. In comparison, the 2019 Changning M_s6.0 earthquake in the Changning salt mining area is associated with high V_p/V_s. expression, suggesting its occurrence is related to fluid injections. In addition, top of the crystalline early Neoproterozoic (pre-Sinian) Sichuan basement is characterized by the 6.5 km/s V_p contour, which is

new for earthquake tomographic studies in the region. Combined with outcrop analysis, we are able to construct a structural framework for induced seismicity in southern Sichuan basin, which unravels the structural architecture of induced seismicity.

KEYWORDS

induced-seismicity, trigger-mechanism, double-difference, seismic tomography, basement characterization, fluid injection

1 Introduction

Induced seismicity resulting from subsurface fluid injection activities has been documented globally (Ellsworth, 2013; Lei et al., 2020), including waste water disposal in midcontinental United States, shale gas hydraulic fracturing in western Canada, and shale gas development in southern Sichuan basin. As the second largest unconventional shale gas production area in the world, the Sichuan basin has experienced abrupt increase in earthquake activity since the mass production of shale gas began in 2014 (Lei et al., 2020). In southern Sichuan basin, there are mainly three shale gas production fields, including the Changning-Zhaotong field, the Weiyuan field, and the Fuling field (Lei et al., 2020). To the north of the Changning-Zhaotong shale gas field, there is a salt mining field. In both Changning shale gas field and salt mining field on the Jianwu syncline and the Changning-Shuanghe anticline system (Figure 1) respectively, a few devastating earthquakes coupled with a considerable number of seismic events of M_s>3.0 (felt seismicity) have been induced by both prolonged and temporary subsurface fluid injections (Ruan et al., 2008; Sun et al., 2017; Lei et al., 2019b; Tan et al., 2020), respectively. Prolonged injections are mainly related to wastewater disposal and salt mining operations and last for a couple of years to some decades (Lei et al., 2008; Zhang et al., 2012; Lei et al., 2013). In contrast, temporary injections are characteristic of hydraulic fracturing at designated well pads for shale gas exploitation and are typically carried out for only a few months (Lei et al., 2017; Lei et al., 2019a; Meng et al., 2019; Tan et al., 2020). In the shale gas hydraulic fracturing region, the concentration of induced seismicity was only on a handful of hydraulic fracturing sites (Lei et al., 2020), similar to the observation of Atkinson et al. (2016) on other zones.

A swarm of induced earthquakes with magnitudes reaching M_s6.0 battered Changning and the neighboring towns (Lei et al., 2019b; Yi et al., 2019; Liu and Zahradník, 2020) after the 2018 Xingwen M_s5.7 main shock that was interpreted to have resulted from hydraulic fracturing for shale gas production (Lei et al., 2019a). This rise in the magnitude and frequency of induced seismicity has aroused increasing concern of potential risks in shale gas exploitation and salt mining operations in this region. Therefore, further investigation of the source mechanisms, source locations and subsurface velocity architecture are imperative to understand induced seismicity in the Changning-Xingwen region.

Neoproterozoic Sichuan basement rocks constitute portions of the Precambrian Igneous complex, which controls structural deformation and spans the entire Sichuan Basin with outcrop equivalents that bound the edges of the basin (Liu et al., 2021). Therefore, to better understand the cause of earthquake activity in southern Sichuan basin, it is important to have detailed comprehension of seismicity induced by fluid injection and improved understanding of the structural morphology of the characteristic down-to-basement faults. Previous research works by Lei et al. (2017), Lei et al. (2019a), Meng et al. (2019) and Tan et al. (2020) were primarily focused on earthquake location and focal mechanism determination. Lei et al. (2017), Lei et al. (2019a) and Yi et al. (2019) mainly utilized the conventional cut-and-paste (CAP) inversion method to calculate the centroid depths and focal mechanisms of some moderate to strong earthquakes. However, while centroid depths and focal mechanisms are helpful for understanding the relationship between induced seismicity and fluid injection activity, they do not provide the accurate structural framework for the occurrence of induced seismicity. InSAR data have been used to infer that the Changning anticline is characterized by a single seismogenic fault (Wang S. et al., 2020), which is highly unlikely given the several faults that deform the anticline (Figure 1C). Recently, Wang et al. (2022) applied InSAR inversions to define three seismogenic faults beneath the Jianwu syncline, however, they could only achieve resolution accurate to 10 by 10 km, which is lower than the 5 by 5 km resolution achieved by the earthquake tomographic inversion of this study.

In general, accurate characterization of the structural framework controlling seismicity beneath a seismogenic zone results from detailed interpretation of seismogenic faults from reflection seismic profiles, tomographic velocity models and accurately relocated earthquake lineaments. Unfortunately, only very few seismic reflection profiles are publicly available (e.g., Liu et al., 2021). There exist, however, quite a number of tomographic studies that investigate parts of or the entire Sichuan basin. Wang et al. (2013) utilized ambient noise tomography to obtain S-wave velocity model beneath the entire Sichuan basin with spatial resolution only as good as ~50 km by 50 km within our study area. At this resolution, only regional scale velocity features are imaged, with detailed reservoir

scale features essentially muted out. Up to now, the most prominent study that covers the entire Sichuan basin is the study by Wang et al. (2016), which incorporated a suite of geological and geophysical data to obtain three-dimensional seismic velocity structure beneath the Sichuan basin. At this resolution, basin-scale geologic features are imaged including the structure of the crystalline Sichuan basement. However, detailed field or reservoir scale structural imaging is lacking in most parts of the basin due to the poor coverage of sparsely distributed seismic reflection profiles and seismic events.

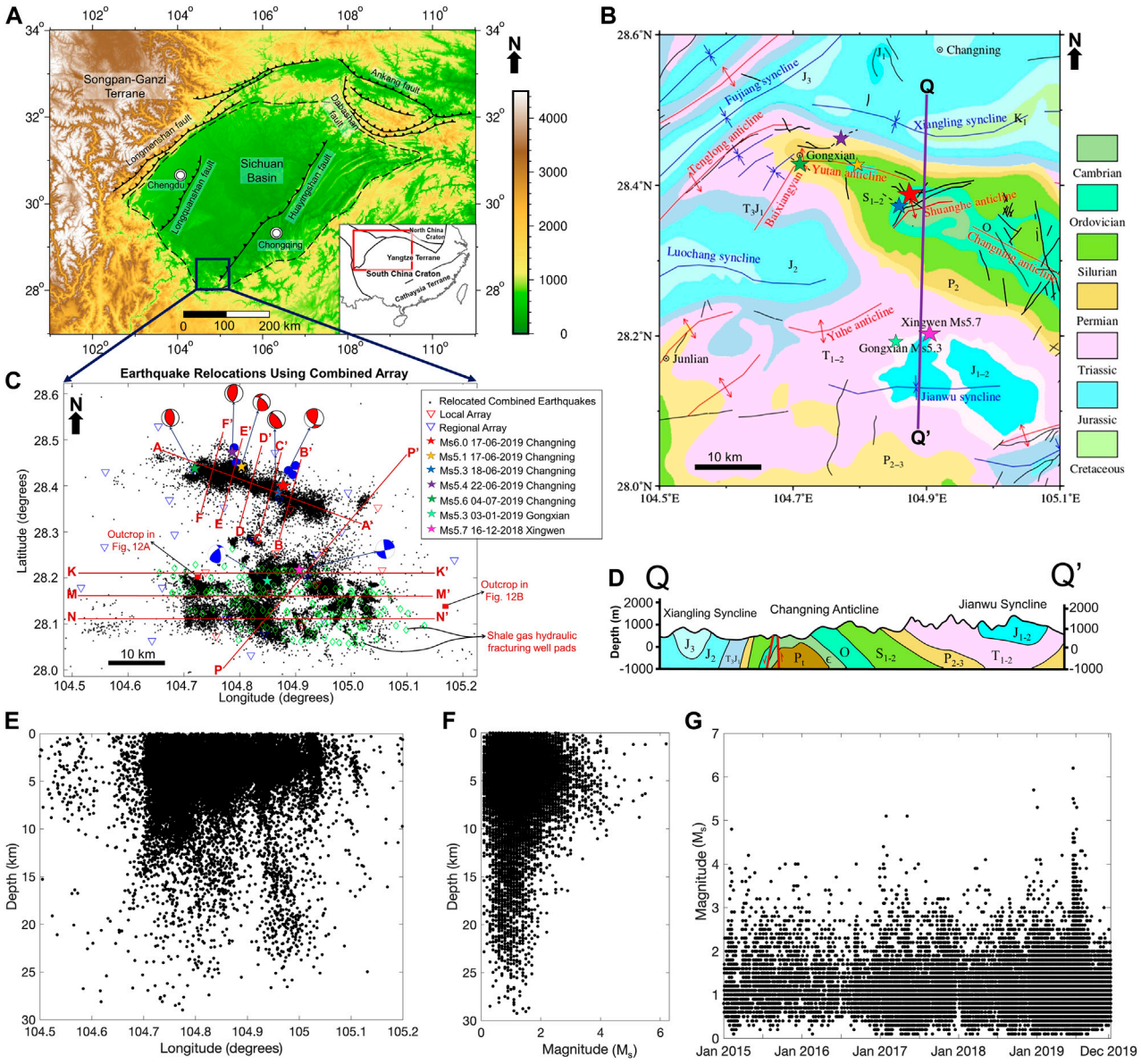

FIGURE 1
(A) Topographic map of Sichuan basin showing area studied and prominent thrust structures. **(B)** Distribution of relocated epicenters (dots), seismic stations (triangles), and shale gas hydraulic fracturing well pads (diamonds) within the target study area. Beachballs with red and blue tension quadrants represent focal mechanisms of M_S>5.0 earthquakes after Wang et al. (2020) and Lei et al. (2019b) within the salt mine and shale gas regions respectively. Red squares denote outcrop locations while blue circles represent zones of co-seismic surface deformations. **(C)** Tectonic and geological settings map of southern Sichuan basin, modified from Zuo et al. (2020). Red lines with outward pointing arrows are anticlines, blue lines with inward pointing arrows are synclines, black lines are mapped seismic-scale faults and black dashed lines are previously unmapped faults. **(D)** Cross-section showing the structural architecture of the Xingwen shale gas and Changning salt mining zones corresponding to Jianwu synclinal region and Changning-Shuanghe anticlinal system respectively, modified from Wang S. et al. (2020). **(E)** Vertical view of relocated earthquakes. **(F)** Magnitude distribution with depth. **(G)** Magnitude distribution with time.

In the southern Sichuan basin, there has been continuous influx of body wave arrival time data, derived from continuous monitoring of natural earthquakes and induced seismicity with different networks of seismic stations. This continuous flow of data has led to several seismic studies within the region, many of which focused on seismicity location and focal mechanism determination. A couple of researchers have recently utilized varying portions of this data flow to determine velocity models at these scales (Long et al., 2020; Zhang et al., 2020; Zuo et al., 2020). Pioneering seismic tomographic study of the region is that of Long et al. (2020), which used 5,252 events recorded on relatively sparse seismic stations and 1-D initial velocity model developed from large-scale tomographic results of Zhao and Zhang (1987). They only obtained V_p (P-wave velocity) and V_s (S-wave velocity) models with spatial resolution of 10 km by 10 km in the longitude and latitude directions, which showed that generally seismicity in this region is predominantly situated in high V_p and high V_s zones, suggesting them to be structurally controlled. Later work by Zhang et al. (2020) utilized a dataset of 8,818 seismic events, which were recorded by a local array of 39 seismic stations between the first of December 2018 and the fourth of July 2019 to determine the velocity structure of the region with similar resolution as Long et al. (2020). They obtained similar V_p and V_s results with Long et al. (2020) with the exception of characterization of low V_p associated with high V_s and low V_p/V_s expressions beneath the southern part of the studied region that correlates with the Jianwu syncline from 4 to 16 km depths. These low V_p zones were inferred as evidence of presence of deep fluids (Zhang et al., 2020), thereby suggesting fluid induced mechanism for these earthquakes. However, this inference is highly skeptical without commensurate low V_s expression, which corresponds to high V_p/V_s ratio. Given that the region has undergone extensive fluid injection involving over 200 wells (Figure 1B) since 2014, it is imperative that the V_s model should reflect features related to fluid distribution. Recently, Zuo et al. (2020) used a more complete version of the regional data set made up of 24,640 earthquakes, recorded by an array of 86 seismic stations to determine the crustal velocity structure of the region up to 5 km by 5 km resolution in the longitude and latitude directions. Their results show obvious high V_s and low V_p/V_s ratio features for seismicity within the region, suggesting no fluid influence on seismicity. Even though these studies imaged the subsurface at this important seismogenic environment, they could not resolve structures clearly representative of fluid influence and their resolvability of local geologic features is also limited due to sparse catalog travel time data utilized in the tomography and the 1-D initial velocity models that were derived from poorly resolved travel time tomography (Zhao and Zhang, 1987) and ambient noise tomography (Lei et al., 2017) results, which are not as accurate as vertical seismic profiles or reflection seismic velocities. We posit that velocity structure beneath this region can be improved by utilizing a more precise 1-D starting velocity model and incorporating denser local catalog data, in the absence of adequate well and seismic data that is essential for the construction of a reliable 3D velocity model.

In this study, we aim at enhancing earthquake locations and consequently better constrain velocity models to improve understanding of the structural framework for induced seismicity in the Changning region, southern Sichuan basin by incorporating local temporary seismic stations. Basically, we combined earthquake catalog data of Zuo et al. (2020) and arrival times recorded by temporary local stations in Tan et al. (2020). More accurate relocations of induced seismicity and crustal velocity structure are determined by V_p/V_s consistency-constrained double-difference seismic tomography (Guo et al., 2018). In addition, we describe the fault and fracture patterns of the Paleozoic sedimentary strata exposed in southwestern Sichuan Basin. These investigations combine to provide better understanding of the controlling structural framework for induced seismicity in the Changning region. This study also supplies the first map of basement structure of southern Sichuan basin from the inverted velocity model, and provides direct indication of linkage between basement structure and induced earthquakes, as well as reveals likely avenues for the migration of injected fluids upward into the overlying siliceous quartz-rich Tertiary rocks resulting in the shallow initiation point of the main shock, and downward to the basement complex from the injection intervals, which are an indispensable tool for rapid generation of induced seismicity.

2 Tectonic and geologic setting

2.1 Basin evolution

The Sichuan Basin is a large intracontinental basin in western China, which has undergone various structural transformations in the vicinity of the Tibetan Plateau (Liu et al., 2012). It is situated on the western edge of the south China craton (Figure 1A), which is bounded in the northwest by the Yangtze platform and in the southeast by the Cathaysia block (Liu et al., 2012; Liu et al., 2017; Liu et al., 2021). Recently, the basin has gone through a transformation from a comparatively stable craton stage to an unstable stage that is marked by convoluted deformation (Wang, 1989). The late Paleozoic to middle Mesozoic Qinling Orogenic belt detached the basin from the North China craton (Meng and Zhang, 2000; Dong et al., 2011), while the fold and thrust belts of Longmenshan-Daliangshan separated it from the Mesozoic-Cenozoic eastern Tibetan Plateau (Roger et al., 2010; Liu et al., 2013). According to Meng and Zhang (2000), the Qinling orogenic belt underwent an extensive tectonic past and is thought to have experienced collision along the Shangdan

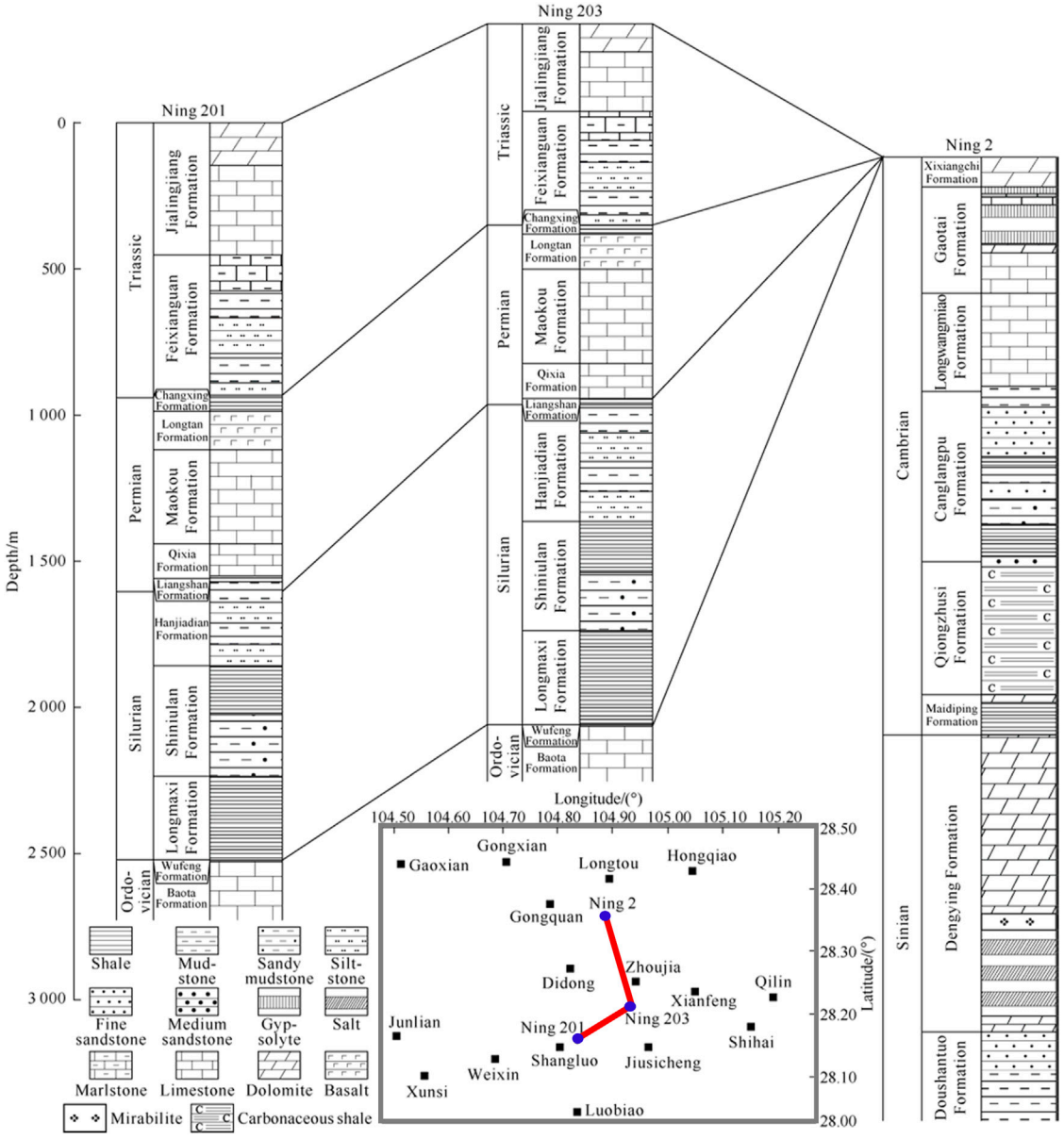

FIGURE 2
Comparison of stratigraphic sections of the Changning anticline and Jianwu syncline, modified from He et al. (2019). Note: red solid line represents cross-section profile, while blue circles denote wellhead positions.

suture area of middle Paleozoic and the Mianlue suture area of middle to late Triassic periods. The subsequent two-phase collision of the North and South China cratons along the Mianlue suture area applied serious effect on the development of the Sichuan Basin (Liu et al., 2005) and entire Yangtze terrace (Liu et al., 2021).

Following the Early Triassic, two major tectonic periods were responsible for the structural configuration of the eastern Tibetan Plateau: Late Triassic thrusting that is composed of sinistral strike-slip motions (Chen and Wilson, 1996; Deng et al., 2012; Yan et al., 2018) and Cenozoic fault reactivations under E-W compression (Burchfiel et al., 1995), which grew into prevailing deformation that involved the crystalline basement beneath the southern part of Longmenshan and Daliangshan (Deng et al., 2018; Tian et al., 2018). Wilson et al. (2006) and Royden et al. (2008) described the reactivation of preexisting structures as the product of late Cenozoic eastward or southeastward thrust of the Tibetan Plateau. Slip on these preexisting structures is believed to be the source of frequent microearthquakes (M_s<3) and several moderate-to-major (M_s>3) earthquakes in the Sichuan basin.

Therefore, the tectonostratigraphic configuration of the Sichuan basin is believed to be mainly controlled by thrust belts that circumscribe the basin, which comprises the Longmenshan belt to the west, the Dabashan to the north, the Eastern Sichuan belt to the east, and the Kangdian belt to the south (Wang et al., 2016) (Figure 1A). Within the basin, however, structural deformation is mainly characterized by a complex array of thrust and normal faults, with some strike-slip counterparts (Liu et al., 2021).

2.2 Stratigraphy

The Sichuan basin was developed from Sinian to Late Triassic period, during which a tenuous, deficient sequence of marine and non-marine debris accumulated (Burchfiel et al., 1995; Jia et al., 2006). The basin transformed to completely non-marine in the course of the Late Triassic Indosinian orogeny, as a result of the closing of the Paleo-Tethys (Chen and Wilson, 1996). During the orogenic deformation, the Sichuan foreland basin was formed by the thrusting of the Longmenshan toward the basin (Burchfiel et al., 1995; Li et al., 2003; Jia et al., 2006). The areal extent of the resultant Sichuan basin is approximately 190,000 km^2 and it contains Sinian to Quaternary sediments with thickness ranging from 5 to 12 km (Zhai, 1992; Li et al., 2005). Strata overlying Cretaceous rocks in the southwestern part of the Sichuan basin mostly consists of Early Tertiary sediments that are composed of fluvial lacustrine red siltstones and sandstones (Burchfiel et al., 1995; Chen and Wilson, 1996; Zhou et al., 2002; Jia et al., 2006), which are highly rich in quartz and silica content. Situated to the west, however, is a thin foreland basin exclusively composed of Quaternary sediments (Burchfiel et al., 1995; Hubbard and Shaw, 2009; Hubbard et al., 2010), which developed in the Late Cenozoic as a result of rapid uplift of the Longmenshan area (Kirby et al., 2002). Most outcrop occurrences of sedimentary strata within the basin are of Mesozoic to Cenozoic age (Wang et al., 2016). Figure 2 shows the stratigraphic column of three wells Ning 201 and 203 drilled within the Shale gas block in the Jianwu syncline and Ning 2, which was drilled on the salt mine block in the Changning anticline. These stratigraphic sections reveal younger formations that correspond to low V_p and V_s values in the Jianwu area, in contrast to the older formations associated with high V_p and V_s values that characterize the Changning anticline area, thus, buttressing the effect of complex tectonic deformations on strata within the southern Sichuan basin. At the base of the Sichuan sedimentary sequence is the faulted crystalline Neoproterozoic basement complex that developed during the complex magmatic tectonic evolution known as the Yanshanian orogeny (Li and Li, 2003; Yan et al., 2003). Outcrop equivalents of these crystalline basement rocks can be seen at the outskirts of the basin, and reveal the characteristic fault framework of the basement.

2.3 Seismic activity

The southwestern Sichuan Basin (our study area) is bounded on the west by Qinghai-Tibet block, and on the south by the mountain transition range of the Yungui Plateau (Figure 1A). The most prominent structural feature is the Changning-Shuanghe compound anticlinal system that trends in the NWW to SEE direction, and primarily consists of Baixiangyan-Yutan, Shuanghe, Changning and Tenglong anticlines (Figures 1C,D). The Changning M_s6.0 earthquake of June 2019 occurred on the Changning anticline within our study area (Figures 1B,C). Higher (steeper) limb dips characterize the northern part of the Changning-Shuanghe anticlinal system, as opposed to lower (gentle) limb dips observed in the southern part (Zuo et al., 2020), and Cambrian strata are revealed with in the core. Axial direction of the maximum horizontal principal stress was determined by Lei et al. (2019a) to be 77° within the Changning-Shuanghe anticlinal system. The foreshocks and aftershocks of M_s6.0 Changning earthquake mostly occur along the Changning anticlinal axis. The extended source region of southwestern Sichuan basin is believed to be bounded by the northeast-southwest trending active major Huayingshan fault, which is characterized by thrust and dextral strike-slip movements (Deng et al., 2003). The crestal and limb regions of the Changning-Shuanghe anticlinal systems are believed to be predominantly characterized by several mini high-angle thrust and normal faults (Wang et al., 2016; Liu et al., 2021). On the other hand, focal mechanisms determined by Lei et al. (2017) show the shale gas region within the Jianwu syncline, as having maximum horizontal principal stress direction of approximately N100°E to N115°E, which conforms to results gotten from *in-situ* rock stress measurements by Wang et al. (2016). The Jianwu and Luochang synclines are large with gentle intrasynclinal structural morphology and Jurassic aged topmost layer (Zuo et al., 2020). Nevertheless, two major earthquakes—2018 Xingwen M_s5.7 and 2019 Gongxian M_s5.3 shocks occurred on the Jianwu syncline (Figures 1B,C), whose seismogenic structures were well constrained by InSAR inversions (Wang et al., 2022). These synclines are mostly characterized by high-angle large scale tectonic faults and fractures that are well developed and trend mainly in the EW, NE and NNW directions (Shi et al., 2019; Wang et al., 2022).

3 Data and methodology

3.1 Data availability

We utilize combined seismic phase arrivals from 86 regional stations of Zuo et al. (2020) and 10 local stations (Figure 3). The

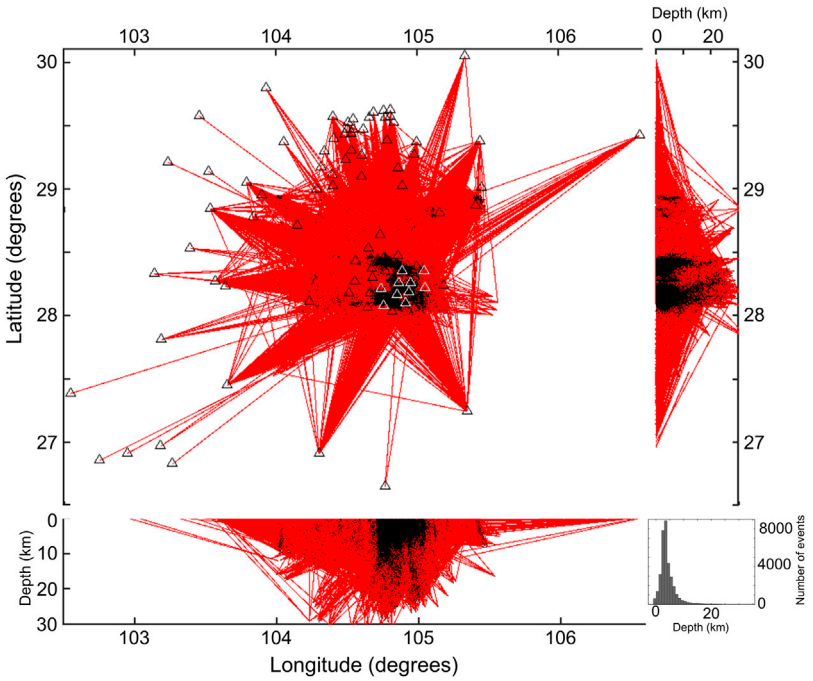

FIGURE 3
Coverage of seismic ray paths involved in the joint inversion. Black dots represent seismic events recorded by the combined array. Black triangles represent regional array stations used in Zuo et al. (2020), and white triangles represent our local stations, respectively, while red lines represent ray paths.

regional stations recorded phase arrivals of about 34,296 individual seismic events within our study area from the first of January 2015 to the 31st of August 2019 (Zuo et al., 2020). Our local stations on the other hand, recorded seismic phase arrivals of about 15,126 earthquakes from the 19th of January 2019 to the 10th of December 2019.

Epicentral distances to be considered during data selection was set to be below 150 km, similar to Zuo et al. (2020), and data with substantial deviations from the time-distance curves were effectively removed (Figure 4A). The earthquakes are determined based on the requirement of at least 8 phase arrivals, both for the regional and local arrays. Analogous to the regional data from Zuo et al. (2020), the distance between any given event pair was set under 10 km for calculating the event-pair differential times, with a maximum number of neighbors of 20. Overall, phase data of 36,314 (24,640 regional array and 11,674 local array) earthquakes with high signal-to-noise-ratio were selected for seismic tomography. The chosen regional array seismic events consisted of 161276P-wave absolute, 161515S-wave absolute, 148818S-P absolute, 1575384P-wave relative, 1569036S-wave relative and 1447388S-P relative arrival data, while those of the local array included 83577P-wave absolute, 74724S-wave absolute, 65546S-P absolute, 2196834P-wave relative, 1988838 S-wave relative and 1916632S-P relative arrival data. Detailed explanation of the meaning of the data and inversion terminologies utilized in this section can be found in the manual for TomoDD (Zhang and Thurber, 2003; Zhang et al., 2009). We utilized an initial one-dimensional (1-D) velocity model that was developed as an average based on vertical seismic profile (VSP) from a well located about 40 km northwest of our study area and modelled reflection seismic P-wave velocity data within our study area from Wang et al. (2016), see Figure 4B. Average velocity values were utilized for depths shallower than 5 km, while the velocity values of the deeper levels were determined solely from the results of the modelled reflection seismic P-wave velocity data. This initial velocity model was preferred to the 1-D initial velocity model used by Zuo et al. (2020) (Figure 4B), which was proposed by Lei et al. (2017) based on results of seismic ambient noise tomography, because VSP and reflection seismic velocities are superior and more accurately express the geology of the area. As expected, the initial residuals are smaller and better distributed around 0 s, with an improved approximate Gaussian distribution (Supplementary Figure S1). By adopting a fixed V_p/V_s of 1.73, which is an average crustal V_p/V_s estimated for the Sichuan basin by Lei et al. (2017), we derive the initial one-dimensional V_s model. This V_s model was preferred to the V_s from the VSP in order to ensure that fluid changes resulting from widespread injection in the region are better constrained, without the introduction of velocity artifacts, which would have arisen from the sole use of the V_s from VSP. Generally, P-wave velocities

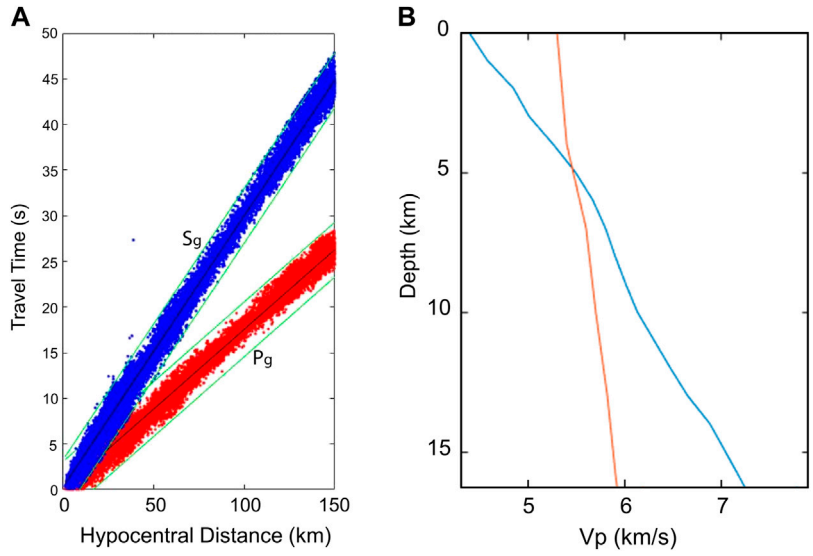

FIGURE 4
(A) Time–distance curves of P-wave phase data in red and S-wave phase data in blue. Black lines represent the linear fitting of travel time against hypocentral distance, and the green lines denote tolerance limits for data with large deviations. Sg and Pg denote direct S- and P-wave arrivals, respectively. **(B)** Initial 1D P-wave velocity model. Blue line denotes the model used in this study, while red line denotes that used in Zuo et al. (2020).

are less affected by injected fluids, which significantly alter S-wave velocities. Therefore, V_p is more suitable for regional velocity estimation than the V_s.

3.2 Seismic tomography method and model resolution analysis

To carry out seismic tomography, we use a recently updated version of the original double difference seismic tomography (TomoDD) method developed by Zhang and Thurber (2003), Zhang and Thurber (2006). The tomoDD method inverts the three-dimensional V_p, V_s models and earthquake locations using both absolute and relative arrival times, which can improve earthquake locations and velocity structure in the source area. Zhang et al. (2009) improved the TomoDD method by expanding it to include inversion of V_p/V_s with S-P (T_s-T_p, where T_s is the arrival time of S-wave and T_p is the arrival time of P-wave) differential data. Due to the relative paucity of S-P data, the recovered V_p/V_s model, though reliable, lacked good resolution (Guo et al., 2018). On the other hand, dividing inverted V_p model by the corresponding V_s model can also yield a V_p/V_s model. Unfortunately, V_p/V_s model inverted in this manner is highly unreliable, even though it typically shows higher resolution, making the resultant model very challenging for any meaningful geologic interpretation (Eberhart-Phillips, 1990; Huang et al., 2014). This issue is resolved by the V_p/V_s model consistency-constrained double-difference seismic tomography (TomoDDMC) by Guo et al. (2018). TomoDDMC utilizes P-wave, S-wave and S-P data to obtain reliable V_p/V_s model with enhanced resolution, as well as generate accurate V_p and V_s models and earthquake relocations. Therefore, we employ TomoDDMC to carry out joint inversion of the 3-D V_p, V_s and V_p/V_s models in the southern Sichuan basin.

Taking into consideration the distribution of stations and recorded seismicity, we set the coordinate origin at 104.8°E and 28.3°N, which corresponds to the center of our study area. The *X*-axis is oriented to the east while the *Y*-axis is oriented to the north. Along the *X*-axis and *Y*-axis, grid nodes were situated at −300, −60, −45, −30, −20, −15, −10, −5, 0, 5, 10, 15, 20, 30, 45, 60, 300 km, similar to Zuo et al. (2020). The grid nodes for the *Z*-axis in the downward vertical direction were densely situated at −100, −2, 0, 1, 2, 3, 4, 5, 6, 7, 8, 9, 10, 11, 12, 13, 14, 15, 16, 17, 18, 19, 20, 30, 200 km depths below the mean sea level (MSL). Coverage of seismic ray paths are displayed in Figure 3. TomoDDMC applies two major constraints—damping, which constrains model slowness and earthquake relocations, as well as smoothing that only constrains the model slowness. The L-curve method for establishing trade-offs for model solution norm and data residual norm, developed by Eberhart-Phillips (1986) was applied to obtain the optimal damping and smoothing parameters for the joint inversion. Figure 5 shows the determined optimal damping and smoothing parameters for inversion to be 800 and 80, respectively.

The reliability and quality of tomographic inversion models are typically estimated from checkerboard resolution test, which

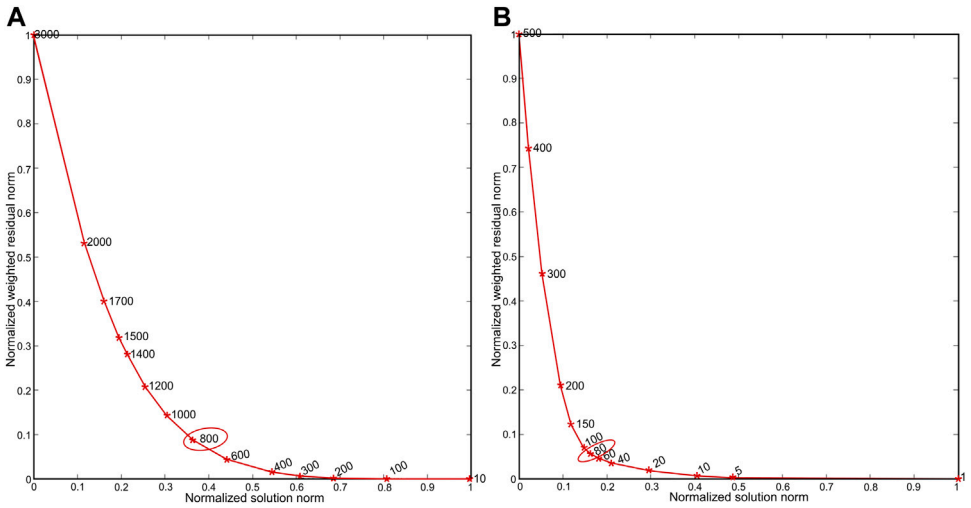

FIGURE 5
Trade-off curves. **(A)** L-curve for selection of damping parameter. **(B)** L-curve for selection of smoothing parameter. Optimal parameters selected are enclosed within the red ovals.

was originally developed by Humphreys and Clayton (1988), as well as from restoration test developed by Zhao and Hasegawa (1993). First, we constructed a synthetic checkerboard velocity model that comprised of alternating perturbations to the initial 3-D V_P and V_P/V_S models of ±5% and ±10% respectively. The corresponding alternating perturbations of the synthetic V_S checkerboard model were computed from the synthetic V_P and V_P/V_S models to be approximately +5.5% and −4.5%. Then, we applied the pseudo-bending ray tracing algorithm by Um and Thurber (1987) to calculate the synthetic phase arrivals, using our checkerboard model and the same distribution of seismicity (catalog data) and stations within the study area. The final step involved inversion of the synthetic input dataset with identical inversion parameters as were utilized in the inversion of the real data. On the other hand, the restoration test was similar to the checkerboard test but synthetic travel times are calculated using the seismicity relocations and V_P, V_S and V_P/V_S models inverted with TomoDDMC. The checkerboard resolution test and restoration test results are displayed in Figure 6 and Supplementary Figure S2, respectively. It is clear that our inversion is of high resolution (5 km by 5 km) and reliability from 0 to ~13 km, with the exception of some peripheral areas. Supplementary Figure S3 shows that resolution deteriorates with finer horizontal grid spacing of 2.5 km by 2.5 km, therefore, confirming that the best obtainable resolution with the current dataset is 5 km by 5 km in the horizontal directions. The final root-mean-square (RMS) travel time residuals are well minimized from 1.5 s to 0.2 s after inversion, with the comprehensive initial and final RMS values for all travel time data being 0.944 s and 0.056 s, respectively. The residuals are roughly distributed around 0 s and have an approximate Gaussian distribution, indicating that the final models can fit the data (Figure 7).

We employ the bootstrapping uncertainty analysis (Efron and Gong, 1983; Efron and Tibshirani 1991), which is based on data resampling to estimate the uncertainties associated with our relocated earthquakes. In this study, we randomly resample our catalog phase arrival data 50 times, and subsequently utilize TomoDDMC to invert the 50 sets of resampled data and obtain their corresponding seismicity relocations. This is followed by computation of the uncertainties of the relocated seismicity in longitude, latitude and vertical directions. We also examined the spatiotemporal location uncertainties associated with the sparse stations of the 2015–2017 events and the dense stations of the 2018–2019 events. The histograms of the estimated location uncertainties in different directions and periods for the relocated seismicity in this study are presented in Figure 8 and Supplementary Figures S4, S5.

4 Results

4.1 Seismicity relocation and focal mechanisms

Application of TomoDDMC resulted in the relocation of a total of 35,039 earthquakes. The relocated seismicity is distributed into clusters both in plan and vertical views, as seen in Figures 1B,E and the subsequent profiles, indicating improved relative event locations. Likewise, incorporation of

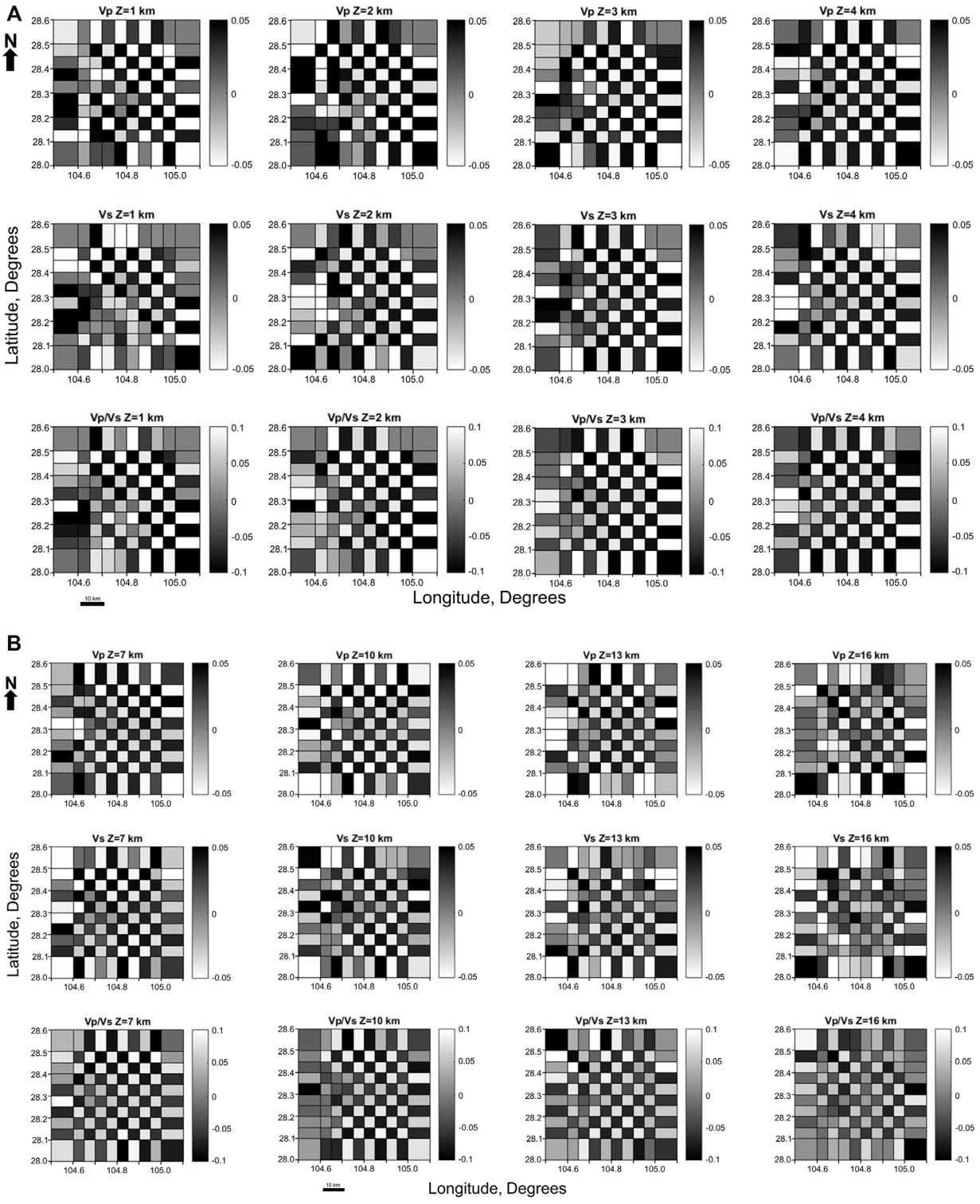

FIGURE 6
Inverted V_p, V_s and V_p/V_s checkerboard resolution for **(A)** 1–4 km depth slices. **(B)** 7, 10, 13 and 16 km depth slices. The checkerboard size is 5 km by 5 km in the horizontal; directions.

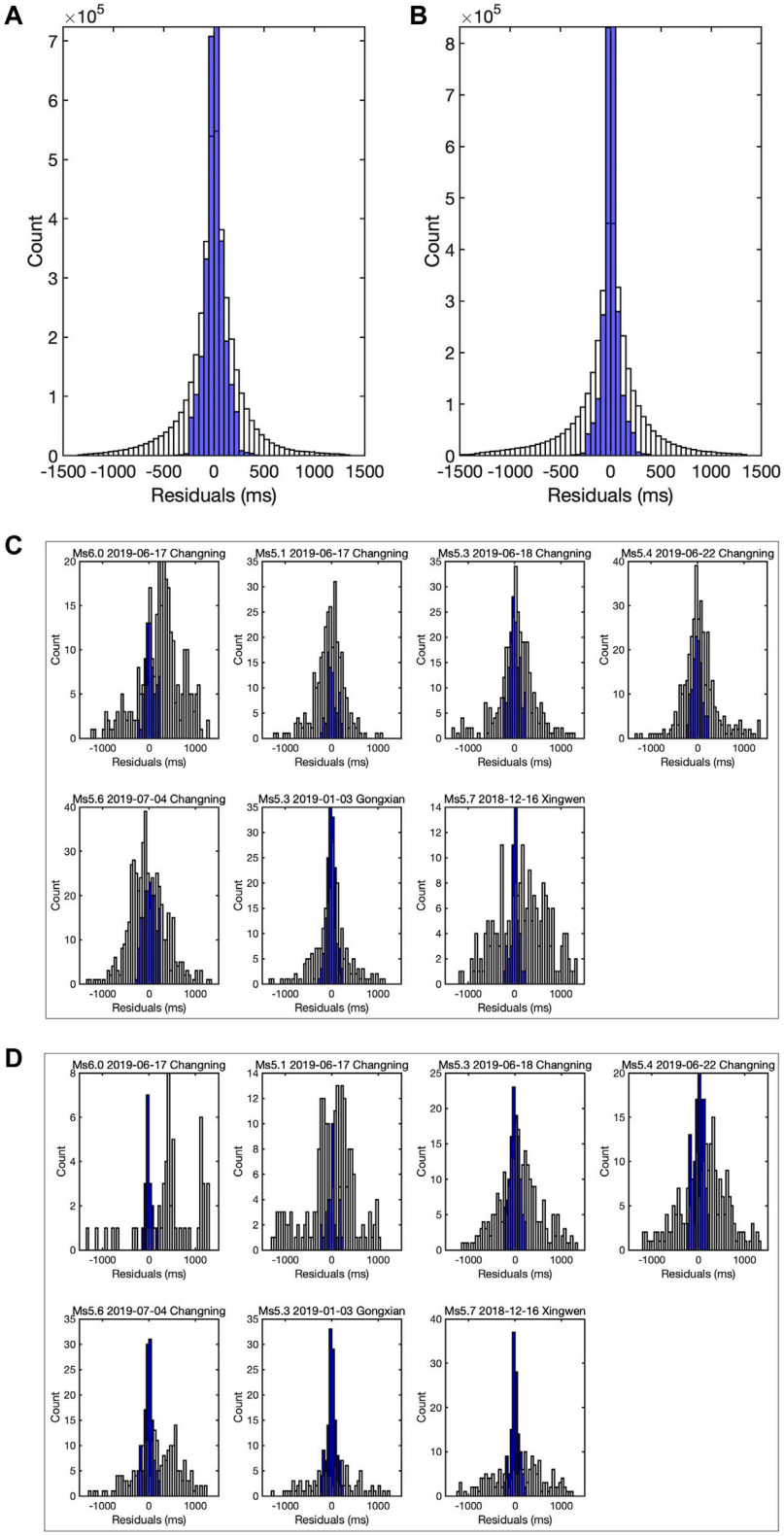

FIGURE 7
Histograms of travel time residuals before and after inversion. Note that white and blue bars denote residuals before and after inversion respectively. **(A)** Full P-wave. **(B)** Full S-wave. **(C)** P-wave residuals for the seven major earthquakes. **(D)** S-wave residuals for the same major earthquakes in c.

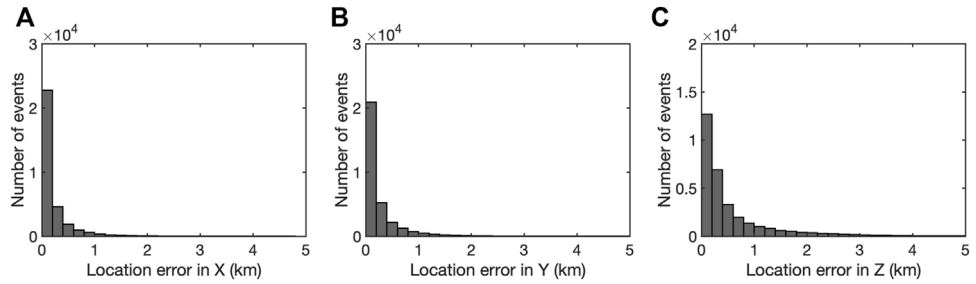

FIGURE 8
Comprehensive seismicity relocation uncertainties in different directions estimated by the bootstrapping method. **(A)** X (Longitude). **(B)** Y (Latitude). **(C)** Z (Vertical).

absolute arrival times of new additional data in the seismic tomography resulted in well resolved absolute seismic locations, with RMS relocation uncertainties estimated from bootstrapping method as low as 0.102, 0.119 and 0.274 km in longitude, latitude and vertical directions. Based on Guo and Zhang (2017), the location uncertainties estimated in this way mostly refer to relative event locations. Further examination shows location uncertainties as low as 0.085 km (longitude), 0.09 km (latitude) and 0.217 km (vertical) for 2018–2019 events, and 0.152 km (longitude), 0.179 km (latitude) and 0.349 km (vertical) for 2015–2017 events. It is clear that 2015–2017 events have larger location errors in comparison with the comprehensive data, while the 2018–2019 events have smaller location errors, suggesting that the uncertainties obtained with the complete data set can be interpreted as a tradeoff result. It is also important to note that location uncertainties for the 2015–2017 events are comparable to the complete data set, suggesting that the effect from the sparsely recorded events of 2015–2017 can be ignored.

Enhanced seismic relocations delineate very clear planar features of traces of active preexisting faults that characterize the Changning salt mine and shale gas regions, many of which are believed to be sub-seismic. Based on the combined data from our local array and the regional array, seven major induced earthquakes (M_s>5) within the study area are accurately relocated (Figure 1B). The relocation results of the Changning M_s6.0 main shock that is said to be fluid induced (Ruan et al., 2008; Zeng et al., 2014; Zhu and He, 2014; Sun et al., 2017; Lei et al., 2019b; Yi et al., 2019; Liu and Zahradnik, 2020), the associated M_s > 5 aftershocks situated within the Changning salt mining area and the M_s5.3 Gongxian and M_s5.7 Xingwen earthquakes that occurred within the shale gas block are listed in Supplementary Table S1. Given the consistency in the centroid depth, spatial orientation and rupture distribution of the source faults of the 27 January 2017 M_s5.1 Xingwen earthquake, 16 December 2018 M_s5.7 Xingwen earthquake and the 3 January 2019 Ms5.3 Gongxian earthquake, determined from centroid moment solutions (Lei et al., 2017; Lei et al., 2019b; Yi et al., 2019) and recent InSAR inversions (Wang et al., 2022), we utilize their results in comparatively assessing the uncertainties of our results (Supplementary Table S2). We find that the focal depth results determined by our study agree with the shallower centroid depths obtained for these major earthquakes with thrust, strike-slip and thrust focal mechanisms, respectively. This buttresses the enhanced resolution and location accuracy achieved in this study, which is also supported by the trivial relative location errors computed as a result of utilizing a robust data set and seismic tomographic method of 5 by 5 km higher resolution. The spatio-temporal distribution of earthquake magnitude in Figures 1F,G show that majority of seismicity beneath the study area have M_s<3.0 and are spread between 0 and 27 km, while the events with M_s>3.0 occur shallower between 0 and 9 km.

4.2 3-D V_p, V_s and V_p/V_s models

4.2.1 Depth slices

We show depth slices of V_p, V_s and V_p/V_s models and earthquakes plotted within 1 km above and below the depth slices in Figure 9. The tomographic results reveal crustal structures characterized by pronounced velocity heterogeneities within 0–10 km depth range, which correlate with the background regional geology. The 1-km depth slice shows a high velocity region beneath the Changning-Shuanghe anticlinal system. This is flanked by low velocity regions that can be related to mini basinal areas with younger sediments in the NE, NNW and NW, which correspond to the Xiangling, Fujiang and Luochang synclines, respectively. The V_s structure at this depth generally shows similar trends beneath the anticlinal and synclinal regions as described for V_p structure. The high V_p trend continues beneath the Shuanghe anticline up to 6 km depth (Figure 9 and Supplementary Figure S6), beyond which, a southwest trending low V_p expression appears (Supplementary Figure S6). This low V_p expression is bounded to the east and

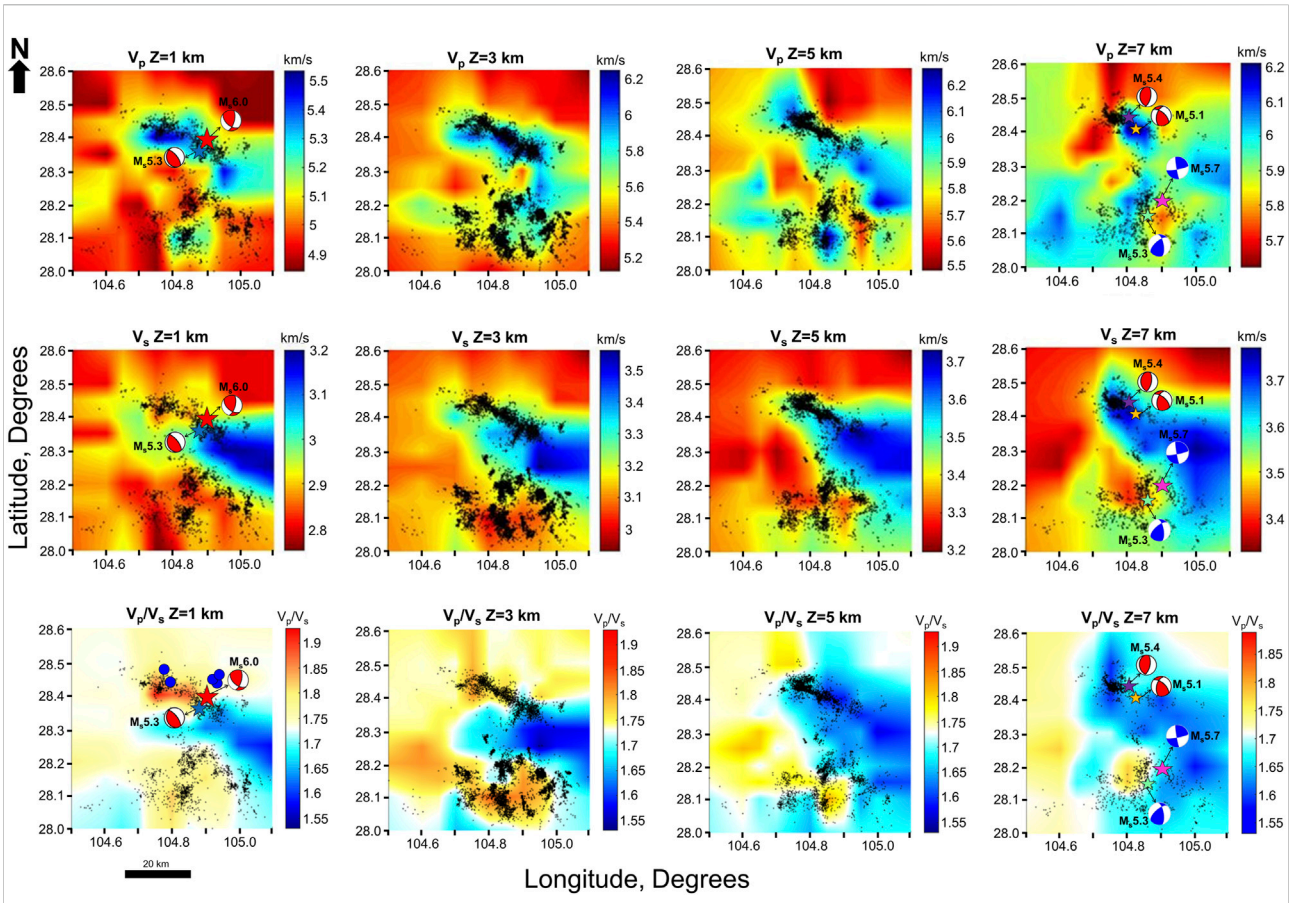

FIGURE 9
Depth slices of V_p, V_s and V_p/V_s models at 1, 3, 5 and 7 km. Black dots represent the vertical projection of earthquakes within 1.0 km on both sides of horizontal section, while blue circles on V_p/V_s slice at 1 km depth are zones of co-seismic surface deformations. The projected epicenters of the M_s6.0 earthquake and its M_s>5.0 aftershocks, Gongxian M_s5.3 earthquake and Xingwen M_s5.7 earthquake are denoted by stars with colors matching the legend in Figure 1B, while their respective focal mechanisms are displayed on the sides.

west by high V_p expressions. Similarly, the anticlinal region is mainly characterized by high V_s expression up to 7 km depth (Figure 9). Below 7 km, relatively homogeneous V_s structure that is characterized by sparse seismicity is observed (Supplementary Figure S7). Structural result of V_p/V_s shows segmentation at 1 km depth slice, with low V_p/V_s and high V_p/V_s expressions on the eastern and western parts of the Changning-Shuanghe anticline, respectively (Figure 9). This segment-style V_p/V_s expression is observed up to 2 km (Supplementary Figure S8). At 4 km slice, low V_p/V_s expression covers the Changning-Shuanghe anticlinal region up to 7 km depth. Below 7 km, the V_p/V_s structure becomes less heterogeneous and predominantly characterized by low V_p/V_s expression (Supplementary Figure S8).

Within the Jianwu synclinal region (shale gas region), low V_p and V_s expressions are revealed at 1 km depth slice (Figure 9). Predominantly, rocks of high V_p expressions are revealed beneath the Yuhe anticline up to 16 km, while beneath the Jianwu syncline rocks with typically low V_p expressions in comparison with V_p expression of rocks at the same depth level beneath the Changning anticlinal system are mostly revealed up to 4 km (Figure 9 and Supplementary Figure S6). On the other hand, low V_s expression is revealed within the Jianwu syncline (shale gas region) up to 4 km depth, beyond which V_s is mostly high (Supplementary Figure S7). The resultant V_p/V_s model reveals low (~1.6) to moderately high V_p/V_s expressions (~1.75) within the region at 1 km depth slice. Also, very high V_p/V_s expression (~1.76–~1.88) is revealed at 3 km (Supplementary Figure S8) and 4 km (Figure 9) depth slices. Below 4 km depth, low V_p/V_s feature dominates in the east, while the west is characterized by high V_p/V_s (Figure 9 and Supplementary Figure S8). This V_p/V_s trend continues up to 13 km depth slice, which reveals an east to west trending high V_p/V_s expression in the eastern part of the Jianwu syncline (Supplementary Figure S8).

4.2.2 Vertical cross sections

Ten vertical cross-sections along strategic profiles outlined on Figure 1B are presented in this section. The corresponding

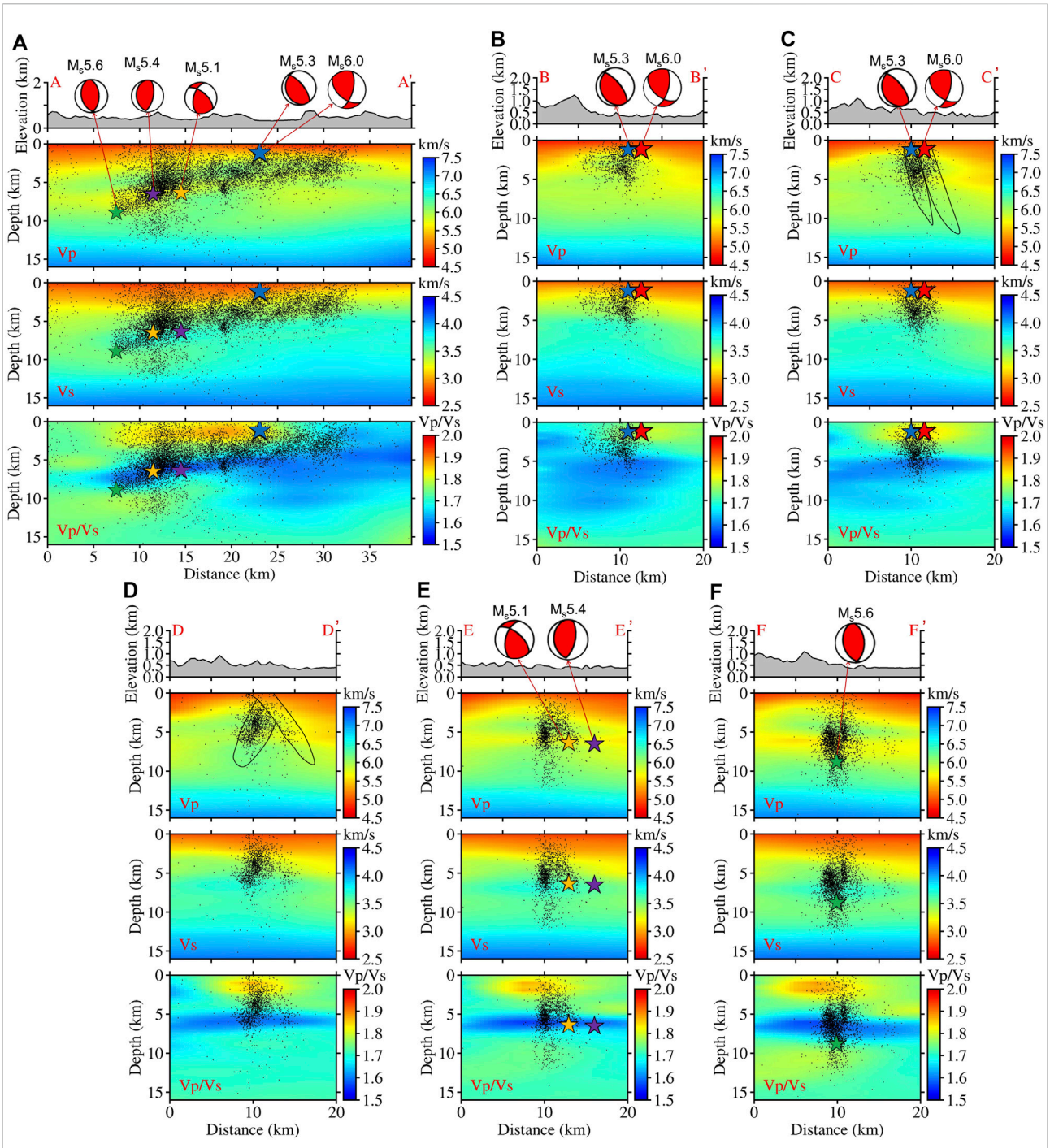

FIGURE 10
Cross-sections of V_p, V_s and V_p/V_s models along different vertical profiles within Changning salt mining region. **(A)** AA′. **(B)** BB′. **(C)** CC′. **(D)** DD′. **(E)** EE′. **(F)** FF′. Black dots are horizontal projections of seismic events within 2.5 km on both sides of the profile. The green, purple, yellow and blue stars on profile AA′ represent the aftershocks with M_s > 5, while the red star behind the blue star represents the M_s 6.0 Changning main shock. The corresponding focal mechanisms for the M_s>5.0 earthquakes are also represented. See Figure 1B for profile directions.

surface topography of each profile is also shown. The profiles show systematic structural velocity changes that are consistent with Wang et al. (2016), Long et al. (2020), but differ in several ways from Zhang et al. (2020) and Zuo et al. (2020), as well as imaged deeper than the 10 km threshold of Long et al. (2020).

Along profile AA' (Figure 10A), we observe low V_p and V_s features up to ~3 km depth. The relatively flat morphology of the

northwest to southeast trending Changning anticline is visible on the V_p expression of this profile. We observe layers of low and high seismic velocities (V_p and V_s) below 3 km depth. It can also be seen that the earthquakes correlate with moderately high to high V_p, high V_s and very low V_p/V_s zone. This zone shallows upward from about 10 km depth in the northwestern part (A) to about 2 km depth in the southeastern part (A'). The Changning M_s6.0 main shock is situated at the transition zone between high V_p/V_s and low V_p/V_s expressions. It obviously occurs in a contrasting structural environment, similar to the M_s>5.0 aftershocks.

Profiles BB′, CC′, DD′, EE′ and FF′ that run in the southwest (SSW) to northeast (NNE) direction, perpendicular to AA′ are evenly spaced by ~4 km and are displayed in Figures 10B–F. These results evidently show that the seismic events are predominantly situated within zones characterized by high V_p and V_s, or along the edge of low V_p and V_s expressions, which are associated with low V_p/V_s zones. The earthquakes displayed on profile BB′ clearly show earthquake clusters that extend up to about 5 km depth, with the source zone of the Changning mainshock and associated M_s5.3 aftershock characterized by low V_s and high V_p/V_s expressions. Profile CC′ shows earthquakes that form two separate lineaments that dip towards the northeast (Figure 10). On the other hand, profile DD′ shows earthquakes that form two separate lineaments, one of which is densely populated with seismic events and the other that is characterized by sparse seismicity. Both clusters have varying dips that are similar to the lineaments on profile EE' (Figure 10). Along profile EE′, the relocated earthquakes evidently form two lineaments similar to profile DD′, with the lineament with more seismic events dipping to the south at very high angles (~85°), while the other dips to the north at lower angles (~40°). In addition, the M_s5.1 and M_s5.4 aftershocks of the Changning mainshock align with the northeast dipping lineament of relocated earthquake clusters. On profile FF', the relocated earthquakes are distributed along two nearly vertical lineaments. The profile also shows that the southernmost lineament is wider than the northernmost lineament. In general, the anticlinal morphology of the Changning anticline is clearly visible on the V_p models along these five profiles, to the extent that the steeper NNE structure is evident.

Profile KK′ extracted within the Changning shale gas block, shows earthquake clusters that are generally situated within moderately low V_p and V_s zones, which typically correlate to low V_p/V_s zones (Figure 11A). MM′ profile reveals a western part with earthquake distributions and velocity structure of similar characteristics to those of KK′ described above (Figure 11B). On the other hand, profile NN′ and eastern part of MM' show earthquake clusters that are characterized by moderately lowered V_p and low V_s expressions, which correspond to moderately high V_p/V_s expression (Figures 11B,C). However, a few planar seismic clusters are situated within and around low V_p/V_s zones at the distal flanks of the moderately high V_p/V_s expression. These profiles show that lineaments of relocated earthquakes with varying dips and strikes are clearly resolved by seismic tomography.

5 Discussions

Several upper crustal-scale earthquake relocation and tomographic studies, which utilized P- and S-wave phase arrival data have been executed for Sichuan Basin (Chen et al., 2017; Improta et al., 2017; Chen et al., 2018; Wang and Kao, 2019; Long et al., 2020; Tan et al., 2020; Zhang et al., 2020; Zuo et al., 2020). These analyses were carried out with distinct data sets, different methods and varying model resolutions. The high-resolution crustal velocity structure obtained from this study with good model resolution up to 16 km depth, revealed accurate velocity characteristics of the structural controls on induced seismicity within the southern Sichuan Basin. The results show low V_p and V_s expressions beneath the mini basinal and synclinal areas up to 1 km depth (Figure 9), which are believed to be composed of younger sedimentary rocks (Figure 1C). These mini basinal areas include the Xiangling, Fujiang, Luochang and Jianwu synclines (Figure 1C). In contrast, higher V_p and V_s expressions are revealed beneath the Changning-Shuanghe anticline system and Yuhe anticline up to 1 km depth, as a result of the older more consolidated rocks elevated to this level by compression. To our understanding, this is the first study that incorporates additional catalog arrival data from local stations with very short epicentral distances (4–40 km) to the Changning M_s6.0 main shock and aftershocks compared to previous studies, to obtain high resolution velocity structure beneath the southern Sichuan basin and accurately relocate the highly destructive M_s6.0 Changning earthquake, associated aftershocks and general seismicity beneath the studied region. The estimation of *in situ* V_p/V_s ratios using the Wadati diagram (Wadati, 1933) and the method by Lin and Shearer (2007) that is based on differential times of cross-correlated waveforms, yielded low and high V_p/V_s ratios for selected clusters within the salt mining field on the Changning-Shuanghe anticline system (Supplementary Figure S9) and the shale gas field on the Jianwu syncline (Supplementary Figure S10), respectively, which correlate with the V_p/V_s expressions resolved by seismic tomography, thereby validate our inverted velocity models and relocated earthquakes.

Compared to velocity models of Zuo et al. (2020), overall, our V_p and V_s models are relatively lower above ~5 km depth and higher below ~5 km depth (Supplementary Figure S10, 11). This is mainly because the two studies use different initial velocity models (Figure 4B). For the same regional dataset, the RMS travel time residual for the initial 1-D models used in Zuo et al. (2020) is 0.7391 s, while it is 0.3297 s for the initial 1-D models used in this study. This indicates that the 1-D initial models used in this study are more appropriate for the area in the absence of reliable 3-D model, which is preferable, given its robustness.

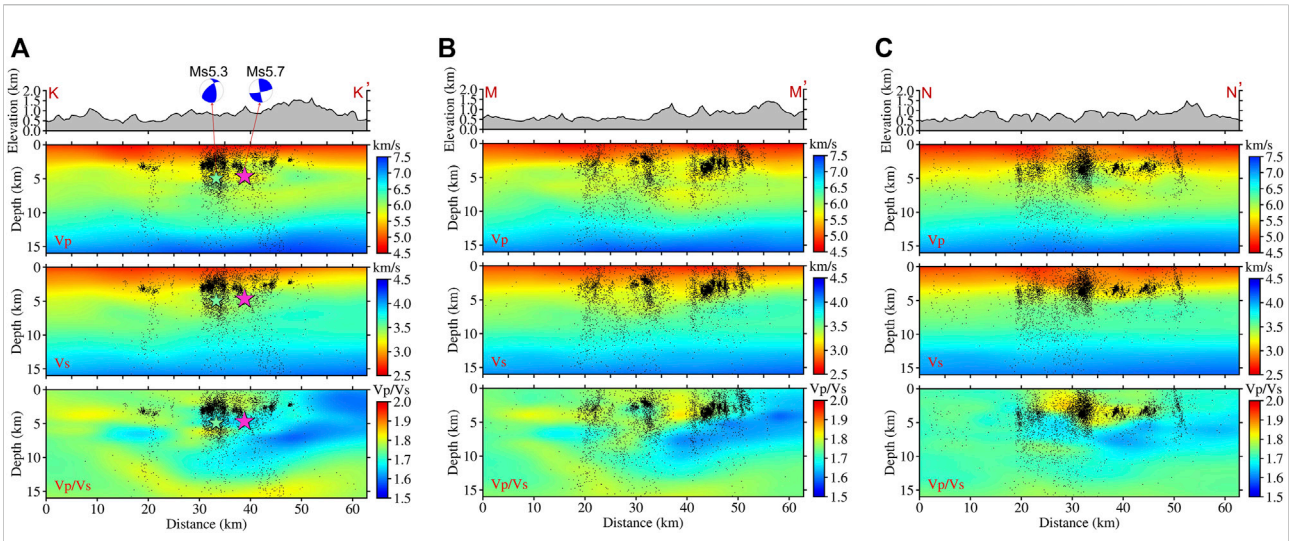

FIGURE 11
Cross-sections of V_p, V_s and V_p/V_s models along different vertical profiles within Xingwen shale gas exploitation region. **(A)** KK′. **(B)** MM′. **(C)** NN′. Black dots are horizontal projections of seismic events within 2.5 km on both sides of the profile. The lemon green and pink stars on profile KK′ represent the M_s 5.3 Gongxian and M_s 5.7 Xingwen earthquakes, respectively. See Figure 1B for profile directions.

Next, we interpret the resultant velocity models and discuss the characteristic connection between structural deformations, relocated seismicity and prolonged fluid injection beneath the southern Sichuan Basin. Our principal conclusions are described in detail based on geologic, tomographic, outcrop, induced seismicity and reflection seismic observations.

5.1 Earthquake locations for large induced earthquakes in southwestern Sichuan basin

Due to the usage of local stations, our study yielded enhanced earthquake relocation results. The Changning M_s6.0 earthquake was relocated at hypocenter of 1.6 km, with aftershocks of moderate to major magnitudes that span 1.7 km–9.1 km (Figure 10). The focal depth of this main shock is obviously shallower than the corresponding centroid depth of 3 km computed by Yi et al. (2019) using the cut-and-paste method. The hypocenter estimated from TomoDDMC represents the rupture initiation point using P- and S-wave first arrivals, while the centroid depth represents the average depth of the rupture area of the earthquake. Therefore, a hypocenter relocated at 1.6 km for the Changning main shock is consistent with deeper centroid depth. Display of the relocated epicenters of the Changning M_s6.0 earthquake and associated M_s>5.0 aftershock sequence on the Changning geologic map (Figure 1C) reveals alignment with some previously interpreted faults, thereby suggesting that the sequence ruptured several faults in an interchanging style following the mainshock. Previous InSAR inversions show that the Changning M_s6.0 mainshock initiated at depth shallower than 3 km, with the sequence rupturing a single seismogenic fault in the SE-NW direction (Wang S. et al., 2020), which is extremely improbable, given that several faults segment the Changning anticline (Liu et al., 2021). However, our interpretation of geometry comprising of multiple faults is further supported by the postulation of rupture geometry involving a previously mapped major fault and slip on a shallow blind fault for the Changning mainshock by Yang et al. (2020).

Similarly, the obtained centroid depths of 3 km and 1.8 km for the Xingwen M_s5.7 and Gongxian M_s5.3 respectively, using the generalized cut-and-paste method (Lei et al., 2019b), validates the corresponding deeper hypocenters of 5.6 km and 5.9 km from this study, respectively (Figure 11A). Likewise, our results are consistent with the 1.0 km and 1.6 km centroid depths obtained from InSAR inversions by Wang et al. (2022). In order to further validate our earthquake relocation results, we compared the arrival times predicted by our velocity model with the picked arrival times on individual waveforms, and great matching is observed (Supplementary Figure S11).

5.2 Structural velocity relationship with relocated seismicity in Changning salt mining zone

From the depth slices and vertical cross-sections of V_p, V_s and V_p/V_s images, our results show that the Changning M_s6.0 main shock occurred at the transitional area from low-V_s region to high-V_s region that is characterized by moderately high V_p/V_s

expression (Figure 10). The depth slice at 1 km through our velocity model remarkably outlines two zones marked by low V_s that corresponds to high V_p/V_s expression and high V_s that corresponds to low V_p/V_s expression, which correlate with the Yutan anticline and the Changning-Shuanghe anticline respectively. The characteristic high V_p/V_s expression beneath the Yutan anticline at this level could be due to considerably lowered V_s, possibly resulting from accumulation of severe water loss resulting from long term injection of fluids by salt mining operation in the region. In addition, given that the Yutan and the Changning-Shuanghe anticlines dip towards the northwest, it is highly likely for injected fluids to migrate to the northwestern Yutan anticline, thus significantly lowering V_s. On the other hand, the high V_s expression beneath the Changning-Shuanghe anticline that corresponds to low V_p/V_s expression is believed to be representative of the highly brittle Cambrian to Ordovician aged formations beneath the regions, which have not been influenced by injected fluids due to segmentation by northeast-southwest trending Changning faults and northwestern fluid migration. Our result is partly consistent with the preceding research by Zuo et al. (2020), which found that the Changning M_s6.0 earthquake is situated at the edge of a high velocity expression (see Supplementary Figures S10, S11 for the differences), and agrees with extreme water loss reported to be associated with decades long dissolution salt mining in the region (Ruan et al., 2008; Sun et al., 2017; Lei et al., 2019b; Yi et al., 2019; Liu and Zahradnik, 2020). Similarly, while studying the significance of tomographic edge zones for large earthquakes in Taiwan, Wang and Kao (2019) reached the conclusion that major earthquakes are located within the transition zone from high V_p/V_s to low V_p/V_s expression. Likewise, the Changning M>5 aftershocks are also located within structural velocity area that is analogous to the Changning M_s6.0 main shock (Figure 10). Generally, seismicity beneath the Changning-Shuanghe anticlinal system in the Changning salt mining region is associated with zones of relatively high V_p and high V_s expressions that mainly correspond to a dipping significantly low V_p/V_s area (Figure 10). The high V_s and low V_p/V_s expressions correspond to zones that are predominantly composed of highly fractured brittle Cambrian to Ordovician aged formations, which can more easily accumulate stresses and thus favor induced seismicity (Lei et al., 2020). This scenario is similar to the tomography study in the San Jacinto fault zone of southern California, where seismicity is clearly associated with low V_p/V_s expressions (Fang et al., 2019). This dipping low V_p/V_s area determined from TomoDDMC is further corroborated by estimated V_p/V_s value of 1.62 from Wadati diagram and *in-situ* V_p/V_s value of 1.62 estimated by the method of Lin and Shearer (2007) using the clustered events located in the low V_p/V_s area (Supplementary Figure S9).

In addition, our results show a high V_p/V_s area that correlates with moderately high V_p and low V_s zones that extends up to ~4 km depth (see depth slices at 1–4 km in Supplementary Figures S6–S8 and Figure 9, as well as cross-sections in Figure 10A), and is relatively centralized on profile AA′, but occurs to the northeastern part of the profiles taken perpendicular to AA' (Figure 10). This zone suggests possible evidence of formations that have been influenced by migrated fresh water resulting from severe water loss due to extensive prolonged injection through several deep wells, within 2.7–3 km interval for salt mining (Lei et al., 2020). Thurber et al. (1995) and Chiarabba and Amato (2003) postulated that shear forces diminish abruptly towards the uppermost end of a fault that terminates within a zone characterized by significant V_p/V_s increase, resulting in upward cut-off of rupture. Similarly, Doi et al. (2013) concluded that an environment characterized by low V_s and relatively high V_p/V_s would significantly inhibit the progress of earthquake ruptures. Figure 10A shows low V_p/V_s expression to the southeast of the Changning main shock and high V_p/V_s zone to the northwest of the main shock that extends from roughly 10 km–25 km along profile AA'. The northwestern high V_p/V_s zone correlates with zones of co-seismic InSAR observations and slip models documented by Wang S. et al. (2020), which found that the Changning M_s6.0 main shock resulted in major deformations from surface to ~3 km depth. Similarly, zones of co-seismic surface deformations of the Changning M_s6.0 main shock determined from field mapping by Jiang et al. (2020), correspond to the edges of the northwesterly high V_p/V_s expression. Figure 1B shows location of the areas that experienced co-seismic surface deformations after Jiang et al. (2020), which are also projected on the V_p/V_s values at 1 km depth slice and are associated with edges of high V_p/V_s expressions, directly above the mainshock and the M_s5.4 aftershock. We observe that this very high V_p/V_s zone that extends up to about 11 km in the northwestern direction is mostly without co-seismic surface deformations, except at its edges directly above the mainshock and the M_s5.4 aftershock, where a few closely spaced co-seismic surface deformations occur (Blue circles in Figure 1B and Vp/Vs at Z=1 km in Figure 9). Considering the clear correlation between the high V_p/V_s expression associated with the Changning Ms6.0 mainshock (This study) and the distribution of co-seismic surface deformations of the Changning M_s6.0 earthquake (Jiang et al., 2020; Wang S. et al., 2020), we infer the rupture associated with the Changning M_s6.0 earthquake to be mostly confined within the low V_p/V_s zone dipping in the northwest direction, which coincides with the northwestward rupture direction determined by Li et al. (2020), with the exception of the zones directly above the mainshock and the M_s5.4 aftershock that are characterized by major faults. The shallow hypocenter of the Changning main shock, associated slip and presence of these major faults are believed to have contributed to the localization of co-seismic surface deformations only in these two zones. Therefore, we posit that the high V_p/V_s zone predominantly acts as an effective upward terminator of rupture, thereby yielding no co-seismic surface deformations, except for regions characterized by seismically active faults.

5.3 Structural velocity relationship with relocated seismicity in Xingwen shale gas block

Within the Changning shale gas block, high-resolution velocity models and seismic relocations reveal the characteristic connections between small seismic events and variations in velocity structure. In general, the relocated earthquakes are profoundly distributed into various clusters, many of which are linear in nature (Figure 11). In general, the seismic events occur as lineaments with high dip angles that substantially agree with the high angle fractures and faults previously interpreted in the region. However, several lineaments of the relocated earthquakes show varying strikes, in comparison with the prior interpreted faults. Therefore, we suggest them to be sub-seismic faults or fractures.

In Figure 11, most small seismic events appear to be situated in low V_s zones and are associated with relatively high V_p/V_s expressions in the central part of the Xingwen shale gas block around latitude 28.1° and longitude 104.9°, likely indicating that they are induced by the high fluid pressures caused by fluid injections for hydraulic fracturing within the zones (Figure 9 and Supplementary Figure S8). From *in-situ* V_p/V_s estimation by the method of Lin and Shearer (2007), high V_p/V_s zone imaged from TomoDDMC also shows relatively higher V_p/V_s (Supplementary Figure S8), supporting the association of seismicity and high V_p/V_s expressions, thereby strengthening the interpretation of these earthquakes as fluid induced. However, we notice that some events are located in relatively low V_p/V_s areas around this high V_p/V_s zone (Figure 9 and Supplementary Figure S8), For example, in the zone around latitude 28.15° and longitude 105.0°, the seismicity is associated with relatively low V_p/V_s values, similar to the results over a small area covering two hydraulic fracturing well pads in Tan et al. (2020). It is also noticed that the M_s5.3 Gongixan and M_s5.7 Xingwen earthquakes are associated with relatively low V_p/V_s expressions (Figure 11). This suggests that low V_p/V_s areas in the depths around 5 km represent zones that could act as asperities for moderately strong earthquakes induced by hydraulic fracturing.

Similarly, Chen et al. (2017), Chen et al. (2018) and Zuo et al. (2020) suggested that the existence of fluid-filled fractures could yield low velocity expressions around hydraulic fracturing zones. Our results largely agree with previous V_p and V_s models obtained by Long et al. (2020), as well as those of Zuo et al. (2020), but with some notable differences. For example, in contrast to the velocity models by Long et al. (2020), Zhang et al. (2020) and Zuo et al. (2020), the shallow subsurface (up to ~4 km depth) in our model is evidently characterized by low V_p and V_s expressions that correlate with low velocity sedimentary strata within this zone. In addition, inverted 3D subsurface magnetic susceptibility model by Wang J. et al. (2020) found evidence of intrusion of the Neoproterozoic basement rock only at about 15 km depth, not at shallow regions as imaged in Long et al. (2020), Zhang et al. (2020) and Zuo et al. (2020).

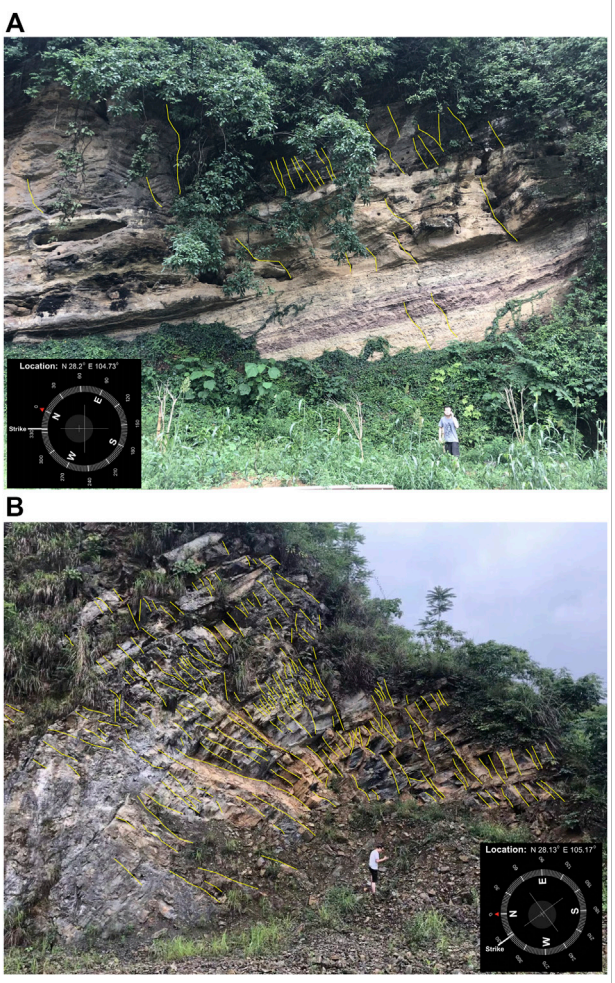

FIGURE 12
Mesozoic to Cenozoic sedimentary outcrops within the Xingwen shale gas region with numerous high-angle fractures of dips that are predominantly >40°, interpreted to be surface equivalents of the deeper well developed thrust and oblique fault zones. **(A)** Outcrop location 1. **(B)** Outcrop location 2.

5.4 Inferred subsurface structural architecture and Sichuan basement characterization

We carried out field work that focused on characterization of the fracture and fault systems in sedimentary outcrops of the Mesozoic to Cenozoic aged formations within the southern part of the studied region (see the red squares in Figure 1B for location of outcrops).

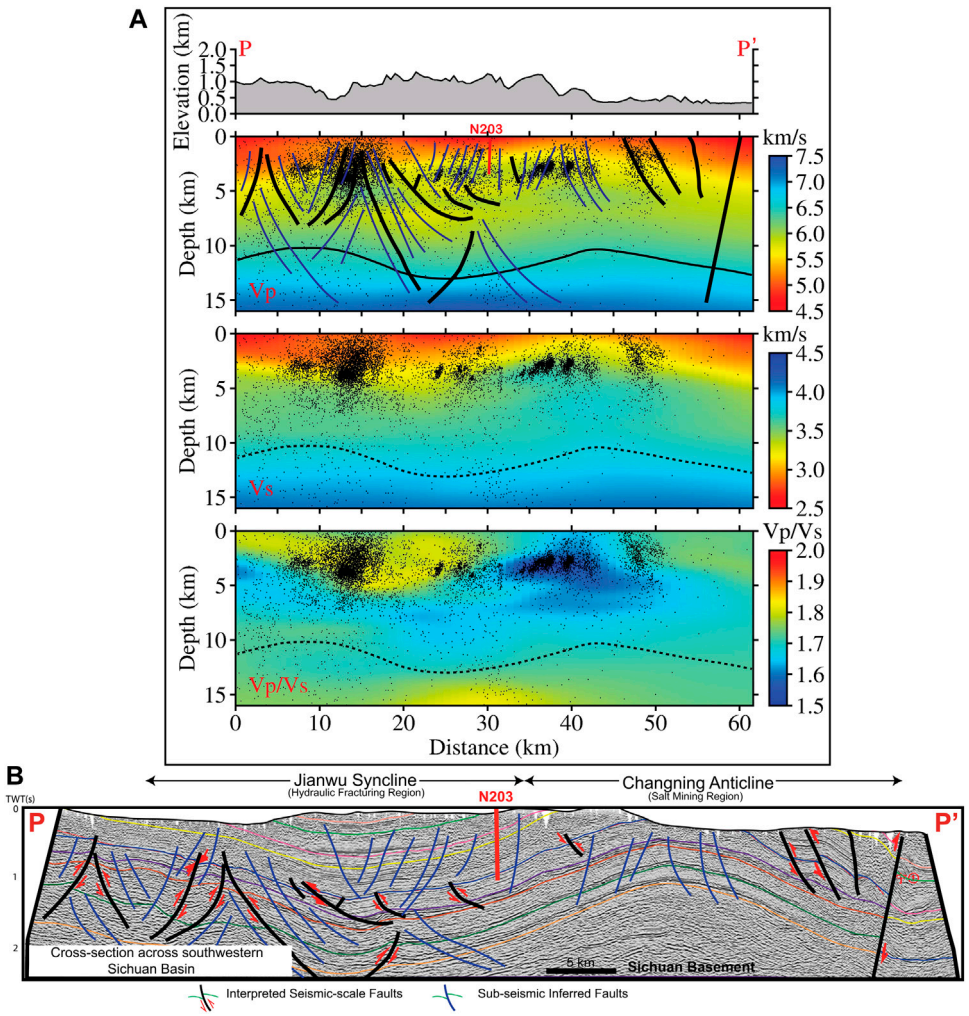

FIGURE 13
Characterization of Sichuan Basement and subsurface fault structures. **(A)** Cross-section of V_p, V_s and V_p/V_s models along PP′ profile showing basement structure with 6.5 km/s V_p contour. Black dots are horizontal projections of seismic events within 2.5 km on both sides of the profile. **(B)** Seismic interpretation of reflection seismic profile alone PP′, modified from He et al. (2019). Thick black lines represent interpreted seismic faults, while blue thin lines represent inferred sub-seismic faults illuminated by the earthquake lineaments.

The exposures reveal numerous high angle fracture networks, many of which exhibit brittle shear features (Figure 12). These brittle shear indicators are prevalent in shear zones characterized by intense rotational tectonic deformation, such as the Sichuan basin (Wang et al., 2016; Lei et al., 2020), which includes our study area. Analysis of the fractures showed thrust and oblique reverse faults to be predominant with a few oblique normal faults that have slight displacements of 2–21 cm.

Even though majority of the fractures are broadly distributed, we discovered various distinct zones of severe deformation with numerous cramped fractures. However, both damage zones predominantly exhibit conjugate shear fracture sets, orderly increment of fracture frequency as the center is approached, dense arrangement of several parallel and bifurcating fractures with miniature local gouges, mineralized fractures and hierarchical fracturing with reverse slip components (Figure 12). Therefore, we interpret these deformation zones as the outcrop equivalents of the deep-seated thrust, normal and strike-slip faults within the Sichuan sedimentary column, and thus posit that the Sinian Dengying Formation (target for salt mining) and Silurian Longmaxi Formation (target for shale gas exploitation), as well as the Tertiary formations (cap rocks) overlying them are highly fractured and faulted. Our interpretation stems from previous works that correlate subsurface faults with their analyzed outcrop counterparts (Segall and Pollard, 1983; Kolawole et al., 2019). It is evident

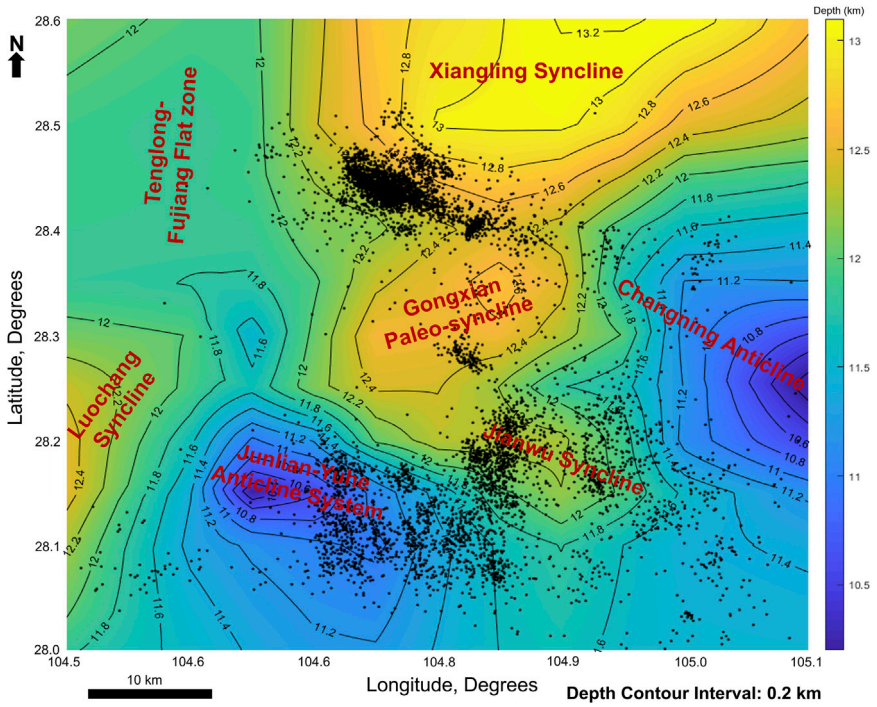

FIGURE 14
Depth structure map of top of basement rocks beneath our study area showing induced seismicity associated with the basement, as well as structural high and low areas that significantly agree with local geology.

from surface (outcrop) and subsurface characterizations of faults and fractures that fracture density and intensity of deformation are maximal at the center, but reduces away from the fracture or fault core (Barton and Zoback, 1992; Sagy et al., 2001).

Our newly obtained high-resolution earthquake locations and V_p, V_s and V_p/V_s models can also be used to characterize the subsurface fault and basement structures beneath the seismically active regions that cover a 4,900 km^2 area, which includes the Changning salt mining and Xingwen shale gas zones. As mentioned, the high-resolution relocated earthquake epicenters are spatially distributed as clusters that form numerous obvious lineaments, some of which align with previously interpreted fault traces. Similar lineament features that no doubt align with some faults interpreted on reflection seismic profile are displayed by the jointly inverted hypocenters (Figures 13A,B). Therefore, interpretation of these lineaments as traces of seismically active faults is reasonable (e.g., Kolawole et al., 2019). This interpretation is further buttressed by the trivial spatial and temporal location uncertainties determined for the 2018 to 2019 seismic events and also for the 2015 to 2017 events, which represent the majority of the down-to-basement lineament clusters. On that note, we interpret the unaligned lineaments as sub-seismic fault traces that are newly illuminated by our relocated hypocenters.

Given the growing induced seismicity beneath the Sichuan Basin, and knowing that slip on basement penetrating faults potentially result in large magnitude earthquakes (Lu et al., 2021), delineation of the basement architecture is of utmost importance. In this study, we estimate the top of the Sichuan basement with the 6.5 km/s P-wave velocity contour (Figure 13A), which was inferred from integrated 3D reflection seismic and well data assisted velocity model by Wang et al. (2016). We went further to extract the depth values of the 6.5 km/s V_p contour along the grid lines and performed enhanced contouring on them to generate the depth structure map of top of basement rocks beneath the southwestern Sichuan Basin (Figure 14). The basement structural map shows superb agreement with existing large scale geologic features in the basin, such as the Changning-Shuanghe anticlinal system, Jianwu syncline, Xiangling syncline, Tenglong anticline, Luochang syncline and Yuhe-Junlian anticlinal system (Figure 1), which are respectively underlain by high, low, low, high, low and high basement morphologies (Figure 14). Overall, the crystalline basement shows P-wave speeds between 6.5 and 7.3 km/s and an undulating top structure with depths ranging

from 10.2 km in the shallow parts to 13 km in the deeper zones. It can be clearly seen that the earthquakes have been induced within the basement and along some basement faults, most of which are concentrated in the Yuhe-Junlian anticlinal system (Figure 14). The deep basement characterization presented here corresponds to the sedimentary foredeeps of the western Longmenshan thrust belt that are composed of Late Triassic to Cretaceous terrigeneous clastics (Wang et al., 2016), and are consistent with their result of top of basement structure depth ranging from 9 to 12 km within southwestern Sichuan basin. Our results are likewise supported by the 3D subsurface magnetic susceptibility model by Wang J. et al. (2020), which found that the southwestern Sichuan Basin is covered by 10–14 km thick non-magnetic sedimentary rocks of Neoproterozoic to Cenozoic period that overly the magnetic pre-Sinian (early Neoproterozoic) Sichuan basement, and are relatively in agreement with the 8 km and 10 km top of basement depth derived from the velocity structure inverted from receiver function of seismic stations ROC and PAL respectively, situated between 100 and 120 km northeast of our study area near Chongqing in the Sichuan basin (Wang et al., 2012). Superimposition of the structural morphology of the top of the basement on the corresponding V_s and V_p/V_s models along profile PP' reveal obvious high V_s and relatively high V_p/V_s characteristics of the Sichuan basement in this region. The enhanced characterization of the V_p, V_s, V_p/V_s and depth structure of the Sichuan basement presented in this study is new for earthquake tomographic studies in the region at remarkably high-resolution of 5 by 5 km in longitude and latitude directions, and we posit that dense seismicity data significantly contributes to improved imaging resolution in earthquake tomography.

6 Conclusion

In this study we present new high-resolution induced seismicity relocations, V_p, V_s and V_p/V_s structures of the upper crust down to 16 km beneath the southern Sichuan basin, using the V_p/V_s consistency-constrained double difference seismic tomography method and extensive high-quality combined phase data of 36,314 earthquakes from our local array and the regional array. These data sets were used to unravel the structural velocity control on induced seismicity beneath the Changning salt mining and Xingwen shale gas regions in the basin. The Changning M_s6.0 main shock and the Changning M_s5.3 aftershock are relocated within the shallow subsurface, above the target Dengying Formation (salt rock), at the transitional area from low-velocity to high-velocity structure that is characterized by moderately high V_p/V_s expression, while the other three major aftershocks of M_s5.1, M_s5.4 and M_s5.6 that likewise occurred on the Changning-Shuanghe anticlinal system are characterized by low V_p/V_s expressions. Generally, seismicity beneath the Changning-Shuanghe anticlinal system in the Changning salt mining region is associated with zones of relatively high V_p and V_s expressions that mainly correspond to an inclined significantly low V_p/V_s area. Within the Xingwen shale gas exploitation area, the Xingwen M_s5.7 main shock and Gongxian M_s5.3 main shock are located around low V_p/V_s expressions, indicating that moderately strong earthquakes in this region could be structurally controlled. For most of the small earthquakes in the Xingwen shale gas block, they are associated with relatively high V_p/V_s expressions, which may indicate regions where seismicity is induced by excess pore fluid pressure due to hydraulic fracturing. In general, the relocated earthquakes are profoundly distributed into various lineaments with dips and strike directions that partly align with previously interpreted faults, suggesting illumination of previously unrecognized pre-existing and potentially sub-seismic faults.

Our results also reveal a crystalline basement complex at the bottom of sedimentary strata, which shows P-wave speeds between 6.5 and 7.3 km/s and has an undulating top structure that conforms with local geology and ranges from 10.2 km in the shallow parts to 13 km in the deeper zones (Figure 14). Detailed structural architecture of the early Neoproterozoic (pre-Sinian) Sichuan basement beneath the Sichuan basin has not been previously resolved by earthquake tomographic studies. A noteworthy observation from this integrated structural evaluation is the clear characterization of down-to-basement lineaments, which are reasonably interpreted as reactivated fault traces beneath the Xingwen hydraulic fracturing area (Figures 10, 11, 13). This serves as a direct indication of the linkage between the Silurian shale, which is the target formation for hydraulic fracturing for shale gas production, and the basal Sichuan basement structures. Where such fluid migration pathways exist, they can promote seismicity generation by prolonged fluid injection. Therefore, we speculate that the Sichuan basement could be susceptible to extensive earthquake occurrence resulting from the reactivation of pre-existing and potentially sub-seismic basement faults and/or fractures.

Data availability statement

The datasets presented in this article are not readily available because we do not have the right to release the waveform data from the regional stations, which have to go through the China Earthquake Administration (CEA) authority. Requests to access the passive seismic data from our local stations should be directed to the corresponding author. TomoDD has been released by the authors through workshops and will soon be available through a repository.

The event locations and velocity models from this study can be accessed *via* https://zenodo.org/record/7312205.

Author contributions

Conceptualization: UA and HZ Methods: UA, HZ, YT, and JQ Interpretation: All Authors Writing: UA and HZ Supervision: HZ.

Funding

This research is supported by National Natural Science Foundation of China under grants U1839205 and 41961134001.

Acknowledgments

We acknowledge the intellectual and material contributions of CAS-TWAS President's Fellowship. We are grateful for the comments from the Editor LL and the two reviewers XL and GR that helped to improve the paper. We thank Shaobo Yang, Sheng Dong, Shoucheng Han, Bingwen Wang and Yuqi Huang for their technical support.

Conflict of interest

The authors declare that the research was conducted in the absence of any commercial or financial relationships that could be construed as a potential conflict of interest.

The handling editor LL declared a past co-authorship with the author YT.

Publisher's note

All claims expressed in this article are solely those of the authors and do not necessarily represent those of their affiliated organizations, or those of the publisher, the editors and the reviewers. Any product that may be evaluated in this article, or claim that may be made by its manufacturer, is not guaranteed or endorsed by the publisher.

Supplementary material

The Supplementary Material for this article can be found online at: https://www.frontiersin.org/articles/10.3389/feart.2022.1082122/full#supplementary-material

References

Atkinson, G. M., Eaton, D. W., Ghofrani, H., Walker, D., Cheadle, B., Schultz, R., et al. (2016). Hydraulic fracturing and seismicity in the western Canada sedimentary basin. *Seismol. Res. Lett.* 87, 631–647. doi:10.1785/0220150263

Barton, C. A., and Zoback, M. D. (1992). Self-similar distribution and properties of macroscopic fractures at depth in crystalline rock in the Cajon Pass scientific drill hole. *J. Geophys. Res.* 97, 5181–5200. doi:10.1029/91jb01674

Burchfiel, B. C., Chen, Z. L., Liu, Z. P., and Royden, L. H. (1995). Tectonics of the Longmen Shan and adjacent regions, central China. *Int. Geol. Rev.* 37, 661–735. doi:10.1080/00206819509465424

Chen, S. F., and Wilson, C. J. L. (1996). Emplacement of the longmen Shan thrust-nappe belt along the eastern margin of the Tibetan plateau. *J. Struct. Geol.* 18, 413–419. doi:10.1016/0191-8141(95)00096-8

Chen, Y., Zhang, H., Miao, Y., Zhang, Y., and Liu, Q. (2017). Back azimuth constrained double-difference seismic location and tomography for downhole microseismic monitoring. *Phys. Earth Planet. Inter.* 264, 35–46. doi:10.1016/j.pepi.2016.10.003

Chen, H., Meng, X., Niu, F., Tang, Y., Yin, C., and Wu, F. (2018). Microseismic monitoring of stimulating shale gas reservoir in SW China: 2. Spatial clustering controlled by the preexisting faults and fractures. *J. Geophys. Res. Solid Earth* 123, 1659–1672. doi:10.1002/2017JB014491

Chiarabba, C., and Amato, A. (2003). V_P and V_P/V_S images 391 in the MW 6.0 colfiorito fault region (central Italy): A contribution to the understanding of seismotectonic and seismogenic processes. *J. Geophys. Res.* 108. doi:10.1029/2001JB001665

Deng, Q., Zhang, P., Ran, Y., Yang, X., Min, W., and Chu, Q. (2003). Basic characteristics of active tectonics of China. *Sci. China, Ser. D. Earth Sci.* 46 (4), 356–372.

Deng, B., Liu, S. G., Jansa, L., Cheng, Y., Li, Z. W., Liu, S., et al. (2012). Sedimentary record of late triassic transpressional tectonics of the longmenshan thrust belt, SW China. *J. Asian Earth Sci.* 48, 43–55. doi:10.1016/j.jseaes.2011.12.019

Deng, B., Liu, S. G., Jiang, L., Zhao, G. P., Huang, R., Li, Z. W., et al. (2018). Tectonic uplift of the Xichang Basin (SE Tibetan Plateau) revealed by structural geology and thermochronology data. *Basin Res.* 30, 75–96. doi:10.1111/bre.12243

Doi, I., Noda, S., Iio, Y., Horiuchi, S., and Sekiguchi, S. (2013). Relationship between hypocentral distributions and V_P/V_S ratio structures inferred from dense seismic array data: a case study of the 1984 Western nagano prefecture earthquake, central Japan. *Geophys. J. Int.* 195, 1323–1336. doi:10.1093/gji/ggt312

Dong, Y. P., Zhang, G. W., Neubauer, F., Liu, X. M., Genser, J., and Hauzenberger, C. (2011). Tectonic evolution of the Qinling orogen, China: Review and synthesis. *J. Asian Earth Sci.* 41, 213–237. doi:10.1016/j.jseaes.2011.03.002

Eberhart-Phillips, D. (1986). Three-dimensional velocity structure in northern California Coast Ranges from inversion of local earthquake arrival times. *Bull. Seismol. Soc. Am.* 76 (4), 1025–1052.

Eberhart-Phillips, D. (1990). Three-dimensional P and S velocity structure in the Coalinga region, California. *J. Geophys. Res.* 95 (B10), 15343–15363. doi:10.1029/jb095ib10p15343

Efron, B., and Gong, G. (1983). A leisurely look at the bootstrap, the jackknife, and cross-validation. *Am. Stat.* 37 (1), 36–48. doi:10.2307/2685844

Efron, B., and Tibshirani, R. (1991). Statistical data analysis in the computer age. *Science* 253, 390–395. doi:10.1126/science.253.5018.390

Ellsworth, W. L. (2013). Injection-induced earthquakes. *Science* 341, 1225942–1226017. doi:10.1126/science.1225942

Fang, H., Yao, H., Zhang, H., Thurber, C., Ben-Zion, Y., and van der Hilst, R. D. (2019). V_p/V_s tomography in the southern California plate boundary region using body- and surface-wave traveltime data. *Geophys. J. Int.* 216, 609–620. doi:10.1093/gji/ggy458

Guo, H., and Zhang, H. (2017). Development of double-pair double difference earthquake location algorithm for improving earthquake locations. *Geophys. J. Int.* 208, 333–348. doi:10.1093/gji/ggw397

Guo, H., Zhang, H., and Froment, B. (2018). Structural control on earthquake behaviors revealed by high-resolution V_P/V_S imaging along the Gofar transform fault, East Pacific Rise. *Earth Planet. Sci. Lett.* 499, 243–255. doi:10.1016/j.epsl.2018.07.037

He, D., Lu, R., Huang, H., Wang, X., Jiang, H., and Zhang, W. (2019). Tectonic and geological setting of the earthquake hazards in the Changning shale gas development zone, Sichuan Basin, SW China. *Pet. Explor. Dev.* 46 (5), 1051–1064. doi:10.1016/S1876-3804(19)60262-4

Huang, H. H., Wu, Y. M., Song, X., Chang, C. H., Lee, S. J., Chang, T. M., et al. (2014). Joint V_p and v_s tomography of taiwan: Implications for subduction-collision orogeny. *Earth Planet. Sci. Lett.* 392, 177–191. doi:10.1016/j.epsl.2014.02.026

Hubbard, J., and Shaw, J. H. (2009). Uplift of the longmen Shan and Tibetan plateau, and the 2008 wenchuan (M = 7.9) earthquake. *Nature* 458 (7235), 194–197. doi:10.1038/nature07837

Hubbard, J. A., Shaw, J. H., and Klinger, Y. (2010). Structural setting of the 2008 Mw 7.9 Wenchuan, China, earthquake. *Bull. Seismol. Soc. Am.* 100 (5B), 2713–2735. doi:10.1785/0120090341

Humphreys, E., and Clayton, R. W. (1988). Adaptation of back projection tomography to seismic travel time problems. *J. Geophys. Res.* 93 (B2), 1073–1085. doi:10.1029/jb093ib02p01073

Improta, L., Bagh, S., De Gori, P., Valoroso, L., Pastori, M., Piccinini, D., et al. (2017). Reservoir structure and wastewater-induced seismicity at the Val d'Agri oilfield (Italy) shown by three-dimensional V_P and V_P/V_S local earthquake tomography. *J. Geophys. Res. Solid Earth* 122 (11), 9050–9082. doi:10.1002/2017jb014725

Jia, D., Wei, G., Chen, Z., Li, B., Zeng, Q., and Yang, G. (2006). Longmen Shan fold-thrust belt and its relation to the Western Sichuan Basin in central China: New insights from hydrocarbon exploration. *Am. Assoc. Pet. Geol. Bull.* 90 (9), 1425–1447. doi:10.1306/03230605076

Jiang, D., Zhang, S., and Ding, R. (2020). Surface deformation and tectonic background of the 2019 M_s 6.0 Changning earthquake, Sichuan Basin, SW China. *J. Asian Earth Sci.* 200, 104493–104517. doi:10.1016/j.jseaes.2020.104493

Kirby, E., Reiners, P. W., Krol, M. A., Whipple, K. X., Hodges, K. V., Farley, K. A., et al. (2002). Late Cenozoic evolution of the eastern margin of the Tibetan Plateau: Inferences from 40 Ar/39 Ar and (U-Th)/He thermochronology. *Tectonics* 21 (1), 1-1–1-20. doi:10.1029/2000TC001246

Kolawole, F., Johnston, C. S., Morgan, C. B., Chang, J. C., Marfurt, K. J., Lockner, D. A., et al. (2019). The susceptibility of Oklahoma's basement to seismic reactivation. *Nat. Geosci.* 12 (10), 839–844. doi:10.1038/s41561-019-0440-5

Lei, X., Yu, G., Ma, S., Wen, X., and Wang, Q. (2008). Earthquakes induced by water injection at ~ 3 km depth within the Rongchang gas field, Chongqing, China. *J. Geophys. Res.* 113, B10310–B10312. doi:10.1029/2008jb005604

Lei, X., Ma, S., Chen, W., Pang, C., Zeng, J., and Jiang, B. (2013). A detailed view of the injection-induced seismicity in a natural gas reservoir in Zigong, southwestern Sichuan Basin, China. *J. Geophys. Res. Solid Earth* 118, 4296–4311. doi:10.1002/jgrb.50310

Lei, X., Huang, D., Su, J., Jiang, G., Wang, X., Wang, H., et al. (2017). Fault reactivation and earthquakes with magnitudes of up to Mw4.7 induced by shale-gas hydraulic fracturing in Sichuan Basin, China. *Sci. Rep.* 7, 7971. doi:10.1038/s41598-017-08557-y

Lei, X., Wang, Z., and Su, J. (2019a). Possible link between long-term and short-term water injections and earthquakes in salt mine and shale gas site in Changning, south Sichuan Basin, China. *Earth Planet. Phys.* 3 (6), 510–525. doi:10.26464/epp2019052

Lei, X., Wang, Z., and Su, J. (2019b). The December 2018 ML 5.7 and January 2019 ML 5.3 earthquakes in south Sichuan Basin induced by shale gas hydraulic fracturing. *Seismol. Res. Lett.* 90 (3), 1099–1110. doi:10.1785/0220190029

Lei, X., Su, J., and Wang, Z. (2020). Growing seismicity in the Sichuan Basin and its association with industrial activities. *Sci. China Earth Sci.* 63, 1633–1660. doi:10.1007/s11430-020-9646-x

Li, W. X., and Li, X. H. (2003). Adakitic granites within the NE jiangxi ophiolites, south China: geochemical and Nd isotopic evidence. *Precambrian Res.* 122, 29–44. doi:10.1016/s0301-9268(02)00206-1

Li, Y., Allen, P. A., Densmore, A. L., and Qiang, X. (2003). Evolution of the longmen Shan foreland basin (western sichuan, China) during the late triassic indosinian orogeny. *Basin Res.* 15, 117–138. doi:10.1046/j.1365-2117.2003.00197.x

Li, J., Xie, Z. Y., Dai, J. X., Zhang, S. C., Zhu, G. Y., and Liu, Z. L. (2005). Geochemistry and origin of sour gas accumulations in the northeastern Sichuan Basin, SW China. *Org. Geochem.* 36 (12), 1703–1716. doi:10.1016/j.orggeochem.2005.08.006

Li, W., Ni, S., Zang, C., and Chu, R. (2020). Rupture directivity of the 2019 Mw 5.8 changning, sichuan, China, earthquake and implication for induced seismicity. *Bull. Seismol. Soc. Am.* 110, 2138–2153. doi:10.1785/0120200013

Lin, G., and Shearer, P. M. (2007). Estimating local V_p/V_s ratios within similar earthquake clusters. *Bull. Seismol. Soc. Am.* 97, 379–388. doi:10.1785/0120060115

Liu, J., and Zahradník, J. (2020). The 2019 Mw 5.7 changning earthquake, Sichuan Basin, China: A shallow doublet with different faulting styles. *Geophys. Res. Lett.* 47. doi:10.1029/2019gl085408

Liu, S. F., Steel, R., and Zhang, G. W. (2005). Mesozoic sedimentary basin development and tectonic implication, northern Yangtze block, eastern China: Record of continent–continent collision. *J. Asian Earth Sci.* 25, 9–27. doi:10.1016/j.jseaes.2004.01.010

Liu, S. G., Deng, B., Li, Z. W., and Sun, W. (2012). Architecture of basin-mountain systems and their influences on gas distribution: A case study from the Sichuan basin, south China. *J. Asian Earth Sci.* 47, 204–215. doi:10.1016/j.jseaes.2011.10.012

Liu, S. G., Deng, B., Li, Z. W., Jansa, L., Liu, S., Wang, G. Z., et al. (2013). Geological evolution of the longmenshan intracontinental composite orogen and the eastern margin of the Tibetan plateau. *J. Earth Sci.* 24 (6), 874–890. doi:10.1007/s12583-013-0391-5

Liu, S. G., Deng, B., Jansa, L., Li, Z., Sun, W., Wang, G., et al. (2017). Multi-stage basin development and hydrocarbon accumulations: A review of the Sichuan Basin at eastern margin of the Tibetan plateau. *J. Earth Sci.* 29, 307–325. Available at: http://en.earth-science.net. doi:10.1007/s12583-017-0904-8

Liu, S. G., Yang, Y., Deng, B., Zhong, Y., Wen, L., Wei, S., et al. (2021). Tectonic evolution of the Sichuan Basin, southwest China. *Earth. Sci. Rev.* 213, 103470. doi:10.1016/j.earscirev.2020.103470

Long, F., Zhang, Z. W., Qi, Y. P., Liang, M. J., Ruan, X., Wu, W. W., et al. (2020). Three dimensional velocity structure and accurate earthquake location in Changning–Gongxian area of southeast Sichuan. *Earth Planet. Phys.* 4 (2), 1–15. doi:10.26464/epp2020022

Lu, R., He, D., Liu, J.-Z., Tao, W., Huang, H., Xu, F., et al. (2021). Seismogenic faults of the changning earthquake sequence constrained by high-resolution seismic profiles in the southwestern Sichuan Basin, China. *Seismol. Res. Lett.* 92, 3757–3766. doi:10.1785/0220200302

Meng, Q. R., and Zhang, G. W. (2000). Geologic framework and tectonic evolution of the Qinling orogen, central China. *Tectonophysics* 323, 183–196. doi:10.1016/s0040-1951(00)00106-2

Meng, L., McGarr, A., Zhou, L., and Zang, Y. (2019). An investigation of seismicity induced by hydraulic fracturing in the Sichuan Basin of China based on data from a temporary seismic network. *Bull. Seismol. Soc. Am.* 109 (1), 348–357. doi:10.1785/0120180310

Roger, F., Jolivet, M., and Malavieille, J. (2010). The tectonic evolution of the songpan-garze (north tibet) and adjacent areas from proterozoic to present: A synthesis. *J. Asian Earth Sci.* 39, 254–269. doi:10.1016/j.jseaes.2010.03.008

Royden, L. H., Burchfiel, B. C., and van der Hilst, R. D. (2008). The geological evolution of the Tibetan Plateau. *Science* 321, 1054–1058. doi:10.1126/science.1155371

Ruan, X., Cheng, W., Zhang, Y., Li, J., and Chen, Y. (2008). Research of the earthquakes induced by water injections in salt mines in Changning, Sichuan. *Earthq. Res. China* 24 (3), 226–234. doi:10.3969/j.issn.1001-4683.2008.03.004 (in Chinese).

Sagy, A., Reches, Z. E., and Roman, I. (2001). Dynamic fracturing: field and experimental observations. *J. Struct. Geol.* 23, 1223–1239. doi:10.1016/s0191-8141(00)00190-5

Segall, P., and Pollard, D. D. (1983). Nucleation and growth of strike slip faults in granite. *J. Geophys. Res.* 88, 555–568. doi:10.1029/jb088ib01p00555

Shi, X., Tong, Y., Liu, W., Zhao, C., Liu, J., and Fang, J. (2019). Analysis of seismic-scale fracture system of shale reservoir and its petroleum significance: a case study of well Ning 201 area of changning block, Sichuan Basin. *Mar. Orig. Petrl. Geol.* 24 (4), 87–96. doi:10.3969/j.issn.1672-9854.2019.04.009 (in Chinese with English abstract).

Sun, X. L., Yang, P. T., and Zhang, Z. W. (2017). A study of earthquakes induced by water injection in the Changning salt mine area, SW China. *J. Asian Earth Sci.* 136, 102–109. doi:10.1016/j.jseaes.2017.01.030

Tan, Y., Hu, J., Zhang, H., Chen, Y., Qian, J., Wang, Q., et al. (2020). Hydraulic fracturing induced seismicity in the southern Sichuan Basin due to fluid diffusion inferred from seismic and injection data analysis. *Geophys. Res. Lett.* 47 (4). doi:10.1029/2019GL084885

Thurber, C. H., Atre, S. R., and Eberhart-Phillips, D. (1995). Three-dimensional V_p and v_p/v_s structure at loma prieta, California, from local earthquake tomography. *Geophys. Res. Lett.* 22, 3079–3082. doi:10.1029/95gl03077

Tian, Y. T., Kohn, B. P., Qiu, N. S., Yuan, Y. S., Hu, S. B., Gleadow, A. J. W., et al. (2018). Eocene to miocene out-of-sequence deformation in the eastern Tibetan plateau: Insights from shortening structures in the Sichuan Basin. *J. Geophys. Res. Solid Earth* 123, 1840–1855. doi:10.1002/2017JB015049

Um, J., and Thurber, C. (1987). A fast algorithm for two-point seismic ray tracing. *Bull. Seismol. Soc. Am.* 77 (3), 972–986. doi:10.1785/bssa0770030972

Wadati, K. (1933). On the travel time of earthquake waves. Part II. *Geophys. Mag.* 7, 101–111.

Wang, Z., and Kao, H. (2019). The significance of tomographic edge zones for large earthquakes in Taiwan. *J. Geophys. Res. Solid Earth* 124 (11), 11822–11839. doi:10.1029/2019jb017875

Wang, X., Ma, S., Lei, X., Guo, X., Wang, Q., Yu, G., et al. (2012). Fine velocity structure and relocation of the 2010 ml5.1 earthquake sequence in the Rongchang gas field. *Earthq. Res. China* 20 (4), 467–478.

Wang, X., Ma, S., Guo, Z., Lei, X., Xia, Y., Guo, X., et al. (2013). S-wave velocity of the crust in Three Gorges Reservoir and the adjacent region inverted from seismic ambient noise tomography. *Chin. J. Geophys.* 56 (12), 1–11. doi:10.6038/cjg20131201 (In Chinese).

Wang, M., Hubbard, J., Plesch, A., Shaw, J. H., and Wang, L. (2016). Three-dimensional seismic velocity structure in the Sichuan basin, China. *JGR. Solid Earth* 121, 1007–1022. doi:10.1002/2015JB012644

Wang, S., Jiang, G., Lei, X., Barbour, A. J., Tan, X., Xu, C., et al. (2022). Three Mw ≥ 4.7 earthquakes within the Changning (China) shale gas field ruptured shallow faults intersecting with hydraulic fracturing wells. *JGR. Solid Earth* 127, e2021JB022946. doi:10.1029/2021JB022946

Wang, J., Yao, C., Li, Z., Zheng, Y., Shen, X., Zeren, Z., et al. (2020). 3D inversion of the Sichuan Basin magnetic anomaly in South China and its geological significance. *Earth Planets Space* 72, 40–10. doi:10.1186/s40623-020-01167-5

Wang, S., Jiang, G., Weingarten, M., and Niu, Y. (2020). InSAR evidence indicates a link between fluid injection for salt mining and the 2019 Changning (China) earthquake sequence. *Geophys. Res. Lett.* 46, e2020GL087603. doi:10.1029/2020GL087603

Wang, B. J. (1989). *The sichuan hydrocarbon province. Volume 10 of petroleum geology of China*. Beijing: Petroleum Industry Press, 516. (in Chinese).

Wilson, C. J. L., Harrowfield, M. J., and Reid, A. J. (2006). Brittle modification of triassic architecture in eastern tibet: implications for the construction of the cenozoic plateau. *J. Asian Earth Sci.* 27, 341–357. doi:10.1016/j.jseaes.2005.04.004

Yan, D. P., Zhou, M. F., Song, H. L., Wang, X. W., and Malpas, J. (2003). Origin and tectonic significance of a mesozoic multi-layer over-thrust system within the Yangtze block (south China). *Tectonophysics* 361, 239–254. doi:10.1016/s0040-1951(02)00646-7

Yan, D. P., Qiu, L., Wells, M. L., Zhou, M. F., Meng, X. K., Lu, S., et al. (2018). Structural and geochronological constraints on the early mesozoic north longmen Shan thrust belt: Foreland fold-thrust propagation of the SW qinling orogenic belt, northeastern Tibetan plateau. *Tectonics* 37, 4595–4624. doi:10.1029/2018TC004986

Yang, Y., Hu, J., Chen, Q., Lei, X., Zhao, J., Li, W., et al. (2020). Shallow slip of blind fault associated with the 2019 M_s 6.0 Changning earthquake in fold-and-thrust belt in salt mines of Southeast Sichuan, China. *Geophys. J. Int.* 224, 909–922. doi:10.1093/gji/ggaa488

Yi, G. X., Long, F., Liang, M. J., Zhao, M., Wang, S. W., Gong, Y., et al. (2019). Focal mechanism solutions and seismogenic structure of the 17 June 2019 M_S6.0 Sichuan Changning earthquake sequence. *Chin. J. Geophys.* 62 (9), 3432–3447. doi:10.6038/cjg2019N0297 (in Chinese).

Zeng, X., Han, L., and Shi, Y. (2014). The april 24, 2013 changning ms 4.8 earthquake: A felt earthquake that occurred in paleozoic sediment. *Earthq. Sci.* 27 (1), 107–115. doi:10.1007/s11589-014-0062-3

Zhai, G. M. (1992). *Petroleum geology of China*. Beijing: Petroleum Industry Press. (in Chinese).

Zhang, H., and Thurber, C. H. (2003). Double-difference tomography: The method and its application to the Hayward fault, California. *Bull. Seismol. Soc. Am.* 93 (5), 1875–1889. doi:10.1785/0120020190

Zhang, H., and Thurber, C. H. (2006). Development and applications of double-difference seismic tomography. *Pure Appl. Geophys.* 163, 373–403. doi:10.1007/s00024-005-0021-y

Zhang, H., Thurber, C. H., and Bedrosian, P. (2009). Joint inversion for V_p, v_s, and v_p/v_s at SAFOD, parkfield, California. *Geochem. Geophys. Geosyst.* 10 (11). doi:10.1029/2009GC002709

Zhang, Z., Cheng, W., Liang, M., Wang, X., Long, F., Xu, Y., et al. (2012). Study on earthquakes induced by water injection in Zigong-Longchang area, Sichuan. *Chin. J. Geophys.* 55, 1635–1645. doi:10.6038/j.issn.0001-5733.2012.05.021

Zhang, B., Lei, J., and Zhang, G. (2020). Seismic evidence for influences of deep fluids on the 2019 Changning M_s 6.0 earthquake, Sichuan Basin, SW China. *J. Asian Earth Sci.* 200, 104492–104512. doi:10.1016/j.jseaes.2020.104492

Zhao, D., and Hasegawa, A. (1993). P wave tomographic imaging of the crust and up-per mantle beneath the Japan Islands. *J. Geophys. Res.* 98, 4333–4353. doi:10.1029/92jb02295

Zhao, Z., and Zhang, R. S. (1987). Primary study of crustal and upper mantle velocity structure of Sichuan province. *Acta Seismol. Sin.*9 (2), 154–166. (in Chinese).

Zhou, M. F., Yan, D. P., Kennedy, A. K., Li, Y. Q., and Ding, J. (2002). SHRIMP U-Pb zircon geochronological and geochemical evidence for Neoproterozoic arc-magmatism along the Western margin of the Yangtze block, South China. *Earth Planet. Sci. Lett.* 196, 51–67. doi:10.1016/s0012-821x(01)00595-7

Zhu, H., and He, C. (2014). Focal mechanism changning character of earthquake sequence induced by water injection: A case study of changning sequence, sichuan province. *Earth Sci. J. China Univ. Geosci.* 39 (12), 1776–1782. doi:10.3799/dqkx.2014.161

Zuo, K., Zhao, C., and Zhang, H. (2020). 3D crustal structure and seismicity characteristics of changning–xingwen area in the southwestern Sichuan Basin, China. *Bull. Seismol. Soc. Am.* 110, 2154–2167. doi:10.1785/0120200085

frontiers | Frontiers in Earth Science

TYPE Methods
PUBLISHED 27 March 2023
DOI 10.3389/feart.2023.1073684

OPEN ACCESS

EDITED BY
Eleftheria Papadimitriou,
Aristotle University of Thessaloniki,
Greece

REVIEWED BY
Mircea Radulian,
National Institute for Earth Physics,
Romania
Risheng Chu,
Institute of Geodesy and Geophysics
(CAS), China

*CORRESPONDENCE
G. M. Adinolfi,
guidomaria.adinolfi@unito.it

SPECIALTY SECTION
This article was submitted to Solid Earth Geophysics, a section of the journal Frontiers in Earth Science

RECEIVED 18 October 2022
ACCEPTED 13 March 2023
PUBLISHED 27 March 2023

CITATION
Adinolfi GM, De Landro G, Picozzi M, Carotenuto F, Caruso A, Nazeri S, Colombelli S, Tarantino S, Muzellec T, Emolo A, Zollo A, Orefice A, Ulivieri B, Calcagni D and Piantanida M (2023), Comprehensive study of micro-seismicity by using an automatic monitoring platform.
Front. Earth Sci. 11:1073684.
doi: 10.3389/feart.2023.1073684

Comprehensive study of micro-seismicity by using an automatic monitoring platform

G. M. Adinolfi[1]*, G. De Landro[2], M. Picozzi[2], F. Carotenuto[2], A. Caruso[3], S. Nazeri[2], S. Colombelli[2], S. Tarantino[4], T. Muzellec[2], A. Emolo[2], A. Zollo[2], A. Orefice[5], B. Ulivieri[5], D. Calcagni[6] and M. Piantanida[7]

[1]Department of Earth Sciences, University of Turin, Turin, Italy, [2]Department of Physics "Ettore Pancini", University of Naples Federico II, Naples, Italy, [3]Technical Department, Rete Ferroviaria Italiana S.p.A., Rome, Italy, [4]Istituto Nazionale di Geofisica e Vulcanologia (INGV), L'Aquila, Italy, [5]Department of Geodynamic and Geophysical Monitoring, Eni S.p.A., Milan, Italy, [6]Department of Geology and Geophysics Operations and Services, Eni S.p.A., Milan, Italy, [7]Department of Technical Computing for Geosciences and Subsurface Operations, Eni S.p.A., Milan, Italy

A modern digital seismic network, with many stations optimally distributed on the earthquake causative seismic zone, enables detection of very low magnitude earthquakes and determination of their source parameters. It is essential to associate to such kind of networks procedures to analyze the huge amount of continuously recorded data for monitoring the space-time-magnitude evolution of natural and/or induced seismicity. Hence, the demand for near-real-time, automated data collection and analysis procedures for assisting seismic network operators in carrying out microearthquake monitoring is growing. In response to this need, we designed a computational software platform, TREMOR, for fast and reliable detection and characterization of seismicity recorded by a dense local seismic network. TREMOR integrates different open-source seismological algorithms for earthquake signal detection, location, and source characterizations in a fully automatic workflow. We applied the platform in play-back mode to the continuous waveform data recorded during 1 month at the Japanese Hi-net seismic network in the Nagano region (Japan) and compared the resulting catalog with the Japan Meteorological Agency bulletin in terms of number of detections, location pattern and magnitudes. The results show that the completeness magnitude of the new seismic catalog decreased by 0.35 units of the local magnitude scale and consequently the number of events increased by about 60% with respect to the available catalog. Moreover, the fault plane solutions resulted coherent with the stress regime of the region, and the Vp/Vs ratio well delineated the main structural features of the area. According to our results, TREMOR has shown to be a valid tool for investigating and studying earthquakes, especially to identify and monitor natural or induced micro-seismicity.

KEYWORDS

seismic monitoring, micro-seismicity, earthquake detection and location, source parameter, seismic network, computational platform, Nagano, Japan

1 Introduction

Automatic detection, location, and source characterization of small magnitude events are challenging tasks for seismic monitoring, both in active fault zones and in areas of underground resources exploitation. A reliable and fast characterization of natural and/or induced seismicity is indeed crucial for seismic hazard analyses, and an *a priori* condition for correctly managing field operations in exploitation areas (Oye and Roth, 2003; Tomic et al., 2009; Goertz-Allmann et al., 2011; Yukutake et al., 2011; Zollo et al., 2014; Grigoli et al., 2017; Li et al., 2019; Lomax and Savvaidis, 2019; Verdon et al., 2019). Given recent technological developments, the availability of real-time and continuous data from local, dense networks has significantly increased, allowing detection of ultra and micro earthquakes ($M \leq 0$) and building of complete seismic catalogs with magnitude down to very low, even negative, values (Poiata et al., 2016; De Landro et al., 2019). The comprehensive study of micro-seismicity can provide a valuable description of the geological medium properties and earthquake related processes in the investigated crustal volumes, such as for instance the identification and geometrical characterization of active fault structures (Shearer, 2002; Hauksson and Shearer, 2005; Lin et al., 2007; De Landro et al., 2015; Adinolfi et al., 2019; Battimelli et al., 2019; Adinolfi et al., 2022), the study of the regional stress field (De Matteis et al., 2012; Terakawa, 2017; Maeda et al., 2020; De Matteis et al., 2021), the small-scale variability of faulting style, stress and strength (Prieto et al., 2004; Hardebeck, 2006; Syracuse et al., 2010; Adinolfi et al., 2015; Stabile et al., 2012; Festa et al., 2021), and the assessment of seismic hazard (Schorlemmer and Wiemer, 2005; Bernard et al., 2006; Emolo et al., 2011). Such achievements have led to an increasing demand for managing and analyzing large amounts of seismic data, mostly consisting of small-magnitude seismic events with signals comparable to or even below the noise level, for which analysts' manual operations are unfeasible (Yoon et al., 2015; Perol et al., 2018; Mousavi et al., 2019; Scafidi et al., 2019; Scala et al., 2022). Seismic monitoring is moving towards the development of fully automated and robust processing approaches, able to exploit the nowadays available huge amount of continuous data and to speed up seismic analyses, which are important for seismic risk assessment and reduction practices (Spallarossa et al., 2021a).

In this work, we present a novel AuTomatic, iteRativE, Modular computational platform for mOnitoring micRo-seismicity (i.e., TREMOR[1]), and its application to the Nagano microseismicity. TREMOR integrates different open-source seismological algorithms for detecting, locating and characterizing very small earthquakes in a fully automatic way (Figure 1). Innovatively, TREMOR provides, together with the standard estimates of earthquake locations, the local, moment, and energy magnitudes, fault plane solutions and the V_P/V_S ratio at each recording station, as a function of space and time with the aim of monitoring the medium properties.

We applied the platform to the continuous waveforms recorded during May 2011 at 25 stations of the Japanese Hi-net seismic network (https://doi.org/10.17598/NIED.0003) (Obara et al., 2005) located in an area of about 70 km × 75 km in the Nagano region. This area was selected considering: 1) the high station density, with mean station spacing of about 10 km; 2) the high rate of micro-seismicity (more than 100 events per month); and 3) the high quality of waveform recording (since most stations are in boreholes). The platform performance is evaluated by comparing its results with respect to the Japan Meteorological Agency (JMA, https://www.jma.go.jp/jma/indexe.html) catalog obtained with the same network.

2 Automatic monitoring platform

The computational platform TREMOR is designed using a Python modular architecture (version 3.6.9), in which each step of the data processing is performed by a specific module. The software block diagram is shown in Figure 1. The main outputs of the analysis are: 1) an earthquake catalog, which contains the time, location, and magnitudes of earthquakes, together with auxiliary information such as phase readings, fault plane solutions and strong motion parameters; and 2) a catalog of earthquake waveforms which contains the seismic traces, windowed around the origin time, of the seismic events plus other information including the seismic station coordinates and the earthquake time, location, magnitude, and phase readings.

The innovations of TREMOR are represented by the estimation of: 1) the earthquake source parameters, 2) the ground motion and 3) the medium properties. In fact, unlike other software used for seismic monitoring, TREMOR calculates energy and moment magnitudes and focal mechanism automatically. The estimation of these parameters for micro-seismicity represents a significant advance towards a complete characterization of the seismic source. Moreover, TREMOR provides ground motion estimates in terms of peak ground velocity (PGV) and acceleration (PGA) with the aim to give more accurate metrics relevant in earthquake engineering and seismic hazard studies. Finally, TREMOR calculates the V_P/V_s ratios to gather information on the physical properties of the medium, which are very useful for studying the influence of fluids in generating earthquakes.

In the following we present a brief description of the methods used in the different platform modules, especially the innovative ones of TREMOR. More details on the platform architecture and moduli interactions can be found in the Supplementary Material.

2.1 Earthquake detection

Earthquake detection is carried out following the coherence-based approach proposed by Adinolfi et al. (2020). The detection module performs a time-shifting and stacking of characteristic functions computed on seismic traces recorded at different stations, aiming to identify and preliminarily locate earthquakes inside a pre-defined spatial grid of potential source locations. In this module, only the S-wave arrivals are used for the detection. Then, the module classifies detected seismic events as real or false based on the presence of a minimum number of triggered stations, their

1 TREMOR is the advanced version of AMEDASC, the Automatic Micro-Earthquake Detection And Source Characterization software platform, developed as part of a research project funded by ENI-UNINA (Copyright © 2019-2021 ENI-UNINA). The modules of focal mechanism and V_p/V_s ratio computation are not provided in AMEDASC.

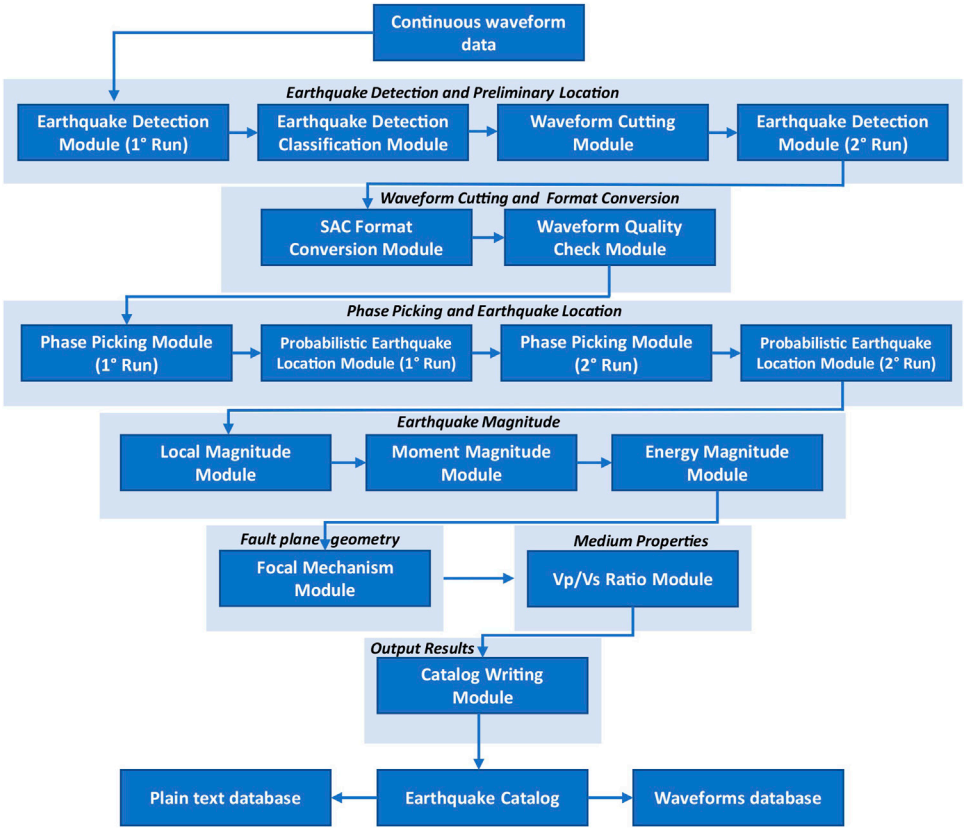

FIGURE 1
Workflow of the processing scheme implemented in the computational earthquake monitoring platform. Computational modules inside the program are shown.

distances from the epicenter, and the coherence of their arrival times (see Heimann et al., 2017; Adinolfi et al., 2019).

2.2 Phase picking

The picking of P- and S-wave arrival times is based on the algorithm of Ross and Ben-Zion (2014) using the triggered stations from the Earthquake Detection Module. Specifically, the P-pick is performed by requiring the exceedance of a threshold of the STA/LTA characteristic function around the theoretical P-wave arrival time. The S-pick is performed by searching the maximum point of the kurtosis derivative function.

2.3 Probabilistic earthquake location

This module implements the procedure proposed by Zollo et al. (2021) for event locations following a probabilistic approach based on the P- and S-phase picks and the travel-time grids generated by the NLLoc software (Lomax et al., 2000; http://alomax.free.fr/nlloc). The module gives as output the earthquake location and a map of the PDF distribution with the maximum likelihood hypocenter. The location errors are defined by considering the 31% and 68% significance levels of the probability density function (PDF), which corresponds to ±1σ.

2.4 Energy magnitude

This module exploits an approach proposed by Picozzi et al. (2017) for earthquake early warning purposes and extended to monitoring applications by Picozzi et al. (2018, 2019), and Spallarossa et al. (2021b). For each record, it obtains an estimate of the apparent energy by integrating the S-transform instantaneous spectrum, after correcting it for the geometrical spreading. Then, the event radiated energy is computed as the average among single station estimates. The corrective factor for geometrical spreading is set in the configuration file. In addition, this module measures peak ground velocity (PGV) and acceleration (PGA) for the three component recordings.

2.5 Moment magnitude

With the aim of determining the seismic moment (M_0) and the moment magnitude (M_w) of an earthquake, this module exploits the time evolution of the P-wave amplitude as proposed by Colombelli et al. (2014, 2015), and Nazeri et al. (2019). The logarithm of the P-wave peak (acceleration and velocity) amplitude is measured on the vertical component of recorded waveforms, in expanding time windows after the P-wave arrival, and after correction of the amplitude for the

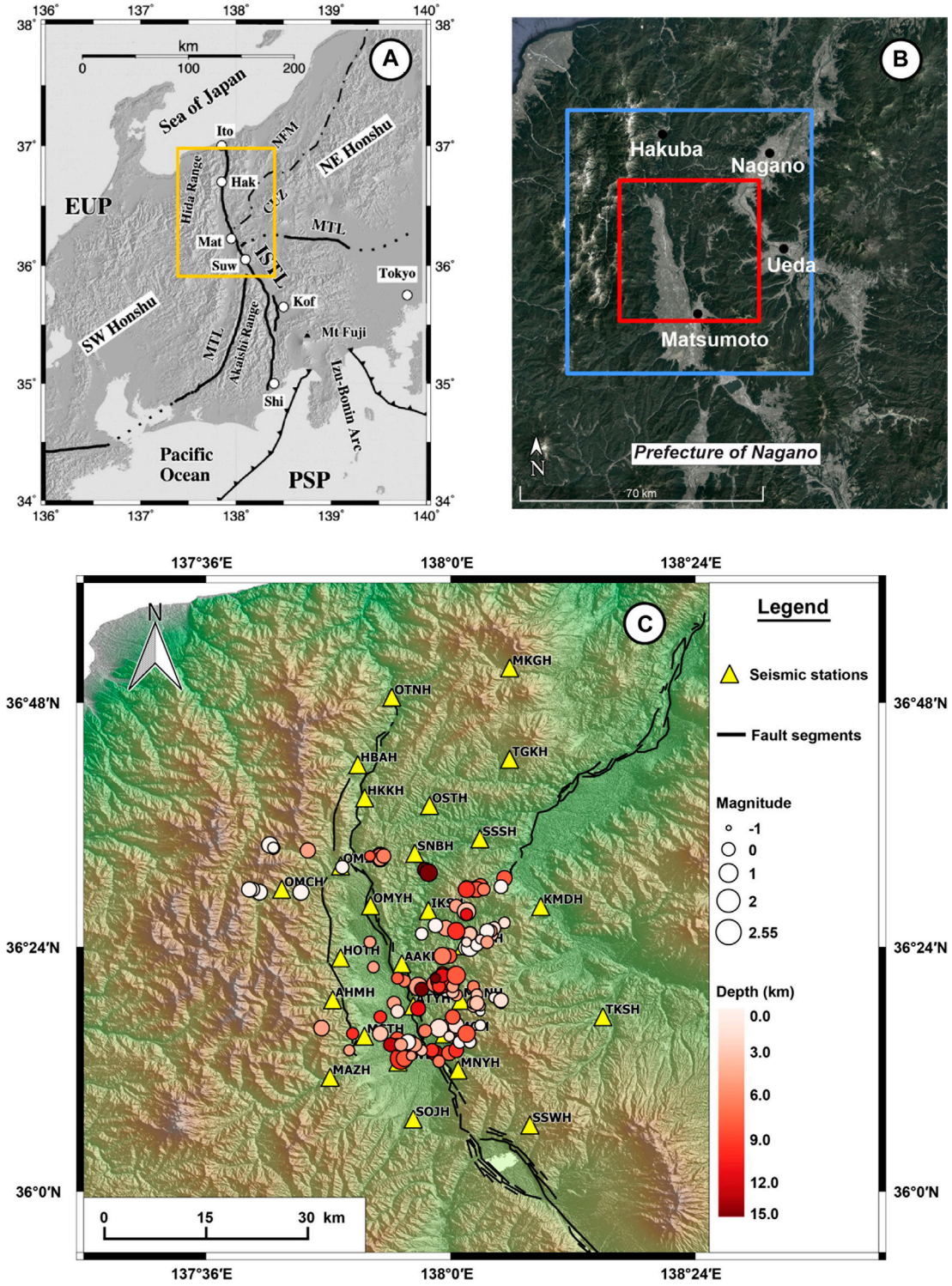

FIGURE 2
Location map of the study area **(A, B)** and epicentral map of the JMA earthquakes used as reference catalog in this study **(C)**. **(A)** Location of the area of interest, Nagano prefecture, along the ISTL line. The yellow contoured area is the location of the area plotted in the **(B)** and **(C)** panels (modified after Panayotopoulos et al., 2016). **(B)** The blue rectangle (70 km × 75 km) shows the location of the volumetric grid of potential hypocenters investigated in this work, the red rectangle delineates the target area (40 km × 40 km) used for the final selection of events. **(C)** Circles depict micro-seismicity recorded by the Japanese seismographic network Hi-net (yellow triangles) during May 2011 occurred within the target area [red square in **(B)**]. This area is the region best covered by the selected seismic network stations. The earthquake locations are from the JMA catalog. The sizes and colors of the circles are coded according to the magnitude and depth of the earthquakes, respectively.

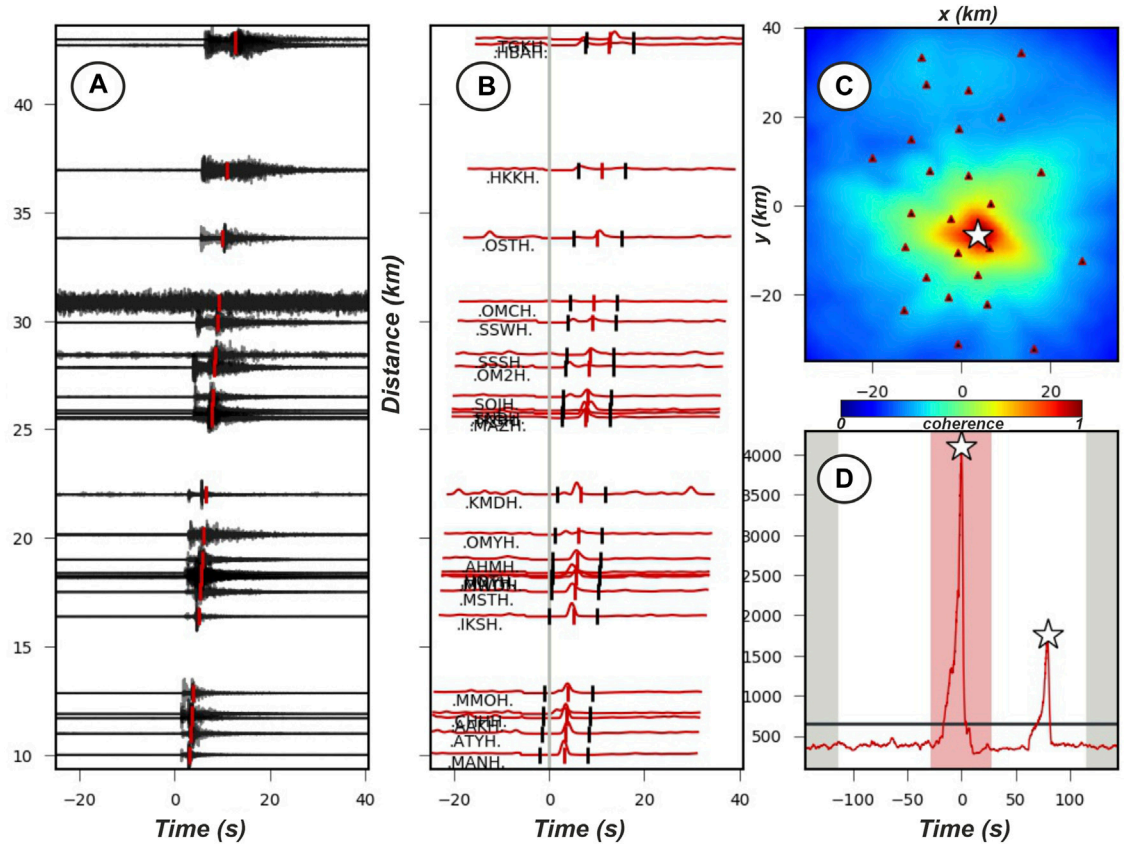

FIGURE 3
Example of arrival-time coherence detection for an M_V 2.5 earthquake on 16/05/2011 at 13:25:04 (JST). **(A)** Waveforms used for detections sorted by epicentral distance. **(B)** Characteristic functions (normalized amplitude) calculated for each station. They are corrected according to the S-wave velocity (red lines) for the travel time and stacked to obtain the final global image function in **(D)**. The markers indicate the best fit arrival times for the P- and S-phases. The black markers indicate the time window over which the characteristic function amplitude is considered for the definition of triggered or not-triggered stations. **(C)** Stack of the coherence map for the search region with available seismic stations (black triangles) and the event detected (white star at 0 s). The color bar shows coherence values. **(D)** Global image functions corresponding to the best fit of the source position along a processing time window centered on the origin time of the detected earthquake. The white star indicates the detected event above a fixed threshold value (black line). The white star on the right, at 75 s, is a second event, which was subsequently detected.

geometrical spreading. Corrective factors are set in a configuration file.

2.6 Focal mechanism

This module inverts the observed, absolute initial P-wave peak amplitudes, corrected for the geometrical attenuation effect, and the P- polarities to estimate focal mechanisms in a Bayesian framework (Tarantino et al., 2019). Data for the focal mechanism estimation are selected using an SNR threshold, which is set in the configuration file along with the minimum number of readings to perform the estimation.

2.7 V_P/V_S ratio

This module evaluates the average V_P/V_S ratio along the ray paths to each seismic station from observations of the difference between P- and S- arrival times divided by the P-wave travel time from the source to the station (Wadati and Oki, 1933; Kisslinger and Engdahl, 1973; Lucente et al., 2010; Chiarabba et al., 2009). The temporal evolution of the V_P/V_S ratio for a set of stations can enable identification of both spatial and temporal changes in the medium properties (Amoroso et al., 2018; De Landro et al., 2022).

3 Application to Nagano region (Japan)

3.1 Data pre-processing

We validated the TREMOR platform by applying it to a dataset of continuous waveforms from the Northern Nagano region (Japan) that was recorded by the Japanese High Sensitivity Seismograph Network (Hi-net, https://www.hinet.bosai.go.jp/), operated by the National Research Institute for Earth Science and Disaster Prevention (National Research Institute for Earth Science and Disaster Resilience, 2019). We selected the Nagano area in Honshu, Japan, for two reasons: 1) its high seismogenic potential and seismicity due to the presence of

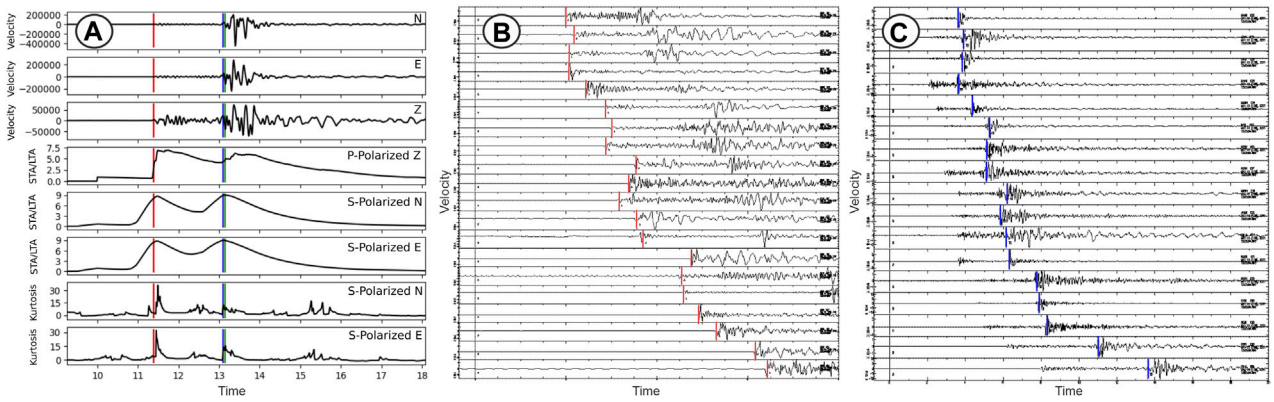

FIGURE 4
Example of P- and S- phase-picking for the M_V 2.5 earthquake on 16/05/2011 at 13:25:04 (JST) in the Nagano region. **(A)** (From the top): 1) the 3-C velocity waveforms, 2) the STA/LTA characteristic functions for the P- (vertical) and S- waves (horizontal) polarized components, and 3) the kurtosis characteristic function calculated for the S-polarized horizontal components. The red and blue vertical lines show the P- and S-wave picks, respectively. **(B)** Seismic sections for vertical and **(C)** horizontal components of the stations for which a P-pick (red vertical line) and S-pick are available.

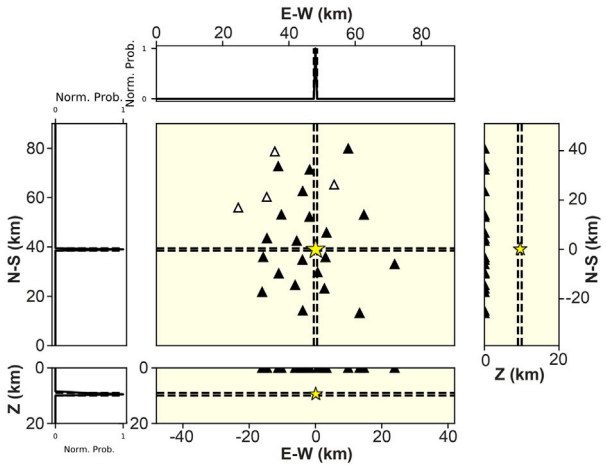

FIGURE 5
Example of probabilistic earthquake location for the M_V 2.5 earthquake which occurred on 16/05/2011 at 13:25:04 (JST) in the Nagano region. The earthquake location in the horizontal and vertical planes, with uncertainties (dotted lines), is marked by a yellow star. The normalized probability density function is shown along N-S and E-W directions and along a vertical section.

the Itoigawa–Shizuoka Tectonic Line (ISTL), which cuts the Island of Honshu and extends for ~150 km from Itoigawa City on the Sea of Japan to Shizuoka City on the Pacific Ocean (Figure 2A); and 2) the high station density in this area, with an average inter-station distance of about 10 km over a maximum aperture of 70 km.

The ISTL strikes NNE–SSW to NNW–SSE and is one of the most active faults in Japan, since it forms one arm of the triple junction of the Eurasian, North American, and Philippine Sea plates. The northernmost segment of the ISTL, the Kamishiro fault, has been shown to be an active thrust fault (Sato et al., 2004; Takeda et al., 2004). On the other hand, the Otari–Nakayama fault, which runs parallel to the Kamishiro and East Matsumoto Basin faults, shows no geomorphological evidence of late Quaternary activity (Matsuta et al., 2004; Ueki, 2008).

We selected a study area of about 40 km × 40 km (blue rectangle in Figure 2B) internal to the larger area covered by the network and collected continuous three-component velocity recordings from 25 borehole stations of Hi-net network in and near this area, (yellow triangles in Figure 2C) with a sampling rate of 100 Hz. Continuous waveform data were downloaded from NIED Hi-net website (https://www.hinet.bosai.go.jp/). We considered the period from the 1st to the 31st of May 2011, for which the Japan Meteorological Agency (JMA) reported 101 earthquakes with magnitudes ranging between −0.6 and 2.6 and depths up to 15 km (Figure 2C, circles). The JMA catalog magnitude of completeness estimated for this time period is 0.2.

Before running the code, we formatted the data in mseed format, organized it in files of one-hour length, and wrote input files with all necessary information (e.g., seismic network, velocity model).

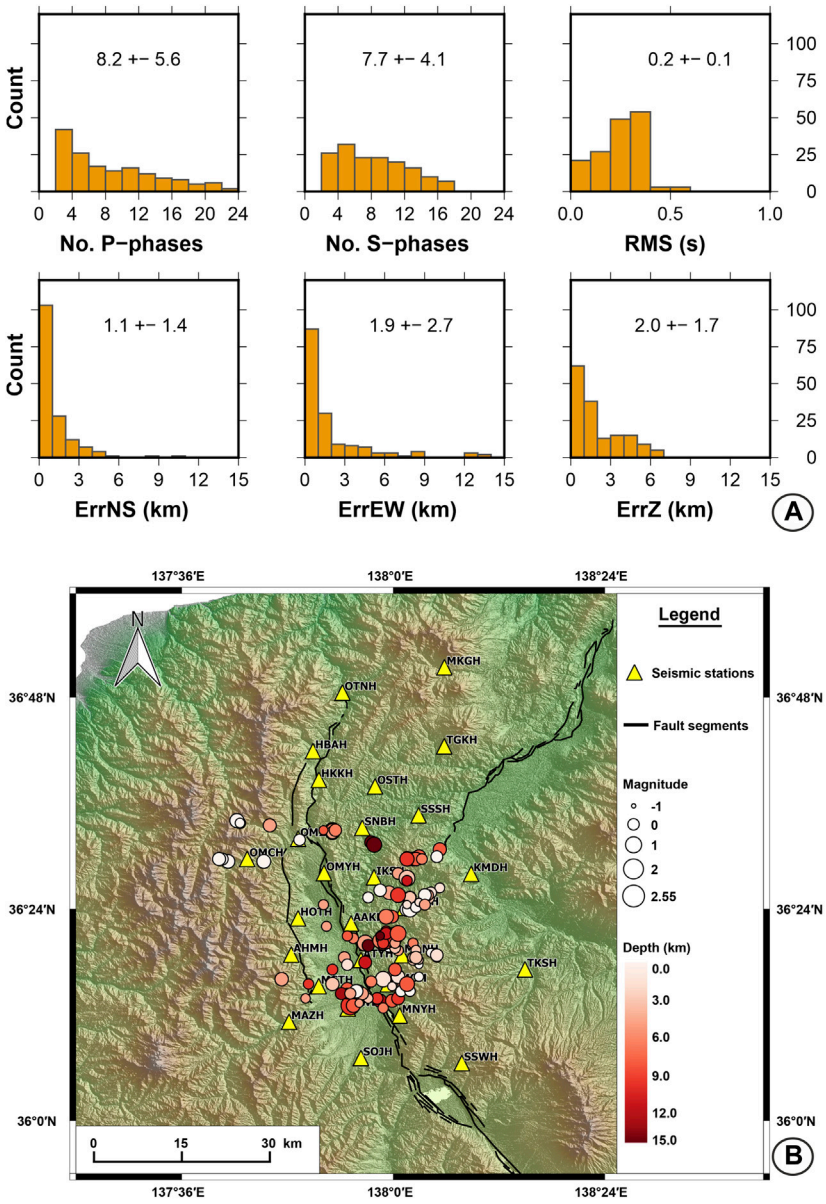

FIGURE 6
Results of TREMOR application to Nagano seismicity occurred during May 2011, in terms of location quality **(A)** and earthquake spatial distribution **(B)**. **(A)** Histograms for numbers of P- and S- readings, RMS of travel time residuals, and horizontal and vertical errors for the earthquake locations. For each histogram, the mean and standard deviation values are reported. **(B)** Earthquake epicenters located by the platform inside the target area (red square in Figure 2B) for the Nagano region during the time period analyzed. Symbols and colors are the same as in Figure 2C.

Moreover, we modified each control file for TREMOR modules with a set of parameters properly tuned for the characteristics of Nagano seismicity to be analyzed (for more details see Supplementary Tables S1–S6).

3.2 Earthquake detection

For the earthquake detection, we defined a 3D grid of potential source locations with a size of 70 km × 75 km × 20 km, with spacing equal to 1.5 km and centered on the barycenter of the seismic network used (blue rectangle in Figure 2B). For the parameter tuning, a specific analysis on a 10-day training dataset was carried out by modifying the parameters and optimizing them based on the number of real and false detections. After a visual inspection of the waveforms, we compared the preliminary results of this analysis with seismicity data from the JMA catalog. The chosen detection parameters are: coherence greater than 700, a signal-to-noise ratio greater than or equal to 3, which is used for the definition of triggered stations (with 10 s of signal, 3 s of noise), and three triggered stations among the 10 closest stations to the epicenter. Figure 3 shows an example of the detection module application for an M_V 2.5 earthquake (velocity magnitude as calculated by

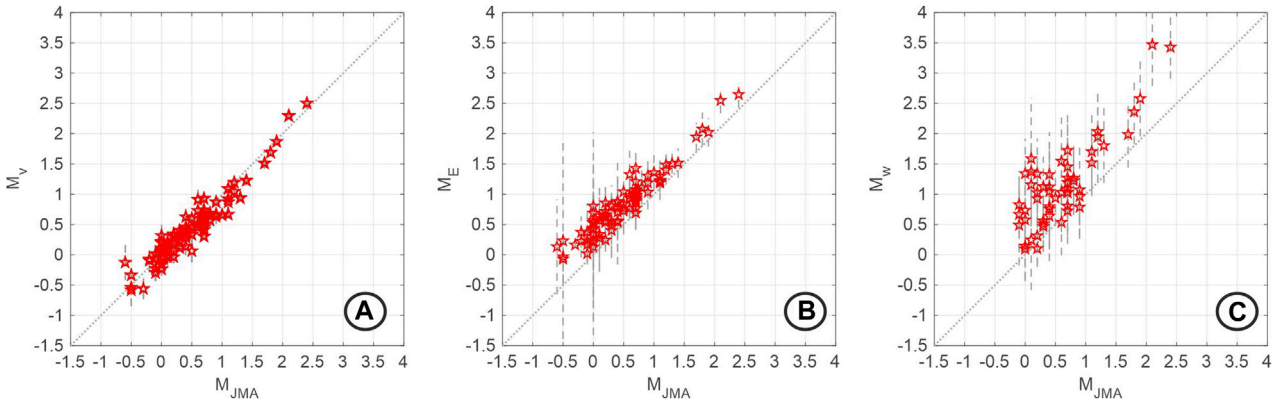

FIGURE 7
Magnitude estimates for the earthquakes identified by TREMOR in the Nagano region. From left to right, calculated M_v **(A)**, M_E **(B)** and M_w **(C)** are plotted versus M_{JMA}. M_{JMA} stands for velocity magnitude calculated by JMA.

JMA), which occurred on 16/05/2011 at 13:25:04 (JST) in the study area. Waveforms (Figure 3A) and characteristic functions (Figure 3B, normalized amplitudes) are calculated for each station to evaluate the vertical stack of the coherence map for the search region (Figure 3C) and global image functions corresponding to the best fit source time (Figure 3D).

Despite this positive performance, it is worth noting that the TREMOR event detection algorithm missed 5 earthquakes which are in the JMA catalog, with Mv < 0, while other six events that were external to the seismic network and target area which were mislocated at the border of the location grid. These cases can occur when very small magnitude events (M_v < 0) are not detected or are detected with low SNR, resulting in mis-location inside the target area or at the border of the grid due to too few and/or incorrect phase readings.

3.3 Earthquake location

To properly set the parameters that guide the picking procedure, we performed an optimization analysis based on comparisons between manual and automatic P-wave arrival time identifications on a sub-set of Nagano events. We explored a wide range of possible parameters and selected as the "best" configuration the one that minimizes the average differences between manual and automatic picks, for all source-station pairs and for both the vertical and horizontal components (average on the order of 0.05 s). In the optimization procedure, we also tried to minimize the number of missed picks (less than 15% for the "best" parameters). The picking parameters that we selected are listed in the Supplementary Table S4.

For the earthquake locations, we used the same 1D velocity models that JMA uses for locating Japanese seismicity (Ueno, 2002). We parameterized the crustal structure using a 3D grid with spacing 0.5 km and size of 70 km × 75 km × 20 km. The theoretical travel times from the grid nodes to the seismic stations were calculated using the Eikonal finite-difference scheme of (Podvin and Lecomte, 1991), as implemented by the Non LinLoc software (Lomax et al., 2000) for absolute earthquake locations in 3D velocity media. We used the same 3D grid for both location steps during the analysis. We located earthquakes with at least 2 P- and 2 S-phase picks, after discarding arrival times with residuals for P- and S-waves higher than 0.5 s and 1 s, respectively. Although it is common practice to use a higher minimum number of phases, we have chosen to use only four phases to maximize the number of micro-earthquake locations.

Figure 4 shows an example of the picking module application for an M_V 2.5 earthquake which occurred on 16/05/2011 at 13:25:04 (JST) in the study area. The characteristic functions (Figure 4A) and the phase picking on the vertical (Figure 4B) and horizontal (Figure 4C) velocity records are shown.

Figure 5 shows the probabilistic location for the same event. After the first run of data processing with the defined spatial grid, 406 earthquakes were detected by the platform of which 339 were effectively located. Based on their location, pick number, and location quality, 157 earthquakes were identified as located within the smaller target grid (red rectangle in Figure 2B). Of the 157 events, 96 are also in the JMA catalog. Five events in the JMA catalog (with M ≤ 0) were missed by TREMOR, while it provided 61 new detections. After visual inspection, we confirmed that all of the new detected events are real earthquakes, with no false detections.

For the 157 detected and located events in the study area, TREMOR provided 1286 P-wave picks and 1216 S-wave picks in the two steps of phase picking. To evaluate the quality and robustness of the automatic picking, we manually picked a subset of 100 events among the final catalog, selected in order to be representative in terms of location and magnitude of the entire seismicity, and we compared the automatic and manual P and S picks (see Supplementary Material). The mean values of the time differences between manual and automatic P- and S-wave onsets are equal to −0.06 and 0.08 s, respectively, with standard deviations of 0.29 and 0.31 (Supplementary Figure S1). These mean values, along with the histograms in Supplementary Figure S1, indicate that the automatic arrival time picks tend to be slightly later than the manual picks.

In the first step of the locations, the events were located with mean errors of 1.2, 2.0, and 2.0 km for the NS, EW and vertical directions, respectively, with an average root-mean-square (RMS) of 0.5 s and a mean of 5 P- and 5 S- phases. The final earthquake locations, shown in Figure 6, have mean location errors equal to 1.1, 1.9, 2.0 km along the NS, and EW horizontal and vertical directions, respectively, a mean RMS (weighted) of 0.2 s, and a mean of 8 P- and 8 S-phases per event (Figure 6A).

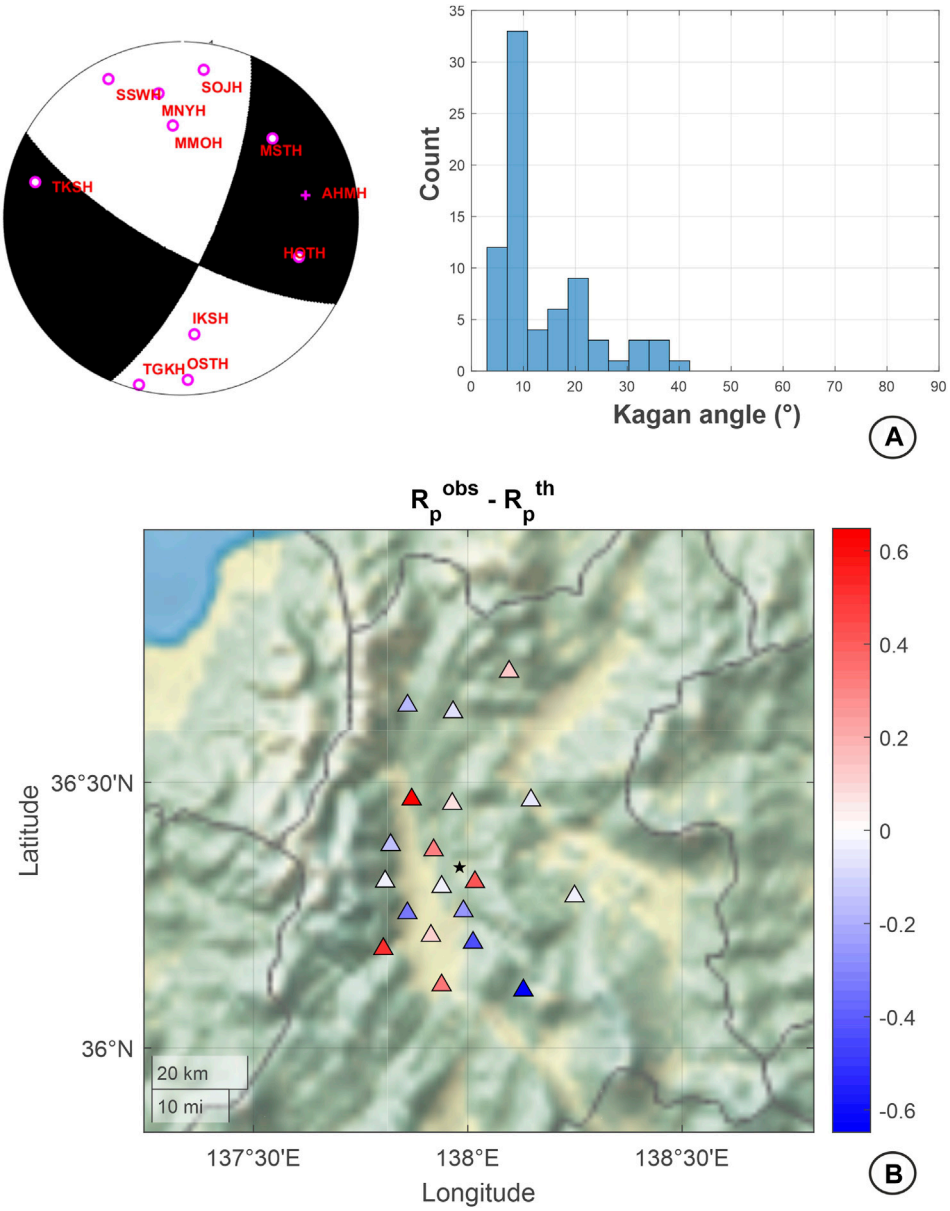

FIGURE 8
Example of fault plane solution computed for the M_V 2.5 earthquake on 16/05/2011 at 13:25:04 (JST) in the Nagano region. **(A)** On the left: focal mechanism solution with the largest probability. The open circles correspond to automatic negative polarities; the crosses are for automatic positive polarities. Station names are labeled in red. On the right: Kagan angle distribution between the best solution and all solutions up to 95% of the maximum of the probability. **(B)** Map of epicenter location and seismic stations used for focal mechanism calculus. The color-bar refers to the residual between the observed and predicted P-wave amplitude at the available stations.

The seismicity pattern delineated by the 157 located events correlates well with the main seismicity features of the area (Figure 6B; Supplementary Figure S2). The seismicity appears mainly aligned along the two segments of the ISTL, the Kamishiro and the Otari–Nakayama faults, down to a depth of 15 km, under the currently dominant east–west compressional stress field (Ando et al., 2017; Panayotopoulos et al., 2014; Panayotopoulos et al., 2016). The hypocenters of the 157 events show the same features of the earthquakes clustered mainly along Otari–Nakayama fault and its NE branch fault, in the southern and eastern part of Matsumoto basin, defining in depth an E-dipping plane (Supplementary Figure S2).

3.4 Earthquake characterization

The JMA assigns earthquakes a velocity magnitude (M_{JMA}), determined from the maximum amplitudes of velocity seismograms (Funasaki and Earthquake Prediction Information Division, 2004). Unfortunately, we could not use the M_v relation directly because the distance and depth corrections are not accessible from JMA web service. So, to better compare our results with those of the JMA catalog, we calculated a velocity magnitude (M_v) based on a linear regression between the maximum horizontal velocities at selected seismic stations and JMA catalog magnitudes. Looking at Figure 7, a

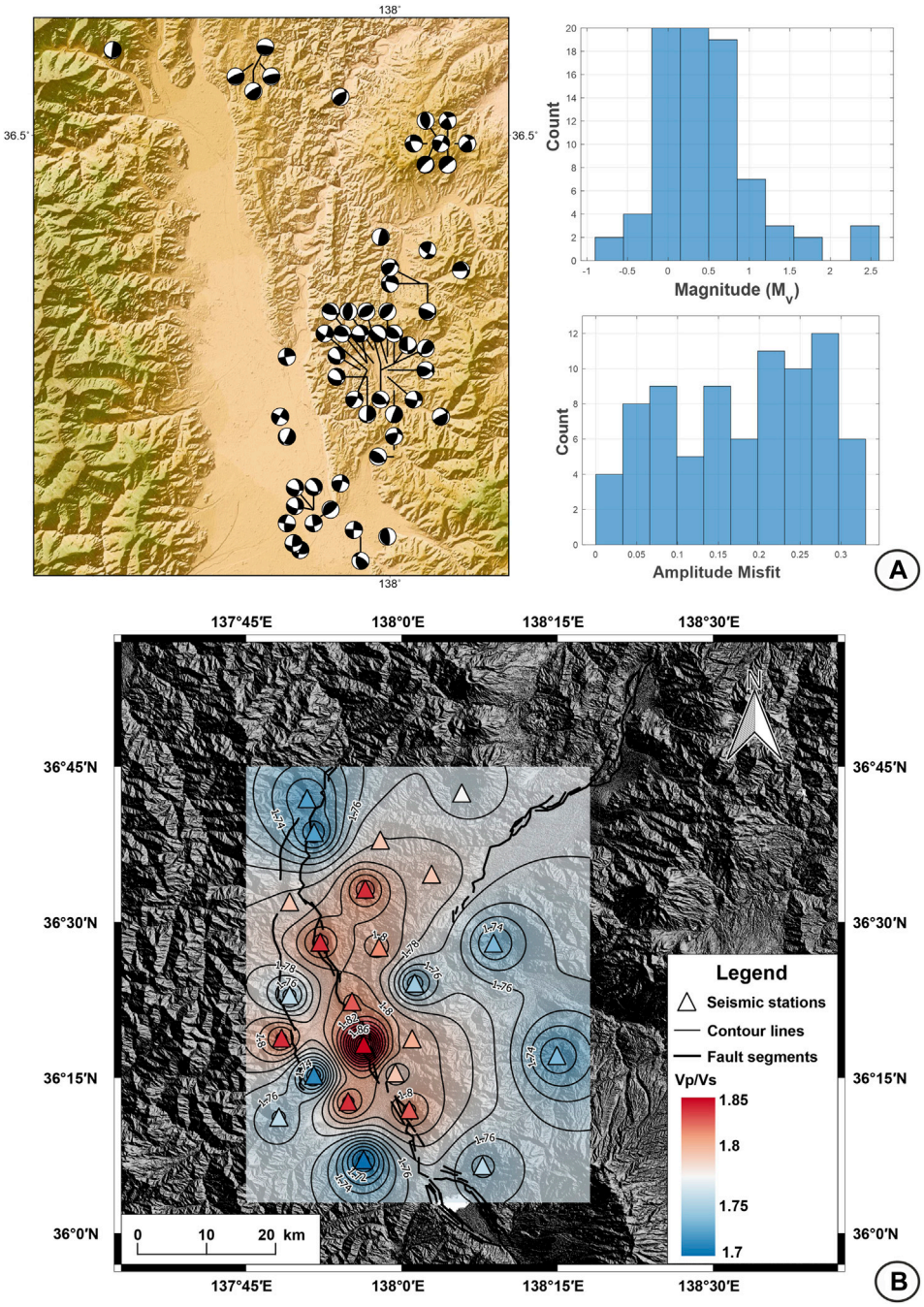

FIGURE 9
(A) On the left: plot of our focal mechanism solutions for the Nagano region with at least six P-wave readings. On the right: histograms of the magnitude distribution and of the P-wave amplitude misfits for the computed fault plane solutions. **(B)** Spatial distribution of the V_P/V_S ratio in the Nagano region. The ratios, computed at each seismic station (triangles) and interpolated, are indicated by the contour lines and colors.

good agreement exists between the magnitude estimates of TREMOR and the JMA magnitude values. Approximately linear scaling relations with M_{JMA} are evident for M_v, M_e and M_w, with mean differences of 0.09, −0.34, −0.55 and standard deviations of 0.17, 0.17, 0.39, respectively.

Fault plane solutions range from reverse to strike-slip (Figures 8, 9A), in accordance with the complex stress regime of this region. We found 57 focal mechanism solutions with an average RMS equal to 0.18 and a mean mismatch on polarity equal to 0.21 (see Supplementary Material). Matsumoto basin is characterized by the interaction of the Kamishiro fault with dip 30°–45° SE and the Otari-Nakayama fault that dips more steeply, at 50°–65° SE. According to Panayotopoulos et al. (2016), focal mechanism solutions for aftershocks of the 2014, M 6.7 Northern Nagano earthquake exhibit both reverse and left-lateral components, with a large strike-slip component distributed along a branch fault with a steep dip-angle (i.e., Otari-Nakayama), consistent with the fault plane solutions estimated by TREMOR.

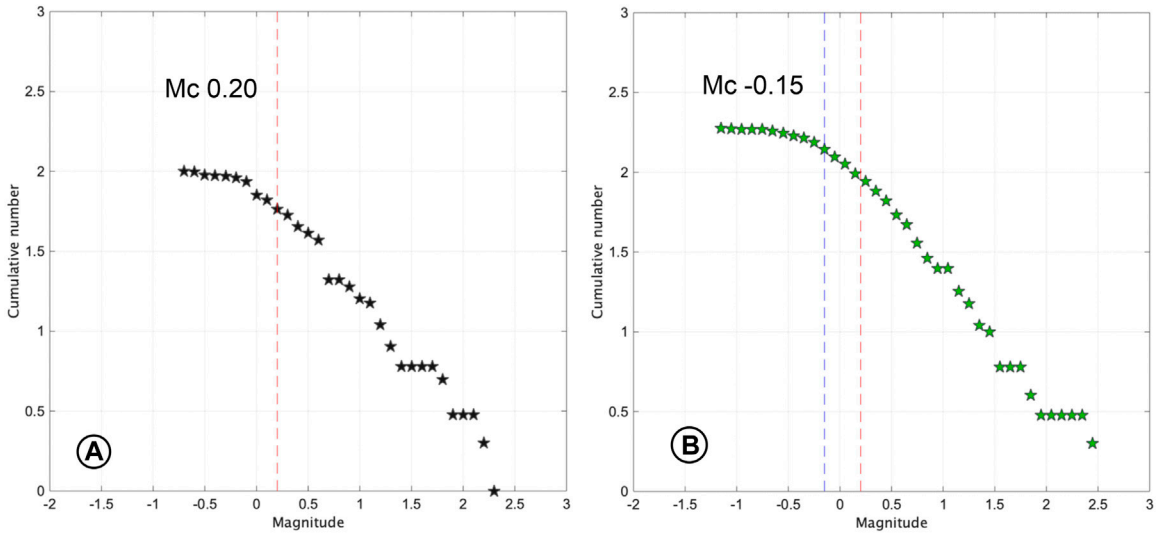

FIGURE 10
Gutenberg-Richter cumulative frequency-magnitude plots for **(A)** the JMA catalog and **(B)** the catalog retrieved in this study by the computational platform. Data are for the seismicity in the Nagano region (target area) during May 2011. The magnitudes are velocity magnitude, M_v. The completeness magnitude M_c for both catalogs is indicated with dashed lines.

In order to validate the V_P/V_S values obtained by the automatic module application, we compared our results with the tomographic results from the work of Panayotopoulos et al. (2014) (Figures 6C, 8). First, we calculated a V_P/V_S ratio value for each station by averaging the values obtained for the entire month (Supplementary Figure S3). Then, we interpolated the V_P/V_S ratios at the stations to obtain a map that can be compared to the tomographic image. The V_P/V_S map shown in Figure 9B agrees with the results by Panayotopoulos et al. (2014)). Indeed, they found a range of V_P/V_S ratio between 1.5 and 1.9, high V_P/V_S anomalies along the ISTL fault and a mean V_P/V_S value of about 1.73 for the other areas.

Figure 10 compares the frequency-magnitude distributions (Gutenberg and Richter, 1942; Aki, 1965; Wiemer, 2001) for the TREMOR and JMA catalogs for the same area and time period. We observe that the TREMOR catalog has more small-magnitude events than the JMA catalog and a lower magnitude of completeness, Mc, of M_v −0.12. In comparison, the JMA catalogue is complete for M_v 0.20 and larger.

4 Discussion and conclusion

We have presented a software platform for microearthquake monitoring, TREMOR, which combines a series of open-software and newly developed algorithms useful for monitoring and studying of natural or induced seismicity. Through TREMOR, a complete and detailed analysis of seismicity can be performed. After an appropriate tuning of a set of input parameters, the continuous seismic waveforms are automatically analyzed to obtain a high-resolution catalog of seismicity which occurred within a target area in a defined time period.

As a consequence of the rapid development of dense seismic networks and the need for reliable catalogs for monitoring purposes, in recent years the research in this field has gradually shifted from the traditional standard processing workflow where each event is identified and characterized by analysts to advanced automatic processing and interpretation techniques. TREMOR includes algorithms for detecting weak seismic signals and characterizing each event in terms of local magnitude, moment magnitude, seismic energy, and focal mechanism, with the goal of producing an informative seismic catalog that is potentially complete to very small magnitudes. TREMOR provides a detailed analysis of earthquake source by computing M_e and M_w, offering a clearer picture of the seismicity and the physics of the rupture process. Although representing a challenge for small earthquakes, one of the most innovative tasks of TREMOR is the focal mechanism computation. This information has become a routine analysis by seismological agencies only for earthquakes of $M \geq 4$. As evidenced by the Nagano application, TREMOR can reliably calculate fault plane solutions even for small magnitude earthquakes, when recorded by a dense seismic network. The information on the geometry of the rupture provided by the focal mechanisms is essential for identifying the fracture patterns or activated fault segments for seismotectonic studies or for monitoring the space-time evolution of seismicity during the underground industrial operations. Moreover, peak ground motion parameters computed by TREMOR for small magnitude events represent a novelty, very useful to have a robust metric of the ground shaking or to compute detailed maps of temporal/spatial variability of ground-motions. In addition to the seismic source characterization, a module for the near-real-time monitoring of the V_P/V_S ratio is also included. Although the limitation of the calculated V_P/V_S ratio, as the assumption that this is constant along the ray-path, the obtained values can be used as first order estimates. The latter quantity is directly correlated with the presence of fluids within the crust (Thurber et al., 1995; De Landro et al., 2020) and the analysis of its spatio-temporal variations allows for the 4D imaging of large-scale medium properties (Amoroso et al., 2018; De Landro et al., 2022).

The main advantages of the computation platform can be summarized as follows.

1. Full-automatic processing. After the parameter tuning and the setting of control files, continuous waveform data are analyzed from earthquake detection to source parameter determination without

any manual effort by an operator. Furthermore, by selecting near-real-time processing (batch-mode), the data analysis could be programmed in time according to raw-data timeslot. Once configured, the platform automatically: 1) searches the waveform data availability recursively, makes the conversion of the data into the necessary format (mseed), runs the processing for the time slots of raw data, and deletes the data already processed to save disk space.

2. Complete and detailed seismic analysis. TREMOR enables study of seismicity starting with the identification of events from continuous waveform data to their characterization in terms of the magnitudes M_L, M_w and M_e, peak ground motion parameters, and fault plane solutions. In addition, through the analysis of V_P/V_S ratios, the platform provides information about the medium properties of an area. This analysis represents the main innovation brought by TREMOR which, unlike the common softwares used for seismic monitoring, offers an in-depth characterization of the seismic source, even in the case of micro-seismicity, in terms of momentum and energy magnitude and fault kinematics.
3. Iterative, refining earthquake location. TREMOR is designed to perform two-step of processing for phase picking and earthquake location in order to: 1) reduce location errors by refining the phase picks, guided by predicted arrival times for a preliminary location; 2) obtain more robust solutions by adding more arrival time picks; and 3) reduce the number of false detections that can occur if a settable minimum number of spurious or unrelated phase readings is identified on the seismic recordings.
4. Modular architecture. The platform involves separating the data processing into independent building blocks or modules, each containing all of the parts needed to execute a single step of the analysis. Moreover, in post-earthquake processing, each module can be activated or dis-activated to run modules separately. This functionality can be very useful for focusing on specific seismological analyses, repeating analyses when necessary, or parameter tuning of the platform module. Moreover, the modularity allows users to quickly update the platform with new modules that carry out new processing functions or analyses, or to quickly modify those already present.

As demonstrated for our test case in the Nagano region, TREMOR can very successfully monitor micro-seismicity recorded by local dense seismic networks and can be a valid tool for investigating and studying natural or induced earthquakes by seismological agencies or laboratories at local scales. Future tests of TREMOR will focus on seismic sequences of moderate magnitude ($M > 5$) earthquakes and multiple earthquakes repeated over time as in the case of a swarm or seismic sequence. Furthermore, we want to expand the use of TREMOR to seismic networks at regional scales (>100 km). Such large-scale applications with large numbers of seismic stations requires optimization of PC memory demand and reduction of computational times.

Data availability statement

Publicly available datasets were analyzed in this study. This data can be found here: https://www.hinet.bosai.go.jp/.

Author contributions

AZ, MP, GA, and GL contributed to the conceptualization of the paper. GA and FC developed the computational platform and assembled the modules. All authors participated in developing computational modules. GA and GL carried out the analysis, wrote the paper and prepared the figures. GA, GL, MP, and AZ reviewed and edited the paper. All authors approved the final version.

Funding

This work has been supported by: 1) ENI-UNINA project, Framework Agreement ENI Spa—UNINA No. 4400007890, Application Contract No. 2500033423 and 2) PRIN-FLUIDS project, Detection and tracking of crustal fluid by multi-parametric methodologies and technologies, PRIN-MIUR programme, Grant No. 20174X3P29.

Acknowledgments

We sincerely thank the Editor in Chief Valerio Acocella and Handling Editor Eleftheria Papadimitriou, and two reviewers for their constructive suggestions, which contributed to the improvement of our paper.

Conflict of interest

AC was employed by Rete Ferroviaria Italiana S.p.A. and AO, BU, DC, and MP were employed by Eni S.p.A.

The remaining authors declare that the research was conducted in the absence of any commercial or financial relationships that could be construed as a potential conflict of interest.

The authors declare that this study received funding from Eni-Spa. The funder had the following involvement in the study: decision to publish and approval of the final version of the manuscript.

Publisher's note

Supplementary material

The Supplementary Material for this article can be found online at: https://www.frontiersin.org/articles/10.3389/feart.2023.1073684/full#supplementary-material

References

Adinolfi, G. M., Cesca, S., Picozzi, M., Heimann, S., and Zollo, A. (2019). Detection of weak seismic sequences based on arrival time coherence and empiric network detectability: An application at a near fault observatory. *Geophys. J. Int.* 218 (3), 2054–2065. doi:10.1093/gji/ggz248

Adinolfi, G. M., De Matteis, R., Orefice, A., Festa, G., Zollo, A., de Nardis, R., et al. (2015). The September 27, 2012, ML 4.1, Benevento earthquake: A case of strike-slip faulting in Southern Apennines (Italy). *Tectonophysics* 660, 35–46.

Adinolfi, G. M., Picozzi, M., Cesca, S., Heimann, S., and Zollo, A. (2020). An application of coherence-based method for earthquake detection and microseismic monitoring (Irpinia fault system, Southern Italy). *J. Seismol.* 24, 979–989. doi:10.1007/s10950-020-09914-7

Adinolfi, G. M., De Matteis, R., De Nardis, R., and Zollo, A. (2022). A functional tool to explore the reliability of micro-earthquake focal mechanism solutions for seismotectonic purposes. *Solid Earth.* 13 (1), 65–83. doi:10.5194/se-13-65-2022

Aki, K. (1965). Maximum likelihood estimate of b in the formula log N= a-bM and its confidence limits. *Bull. Earthq. Res. Inst. Tokyo Univ.* 43, 237–239.

Amoroso, O., Festa, G., Bruno, P. P., D'Auria, L., De Landro, G., Di Fiore, V., et al. (2018). Integrated tomographic methods for seismic imaging and monitoring of volcanic caldera structures and geothermal areas. *J. Appl. Geophys.* 156, 16–30. doi:10.1016/j.jappgeo.2017.11.012

Ando, R., Imanishi, K., Panayotopoulos, Y., and Kobayashi, T. (2017). Dynamic rupture propagation on geometrically complex fault with along-strike variation of fault maturity: Insights from the 2014 northern Nagano earthquake. *Earth, Planets Space* 69 (1), 130–213. doi:10.1186/s40623-017-0715-2

Battimelli, E., Adinolfi, G. M., Amoroso, O., and Capuano, P. (2019). Seismic activity in the central adriatic offshore of Italy: A review of the 1987 ML 5 Porto San Giorgio Earthquake. *Seismol. Res. Lett.* 90 (5), 1889–1901. doi:10.1785/0220190048

Bernard, P., Lyon-Caen, H., Briole, P., Deschamps, A., Boudin, F., Makropoulos, K., et al. (2006). Seismicity, deformation and seismic hazard in the Western rift of Corinth: New insights from the Corinth Rift Laboratory (CRL). *Tectonophysics* 426 (1-2), 7–30. doi:10.1016/j.tecto.2006.02.012

Chiarabba, C., De Gori, P., and Boschi, E. (2009). Pore-pressure migration along a normal-fault system resolved by time-repeated seismic tomography. *Geology* 37 (1), 67–70. doi:10.1130/G25220A.1

Colombelli, S., Zollo, A., Festa, G., and Picozzi, M. (2014). Evidence for a difference in rupture initiation between small and large earthquakes. *Nat. Commun.* 5 (1), 3958–3965. doi:10.1038/ncomms4958

Colombelli, S., Caruso, A., Zollo, A., Festa, G., and Kanamori, H. (2015). A P wave-based, on-site method for earthquake early warning. *Geophys. Res. Lett.* 42 (5), 1390–1398. doi:10.1002/2014gl063002

De Landro, G., Amoroso, O., Stabile, T. A., Matrullo, E., Lomax, A., and Zollo, A. (2015). High-precision differential earthquake location in 3-D models: Evidence for a rheological barrier controlling the microseismicity at the Irpinia fault zone in southern Apennines. *Geophys. Suppl. Mon. Notices R. Astron. Soc.* 203 (3), 1821–1831. doi:10.1093/gji/ggv397

De Landro, G., Picozzi, M., Russo, G., Adinolfi, G. M., and Zollo, A. (2019). Seismic networks layout optimization for a high-resolution monitoring of induced micro-seismicity. *J. Seismol.* 24, 953–966. doi:10.1007/s10950-019-09880-9

De Landro, G., Amoroso, O., Russo, G., and Zollo, A. (2020). 4d travel-time tomography as a tool for tracking fluid-driven medium changes in offshore oil–gas exploitation areas. *Energies* 13 (22), 5878. doi:10.3390/en13225878

De Landro, G., Amoroso, O., Russo, G., D'Agostino, N., Esposito, R., Emolo, A., et al. (2022). Decade-long monitoring of seismic velocity changes at the Irpinia fault system (southern Italy) reveals pore pressure pulsations. *Sci. Rep.* 12 (1), 1247–1249. doi:10.1038/s41598-022-05365-x

De Matteis, R., Convertito, V., Napolitano, F., Amoroso, O., Terakawa, T., and Capuano, P. (2021). Pore fluid pressure imaging of the Mt. Pollino region (southern Italy) from earthquake focal mechanisms. *Geophys. Res. Lett.* 48 (22), e2021GL094552. doi:10.1029/2021GL094552

De Matteis, R., Matrullo, E., Rivera, L., Stabile, T. A., Pasquale, G., and Zollo, A. (2012). Fault delineation and regional stress direction from the analysis of background microseismicity in the southern Apennines, Italy. *Bull. Seismol. Soc. Am.* 102 (4), 1899–1907. doi:10.1785/0120110225

Emolo, A., Convertito, V., and Cantore, L. (2011). Ground-motion predictive equations for low-magnitude earthquakes in the Campania–Lucania area, Southern Italy. *J. Geophys. Eng.* 8 (1), 46–60. doi:10.1088/1742-2132/8/1/007

Festa, G., Adinolfi, G. M., Caruso, A., Colombelli, S., De Landro, G., Elia, L., et al. (2021). Insights into mechanical properties of the 1980 Irpinia Fault System from the analysis of a seismic sequence. *Geosciences* 11 (1), 28. doi:10.3390/geosciences11010028

Funasaki, J.Earthquake Prediction Information Division (2004)). Revision of the JMA velocity magnitude (in Japanese). *Quart. J. Seis.* 67, 11–20.

Goertz-Allmann, B. P., Goertz, A., and Wiemer, S. (2011). Stress drop variations of induced earthquakes at the Basel geothermal site. *Geophys. Res. Lett.* 38 (9). doi:10.1029/2011GL047498

Grigoli, F., Cesca, S., Priolo, E., Rinaldi, A. P., Clinton, J. F., Stabile, T. A., et al. (2017). Current challenges in monitoring, discrimination, and management of induced seismicity related to underground industrial activities: A European perspective. *Rev. Geophys.* 55 (2), 310–340. doi:10.1002/2016rg000542

Gutenberg, B., and Richter, C. F. (1942). Earthquake magnitude, intensity, energy, and acceleration. *Bull. Seismol. Soc. Am.* 32 (3), 163–191. doi:10.1785/bssa0320030163

Hardebeck, J. L. (2006). Homogeneity of small-scale earthquake faulting, stress, and fault strength. *Bull. Seismol. Soc. Am.* 96 (5), 1675–1688. doi:10.1785/0120050257

Hauksson, E., and Shearer, P. (2005). Southern California hypocenter relocation with waveform cross-correlation, part 1: Results using the double-difference method. *Bull. Seismol. Soc. Am.* 95 (3), 896–903. doi:10.1785/0120040167

Heimann, S., Kriegerowski, M., Isken, M., Cesca, S., Daout, S., Grigoli, F., et al. (2017). *Pyrocko - an open-source seismology toolbox and library*. Potsdam: GFZ Data Services. doi:10.5880/GFZ.2.1.2017.001

Kisslinger, C., and Engdahl, E. R. (1973). The interpretation of the Wadati diagram with relaxed assumptions. *Bull. Seismol. Soc. Am.* 63 (5), 1723–1736.

Li, L., Tan, J., Wood, D. A., Zhao, Z., Becker, D., Lyu, Q., et al. (2019). A review of the current status of induced seismicity monitoring for hydraulic fracturing in unconventional tight oil and gas reservoirs. *Fuel* 242, 195–210. doi:10.1016/j.fuel.2019.01.026

Lin, G., Shearer, P. M., and Hauksson, E. (2007). Applying a three-dimensional velocity model, waveform cross correlation, and cluster analysis to locate southern California seismicity from 1981 to 2005. *J. Geophys. Res. Solid Earth* 112 (B12), B12309. doi:10.1029/2007jb004986

Lomax, A., and Savvaidis, A. (2019). Improving absolute earthquake location in west Texas using probabilistic, proxy ground-truth station corrections. *J. Geophys. Res. Solid Earth* 124 (11), 11447–11465. doi:10.1029/2019jb017727

Lomax, A., Virieux, J., Volant, P., and Berge-Thierry, C. (2000). "Probabilistic earthquake location in 3D and layered models: Introduction of a metropolis-gibbs method and comparison with linear locations," in *Advances in seismic event location*. Editors C. H. Thurber and N. Rabinowitz (Amsterdam: Kluwer), 101–134.

Lucente, F. P., De Gori, P., Margheriti, L., Piccinini, D., Di Bona, M., Chiarabba, C., et al. (2010). Temporal variation of seismic velocity and anisotropy before the 2009 M_W6.3 L'Aquila earthquake, Italy. *Italy. Geol.* 38 (11), 1015–1018. doi:10.1130/g31463.1

Maeda, S., Matsuzawa, T., Okada, T., Katao, H., Yoshida, T., Kosuga, M., et al. (2020). Spatiotemporal variations in the stress field in the northeasternmost part of the NE Japan arc: Constraints from microearthquakes. *Earth, Planets Space* 72 (1), 117–7. doi:10.1186/s40623-020-01245-8

Matsuta, N., Ikeda, Y., and Sato, H. (2004). The slip-rate along the northern Itoigawa-Shizuoka tectonic line active fault system, central Japan. *Earth, Planets Space* 56 (12), 1323–1330. doi:10.1186/bf03353357

Mousavi, S. M., Zhu, W., Sheng, Y., and Beroza, G. C. (2019). CRED: A deep residual network of convolutional and recurrent units for earthquake signal detection. *Sci. Rep.* 9 (1), 10267–10314. doi:10.1038/s41598-019-45748-1

National Research Institute for Earth Science and Disaster Resilience (2019). *NIED hinet, national research institute for earth science and disaster resilience*. Tsukuba-shi, Japan: NIED. doi:10.17598/Q17NIED.0003

Nazeri, S., Colombelli, S., and Zollo, A. (2019). Fast and accurate determination of earthquake moment, rupture length and stress release for the 2016–2017 Central Italy seismic sequence. *Geophys. J. Int.* 217 (2), 1425–1432. doi:10.1093/gji/ggz097

Obara, K., Kasahara, K., Hori, S., and Okada, Y. (2005). A densely distributed high-sensitivity seismograph network in Japan: Hi-net by national research institute for Earth science and disaster prevention. *Rev. Sci. Instrum.* 76 (2), 021301. doi:10.1063/1.1854197

Oye, V., and Roth, M. (2003). Automated seismic event location for hydrocarbon reservoirs. *Comput. Geosci.* 29 (7), 851–863. doi:10.1016/s0098-3004(03)00088-8

Panayotopoulos, Y., Hirata, N., Sato, H., Kato, A., Imanishi, K., Kuwahara, Y., et al. (2014). Investigating the role of the Itoigawa-Shizuoka tectonic line towards the evolution of the Northern Fossa Magna rift basin. *Tectonophysics* 615, 12–26. doi:10.1016/j.tecto.2013.12.014

Panayotopoulos, Y., Hirata, N., Hashima, A., Iwasaki, T., Sakai, S. I., and Sato, H. (2016). Seismological evidence of an active footwall shortcut thrust in the Northern Itoigawa–Shizuoka tectonic line derived by the aftershock sequence of the 2014 M 6.7 northern Nagano earthquake. *Tectonophysics* 679, 15–28. doi:10.1016/j.tecto.2016.04.019

Perol, T., Gharbi, M., and Denolle, M. (2018). Convolutional neural network for earthquake detection and location. *Sci. Adv.* 4 (2), e1700578. doi:10.1126/sciadv.1700578

Picozzi, M., Bindi, D., Brondi, P., Di Giacomo, D., Parolai, S., and Zollo, A. (2017). Rapid determination of P wave-based energy magnitude: Insights on source parameter scaling of the 2016 Central Italy earthquake sequence. *Geophys. Res. Lett.* 44 (9), 4036–4045. doi:10.1002/2017gl073228

Picozzi, M., Bindi, D., Spallarossa, D., Di Giacomo, D., and Zollo, A. (2018). A rapid response magnitude scale for timely assessment of the high frequency seismic radiation. *Sci. Rep.* 8 (1), 8562–8610. doi:10.1038/s41598-018-26938-9

Picozzi, M., Bindi, D., Zollo, A., Festa, G., and Spallarossa, D. (2019). Detecting long-lasting transients of earthquake activity on a fault system by monitoring apparent stress, ground motion and clustering. *Sci. Rep.* 9 (1), 16268–16311. doi:10.1038/s41598-019-52756-8

Podvin, P., and Lecomte, I. (1991). Finite difference computation of traveltimes in very contrasted velocity models: A massively parallel approach and its associated tools. *Geophys. J. Int.* 105 (1), 271–284. doi:10.1111/j.1365-246x.1991.tb03461.x

Poiata, N., Satriano, C., Vilotte, J. P., Bernard, P., and Obara, K. (2016). Multiband array detection and location of seismic sources recorded by dense seismic networks. *Geophys. J. Int.* 205 (3), 1548–1573. doi:10.1093/gji/ggw071

Prieto, G. A., Shearer, P. M., Vernon, F. L., and Kilb, D. (2004). Earthquake source scaling and self-similarity estimation from stacking P and S spectra. *J. Geophys. Res. Solid Earth* 109 (B8). doi:10.1029/2004jb003084

Ross, Z. E., and Ben-Zion, Y. (2014). Automatic picking of direct P, S seismic phases and fault zone head waves. *Geophys. J. Int.* 199 (1), 368–381. doi:10.1093/gji/ggu267

Sato, H., Iwasaki, T., Kawasaki, S., Ikeda, Y., Matsuta, N., Takeda, T., et al. (2004). Formation and shortening deformation of a back-arc rift basin revealed by deep seismic profiling, central Japan. *Tectonophysics* 388 (1-4), 47–58. doi:10.1016/j.tecto.2004.07.004

Scafidi, D., Spallarossa, D., Ferretti, G., Barani, S., Castello, B., and Margheriti, L. (2019). A complete automatic procedure to compile reliable seismic catalogs and travel-time and strong-motion parameters datasets. *Seismol. Res. Lett.* 90 (3), 1308–1317. doi:10.1785/0220180257

Scala, A., Adinolfi, G. M., Picozzi, M., Scotto di Uccio, F., Festa, G., De Landro, G., et al. (2022). Monitoring the microseismicity through a dense seismic array and a similarity search detection technique: application to the seismic monitoring of Collalto Gas-Storage, North Italy. *Energies* 15 (10), 3504. doi:10.3390/en15103504

Schorlemmer, D., and Wiemer, S. (2005). Microseismicity data forecast rupture area. *Nature* 434 (7037), 1086. doi:10.1038/4341086a

Shearer, P. M. (2002). Parallel fault strands at 9-km depth resolved on the Imperial fault, southern California. *Geophys. Res. Lett.* 29 (14), 19-1–19-4. doi:10.1029/2002gl015302

Spallarossa, D., Cattaneo, M., Scafidi, D., Michele, M., Chiaraluce, L., Segou, M., et al. (2021). An automatically generated high-resolution earthquake catalogue for the 2016–2017 Central Italy seismic sequence, including P and S phase arrival times. *Geophys. J. Int.* 225, 555–571. doi:10.1093/gji/ggaa604

Spallarossa, D., Picozzi, M., Scafidi, D., Morasca, P., Turino, C., and Bindi, D. (2021). The RAMONES service for rapid assessment of seismic moment and radiated energy in central Italy: Concepts, Capabilities, and future perspectives. *Seismol. Res. Lett.* 92, 1759–1772. doi:10.1785/0220200348

Stabile, T. A., Satriano, C., Orefice, A., Festa, G., and Zollo, A. (2012). Anatomy of a microearthquake sequence on an active normal fault. *Sci. Rep.* 2 (1), 410–417. doi:10.1038/srep00410

Syracuse, E. M., Thurber, C. H., Wolfe, C. J., Okubo, P. G., Foster, J. H., and Brooks, B. A. (2010). High-resolution locations of triggered earthquakes and tomographic imaging of Kilauea Volcano's south flank. *J. Geophys. Res. Solid Earth* 115 (B10), B10310. doi:10.1029/2010JB007554

Takeda, T., Sato, H., Iwasaki, T., Matsuta, N., Sakai, S. I., Iidaka, T., et al. (2004). Crustal structure in the northern Fossa Magna region, central Japan, modeled from refraction/wide-angle reflection data. *Earth, Planets Space* 56 (12), 1293–1299. doi:10.1186/bf03353353

Tarantino, S., Colombelli, S., Emolo, A., and Zollo, A. (2019). Quick determination of the earthquake focal mechanism from the azimuthal variation of the initial P-wave amplitude. *Seismol. Res. Lett.* 90 (4), 1642–1649. doi:10.1785/0220180290

Terakawa, T. (2017). Overpressurized fluids drive microseismic swarm activity around Mt. Ontake volcano, Japan. *Earth, Planets Space* 69 (1), 87–10. doi:10.1186/s40623-017-0671-x

Thurber, C. H., Atre, S. R., and Eberhart-Phillips, D. (1995). Three-dimensional Vp and Vp/Vs structure at Loma Prieta, California, from local earthquake tomography. *Geophys. Res. Lett.* 22 (22), 3079–3082. doi:10.1029/95gl03077

Tomic, J., Abercrombie, R. E., and Do Nascimento, A. F. (2009). Source parameters and rupture velocity of small M≤ 2.1 reservoir induced earthquakes. *Geophys. J. Int.* 179 (2), 1013–1023. doi:10.1111/j.1365-246X.2009.04233.x

Ueki, T. (2008). Plio-pleistocene behavior of the itoigawa–shizuoka tectonic line in northern Nagano prefecture, central Japan: Paleomagnetism of the omine-SK tephra. *Bull. Earthq. Res. Inst. Univ. Tokyo* 83, 163–173.

Ueno, S. (2002). Improvement of hypocenter determination method by Japan Meteorological Agency. *Kenshinjiho* 65, 123–134.

Verdon, J. P., Baptie, B. J., and Bommer, J. J. (2019). An improved framework for discriminating seismicity induced by industrial activities from natural earthquakes. *Seismol. Res. Lett.* 90 (4), 1592–1611. doi:10.1785/0220190030

Wadati, K., and Oki, S. (1933). On the travel time of earthquake waves. (Part II). *J. Meteorol. Soc. Jpn. Ser. II* 11 (1), 14–28. doi:10.2151/jmsj1923.11.1_14

Wiemer, S. (2001). A software package to analyze seismicity: ZMAP. *Seismol. Res. Lett.* 72 (3), 373–382. doi:10.1785/gssrl.72.3.373

Yoon, C. E., O'Reilly, O., Bergen, K. J., and Beroza, G. C. (2015). Earthquake detection through computationally efficient similarity search. *Sci. Adv.* 1 (11), e1501057. doi:10.1126/sciadv.1501057

Yukutake, Y., Ito, H., Honda, R., Harada, M., Tanada, T., and Yoshida, A. (2011). Fluid-induced swarm earthquake sequence revealed by precisely determined hypocenters and focal mechanisms in the 2009 activity at Hakone volcano, Japan. *J. Geophys. Res. Solid Earth* 116 (B4), B04308. doi:10.1029/2010JB008036

Zollo, A., Orefice, A., and Convertito, V. (2014). Source parameter scaling and radiation efficiency of microearthquakes along the Irpinia fault zone in southern Apennines, Italy. *J. Geophys. Res. Solid Earth* 119 (4), 3256–3275. doi:10.1002/2013JB010116

Zollo, A., Caruso, A., De Landro, G., Colombelli, S., and Elia, L. (2021). A bayesian method for real-time earthquake location using multiparameter data. *J. Geophys. Res. Solid Earth* 126 (3), e2020JB020359. doi:10.1002/essoar.10503363.1

frontiers | Frontiers in Earth Science

TYPE Original Research
PUBLISHED 24 May 2023
DOI 10.3389/feart.2023.1149932

OPEN ACCESS

EDITED BY
Frantisek Stanek,
Czech Academy of Sciences, Czechia

REVIEWED BY
Yuanyuan Fu,
China Earthquake Administration, China
Yujiang Li,
Ministry of Emergency Management, China

*CORRESPONDENCE
Jiwen Huang,
hjwenlion@csu.edu.cn

RECEIVED 23 January 2023
ACCEPTED 05 May 2023
PUBLISHED 24 May 2023

CITATION
Sun Y, Deng S and Huang J (2023), Crustal structure and the seismogenic environment in Yunnan imaged by double-difference tomography. *Front. Earth Sci.* 11:1149932. doi: 10.3389/feart.2023.1149932

Crustal structure and the seismogenic environment in Yunnan imaged by double-difference tomography

Ya Sun[1,2], Shilin Deng[1,2] and Jiwen Huang[1,2]*

[1]Key Laboratory of Metallogenic Prediction of Nonferrous Metals and Geological Environment Monitoring, Ministry of Education, Central South University, Changsha, China, [2]School of Geosciences and Info-Physics, Central South University, Changsha, China

The large-scale faulting and earthquake activities that developed extensively in the Yunnan area are associated with the collision of India and Eurasia. The fine crustal structure can provide a better understanding of the crustal deformation, seismogenic environment, and rupture processes. We performed a new 3-dimensional (3D) P wave velocity structure and seismic relocation using double-difference tomography based on seismic observations. The tomography images show that large-scale low-velocity anomalies spread around the margin of the south Chuan–Dian Block, Xiaojiang fault (XJF), and the Lijiang–Xiaojinhe fault (LJ-XJHF) in the middle and lower crust. There is an obvious high-speed anomaly in the Emeishan large igneous province (ELIP). We infer that the low-velocity anomaly under the LJ-XJHF zone may be derived from the lower crustal flow extruded from the central Tibetan plateau and obstructed by the ELIP, while the velocity anomalies around the XJF might be caused by shear heating, which is associated with the large-deep strike–slip fault and the transmission of stress in the southeast direction. The inversion results also show that the Yangbi earthquake occurred at the NW–SE boundary of high and low velocity from the upper crust to the lower crust, which coincides well with the location of the Yangbi earthquake sequence and the Weixi–Qiaohou fault. Meanwhile, the earthquake relocations show that the aftershocks are mainly distributed at low velocities. All the aforementioned research results indicate that the Yangbi earthquake might be attributed to the intrusion of the soft material flow along the Weixi–Qiaohou fault in the NW–SE direction. These low-viscosity crustal materials would cause brittle fractures and result in NW–SE sinistral strike–slip faults.

KEYWORDS

double-difference tomography, earthquake relocation, Yunnan area, Yangbi earthquake, strike–slip fault

1 Introduction

The collision between India and Eurasia and the resistance of the Yangtze plate resulted in a regional high-stress environment and many destructive earthquakes in the Southeast margin of the Tibetan Plateau (SE Tibet) (Xu et al., 2013; Wang and Burchfiel, 2000; Zhang et al., 2004). The northeast extrusion of the Indian continent into the Eurasian continent has led to the vertical thickening of the crust under the Tibetan Plateau, as well as the crustal flow and migration of deep materials. The stress is not only transferred within the plateau but also

transferred to the margin of the plateau, forming a series of Cenozoic structures and landforms, accompanied by seismic activities and environmental evolution (Wang and Burchfiel, 2000; Zhang et al., 2004; Xu et al., 2013). SE Tibet was, therefore, demonstrated to have undergone intense deformation and a sudden thickening of the crust and surface uplift (Figure 1A). Two representative models have been put forward to simulate the process of crustal deformation and the uplift of SE Tibet. The first model is the rigid block extrusion along the large deep fault with coherent deformation of the crust and upper mantle lithosphere (Tapponnier and Molnar, 1976; Tapponnier et al., 1982). The second model is the general model of lower crustal flow (Royden et al., 1997; Clark and Royden, 2000), which considers the lower crust as the weak material channel that led to decoupled deformation of the lithosphere mantle and crust since no substantial stress transfers from the low-viscosity materials. Both models suggest that the material of the Tibetan Plateau has extruded into SE Tibet from the lower crust under the compressive stress of the uplift of the Tibetan Plateau. However, the specific extrusion model has not been confirmed.

Yunnan has bred a series of unique deep fault zones, mainly including the Nujiang fault, Lancang River fault, and XJF in the N–S direction; Red River fault (RRF) in the NW–SE direction; and LJ-XJHF in the NE–SW direction (Zhang et al., 2004). Yunnan is different from the northern Chuan–Dian Block and other steep plateau boundaries. Its terrain is relatively flat, and the surface gradient is small. In the process of surface uplift and crustal thickening, there is no obvious large-scale shortening in the crust in this region (Figure 1). However, the current GPS observation shows that there is a large-scale surface movement in this area, and the plateau materials flow from the southeast edge to the east–southeast direction (Cheng et al., 2012). Although previous studies have provided many different perspectives and helped study the deformation mechanism of the crust in this region, the specific distributions of these lower-velocity anomalies are always heterogeneous (Yao et al., 2006). The existence and distribution of the crustal channel flow have also been questioned by various scientists in some new studies (Bai et al., 2010; Bao et al., 2020; Dai et al., 2020). Moreover, the relationship between seismic activities and lower crustal flow is also unclear.

On the other hand, in the past 30 years, hundreds of earthquakes with a magnitude above 6.0 have occurred in this area, such as the recent Yangbi earthquake with Ms 6.4 (Long et al., 2021; Zhang et al., 2021) in 2021, the Ludian earthquake with Ms 6.5 in 2014 (Xie et al., 2015), and the Ya'an earthquake with Ms 7.0 (Zhang et al., 2021). It is one of the areas with the strongest crustal deformation and the most frequent seismic activities in China (Xie et al., 2015; Long et al., 2021; Zhang et al., 2021). Most earthquakes occur along the large deep faults and the main tectonic line, such as the RRF, Longmenshan Fault, LJ-XJHF, and XJF. Moreover, the seismogenic mechanism of these earthquakes might be related to the low-velocity region of the crust below the source area, which indicates that the low-velocity region influences the preparation for large earthquakes (Wei et al., 2013; Wei et al., 2019; Wang et al., 2021).

The current stress field state obtained from the GPS observation, combined with the dynamic process of the seismogenic stage, indicates that the earthquake occurrence rate is higher in southwest Yunnan (Kong et al., 2022). The measurement of the stress accumulation of the coseismic, post-earthquake, and inter-earthquake shows that the stress accumulation of the RRF zone, XJF zone, and LJ-XJHF zone is relatively high (Sun et al., 2014; Bao et al., 2020). Recent geophysical studies show that there are two zones of low velocities around the XJF and LJ-XJHF zones (Li et al., 2008; Sun et al., 2014). A GNSS velocity field shows that the XJF zone has a high degree of fault locking and lateral left slip loss rate, which increases the risk of earthquakes (Zhang et al., 2022). Yunnan as the southern part of SE Tibet is the passage zone of the lower crustal material from the center of Tibet to SE Tibet and is an important area to clarify the lithosphere deformation and the seismogenic mechanism for these strong earthquakes. The study of the fine crustal structure and earthquake relocations can reflect available geophysical evidence for the geodynamic model of surface uplift and

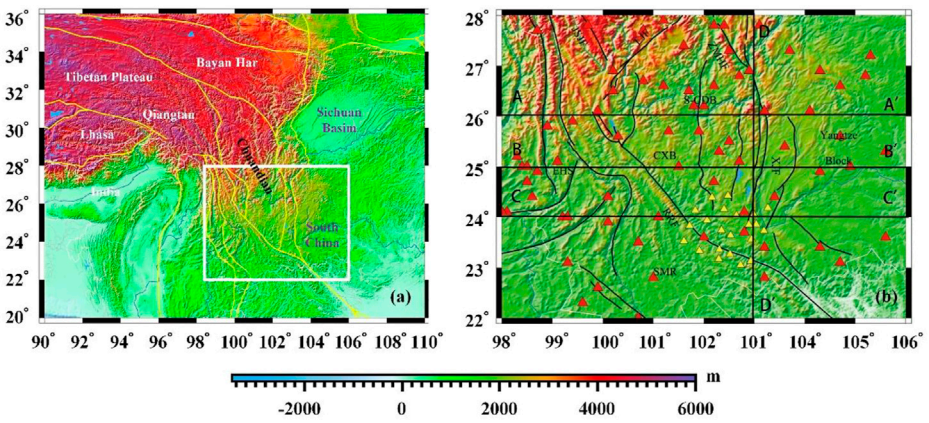

FIGURE 1
(A) Tectonic blocks around the Tibetan plateau. **(B)** Topographic map showing the China Earthquake Administration (CEA) and temporary stations in the southern Chuan–Dian block and its surrounding areas. The red triangle in **(B)** represents the data of the stations of the CEA, and the yellow triangle represents broadband seismic stations installed by Central South University. S-CDB: southern Sichuan–Yunnan block; CXB: Chuxiong Basin; EHS: East Himalayan Block; Yangtze Block: Yangtze plate; SMR: Simao Block; JSJF: Jinshajiang fault zone; LJF: Lijiang fault; ZMHF: Zemuhe fault zone; XJF: Xiaojiang fault zone; RRF: Red River fault zone.

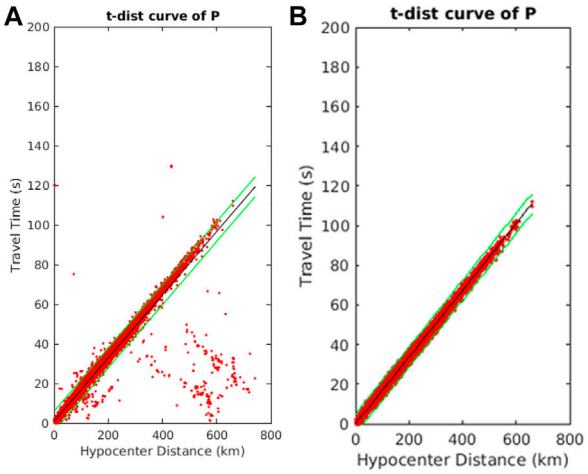

FIGURE 2
Travel time–distance curve of a P wave before selection **(A)** and after selection **(B)**. The data outside the green lines are removed to ensure data quality.

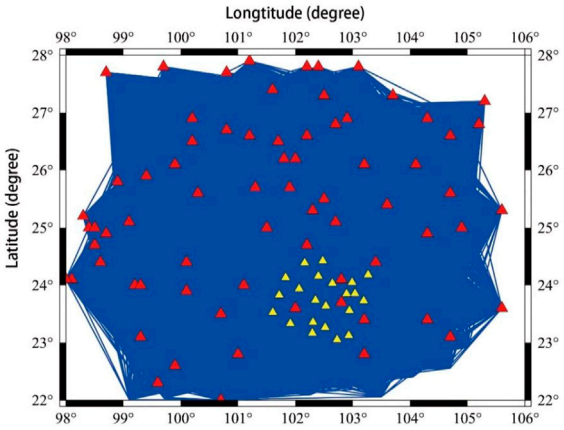

FIGURE 3
Seismic wave ray coverage map; the red triangles represent the data of the CEA, and the yellow triangles represent the data installed by Central South University.

the deep seismogenic environment and mechanism under Yunnan and its surroundings.

Seismic tomography plays an important role in obtaining detailed crustal structure information (Rawlinson et al., 2010; Xin et al., 2019). Many seismic studies have shown and provided valuable geophysical information for the crustal structure and the geodynamic model for surface uplift around SE Tibet (Sun et al., 2012; Lv et al., 2022). However, the distribution of low-velocity anomalies and the relationship between these lower crustal materials and the seismogenic mechanism are still unclear. In this study, we collected a high-quality dataset recorded by the China Earthquake Administration's (CEA) network and a 2-year mobile seismic observation installed by Central South University. We used the collected data to build a new 3D Vp model of the crust of the Yunnan area using the double-difference tomography method (Figure 1B; Waldhauser, 2001; Zhang and Thurber, 2003). The inversion results can give significant information for further understanding the crust structure and the mid-lower crust channel flow and analyzing the deep seismogenic environment and geological structure of the Yangbi area.

2 Data and methods

2.1 Data

We chose 82 seismic stations located in the study region between 98° and 106° in longitude and 22°–28° in latitude recorded by the CEA's network (Zheng et al., 2010) and 22 broadband seismic stations observed for 2 years from 2018 to 2020, which were installed by Central South University. We collected the data of P-wave arrival times from 37,431 earthquakes with magnitudes greater than 1.0 that occurred in Yunnan and its surroundings recorded between January 2009 and December 2020 (https://data.earthquake.cn). Since the first arrival phase was used in the double-difference analysis to invert the crustal structure, we selected the first P-wave arrival time with the smallest travel time and then manually checked the seismograms. The outliers of the P-wave arrival time were further deleted to improve the resolution of the double-difference tomography following two criteria: 1) selecting the phase data with uncertainties smaller than ±9 s, relative to the fitted curve of the major trend of travel time curves for P-wave (Figure 2); 2) the events should be recorded in at least more than eight stations, and the distance between two stations should be larger than 10 km. The number of seismic events was then reduced from 37,431 to 13,590. The number of first P-wave arrivals is 1,743,279. A total of 244,445 differential event pairs were also constructed based on these catalog arrival times. All these P-wave arrivals and the event pairs provide good ray coverage and cross-correlation for reliable double-difference tomography (Figure 3).

2.2 Method

We apply the regional-scale double-difference tomography technique (Zhang and Thurber, 2003) to simultaneously perform seismic tomography and earthquake relocation (Aki and Lee, 1976; Waldhauser and Ellsworth, 2000). Since the travel time between events and stations is calculated in this spherical coordinate system using the finite-difference travel-time algorithm (Aki and Lee, 1976), the double-difference method can produce a more accurate regional-scale seismic velocity structure than the larger-scale seismic velocity structure. Moreover, both the absolute travel time and the relative travel time data are combined to solve the 3D seismic wave velocity of the earthquake source and its surrounding region (Lv et al., 2022).

We first calculate the body-wave travel-time T from an event i to a seismic station k using the ray theory based on the integration along the ray path (Zhang and Thurber, 2003):

$$\tau^i + \int_i^k uds = T_k^i, \quad (1)$$

where $\boldsymbol{u}$ is the slowness, $\boldsymbol{ds}$ is the differential of ray path length, and τ^i is the original time of the event i. Since the relation between the travel time and earthquake event is non-linear, the residual travel-time $\boldsymbol{r}$ can be obtained based on Taylor expansion from Eq. 1. Then, the relation between source parameters and slowness of earthquake event I can be rewritten on each station k:

$$\frac{\partial \boldsymbol{t}_k^i}{\partial \boldsymbol{m}} \Delta \boldsymbol{m}^i + \int_i^k \boldsymbol{\delta u ds} = \boldsymbol{r}_k^i, \tag{2}$$

where $\Delta \boldsymbol{m}^i = (\Delta \mathbf{x}^i, \Delta \mathbf{y}^i, \Delta \mathbf{z}^i, \Delta \boldsymbol{\tau}^i)$ represents the perturbation of source parameters, $\boldsymbol{\delta u}$ is the perturbation of slowness, and $\boldsymbol{r}_k^i = (\boldsymbol{t}^{obs} - \boldsymbol{t}^{cal})_k^i$ is the residual time between the observed differential arrival time and the predicted arrival time, which is the desired perturbation to the hypocenter and velocity structure parameters.

However, the cross-correlation method is used to measure the residual time between different events using the formula $(\boldsymbol{r}_k^i - \boldsymbol{r}_k^j)^{obs}$. We subtract a similar equation for event j measured from station k. The residual time between two events (i and j) at the same station k can be written as follows (Zhang and Thurber, 2003):

$$\frac{\partial \boldsymbol{t}_k^i}{\partial \boldsymbol{m}} \Delta \boldsymbol{m}^i + \int_i^k \boldsymbol{\delta u ds} - \frac{\partial \boldsymbol{t}_k^j}{\partial \boldsymbol{m}} \Delta \boldsymbol{m}^j - \int_j^k \boldsymbol{\delta u ds} = \boldsymbol{r}_k^i - \boldsymbol{r}_k^j, \tag{3}$$

where $\Delta \boldsymbol{m}^{ij} = (\Delta \boldsymbol{dx}^{ij}, \Delta \boldsymbol{dy}^{ij}, \Delta \boldsymbol{dz}^{ij}, \Delta \boldsymbol{d\tau}^{ij})$ is the perturbation of two sources, and the equation can also be simplified as

$$\boldsymbol{dr}_k^{ij} = \boldsymbol{r}_k^i - \boldsymbol{r}_k^j = \left(\boldsymbol{T}_k^i - \boldsymbol{T}_k^j\right)^{obs} - \left(\boldsymbol{T}_k^i - \boldsymbol{T}_k^j\right)^{cal}. \tag{4}$$

$\boldsymbol{dr}_k^{ij}$ is the double difference. $(\boldsymbol{T}_k^i - \boldsymbol{T}_k^j)^{obs}$ is the observed differential travel time between events i and j, and $(\boldsymbol{T}_k^i - \boldsymbol{T}_k^j)^{cal}$ is the calculated differential travel time. When the distance between seismic event pairs is less than the distance between the event and station, the ray path from the earthquake to the station can be approximately regarded as consistent, that is, $\int_i^k \boldsymbol{\delta u ds} = \int_j^k \boldsymbol{\delta u ds}$. Eq. 3 can be written as Eq. 5:

$$\frac{\partial \boldsymbol{t}_k^i}{\partial \boldsymbol{m}} \Delta \boldsymbol{m}^i - \frac{\partial \boldsymbol{t}_k^j}{\partial \boldsymbol{m}} \Delta \boldsymbol{m}^j = \boldsymbol{r}_k^i - \boldsymbol{r}_k^j = \boldsymbol{dr}_k^{ij}. \tag{5}$$

We give an appropriate weight parameter between the differential and the absolute travel time at different stages of inversion (Waldhauser and Ellsworth, 2000).

2.3 Model construction and parameter selection

The inversion formula is obtained by combining the relationship between all seismic event pairs (i, j=1, 2, 3, . . ., N) and all the seismic stations (k=1, 2, 3, . . .):

$$\boldsymbol{WGm} = \boldsymbol{Wd}, \tag{6}$$

where $\boldsymbol{G}$ represents a size of an $M \times 4N$ matrix containing partial derivatives (M is the number of double-difference observations and N is the number of seismic events); $\boldsymbol{d}$ is the data vector; $\boldsymbol{m}$ is the source parameters determined by $\Delta \boldsymbol{m}^i = [\Delta \boldsymbol{x}^i, \Delta \boldsymbol{y}^i, \Delta \boldsymbol{z}^i, \Delta \boldsymbol{\tau}^i]^T$ with a dimension of $4N$; and $\boldsymbol{W}$ is a diagonal matrix weighted for each equation.

The inversion results largely depend on the initial model. Since the crustal structure of the Yunnan area has strong heterogeneity in both vertical and horizontal directions, a one-dimensional initial velocity model cannot invert the accurate result. We then consider the 3D seismic wave velocity model of SWChinaCVM-1.0 observed by the adjoint inversion from body wave and surface wave (Liu et al., 2019; Lv et al., 2022) as the initial model for double-difference tomography in this study (Figure 4). Based on the model resolution and regional seismic ray distribution density, we finally set the node spacing to 0.5° and 1° in our study area and on the edge of the study area, respectively. The vertical grid nodes are set at −5, 0, 1, 5, 10, 15, 20, 25, 30, 35, 40, 50, 60, and 70 km (Figure 5).

To balance the trade-off analysis between data residual variance and model variances, as well as the model smoothness, the L-curve method (Hansen, 1992) is used to obtain the best damping and smoothing factors in inversion. In this study, we choose the best damping factor, 300, and the best smoothing factor, 30 (Figure 6).

2.4 Checkboard test

To estimate the resolution of velocity models and adequacy of the ray path coverage, the checkboard resolution test was used to evaluate the inversion (Zhao et al., 1992). We first add the positive and negative perturbation of 5% to the initial P-wave model and form the input model. The synthetic travel times are then calculated with the same distribution of events and stations as those in real data. The checkboard test is shown in Figure 7, which shows that the velocity anomalies will be well-recovered by travel times from 0 km to 50 km in the study area with good data coverage.

3 Results

3.1 Earthquake distribution after relocation

The seismic event distribution after the relocation is generally consistent with that before relocation. However, the number of seismic relocations is reduced from 23,299 to 19,558. The main reason is attributed to the few data on the arrival time of some seismic events in the inversion process and the lack of good coverage for seismic stations, which lead to the depth of earthquake relocation exceeding the set elevation and locate in the air layer. At the same time, we have deleted the residuals of travel time that are greater than the standard deviation in the inversion. The aforementioned two issues will reduce the number of relocated earthquake events. Moreover, the P-wave residual misfit after the inversion has a smaller range than that before the inversion (Figure 8). The residuals after inversion are concentrated between −2 and 2 s, indicating that the final velocity model is better than the initial model in fitting the actual observation time.

We have drawn the distribution of seismic earthquakes in the horizontal and vertical directions (Figure 9). Vertical cross images along the longitude and latitude after inversion (Figures 9C, D) show that the earthquakes are mainly distributed in the depth of 0–20 km, with less or even no events below 20 km. It also shows that the earthquakes mainly spread in a strip shape in the vertical direction. It indicates that the relocated earthquakes (Figures 9C, D) are more accurate in the vertical direction than those before relocation

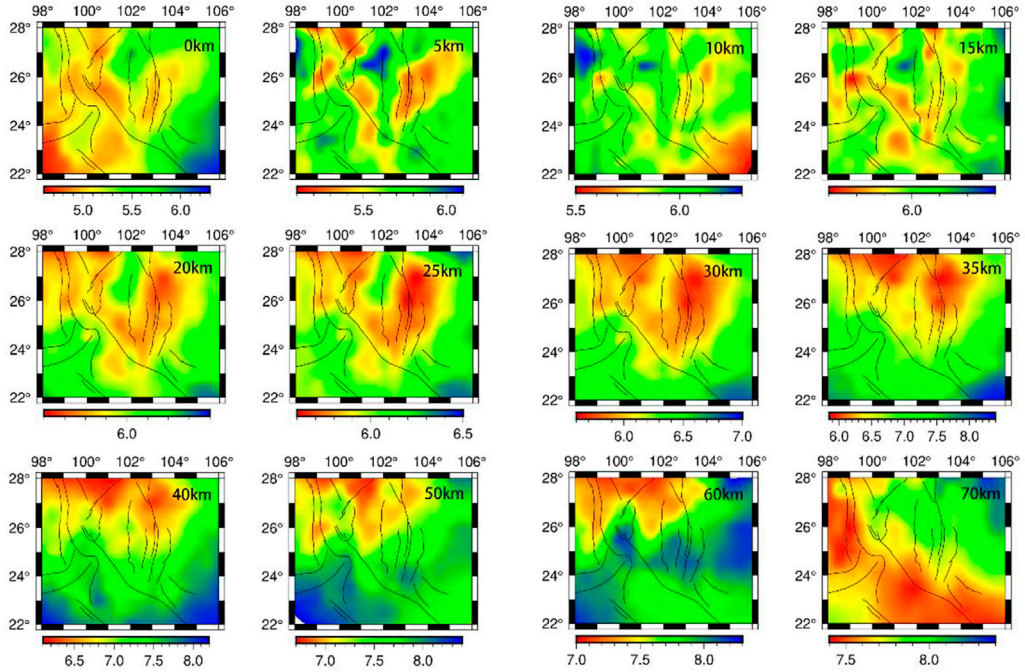

FIGURE 4
3D initial velocity model referred to Lv et al. (2022) and Liu et al. (2019).

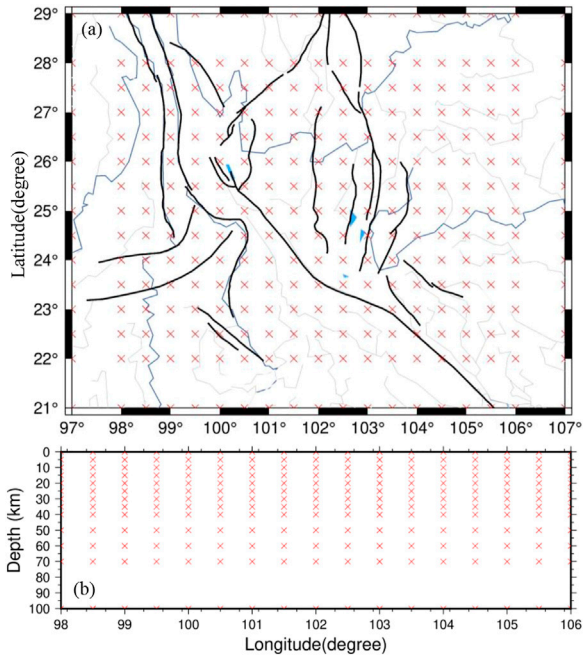

FIGURE 5
3D mesh grid for horizontal **(A)** and E–W vertical cross-section **(B)**. Red crosses represent grid nodes in both horizontal and vertical sections.

(Figures 9B, E). The number of relocated earthquakes in the shallow depth (0–5 km) increases significantly, relative to that before earthquake relocation (Figure 10). Comparing earthquake locations after inversion and before inversion, we found that the relocated earthquake events mainly spread around the fault zone, especially at the south end of the XJHF, XJF zone, and the north section of the RRF zone (Figure 9A).

3.2 Velocity anomalies

The horizontal slices of the 3D Vp models in the depths of 5, 10, 15, 20, 25, 35, 40, and 50 km are shown in Figure 11, which suggest strong lateral heterogeneities in the crust. The vertical profiles of the Vp images along the four lines (AA', BB', CC', and DD') are shown in Figure 12. At shallow depths of 0–15 km, Vp images show that the low-velocity anomaly is widely distributed around the LJ-XJHF, northern RRF, and Zemuhe fault. Meanwhile, the distribution of anomalies is relatively scattered. It indicates that the velocity anomaly area is largely associated with the geological structure at the shallow depth. For the depth of 15–35 km, the extensive low-velocity anomalies extend to the southwest along the LJ-XJHF zone with a belt shape, while the low-velocity anomaly zone along the XJF also appears on the western margin of the Yangtze Craton, which is consistent with the three-dimensional S-wave inversion (Long et al., 2021). We also found that the high-velocity anomalies extend from the surface to 30 km near the center of the southern Chuan–Dian block, which is consistent with the location of the Emeishan large igneous province. For a depth of 20–35 km, our inversion also shows that the high-velocity anomalies are distributed in the Simao Block and Baoshan Block. The vertical image of 103°E shows that the low-velocity anomalies mainly spread in the longitude of 102–105°E (Figures 12AA'–CC') within the depth of 15–35 km (Figure 12DD'), and this low-velocity

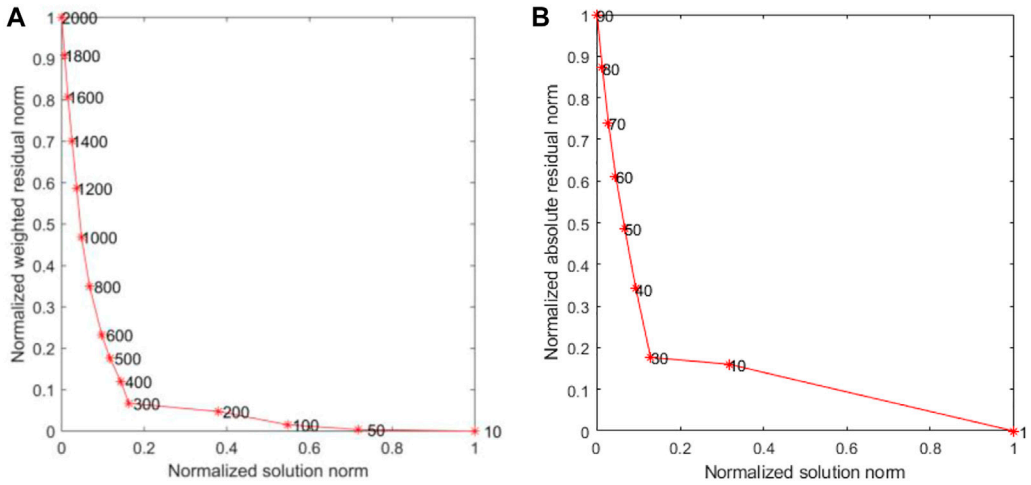

FIGURE 6
L-curve curve, damping factor curve **(A)** and smoothing factor curve **(B)**.

anomaly is continuous from the Zemuhe fault to the intersection of the XJF and RRF. For the vertical seismic profiles of 26 and 25°N, a significant high-velocity anomaly is located around the center of the southern Chuan–Dian block at about 102°E, which separates the low-velocity region into two parts (Figure 12BB'). The vertical P-wave seismic profiles along 26°N, 25°N, 24° N, and 103°E also show that there are obvious low-velocity anomalies in the middle and lower crusts of the XJF and the RRF zones and relatively high-velocity anomalies in the central region of the Chuan–Dian block (Figure 12).

4 Discussion

4.1 Lower crustal flow

Previous studies have generally found that the obvious low-velocity anomalies are widely spread in SE Tibet, especially under the surface of the Chuan-Dian Block (Wei et al., 2013; Bao et al., 2015; Yang et al., 2020). However, the distribution and connection of the low-velocity anomalies in the subsurface, as well as the geodynamics of their deformation, are still unclear.

The horizontal images of the seismic velocity (Figure 11) show a large distribution of low-velocity anomalies at 15–35 km depth below the XJF, LJ-XJHF, and northern RRF zones. The 25-km depth slicing map shows that the low-velocity anomaly is a north–south strip under the Zemuhe fault zone, while it rotates to the southwest along the LJ-XJHF and northern RRF. The distributions of two significant low-Vp anomalies are generally in good agreement with previous research results, including the surface wave tomography (Yao et al., 2010; Bao et al., 2015; Lun et al., 2023) and body wave images (Huang et al., 2019; Deng et al., 2020). Lv et al. (2022) also showed two low-Vp anomaly belts in our study area based on double-difference tomography. The western one distributes from the northwest of the Chuan–Dian block to the LJ-XJH fault and the north part of the RRF, another low-velocity zone around the

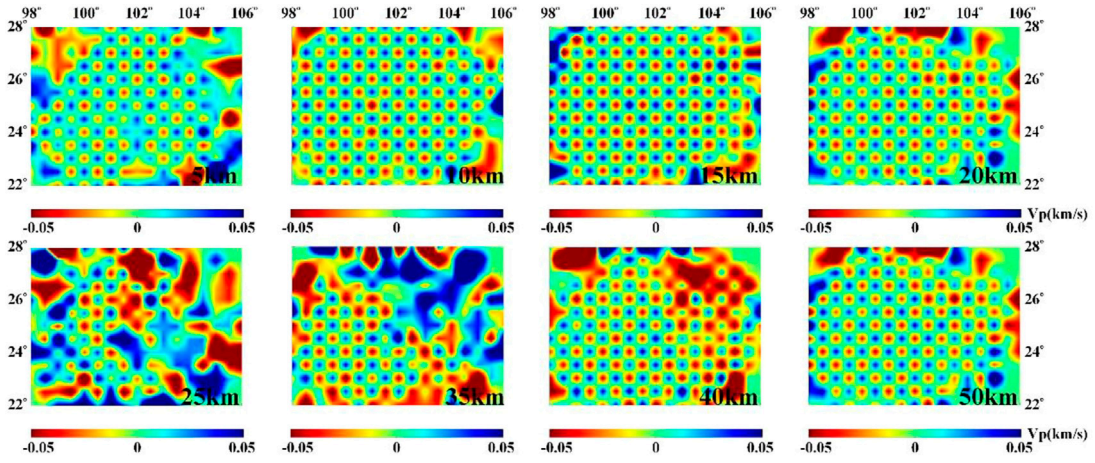

FIGURE 7
Checkboard test for P-wave velocity anomalies at depths of 5, 10, 15,20, 25, 35, 40, and 50 km, respectively.

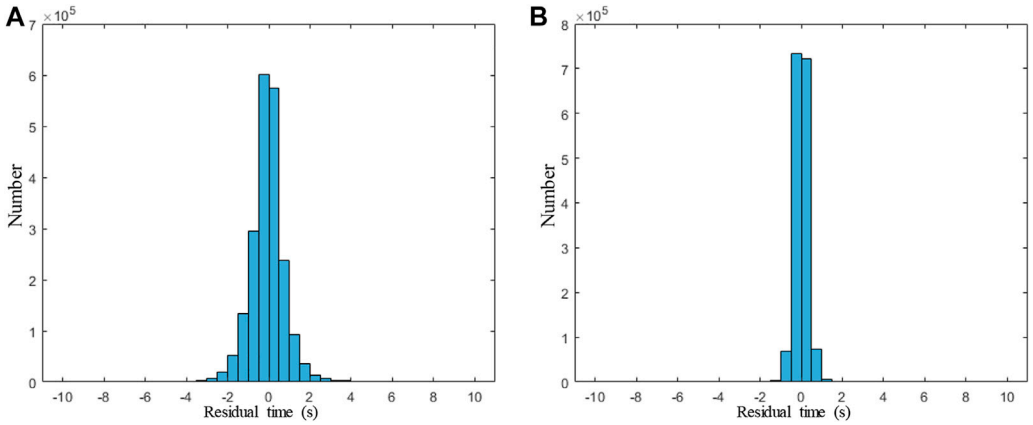

FIGURE 8
Histogram of travel time residuals before **(A)** and after **(B)** relocation for the P-wave.

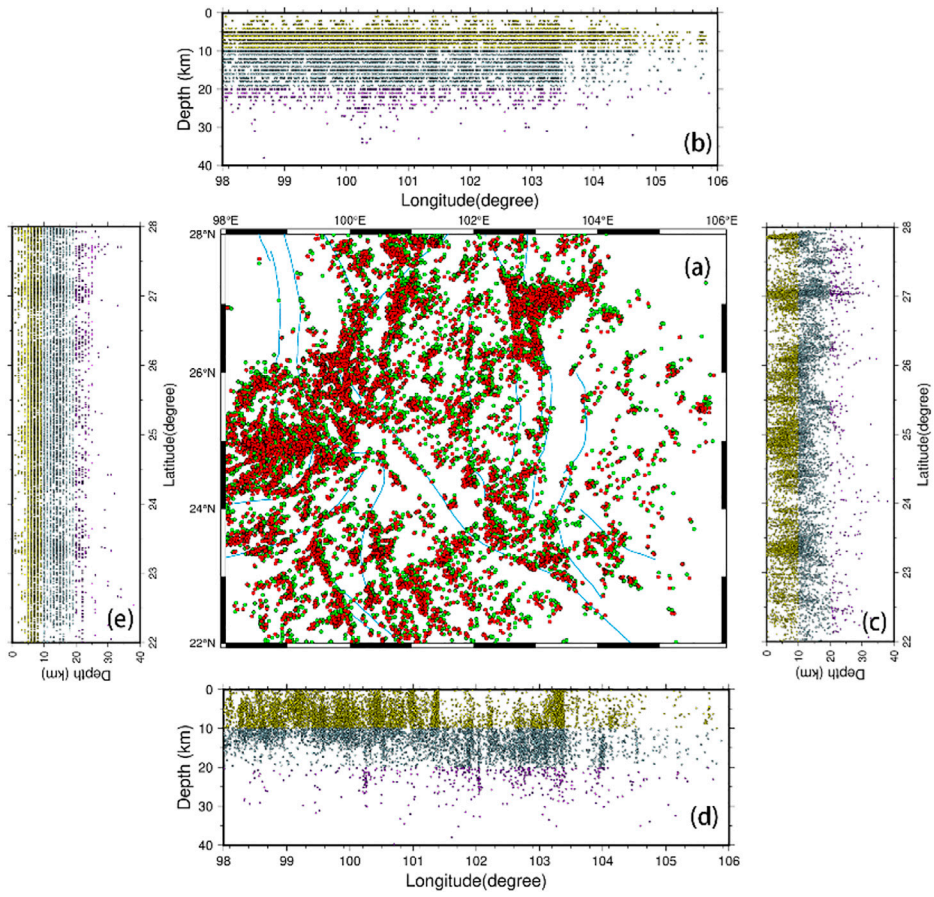

FIGURE 9
Distribution of seismic events in the horizontal profile **(A)**, **(B)** and **(E)** represent seismic events along the longitude and latitude profiles before inversion, respectively. **(C)** and **(D)** represent the relocation of seismic events along the longitude and latitude profiles after inversion, respectively. Red and green dots in **(A)** represent earthquake locations before and after inversion, respectively. Yellow dots represent earthquake locations in the range of 0–10 km, blue dots represent earthquakes in the range of 10–20 km, and purple dots represent earthquakes below 20 km.

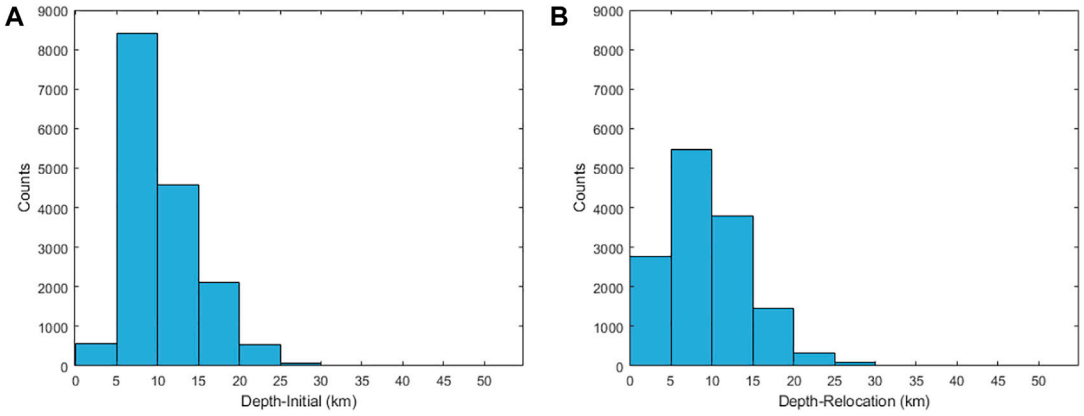

FIGURE 10
Distribution of seismic events in the depth before inversion **(A)** and after inversion **(B)**.

XJF, which are consistent with our results that show significant low velocity at the middle and lower crust in this region. However, the depths of these low-velocity anomalies in this study are 15–35 km, which is relatively less compared to that (20–35 km) found in Lv et al. (2022) and Deng et al. (2020), but similar to that (15–30 km) found in Yang et al. (2020) and Zhang et al. (2020) in the shallow depth. As we know, different data types yield different constraints on the velocity structure. We attribute this difference to the seismic stations that we added, 22 permanent stations around the intersection of the XJF and RRF, which provide good seismic ray coverage and improve the resolution of this area.

Magnetotelluric results (Bai et al., 2010) also show that there are two high-conductivity and low-resistance channels at a depth of 20–40 km. One distributes along the eastern Himalayan syntaxis (EHS) and the other spreads along the Xianshuihe fault zone and XJF zone, which are consistent with the low-velocity zone below the XJF zone in this study. Geochemical data show that the high conductivity of the crust may be caused by thermal, soft material fluid, and partial melting (Liu et al., 2020). Geothermal data (Hedlund et al., 2012) show that the heat flow value in this region reaches 110 mW/m^2, which is far more than the average value of 61 mW/m^2 in Mainland China. The crustal Q-value images (Zhou et al., 2009) also show the low Q-value located near the XJF zone and LJ-XJHF zone. The low Q-value reflects the high attenuation property of the medium in this area, indicating the inelastic property and soft medium associated with temperature change. Seismic wave anisotropy (Sun et al., 2012) shows that the fast wave direction of Ps splitting near the XJF zone is approximate to the N–S direction, indicating that the material

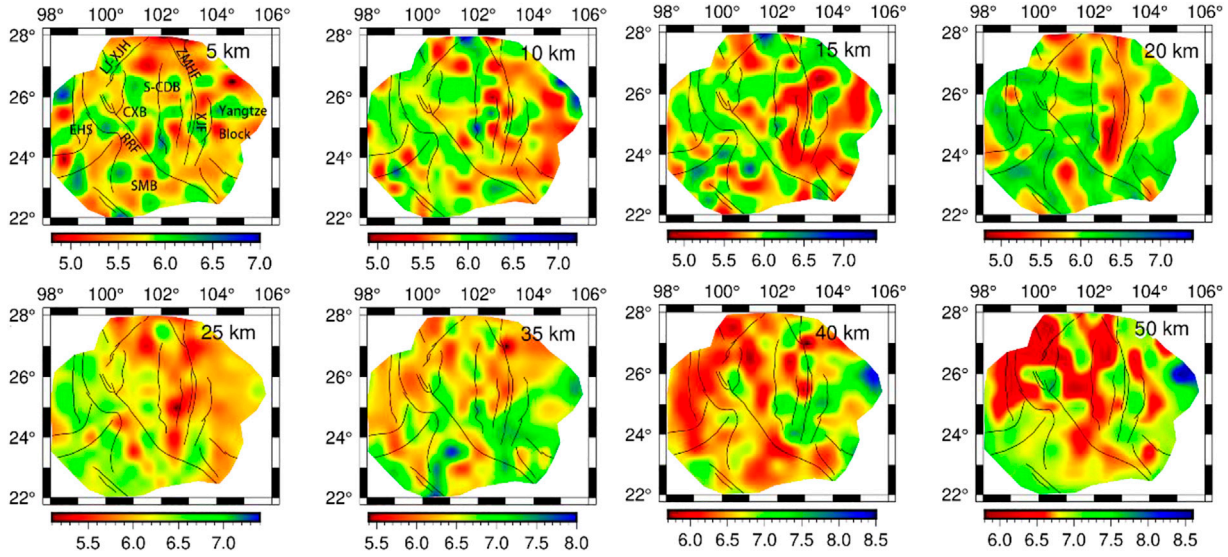

FIGURE 11
Depth slices of P-wave velocity. SMB: Simao Block; S-CDB: South Chuan–Dian Block; RRF: Red River fault; XJF: Xiaojiang fault; ZMHF: Zemuhe fault; LJ-XJHF: Lijiang–Xiaojinhe fault; EHS: East Himalayan Block; SMR: Simao Block; CXB: Chuxiong Basin.

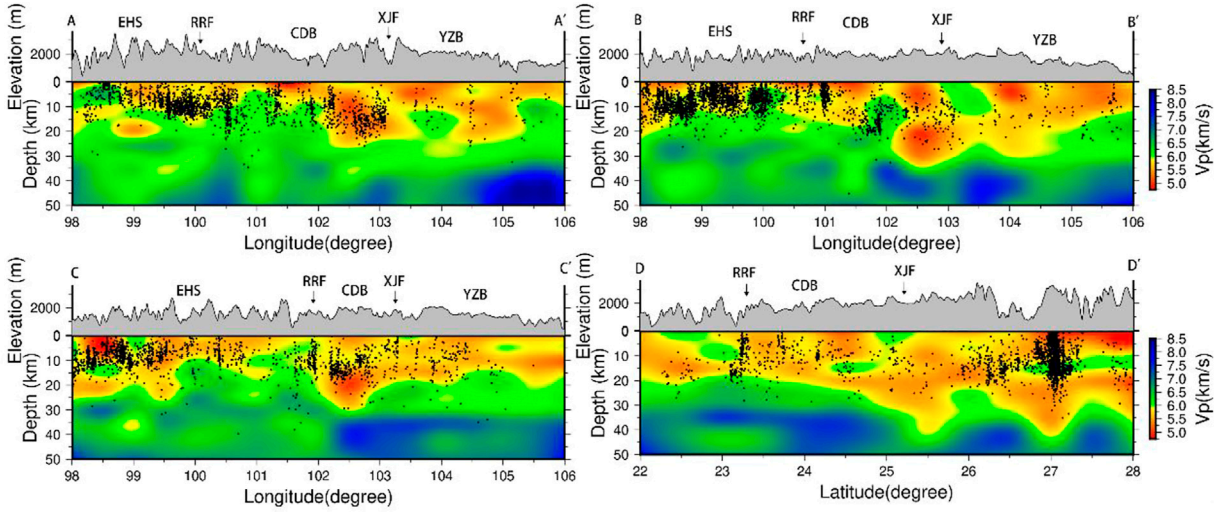

FIGURE 12
P-wave velocity profiles along the latitude of 26°N, 25°N, and 24° N and longitude of 103°E along the **(AA′, BB′, CC′, and DD′)** shown in Figure 1B. CDB: Chuan–Dian Block; RRF: Red River fault; XJF: Xiaojiang fault; YZB: Yangzi Block; EHS: Eastern Himalayan syntaxis. Block dots represent the earthquake relocations.

flow direction is approximately in the N–S direction, while it is in the SW direction near the LJ-XJHF zone, suggesting that the material flow direction is near to southwest direction. The aforementioned results are consistent with those of the low-velocity anomaly distribution area in this paper, inferring that the low-velocity anomaly material under the XJF and LJ-XJHF zones may be the crustal flow from the Tibetan Plateau. However, the inversion results show that the low-velocity anomaly is not widely distributed in the southeast margin of the Tibetan Plateau, mainly distributed along the XJF, LJ-XJHF, and north RRF zone.

P-wave velocity images show a relatively higher-velocity region between two low-velocity regions, which is consistent with the location of the ELIP. It is a volcanic province recognized by the international academic community in China, which is widely distributed in Yunnan, Guizhou, and Sichuan provinces (He et al., 2003). At present, it is generally believed that a large-scale eruption of Emeishan basalt occurred in the center of the Chuan–Dian Block during the late Paleozoic at 256–259 Ma. The analysis of the temporal and spatial distribution of basalt and the geochemical properties of the original magma show that the center of the mantle plume is located west of the Emeishan area (Ma et al., 1993; Xu and Zhong, 2001). The study of peridotite phenocrysts and intrusive bodies confirmed the high magnesium content (MgO>16%) of the original magma in the ELIP (Xu and Zhong, 2001). The seismic exploration profiles (Chen et al., 2022) indicate that the mafic and ultramafic rocks have high P-wave velocities. Then, the high Vp velocity might relate to the intrusion of basic and ultrabasic mantle source materials formed by the activity of mantle plumes into the crust during the Permian period. The lower crustal flow would be blocked by this ultrabasic mantle source material when it extrudes from the north of the Chuan-Dian block to the south, resulting in the lower crustal flow converging near the relatively weak region, such as the XJF and LJ-XJHF and the north RRF.

SE Tibet has always been a seismically active region, with destructive earthquakes having occurred here frequently in recent years. Figure 12 shows that a large number of earthquakes are distributed in the middle–upper crust, and the location of earthquakes has a good relationship with the major faults, especially near the boundary of high- and low-velocity anomalies around the XJF and LJ-XJHF zones (Figure 12). This good relation suggests that the mechanical properties of these regions are weak, and there may be a flow of lower crustal material (Clark and Royden, 2000). Our results are also consistent with those of previous studies that show that the Ludian Ms 6.5 earthquake (Xie et al., 2015) and the 2008 Wenchuan Ms 8.0 earthquake (Lei and Zhao, 2009), and the Changning Ms 6.0 earthquake (Lv et al., 2022) occurred in the boundary of high- and low-velocity anomalies. The good correspondence of the aforementioned characteristics indicates that the large deep fault has a significant effect on the regional seismicity and tectonic evolution process.

4.2 Yangbi earthquake

The Yangbi earthquake occurred on the NW-trending Weixi–Qiaohou fault in 2021 with a magnitude of Ms 6.4 (Long et al., 2021; Lv et al., 2022). The Weixi–Qiaohou fault is located on the western part of the RRF, with dextral strike–slip movement and obvious seismic activity on the Weixi–Qiaohou fault since the Late Quaternary (Sun et al., 2022). Meanwhile, the Weihe–Qiaohou fault has controlled the Weishan Quaternary Basin. Due to the collision between the Indian and Eurasian plateaus and obstruction by the Yangtze Craton, this area has suffered eastward extrusion of the Tibetan Plateau and compression in the east and west directions (Wang et al., 2017). In addition, the Chuan–Dian Block is the junction of the Indian plate subducting to the Burmese plate, and

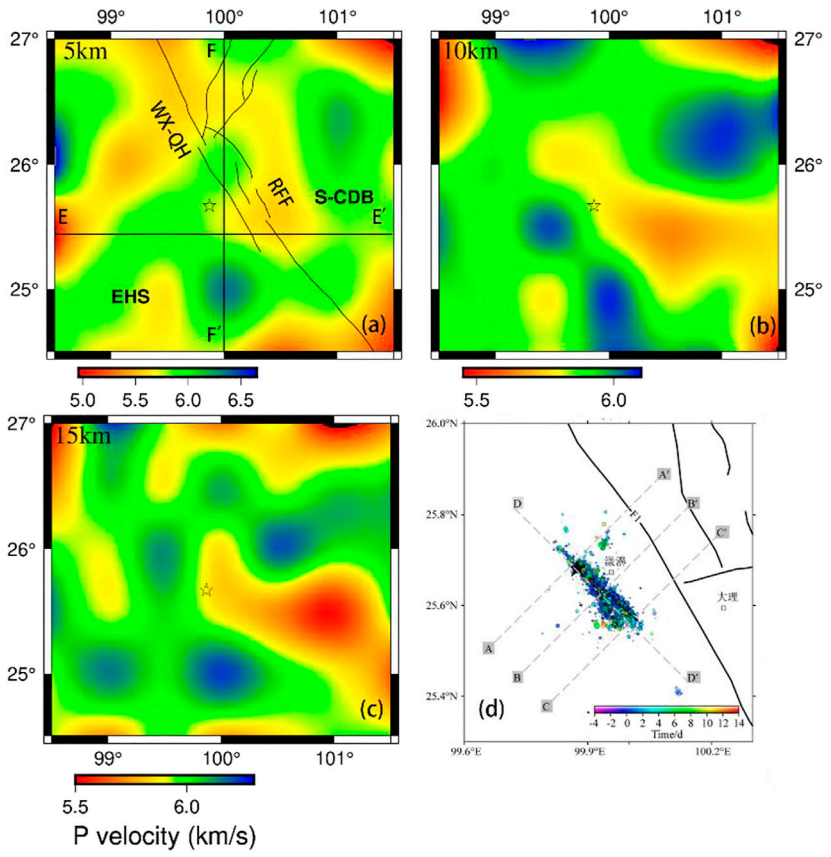

FIGURE 13
Horizontal slice of P-wave velocity and earthquake sequence diagram in the Yangbi earthquake area. **(A–C)** represent the P wave velocity at depth of 5, 10, and 15 km, respectively. The star indicates the location of the Yangbi earthquake. WX-QHF: Weixi–Qiaohou fault; RRF: Red River fault zone. The figure in the lower right region is the earthquake sequence map. **(D)** Referred by Hu et al. (2021)

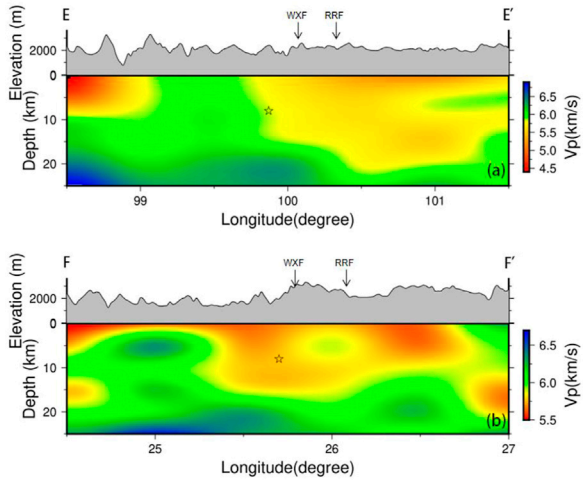

FIGURE 14
P-wave velocity vertical profiles across the Yangbi earthquake with 25 km depth along the EE′ and FF′ in Figure 13A, which is zoomed in from Figure 11. **(A,B)** represent the profiles of EE′ and FF′. The star indicates the location of the Yangbi earthquake. WXF: Weixi fault; RRF: Red River fault zone.

a large-scale fault and extreme seismic activities have developed in this area (Hu et al., 2021).

We enlarged the seismic wave velocity structure in the Yangbi area and drew the three layers and two vertical cross profiles of P-wave velocity (Figures 13A–C, 14A, B). Our results show that there is a clear high- and low-velocity boundary in the Yangbi area, and the velocity anomaly distributes in the NW–SE direction at a depth of 5–15 km (Figures 13A–C, 14). With the increase in depth, the low-velocity anomaly extends to the southeast. Figure 13 shows that the center of the Yangbi earthquake is located in the boundary of high- and low-Vp anomalies, which is consistent with the result of Lv et al. (2022) and Hu et al. (2021). The relocation of the Ms 6.4 Yangbi earthquake sequence shows that the sequence is about 3–13 km away from the nearest known Weixi–Qiaohou fault (Figure 13D), (Li et al., 2022; Lu et al., 2022), indicating that the Yangbi earthquake occurred in the shallow area of the upper crust (Long et al., 2021). Meanwhile, the stress transmitted into the surrounding tectonics caused by the Yangbi earthquake affects the magnitude of Coulomb stress in the southeastern section of the Weixi–Qiaohou fault, significantly increasing the stress in this fracture zone.

The relocation of the earthquake sequence also suggests that the aftershocks of the main earthquake along the northwest segment of the

Weixi–Qiaohou fault are relatively shallow and dense, while those in the southeast part are deeper and dispersed. The seismic cross-sections from the main shock and layer profiles (Figure 14) show that the P-wave low-velocity anomalies extend SE in the deep region and NW in the shallow region. The domain tectonic stress field observed from the focal mechanism solution of the earthquake sequence shows that the seismogenic structure is an NW–SE-trending right-lateral strike–slip movement near the horizontal principal compressive stress. The dislocation type of the main seismogenic fault is generally consistent with that of the Weixi–Qiaohou fault. In addition, the direction of the regional tectonic stress field in the northern segment of the RRF is mainly NNW–SSE (Long et al., 2021). The obvious low-Vp anomalies were distributed around the northern part of the RRF in the upper crust with a depth of 0–15 km, which was interpreted as the weak material flow. The recent ambient noise tomography shows that the lower crustal flow is divided into two ranges in the southern Chuan–Dian block, one along the XJF and the other extending from the LJ-XJHF to the RRF (Liu et al., 2019). Due to the southeast extrusion along the RRF and the clockwise rotation of the southwest Chuan–Dian Block (Long et al., 2021), the extension stress may continue to be transferred southeast along the RRF.

Moreover, the inversion of the b-value shows that the main Yangbi earthquake occurred near the peak values of tidal body strain and Coulomb stress (Hu et al., 2021; Li et al., 2022; Zhang et al., 2022), which reflects the seismic activity of the Yangbi earthquake might be affected by fluid migration (Sun et al., 2022). The high-resolution seismic images of the Yangbi earthquake sequence based on deep learning suggest that a long and narrow strip structure around this area can be analyzed as a channel for material fluid migration (Jin et al., 2019). Geothermal data for regions near the Yangbi earthquake area show that a large number of medium–higher heat flows distribute on the Red River and Weishan–Qiaohou faults (Hu et al., 2000). The observed large low-velocity anomalies around the west of the Yangbi earthquake source have a good correspondence with the low Poisson's ratio and high heat flow (Hu et al., 2000; Liu et al., 2021). The coincidence of these observations implies that the crust here is relatively weak, which might represent the crustal material flow. The studies of earthquake sequences and seismic wave images show that most continual earthquakes occur at the boundary of high- and low-velocity regions (Huang and Zhao, 2004; Mooney et al., 2012), where the large stress and strain energies are easily accumulated (Yang et al., 2021). Combined with the stress, earthquake sequence distribution, and geothermal activity, we infer that cracks were caused by the main Yangbi earthquake around the fault zone. Due to the extrusion of middle and lower crustal flow upwelling along these cracks, the crustal flow further accelerated the fracture of the cracks, resulting in a series of aftershocks.

5 Conclusion

In this study, we construct 3D P-wave velocity images and seismic relocation in the Yunnan region (22°–28°N, 98°–106°E) using the double-difference tomography method, based on the P-wave travel time data recorded by 82 seismic stations in the region from 1 January 2009 to 31 December 2020, and 22 temporary stations installed by Central South University from 2018 to 2020. These results provide some new geophysical evidence for the seismogenic environments of regional earthquakes and the crustal deformation under Yunnan and its surroundings.

(1) The seismic images show that there are two obvious low-velocity zones at a depth of 15–35 km. The east belt distributes along the XJF in the N–S direction, while the west belt extrudes from the LJ-XJHF and rotates to the north RRF. These observations have good correspondence with the high Vp ratio, significant crustal anisotropy, and high heat flow. The coincidence of the aforementioned geophysical observation indicates the existence of two belts of middle-to-lower crustal flow around our study area. The high-seismic velocity region in the central part of the Chuan–Dian Block is located between two low-seismic velocity regions, which is consistent with the distribution of the ELIP.
(2) The seismic images also show that the Yangbi area has an obvious boundary of low and high velocity within the depth of 5–15 km, which is NW–SE-trending and extends to the southeast with the depth. This is consistent with the distribution of aftershock sequences of the Yangbi earthquake and the trend of the WX-QHF zone, indicating that the seismogenesis of the Yangbi earthquake might be related to the regional tectonic stress. Meanwhile, the observed low-velocity anomalies are widespread around the northern RRF, east of the Yangbi area, which was expressed as the lower crustal flow, indicating that the stress continues to be transferred southward along the RRF. The soft materials in the middle and lower crust would drag the upper brittle crust and lead to sinistral strike-slip earthquakes.

Data availability statement

The original contributions presented in the study are included in the article/Supplementary Materials; further inquiries can be directed to the corresponding author.

Author contributions

All authors participated in editing and reviewing the manuscript. YS implemented the methodology and writing—original draft preparation. SD implemented related experiments, earthquake relocation, and tomography. JH was involved in data curation and measuring earthquake relocation. All authors contributed to the article and approved the submitted version.

Funding

This study was supported by the National Natural Science Foundation of China (Grant Nos 42274083 and 41974049).

Acknowledgments

The authors acknowledge the method software application from Haijiang Zhang of the Chinese University of Science and

Technology. Some figures were prepared using the public domain Generic Mapping Tools (GMT).

Conflict of interest

The authors declare that the research was conducted in the absence of any commercial or financial relationships that could be construed as a potential conflict of interest.

Publisher's note

References

Aki, K., and Lee, W. H. K. (1976). Determination of three-dimensional velocity anomalies under a seismic array using first P arrival times from local earthquakes: 1. A homogeneous initial model. *J. Geophys. Res.* 81 (23), 4381–4399. doi:10.1029/JB081i023p04381

Bai, D., Unsworth, M. J., Meju, M. A., Ma, X., Teng, J., Kong, X., et al. (2010). Crustal deformation of the eastern Tibetan plateau revealed by magnetotelluric imaging. *Nat. Geosci.* 3 (5), 358–362. doi:10.1038/ngeo830

Bao, X., Song, X., Eaton, D. W., Xu, Y., and Chen, H. (2020). Episodic lithospheric deformation in eastern Tibet inferred from seismic anisotropy. *Geophys. Res. Lett.* 47 (3), e2019GL085721. doi:10.1029/2019GL085721

Bao, X., Sun, X., Xu, M., Eaton, D. W., Song, X., Wang, L., et al. (2015). Two crustal low-velocity channels beneath SE Tibet revealed by joint inversion of Rayleigh wave dispersion and receiver functions. *Earth Planet. Sci. Lett.* 415, 16–24. doi:10.1016/j.epsl.2015.01.020

Chen, S., Gao, R., Lu, Z., Zhang, X., Li, W., Liang, Y., et al. (2022). Shallow shear wave velocity structure of the Dongshan sag area using surface wave data in a deep reflection profile of the Yuanmou area of Yunnan province, China. *Tectonophysics* 843, 229606. doi:10.1016/j.tecto.2022.229606

Cheng, J., Xu, X. W., Gan, W. J., Ma, W. T., Chen, W. T., and Zhang, Y. (2012). Block model and dynamic implication from the earthquake activities and crustal motion in the southeastern margin of the Tibetan Plateau. *Chin. J. Geophys.* 55 (4), 1198–1212. doi:10.6038/j.issn.0001-5733.2012.04.016

Clark, M. K., and Royden, L. H. (2000). Topographic ooze: Building the eastern margin of Tibet by lower crustal flow. *Geology* 28 (8), 703–706. doi:10.1130/0091-7613(2000)028<0703:tobtem>2.3.co;2

Dai, A., Tang, C. C., Liu, L., and Xu, R. (2020). Seismic attenuation tomography in southwestern China: Insight into the evolution of crustal flow in the Tibetan Plateau. *Tectonophysics* 792, 228589. doi:10.1016/j.tecto.2020.228589

Deng, S., Zhang, W., Yu, X., Song, Q., and Wang, X. (2020). Analysis on crustal structure characteristics of southern Sichuan-Yunnan by regional double-difference seismic tomography. *Chin. J. Geophys.* 63 (10), 3653–3668. doi:10.6038/cjg2020N0383

Hansen, B. E. (1992). Testing for parameter instability in linear models. *J. policy Model.* 14 (4), 517–533. doi:10.1016/0161-8938(92)90019-9

He, B., Xu, Y., and Xiao, L. (2003). Formation mechanism and spatial distribution of igneous rocks in Emei Mountain: New evidence from sedimentary stratigraphy[J]. *Acta Geol. Sin.* 2003 (02), 194–202.

Hedlund, B. P., Cole, J. K., Williams, A. J., Hou, W., Zhou, E., Li, W., et al. (2012). A review of the microbiology of the Rehai geothermal field in Tengchong, Yunnan Province, China. *Geosci. Front.* 3 (3), 273–288. doi:10.1016/j.gsf.2011.12.006

Hu, J., Zhao, T., and Bai, C. Y. (2021). Three-dimensional P and S wave velocity structure and earthquake relocation of the May 21, 2021 Yangbi MS6.4 source region. *Chin. J. Geophys.* 64 (12), 4488–4509. in Chinese. doi:10.6038/cjg2021P0456

Hu, S., He, L., and Wang, J. (2000). Heat flow in the continental area of China: A new data set. *Earth Planet. Sci. Lett.* 179 (2), 407–419. doi:10.1016/S0012-821X(00)00126-6

Huang, J. L., and Zhao, D. P. (2004). Crustal heterogeneity and seismotectonics of the region around Beijing, China. *Tectonophysics* 385 (1–4), 159–180. doi:10.1016/j.tecto.2004.04.024

Huang, Z., Tilmann, F., Comte, D., and Zhao, D. (2019). *P*Wave azimuthal anisotropic tomography in northern Chile: Insight into deformation in the subduction zone. *J. Geophys. Res. Solid Earth* 124 (1), 742–765. doi:10.1029/2018JB016389

Jin, H., Gao, Y., Su, X., and Fu, G. (2019). Contemporary crustal tectonic movement in the southern Sichuan-Yunnan block based on dense GPS observation data. *Earth Planet. Phys.* 3 (1), 53–61. doi:10.26464/epp2019006

Kong, W., Huang, L., Yao, R., and Yang, S. (2022). Contemporary kinematics along the Xianshuihe-Xiaojiang fault system: Insights from numerical simulation. *Tectonophysics* 839, 229545. doi:10.1016/j.tecto.2022.229545

Lei, J., and Zhao, D. (2009). Structural heterogeneity of the Longmenshan fault zone and the mechanism of the 2008 Wenchuan earthquake (Ms 8.0). *Geochem. Geophys. Geosystems* 10 (10), 002590. doi:10.1029/2009GC002590

Li, C., Shan, X., Zhang, G., Zhao, C., Gong, W., and Zhang, Y. (2022). Slip kinematics of the 2021 Yangbi earthquake: Fore-Main-Aftershock sequence rupture along an unknown secondary fault of the weixi–qiaohou fault. *Seismol. Res. Lett.* 93 (3), 1400–1412. doi:10.1785/0220210220

Li, Y., Wu, Q., Zhang, R., Tian, X., and Zeng, R. (2008). The crust and upper mantle structure beneath Yunnan from joint inversion of receiver functions and Rayleigh wave dispersion data. *Phys. Earth Planet. Inter.* 170, 134–146. doi:10.1016/j.pepi.2008.08.006

Liu, C., Yao, H., Yang, H. Y., Shen, W., Fang, H., Hu, S., et al. (2019). Direct inversion for three-dimensional shear wave speed azimuthal anisotropy based on surface wave ray tracing: Methodology and application to Yunnan, southwest China. *J. Geophys. Res. Solid Earth* 124 (11), 11394–11413. doi:10.1029/2018JB016920

Liu, J., Zhang, L., and Du, Y. (2020). Seismic hazard assessment of the mid-northern segment of Xiaojiang fault zone in southwestern China using scenario earthquakes. *Bull. Seismol. Soc. Am.* 110 (3), 1191–1210. doi:10.1785/0120190248

Liu, Y., Li, L., van Wijk, J., Li, A., and Fu, Y. V. (2021). Surface-wave tomography of the Emeishan large igneous province (China): Magma storage system, hidden hotspot track, and its impact on the Capitanian mass extinction. *Geology* 49 (9), 1032–1037. doi:10.1130/G49055.1

Long, F., Qi, Y., Yi, G., Wu, W., Wang, G., Zhao, X., et al. (2021). Relocation of the M S 6.4 Yangbi earthquake sequence on May 21, 2021 in Yunnan Province and its seismogenic structure analysis. *Chin. J. Geophys.* 64 (8), 2631–2646. doi:10.6038/cjg2021O0526

Lu, H., Feng, G., He, L., Liu, J., Gao, H., Wang, Y., et al. (2022). An improved source model of the 2021 M w 6.1 Yangbi earthquake (southwest China) based on InSAR and BOI datasets. *Remote Sens.* 14 (19), 4804. doi:10.3390/rs14194804

Lun, L., Chen, C., Yuanyuan, F., and Hongjian, F. (2023). Multiple surface wave tomography methods and their applications to the Tibetan Plateau. *Rev. Geophys. Planet. Phys.* 54 (2), 174–196. doi:10.19975/j.dqyxx.2022-019

Lv, M., Ding, Z., and Xu, X. (2022). Seismogenic environments of earthquakes on the southeastern margin of the Tibetan Plateau revealed by double-difference tomography. *Tectonophysics* 843, 229603. doi:10.1016/j.tecto.2022.229603

Ma, X., McElhinny, M. W., Embleton, B. J., and Zhang, Z. (1993). Permo-Triassic palaeomagnetism in the Emei mountain region, southwest China. *Geophys. J. Int.* 114 (2), 293–303. doi:10.1111/j.1365-246x.1993.tb03918.x

Mooney, W. D., Ritsema, J., and Hwang, Y. K. (2012). Crustal seismicity and the earthquake catalog maximum moment magnitude (Mcmax) in stable continental regions (SCRs): Correlation with the seismic velocity of the lithosphere. *Earth Planet. Sci. Lett.* 357, 78–83. doi:10.1016/j.epsl.2012.08.032

Rawlinson, N., Pozgay, S., and Fishwick, S. (2010). Seismic tomography: A window into deep Earth. *Phys. Earth Planet. Interiors* 178 (3-4), 101–135. doi:10.1016/j.pepi.2009.10.002

Royden, L. H., Burchfiel, B. C., King, R. W., Wang, E., Chen, Z., Shen, F., et al. (1997). Surface deformation and lower crustal flow in eastern Tibet. *science* 276 (5313), 788–790. doi:10.1126/science.276.5313.788

Sun, Q., Guo, Z., Pei, S., Fu, Y. V., and Chen, Y. J. (2022). Fluids triggered the 2021 Mw 6.1 Yangbi earthquake at an unmapped fault: Implications for the tectonics at the northern end of the Red River fault. *Seismol. Res. Lett.* 93 (2A), 666–679. doi:10.1785/0220210227

Sun, X., Bao, X., Xu, M., Eaton, D. W., Song, X., Wang, L., et al. (2014). Crustal structure beneath SE Tibet from joint analysis of receiver functions and Rayleigh wave dispersion. *Geophys. Res. Lett.* 41, 1479–1484. doi:10.1002/2014gl059269

Sun, Y., Niu, F., Liu, H., Chen, Y., and Liu, J. (2012). Crustal structure and deformation of the SE Tibetan plateau revealed by receiver function data. *Earth Planet. Sci. Lett.* 349, 186–197. doi:10.1016/j.epsl.2012.07.007

Tapponnier, P., and Molnar, P. (1976). Slip-line field theory and large-scale continental tectonics. *Nature* 264 (5584), 319–324. doi:10.1038/264319a0

Tapponnier, P., Peltzer, G. L. D. A. Y., Le Dain, A. Y., Armijo, R., and Cobbold, P. (1982). Propagating extrusion tectonics in Asia: New insights from simple experiments with plasticine. *Geology* 10 (12), 611–616. doi:10.1130/0091-7613(1982)10<611:petian>2.0.co;2

Waldhauser, F., and Ellsworth, W. L. (2000). A double-difference earthquake location algorithm: Method and application to the northern Hayward fault, California. *Bull. Seismol. Soc. Am.* 90, 1353–1368. doi:10.1785/0120000006

Waldhauser, F. (2001). hypoDD-A program to compute double-difference hypocenter locations. doi:10.7916/D8SN072H

Wang, E., and Burchfiel, B. C. (2000). Late Cenozoic to Holocene deformation in southwestern Sichuan and adjacent Yunnan, China, and its role in formation of the southeastern part of the Tibetan Plateau. *Geol. Soc. Am. Bull.* 112 (3), 413–423. doi:10.1130/0016-7606(2000)112<413:lcthdi>2.0.co;2

Wang, F., Shi, W., Zhang, W., Wu, L., Yang, L., Wang, Y., et al. (2017). Differential growth of the northern Tibetan margin: Evidence for oblique stepwise rise of the Tibetan Plateau. *Sci. Rep.* 7 (1), 41164–41169. doi:10.1038/srep41164

Wang, Y., Hu, S., He, X., Guo, K., Xie, M., Deng, S., et al. (2021). Relocation and focal mechanism solutions of the 21 May 2021 M S 6.4 Yunnan Yangbi earthquake sequence. *Chin. J. Geophys.* 64 (12), 4510–4525. doi:10.6038/cjg2021P0401

Wei, L., Qingju, W., Fengxue, Z., Sun, L. Y., Zeng, Z. G., Qu, W., et al. (2019). A new approach to accomplish intraoperative cholangiography in left lateral segmentectomy of living liver donation. *Acta Seismol. Sin.* 41 (2), 155–161. doi:10.12659/AOT.915400

Wei, W., Zhao, D., and Xu, J. (2013). P-wave anisotropic tomography in Southeast Tibet: New insight into the lower crustal flow and seismotectonics. *Phys. Earth Planet. Interiors* 222, 47–57. doi:10.1016/j.pepi.2013.07.002

Xie, Z., Zheng, Y., Liu, C., Xiong, X., Li, Y., and Zheng, X. (2015). Source parameters of the 2014 Ms 6.5 Ludian earthquake sequence and their implications on the seismogenic structure. *Seismol. Res. Lett.* 86 (6), 1614–1621. doi:10.1785/0220150085

Xin, H., Zhang, H., Kang, M., He, R., Gao, L., and Gao, J. (2019). High-resolution lithospheric velocity structure of continental China by double-difference seismic travel-time tomography. *Seismol. Res. Lett.* 90 (1), 229–241. doi:10.1785/0220180209

Xu, Y., and Zhong, S. (2001). Emei Mountain igneous rocky province: Evidence of mantle plume activity and its melting conditions[J]. *Geochemistry* 2001 (01), 1–9. doi:10.19700/j.0379-1726.2001.01.002

Xu, Y., Yang, X. T., and Liu, J. H. (2013). Tomographic study of crustal velocity structures in the Yunnan region southwest China. *Chin. J. Geophys.* 56 (6), 1904–1914. doi:10.6038/cjg20130613

Yang, W., Ding, Z., Liu, J., Cheng, J., Zhang, X., Wu, P., et al. (2021). Velocity structure of the northeastern end of the Bayan Har block, China, and the seismogenic environment of the Jiuzhaigou and Songpan-Pingwu earthquakes: Inferences from double-difference tomography. *Bull. Seismol. Soc. Am.* 111 (4), 2195–2208. doi:10.1785/0120200224

Yang, Y., Yao, H. J., Wu, H. X., Zhang, P., and Wang, M. M. (2020). A new crustal shear-velocity model in Southwest China from joint seismological inversion and its implications for regional crustal dynamics. *Geophys. J. Int.* 220, 1379–1393. doi:10.1093/gji/ggz514

Yao, H., van Der Hilst, R. D., and De Hoop, M. V. (2006). Surface-wave array tomography in SE Tibet from ambient seismic noise and two-station analysis—I. Phase velocity maps. *Geophys. J. Int.* 166 (2), 732–744. doi:10.1111/j.1365-246X.2006.03028.x

Yao, H., van der Hilst, R. D., and Montagner, J. P. (2010). Heterogeneity and anisotropy of the lithosphere of SE Tibet from surface wave array tomography. *J. Geophys. Res. Solid Earth* 115 (B12), B12307. doi:10.1029/2009JB007142

Zhang, H., and Thurber, C. H. (2003). Double-difference tomography: The method and its application to the Hayward fault, California. *Bull. Seismol. Soc. Am.* 93 (5), 1875–1889. doi:10.1785/0120020190

Zhang, P. Z., Shen, Z., Wang, M., Gan, W., Burgmann, R., Molnar, P., et al. (2004). Continuous deformation of the Tibetan Plateau from global positioning system data. *Geology* 32 (9), 809–812. doi:10.1130/G20554.1

Zhang, Y., An, Y., Long, F., Zhu, G., Qin, M., Zhong, Y., et al. (2022). Short-term foreshock and aftershock patterns of the 2021 Ms 6.4 Yangbi earthquake sequence. *Seismol. Res. Lett.* 93 (1), 21–32. doi:10.1785/0220210154

Zhang, Y., Meng, Q., Wang, Z., Lu, X., and Hu, D. (2021). Temperature variations in multiple air layers before the mw 6.2 2014 ludian earthquake, yunnan, China. *Remote Sens.* 13 (5), 884. doi:10.3390/rs13050884

Zhang, Z., Yao, H., and Yang, Y. (2020). Shear wave velocity structure of the crust and upper mantle in Southeastern Tibet and its geodynamic implications. *Sci. China Earth Sci.* 63, 1278–1293. doi:10.1007/s11430-020-9625-3

Zhao, D., Hasegawa, A., and Horiuchi, S. (1992). Tomographic imaging of P and S wave velocity structure beneath northeastern Japan. *J. Geophys. Res. Solid Earth* 97 (B13), 19909–19928. doi:10.1029/92JB00603

Zheng, X. F., Yao, Z. X., Liang, J. H., and Zheng, J. (2010). The role played and opportunities provided by IGP DMC of China National Seismic Network in Wenchuan earthquake disaster relief and researches. *Bull. Seismol. Soc. Am.* 100 (5B), 2866–2872. doi:10.1785/0120090257

Zhou, L. Q., Liu, J., Su, Y. J., Ma, H. S., and Zhou, J. (2009). Tomography for Q of Yunnan region from high-frequency attenuation of S wave. *Chin. J. Geophys.* 52 (6), 1500–1507. doi:10.3969/j.issn.0001-5733.2009.06.011

frontiers | Frontiers in Earth Science

TYPE Original Research
PUBLISHED 30 May 2023
DOI 10.3389/feart.2023.1152348

OPEN ACCESS

EDITED BY
Lei Li,
Central South University, China

REVIEWED BY
Giovanni Martinelli,
National Institute of Geophysics and Volcanology, Section of Palermo, Italy
Fuqiong Huang,
China Earthquake Networks Center, China

*CORRESPONDENCE
Guofu Luo,
153968569@qq.com

RECEIVED 27 January 2023
ACCEPTED 18 May 2023
PUBLISHED 30 May 2023

CITATION
Luo G, Ding F, Xu Y, Luo H and Li W (2023), Strain fields of *Ms* >6.0 earthquakes in Menyuan, Qinghai, China.
Front. Earth Sci. 11:1152348.
doi: 10.3389/feart.2023.1152348

Strain fields of *Ms* >6.0 earthquakes in Menyuan, Qinghai, China

Guofu Luo*, Fenghe Ding, Yingcai Xu, Hengzhi Luo and Wenjun Li

Seismological Bureau of Ningxia Hui Autonomous Region, Yinchuan, China

In predicting earthquakes, it is a major challenge to capture the time factor and spatial isoline anomalies, and understand their physical processes, of the seismic strain field before a strong earthquake. In this study, the seismic strain field was used as representative of seismic activity. The natural orthogonal function expansion method was used to calculate the seismic strain field before the Menyuan *M*s 6.4 earthquakes in 1986 and 2016, and the *M*s 6.9 earthquake in 2022. Time factor and spatial isoline anomaly of the strain field before each earthquake was extracted. We also compared the evolution of the strain field with numerical simulation results under the tectonic stress system at the source. The results showed that the time factor before the earthquakes had high or low value anomalies, exceeding the mean square error of the stable background. The anomalies were concentrated in the first four typical fields of the strain field, which has multiple components. The abnormal contribution rate of the first typical field is the largest (accounting for 42%–49% of the total field). The long- and medium-term anomalies appear 3-4, and 1-2 years before the earthquake, respectively. There were no short or immediate-term anomalies within 3 months of the earthquake. In addition, during the evolution of the strain field, the abnormal area of the spatial isoline changed with the change in time. Usually, the intersection area of the two isoseismic lines of strain accumulation and strain release becomes a potential location for strong earthquakes. Finally, we found that the high strain field values of the 1986 and 2016 *M*s 6.4 earthquakes were equivalent to the numerical simulation results, while the high strain field values of the 2022 Menyuan *M*s 6.9 earthquakes were slightly different, but within the accepted error range. These results indicate that the two methods are consistent. We have shown that the natural orgthagonal method can be used to obtain the spatiotemporal anomaly information of strain field preceding strong earthquakes.

KEYWORDS

Menyuan region China, *Ms* >6.0 earthquakes, seismic strain field, spatiotemporal anomalies, natural orthogonal function expansion method

1 Introduction

The Menyuan region is located in the middle of the eastern region of the Qilian Mountains block on the northeastern boundary of the Tibetan Plateau in China. This orogenic belt has strong tectonic deformation, relatively large topographic gradient variations, and strong movements (Gaudemer et al., 1995; Jiang et al., 2017; Li et al., 2021). The area has long been pushed by the Indian plate, leading to the northeastern expansion of the Tibetan Plateau and the resisting force of the Alxa block (Pan et al., 2022; Yuan et al., 2023). The region has a complex internal geological structure, and the active

Lenglongling and Tuolaishan fault zones that developed mainly during the Holocene belong to the strongly active Qilian-Haiyuan fault zone branch (Zheng et al., 2013). Historically, the following earthquake events were located in areas known for strong earthquake activity (Yuan et al., 2023; Zuo et al., 2023): the 1927 Gansu Gulang *Ms* 8 (Zheng et al., 2004; Liu et al., 2007; Guo et al., 2020), 1986 Menyuan *Ms* 6.4 (Yan et al., 1987; Dang et al., 1988; He et al., 2019), 2016 Menyuan *Ms* 6.4 (Hu et al., 2016; Xu et al., 2016; Guo et al., 2017; Liang et al., 2017; Liu et al., 2019; Zhao et al., 2019; Qu et al., 2021), and 2022 Menyuan *Ms* 6.9 (Fan et al., 2022; Sun et al., 2022; Xu et al., 2022). Recently, several detailed studies have investigated the activity pattern, seismogenic environment and earthquake triggering capacity of the Lenglongling fault zone (Guo et al., 2017; Liu et al., 2018; Zhao et al., 2019). Three *Ms* >6.0 earthquakes in Menyuan are believed to have been associated, predominantly, with the Lenglongling fault, although the 2022 Menyuan *Ms* 6.9 earthquake resulted from the combined activity of the Tuolaishan and Lenglongling faults (Fan et al., 2022; Zhao et al., 2022; Yuan et al., 2023), with ruptures occurring on both sides (Xu, 2022). The 2022 Menyuan *Ms* 6.9 earthquake significantly affected the Jinqianghe and Laohushan faults situated at the eastern side of the Lenglongling fault, increasing the seismic stress and, the probability of strong earthquakes in future (Pan et al., 2022; Yuan et al., 2023).

In recent years, strong seismic activity in the Menyuan area has elicited abundant research, with detailed local and international studies being conducted on the cause, velocity structure, coseismic deformation, and surface rupture of strong earthquakes in the area. Zuo and Chen (2018) and Wang et al. (2022) investigated the three-dimensional body wave velocity structure and seismic relocation of the crust in the Menyuan region, contending that the heterogeneity of the velocity structure showed strong congruity with the two Menyuan *Ms* 6.4 earthquakes. Zhang et al. (2020) found that the 2016 Menyuan *Ms* 6.4 earthquake resulted from the delayed rupture deep in the focus of the 1986 earthquake. Gai et al. (2022), Han et al. (2022), Liang et al. (2022), Li Z et al. (2022), and Pan et al. (2022) studied the distribution of the surface rupture and seismogenic structures of the 2022 Menyuan *Ms* 6.9 earthquake. Yang et al. (2022), Huang et al. (2022), Li Y et al. (2022), and Bao et al. (2022), employing Interferometric Synthetic Aperture Radar (InSAR) data, determined the coseismic deformation of the Menyuan *Ms* 6.9 earthquake. These authors conducted slip inversion of the earthquake, demonstrating that the surface rupture process was a consequence of the combined actions of the Lenglongling and Tuolaishan faults.

The application of field theory to study anomalies before strong earthquakes is relatively new. In China, the orthogonal function expansion method is used to calculate the energy field (Yang and Zhao, 2004), frequency field (Luo et al., 2023) and strain field (Yang et al., 2017; Luo et al., 2018; Luo et al., 2019) before strong earthquakes. This method analyze the relationship to between spatiotemporal anomalies and strong earthquakes. In Japan, India, Europe and the United States, the empirical orthogonal function method is used to calculate deformation fields before and after strong earthquakes (Chang and Chao, 2011; Chao and Liau, 2019; Neha and Pasari, 2022). This method analyzes the co-seismic deformation and gives the motion direction of 3-dimensional deformation.

In this study, we used the natural orthogonal function expansion method to analyze the strain field before 3 *Ms* >6.0 earthquakes in the Menyuan region. We aimed to understand the spatial and temporal anomalies that occur before strong earthquakes, analyze the evolution characteristics of spatial anomalies of the strain field over time, and give the physical interpretation of spatial anomalies and strong earthquake locations. In addition, this is the first time the results of numerical simulation under the tectonic stress system and strain field evolution have been compared.

2 Methodology

Seismic strain was considered a random variable and was broken into temporal and spatial functions using the natural orthogonal function expansion method, also known as the seismic strain field *S* (Yang et al., 2017; Luo et al., 2018). Using the grid method, the strain field was constructed for a particular study region according to the level of seismic activity in the region. A time interval Δt was selected, the observation time was divided into different m periods $t_i = \Delta t \times i (i = 1, 2, ...m)$; and the area was separated into n equal-area elements $\Delta S = \Delta x \times \Delta y$, with center coordinates of $(x_j, y_j) (j = 1, 2, ...n)$. The observed values in each area element in each time-period S_{ij} were calculated and used as the field function value representing the spatiotemporal coordinates $(x_i, y_i, t_j) (i, j = 1, 2, ...n)$.

The seismic energy release was represented by E, Considering that the square root of seismic energy is proportional to the seismic strain, i.e., $\sqrt{E} = c\varepsilon$ (c is the focal-related parameter of the earthquake in the study region, and ε is the seismic focal region cumulative strain parameter), where both parameters reflect strain field changes in the focal region. After assessing the region, the strain field function was established through $S = \sum_i \sqrt{E_i}$, expressed in a matrix form:

$$\boldsymbol{S} = \begin{bmatrix} S_{11} & S_{12} & \cdots & S_{1n} \\ S_{21} & S_{22} & \cdots & S_{2n} \\ \vdots & \vdots & \vdots & \vdots \\ S_{m1} & S_{m2} & \cdots & S_{mn} \end{bmatrix} \tag{1}$$

The Menyuan region has similar seismic blocks, and seismic focal-related parameter c is approximately constant. The field function $S = \sum_i \sqrt{E_i}$ is also known as the seismic strain field, where S_{ij} $(i = 1, 2, ...m, j = 1, 2, ...n)$ is the j th grid and i th time-period of the cumulative seismic strain value. The energy agrees with the formula $LogE = 4.8 + 1.5M$ ($\boldsymbol{E}$ is the energy unit in joules, M is magnitude). We conducted the natural orthogonal function expansion, which involved breaking down matrix S into the sum of the product of orthogonal spatial function x and orthogonal temporal function T:

$$S_{ij} = \sum_{p=1}^{n} T_{ip} X_{pj} \begin{cases} i = 1, 2, \cdots, m \\ j = 1, 2, \cdots, n \end{cases} \tag{2}$$

The orthogonality and normalization conditions were satisfied, as follows:

$$\sum_{j=1}^{n} x_{kj} x_{lj} = \begin{cases} 0 & k \neq l \\ 1 & k = l \end{cases} \tag{3}$$

$$\sum_{i=1}^{m} T_{ik}T_{il} = \begin{cases} 0 & k \neq l \\ \lambda_k & k = l \end{cases} \quad (4)$$

The characteristic equation of the corresponding covariance matrix $R = S'S$ was solved, as follows:

$$\begin{bmatrix} R_{11} & R_{12} & \cdots & R_{1n} \\ R_{21} & R_{22} & \cdots & R_{2n} \\ \cdots & \cdots & \cdots & \cdots \\ R_{n1} & R_{n2} & \cdots & R_{nn} \end{bmatrix} \begin{bmatrix} x_1 \\ x_2 \\ \cdots \\ x_n \end{bmatrix} = \lambda \begin{bmatrix} x_1 \\ x_2 \\ \cdots \\ x_n \end{bmatrix} \quad (5)$$

The eigenvectors $\vec{x}_k$ and eigenvalues λ_k ($k = 1, 2...n$) were obtained. The temporal factor (i.e., weight coefficient sequence) is expressed as:

$$\vec{T}_k = S\vec{x}_k \quad k = 1, 2, \cdots n \quad (6)$$

The eigenvectors $\vec{x}_k$ (strain fields) represent the spatial distribution of seismic strain in the different fields constituting the field, and the temporal factor $\vec{T}_k$ represents temporal changes in strain fields $\vec{x}_k$, reflecting the dynamic characteristics of the strain fields at different times. The eigenvectors corresponding to the first few eigenvalues (in order of large to small) in matrix R satisfied the accuracy of fitting of the total strain field, indicating that the superposition of the first few eigenvectors (strain field) approximated the total strain field. Accordingly, the changes of the first few main strain fields we studied represented the spatiotemporal characteristics of the strain field in the study region. Assuming that the sum of all n eigenvalues was b_0, using the previous typical field l, the accuracy of fitting of the total field r_l was:

$$r_l = \sum_{p=1}^{l} \lambda_p \Big/ b_0 \quad (7)$$

where λ_p represents the p th characteristic root.

The natural orthogonal function expansion method was employed to extract the strain fields corresponding to the largest eigenvalues, which is equivalent to encapsulating the main information of the strain fields in the region. The focus was on the anomalies of the highest strain fields and any strain fields without anomalies or that had a small correlation with strong earthquakes were excluded.

3 Data

3.1 Catalog and calculated parameters

The earthquake data used in this study was derived from the official national earthquake catalog of the China Earthquake Networks Center (CENC). A b-value test was performed on the seismic data in the study region from January 1975 to December 2022, with the lower limit of the smallest complete magnitude of the earthquake being set to M_L 2.7. The probability of moderate and strong earthquakes occurring in the study region is quite small, and the release of strain energy has a significant effect on this region. Therefore, earthquakes with intensities greater than moderate were not considered to belong to the normal seismic activity in our study region, and the upper magnitude limit was set to *Ms* 5.0. We employed the K-K theory (Luo et al., 2019) to remove the aftershocks of *Ms* >5.0 earthquakes. A grid of 0.5° × 0.5°(Yang et al., 2017) was used for the study region, and the time-sliding algorithm was adopted, with a time interval of 12 months, sliding span of 1 month, and the data were discretized. Seismic strain release matrix S was constructed in accordance with Eq. 1, and natural orthogonal function expansion analysis was conducted. Covariance matrix R was solved to obtain the eigenvalues of the field and the main strain fields corresponding to these eigenvalues. The temporal factors corresponding to the eigenvalues of the main fields were obtained, along with the spatial isolines of different study regions.

3.2 Tectonic and geological settings

The study region is located at (100.5°–103.5° E, 35.5°–38.5° N) in the Qilian Mountain block area on the northeastern boundary of the Tibetan Plateau, where a series of approximately parallel faults has developed, that is, inclined toward the NWW, as shown in Figure 1. These parallel faults include the Xunhua Nanshan, Dabanshan, Tuolaishan, Lenglongling, Jinqianghe, Qilian Mountain northern boundary, and Changma–Ebo faults. Moreover, several other NNW-trending faults are present, such as the Wuwei–Tianzhu, Zhuanglanghe, and Riyueshan faults, along with numerous secondary faults. Accordingly, this fault system is an important and active system on the northeastern edge of the Tibetan Plateau (Figure 1A). Over the past 40 years, three consecutive *Ms* >6.0 earthquakes have occurred in the Menyuan region (Figure 1B), with the Lenglongling fault being the seismogenic origin of the 1986 and 2016 *Ms* 6.4 thrust earthquakes (He et al., 2019; Qu et al., 2021). The seismogenic origin of the 2022 strike-slip *Ms* 6.9 earthquake in Menyuan was a combination of the Tuolaishan and Lenglongling faults (Pan et al., 2022; Yuan et al., 2023). The seismic activity of *Ms* >6.0 earthquakes in the Menyuan region could indicate that the earthquakes have accumulated a relatively high strain field capable of triggering strong earthquakes whenever the main active faults slide and rupture (Zuo et al., 2023).

4 Results

4.1 Strain field time factor

We used the natural orthogonal function expansion method to study the spatiotemporal characteristics of the seismic strain fields in the Menyuan region in the 10 years prior to the occurrence of the 1986 and 2016 *Ms* 6.4 earthquakes and the2022 *Ms* 6.9 earthquake. The results are shown in Table 1.

The parameters included the calculation grid and time-period, temporal factors, and time of anomaly of the first four strain fields as well as anomaly types, mean square error, and accuracy of the previous four strain fields. The accuracy of the first four strain fields was above 89%, whereas that of the 2022 *Ms* 6.9 earthquake was above 99 Figure 2 shows the characteristics of strain field changes over time, before the three *Ms* >6.0 earthquakes. In our study, the analyzed the temporal factor of the strain field that exceeded the mean square error as the criterion for anomalies. The anomalies (Luo et al., 2023) were classified based on timing before the

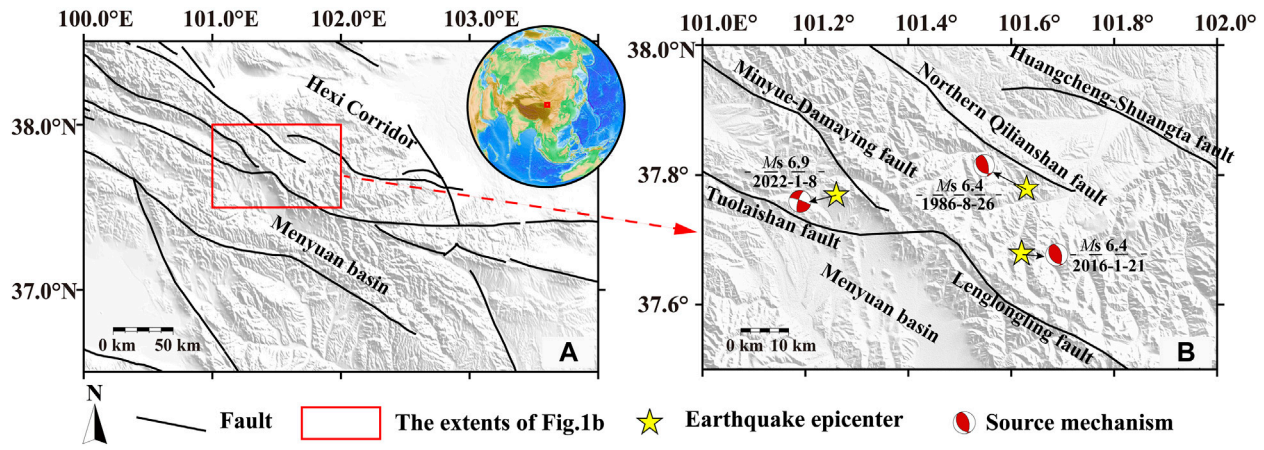

FIGURE 1
(A) Study area of the northeastern margin of the Tibetan Plateau. Black lines show major faults. The red rectangle represents the location of the study area. **(B)** The northeast direction of the red rectangle is the Hexi Corridor, and the south is the Menyuan basin. Regional seismic setting of the 1986, 2016, and 2022 Menyuan earthquakes. The epicenters of the earthquakes are indicated by stars in accordance with data derived from the China Earthquake Networks Center (CENC). The focal mechanism of the 1986 Menyuan *M*s 6.4 earthquake derives from the United States Geological Survey (USGS), that of the 2016 Menyuan *M*s 6.4 earthquake is from Yin et al. (2018), and that of the 2022 Menyuan *M*s 6.9 earthquake is from Xu et al. (2022).

TABLE 1 Strain field temporal factors.

No.	Earthquake	Grids (n,m)	Time span of the data	Temporal factor	Time of anomaly (year-month)	Mean square error	Type of anomaly	Accuracy *r*
1	1986-8-26	(36,137)	1975-01–1986-08	T_1	1984-10–12	±1.2055	medium term	0.8966
				T_2	1980-01–03	±1.0913	Long and medium term	
					1985-04–06			
	M_s 6.4			T_3	1982-04–06	±0.5318	Long term	
				T_4	1982-02–04	±0.4491	Long term	
2	2016-1-21	(36,118)	2006-01–2016-01	T_1	2008-01–03	±3.0313	Long term	0.9720
					2012-05–07			
				T_2	2014-10–12	±2.0792	medium term	
	M_s 6.4			T_3	2007-07–09	±1.9303	medium and long term	
					2014-10–12			
				T_4	2014-01–03	±1.2192	medium term	
3	2022-1-8	(36,118)	2012-01–2022-01	T_1	2019-07–09	±3.0583	Long term	0.9932
					2012-03–05			
				T_2	2014-01–03	±1.2645	Long term	
	M_s 6.9			T_3	2019-08–2020-02	±0.1960	medium term	
				T_4	2018-06–08	±0.1610	Long term	

n, number of grids; m, time interval. T_k is the kth (1 to 4) strain-field time factor.

earthquake as: long-term (10 years), medium-term (1-2 years), short-term (3 months), and imminent (tens of days).

One or several anomalies of the four strain field factors appeared every time before a strong earthquake. Whether the magnitude of the anomaly exceeded the absolute value of the mean square error was used as the criterion for determining whether there was an anomaly. More than two medium-term anomalies appeared before the 1986 and 2016 earthquakes, and one medium-term anomaly appeared before the 2022 earthquake. Two long-term anomalies and no short-term anomalies were detected (Table 1), and the first two

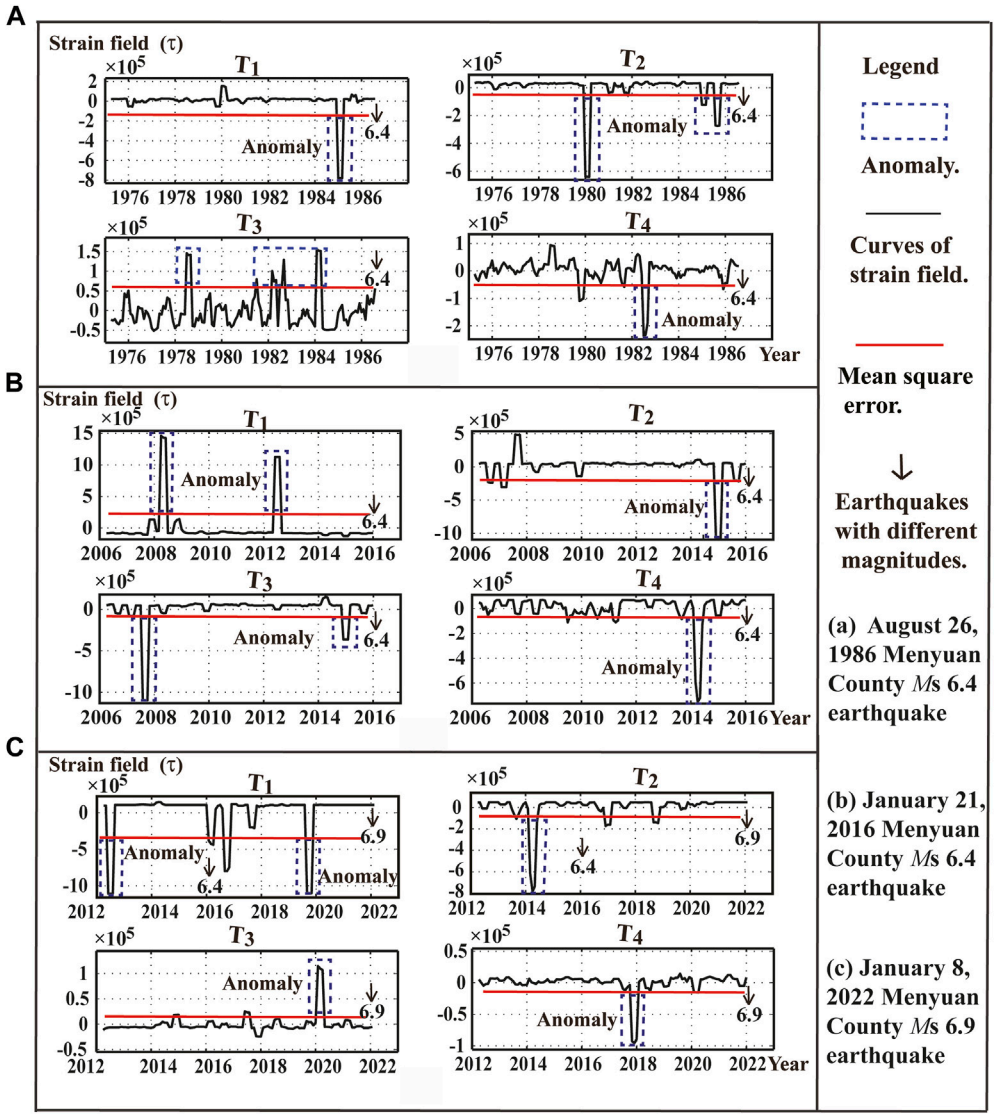

FIGURE 2
Temporal factors of the first four strain fields of three *Ms* ≥6.0 earthquakes. **(A)** August 26, 1986 Menyuan County *Ms* 6.4 earthquake; **(B)** January 21, 2016 Menyuan County *Ms* 6.4 earthquake; **(C)** January 8, 2022 Menyuan County *Ms* 6.9 earthquake. The blue dotted line represents the anomaly, the red line is the mean square error, and the black arrow represents the magnitude of the Ms ≥6.0 earthquake.

temporal anomalies were related to the 2016 earthquake. Generally, the overall changes in the four strain field temporal factor curves were stable before the three *Ms* >6.0 earthquakes. Relatively few anomalies exceeded the threshold (the mean square error, indicated by the red line in Figure 2).

4.2 Strain field spatial evolution

In our study of the seismic strain field spatial isoline evolution patterns in the study region before and after strong earthquakes, the environs of the isoline values (or absolute values) greater than 0.05×10^5 were usually defined as danger zones (Luo et al., 2018). The positive values of the isolines represented seismic strain field release and the negative values represented seismic strain field accumulation. The danger zone in the intersection between strain field release and accumulation usually corresponded to the location of the main shock. Combined with the geological structure in the region, the strain field accumulation and release regions of the active faults could be considered the seismogenic location of future strong earthquakes (Yang et al., 2017; Luo et al., 2019). Figure 3 shows the spatial distribution of the strain fields in the region before and after the August 1986 earthquake. From January to March 1986, two types of large area seismic danger zones—Strain field accumulation and release—Occurred in the middle of the eastern region of the Qilian Mountain. From April to June 1986, the number of anomalies in the seismic danger zone increased, and these were divided into multiple anomalies. From July to September 1986, the area of the two anomalous zones increased, and the earthquake occurred around the two danger zones of the Lenglongling fault. From October to December 1986, the danger zones of the strain field isolines gradually increased in size, before finally slowly disintegrating.

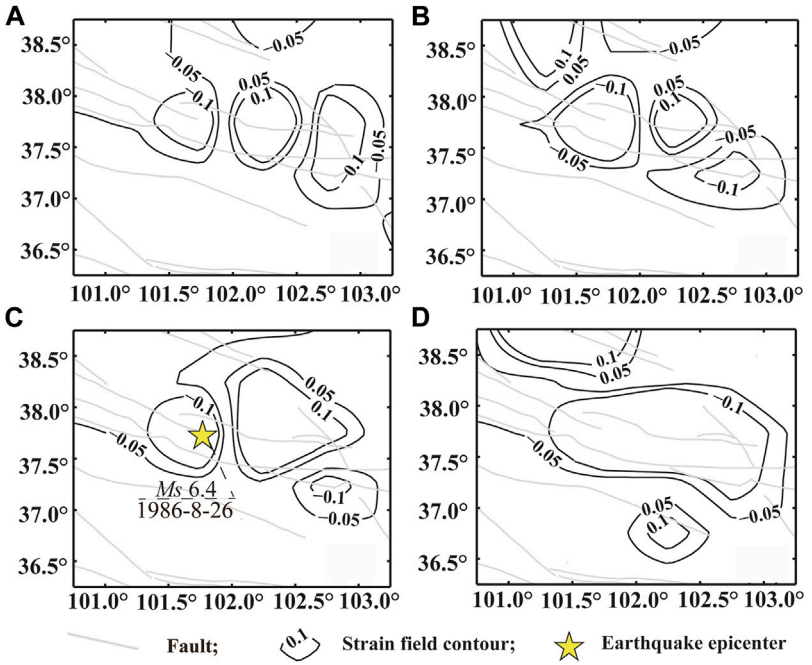

FIGURE 3
Spatial distribution of the strain field before and after the 1986 earthquake. Strain field from **(A)** January to March 1986; **(B)** April to June 1986; **(C)** July to September 1986; **(D)** October to December 1986. The gray and black lines are the fault and strain field contour, respectively. A negative value indicates accumulated strain, and a positive value indicates released strain. Isoline value 0.1 represents 0.1×10^5. The yellow stars represents the epicenter of the Menyuan *Ms* 6.4 earthquake on 26 August 1986.

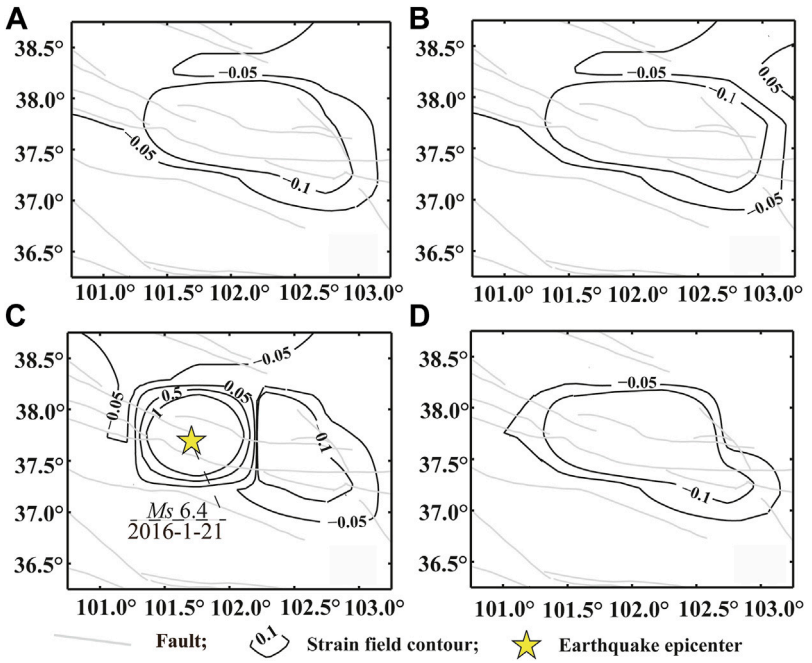

FIGURE 4
Spatial distribution of the strain field before and after the 2016 earthquake. Strain field from **(A)** July to September 2015; **(B)** October to December 2015; **(C)** January to March 2016; **(D)** April to June 2016. The gray and black lines are the fault and strain field contour, respectively. A negative value indicates accumulated strain, and a positive value indicates released strain. Isoline value 0.1 represents 0.1 × 105. The yellow stars represents the epicenter of the Menyuan *Ms* 6.4 earthquake on 21 January 2016.

10.3389/feart.2023.1152348

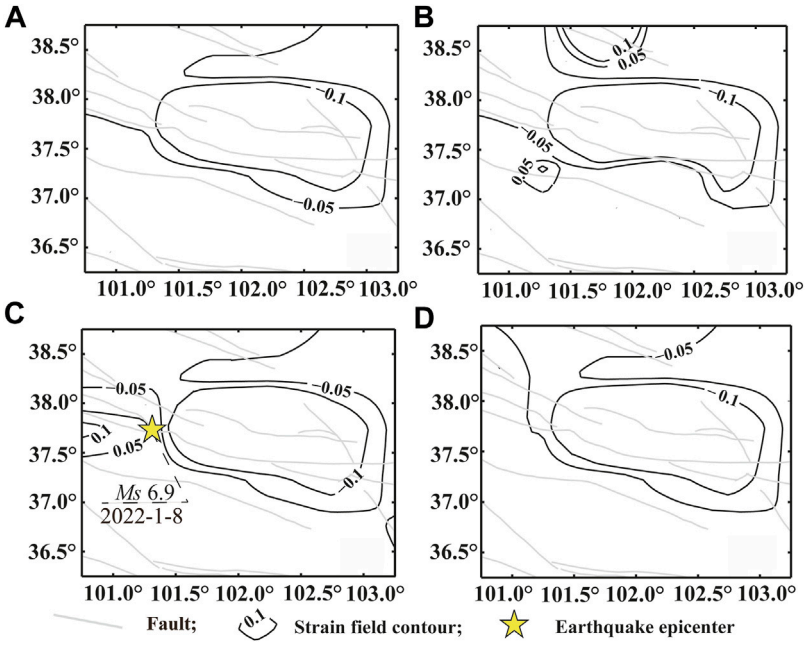

FIGURE 5
Spatial distribution of the strain field before and after 2022 earthquake. Strain field from **(A)** July to September 2021; **(B)** October to December 2021; **(C)** January to March 2022; **(D)** April to June 2022. The gray and black lines are the fault and strain field contour, respectively. A negative value indicates accumulated strain, and a positive value indicates released strain. Isoline value 0.1 represents 0.1×10^5. The yellow stars represents the epicenter of the Menyuan *Ms* 6.9 earthquake on 8 January 2022.

Figure 4 shows the spatial distribution of the strain fields in the region before and after the earthquake in January 2016. A strain-field accumulation danger zone appeared in the middle of the eastern area of the Qilian Mountain from July to September 2015. The area of the strain-field danger zone remained unchanged from October to December 2015, although a strain field release danger zone appeared in the northeast of the study region. From January to March 2016, the two large areas of strain field accumulation and release seismic danger zone anomalies appeared to converge and split into multiple anomalies. Here, at the same time, the earthquake occurred in the center of the anomalous zone. However, no main shock occurred at the intersection of the danger zone. From April to June 2016, the strain-field isoline danger zone gradually enlarged and, ultimately, slowly disintegrated.

Figure 5 shows the spatial distribution of the strain fields in the region before and after earthquake in January 2022, where a strain field accumulation danger zone surfaced in the middle eastern Qilian Mountain from July to September 2021. From October to December 2015, the strain-field danger zone area decreased, and a strain-field release danger zone simultaneously appeared in the north- and southwest of the danger zone, forming an anomalous intersection of these strain field accumulation and release danger zone areas. From January to March 2016, strain field accumulation and release anomalous danger zones formed along the intersection of the Tuolai Mountain fault and the Lenglongling fault zone and, at the same time, the earthquake occurred at the intersection of the danger zone. From April to June 2022, the strain-field isoline danger zones gradually increased before finally slowly disintegrating.

A comparison of Figures 3–5 indicated differences in the strain field isoline anomaly evolution patterns before and after the earthquakes. There were also similarities in that the anomalies in strain accumulation and release first appeared in the study region, followed by several anomalous areas appearing. Additionally, the danger zone increased in size before slowly disappearing after the main earthquake. These findings explained the inference (Zhang et al., 2020) that the 2016 Menyuan *Ms* 6.4 earthquake was the result of delayed rupture deep in the focus of the 1986 Menyuan *Ms* 6.4 earthquake. Moreover, our findings were consistent with those of He et al. (2019) that the 2016 Menyuan *Ms* 6.4 earthquake was a repeating earthquake of the 1986 Menyuan *Ms* 6.4 event.

4.3 Relationship between spatial anomalies and strong earthquakes

The study region has long been subjected to the northeasterly pushing of the Tibetan Plateau and resistance from the Alxa block, which has led to the gradual deformation of the Haiyuan-Qilian Mountain fault zone, as well as accumulation of considerable seismic strain that has formed a locked seismogenic unit. The high concentration of stress and strain in the environs of the locked zone has led to earthquakes or fault branches in the Haiyuan-Qilianshan fault zone. Such events have triggered changes in the accumulation of stress and strain, which, in turn, has altered the spatial distribution of the seismic strain field. Accordingly, seismogenic information on the 1986 Menyuan *Ms* 6.4, 2016 Menyuan *Ms* 6.4, and 2022 Menyuan *Ms* 6.9 earthquakes

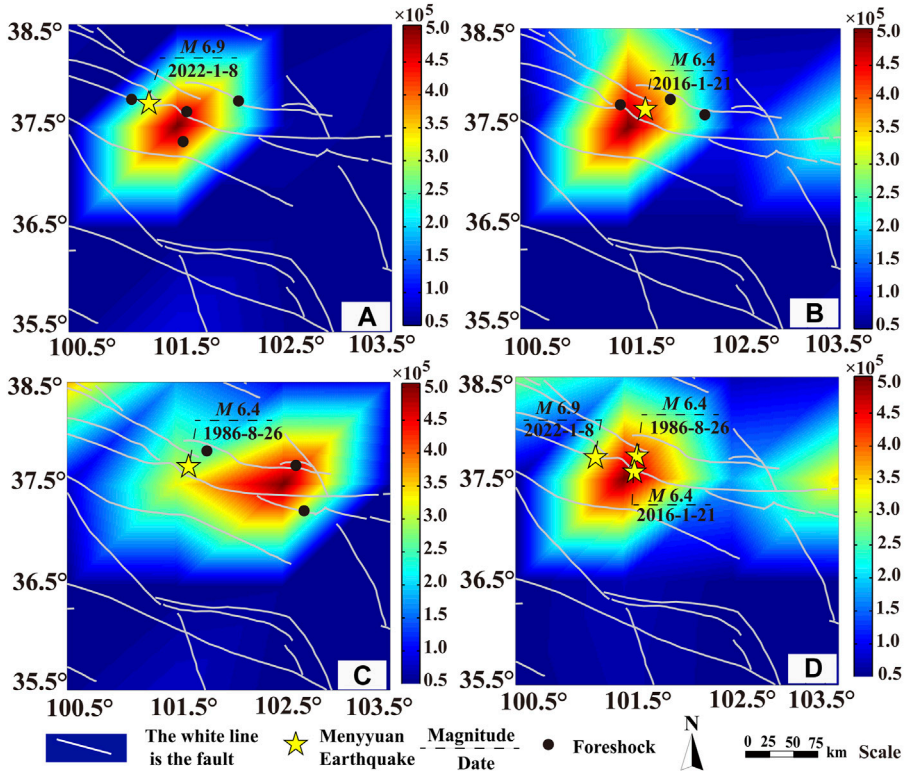

FIGURE 6
Spatial distribution of the seismic strain in the study area from 1975 to 2022. Spatial distribution of the seismic strain field from **(A)** 1 February 2016 to 7 January 2022; **(B)** 1 January 2006 to 20 January 2016; **(C)** 1 January 1975 to 25 August 1986; **(D)** 1 January 1975 to 31 December 2022. The white line is the fault, the yellow stars represents the epicenter of the *Ms* ≥6.0 earthquake and the black point is the epicenter of *Ms* 3–5 foreshocks. The area enclosed by sky blue, yellow, and red is the abnormal area of the seismic strain field.

was included in this study of the seismic strain field in the Menyuan region, where the dynamic processes of strong earthquakes are reflected.

Figure 6A shows the spatial distribution of the seismic strain field from 1 February 2016 to 7 January 2022. The seismic strain anomalies were concentrated mainly in the Lenglongling and Sunan–Qilian faults in a hexagonal distribution and a northeast direction. The center of the anomalies was located on the Lenglongling fault, with a value of approximately 4.3×10^5; however, 2022 earthquake occurred on the boundary of the strain field anomaly with a value of approximately 2.5×10^5. Figure 6B shows that the seismic strain field anomalies from 1 January 2006 to 20 January 2016 were concentrated around the Lenglongling fault and followed a hexagonal distribution in a northeast direction, with a larger area of anomalies. The 2016 earthquake occurred near the high anomalous value area (4.5×10^5). Figure 6B shows that the seismic strain field anomalous area was larger from 1 January 1975 to 25 August 1986, was moving in an easterly direction, and was concentrated mainly around the Gulang and Huangcheng-Shuangta faults. The 1986 earthquake occurred at the boundary of the anomaly, with a value of approximately 2.8×10^5. Figure 6C shows two high-value areas that appeared in the seismic strain field anomalies from 1 January 1975 to 31 December 2022. The high-value northeastward-trending hexagonal anomalous area was centered on the Lenglongling fault and corresponded to all three earthquakes. Another high strain field anomalous value in Tianzhu County, Gansu Province could indicate a seismogenic unit of future strong earthquakes. A comparison between Figures 6A–C showed that the seismic strain field high anomalous values were concentrated predominantly around the Lenglongling fault, with the environs of the high anomalous value area corresponding mainly to the three Menyuan *Ms* >6.0 earthquakes east of the Lenglongling fault. The vicinity of the Tianzhu fault could be a seismogenic unit of future strong earthquakes. These areas predicted as sites for potential future strong earthquakes were consistent with the strong earthquake danger zones proposed by Xu et al. (2022), Fan et al. (2022), and Yuan et al. (2023).

5 Discussion

5.1 Comparison between seismic strain field and tectonic stress

This study aimed to understand the strain field factors that contributed to three earthquakes in the Menyuan region in 1986, 2016 and 2022. These factors determined the outcome of the relative shear stress produced by the two focal mechanism solution nodal planes of the 2022 Menyuan *Ms* 6.9, 2016 Menyuan *Ms* 6.4, and 1986 Menyuan *Ms* 6.4 earthquakes (Figure 7). The outcomes of the focal mechanism solutions of the three earthquakes were consistent

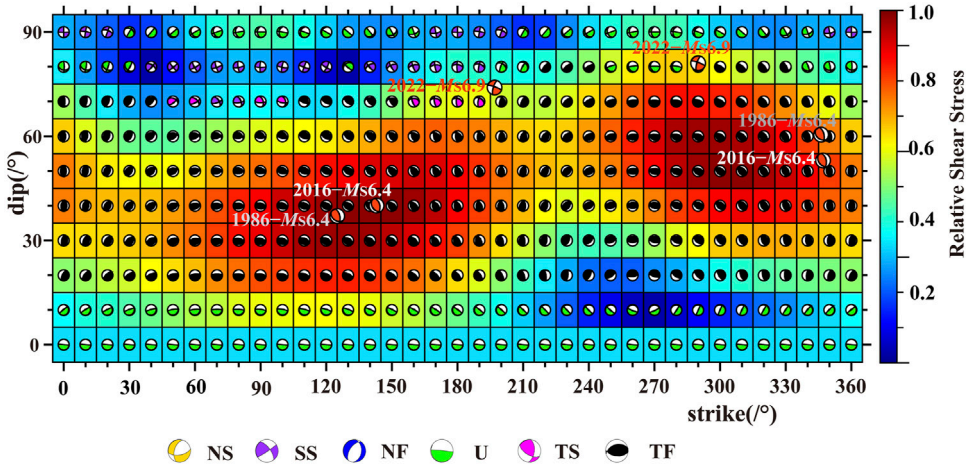

FIGURE 7
Simulated focal mechanisms and relative shear stress of the stress system in the Menyuan region. The abscissa is the strike of the focal mechanism, and the ordinate is the dip angle. NS represents the positive fault-and-strike slip type, SS represents the strike-slip type, NF represents the positive fault-and-strike slip type, TS represents the reverse fault-and-strike slip type, TF represents the reverse fault-and-strike type, and U represents uncertain focal mechanism solutions. Theoretical simulation results are compared with the source mechanism solutions of three actual source Menyuan earthquakes, with magnitudes 6 or above (using the source mechanism solution results in Figure 1). The red characters represent the *Ms* 6.9 Menyuan earthquake in 2022, white characters represent the *Ms* 6.4 Menyuan earthquake in 2016, and the gray characters represent the *Ms* 6.4 Menyuan earthquake in 1986. Grid squares represent shear stress from low (blue) to high (red).

TABLE 2 Relationship between temporal and spatial anomalies of the strain field and foreshock activity.

No.	Earthquake	Foreshock	Foreshock location (°N,°E)	Foreshock magnitude (*Ms*)	Temporal factor	Relationship between foreshock and isoline anomaly	Distance between foreshock and earthquake (km)
1	1986-8-26	1982-6-8	37.67, 102.57	4.0	T_3、T_4	Isoline anomaly edge	43
	Menyuan	1984-12-7	37.23, 102.68	4.7	T_1	Isoline anomaly cente	88
	M_s 6.4	1985-7-14	37.83, 101.82	4.1	T_2	Isoline anomaly edge	110
2	2016-1-21	2012-5-11	37.75, 102.00	4.9	T_1	Isoline anomaly edge	32
	Menyuan	2014-3-12	37.62, 102.27	3.6	T_4	Isoline anomaly edge	55
	M_s 6.4	2014-9-20	37.73, 101.53	5.0	T_2、T_3	Isoline anomaly cente	12
3	2022-1-8	2018-8-26	37.70, 102.23	3.7	T_4	Isoline anomaly edge	86
	Menyuan	2019-7-27	37.82, 100.98	3.1	T_1	Isoline anomaly edge	24
	M_s 6.9	2019-8-9	37.70, 101.58	4.9	T_1、T_3	Isoline anomaly cente	30
		2019-8-22	37.23, 101.82	3.3	T_1、T_3	Isoline anomaly cente	78

with the results shown in Figure 1. Figure 7 shows that the relative shear stress generated by the stress tensor on the 2022 Menyuan *Ms* 6.9 earthquake focal mechanism solution (Xu et al., 2022) nodal plane I (strike 290°, dip angle 81°) was 0.64, and the relative shear stress generated on nodal plane II (strike 197°, dip angle 74°) was 0.52. The relative shear stress generated by the stress tensor on the 2016 Menyuan *Ms* 6.4 earthquake focal mechanism (Yin et al., 2018) nodal plane I (strike 143°, dip angle 40°) was 0.99; whereas the relative stress generated on nodal plane II (strike 347°, dip angle 53°) was 0.83. The relative shear stress generated by the stress tensor on the 1986 *Ms* 6.4 earthquake focal mechanism [United States Geological Survey (USGS)] nodal plane I (strike 125°, dip angle 37°) was 0.98, and the relative shear stress generated on nodal plane II (strike 346°, dip angle 60°) was 0.81. These values indicated that the relative shear stress of the two Menyuan *Ms* 6.4 earthquakes in 2016 and 1986 reached a maximum (the maximum shear stress was 1), i.e., the accumulated stress was released completely, with a relatively significant effect on the environs of the earthquake focus. The relative shear stress of the 2022 Menyuan *Ms* 6.9 earthquake only exceeded the average value, and the complete release of the accumulated stress in the tectonic area had negligible effect on the environs of the earthquake focus. The strain field results

were consistent with the numerical simulation results under the tectonic stress system for the 1986 and 2016 earthquakes. The results for the 2022 earthquake were slightly different, but still within the acceptable error range.

5.2 Factors affecting strain field anomalies

We found that the main factors affecting the temporal and spatial anomalies of the seismic strain field are the occurrence of magnitude-4-5 foreshocks or clusters and the intensity and frequency of foreshock activity (Table 2). The largest foreshocks or clusters were usually located in the center of a spatial anomaly and the first time factor anomaly. The activity level of foreshocks increased significantly before the three earthquakes, which was mainly characterized by high intensity and high frequency foreshocks. In 1986 and 2016, there were several foreshocks of magnitude 4-5 in the region 4 years prior to the earthquakes. Additionally, a *M*s 4.9 earthquake cluster occurred in the region 3 years prior to the 2022 earthquake. The strongest foreshock or cluster is usually located in the center of spatial anomaly and distributed in the first time factor anomaly of the strain field.

By comparing the difference between the seismic strain field method and the seismic frequency field method (Luo et al., 2023), the method chosen to study the temporal and spatial anomaly characteristics around strong earthquakes mainly determines the level of foreshock activity around the source. If the frequency of foreshocks around the source increases significantly, and the intensity of the earthquake is magnitude 3-4, the seismic frequency field method is preferred. If the foreshock frequency around the source increases, it is mainly caused by earthquakes of magnitude 4-5, the seismic strain field method is more suitable. If the foreshock activity around the source is of high frequency and high intensity, either method may be used. Usually, a comparative study of both methods is more reliable conclusions.

5.3 Application of orthogonal function method in earthquake prediction

Many groups consider the spatiotemporal empirical orthogonal function method to be a state-of-the-art toolkit in the study of prediction, evaluation, and detection of small-scale and, short-term and long-term variation in data sets (Dawson, 2016; Chao and Liau, 2019; Neha and Pasari, 2022). Therefore, in this study, the natural orthogonal function method was used to extract the temporal and spatial anomalies of the seismic strain field, analyze the relationship between the anomalies and strong earthquakes, and predict the likelihood of an earthquake occurring. Prediction of earthquakes has always been a controversial scientific issue, but has been carried out systematically in China. In recent years, significant progress has been made in short-and medium-term prediction techniques based on seismicity (Huang et al., 2017). These are generally divided into a physical process-based model and smooth seismic activity model (Tiampo and Sihchernakov, 2012) with 7 new methods in the former and 10 in the latter. The natural orthogonal function expansion method used in this study is the 11th method of the smooth seismic activity model, and the latest development in the field of statistical seismology. It provides more spatiotemporal information for earthquake prediction than other methods.

6 Conclusion

This study investigated the spatiotemporal anomalies of the seismic strain field before and after three *M*s >6.0 earthquakes in the Menyuan region. We found that there were long- and medium-term anomalies before the earthquakes in the first four strain fields. Additionally, the more abnormal the anomalies were, the higher their predictive ability became. We found that the intersection region of strain accumulation and strain release became the potential location for strong earthquakes and the danger region gradually disappeared −3–6 months after the event. Seismic strain field results were consistent with numerical simulation results for the 1986 and 2016 earthquakes but less reliable for the 2022 earthquake.

Due to the relatively short time that the seismic catalog has been available, longer seismic observation data will be needed in the future to evaluate and revise the feasibility and effectiveness of the method used in this study.

Data availability statement

The raw data supporting the conclusion of this article will be made available by the authors, without undue reservation.

Author contributions

All authors contributed to the conception and design of this study. GL, HL, and WL prepared the material, collected the data, and performed the analysis. The first draft of the manuscript was written by GL and YX, and all authors provided their feedback. All authors contributed to the article and approved the submitted version.

Funding

This work was supported by the Ningxia Natural Science Foundation Project (2021AAC03483) and Technology Spark Plan Project (XH18052).

Acknowledgments

We are very thankful to the reviewers for their valuable revision suggestions, and especially to the responsible editors for their patient answers and help. Some of the figure were prepared using MATLAB and GMT.

Conflict of interest

The authors declare that the research was conducted in the absence of any commercial or financial relationships that could be construed as a potential conflict of interest.

Publisher's note

References

Bao, X., Zhang, R., Wang, T., Shama, A., Zhan, R., Lv, J. C., et al. (2022). The source mechanism and fault movement characterization of the 2022 *Mw* 6.7 Menyuan earthquake revealed by the joint inversion with InSAR and teleseismic observations. *Front. Environ. Sci.* 10, 917042. doi:10.3389/fenvs.2022.917042

Chang, E. T. Y., and Chao, B. F. (2011). Co-seismic surface deformation of the 2011 off the Pacific coast of Tohoku earthquake: Spatiotemporal EOF analysis of GPS data. *Earth, Planets Space*. 63, 649–654. doi:10.5047/eps.2011.07.002

Chao, B. F., and Liau, J. R. (2019). Gravity changes due to large earthquakes detected in GRACE satellite data via empirical orthogonal function analysis. *J. Geophys. Res. Solid Earth*. 124, 3024–3035. doi:10.1029/2018JB016862

Dang, G. M., Tu, D. L., Ye, J. Q., Zhang, R. B., and Jia, Y. H. (1988). Seismic damage and intensity distribution of the Menyuan earthquake *Ms* 6.4 in 1986. *Northwest. Seismol. J.* 10 (3), 5–97. (in Chinese).

Dawson, A. (2016). Eofs: A library for eof analysis of meteorological, oceanographic, and climate data. *J. Open Res. Softw.* 4, 256. doi:10.5334/jors.122

Fan, L. P., Li, B. R., Liao, S. R., Jiang, C., and Fang, L. H. (2022). Precise earthquake sequence relocation of the january 8 2022, Qinghai menyuan *ms* 6.9 earthquake. *Earthq. Sci.* 35, Q20220008. doi:10.1016/j.eqs.2022.01.021

Gai, H. L., Li, Z. M., Yao, S. H., and Li, X. (2022). Preliminary investigation and research on surface rupture characteristics of the 2022 Qinghai Menyuan *Ms* 6.9 earthquake. *Seismol. Geol. (in Chin.* 44, 238–255. doi:10.3969/j.issn.0253-4967.2022.01.015

Gaudemer, Y., Tapponnier, P., Meyer, B., Peltzer, G., Shunmin, G., Zhitai, C., et al. (1995). Partitioning of crustal slip between linked, active faults in the eastern Qilian Shan, and evidence for a major seismic gap, the 'Tianzhu gap', on the Western Haiyuan Fault, Gansu (China). *Geophys. J. Int.* 120, 599–645. doi:10.1111/j.1365-246X.1995.tb01842.x

Guo, P., Han, Z. J., An, Y. F., Jiang, W. L., Mao, Z. B., and Feng, W. (2017). Activity of the lenglongling fault system and seismotectonics of the 2016 *Ms* 6.4 Menyuan earthquake. *Chin. Sci. Earth Sci.* 60 (5), 929–942. doi:10.1007/s11430-016-9007-2

Guo, P., Han, Z., Gao, F., Zhu, C., and Gai, H. (2020). A new tectonic model for the 1927 M 8.0 Gulang earthquake on the NE Tibetan plateau. *Tectonics* 39. doi:10.1029/2020TC006064

Han, S., Wu, Z. H., Gao, Y., and Lu, H. F. (2022). Surface rupture investigation of the 2022 Menyuan *Ms* 6.9 earthquake, Qinghai, China: Implications for the fault behavior of the Lenglongling fault and regional intense earthquake risk. *J. Geomech. (in Chin.* 28, 155–168. doi:10.12090/j.issn.1006-6616.2022013

He, X. H., Zhang, Y. P., Shen, X. Z., Zheng, W. J., and Zhang, D. L. (2019). Examination of the repeatability of two *Ms* 6.4 Menyuan earthquake in Qinlian-Haiyuan fault zone (NE Tibetan Plateau) based on source parameters. *Phys. Earth Planet. Inter*. doi:10.1016/j.pepi.2019.106408

Hu, C. Z., Yang, P. X., Li, Z. M., Huang, S. T., Zhao, Y., Chen, D., et al. (2016). Seismogenic mechanism of the 21 january 2016 menyuan, Qinghai *ms* 6.4 earthquake. *Chin. J. Geophys. (in Chin.* 59 (3), 1637–1646. doi:10.6038/cjg20160509

Huang, F. Q., Li, M., Ma, Y. C., Han, Y. Y., Tian, L., Yan, W., et al. (2017). Studies on earthquake precursors in China: A review for recent 50 years. *Geod. Geodyn.* 8, 1–12. doi:10.1016/j.geog.2016.12.002

Huang, C. C., Zhang, G. H., Zhao, D. Z., Shan, X. J., Xie, C. D., Tu, H. W., et al. (2022). Rupture process of the 2022 *Mw* 6.6 Menyuan, China, earthquake from joint inversion of acceleration data and InSAR measurements. *Remte Sens.* 14, 5104. doi:10.3390/rs14205104

Jiang, W., Han, Z., Guo, P., Zhang, J., Jiao, Q., and Kang, S. (2017). Slip rate and recurrence intervals of the east Lenglongling fault constrained by morphotectonics: Tectonic implications for the northeastern Tibetan Plateau. *Lithosphere* 9 (3), 417–430. doi:10.1130/L597.1

Li, H. B., Pan, J. W., Sun, Z. M., Si, J. L., Pei, J. L., Liu, D. L., et al. (2021). Continental tectonic deformation and seismic activity: A case study the Tibetan plateau. *Acta Geol. Sin. (in Chin.* 95, 194–213. doi:10.19762/j.cnki.dizhixuebao.2021051

Li Y, Y., Jiang, W., Li, Y., Shen, W., He, Z., Li, B., et al. (2022). Coseismic rupture model and tectonic implication of the January 7 2022, Menyuan *Mw* 6.6 earthquake constraints from InSAR observations and field investigation. *Remote Sens.* 14, 2111. doi:10.3390/rs14092111

Li Z, Z. M., Gai, H. L., Li, X., Yuan, D. Y., Xie, H., Jiang, W. L., et al. (2022). Seismogenic fault and coseismic surface deformation of the Menyuan *Ms* 6.9 earthquake in Qinghai, China. *Acta Geol. Sin. (in Chin.* 96 (1), 330–335. doi:10.19762/j.cnki.dizhixuebao.2022124

Liang, S. S., Lei, J. S., Xu, Z. G., Zou, L. Y., and Liu, J. G. (2017). Relocation of the aftershock sequence and focal mechansim solutions of the 21 January 2016 Menyuan, Qinghai, *Ms* 6.4 earthquake. *Chin. J. Geophys.* 60 (6), 2091–2103. (in Chinese). doi:10.6038/cjg20170606

Liang, K., He, Z. T., Jiang, W. L., Li, Y. S., and Liu, Z. M. (2022). Surface rupture characteristics of the menyuan *ms* 6.9 earthquake on january 8, 2022, Qinghai Province. *Seismol. Geol. (in Chin.* 44, 256–278. doi:10.3969/j.issn.0253-4967.2022.01.016

Liu, J., Klinger, Y., Xu, X. W., Lasserre, C., Chen, G., Chen, W., et al. (2007). Milennial recurrence of large earthquakes on the Haiyuan fault near Songshan, Gansu Province, China. *Bull. Seismol. Soc. Am.* 97, 14–34. doi:10.1785/0120050118

Liu, Y. G., Zhang, Y., Zhang, Y. F., and Shan, X. J. (2018). Source parameters of the 2016 Menyuan earthquake in the northeastern Tibetan Plateau determined from regional seismic waveforms and InSAR measurements. *J. Asian Earth Sci.* 158, 103–111. doi:10.1016/j.jseaes.2018.02.009

Liu, M., Li, H., Peng, Z., Ouyang, L., Ma, Y., Ma, J., et al. (2019). Spatial-temporal distribution of early aftershocks following the 2016 *Ms* 6.4 Menyuan, Qinghai, China Earthquake. *Tectonophysics* 766, 469–479. doi:10.1016/j.tecto.2019.06.022

Luo, G. F., Liu, Z. W., Ding, F. H., Ma, H. Q., and Yang, M. Z. (2018). Research on the seismic strain field prior to the 2017 Jiuzhaigou, Sichuan *Ms* 7.0 earthquake. *China Earthq. Eng. J.* 40, 1322–1330. doi:10.3969/j.issn.1000-0844.2018.06.1322

Luo, G. F., Liu, Z. W., Luo, H. Z., and Ding, F. H. (2019). Effect of the strain field of Wenchuan 8 earthquake on the strong earthquake around the epicenter. *Prog. Geophys.* 34, 0908–0918. (in Chinese). doi:10.6038/pg2019CC0454

Luo, G., Ding, F., Ma, H., and Yang, M. (2023). Pre-quake frequency characteristics of *Ms* ≥7.0 earthquake in mainland China. *Front. Earth Sci.* 10, 10–992858. doi:10.3389/feart.2022.992858

Neha, and Pasari, S. (2022). A review of empirical orthogonal function (EOF) with an emphasis on the co-seismic crustal deformation analysis. *Nat. Hazards*. 110, 29–56. doi:10.1007/s11069-021-04967-4

Pan, J. W., Li, H. B., Marie-Luce, C., Liu, D. L., Li, C., Liu, F. C., et al. (2022). Coseismic surface rupture and seismic structure of the 2022 *Ms* 6.9 Menyuan earthquake, Qinghai Province,China. *Acta Geol. Sin.* 96, 215–231. doi:10.19762/j.cnki.dizhixuebao.222125

Qu, W., Liu, B., Zhang, Q., Gao, Y., Chen, H., and Wang, Q. (2021). Sentinel-1 InSAR observations of co- and post-seismic deformation mechanisms of the 2016 Mw 5.9 Menyuan Earthquake, Northwestern China. *Adv. Space Res.* 68, 1301–1317. doi:10.1016/j.asr.2021.03.016

Sun, A. H., Gao, Y., Zhao, G. F., Ren, C., and Liang, S. S. (2022). Seismic structure and *b* -value in the focal area of the 8th January 2022 Mengyuan, Qinghai *Ms* 6.9 earthquake. *Chin. J. Geophys.* 65, 1175–1183. (in Chinese). doi:10.6038/cjg2022Q0030

Tiampo, K. F., and Shcherbakov, R. (2012). Seismicity-based earthquake forecasting techniques: Ten years of progress. *Tectonophysics* 522–523, 89–121. doi:10.1016/j.tecto.2011.08.019

Wang, Q., Xiao, Z., WuLi, Y. S. Y., and Gao, Y. (2022). The deep tectonic background of the *ms* 6.9 menyuan earthquake on january 8, 2022 in Qinghai Province. *Acta Seismol. Sin.* 44, 211–222. doi:10.11939/jass.20220010

Xu, D. Z., Zhu, C. B., Meng, X. G., Li, Y., Sun, Q., and Zhang, K. (2016). Fault activity characteristics in the northern margin of the Tibetan Plateau before the Menyuan *Ms* 6.4 earthquake. *Geod. Geodyn.* 7, 261–267. doi:10.1016/j.geog.2016.07.001

Xu, Y. C., Guo, X. Y., and Feng, L. (2022). Relocation and focal mechanism solutions of the *ms* 6.9 menyuan earthquake sequence on january 8, 2022 in Qinghai Province. *Acta Seismol. Sin.* 44, 195–210. doi:10.11939/jass

Yan, Z. D., Zhang, C., and Xiao, L. Z. (1987). The sequence characteristics of Menyuan earthquake on August 26, 1986. Northwest. *Seismol. J.* 9, 89–93. (in Chinese).

Yang, M. Z., and Zhao, W. M. (2004). Statistical analysis of seismic activity energy field in Ningxia and its adjacent areas. *J. E arthritis* 26, 516–522. (in Chinese).

Yang, M. Z. M., Luo, H. Q., Xu, G. F., and Xu, X. Q. (2017). Research on the seismic strain field before strong earthquakes above *Ms* 6.0 in Chinese mainland. *Chin. J. Geophys.* 60, 3804–3814. doi:10.6038/cjg20171010

Yang, H. F., Wang, D., Guo, R., Xie, M., Zang, Y., Wang, Y., et al. (2022). Rapid report of the 8 january 2022 *Ms* 6.9 menyuan earthquake, Qinghai, China. *Earthq. Res. Adv.* 2, 1–14. doi:10.1016/j.eqrea.2022.100113

Yin, X. X., Zhao, L. L., Yang, L. M., Chen, J. F., Zuo, K. Z., and Pu, J. (2018). Research on focal mechanism and south depth of Menyuan, Qinghai *M*s 6.4 earthquake. *J. Geod. Geodyn.* 38, 624–628. (in Chinese). doi:10.14075/j.jgg.2018.06.015

Yuan, D. Y. X., Su, H., Li, R. H., Wen, Z. M., Si, Y. M., Xue, G. J., et al. (2023). Characteristics of co-seismic surface rupture zone of Menyuan *M*s 6.9 earthquake in Qinghai Province on January 8, 2022 and seismogenic mechanism. *Chin. J. Geophys. (in Chin.* 66, 229–244. doi:10.6038/cjg2022Q0093

Zhang, Y., Shan, X. J., Zhang, G. H., Zhong, M. J., Zhao, Y. J., Wen, S. Y., et al. (2020). The 2016 *M*w 5.9 menyuan earthquake in the qilian orogen, China: A potentially delayed depth-segmented rupture following from the 1986 *M*w 6.0 menyuan earthquake. *Seismol. Res. Lett.* 91, 758–769. doi:10.1785/0220190168

Zhao, L. Q., Zhan, Y., Sun, X. Y., Hao, M., Zhu, Y. Q., Chen, X. B., et al. (2019). The hidden seismic structure and dynamic environment of the 21 January Menyuan, Qinghai *M*s 6.4 earthquake derived from magnetotelluric imaging. *Chin. J. Geophys. (in Chin.* 62 (6), 2088–2100. doi:10.6038/cjg2019M0204

Zhao, L. Q., Sun, X. Y., Zhan, Y., Yang, H. B., Wang, Q. L., Hao, M., et al. (2022). The seismic model of the Menyuan *M*s 6.9 earthquake on January 8, 2022, Qinghai Province and segmented extensional characteristics of the Lenglongling fault. *Chin. J. Geophys.* 65, 1536–1546. (in Chinese). doi:10.6038/cjg2022Q0051

Zheng, W. J., Yuan, D. Y., Zhang, D. L., He, W. G., and Guo, H. (2004). Rupture property in the Gulang *M*s 8.0 earthquake, 1927 and Numerical simulation of rupture mechanism. *Earthq. Res. China* 20, 353–363. (in Chinese).

Zheng, W. J., Zhang, P. Z., He, W. G., Yuan, D. Y., Shao, Y. X., Zheng, D. W., et al. (2013). Transformation of displacement between strike-slip and crust shortening in the northern of the Tibetan Plateau; Evidence from decadent GPS measurements and late Quaternary slip rates on faults. *Tectonophysics* 584, 267–280. doi:10.1016/j.tecto.2012.01.006

Zuo, K. Z., and Chen, J. F. (2018). 3D body-wave velocity structure of crust and relocation of earthquake in the Menyuan area. *Chin. J. Geophys.* 61, 2788–2801. (in Chinese). doi:10.6038/cjg2018L0537

Zuo, K. Z., Luo, Y., ZhaoChen, C. P. J. F., and Yi, X. X. (2023). Spatiotemporal distribution characteristics of seismicity and seismogenic environment in the Menyuan area, Qinghai Province. *Chin. J. Geophys.* 66, 1460–1480. (in Chinese). doi:10.6038/cjg2022

frontiers | Frontiers in Earth Science

TYPE Original Research
PUBLISHED 07 June 2023
DOI 10.3389/feart.2023.1176921

OPEN ACCESS

EDITED BY
Frantisek Stanek,
Czech Academy of Sciences, Czechia

REVIEWED BY
Kit Chambers,
Motion Signal Technologies Limited, United Kingdom
Ge Jin,
Colorado School of Mines, United States

*CORRESPONDENCE
Jean Lecoulant,
jean.lecoulant@ucalgary.ca

RECEIVED 01 March 2023
ACCEPTED 22 May 2023
PUBLISHED 07 June 2023

CITATION
Lecoulant J, Ma Y, Dettmer J and Eaton D (2023), Strain-based forward modeling and inversion of seismic moment tensors using distributed acoustic sensing (DAS) observations. *Front. Earth Sci.* 11:1176921. doi: 10.3389/feart.2023.1176921

Strain-based forward modeling and inversion of seismic moment tensors using distributed acoustic sensing (DAS) observations

Jean Lecoulant*, Yuanyuan Ma, Jan Dettmer and David Eaton

Department of Geosciences, University of Calgary, Calgary, AB, Canada

This study used a waveform inversion of distributed acoustic sensing (DAS) data, acquired in two horizontal monitoring wells, to estimate the moment tensor (MT) of two induced microearthquakes. An analytical forward model was developed to simulate far-field tangential strain generated by an MT source in a homogeneous and anisotropic medium, averaged over the gauge length along a fiber of arbitrary orientation. To prepare the data for inversion, secondary scattered waves were removed from the field observations, using *f-k* filtering and time-windowing. The modeled and observed primary arrivals were aligned using a cut-and-paste approach. The MT parameters were inverted via a least-squares approach, and their uncertainties were determined through bootstrap analysis. Using simulated data with additive noise derived from the field data and the same fiber configuration as the monitoring wells, the inversion method adequately resolved the MT. Despite the assumption of Gaussian noise, which underlies the least-squares inversion approach, the method was robust in the presence of heavy-tailed noise observed in field data. When the inversion was applied to field data, independent inversion results using P-waves, S-waves, and both waves together yielded results that were consistent between the two events and for different wave types. The agreement of the inversion results for two events resulting from the same stress field illustrated the reliability of the method. The uncertainties of the MT parameters were small enough to make the inversion method useful for geophysical interpretation. The variance reduction obtained from the data predicted for the most probable MT was satisfying, even though the polarity of the P-waves was not always correctly reproduced.

KEYWORDS

distributed acoustic sensing, moment tensor inversion, strain, forward modeling, bootstrap analysis, uncertainties, magnitude, induced seismicity

1 Introduction

Anthropogenic earthquakes are a worldwide phenomenon associated with oil and gas production, geothermal projects, carbon capture and storage, and other industrial processes (Ellsworth, 2013; Atkinson et al., 2016). In Canada, induced earthquakes have been associated with a small fraction of hydraulic fracturing operations, including those in the Duvernay and Montney plays. In the Montney of northern British Columbia, significant numbers and magnitudes (M_w) of events have been observed, including an $M_w > 4$ earthquake sequence in 2018. The occurrence of these events has caused many challenges to regulators, operators, and residents in the area. Nonetheless, the physical processes that

lead to the activation of existing faults due to hydraulic fracturing remain poorly understood in this area. This lack of knowledge makes it difficult to implement a meaningful regulatory framework.

Distributed acoustic sensing (DAS) systems consist of optical fiber connected to an interrogator unit, which emits a laser pulse into the fiber and records Rayleigh-backscattered light on a photonic sensor (Parker et al., 2014). Changes in phase due to the fiber undergoing deformation under seismic strain make this strain measurable. Thus, DAS gives access to a different observable quantity to characterize the seismic wavefield compared to displacement or particle velocity provided by more traditional methods. It also offers an almost continuous sampling in space and time, measuring strain over kilometers with a resolution of a few meters and with a large frequency band, from ~1 Hz to ~10 kHz (Daley et al., 2013). In addition, the sensor only consists in a commercial optic fiber, making it cost-effective and easy to deploy without modifying existing boreholes and taking advantage of previous installations. All these advantages have led to a large variety of applications, including CO_2 storage surveys (Daley et al., 2013), ambient noise interferometry (Dou et al., 2017), regional seismometry (Lindsey et al., 2017), microseismics (Karrenbach et al., 2017), and induced seismicity (Lellouch et al., 2021). In the last context, DAS deployed near the injection well provides closer proximity to the source than surface geophones. The main limitation of DAS is that instead of providing a three-component measurement, as seismometers, it only measures strain coaxial to the optic fiber, which is one component.

The seismic source can be described as a dislocation propagating at a finite speed over an extended surface (e.g., Burridge and Knopoff, 1964). However, in the far field, the source can be approximated by a point whose energy is released by six force-couples following an unknown function of time. This source parametrization is known as the centroid moment tensor (CMT) and can be simplified into the moment tensor (MT) if the position and depth of the point source are assumed to be known. The inversion of the MT is a linear problem that can be solved using a linear least-squares approach in either the time or in frequency domains (Jost and Herrmann, 1989). Once the position of the source and the MT are separately inverted, they can be used as initial solutions that are perturbated together in an iterative procedure to solve the non-linear problem of the CMT inversion (Dziewonski et al., 1981). This method has been automated and is routinely used to create the Global CMT catalog (Ekström et al., 2012). The non-linear problem of CMT inversion can also be solved using Bayesian inference (Wéber, 2006; Stähler and Sigloch, 2014), which is an efficient way to obtain the uncertainty of the inverted parameters and the covariance of the data. This method has led to the development of the ISOLA software (Vackář et al., 2017), based on waveform inversion, and BEAT (Vasyura-Bathke et al., 2020), which can take advantage of seismic and geodetic data.

Although the measurement of a single component of strain (rate) rather than 3C particle velocity or displacement introduces some complications, progress has been made toward full MT inversion of DAS data. With field data from a single linear fiber, a microseismic source cannot be localized with a unique position; nevertheless, a classification based on amplitude analysis and polarity can be applied to obtain information on the nodal planes (Cole et al., 2018). Using simulated data produced by an analytical model, the resolvability of the MT for compressional waves (P-waves), shear waves (S-waves), and a variable number of non-coplanar wells has been studied (Vera Rodriguez and Wuestefeld, 2020). In simulated data produced by ray tracing, the characteristics of S-waves measured by a single fiber provide additional constraints on the position of the source, whereas the polarity reversals in P- and S-waves help constrain the fault plans (Baird et al., 2020). In data produced by a one-component sensor in a laboratory experiment, machine learning and waveform fitting MT solutions showed discrepancies mainly localized in the azimuthal direction (Vera Rodriguez and Myklebust, 2022), which cannot be resolved with only one fiber. Most of these studies focused on the information that could be extracted from a single fiber. This is probably the most widely applicable case in an industrial context, since operational constraints do not necessarily allow for multiple fibers; however, a full inversion of the MT is not achievable in this configuration.

This paper illustrated the full MT inversion of field data acquired by two DAS fibers deployed in the Montney Formation. Our method was applied to two induced seismic events that occurred within 1 h and 100 m away from each other. For the calculation of the Green functions used in the inversion, while avoiding the inaccuracies linked to the conversion of strain data into displacement data, and those associated with the spatial differentiation of simulated displacement to obtain strain, we designed an analytical forward model to predict the far-field terms of the strain generated in a homogeneous isotropic medium by an MT along a fiber of arbitrary geometry (**Section 2.1**). The field data were filtered to remove reflections and time-windowed to remove secondary arrivals (**Section 2.3**). Only the first arrivals of the P- and S-waves were kept, as they best compared with the arrivals predicted by the forward model, with very simplified assumptions. The difference in arrival times between field data and simulated data was measured using cross-correlation, and the latter was time-shifted to the arrival time of the field data. This procedure was applied to produce the Green functions for the six independent components of the MT, for the two centroid solutions for the two events of interest. With the assumption of no volume change, the least-squares solution provided the linear combination of Green functions that best approximated the field data. The uncertainties of the inverted parameters were determined through bootstrap analysis (**Section 2.4**). This method was first validated using synthetic data produced with the forward model. It is possible to resolve the MT, even if the data are polluted with the non-Gaussian noise observed in field data. The MT error increased with the decreasing signal-to-noise ratio (SNR) but remained reasonable for the SNR of the events of interest.

The inversion method was then applied to the field data. Small differences were observed between the inversion of P-waves and the inversion of S-waves, with the inversion of both P- and S-waves almost identical to the last. The three types of inversion, however, remained in relatively good agreement. The important similarity between the MT inverted for the two events of interest justified our confidence in the method. The uncertainties were small enough to encourage future geological interpretation.

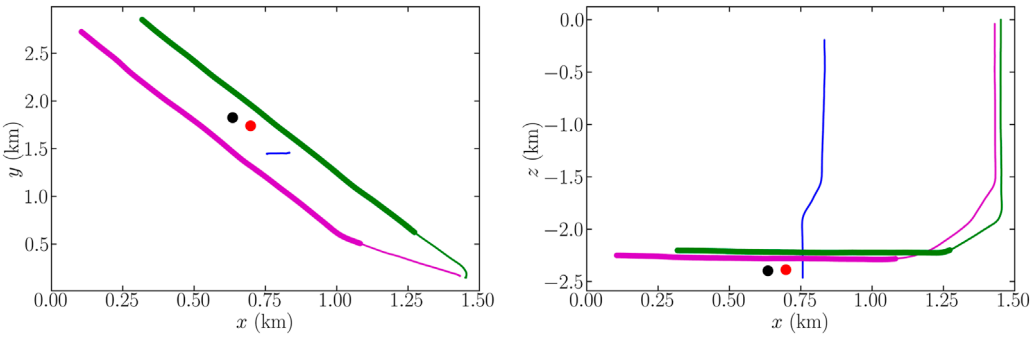

FIGURE 1
Geometry of wells H (blue), J (green), and M (cyan) and the position of the source of Events 1 (red) and 2 (black). The channels of wells H and J used in the inversion are emphasized (thick lines).

2 Materials and methods

2.1 Forward modeling of strain

The far-field terms (i.e., terms with an amplitude that decays as $1/r$) of the displacement generated along the direction i in an isotropic homogeneous medium of density ρ, P-wave velocity α, an S-wave velocity β, at a distance r from a seismic point source characterized by moment tensor $\mathbf{M}$, is given at any time t by u_j^P for P-waves and u_j^S for S-waves (Aki and Richards, 2009):

$$u_i^P = \frac{1}{4\pi\rho\alpha^3}\frac{m\gamma_i}{r}s_t(t-r/\alpha),$$
$$\text{and } u_j^S = -\frac{1}{4\pi\rho\beta^3}\frac{m\gamma_i-\gamma_i'}{r}s_t(t-r/\beta), \tag{1}$$

where s_t is the far-field source time function, γ_i is the ith component of the unit vector pointing from the source to the point where strain is measured, $m = \gamma_p M_{pq}\gamma_q$, and $\gamma_i' = \gamma_p M_{pi}$. Note that Einstein summation over p and q is applied.

Equation 1 is used to derive the far-field terms of the strain generated by a seismic source in a homogeneous medium (Eaid, 2022). The contribution of P-waves to the strain exerted over direction i by direction j is

$$\epsilon_{ij}^P = -\frac{1}{4\pi\rho}\frac{m\gamma_i\gamma_j}{\alpha^4 r}\dot{s}_t(t-r/\alpha). \tag{2}$$

Similarly, the contribution ϵ_{ij}^S for S-waves is

$$\epsilon_{ij}^S = \frac{1}{4\pi\rho}\frac{m\gamma_i\gamma_j-\Gamma_{ij}}{\beta^4 r}\dot{s}_t(t-r/\beta), \tag{3}$$

where $\Gamma_{ij} = (\gamma_i\gamma_j' + \gamma_i'\gamma_j)/2$. Once the components ϵ_{ij} of the strain tensor are obtained by summing the contributions of P- and S-waves, the tangential strain $\epsilon_{tt}(s)$ measured by DAS along a fiber at an arclength s can be derived as follows. Assuming a constant strain over the gauge length G_L (Eaid, 2022) gives

$$\begin{aligned}\epsilon_{tt}(s) = \frac{1}{G_L}\Bigg(&\epsilon_{xx}\int_{-G_L/2}^{G_L/2}T_x(u)^2\mathrm{d}u + 2\epsilon_{xy}\int_{-G_L/2}^{G_L/2}T_x\times(u)\,T_y(u)\,\mathrm{d}u\\ &+2\epsilon_{xz}\int_{-G_L/2}^{G_L/2}T_x(u)\,T_z(u)\,\mathrm{d}u + \epsilon_{yy}\int_{-G_L/2}^{G_L/2}T_y(u)^2\mathrm{d}u\\ &+2\epsilon_{yz}\int_{-G_L/2}^{G_L/2}T_y(u)\,T_z(u)\,\mathrm{d}u + \epsilon_{zz}\int_{-G_L/2}^{G_L/2}T_z(u)^2\mathrm{d}u\Bigg),\end{aligned} \tag{4}$$

where T_x, T_y, and T_z are the three components of the unit vector $\widehat{\mathbf{T}}$ tangential to the fiber. A fiber whose position is known with finite precision can be approximated by multiple linear segments. If the lengths of these segments are larger than half the gauge length, it is convenient to break the integrals in Equation (4) into two halves: one between $-G_L/2$ and 0 and one between 0 and $G_L/2$. Over these two halves, $\widehat{\mathbf{T}}$ can be considered constant, and for the strain ϵ_{tt}^i measured at the ith point along the fiber, Equation 4 simplifies to

$$\begin{aligned}\epsilon_{tt}^i = \frac{1}{2}\Big[&\left(T_{i-1,x}^2 + T_{i,x}^2\right)\epsilon_{xx} + \left(T_{i-1,y}^2 + T_{i,y}^2\right)\epsilon_{yy} + \left(T_{i-1,z}^2 + T_{i,z}^2\right)\epsilon_{zz}\Big]\\ &+\left(T_{i-1,x}T_{i-1,y} + T_{i,x}T_{i,y}\right)\epsilon_{xy} + \left(T_{i-1,x}T_{i-1,z} + T_{i,x}T_{i,z}\right)\epsilon_{xz}\\ &+\left(T_{i-1,y}T_{i-1,z} + T_{i,y}T_{i,z}\right)\epsilon_{yz},\end{aligned} \tag{5}$$

where $T_{i,x}$, $T_{i,y}$, and $T_{i,z}$ are the three components of the unit vector pointing from the ith to the $(i+1)$th point of the fiber.

To calculate the strain at the ith point of the fiber, Equations 2, 3 are applied to obtain the six components of the strain field. By means of the vector pointing from the ith to the $(i+1)$th point of the fiber and of the vector pointing from the $(i-1)$th to the ith point of the fiber, the six components of the strain field can be projected to create the tangential strain at the ith point of the fiber, according to Equation 5.

2.2 Data provenance

The DAS data considered in this study were acquired on three fibers with a 4 m gauge length and a 2000 Hz sampling frequency located in two horizontal wells (referred to as H and J) and one vertical well (referred to as M) within the Montney Formation, British Columbia, Canada. The three wells are shown in Figure 1,

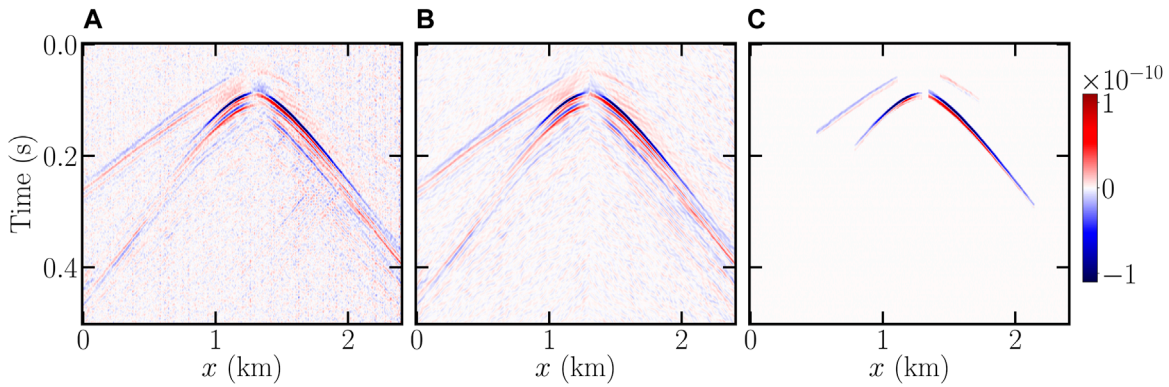

FIGURE 2
Strain measured during Event 1 along well H: pre-processed data **(A)**, data after filtering in the wavenumber–frequency domain **(B)**, and data after time-windowing and muting of channels with poor SNR **(C)**.

in addition to the location of the two events of interest, Event 1 and Event 2. These microseismic events occurred at 1 h intervals within a radius of ~100 m after stimulation in an adjacent well (not shown). The sources are located based on the DAS data, ray tracing, and grid search (Ma et al., 2023). A downhole three-component geophone array in well H, operating concurrently with the DAS acquisition system was utilized to estimate magnitudes based on the Brune model (Brune, 1970). The estimated moment magnitudes were −0.8 (Event 1) and −0.5 (Event 2). Data from the three wells were used to locate the source with an uncertainty of ±20 m, but only data from the two horizontal wells H and J were used in MT inversion. It would have been impossible to approximate the data from a vertical well with a forward model assuming a homogeneous medium.

2.3 Data processing

The simple forward model presented in **Section 2.1** can only predict strain propagating in isotropic homogeneous media. However, the Montney Formation shows numerous reflections from lithographic boundaries and fractures (Ma et al., 2022). Therefore, we applied data processing to select the direct arrivals of the P- and S-waves, enabling the quantitative comparison between observed and predicted data, which is crucial for the inversion.

After conversion from phase to strain, we removed constant bias, spikes, and system noise. Then, data were bandpass-filtered between 10 and 150 Hz. **Figure 2A** shows the strain measured for Event 1 along well H after this pre-processing. The successive arrivals of the P- and S-waves are clearly visible but are followed by secondary arrivals due to reflections from the horizontal layers of the Montney Formation (Karrenbach et al., 2017). In addition, where the primary and secondary arrivals cross fault planes, they generate reflected waves that propagate in a direction opposite to that of the direct waves, which makes them noticeable in a time–distance diagram (Ma et al., 2022; Staněk et al., 2022). To the right of the apex, the first arrivals propagated rightward and leftward to the left of the apex. Hence, it was straightforward to remove reflected waves by using filtering in the wavenumber–frequency domain to filter out waves propagating leftward on the right of the apex and rightward on the left of the apex. In this process, the position of the apex was defined manually. Noise with wavelengths <24 m was also filtered out. **Figure 2B** shows the data after filtering in the wavenumber–frequency domain. Secondary arrivals were removed by time-windowing, zero-padding the data above and below hyperbolas parallel to the direct arrivals. Finally, channels with a poor SNR, particularly around and at a large distance from the apex, were muted. **Figure 2C** shows the final data used for inversion.

To illustrate the ability of the forward model to predict useful data, we simulated the strain generated along wells H, in a medium with a density $\rho = 2{,}650\ \mathrm{kg\ m^{-3}}$, P-wave velocity $\alpha = 5.1\ \mathrm{km\ s^{-1}}$, and S-wave velocity $\beta = 3.5\ \mathrm{km\ s^{-1}}$ by a source at the location predicted for Event 1. The environmental parameters were based on observations in the Montney Formation at the depth of the wells. The source is characterized by a double-couple moment tensor

$$\mathbf{M} = \frac{1}{\sqrt{2}} \begin{pmatrix} -M_0 & 0 & 0 \\ 0 & M_0 & 0 \\ 0 & 0 & 0 \end{pmatrix}, \tag{6}$$

with $M_0 = 7.08 \times 10^7$ Nm to mimic the moment magnitude of $M_w = -0.8$ for Event 1. To match the observed data, we used the first derivative of a Gaussian as a far-field source time function

$$\dot{s}_t(t - r/c) = (t - r/c)\, \mathrm{e}^{-\pi^2 f^2 (t - r/c)^2}, \tag{7}$$

where $c = \alpha$ or β, depending on the consideration of P- or S-waves, and f is the dominant frequency of the signal. We used this source time function for the remainder of the present study. The frequency f was chosen for each event, well, and type of wave by generating simulated data for various frequencies between 75 and 115 Hz. In the frequency–wavenumber domain, the simulated data were then summed along the wavenumber axis to create an aggregated spectrum. The coefficient of determination for this aggregated spectrum and the coefficient of determination created from observed data were finally computed (**Figure 3**). The frequency

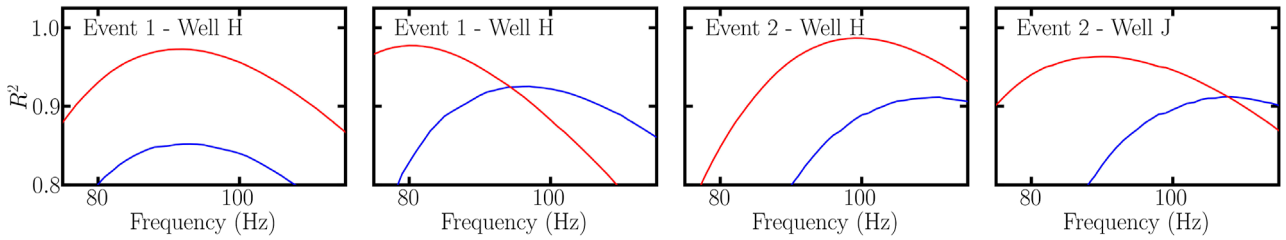

FIGURE 3
Coefficients of determination of the regression between the aggregated spectra of the observed and simulated data for various frequencies. Blue: P-waves; red: S-waves.

TABLE 1 Frequencies used to calculate the simulated data for two seismic events, two wells, and P- and S-waves.

	Well H		Well J	
	P-wave	S-wave	P-wave	S-wave
Event 1	93	92	97	80
Event 2	111	99	108	90

with the highest coefficient of determination for each event, well, and type of wave was kept as the frequency for producing simulated data thereafter (Table 1). The chosen frequencies were higher for P-waves than for S-waves, which may reflect higher inelastic attenuation on S-waves than on P-waves. For this first example, $f = 100$ Hz.

Figure 4A shows the strain simulated along well H with the forward model using the previous environmental parameters. The first obvious difference compared to the observed data (Figure 2) is the polarity of the signals. The double-couple source in equation 6 likely differs from the actual moment tensor, but only inversion can provide a better approximation. Another difference is that the strain amplitudes were up to 3.70×10^{-10} for the predicted data, but only 1.51×10^{-10} for the observed data. This result indicated that the magnitude estimated from geophone data was likely too high. Despite these differences in polarity and amplitudes, the predicted data correctly represented the direct arrivals of the P- and S-waves as two successive parabolas and their general appearance in the time–distance diagram. However, small differences remained in the arrival times, which are likely due to errors in the source position, inhomogeneity, and/or anisotropy in the medium.

These arrival-time differences can cause erroneous inversion results. To overcome this issue, we shifted the predicted traces (Figure 4A) based on the maximum cross-correlation between the absolute values of the predicted and the processed observed data, where only primary arrivals of the P- and S-waves were conserved (Figure 2A). The lags used in this procedure are shown in Figure 5 for the two events and two wells. This approach was similar to the well-known cut-and-paste method used in waveform inversion (Zhu and Helmberger, 1996). Its advantage is that it makes inversion insensitive to inaccuracies in arrival times when applying a forward model with homogeneous velocities to the multi-layered Montney Formation. Previously muted channels were also muted in the predicted data.

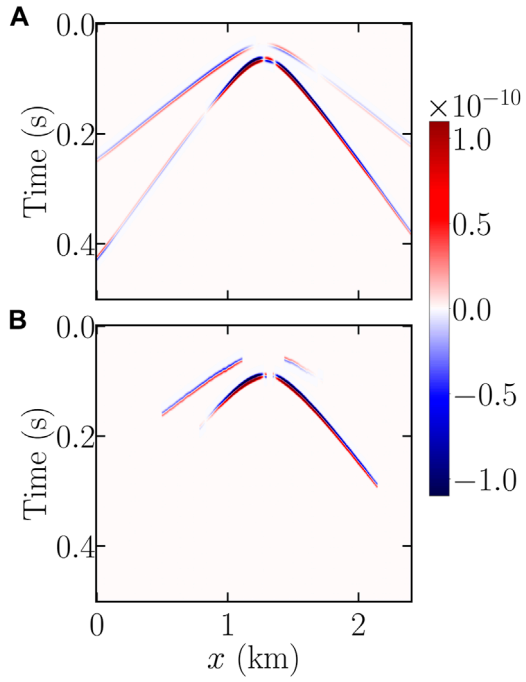

FIGURE 4
Strain along well H simulated for Event 1 using the forward model: output of the simulation **(A)** and after time-shift to match the observed arrivals **(B)**. The color scale is saturated to help visualize the P-waves.

2.4 Inversion method

Herein, we present the results for the inversion of the strain data measured along wells H and J for moment tensors of the two events. The forward model (Section 2.1) generated the six independent Green functions for the inversion. The Green functions were calculated in the same way as the predicted data in Section 2.3 with identical environmental parameters and source time function. However, the six independent components of the moment tensor were chosen instead of the moment tensor shown in Equation 6. In addition, the centroids were the two event locations. Run on one core of an AMD Ryzen 7 5800X 8-Core 4.4 GHz processor, the calculation of the six Green functions along one well required 0.37 s to complete. The Green functions were

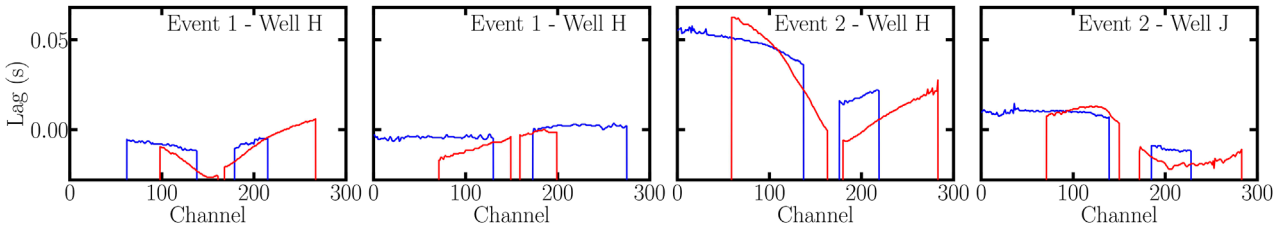

FIGURE 5
Lags between the arrivals of simulated and observed P-waves (blue) and S-waves (red).

time-shifted according to Section 2.3. Our hypothesis was that the simplified forward model presented in Section 2.1 could correctly predict the polarity and amplitude of the primary arrivals of the P- and S-waves, although it was unable to reproduce their arrival times or the complex secondary arrivals. This approach also supposed that the paths between the seismic sources and the fibers were short enough for ignoring the effects of inelastic attenuation and wave dispersion.

Once the Green functions are computed, the moment tensor can be inverted, taking the least-squares solution of the linear matrix equation $\mathbf{Am} = \mathbf{d}$, where $\mathbf{d}$ is a vector of observation data of length N, $\mathbf{A}$ is a $6 \times N$ matrix that contains the Green functions, and $\mathbf{m}$ is a vector of length 6 containing the moment tensor parameters.

To quantify parameter uncertainties, we applied the bootstrap method (Efron and Tibshirani, 1986; Tichelaar and Ruff, 1989). For this purpose, 225 of the 300 channels available after data processing were selected randomly, and the least-squares solution was computed. This process was repeated 10,000 times through a sampling scheme with replacement where each of the 300 channels had the same probability of being sampled. Taking statistical inferences from the 10,000 samples provided uncertainty estimates. Run on one core of an AMD Ryzen 7 5800X 8-Core 4.4 GHz processor, the bootstrap analysis required 150 s to complete.

We present the results in terms of the moment tensor parametrization proposed by Tape and Tape (2012). In this Lune representation, the moment tensor of unit magnitude is characterized by the five parameters of strike angle, slip angle, dip angle, latitude u that gives the amount of volume change, and longitude v that describes the mechanism on a scale from double-couple to positive or negative compensated linear vector dipole (CLVD). A pure isotropic explosion yields $u = 0$, and an absence of volume change corresponds to $u = 3\pi/8 \simeq 1.178$. The longitude v is equal to 0 for a pure double-couple, equal to $-1/3$ for a pure negative CLVD, and equal to $+1/3$ for a pure positive CLVD.

3 Results

3.1 Results for the simulated data

First, we present inversion results for noisy simulated data generated using the forward model and a known moment tensor. The noise was taken from DAS observations in the two wells during a period of relative quiescence. The observed distribution of the absolute value of the seismic noise along well H is shown in Figure 6A. It is clearly heavy-tailed, as the best fit obtained with a Gaussian distribution underestimates the probability of the largest events. A heavier-tailed distribution is the Student's t-distribution

$$f(x) = \frac{\Gamma((\nu+1)/2)}{\sqrt{\pi\nu}\,\Gamma(\nu/2)}\left(1 + (x/b)^2/\nu\right)^{-(\nu+1)/2}, \tag{8}$$

where Γ is the gamma function, ν is the number of degrees of freedom, and b is the scale parameter. We obtained a better agreement between the noise and the Student's t distribution with parameters $\nu = 6.54$ and $b = 5.1 \times 10^{-11}$ than for a Gaussian distribution. For a sample of the length used for the inversion (0.5 s long, sampled at 2000 Hz, and for 300 channels, resulting in 3×10^5 data), the Kolmogorov–Smirnov test with a threshold p-value of 0.05 failed to reject the Student's t-distribution ($p = 0.833$). The p-value started dropping below 0.05 for samples $>6 \times 10^6$ data points. For a sample of 3.6×10^7 data points (1 of data), the observed distribution appeared less heavy-tailed than the best t-Student's fit (Figure 6B). Nonetheless, the Student's t-distribution was a closer match than a Gaussian distribution.

The noise distribution was not the same along the two wells, nor was it stable over time. The latter explains why Event 1, despite causing strain one order of magnitude lower than that for Event 2, still showed a similar SNR. The best fits with a Student's t for the last 0.5 s of noise before each event occurred showed the same one order of magnitude difference in the b parameter. For Event 1, we obtained $\{\nu = 6.89, b = 3.49 \times 10^{-12}, p = 0.051\}$ along well H, and $\{\nu = 10.83, b = 4.46 \times 10^{-12}, p = 0.550\}$ along well J. For Event 2, we obtained $\{\nu = 6.45, b = 5.23 \times 10^{-11}, p = 0.542\}$ along well H, and $\{\nu = 9.88, b = 6.70 \times 10^{-11}, p = 0.881\}$ along well J. ν looked stable over time but the scale parameter b was 15 times larger before Event 2 that before Event 1, which explains the similar SNR between both events, despite the observed strain being ten times larger in Event 2 than in Event 1. This lack of stability over time can account for the difficulty in fitting a long noise sample with a Student's t.

The moment tensor used for generating the simulated data can be expressed in the Lune representation as $u = 3\pi/8$, $v = -0.2$, with a strike of 105°, a slip of 40°, a dip of 12°, and an amplitude of $M_0 = 7.08 \times 10^8$ Nm. The simulated data were contaminated with noise for various SNRs ranging from 0.1 to 10 (two orders of magnitude). The SNR was defined as the ratio of the maximum amplitude of the signal over the maximum amplitude of the noise. The noise was normalized to obtain the same SNR in the data acquired along the two wells, even if the seismic source was located at different distances from the wells.

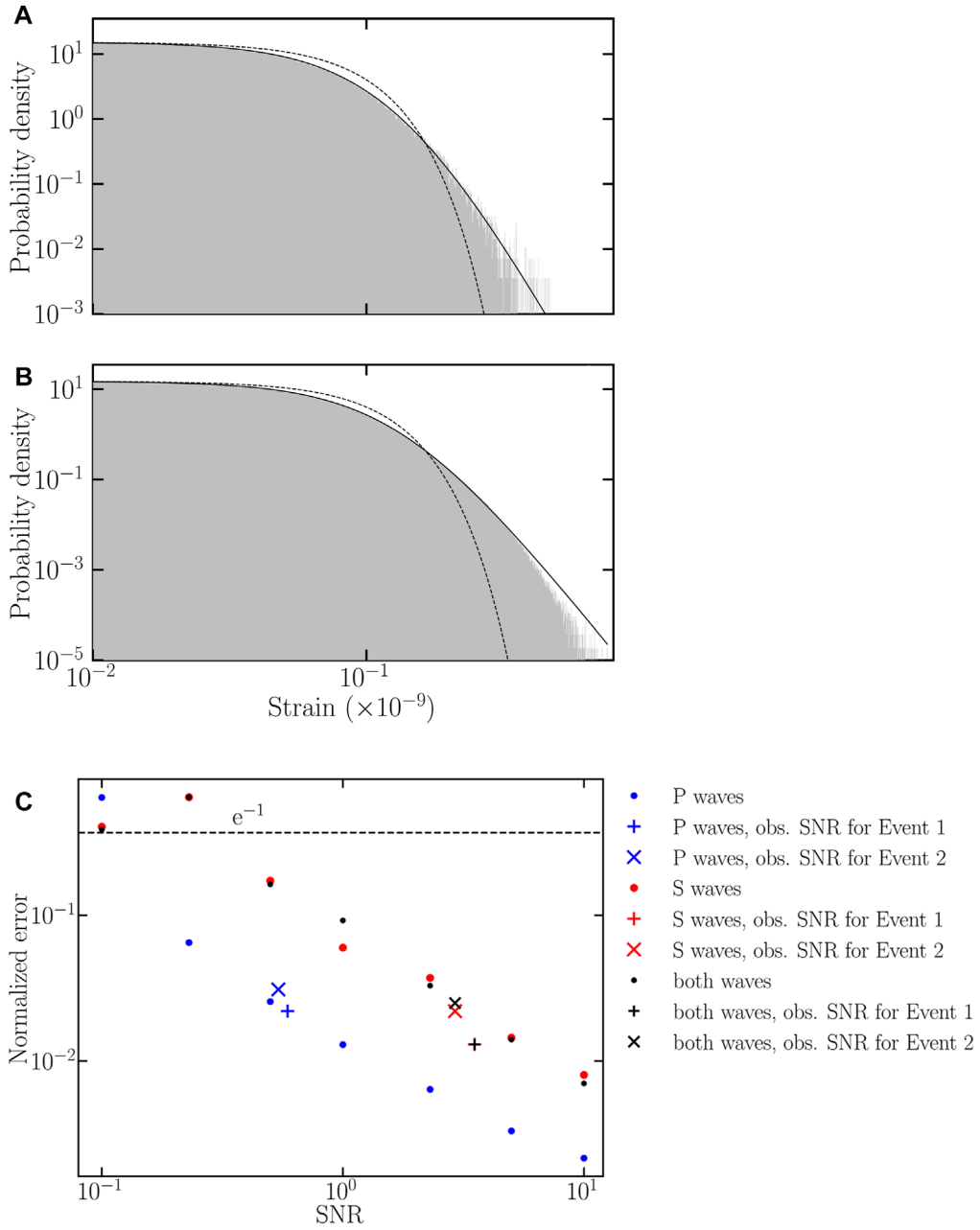

FIGURE 6
(A) Distribution of the absolute value of the seismic noise along well H for 3×10^5 data points (gray histogram) where no events were present. The best fits with a Student *t*-distribution (black) and a Gaussian distribution (black dash line) are shown. **(B)** Distribution of the seismic noise for 3.6×10^7 data points and best fits. **(C)** Normalized errors versus SNR when inverted from P-waves (blue), S-waves (red), or both P- and S-waves (black). Results with identical SNR along the two wells are shown as dots and results with the observed SNR (different along each well) are given by pluses for Event 1 and crosses for Event 2. The black dashed line is the e^{-1} threshold of the acceptable error.

Another case was considered with the SNR measured for the observed data. For Event 1, the SNR was 0.59 for the P-waves and 3.52 for the S-waves along well H, and 0.83 for the P-waves and 5.24 for the S-waves along well J. For Event 2, the SNR was 0.55 for the P-waves and 5.3 for the S-waves along well H, and 0.70 for the P-waves and 2.92 for the S-waves along well J. In a manner similar to that of Eaton and Forouhideh (2011), the inversion method was applied to the noisy simulated data, and the normalized error was computed as follows:

$$E = \frac{1}{9}\left[\sum_{i=1}^{3}\sum_{j=1}^{3}\left(\widehat{M}_{ij} - M_{ij}\right)\right]^{1/2}, \tag{9}$$

where M_{ij} are the elements of the moment tensor used for generating simulated data and $\widehat{M}_{ij}$ are the elements of the inverted moment tensor. Both moment tensors were normalized to unity to compute

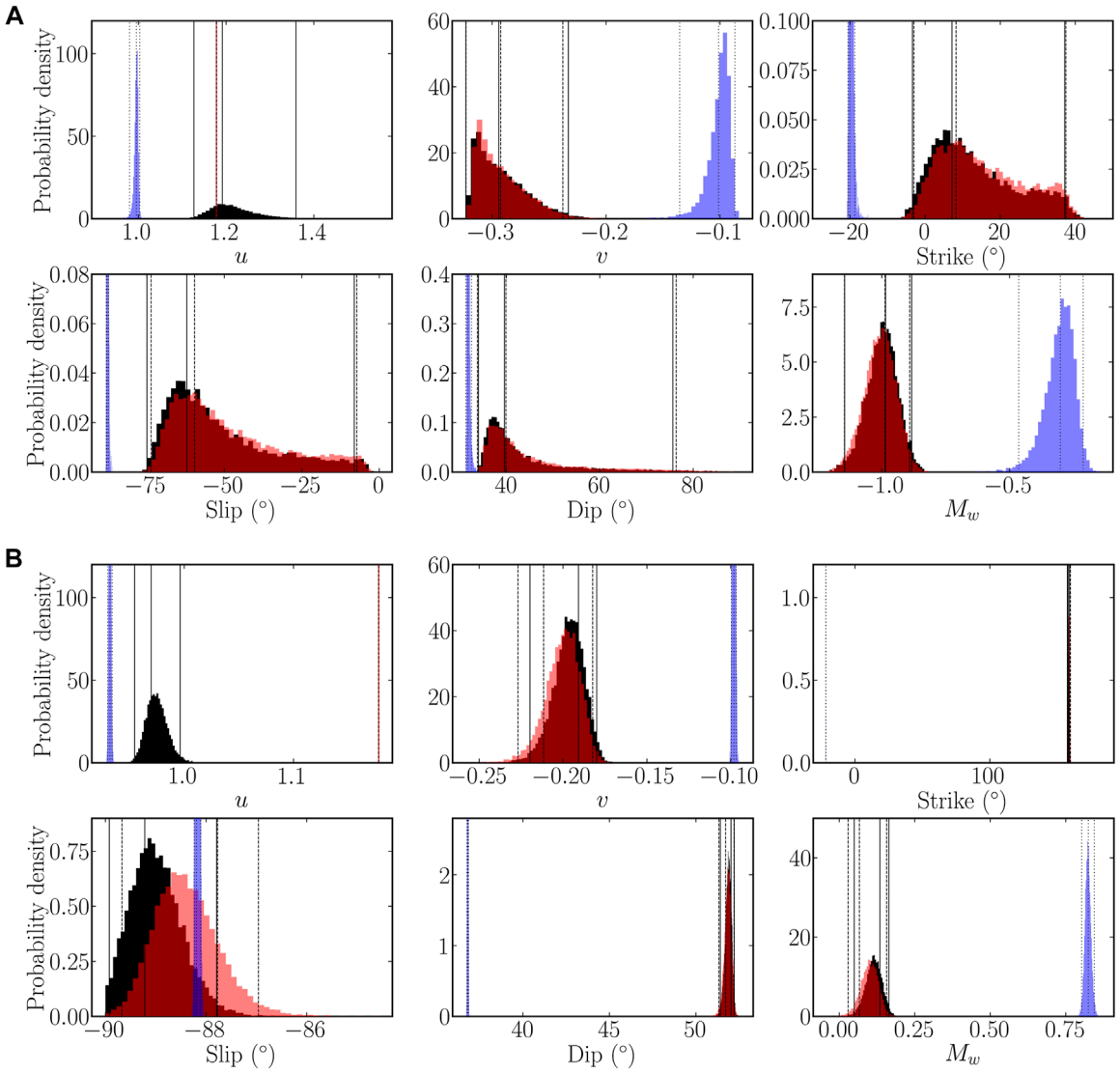

FIGURE 7
Histograms of the distributions of the source parameters for Event 1 **(A)** and Event 2 **(B)** sampled by bootstrapping and inverted using S-waves (red), P-waves (blue), and both P- and S-waves (black). From left to right, the vertical lines show the lower bound of the 95% uncertainty, the most probable value, and the upper bound of the 95% uncertainty for source parameters inverted using S-waves (dotted line), P-waves (dash line), and both P- and S-waves (solid line).

the normalized error. Consequently, the normalized error did not account for the error in the inversion of the magnitude.

Figure 6C shows the normalized errors versus SNR, when inverting using different types of waves. When the SNR was the same along both wells, and at a given SNR, inversion of the P-waves gave the smallest normalized errors. Inversion of only the S-waves and inversion of both P- and S-waves gave similar errors. The normalized errors decreased with increasing SNR, following a logarithmic trend.

The threshold of acceptable errors of e^{-1} (~0.3679) was exceeded for SNR ≤0.23 for the inversion of the S-waves and the inversion of both P- and S-waves. Similarly, for an SNR of ≤0.1 for the inversion of P-waves. When the SNR values based on observed data were used, the lower SNR for P-waves resulted in the inversions of the different types of waves not having significantly different normalized errors. For Event 1, the normalized errors were 0.022 for P-waves, 0.013 for S-waves, and 0.013 for the joint inversion of the P- and S-waves. For Event 2, the normalized errors were 0.031 for P-waves, 0.022 for S-waves, and 0.025 for the joint inversion of the P- and S-waves. In Figure 6C, these normalized errors appear consistent with the others when plotted with the SNR of the well with the lower SNR.

These results showed that in a case with no theoretical error, our method produced reliable results, even for non-Gaussian noise. This is important since the least-squares method makes assumes Gaussian-distributed noise in the data. With the SNR measured from the observed data, the inversion of the P- and S-waves appeared to be as reliable as the inversion of S-waves alone and the largest error appeared in the inversion of the P-waves.

10.3389/feart.2023.1176921

TABLE 2 Most probable values with the bounds of the 95% uncertainty of the source parameters inverted using S-waves, P-waves, and both P- and S-waves.

	P-waves	S-waves	P- and S-waves
Event 1			
u	0.996	1.178	1.19
	[+0.008, −0.016]	±0	[+0.17, −0.06]
v	−0.10	−0.29	−0.29
	[+0.01, −0.03]	[+0.06, −0.03]	[+0.03, −0.07]
Strike (°)	−20.1	8	7
	[+1.3, −0.5]	[+29, −11]	[+30, −11]
Slip (°)	−87.8	−60	−62
	[+0.5, −0.3]	[+52, −14]	[+54, −13]
Dip (°)	31.8	40	40
	[+0.8, −0.5]	[+36, −6]	[+37, −6]
M_w	−0.30	−1.0	−1.0
	[+0.09, −0.16]	[+0.1, −0.2]	[+0.1, −0.2]
Event 2			
u	0.932	1.178	0.962
	±0.002	±0	[+0.035, −0.007]
v	−0.098	−0.21	−0.19
	[+0.001, −0.002]	[+0.003, −0.002]	[+0.01, −0.03]
Strike (°)	−21.66	159.2	157.8
	[+0.07, −0.05]	[+0.6, −1.4]	[+1.3, −0.3]
Slip (°)	−88.19	−87.8	−89.3
	[+0.08, −0.05]	±1	[+1.5, −0.7]
Dip (°)	36.81	51.7	52.0
	±0.05	[+0.3, −0.4]	[+0.2, −0.6]
M_w	0.82	0.07	0.13
	±0.02	[+0.09, −0.04]	[+0.04, −0.08]

3.2 Results for the observed data from wells J and H

This section presents the inversion results for the field observations made on two wells (J and H). We carried out three types of inversions and compared the results for these cases: S-waves only, P-waves only, and the joint inversion of P- and S-waves. The uncertainty estimates for the inverted source parameters, obtained by bootstrapping are shown in **Figure 7**. **Table 2** gives the most probable values of the inverted parameters and the bounds of the 95% uncertainty interval.

The three types of inversion exhibited unimodal distributions for both events. The inversion of the u parameter using S-waves naturally gave the theoretical value for no volume change: $u = 3\pi/8 \simeq 1.178$. The inversion of this parameter using P-waves points toward a small positive isotropic component. The inversion using P- and S-waves was consistent with an absence of a volume change for Event 1 and suggested a small positive isotropic component for Event 2. The inverted explosive component was not necessarily linked to fluid injection. It can, in fact, account for the complexity of the source; for example, if the rupture propagates along a curved fault plane.

For the five other parameters, the inversion results obtained from S-waves alone were nearly identical to those for both P- and S-waves together. Both of these types of inversion point toward a large negative CLVD component for Event 1 ($v = -0.29$) and a slightly smaller one for Event 2 ($v = -0.21$ from S-waves and $v = -0.19$ from P- and S-waves). By contrast, the inversion of the P-waves appears more biased toward a smaller CLVD component, with $v \simeq 0.1$ for both events. The inversion of P-waves also exhibited smaller uncertainties for the v parameter. A CLVD component is not unexpected for an induced earthquake resulting from fluid injection (Baig and Urbancic, 2010).

For the three angle parameters, the inversion of the P-waves always yielded the smallest uncertainties. This probably occurred due to the polarity reversal visible in the P-wave data, but not in the S-wave data, which helped to resolve the nodal planes. The three inversion types gave close values for Event 1, even if the uncertainties did not overlap. The uncertainties obtained by the inversion of the S-waves or P- and S-waves were large, several tens of degrees, while the uncertainties for the inversion of P-waves were below 2°. For Event 2, a difference of 180° was observed between the strikes inverted using P-waves and S-waves or P- and S-waves, corresponding to a classical ambiguity of the employed parametrization. The inversion of the dip also gave two disjoint values, with a difference of 18°, whereas the uncertainties of the slip values given by the three inversion types overlapped. All the uncertainties were below 2°.

For both events, the inversion of P-waves yielded the largest magnitude. For Event 1, the magnitude estimate from geophone data ($M_w = -0.8$) was within the uncertainties of the magnitude derived from the S-waves or P- and S-waves ($M_w = -1.0$). For Event 2, the magnitude estimate from geophone data ($M_w = -0.5$) was well below the value inverted from S-waves ($M_w = -0.07$), P- and S-waves ($M_w = -0.13$), and P-waves ($M_w = 0.82$). The different values obtained from the different waves can reflect differences in the transmission coefficients between the layers of the Montney Formation. This effect is expected to be more noticeable for Event 2 than for Event 1, since its sources are buried deeper.

Figure 8 presents the results in terms of lower-hemisphere projections of the moment tensor, often referred to as beachballs, and using the north-west-up coordinate system. To visualize the uncertainty of the moment-tensor parameters, we use fuzzy beachballs, where the gray-scale represents the uncertainty (the probability density of the ensemble of solutions from bootstrapping in the lower-hemisphere projection). Magnitudes are ignored in **Figure 8**.

The inverted mechanisms were generally consistent between the two events and the three types of inversion. For both events, the moment tensors inversions of S-waves and of both P- and S-waves gave very similar results. Event 2 showed a difference in the greater closeness between the black areas of the fuzzy beachball for the moment tensor inverted from P- and S-waves, which illustrated its greater similarity to a double-couple. With $v = 0$, the two black

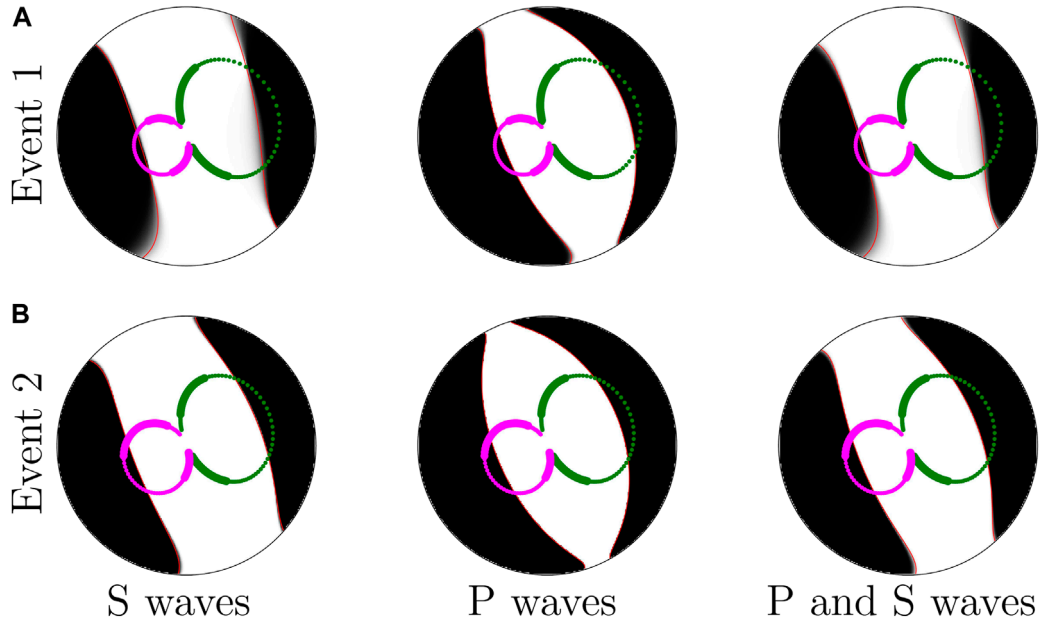

FIGURE 8
Fuzzy beachballs showing the moment tensors and their uncertainties inverted for Event 1 **(A)** and Event 2 **(B)** using, from left to right: S-waves; P-waves; both P- and S-waves. The red lines show the most probable moment tensor for each case. The scatter plot shows the projection on the beachballs of the 300 channels of well H (magenta) and well J (green) used in the inversion. Channels that are not muted in the P-wave data are magnified.

areas indeed intersected at the two poles of the beachball. The similarity between the moment tensors inverted using S-waves and both P- and S-waves was mainly due to the significantly larger amplitude of S-waves compared to P-waves in the data. Their agreement should not necessarily lead to the conclusion that their results are more reliable than the one obtained using P-waves only.

The most probable moment tensor inverted based on S-waves, P-waves, and both P- and S-waves was used to generate simulated data using a linear combination of the Green functions. The agreement of these simulated data with field data made it possible to evaluate the accuracy of our inversion method. A first qualitative assessment can be carried out by comparing the time–distance diagrams of simulated and field data (**Figure 9**). For both events, the polarity of the S-wave arrival was correctly reproduced in simulated data, with a negative strain followed by a positive strain. The polarity of the P-wave arrival was also correctly reproduced along well J. Along well H, the P-wave on the right of the apex showed a polarity reversed with respect to the left of the apex. In the simulated data, only the channels closest to the apex showed the correct positive polarity while a polarity reversal appeared further on the right. In the simulated data based on the inversion of the P-waves, a significant number of channels showed correct polarity; however, in simulated data based on the inversion of both P- and S-waves, only a few channels showed positive polarity. The amplitude of the strain measured for Event 1 along well H was correctly reproduced in simulated data; however, the simulated strain was almost twice as weak as the observed strain in all the other cases, which suggested that the magnitude of both events was undervalued.

For a quantitative evaluation of the data fit of the inversions, we used variance reduction

$$VR = 1 - \frac{(x_i - d_i)^2}{d_i^2}, \tag{10}$$

where i is the channel, x_i is the simulated strain, and d_i is the observed strain. The variance reduction takes the value 1 when the simulated and observed strains are identical. Along with this variance reduction, **Figure 10** gives the variance reduction obtained when the observed and simulated data were normalized to their maximums, which removed the effect of the amplitude of the strain for focusing on its polarity and the shape of the signal. Note that for noisy data, a variance reduction of unity implies over-fitting of the data.

In both events, the best variance reductions occurred relatively close to the apex and decreased far from the apex. This could be due to the inelastic attenuation not being considered in the forward model, especially since the decreased variance reduction was moderated when looking at normalized signals. The paths between the seismic sources were indeed shorter close to the apex. Another possible explanation is the limited azimuthal coverage of the DAS. The difficulty in reproducing the polarity of the P-waves along well H was responsible for a clear drop in the variance reduction, which did not appear when the two types of waves were taken together, due to the larger amplitude of S-waves. For Event 2, the variance reduction for S-waves dropped below 0.5 along

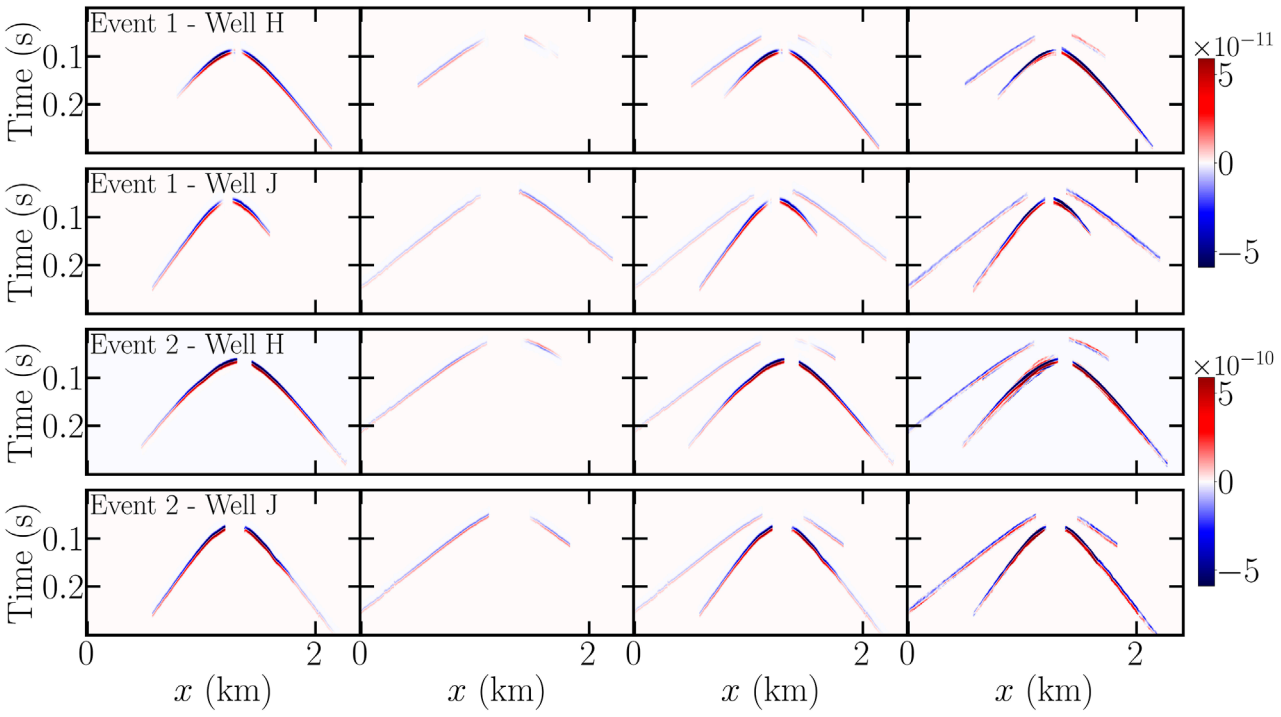

FIGURE 9
Simulated data for Event 1 (rows 1 and 2) and Event 2 (rows 3 and 4) at wells H (rows 1 and 3) and J (rows 2 and 4) based on the most probable moment tensors inverted using S-waves (column 1), P-waves (column 2), and both P- and S-waves (column 3). Field data are given for comparison (column 4). The color scale is saturated to help visualize the P-waves.

well J for channels 218 to 299 ($x \gtrsim 1.7$ km, **Figure 10A**, right), which was linked to a sudden drop in the measured strain in the observed data (**Figure 2**). This was probably a path effect, perhaps due to a region of the ground with higher inelastic attenuation. In any case, the polarity of the strain or the shape of the signal were unaffected, and the variance reduction calculated for data normalized to their maximum was, therefore, quite good (>0.5).

The difference between field data and the simulated data based on the most probable moment tensors and the signification of the variance reduction could be better understood using direct comparisons of signals (**Figure 11**). Despite the relatively good variance reductions ($VR > 0.5$) obtained on channel 191 of well H for both events, the two problems already described are made very clear: the polarity of the P-waves was not correctly reproduced when inverting from both P- and S-waves and the amplitude of the simulated data was smaller than the amplitude of the field data. Unexpectedly, for Event 1, the difference in amplitude was slightly smaller when inverted from both P- and S-waves, which probably explains the better variance reduction than when inverting from S-waves alone, despite the incorrect polarity predicted for the P-waves.

4 Discussion

The inversion of geophysical data relies on fast and accurate forward modeling, used for generating the predicted data that are compared to observed data. In this study, we choose a forward model able to simulate strain, which avoids the sources of uncertainty linked to the conversion of the observed strain data into displacement data. We did not retain the possibility of employing a state-of-the-art forward model written for predicting displacement before applying spatial differentiation to approximate the strain, which may introduce artifacts in the simulated data. Therefore, the strain was obtained by analytically calculating the far-field components of the strain in a homogeneous and anisotropic medium before projecting those components on the fiber of interest and averaging the tangential strain on the gauge length of the DAS sensor.

The field data acquired in the Montney Formation showed secondary arrivals and numerous reflections from lithographic boundaries and fractures and must be prepared for inversion. The reflections were removed using *f-k* filtering, and only the primary arrivals were kept using time-windowing. The channels with too low an SNR were muted. The simulated data were shifted to the arrival times of the observed primary arrivals, using cross-correlation of both signals at each channel, in an approach similar to the cut-and-paste method. The method was made insensitive to the inaccuracies in the prediction of the arrival times. However, our inversion method expected that the polarity and amplitude of the first arrivals of the P- and S-waves were correctly predicted by the forward model. Thus, we supposed that the amplitude was mainly affected by geometrical attenuation. Indeed, our method does not account for inelastic attenuation or the effects of heterogeneities, such as layers with different velocities and transmission coefficients in the Montney Formation. For the two events of interest, the short

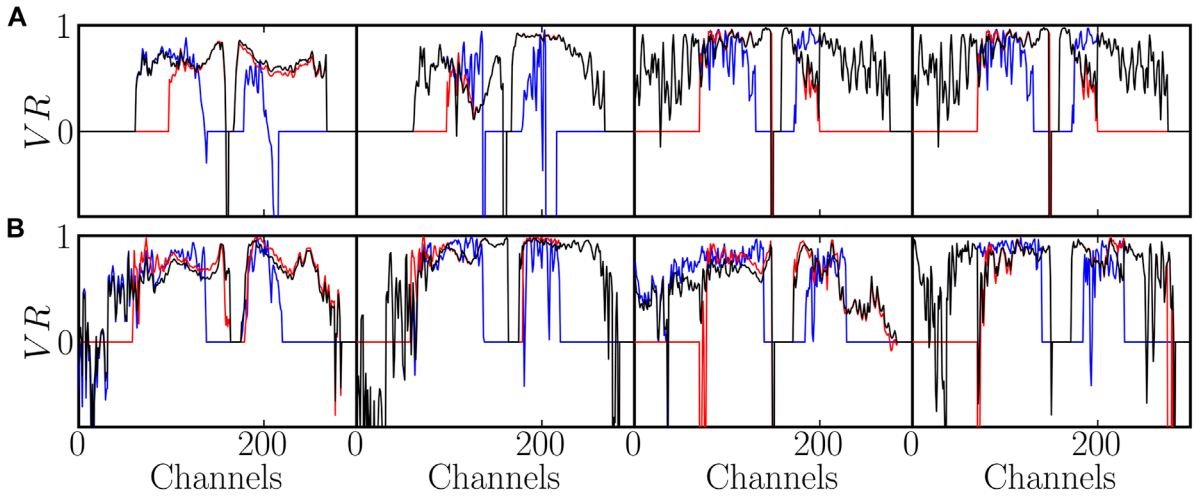

FIGURE 10
Variance reduction for Event 1 **(A)** and Event 2 **(B)** with the simulated data (columns 1 and 3) and normalized simulated data (columns 2 and 4) at well H (columns 1 and 2) and well J (columns 3 and 4), based on the most probable moment tensors inverted using S-waves (red), P-waves (blue), and both P- and S-waves (black). The value *VR* =0 is arbitrarily assigned to channels with no data.

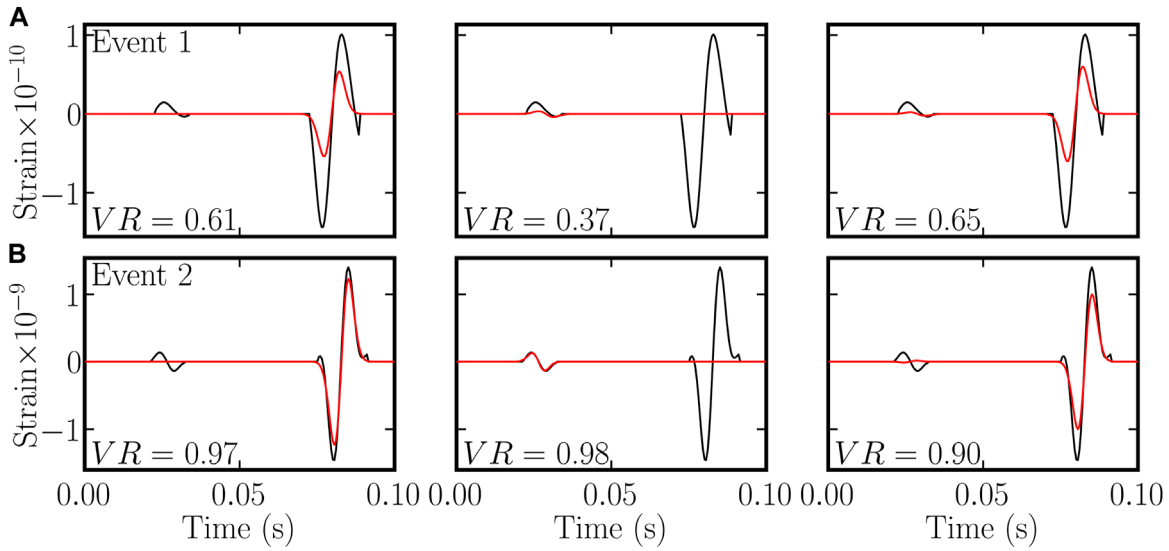

FIGURE 11
Field (black) and simulated (red) data from channel 191 of well H for Event 1 **(A)** and Event 2 **(B)**. Simulated data are based on the most probable moment tensors inverted using S-waves (left), P-waves (center), and both P- and S-waves (right).

distances between the sources and the fibers (180 m for Event 1 and 210 m for Event 2) made these assumptions reasonable.

The linear problem of MT inversion (six dimensions) was solved with the least-squares method, using the processed data and the Green functions calculated by the forward model and time-shifted to the arrival times of the field data. However, the least-squares inversion relied on the assumption of Gaussian noise, and the observed noise was better approximated by a heavy-tailed Student's *t* distribution. The uncertainties in the inverted parameters were provided by bootstrap analysis. We checked the robustness of our inversion method under heavy-tailed noise by applying it to data predicted by the forward model and polluted with different levels of real noise. Measured by normalized errors, the performances of the inversion method for this case without theoretical error appeared satisfying with the SNR found in real data.

The inversion method was applied to field data from two seismic events that occurred within 1 h with sources located approximately 100 m from each other. Magnitude aside, the inversion results were consistent between the two events for a given type of wave, which was expected since they both resulted from the same stress field. For a given event, the inversion results were consistent between the three types of inversion: using P-waves alone, S-waves alone, and both P- and S-waves together. The uncertainties

in the inverted parameters were small enough to make possible future geological interpretations. The accuracy of the inversion method was evaluated by comparing the observed data to the data predicted for the most probable MT. The polarity of the S-waves was correctly reproduced for both fibers and both events; however, a polarity change in the P-waves along well H did not appear in predicted data for the joint inversion of the P- and S-waves. Thus, our assumption of no path effect on the polarity may be incorrect for P-waves. The evaluation can be refined using variance reduction. This shows the possible effect of inelastic attenuation on the amplitude of the measured strain. Comparisons of the observed and predicted signals for a single location highlighted a possible underestimation of the magnitudes for both events.

This paper provides encouraging results supporting a new method for inverting MT from DAS data. However, this method should be validated by comparison to a state-of-the-art inversion method, for example, in a dataset where both DAS data and abundant seismometer data are available. Then, the inversion method must be systematized and applied to a large number of events to improve our understanding of the local geology and fault activation under hydraulic fracturing in the Montney Formation. The forward model must be improved to reduce the theoretical errors that arise from simplifying assumptions. While keeping the hypothesis of a homogeneous and isotropic medium, the terms of the intermediate and near field could easily be considered, which is expected to improve the resolvability of the MT in events where the source is close enough to the wells (e.g.,Vera Rodriguez and Wuestefeld, 2020). The resolvability of the moment tensor using strain-simulated and field data was studied by Luo et al. (2021). It would be crucial to work with a forward model able to consider more complex environments, such as layered or anisotropic mediums. Finally, the inversion procedure itself should be improved to invert for source location, source time function, or more complex parametrizations of the source, which would force the use of non-linear methods.

Data availability statement

The data analyzed in this study is subjected to the following licenses/restrictions: the data are proprietary. Requests to access these datasets should be directed to jean.lecoulant@ucalgary.ca.

Author contributions

JL contributed to developing the inversion method, performing the DAS data analysis, and drafting the paper. YM contributed to processing the raw data, as well as localizing and selecting the seismic events of interest. JD contributed to the elaboration of the moment tensor inversion and critical revision of the paper. DE contributed to the results interpretation and critical revision of the paper. All authors contributed to the article and approved the submitted version.

Funding

JL thanks the Natural Sciences and Engineering Research Council of Canada (NSERC) for the financial support (Grant No. ALLRP\548576-2019) through the Alliance program.

Acknowledgments

The authors are grateful to ConocoPhillips Canada for permission to publish the DAS examples. The authors thank Mahdi Hamidbeygi and Pejman Shahsavari for useful discussions about the observed noise distribution.

Conflict of interest

The authors declare that the research was conducted in the absence of any commercial or financial relationships that could be construed as a potential conflict of interest.

Publisher's note

References

Aki, K., and Richards, P. G. (2009). "*Quantitative seismology* (mill valley, calif: Univ. Science books," in *corr*, 2. print edn.

Atkinson, G. M., Eaton, D. W., Ghofrani, H., Walker, D., Cheadle, B., Schultz, R., et al. (2016). Hydraulic fracturing and seismicity in the western Canada sedimentary basin. *Seismol. Res. Lett.* 87, 631–647. doi:10.1785/0220150263

Baig, A., and Urbancic, T. (2010). Microseismic moment tensors: A path to understanding frac growth. *Lead. Edge* 29, 320–324. doi:10.1190/1.3353729

Baird, A. F., Stork, A. L., Horne, S. A., Naldrett, G., Kendall, J.-M., Wookey, J., et al. (2020). Characteristics of microseismic data recorded by distributed acoustic sensing systems in anisotropic media. *GEOPHYSICS* 85, KS139–KS147. doi:10.1190/geo2019-0776.1

Brune, J. N. (1970). Tectonic stress and the spectra of seismic shear waves from earthquakes. *J. Geophys. Res.* 75, 4997–5009. doi:10.1029/JB075i026p04997

Burridge, R., and Knopoff, L. (1964). Body force equivalents for seismic dislocations. *Bull. Seismol. Soc. Am.* 54, 1875–1888. doi:10.1785/BSSA05406A1875

Cole, S., Karrenbach, M., Kahn, D., Rich, J., Silver, K., and Langton, D. (2018). "Source parameter estimation from DAS microseismic data," in *SEG technical program expanded abstracts 2018* (Anaheim, California: Society of Exploration Geophysicists), 4928–4932. doi:10.1190/segam2018-2995716.1

Daley, T. M., Freifeld, B. M., Ajo-Franklin, J., Dou, S., Pevzner, R., Shulakova, V., et al. (2013). Field testing of fiber-optic distributed acoustic sensing (DAS) for subsurface seismic monitoring. *Lead. Edge* 32, 699–706. doi:10.1190/tle32060699.1

Dou, S., Lindsey, N., Wagner, A. M., Daley, T. M., Freifeld, B., Robertson, M., et al. (2017). Distributed acoustic sensing for seismic monitoring of the near surface: A traffic-noise interferometry case study. *Sci. Rep.* 7, 11620. doi:10.1038/s41598-017-11986-4

Dziewonski, A. M., Chou, T.-A., and Woodhouse, J. H. (1981). Determination of earthquake source parameters from waveform data for studies of global and regional seismicity. *J. Geophys. Res. Solid Earth* 86, 2825–2852. doi:10.1029/JB086iB04p02825

Eaid, M. (2022). *Distributed acoustic sensing: Modelling, full waveform inversion, and its use in seismic monitoring*. Calgary, AB: Ph.D. thesis, University of Calgary. doi:10.11575/PRISM/39485

Eaton, D. W., and Forouhideh, F. (2011). Solid angles and the impact of receiver-array geometry on microseismic moment-tensor inversion. *GEOPHYSICS* 76, WC77–WC85. doi:10.1190/geo2011-0077.1

Efron, B., and Tibshirani, R. (1986). Bootstrap methods for standard errors, confidence intervals, and other measures of statistical accuracy. *Stat. Sci.* 1, 54–75. Publisher: Institute of Mathematical Statistics.

Ekström, G., Nettles, M., and Dziewoński, A. (2012). The global CMT project 2004–2010: Centroid-moment tensors for 13,017 earthquakes. *Phys. Earth Planet. Interiors* 200-201, 1–9. doi:10.1016/j.pepi.2012.04.002

Ellsworth, W. L. (2013). Injection-induced earthquakes. *Science* 341, 1225942. doi:10.1126/science.1225942

Jost, M. L., and Herrmann, R. B. (1989). A student's guide to and review of moment tensors. *Seismol. Res. Lett.* 60, 37–57. doi:10.1785/gssrl.60.2.37

Karrenbach, M., Kahn, D., Cole, S., Ridge, A., Boone, K., Rich, J., et al. (2017). Hydraulic-fracturing-induced strain and microseismic using *in situ* distributed fiber-optic sensing. *Lead. Edge* 36, 837–844. doi:10.1190/tle36100837.1

Lellouch, A., Schultz, R., Lindsey, N., Biondi, B., and Ellsworth, W. (2021). Low-magnitude seismicity with a downhole distributed acoustic sensing array—examples from the FORGE geothermal experiment. *J. Geophys. Res. Solid Earth* 126. doi:10.1029/2020JB020462

Lindsey, N. J., Martin, E. R., Dreger, D. S., Freifeld, B., Cole, S., James, S. R., et al. (2017). Fiber-optic network observations of earthquake wavefields. *Geophys. Res. Lett.* 44. doi:10.1002/2017GL075722

Luo, B., Jin, G., and Stanek, F. (2021). Near-field strain in distributed acoustic sensing-based microseismic observation. *GEOPHYSICS* 86, P49–P60. doi:10.1190/geo2021-0031.1

Ma, Y., Eaton, D., Igonin, N., and Wang, C. (2023). Machine learning-assisted processing workflow for multi-fiber DAS microseismic data. *Front. Earth Sci.* 11, 1096212. doi:10.3389/feart.2023.1096212

Ma, Y., Eaton, D. W., and Wang, C. (2022). "Fracture imaging using DAS-recorded microseismic reflections," in *Second international meeting for applied geoscience and energy* (Houston, Texas: Society of Exploration Geophysicists and American Association of Petroleum Geologists), 587–591. doi:10.1190/image2022-3745381.1

Parker, T., Shatalin, S., and Farhadiroushan, M. (2014). Distributed Acoustic Sensing – a new tool for seismic applications. *First Break* 32. doi:10.3997/1365-2397.2013034

Stähler, S. C., and Sigloch, K. (2014). Fully probabilistic seismic source inversion – Part 1: Efficient parameterisation. *Solid earth.* 5, 1055–1069. doi:10.5194/se-5-1055-2014

Staněk, F., Jin, G., and Simmons, J. (2022). Fracture imaging using DAS-recorded microseismic events. *Front. Earth Sci.* 10, 907749. doi:10.3389/feart.2022.907749

Tape, W., and Tape, C. (2012). A geometric setting for moment tensors: A geometric setting for moment tensors. *Geophys. J. Int.* 190, 476–498. doi:10.1111/j.1365-246X.2012.05491.x

Tichelaar, B. W., and Ruff, L. J. (1989). How good are our best models? Jackknifing, bootstrapping, and earthquake depth. *Eos, Trans. Am. Geophys. Union* 70, 593. doi:10.1029/89EO00156

Vackář, J., Burjánek, J., Gallovič, F., Zahradník, J., and Clinton, J. (2017). Bayesian ISOLA: New tool for automated centroid moment tensor inversion. *Geophys. J. Int.* 210, 693–705. doi:10.1093/gji/ggx158

Vasyura-Bathke, H., Dettmer, J., Steinberg, A., Heimann, S., Isken, M. P., Zielke, O., et al. (2020). The bayesian earthquake analysis tool. *Seismol. Res. Lett.* 91, 1003–1018. doi:10.1785/0220190075

Vera Rodriguez, I., and Myklebust, E. B. (2022). Deep compressed seismic learning for fast location and moment tensor inferences with natural and induced seismicity. *Sci. Rep.* 12, 15230. doi:10.1038/s41598-022-19421-z

Vera Rodriguez, I., and Wuestefeld, A. (2020). Strain microseismics: Radiation patterns, synthetics, and moment tensor resolvability with distributed acoustic sensing in isotropic media. *GEOPHYSICS* 85, KS101–KS114. doi:10.1190/geo2019-0373.1

Wéber, Z. (2006). Probabilistic local waveform inversion for moment tensor and hypocentral location. *Geophys. J. Int.* 165, 607–621. doi:10.1111/j.1365-246X.2006.02934.x

Zhu, L., and Helmberger, D. V. (1996). Advancement in source estimation techniques using broadband regional seismograms. *Bull. Seismol. Soc. Am.* 86, 1634–1641. doi:10.1785/BSSA0860051634

Frontiers in Earth Science

Investigates the processes operating within the major spheres of our planet

Advances our understanding across the earth sciences, providing a theoretical background for better use of our planet's resources and equipping us to face major environmental challenges.

Discover the latest Research Topics

See more →

Frontiers

Avenue du Tribunal-Fédéral 34
1005 Lausanne, Switzerland
frontiersin.org

Contact us

+41 (0)21 510 17 00
frontiersin.org/about/contact